THE INFLUENCE OF NON-METALLIC INCLUSIONS UPON THE PROPERTIES OF LINEPIPE STEELS

DARYL PAUL HILL

DOCTOR OF PHILOSOPHY

THE UNIVERSITY OF ASTON IN BIRMINGHAM

October 1986

SYNOPSIS

The University of Aston in Birmingham

The Influence of Non-metallic Inclusions upon the Properties of Linepipe Steels

Daryl Paul Hill Doctor of Philosophy October 1986

The principal aim of this work was to determine the role of non-metallic inclusions in the process of hydrogen stepwise cracking(SWC). Additionally, the influence of inclusions upon the notch ductility of hydrogen charged (HC) and uncharged (UN) tensile specimens was examined.

To obtain a basis for experiment a series of low carbon-manganese steels were prepared by induction melting.In order to produce variations in the composition, morphology, volume fraction, size and distribution of the inclusions the steel chemistry was adjusted prior to casting by additions of deoxidiser and Ca-Si injection. Sections of each ingot were hot rolled . Metallography, image analysis, mechanical tests and hydrogen SWC tests were then carried out .

The volume fraction, morphology, and shape of inclusions influenced the tensile ductility of the steels. Marked anisotropy was found in the steels containing type II MnS inclusions at all rolling temperatures, whereas, the fully Ca treated steel was isotropic. It was found that several inclusion parameters (projected length P_L, mean free distance MFD, nearest-neighbour distance NND) correlated with fracture strain. An increase in inclusion volume fraction and/or the dimension of inclusions on a plane parallel to the plane of fracture lead to a decrease in fracture strain.

The inclusion parameters did not correlate with the fracture strains for the HC tensile specimens, however, large or clusters of inclusions acted as the principal sites for crack initiation. "Fisheyes" or areas of "flat" fracture were often found on these fracture surfaces.

The criteria for SWC initiation was found to be either large inclusions or clusters of inclusions. As the P_L of inclusions increased the probability of large SWCs occurring increased. SWC initiation at inclusions was believed to occur at a critical concentration of hydrogen . Factors which assisted the concentration of hydrogen at inclusions were discussed. None of the proposed mechanisms of hydrogen embrittlement could be identified as the single cause of SWC.

Non-metallic inclusions,calcium silicide injection, image analysis, stepwise cracking, hydrogen embrittlement

ACKNOWLEDGEMENTS

Various circumstances have made the completion of this work somewhat of a marathon, and in order to get to this final stage I would like to thank many of the technical staff (past and present) within what was once the Department of Metallurgy and Materials (now Production and Mechanical Engineering) at Aston University, for their assistance and encouragement under often very difficult circumstances.

In particular I would like to thank my supervisor Dr J C Billington for his encouragement and patience over this period of time and Dr A Nadkarni for many useful discussions.

Not least of all I would like to thank the numerous secretaries in different parts of the country who have been patient enough to put up with the many changes I have made to the text.

CONTENTS

		Page
1.0	SECTION 1 - INTRODUCTION	1
1.1	Aims	6
2.0	SECTION 2 - LITERATURE REVIEW	7
2.1	The control of inclusions in steel. Introduction	7
2.1.0	Oxide and sulphide inclusions - basic observations	7
2.1.1	The thermodynamics of oxides and sulphides	13
2.1.2	Kinetics : The formation and separation of inclusions in steel	24
2.1.2.0	Melt additions	28
2.1.2.1	Nucleation of inclusions	31
2.1.2.2	Inclusion growth	33
2.1.2.3	The separation of inclusions	37
2.1.3.0	Inclusion shape control	43
2.2	Hydrogen induced stepwise cracking in linepipe steels. Introduction	52
2.2.1	Stepwise cracking in linepipe - field failures	52
2.2.1.1	Stepwise cracking - definition and appearance	53
2.2.1.2	Environmental conditions	57
2.2.1.3	Compositional and microstructural effects	60
2.2.2.0	Mechanisms of stepwise cracking. Introduction	67
2.2.2.1	The process of stepwise cracking	68
2.2.2.2	Metallography and fractography of cracking	70

		Page
2.2.2.3	Mechanisms of hydrogen embrittlement	73
2.2.2.4.0	Fracture and hydrogen embrittlement(HE)	79
2.2.2.4	Ductile fracture	84
2.2.3	The effect of non-metallic inclusions upon stepwise cracking. Introduction	92
2.2.3.1	Inclusion morphology and composition	92
2.2.3.2	Inclusion volume fraction	96
2.2.2.4	Size, shape and distribution of inclusions	103
3.0	SECTION 3 - EXPERIMENTAL PROCEDURE	111
3.1	Material preparation	111
3.1.0	Experimental melts	111
3.1.1	Melting procedure	113
3.1.2	Deoxidation and alloy additions	115
3.1.3	Calcium silicide injection	117
3.1.4	Casting	119
3.1.5	Ingot sectioning and identification	119
3.1.6	Hot rolling	120
3.1.7	Sectioning of the rolled plate	122
3.2	Material testing	124
3.2.0	Hydrogen sulphide exposure testing	124
3.2.1	Test solution	124
3.2.2	Test procedure	125
3.2.3	Stepwise cracking tests	125
3.2.3.0	Specimen preparation	125
3.2.3.1	Specimen examination	126
3.2.3.1.0	Surface blisters	126
3.2.3.1.1	Analysis of stepwise cracking	126

		Page
3.2.4	Further stepwise cracking tests	128
3.2.5	Hydrogen analysis	128
3.2.6	Notched tensile tests	129
3.2.6.0	Hydrogen charged notched tensiles	130
3.2.6.1	Testing procedure	131
3.2.6.2	Stress and strain measurements	132
3.2.7	Hardness testing	132
3.3	Chemical analysis	134
3.4	Metallography and fractography	134
3.4.0	General metallographic preparation	134
3.4.1	Ingot structure	134
3.4.2.0	Image analysis	135
3.4.2.1	Specimen preparation for inclusion analysis	135
3.4.2.2.0	Inclusion analysis	136
3.4.2.2.1	As cast ingot	136
3.4.2.2.2	Rolled plate	136
3.4.2.3	Microstructural analysis	137
3.4.3	Notched tensile specimens	137
3.4.4.0	Scanning electron microscopy	138
3.4.4.1	In-situ inclusion analysis	138
3.4.4.2	Microscopy and fractography	139
4.0	SECTION 4 - EXPERIMENTAL RESULTS	142
4.1	Chemical analysis	142
4.1.0	Ingot	142
4.1.1	Rolled plate	142
4.2	Ingot analysis	144
4.2.0	Macrostructure and sulphur print	144

		Page
4.2.1	Metallographic examination	144
4.2.2	Inclusion size analysis	147
4.2.3	Inclusion composition	149
4.3	Rolled plate	153
4.3.0	Metallography	153
4.3.0.0	Microstructural observations	153
4.3.0.1	Quantitative metallography	162
4.3.1.0	Inclusions	162
4.3.1.1	Metallographic observation	162
4.3.1.2	Inclusion relative plasticity	168
4.3.2.0	Quantitative analysis of inclusions	171
4.3.2.1	Data from image analysis	171
4.3.2.2	Inclusion parameters	173
4.3.2.3	Statistical analysis of inclusion parameters	174
4.3.2.4	Computer applications	184
4.4	Mechanical tests	187
4.4.0	Hounsfield tensile tests	187
4.4.1	Notched tensile tests	195
4.4.2	Fractography and metallography	202
4.4.3	Quantitative analysis	223
4.4.4	Vickers hardness	232
4.5.0	Stepwise cracking tests	232
4.5.1	Surface blisters	236
4.5.2	Metallography and fractography	236

		Page
5.0	SECTION 5 - DISCUSSION OF RESULTS	253
5.1	Introduction	253
5.2	Production of cast ingots	254
5.2.0	Factors affecting melting and inclusion control	254
5.2.1	Melt out	254
5.2.2	Deoxidation and removal of primary inclusions	255
5.2.3	Calcium silicide injection	259
5.2.4	Steel compositions	262
5.3	Inclusions in the as cast steels	264
5.3.0	Size distribution	264
5.3.1	Inclusion composition and morphology	268
5.4	Statistics, image analysis and inclusion parameters in the rolled steel	269
5.5	Deformation of inclusion during hot rolling	272
5.6	Inclusions, anisotropy and tensile ductility	277
5.7	The influence of hydrogen upon tensile ductility and anisotropy (notched specimens)	285
5.8	The role of inclusions in hydrogen step-wise cracking	292
5.9	Stepwise cracking in linepipe steels - implications	307
6.0	SECTION 6 - CONCLUSIONS	312
7.0	SECTION 7 - SUGGESTIONS FOR FURTHER WORK	319
	APPENDICES	321
	REFERENCES	375

LIST OF FIGURES

		Page
Figs.1 to 57	Literature review	2 to 109
Fig.58	Furnace layout, refractories and argon supply	112
Fig.59	Calcium silicide injection apparatus	118
Fig.60	Sectioning of the cast ingot	121
Fig.61	Sectioning of the rolled plate	123
Fig.62	Hydrogen sulphide test cell	118
Fig.63A	Sectioning of SWC coupons	127
Fig.63B	Measurement of SWC	127
Fig.63C	Small size SWC specimens	127
Fig.64	Design of notched tensile specimen	133
Fig.65	Specimen orientation and sampling scheme for image analysis	133
Fig.66	Cross sectioning of tensile specimen	140
Fig.67	Examination of fracture surfaces by SEM	140
Figs.68 to 71	Inclusion size distribution	150 to 151
Fig.72	Log-normal probability graph of the inclusion size distribution for the mid-sections of the as cast ingots	152
Fig.73	Increase in inclusion iron content with decreasing inclusion size	154
Figs.74 to 77	Variation of inclusion composition with inclusion size	155 to 158
Fig.78	Inclusion relative plasticity	170
Fig.79	Diagram showing planes, directions and inclusion dimensions	172
Figs.80 to 85	Histograms of the frequency distributions inclusions parameters	175 to 177

		Page
Figs.86 to 90	Log-normal probability plots of inclusion parameters	179 to 183
Fig.91	Flow diagram of computer program	185
Fig.92	Hounsfield fracture strain versus inclusion % area fraction	188
Fig.93	Hounsfield fracture strain versus the projected inclusion length per unit area on a plane parallel to the fracture plane	189
Fig.94	Hounsfield fracture strain versus the reciprocal of the MFD between inclusions in a direction parallel to the tensile direction	190
Fig.95	Observed and calculated fracture strains for Hounsfield specimens	194
Figs.96 to 99	Typical effective stress versus effective plastic strain for notched uncharged and hydrogen charged specimens	196 to 197
Figs.100 and 101	The fracture strain of the uncharged and hydrogen charged tensile specimens versus the inclusion projected length per unit area on a plane parallel to the fracture	198 and 199
Figs.102 and 103	The fracture strain of the uncharged and the hydrogen charged tensile specimens versus the reciprocal of the MFD between inclusions in a direction parallel to the tensile direction	200 and 201

		Page
Figs.104 and 105	The percentage loss in fracture strain between the Hounsfield and the notched tensile specimens and notched and hydrogen charged notched tensile specimens versus the projected length of inclusion per unit area on a plane parallel to the fracture plane	203 and 204
Figs.106 to 117	The areal density,% area fraction and total length of voids versus the distance Z(mm) from the fracture surface	226 to 231
Fig.118	The % area fraction of inclusions versus the CLR	238
Fig.119	The projected length of inclusions on a plane parallel to the plane of cracking versus the CLR and CTR (Tests 1 and 2)	239
Fig.120	The projected length of inclusions parallel to the plane of cracking versus the CLR and CTR measured upon the side faces of Test 2	240
Fig.121	The probability of exceeding a projected length of 1.4mm/mm^2 versus the CLR and CTR (Tests 1 and 2)	241

LIST OF PLATES

		Page
Plate 1	Sulphur print of as cast ingot	145
Plate 2	Macro-etch of as cast ingot	146
Plates 3 to 6	As cast inclusion morphologies	148
Plates 7 and 8	Inclusion X-ray maps	160 to 161
Plates 9 to 14	Steel microstructures	164 to 166
Plate 15	Reoriented MnS network in rolled steel	186
Plate 16	SEM - Cluster of MnS inclusions forming largevoid on fracture surface. Steel F rolled at 1100°C	186
Plates 17 tol9	Macros of typical notched fracture surfaces for uncharged and hydrogen charged specimens	206
Plates 20 to 26	SEM - Typical examples of the fracture surface for the Hounsfield specimens tested longitudinally. Steel L rolled at 900°C	207 to 208
Plates 27 to 30	SEM - Comparison of fracture surfaces between hydrogen charged and uncharged specimens. Steel L rolled at 900°C	209
Plates 31 to 34	SEM - Comparison of fracture surfaces between hydrogen charged and uncharged specimens. Steel M rolled at 900°C	210
Plates 35 to 39	SEM - Comparison of fracture surfaces between hydrogen charged and uncharged specimens. Steel K rolled at 900°C	211

		Page
Plates 40 to 45	SEM - Deformed MnS inclusions on the fracture surface of steel L rolled at 900 for both the charged and uncharged specimens	212
Plates 46 and 47	Effect of inclusion anisotropy on the fracture appearance of steel rolled at 1100°C	214
Plates 48 and 49	Anomalous fracture phenomenon as a result of hydrogen and inclusion interaction in steel L rolled at 1100°C	214
Plates 50 to 52	Anomalous fracture phenomenon associated with non-metallic inclusions as a result of hydrogen charging. Steel F rolled at 1100°C	215
Plates 53 to 58	"Fisheye" type fracture associated with alumina inclusions and X-ray maps of fracture area. Steel F rolled at 900°C	216
Plates 59 to 61	"Fisheye" type fracture associated with MnS and alumina inclusion clusters. Steel F rolled at 900°C	217
Plates 62 to 67	Typical "fisheye" type fracture associated with inclusions (Al_2O_3 and (Ca,Mn,S)phases) and detail of resultant fracture surface. Steel M rolled at 1100°C	218
Plates 68 to 72	Axial cross-section of notched tensile specimens. Steel F rolled at 1100°C	220
Plates 73 to 77	Axial cross-section of hydrogen charged notched tensile specimens. Steel F rolled at 1100°C	221

		Page
Plates 78 to 83	Detail of void formation at inclusions and carbides, axial cross-section of steels K and L rolled at 1100°C, uncharged	222
Plates 84 to 87	Detail of cracks in axial cross-section of steel K rolled at 1100°C and hydrogen charged	224
Plates 88 and 89	Example of cracks occurring predominantly in the pearlite bands and running perpendicular to the tensile axis. Steel M rolled at 1100°C hydrogen charged	225
Plates 90 and 91	Macro of typical blister on the surface of a steel specimen after immersion in the NACE solution for 96 hours and cross section of a blister	245
Plates 92 to 94	Typical cleavage fracture surfaces. Steel K rolled at 1100°C and fractured at liquid nitrogen temperature	246
Plates 95 to 97	Steel L rolled at 900°C immersed for 96 hours in the NACE solution and then fractured at liquid nitrogen temperatures to reveal the fracture appearance caused by SWC	247
Plates 98 to 100	Typical example of (solitary) SWC associated with large silicate inclusion. Steel K rolled at 1100°C	248
Plates 101 to 106	SWC associated with large inclusion and X-ray maps to of inclusion and ruptured area in front of main crack. Steel K rolled at 1100°C	249

		Page
Plates 107 to 109	Typical example of SWC steel F rolled at 750°C	250
Plates 110 to 113	Elemental (Mn,S and P) concentration profiles across area containing SWC. Steel F rolled at 750°C	251
Plates 114 to 118	Example of SWC initiation at very small inclusions and composition maps. Steel F rolled at 750°C	252

LIST OF TABLES

		Page
Table 1.1	Steelmaking technologies to meet property requirements for linepipe	5
Table 2.1	Solubility products of oxides,sulphides and nitrides in liquid steel	16
Table 2.2	Phsyico-chemical and technological properties of alloying agents	17
Table 2.3	Influence of stirring upon inclusion separation	39
Table 2.4	Formation mechanisms of inclusions in Ca-treated steels	51
Table 2.5	Typical compositions of linepipe for various service conditions	61
Table 2.6	Variables used in ductile fracture mechanisms involving second phase particles	87
Table 3.1	Details of steelmaking	116
Table 3.2	Rolling schedule	120
Table 4.1	Chemical analysis of as cast ingots	142
Table 4.2	Chemical analysis of steel plate	143
Table 4.3	As cast inclusion compositions - summary	159
Table 4.4	Grain size and % pearlite fraction	167
Table 4.5	Inclusion relative plasticity and aspect ratio	169
Table 4.6	Fracture model data and results	193
Table 4.7	Vickers hardness	232
Table 4.8	Results of SWC tests - Test 1	233
Table 4.9	Results of SWC tests - Test 2	234
Table 4.10	Results of SWC tests, side faces - Test 2	235
Table 4.11	Blister size distribution	242 and 243
Table 4.12	Statistical analysis of blister size distribution	244

1.0 INTRODUCTION

From the onset of adopting large diameter linepipe to transport oil and natural gas in the early 1950's there has been a continuous development in the properties of the steels used in their fabrication (1,2).

The evolution has been achieved through an improved understanding of structure/property relationships and advances in steelmaking technology allowing increasingly tighter control over steel chemistry. The result is that today, tough, weldable, high strength low alloy steels (HSLA) are available for a range of pipeline applications (Fig.1).

A consistent trend in the development of these steels has been towards lower sulphur levels, primarily as a means of improving toughness and ductility by reducing the deleterious effect of sulphide inclusions (2).

In the late sixties deoxidation by aluminium (Al) and low temperature finish rolling (controlled rolling) were adopted in order to obtain fine-grained steels. This development was introduced to improve resistance to brittle fracture by lowering the impact transition temperature (ITT). However, several pipes unexpectedly failed in service by longitudinal propagating ductile fractures (1). Because of this, increased levels of transverse shelf energy were specified. This initiated a sequence of changes in steel making aimed at raising the overall level of toughness, and reducing toughness anisotropy.

Anisotropy was found to be caused by a combination of factors; Al-killed steels promoted the formation of intergranular type II manganese sulphide (MnS) inclusions and low-temperature rolling ($< 700^{\circ}C$), resulted in the elongation and reorientation of these MnS networks in the rolling direction (4,85).

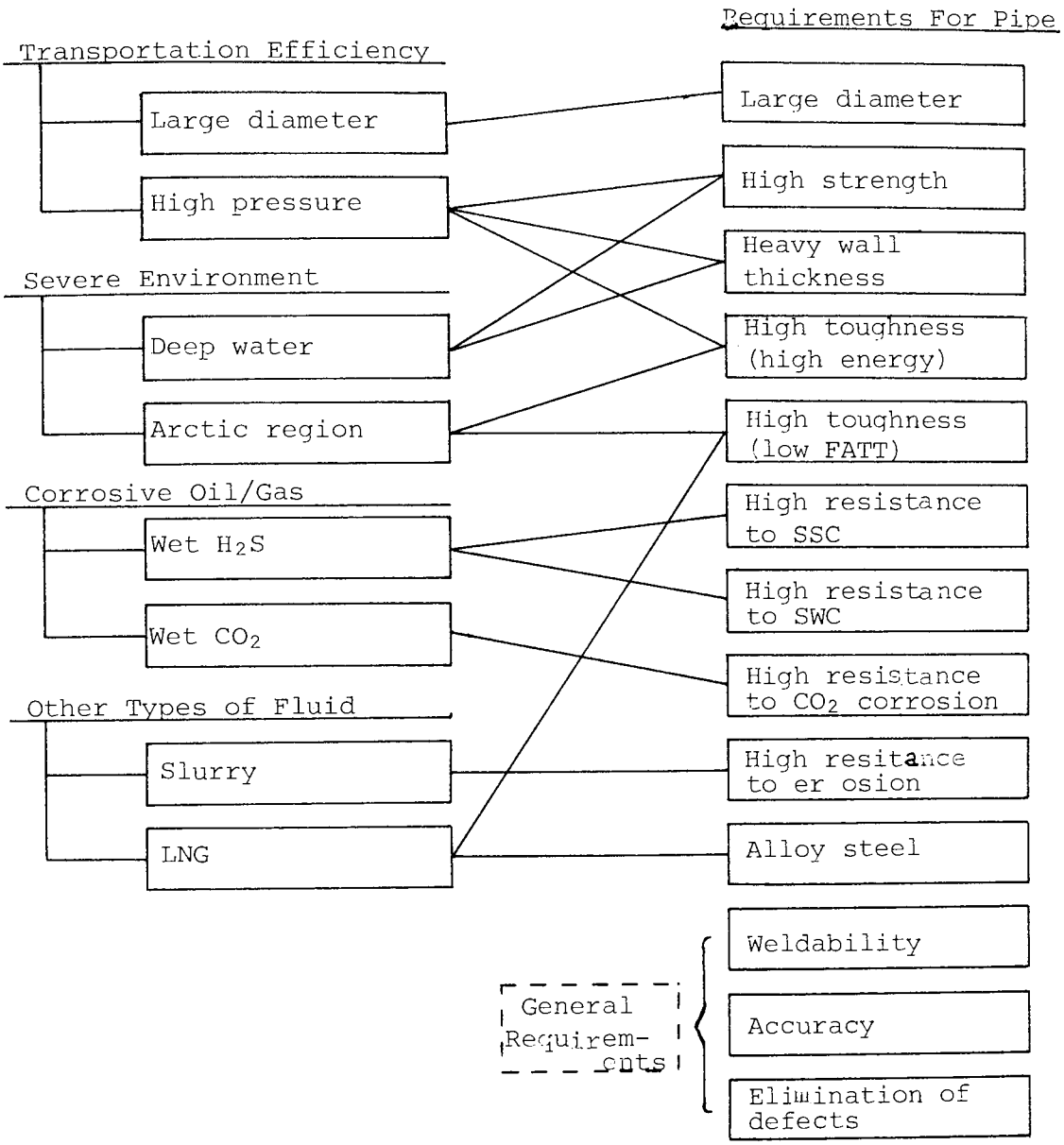

FIG.1 : Factors determining property requirements in pipeline steels (9).

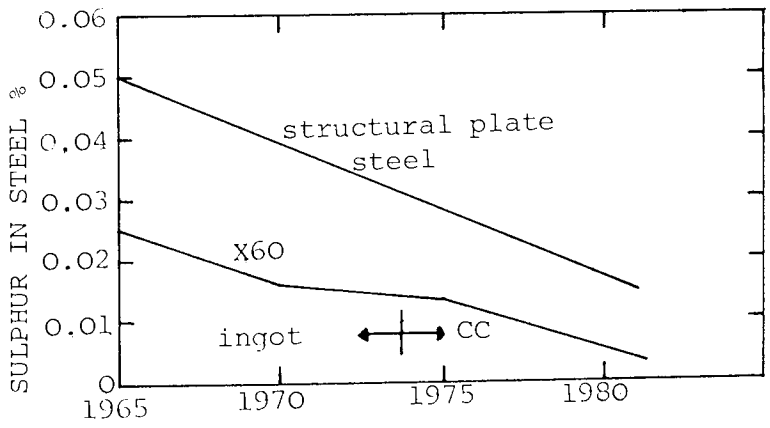

FIG.2 : Steelplant sulphur limits (5).

To combat this, and satisfy the demands for increased toughness, sulphur levels in steel were further reduced (Fig.2) (5) and sulphide inclusion shape control was introduced. Initially rare earth metal (REM) additions were made for shape control as they offered an effective means of reducing anisotropy without costly desulphurisation (2). Around the mid-seventies, however, the powder injection process (e.g. calcium silicide) became commercially viable. This marked a turning point in the manufacture of HSLA steels for linepipe, as in combination with the adoption of continuous casting, large tonnages of low sulphur steels with inclusion shape control could be produced economically (6).

At about this time, several reports appeared in the literature concerning the occurrence of linepipe failures in sour gas service (hydrogen sulphide (H_2S) environment) (7,8). The form of cracking, known as stepwise cracking (SWC),was thought to be caused by hydrogen (produced by corrosion) which was absorbed by the steel where inclusions specifically MnS, were considered to act as preferential sites for hydrogen concentration and subsequent crack initiation (85).

Since then considerable interest has been shown by the oil and gas producers for linepipe which offers resistance to this type of failure, principally as an increasing number of oil and gas reserves now contain high levels of H_2S. This has resulted in the adoption of sophisticated steel making techniques whereby sulphur and oxygen are reduced to very low levels through the injection of calcium alloys, lime-alumina slag practice and argon stirring in the ladle. The ultimate aim being the control of inclusion volume fraction, distribution and shape, and thereby the number of sites where SWC can develop (92).

Presently a typical steel producer offers the following (Table 1.1) to meet the property requirements for linepipe (9).

It can be seen that the control of inclusions is considered indispensable for sour gas/oil pipe and is now more important for these applications than other property requirements.

Under these circumstances it might be expected that the probability of SWC occurring is minimal, and this is certainly true. Nonetheless, cracking has been found to occur in some laboratory tests in steels with compositions which satisfy these conditions (10). It is also interesting to note that in a recent study (11) during hydrostatic burst tests of pipe, which had previously been exposed to a sour environment, even the occurrence of a limited amount of SWC caused a deterioration in the property of the pipe. Indeed pipes which were found to be free of SWC, as determined by standard metallographic examination (7), proved to exhibit evidence of a well documented form of hydrogen damage i.e flakes (or "fisheyes") (12) on the fracture surface after hydrostatic bursting. This phenomenon has been shown previously by several authors also to be frequently associated with non-metallic inclusions (13,14,15).

TABLE 1.1 STEELMAKING TECHNOLOGIES TO MEET PROPERTY REQUIREMENTS FOR LINEPIPE (9) .

APPLICATIONS / STEELMAKING	HIGH STRENGTH HEAVY WALLED PIPE	LOW TEMP. APPLICATION PIPE	SOUR GAS/OIL PIPE
CLEAN STEEL			
S < 0.006%	O		
S < 0.002%	Δ	●	●
P < 0.020%	O		O
P < 0.010%		●	Δ
O < 0.003%	Δ	●	●
H < 1.5ppm	●	O	Δ
N < 40 ppm	O	●	Δ
CALCIUM TREATMENT Ca 15 to 35 ppm	Δ	●	●
LOW-CARBON STEEL	●	●	●
INCLUSION CONTROL	O	O	●
NARROW RANGE CONTROL OF CHEMICAL COMPOSITIONS	●	●	●

NOTATION:

● : INDISPENSABLE

O : NECESSARY

Δ : DESIRABLE

1.1 AIMS

The purpose of this work was to determine the role of non-metallic inclusions in the cracking of steels exposed to a wet H_2S environment.

To obtain a basis for experiment a series of low-carbon manganese steels were prepared, by induction melting: these were cast as 18Kg ingots. In order to produce variation in the composition, morphology, volume fraction, size and distribution of inclusions, the steel chemistry was adjusted prior to casting by additions of deoxidiser and desulphuriser.

Sections of each ingot were subsequently hot rolled at temperatures between 750 and 1100° C.

The steel plate was then cut up to produce specimens for metallography, mechanical testing and hydrogen cracking tests.

Information on the following was obtained:

1) Inclusion parameters;

   A) As cast ingot;

      1) size distribution

      2) composition

      3) morphology

   B) Hot rolled steel;

      1) volume fraction

      2) shape

2) The effect of hot rolling upon inclusion deformation.

3) The anisotropy of tensile ductility, and the effect of hydrogen and inclusions upon tensile ductility.

4) The role of inclusions in hydrogen step wise cracking.

2.0 LITERATURE REVIEW

This is presented in two principal sections as reflecting the nature of the investigation. The first part deals with the control of inclusionsin steel whilst the second covers the effect of inclusions upon step-wise cracking in linepipe steels.

2.1 THE CONTROL OF INCLUSIONS IN STEEL

INTRODUCTION

Inclusions in steel are inherently controlled though steel making practice where the chemical refining processes of deoxidation and desulphurisation determine the final inclusion properties (16). These processes provide the means of governing oxygen and sulphur levels in the molten steel, and the composition of the deoxidation and desulphurisation products, i.e. the inclusions, formed in the melt and during solidification (17).

The following section reviews the literature concerned with the control of inclusions in steel through the practice of deoxidation, desulphurisation and inclusion shape control. This discussion is confined to the later stages of steel making i.e. ladle metallurgy and more specifically to the production of clean, high strength low alloy (HSLA) steels such as those used for linepipe.

2.1.0 OXIDE AND SULPHIDE INCLUSIONS - BASIC OBSERVATIONS.

During ladle deoxidation and desulphurisation oxygen and sulphur are removed from the steel bath by diffusion controlled exchange reactions between the metal and a suitable slag or the formation and separation of non-metallic inclusions (16,85).

In an early review of inclusions in steel KIESSLING and LANGE (19) discussed the factors affecting the formation of oxide and sulphide inclusions. They determined that both types of inclusion were formed by precipitation from the melt and that although the mechanisms of sulphide and oxide formation were very similar it was possible to make distinctions. These were distinctions of degree rather than of the character of the reaction. Firstly, under most conditions encountered in steel making practice, the steel will hold sulphur in solution without the precipitation of sulphides until it has cooled below the normal teeming temperature. Secondly, temperature has a greater effect on the solubility of the usual sulphides in steel than on most of the oxide inclusions. Consequently, they reported that the precipitation of sulphide inclusions occurred during solidification, from the interdendritic liquid, and was greatly influenced by segregation, whereas oxide inclusions primarily formed in the melt. For both oxygen and sulphur they reported that their solubility in solid steel was negligible, but the oxygen level in the molten steel was dependent upon the effect of other elements in addition to iron. Deoxidation being accomplished by the addition of elements which have a greater affinity for oxygen than iron.

Although these comments were made some ten years before the introduction of modern ladle metallurgy they contain within them the essential factors influencing the formation of inclusions in steel that are equally valid today. That is, the effect of temperature upon the solubility of oxygen and sulphur in steel and the effect of elements that are added to steel which have a higher affinity for oxygen and/or sulphur than iron resulting in lower soluble oxygen and sulphur levels. Both these processes lead to the formation of inclusions and, hence, are the means whereby inclusions can be controlled in steel.

The mechanisms of inclusion formation reported above are by no means mutually exclusive and will occur on a cooperative basis during ladle refining and casting. Studies by PICKERING (22), PLOCKINGER (20) and BERGH (87) have illustrated how inclusion composition and density change continuously during the processing of liquid steel.

HOLAPPA (24) discusses the situation for a normal aluminium killed steel (Al ≃ 0.02%). Deoxidation carried out in the ladle reduces the soluble oxygen content to as low as 5ppm at 1600° C with the majority of oxygen remaining suspended in the melt as alumina (Al_2O_3) inclusions. (The solubility of oxygen in liquid iron has been determined at approximately 0.23% at 1600° C (21)). JANKE (35) reports that total oxygen levels in aluminium killed melts have been found to be between 0.003-0.012%, whilst the dissolved oxygen level is estimated to be below 0.001% (10ppm) in agreement with the above data. Sulphur, on the other hand, which is dissolved in the liquid metal (ladle concentrations of sulphur in most steels of this type are in the range 0.01 - 0.02% (17,25)) does not precipitate as sulphide inclusions in the melt before casting. During solidification, however, due to the temperature drop and the enrichment of the remaining liquid steel with elements which are insoluble in the solid state (e.g. Mn,S and P), sufficient concentrations of Mn and S occur to exceed their solubility product precipitating MnS inclusions. In normal Al killed steels, type II intergranular MnS inclusions are formed (24). Similar observations to these for Al killed steels have been made by SAXENA et al (36,37).

The alumina inclusions formed in the melt at constant steel temperature are referred to by HOLAPPA (24) as primary deoxidation products. Further inclusions formed during casting (i.e. cooling leading to increased oxygen rejection) are called secondary deoxidation products and, inclusions occurring upon solidification are known as tertiary

deoxidation products, this period of inclusion formation also encompasses the precipitation of MnS. The distinction between stages in inclusion formation during deoxidation has been made by several authors (26,27,28,19). KIESSLING and LANGE (19) comment that the significant point of this classification is that primary deoxidation products have a greater opportunity to escape from the steel than those which form due to a fall in temperature. From this it can be concluded that secondary and primary inclusions, which do not separate from the melt will become trapped in the solidified ingot along with nearly all the inclusions produced as a result of solute rejection and segregation i.e. tertiary products.

This sequence of events will determine the distribution and composition of inclusions within the ingot, as typically shown in sulphur prints and macro-etched cast steel ingots (32,86,93,105). The total volume fraction will be dependent upon the successful separation of inclusions (36), and therefore, the quantity of primary, secondary or tertiary inclusions remaining in the solidified ingot.

For normal aluminium killed steels, it has been shown that there is little opportunity for sulphide inclusions to separate from the melt, and even when the ladle sulphur levels are very low (<0.005%), the tendency for sulphur to segregate can result in areas within the ingot where MnS precipitation occurs on an extensive intergranular scale (85).

This effect has been studied by GASPARD et al (38), in a series of aluminium killed steels. By using quantitative metallography and thermodynamic analysis they determined the effect of oxygen, sulphur, carbon and manganese content upon the extent of interdendritic segregation and manganese sulphide formation. The results are presented in terms of the Mn and S content of the steel as it affects the

occurrence of large MnS inclusions (Fig.3). From this it may be seen that S levels of less than 0.005% are required in steels with Mn contents of 1.5% to prevent excessively long MnS inclusions, which would otherwise be detrimental to steel properties.

This point is discussed further by TURKDOGAN (31) who comments that when the sulphur level in steel is less than 0.01%, there is not enough sulphur in the system for the formation of a continuous network of interdendritic sulphide inclusions. However, the macro segregation that is inherent to the solidification process, both in continuous and ingot casting, (leading to clustering and segregation of oxide inclusions also) (31,32) is responsible for the accumulation of impurity-enriched liquid in certain regions of the casting, resulting in localised precipitation of relatively large manganese sulphides, even when the steel contains as little as 0.002% sulphur. Consequently, in linepipe quality steels containing 1.2 to 1.5% manganese, desulphurisation to less than 0.002% is carried out in order to prevent the formation of detrimental sulphide inclusions and fulfil compositional requirements (e.g.Table 1.1), (9,31,39).

A further source of oxide inclusions in steel occurs as a result of reoxidation, where oxygen from the atmosphere, refractories or slag leads to the formation of inclusions (29,30,31,32,33).

The significance of the reaction has been found difficult to evaluate as it can occur throughout ladle treatments and casting. However, a recent study by LINDENBERG and VORWERK (30) of atmospheric reoxidation of steel has found that the inclusion morphology is different to those produced by normal deoxidation and that this may offer a basis for investigation.

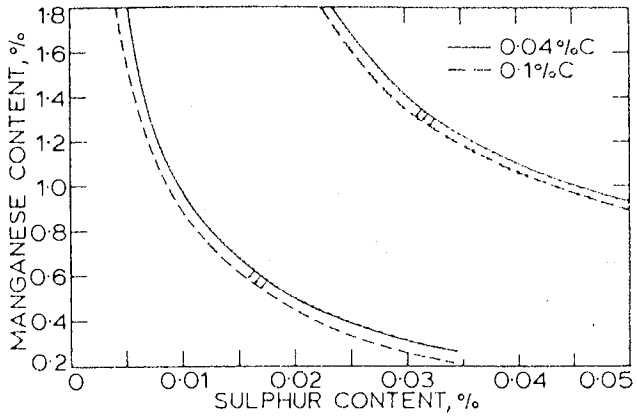

FIG.3 : The influence of manganese and sulphur contents on the inclusion level of aluminium steels with two carbon contents (38).

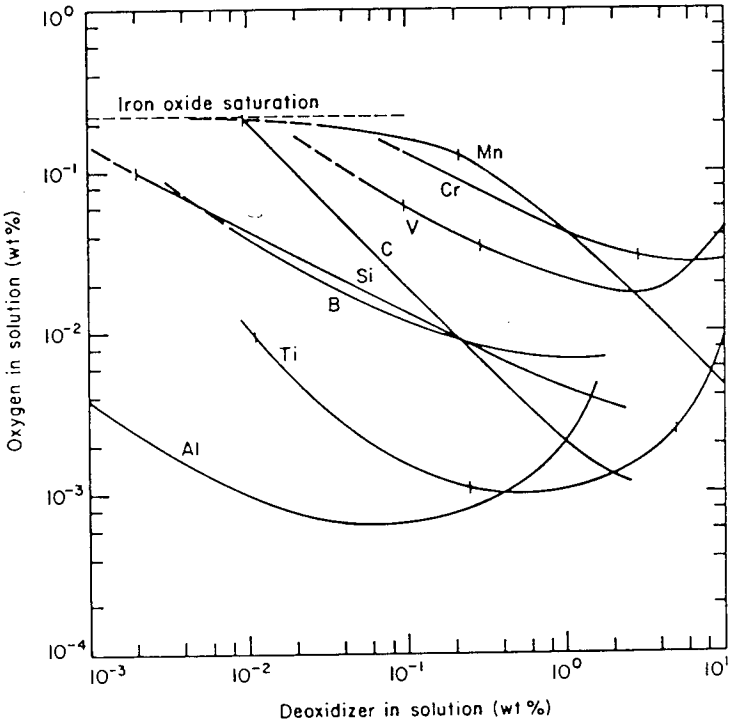

FIG.4 : Deoxidation equilibria in liquid iron at 1600°C (18).

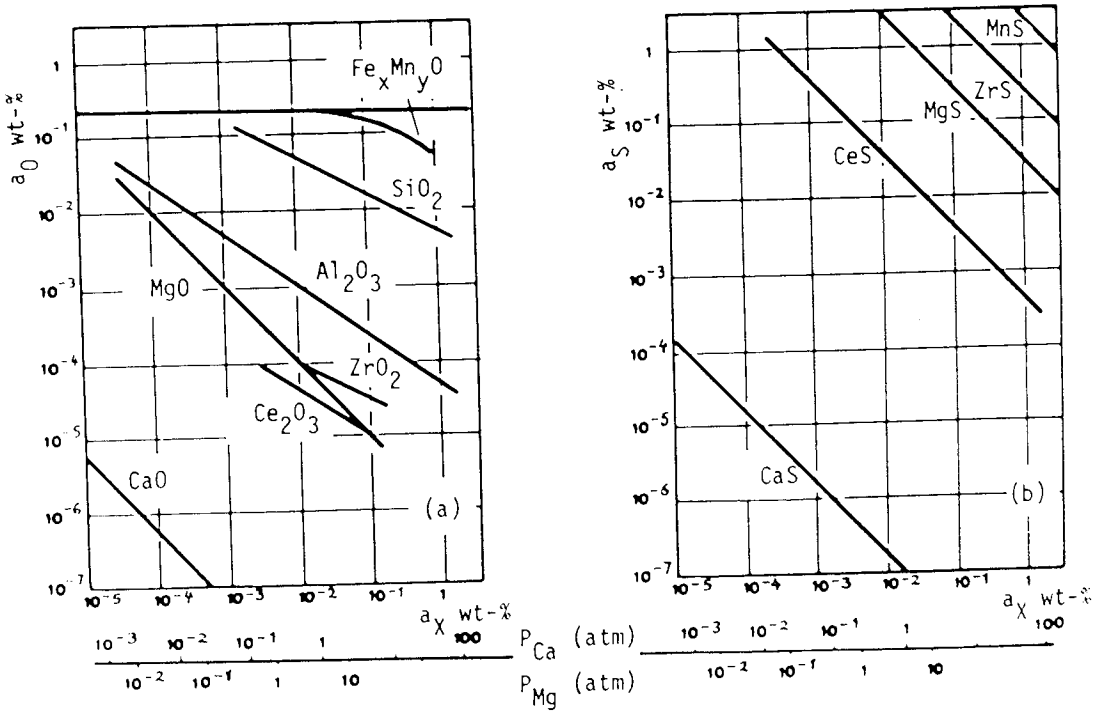

FIG.5 : Activity of oxygen and sulphur in equilibrium with various desulphurisers in liquid iron at 1600°C (50).

Numerous authors have discussed the causes of, and methods for, preventing reoxidation, primarily as it effectively detracts from attempts to deoxidise (24,40,41). An investigation by KAY et al (33) into the effect of rare earth-oxygen-sulphur reactions in molten steel has also pointed out that reoxidation by interaction with refractories, slags and the atmosphere can result in oxidation of sulphide and oxysulphide phases,with sulphur reverting to the melt. If this reversion is excessive, iron manganese sulphides may eventually form with a consequent loss of inclusion control.

This observation has also been made by other authors (30,41,95), thus reoxidation may possibly reduce the effectiveness of desulphurisation as well as increase the number of oxide inclusions.

Finally, in his review of the ladle treatment of liquid steel TURKDOGAN (17) comments that the close control of deoxidation is a necessity to accomplish two primary objectives: i) to lower the residual oxygen content in solution in the steel to the desired level, and ii) to separate inclusions from the melt prior to casting. And in agreement with KAY et al (33), above, he comments that deoxidation is perhaps the most important reaction which directly affects the efficiency of ladle desulphurisation, steel cleanliness (low inclusion count), soundness of casting, and the form of sulphide inclusions. The importance of deoxidation to the production of low sulphur steels is discussed in the following section.

2.1.1 THE THERMODYNAMICS OF OXIDES AND SULPHIDES

The thermodynamics of deoxidation and desulphurisation reactions of interest to the steelmaker have been investigated by many workers (42,43,44,45), and comprehensive reviews are available by BODSWORTH and BELL (21) and more recently TURKDOGAN (17) and PEHLKE and FUWA (85).

These contain tabulated thermodynamic data collected from the literature which are generally held to be reliable.

The affinity of an element for oxygen and sulphur can be determined by the standard free energy change associated with the reactions:-

$$\underline{Mx} + \underline{Oy} = (MxOy) \qquad \ldots\ldots 1$$

$$\underline{Mx} + \underline{Sz} = (MxSz) \qquad \ldots\ldots 2$$

where x,y and z reflect stoichiometry.

A large negative value of standard free energy indicates a strong reaction and a stable product (21,47).

In many cases the above reactions have been investigated in terms of the equilibrium constant or the solubility product for steelmaking (17,18,21,23,29). The standard free energy change is related to the equilibrium constant by the GIBBS equation (47),

$$\Delta G^{o} = - RT \ln K \qquad \ldots\ldots 3$$

The equilibrium constants for reactions 1 and 2 are given by:-

$$K_1 = \frac{a(MxOy)}{a\underline{Mx}.a\underline{Oy}} \qquad \ldots\ldots 4$$

$$K_2 = \frac{a(MxSz)}{a\underline{Mx}.a\underline{Sz}} \qquad \ldots\ldots 5$$

a= activity.

These equations must be interpreted carefully because it is assumed that the components are at equilibrium and in their standard states i.e pure substances, atmospheric pressure (47). For steelmaking KIESSLING and LANGE (19) have noted that these conditions are rarely approached, as molten steel is a dilute solution of numerous elements in iron, and for many of them the solution is far from saturation and their activity is not unity.

To overcome this restriction, the assumptions contained in HENRY's law, for infinitely dilute solutions, is applied (47). The activity of an element in solution being defined by its concentration in weight per cent, where the standard state is taken as 1 wt %.

By applying this law the solubility of the deoxidation product in liquid steel can then be represented as (17),

$$MxOy = x\underline{M} + y\underline{O} \qquad \ldots\ldots 6$$

$$K = {}^{a}\underline{M}^{x} \cdot {}^{a}\underline{O}^{x} / aMxOy \qquad \ldots\ldots 7$$

The solute activities are then equivalent, at infinitely dilute solution, to the weight percent of solute in the steel i.e. $a_i \equiv wt\%_i$. FRUEHAN (18) and OLETTE and GATELLIER (50) have presented some of the more common deoxidation equilibria (Fig.4), here the oxygen and alloying elements in solution are in equilibrium with the appropriate gas, liquid or solid oxide phase at 1600°C e.g. pure $Al_2 O_3$ at unit activity.

Similar equilibrium relationships have been determined for desulph urisers, and these are shown in Fig.5 (50,24). Table 2.1 is a compilation of data by OLETTE and GATELLIER (50) showing the solubility products for the more common reactions in steelmaking for oxides and sulphides (and nitrides).

These diagrams (Fig.4 and 5) reflect the relative ability of elements to form oxide and sulphide phases, and give some indications of why elements such as calcium and aluminium are used to obtain very low levels of oxygen and sulphur in steel. However, as pointed out by EL GAMMAL (53), this is not an exclusive measure of their technical suitability, as factors such as solubility, density and vapour pressure etc. must also be considered. In Table 2.2 the more important physical and chemical properties of alloying elements found in steel are presented from ABRATIS and LANGHAMMER (70).

Element	oxide	$\log_{10} K$	K 1 600 °C	sulphide	$\log_{10} K$	K 1 600 °C	nitride	$\log_{10} K$	K 1 600 °C
Al	$FeAl_2O_4$	$-\frac{70\,320}{T} + 23.38$	$6.9 \cdot 10^{15}$	Al_2S_3		1C[3]	AlN	$-\frac{12\,950}{T} + 5.58$	$4.6 \cdot 10^{-2}$
	Al_2O_3	$-\frac{62\,680}{T} + 20.54$	$1.2 \cdot 10^{13}$						
B	B_2O_3		$1.5 \cdot 10^{8}$				BN	$-\frac{10\,000}{T} + 4.64$	0,2
C	CO (gaz)	$-\frac{1\,168}{T} - 2.07$	$2.05 \cdot 10^{3}$						
Ca	CaO		$6.2 \cdot 10^{-11}$	CaS		$1.3 \cdot 10^{-9}$	Ca_3N_2		$1.2 \cdot 10^{11}$
Ce	Ce_2O_3	$-\frac{68\,500}{T} + 19.6$	10^{17}	CeS	$-\frac{20\,600}{T} + 6.39$	$2.5 \cdot 10^{5}$			
Cr	$FeCr_2O_4$	$-\frac{50\,700}{T} + 21.70$	$4 \cdot 10^{6}$						
	Cr_2O_3	$-\frac{40\,740}{T} + 17.78$	$1.1 \cdot 10^{4}$						
La	La_2O_3	$-\frac{62\,050}{T} + 14.10$	$9.3 \cdot 10^{20}$	LaS	$-\frac{26\,000}{T} + 8.98$	$1.3 \cdot 10^{-6}$			
Mg	MgO		$1 \cdot 10^{6}$	MgS		$3 \cdot 10^{-3}$			
Mn	$(FeO\text{-}MnO)_{liq}$	$-\frac{12\,760}{T} + 5.57$	$5.8 \cdot 10^{-2}$	MnS		2.7			
	$(FeO\text{-}MnO)_{sol}$	$-\frac{15\,050}{T} + 6.70$	$4.7 \cdot 10^{-2}$						
Nb	$FeNb_2O_6$	$-\frac{88\,300}{T} + 36.76$	$4.1 \cdot 10^{13}$				NbN	$-\frac{11\,100}{T} + 5.40$	0,3
	NbO_2	$-\frac{32\,780}{T} + 13.92$	$2.6 \cdot 10^{4}$						
Si	SiO_2	$-\frac{31\,040}{T} + 12.0$	$2.7 \cdot 10^{5}$						
Ta	$FeTa_2O_6$	$-\frac{79\,300}{T} + 28.43$	$1.2 \cdot 10^{11}$				TaN	$-\frac{15\,410}{T} + 7.80$	0,4
	Ta_2O_5	$-\frac{63\,100}{T} + 21.90$	$1.6 \cdot 10^{12}$						
Ti	TiO_2		$5 \cdot 10^{7}$	TiS	$-\frac{8\,000}{T} + 4.02$	0.56	TiN	$-\frac{19\,755}{T} + 7.78$	$1.7 \cdot 10^{3}$
	Ti_3O_5		$3.5 \cdot 10^{16}$						
	Ti_2O_3		$2.7 \cdot 10^{13}$						
U	UO_2		$5.9 \cdot 10^{11}$	US		$1.6 \cdot 10^{4}$			
V	FeV_2O_4		$8.3 \cdot 10^{8}$						
	V_2O_3		$3.5 \cdot 10^{6}$						
	VO	$-\frac{15\,530}{T} + 6.66$	$2.3 \cdot 10^{2}$						
Zr	ZrO_2	$-\frac{40\,750}{T} + 11.80$	$1.1 \cdot 10^{10}$	ZrS		0,3	ZrN	$-\frac{13\,330}{T} + 4.80$	$4.8 \cdot 10^{-3}$

TABLE 2.1 Solubility products of oxides, sulphides and nitrides in liquid steel (50) .

	Al	C	Ca	Ce	Mg	Mn	Nb	Si	Ti	V	Zr
Solubility in Fe at 160°C (wt. *%)	tot.	5.4	0.03	tot.	v.l.*	tot.	35 - 38	tot.	97	67	40 - 42
Specific heat capacity at 20°C (kJ/kg K)	0.90	0,69	0.65	0.23	1.02	0.48	0.27	0.71	0.53	0.48	0.28
Melting Point(°C)	659	3800	850	804	650	1244	2467	1412	1660	1917	1852
Latent heat of fusion (kJK/kg)	396	-	233	63	373	262	(288)	1411	(437)	(293)	(252)
Boiling Point (°C)	2450	-	1489	3810	1105	2051	4734	3219	3302	3379	4504
Latent heat of evaporation (kJ/kg)	10541	-	4032	2181	5423	4093	-	10594	(8828)	-	(4590)
Enthalpy $\Delta H°$ at 1600°C 9kJ/kg)	2197	2683	5257	462	7368	1478	476	3256	1094	1001	567
Heat conductivity at 0°C (kJ/mhK)	850	42 - 419	742	39	565	28	192	606	80	110	83
Oxygen affinity (free enthalpy of reaction $\Delta G^{1600°C}$) (kJ/mole)	- 491.1	- 283	- 219.8	- 297.4	- 756.6	- 345.1	- 45.5	- 126.7	- 162.1	- 244.1	- 206.6
Density at 20°C (g/cm^3)	2.7	2.3	1.53	6.81	1.7	7.4	7.6	2.3	4.5	6.2	6.4
Brinell hardness HB	16	-	13	21	-	-	250	-	160	260	160
Range of alloying (wt. *%)	0.020 - 5	0.005 - 1.0	-	0.1 - 0.5		0.30 - 14	0.02 - 4.5	0.3 - 4	0.01 - 10	0.05 - 4	0.002 - 1.25

Values in parentheses are of uncertain reliability

+
* very low

TABLE 2.2 Physico Chemical and technological properties of alloying elements (70).

In addition elements may act together during deoxidation/desulphurisation producing lower residual oxygen and sulphur levels. This has been observed by a number of authors (27,38,51,52,53,54).

For the case of aluminium deoxidation of a simple iron-oxygen melt GUSTAFSSON and MELLBERG (51) found, that upon additions of calcium in such quantities that a liquid $CaO-Al_2O_3$ - inclusion formed, the equilibrium oxygen content (soluble) decreased as the activities of the oxides in the product were reduced. OZTURK and TURKDOGAN (52) confirmed these observations and produced a diagram (Fig.6) from data calculated by REIN and CHIPMAN which shows how the activity of both Al_2O_3 and lime (CaO) vary with the composition of the oxide phase.

These observations were discussed in terms of the equilibrium constant by EL GAMMAL (53); for a constant activity of the reagent metal $a\underline{M}$ the equilibrium oxygen (or sulphur) in the metal will decrease by a value directly related to the decrease in the activity of the reaction product when these are chemically bonded or diluted viz;

$$K = \frac{a(MO)}{a\underline{M} \cdot a\underline{O}} \qquad (MO)\ \text{Dissolved In Slag} \qquad \ldots\ldots 8$$

$$K = \frac{a\langle MO.OX\rangle}{a\underline{M}.a\underline{O}.a\underline{XO}} \qquad \langle MO\rangle\ \text{Chemically Bonded} \qquad \ldots\ldots 9$$

For example, FRUEHAN (18) has shown that for a steel containing 0.002% Al in equilibrium with a 50% CaO- 50% Al_2O_3 slag the equilibrium oxygen content was 8ppm, whereas for Al alone it was 22ppm, (Fig.7).

Finally from inspection of Figs.4 and 5 it can be observed that elements which have a strong affinity for sulphur are also strong oxide formers. This is particularly so for calcium and has an important bearing upon the production of low sulphur steels ($<0.002\%$) (24,31,85).

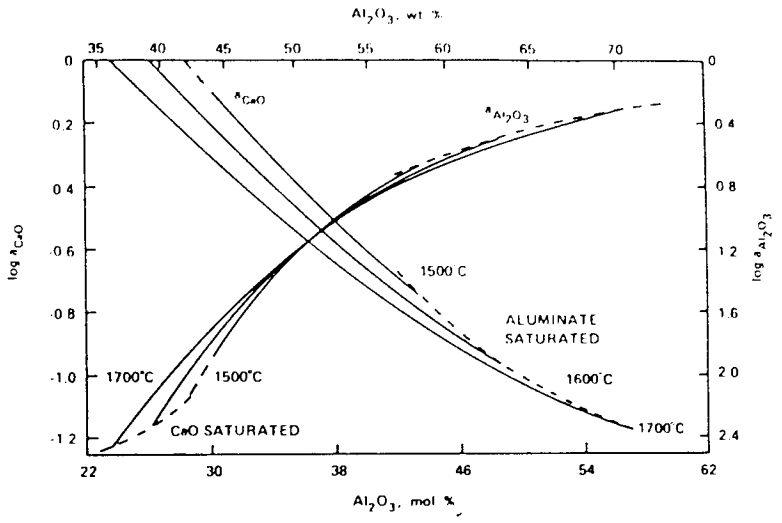

FIG.6 : Activities of oxides in $CaO-Al_2O_3$melts (52).

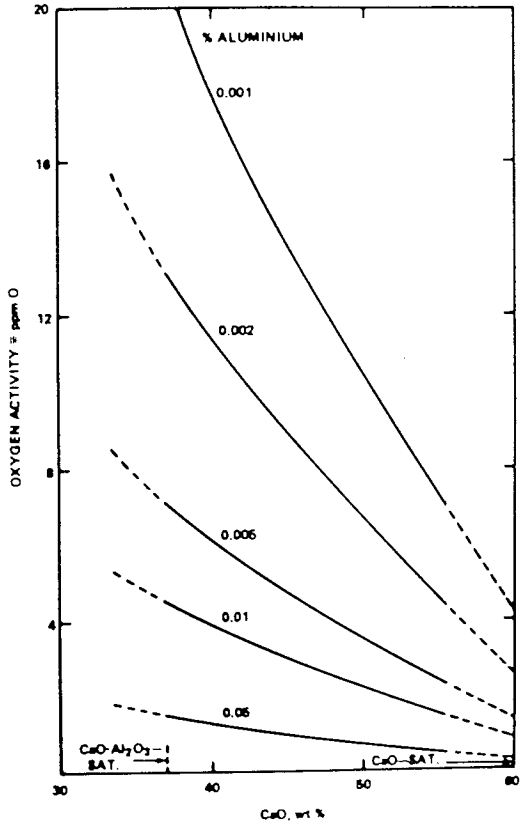

FIG.7 : Deoxidation equilibria for Fe-Al melts (52).

The success of the desulphurisation operation depends upon achieving a very low oxygen level in the melt (18,80,85). In steels which have not been deoxidised sufficiently the addition of a desulphurising element eg. Ca, Mg or REM will result initially in the formation of the oxide phase. Hence, to achieve desulphurisation to very low levels it has been found necessary to fully kill the steel with aluminium before sulphur reduction is attempted (18,24,31,34).

The overall reaction to be considered is that involving an oxide and sulphide (24,31,34,37,58),

$$\underline{M} + \underline{O} = (MO) \qquad \ldots\ldots 10$$

$$\underline{M} + \underline{S} = (MS) \qquad \ldots\ldots 11$$

which combined gives,

$$(MO) + \underline{S} = (MS) + \underline{O} \qquad \ldots\ldots 12$$

where the equilibrium constant is given by,

$$K = \frac{a(MS) \cdot a\,\underline{O}}{a(MO) \cdot a\,\underline{S}} \qquad \ldots\ldots 13$$

When the metal oxide (MO) and metal sulphide (MS) have unit activity the equilibrium constant is given by the ratio of activities (18,24,31,37,58,59),

$$K = \frac{a\underline{O}}{a\underline{S}} \qquad \ldots\ldots 14$$

Fig.9 gives examples for the alkaline earth sulphide/oxide and cerium oxysulphide/oxide equilibria calculated by TURKDOGAN (31). For a given level of deoxidation, the higher the equilibrium ratio aO/aS the lower will be the residual sulphur in the steel. The ability of calcium to desulphurise, in comparison with other elements is clearly very favourable on thermodynamic grounds.

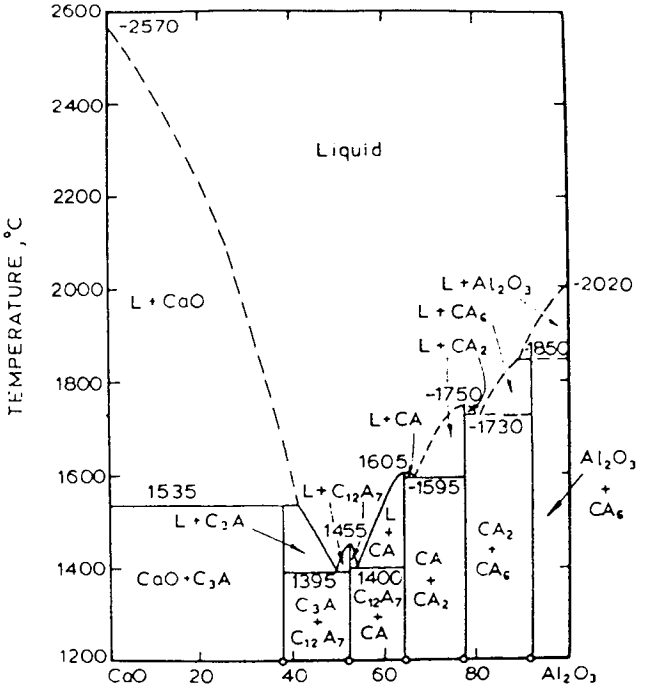

FIG.8 : Phase diagram of the $CaO-Al_2O_3$ system (102).

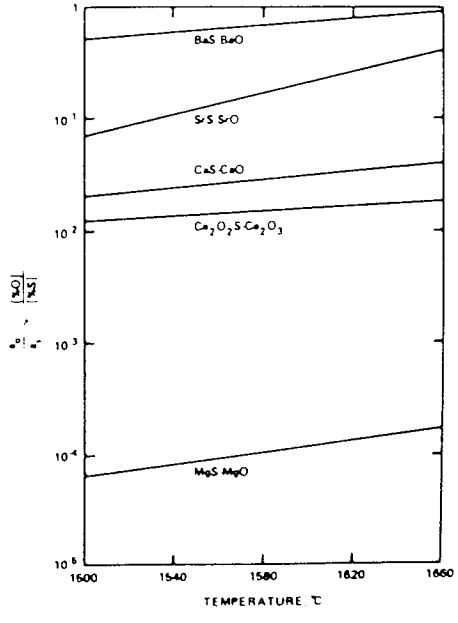

FIG.9 : Oxygen/sulphur activity ratio in liquid iron for the indicated sulphide-oxide equilibrium at 1600 C^{o} (49).

To give some indication of the oxygen activity required to obtain low levels of sulphur in steel SHALIMOV (59) has made calculations (on the basis of equations 10 and 11) and determined the equilibrium constant (equation 13) for the case of calcium as,

$$\log K = \frac{-5150}{T} + 1.191 = \frac{aO}{a\underline{S}} \qquad \ldots\ldots 15$$

to obtain sulphur levels of 0.02, 0.01 and 0.003% the oxygen activities required would be .0005, .0003 and .0001% respectively. These values are in close agreement with calculations made by SAXENA (37) and FRUEHAN (18).

In aluminium killed steels the already low oxygen activity is decreased further by the addition of calcium as a result of the formation of calcium aluminates, (56), as discussed earlier i.e mixed deoxidants (see Fig.8) (51,52). When the oxygen activity becomes sufficiently low (dependent upon the prior oxygen and sulphide levels -SHALIMOV (59)) then calcium sulphide formation occurs by the reaction (31,52),

$$CaO + \tfrac{2}{3}\underline{Al} + \underline{S} = CaS + \tfrac{1}{3}Al_2O_3 \qquad \ldots\ldots 16$$

The calcium sulphide produced is then absorbed in the calcium aluminate phase (whether this is the top slag or the calcium aluminate inclusions in the melt), its capacity for sulphur being dependent upon the ratio of CaO to Al_2O_3 (54). Fig.10, after TURKDOGAN (31), is a compilation of results from several investigators showing the sulphur capacity of lime/alumina phases at different temperatures. Only when these become saturated and sufficient calcium is available, is it possible for a CaS phase to occur in the melt (88). This is rarely observed in practice as there is normally sufficient slag available to absorb all the sulphur.

Recent articles by OZTURK et al, (52) and PEHLKE and FUWA (85) discuss in full the factors influencing the sulphur capacity of lime-alumina slags. The importance of deoxidation in promoting desulphurisation, as determined above (Equation 16) is shown in Fig.11 after FRUEHAN (18).

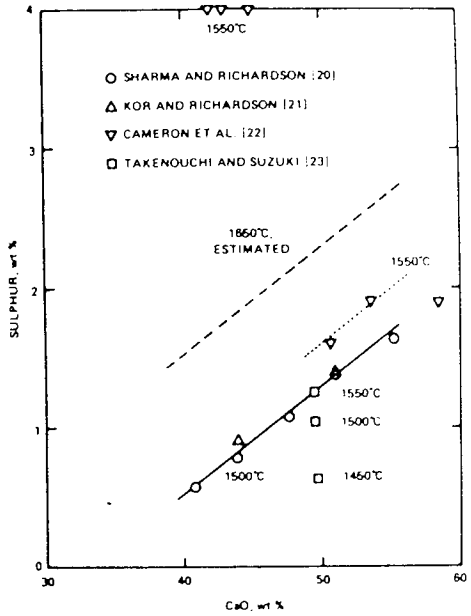

FIG.10 : Solubility of CaS in $CaO-Al_2O_3$melts (31).

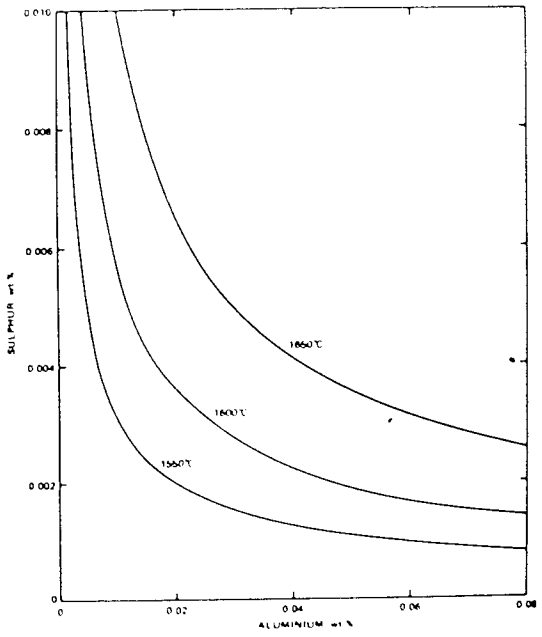

FIG.11 : Calculated relationship between sulphur and aluminium contents in liquid Fe in equilibrium with 56 percent CaO - 44 percent Al_2O_3 (18).

Here, the equilibrium sulphur level for a typical inclusion content (56%CaO-44%Al_2O_3) is found to decrease with increasing aluminium as a direct result of lower oxygen levels. The effect of temperature in lowering the soluble oxygen content is also apparent.

The control of deoxidation and desulphurisation equilibria is of critical importance in the commercial production of large tonnages of low sulphur steels. In the various ladle practices used industrially the essential feature, in all cases, is deoxidation. To achieve this, and so produce low sulphur HSLA steels, aluminium deoxidation and a lime alumina slag practice are used together with a combination of argon stirring, powdered slag or calcium silicide injection almost without exception (85). Extensive details of the various practices have been reported in the literature (34,37,54,55,56,57,58,85). A typical example of desulphurisation and deoxidation occurring during calcium silicide injection of a 145 ton melt, aluminium killed (0.03-0.05%) with a synthetic slag covering of 85% CaO and 15% CaF_2 is shown in Fig.12 after TIVELIUS et al (57). Calcium silicide injection can be seen to cause a dramatic decrease in both the oxygen and sulphur levels. This is due to the formation of liquid inclusions comprising of $CaO-Al_2O_3$- CaS and, with high concentrations of calcium, possibly CaS or Ca(OS), which quickly separate from the melt and are absorbed in the slag (39). Note also the increased hydrogen content of the steel after injection.

2.1.2 KINETICS: THE FORMATION AND SEPARATION OF INCLUSIONS IN STEEL

INTRODUCTION

A complete awareness of the thermodynamics affecting oxide and sulphide formation is a necessity in controlling the levels of oxygen and sulphur in steel. However, this information is only useful in determining whether a reaction is possible, identifying the initial and final states at equilibrium. It does not provide answers concerning the rate at which

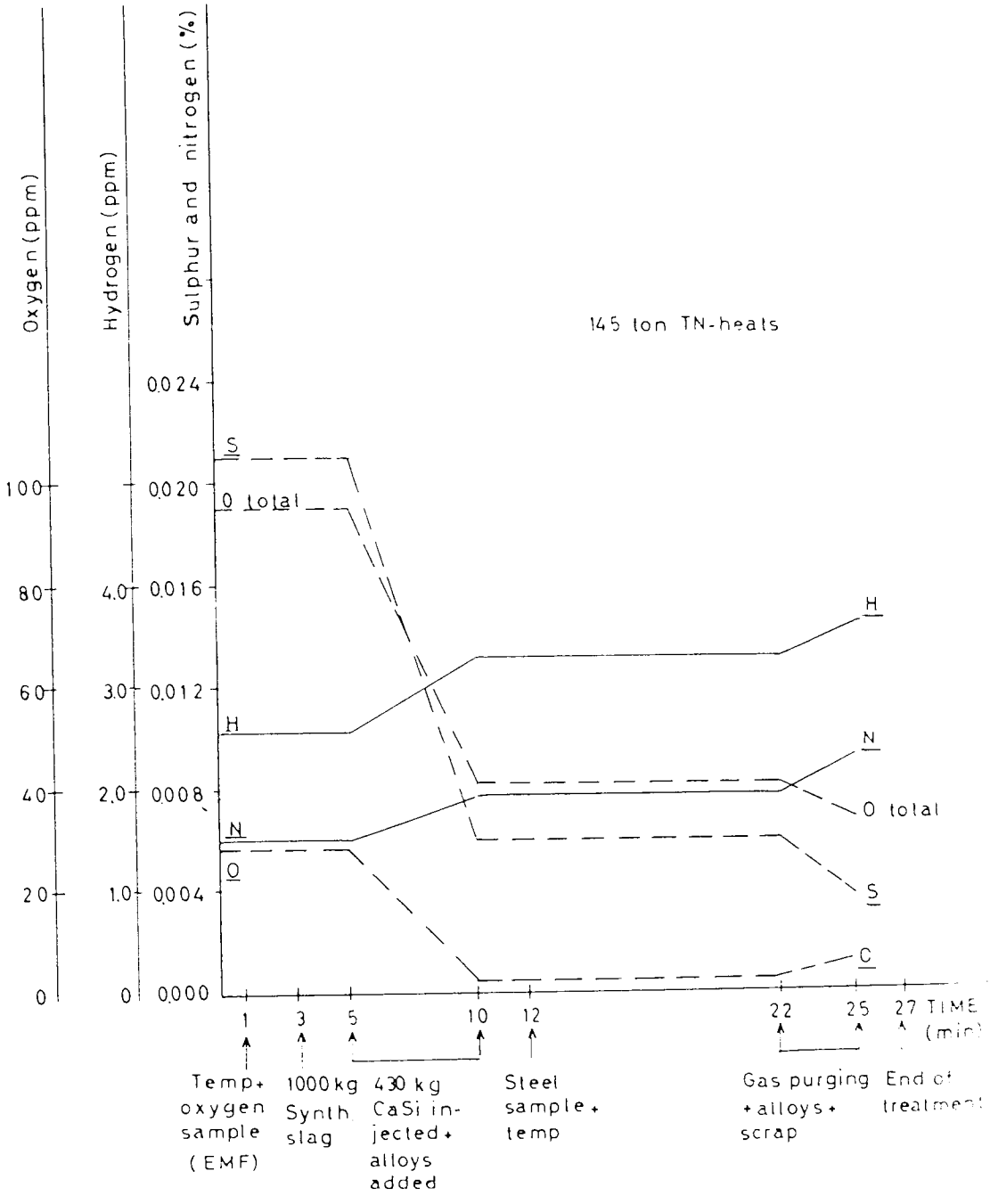

FIG.12 : Hydrogen, oxygen, sulphur and nitrogen contents as a function of time for a 145 ton Al killed CaSi injected melt (57).

a reaction takes place nor the mechanisms involved (47). These aspects are determined by kinetics and are considered by a number of workers as the single most important factor affecting steel cleanness (25,61).

The formation and separation of inclusions in steel is a process which involves a series of reactions over a period of time. Under steelmaking conditions these occur dynamically, specific reactions prevailing where thermodynamic and kinetic conditions are satisfied. Consequently, this has caused difficulties in identifying the significance of individual reactions (62,68).

One of the first investigations which set out to clarify this situation was carried out by PLOCKINGER (20,63). He conducted a series of experiments designed to catalogue the reactions taking place during deoxidation, in order to determine the factors and conditions producing "clean steel". He observed the effect of different deoxidants upon oxygen level during steelmaking with time (Fig.13) and more importantly made a distinction between oxygen in solution and combined as an oxide (Fig.14). He found that oxygen is quickly tied up after the addition of deoxidiser but the reaction products, oxide inclusions, remain in suspension for a considerable time afterwards. He also noted that stirring the melt increased the inclusion separation rate for all compositions (shown in Fig.13 for the teeming period) and that the surface properties of the deoxidation products could influence their removal from the liquid steel. These early observations have proved to be important factors in the production of clean steels during modern ladle practice.

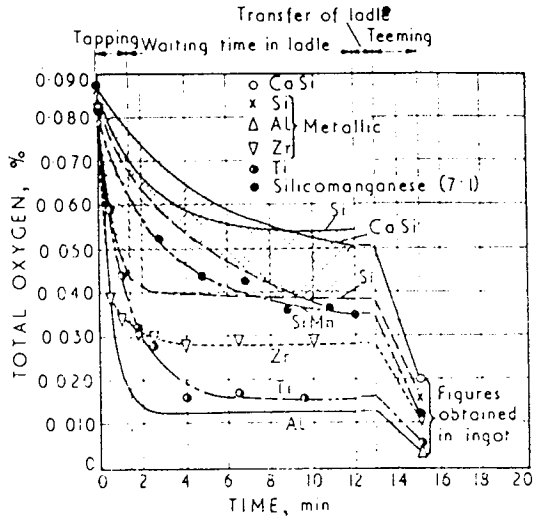

FIG.13 : Change in total oxygen content after addition of different deoxidizers (20).

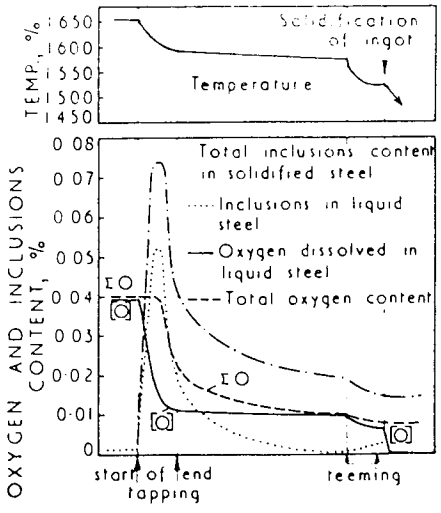

FIG.14 : Schematic representation of deoxidation in the ladle (20).

From this initial study four basic stages of deoxidation are now recognised (25,62,64,68);

i) Solution of the deoxidising agent in the bath

ii) The nucleation of deoxidation products

iii) Growth of nuclei

iv) The elimination of inclusions.

These factors have subsequently been studied individually and collectively on a laboratory scale and during commerical practice, a number of reviews appearing, as development and understanding has progressed (16,20,25,26,62,65,66,67).

The majority of early investigations were concerned with the phenomena leading to primary deoxidation, as the formation of inclusions in the melt meant that they had the opportunity to escape and hence improve the steel cleanness. However, many of these phenomena are equally relevant (when the thermodynamic requirements have been satisfied) to sulphide formation and separation during ladle metallurgy. The following section discusses kinetic factors which are significant in this practice.

2.1.2.0 MELT ADDITIONS

To reduce the amounts of oxygen and sulphur in liquid steel, intimate contact between the reacting elements is required. The authors, who have studied the processes of deoxidation and desulphurisation are in agreement that after the addition of the deoxidant and desulphuriser it is the solution and mixing steps which limit inclusion formation (62,67,68).

OLETTE et al (69) in a study of the deoxidation of liquid iron by aluminium found that additions of liquid aluminium resulted in a considerably quicker reduction in the soluble oxygen content of the steel compared to a solid addition. The slower reaction of solid aluminium was

considered to be caused by the formation of a layer rich in small alumina inclusions adjacent to the dissolving solid, holding back the diffusion of aluminium and thus restricting homogenisation (68).

Investigations by ABRATIS and LANGHAMMER (70) found that deep injection of aluminium powder resulted in improved deoxidation. They explained that as aluminium has a low density, it tends to float after addition, and remain upon the surface of the molten steel, where atmospheric oxidation may take place reducing its yield. The overall performance was found to be dependent upon particle size and gas flow rate.

GUTHRIE et al (71) have made similar observations by investigating the rate of solution and buoyancy effects of deoxidants fired into quiescent steel baths at various velocities and particle sizes. They found that low density deoxidants such as aluminium can refloat before complete dissolution even when projected at very high velocities.

KUSAKAWA and SHIOHARA (72) have experimented with additions of solid and liquid aluminium, silicon and calcium silicide into quiescent molten iron baths. They draw similar conclusions to OLETTE et al (69) regarding the additions of solid and liquid aluminium, explaining that a heat loss occurs upon the addition of solid aluminium, resulting in convection currents leading to the diffusion and concentration of aluminium in these areas (Fig.15). Whereas for liquid additions this does not occur and homogenisation was simply achieved by diffusion. For calcium silicide on the other hand, transportation into the molten iron was found to be caused by the explosive nature of the addition.

In commercial practice a complex situation arises due to the variation in temperature and flow patterns found in different ladle systems. A recent article on a new method for refining of molten steel in the ladle, known

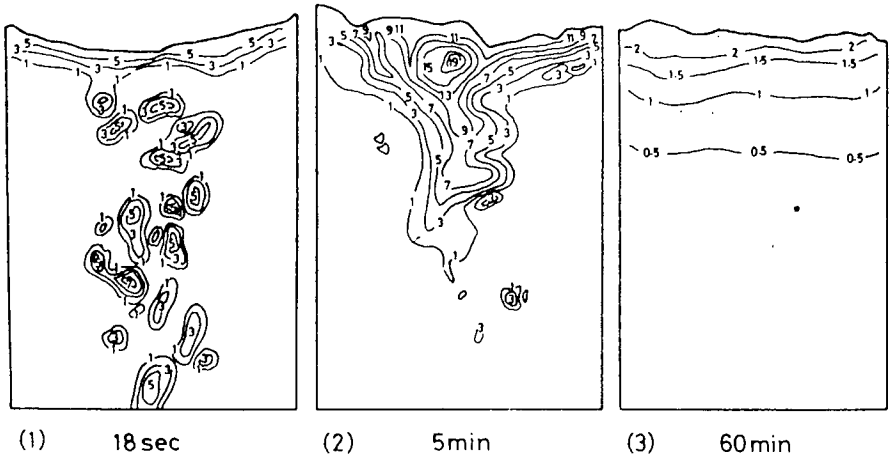

FIG.15 : Changes in the iso-concentration curves of aluminium in the specimen with time (solid addition) (72) .

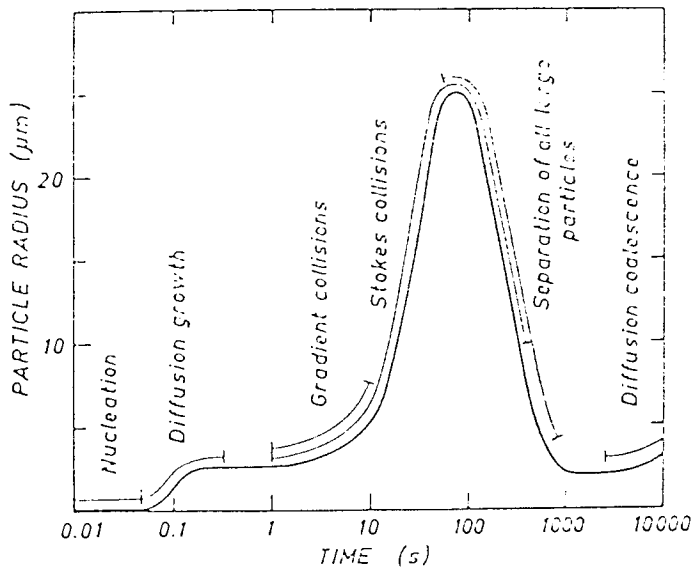

FIG.16 : Characteristic dimensions of silica particles during deoxidation (77) .

as the pulsating mixing process (PM) by FUJII et al (73) compares the effectiveness of this process, in deoxidising steel with aluminium, to established methods. They conclude that for deoxidation and trimming operations the PM process is much superior to argon bubbling and equal to the RH or DH vacuum methods. This result highlights the importance of stirring intensity upon the effectiveness of these processes.

2.1.2.1 NUCLEATION OF INCLUSIONS

A number of studies have been undertaken to determine the factors controlling the nucleation of inclusions in steel, often in connection with the theory of homogeneous nucleation (25,62,72,74 ,75).

VON BOGDANDY (74) in his initial work developed experimental procedures to determine the degree of supersaturation required to produce nucleation. Difficulties were found, however, in accurately measuring values of interfacial energy between the melt and the reaction product (75) and also interference by heterogeneous nucleation could never be ruled out (61).

Nevertheless, estimates of the supersaturation required to produce homogeneous nucleation have been made for several important deoxidiers. The supersaturation values are defined by the ratio (62),

$$a = \frac{K\ EFFECTIVE}{K\ EQUILIBRIUM} \qquad \ldots\ldots 17$$

K EFFECTIVE is the measured and K EQUILIBRIUM is the equilibrium constant for the reaction;

$$(M)^X + (O)^Y = MxOy \qquad \ldots\ldots 18$$

GRETHEN and PHILIPPE (62) report the following supersaturation values from the literature;

Zr: $aZrO_2 = 4.10^8$

Al: $10^4 < a\ Al_2O_3 < 10^7$

Ti: $aTiO_2 = 10^3$

The present understanding of the nucleation process may be summarised as follows:

i) Homogeneous nucleation is possible for strong deoxidisers, such as those given above, particularly where high levels of supersaturation occur, e.g. at high local concentrations near dissolving deoxidants, by solute rejection during solidification and by atmospheric oxidation during tapping and teeming (64).

ii) Heterogeneous nucleation will predominate in industrial practice due to the presence of substrates already in the melt and oxide particles present in the deoxidation alloys i.e. the level of supersaturation will always be less than that required for homogeneous nucleation (61) and,

iii) The interfacial tension between the melt and the nucleating phase is reported to be probably as important as the free energy change for nucleation (76),

$$\Delta G^*_N = \frac{16\ \Pi\ \gamma^3}{3\ (\Delta Gv)^2} \qquad \ldots\ldots 19$$

ΔG^*_N = free energy of formation of a nucleus capable of growth.

γ = melt/nucleus interfacial energy

ΔG_v = free energy change due to the transition of a molecule from the melt to the nucleus.

Particularly where surface active elements e.g. sulphur (61) are present in iron, which lower its surface tension, (See Fig.20).

Finally, GRETHEN and PHILIPPE (62) comment that nucleation is promoted by homogenisation, mixing areas of high oxygen content with areas of high deoxidant, and the nucleation stage effectively terminates when the distribution of deoxidant and oxygen in the melt no longer ensures the necessary supersaturation.

2.1.2.2 INCLUSION GROWTH

Several mechanisms have been proposed as contributing to inclusions growth. The initial stages are thought to be diffusion controlled (26,17) whilst growth by collisions is believed to be responsible once the majority of oxygen has been fixed by the deoxidant (17,68,77). Other processes such as BROWNIAN motion and OSTWALD ripening have also been considered (17,64,72), but have been discounted on account of their slow reaction rates.

An investigation by LINDBORG and TORSSELL (77) studied the growth and separation of silica particles in liquid iron. Fig.16 shows a schematic representation based upon their findings. They concluded that diffusional processes of growth cease to contribute significantly to the increase in inclusion size within a second, when the inclusion radius reaches approximately 2μm; subsequent growth to sizes greater than 20μm is attributed to collisions, owing to movements in the bath and differences in the rate of ascent.

Similar results have been obtained by GATELLIER and OLETTE (68) for both silicon and aluminium deoxidation of 1kg laboratory melts of liquid iron. In these experiments, however, the soluble oxygen content of the melt was monitored continuously with an oxygen probe. Their results are

presented in terms of total oxygen, soluble oxygen and oxygen present as inclusions versus time (Fig.17 and 18) and inclusion size distribution with time (Fig.19). These results show that soluble oxygen levels are fixed within seconds and total oxygen levels become constant after about 15 minutes. However, the inclusion size distributions differ for the two deoxidants, alumina inclusions appear to have a constant size distribution whereas the silicon inclusions grow in size initially then become smaller again as deoxidation becomes complete.

This suggested to GATELLIER and OLETTE (68) that two different separation mechanisms were occurring and appeared to be supported by calculations of inclusion separation rates made on the basis of STOKE's law. The larger silica inclusions which were believed to occur by coalescence, were able to separate from the melt, theoretically, within the practical times recorded, whereas, the smaller alumina inclusions (3 to 4 μm) were calculated to have an escape velocity of 2cm/hour which did not agree with the levels of total oxygen recorded after fifteen minutes. This anomaly was resolved when successive microsections of the aluminium killed steel were made, and it was discovered that clusters of connected alumina inclusions existed within the steel. These clusters, which it was believed formed by collision, were then of sufficient size to separate out from the melt within the times recorded. The apparent difference in separation was, therefore, due to the different inclusion morphologies. In both cases growth occurred, however, alumina clusters formed as a result of collisions and sintering of solid alumina particles whereas silica inclusions remained spherical as they formed in the liquid state in the melt. The morphology and growth of alumina inclusions has since been well documented in the literature (78,79), and similar growth mechanisms have also been observed for solid calcium aluminates ($CaO.6Al_2O_3$) (79).

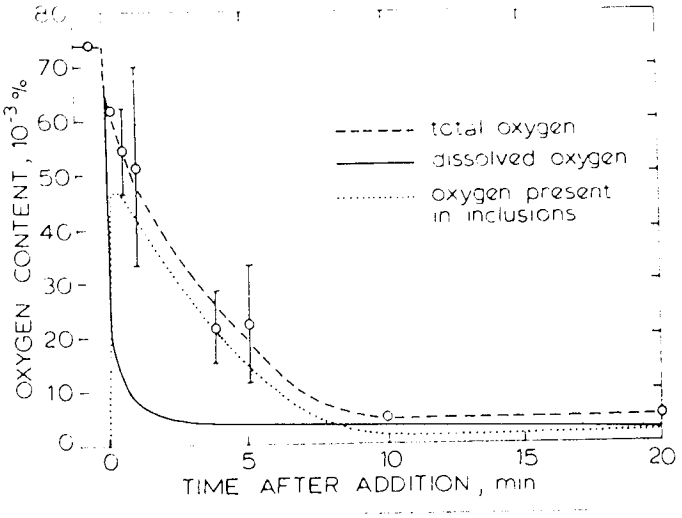

FIG.17 : Deoxidation by aluminium at 1600°C (68) .

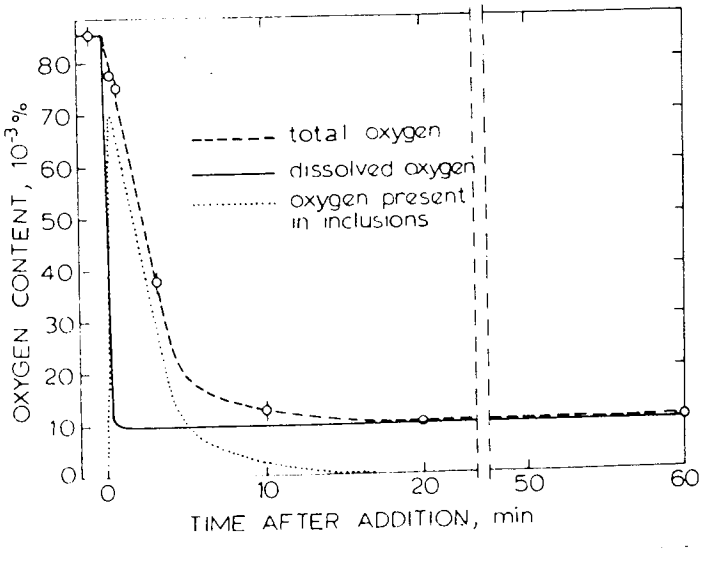

FIG.18 : Deoxidation by silicon at 1600°C (68) .

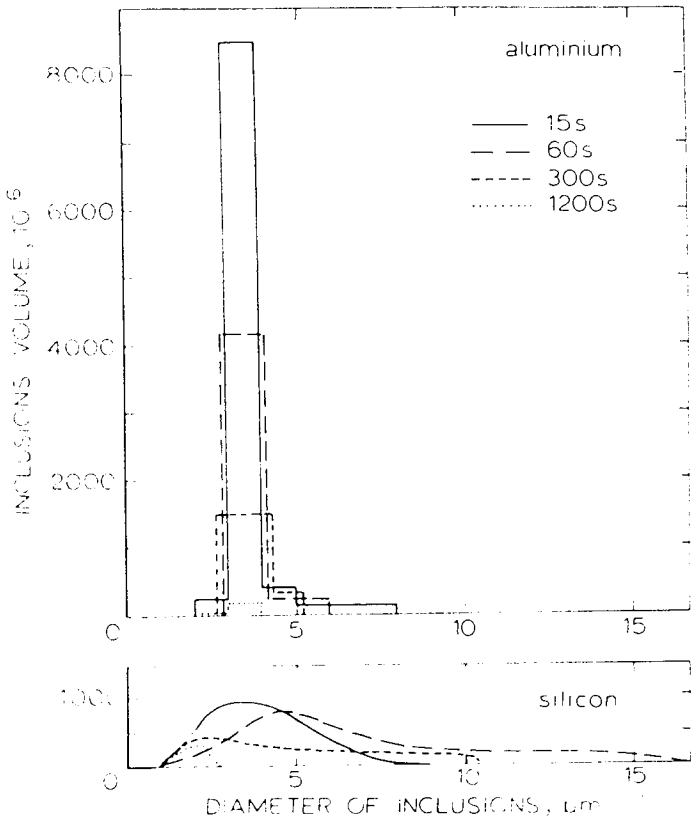

a aluminium; *b* silicon

FIG.19 : Size distribution of inclusions during a deoxidation run (68) .

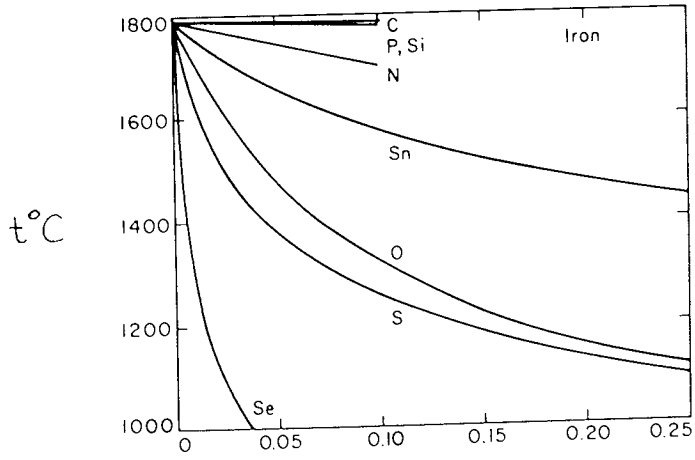

FIG.20 : Effect of solutes on the surface tension of liquid iron at 1550°C (17) .

Prompted by these findings, investigations were subsequently carried out to ascertain the important phenomena promoting inclusion growth by collision (64,80,81). From these studies it became clear that several factors were involved; the interfacial tension between the inclusion and the melt, the viscosity of liquid inclusions, and the agitation of the melt (62). These factors are discussed in the following section on separation as they have a controlling influence on this process also.

2.1.2.3 THE SEPARATION OF INCLUSIONS

In laboratory tests and industrial practice investigators have often reported that stirring greatly improved the rate of deoxidation (20,66,73,77), and this has similarly been found to be the case for ladle desulphurisation (31,82,85) (See Fig.12 for example) (57). However, as the soluble oxygen content of deoxidised steels was found to be quickly fixed (see Fig.14 and 17 for example) (20,68) it became clear that it was the physical separation of the resulting inclusions which dictated the total oxygen concentration in the final steel. Hence, stirring must have a significant effect upon this stage of the process. This is indeed the opinion of TURKDOGAN (20) who states that the slow step in deoxidation is the flotation of inclusions that are less than 20μm in diameter and that rapid inclusion growth and flotation is enhanced by stirring of the melt, a view which has also been expressed by other authors (18,66,68).

To determine the factors influencing the separation of different types of deoxidant earlier studies considered the flotation of inclusions from quiescent melts by STOKE's law (62). For this case flotation is controlled by inclusion size and density, which in turn is influenced by the density and viscosity of the steel. Although some model systems were found to show a reasonable agreement between experiment and theory (62,69) a number of anomalies were recognised. PARKER (64) discussed

some of these in a review article noting the following objections; similar separation rates have been observed for different inclusion morphologies and inclusions with dissimilar densities and also large liquid inclusions (which need not be spherical) may break up during ascent decreasing their capacity for separation by flotation. He concluded that it is difficult to imagine a real deoxidation situation in which the steel is completely quiescent. In industrial ladle practices this is undeniably true, hence, although separation rates in quiescent baths may be influenced by inclusion size and density, during ladle practice, when stirring is often encouraged, other factors must also be responsible.

TORSSELL and OLETTE (83) have investigated the influence of stirring upon the deoxidation of iron with Al and Si. In a series of experiments, they varied the speed of an alumina propeller situated in the centre of a crucible containing the molten iron. Their results were presented using an analogy with the decay of radio active elements to determine the time at which half of the oxygen had been removed (Table 2.3). From these it is clear that as the stirring intensity increased so did the deoxidation rate and that this had a greater influence upon the aluminium deoxidised melt than the silicon one. PLOCKINGER (20) had observed similar results for deoxidation, by various elements, in commercial practice (See Fig.13). GATELLIER and OLETTE (68) commenting on the results above also noted that under industrial conditions electromagnetic stirring and inert gas bubbling produced a faster decrease in oxygen. However, in addition they suggested that if the stirring was too vigorous, some of the rising inclusions could be submitted to a physical reversion into the melt and in this case the stirring effect would not be advantageous.

Another factor which has been considered important to mechanisms of inclusion growth by collision and the physical separation of inclusions

TABLE 2.3 Influence of stirring upon deoxidation (68) .

	SILICON			ALUMINIUM		
Mechanical stirring, rev/min	Period,s Mean value	Standard deviation	Number of runs	Period,s Mean value	Standard deviation	Number of runs
without	128	14	4	119	34	17
50 - 60	120	10	2	63	7	2
320 - 550	58	16	3	42	2	1

from the bath, is surface tension. PLOCKINGER (20) felt that this might play a role in the separation of inclusions and LINDBORG and TORSSELL (77) stated that a high interfacial tension between the inclusion phase and melt would encourage the growth of inclusions by collisions.

This aspect has been throughly investigated by KOZAKEVITCH and OLETTE (80). These authors considered the ability of solid inclusions to coalesce, emerge at a slag-metal interface and a metal-gas interface, interms of the interfacial energy and the contact angle between the inclusion and the melt. If the free surface energy of the system i.e. melt and inclusion can be reduced by the formation of an interface e.g. inclusion-inclusion, which produces an overall decrease in the metal-inclusion interface, then there is a certain energy per contact unit area necessary to separate them, KOZAKEVITCH and OLETTE presented the following relationship for cohesion between two inclusions:

$$\Delta G = 2 (\gamma s - \gamma sm) = 2\gamma m \cos \theta \qquad \ldots\ldots 20$$

γm = surface tension of the melt

γs = surface tension of the solid oxide

γsm = interfacial tension of the solid oxide/melt

θ = contact angle.

They concluded that contact will be maintained if ΔG remains negative which is brought about by $\gamma s < \gamma sm$ or $\theta > 90$. Their experimental investigations revealed a number of important results: alumina was found to have a contact angle of 140° , this explained its ability to form clusters and its superior rate of separation compared to silica (contact angle of 115°) in agitated baths (68). The conditions of the melt were also found to influence separation rates, low oxygen and sulphur in solution increasing the melt surface tension and thus facilitating removal. Fig.20 from TURKDOGAN (49) shows the effect of various elements

upon the surface tension of iron at 1550°C . Additionally a slag cover was determined to be always beneficial for inclusion separation even if the particles did not dissolve in it and the removal of inclusions by attachment to refractory was also considered important.

Later studies have confirmed the principles defined above (16,32,76,78). PARKER (64) noted that for liquid inclusions, coalescence would be favoured by a low inclusion viscosity as well as high interfacial energy between the inclusion and the melt. A more recent review by RIBOUD and GATELLIER (16) summarises the important factors affecting liquid and solid inclusion separation as follows; " for large liquid inclusions emersion, although always thermodynamically possible, may present a slow stage and could be retarded by high oxygen or sulphur activities; in these cases, the probability of emersion for an inclusion brought temporarily to an interface could decrease"; and for solid inclusions, "the value of their wetting angle by metal is very important. The angle should be larger than 90°to make cluster formation possible and it should also be as large as possible to increase the relative proportion of the emersed part of the clusters (Fig.21)". Here again they commented that high oxygen levels are unfavourable for the emersion of alumina or spinel inclusions, particularly when the manganese level of the steel is high. They concluded that these factors tend to confirm that it is easier to clean an already low sulphur killed steel and, therefore, reoxidation of any description would be detrimental to steel cleanliness (See Fig.20).

LUYCKX (66) has considered the mechanisms of inclusion separation in carbon steel ladles. He comments that the separation of inclusions is influenced (directly or indirectly) by i) flotation, which is only dominant for liquid inclusions, ii) an open meniscus and iii) slag or refractory surfaces, the actual mechanism being overwhelmingly controlled

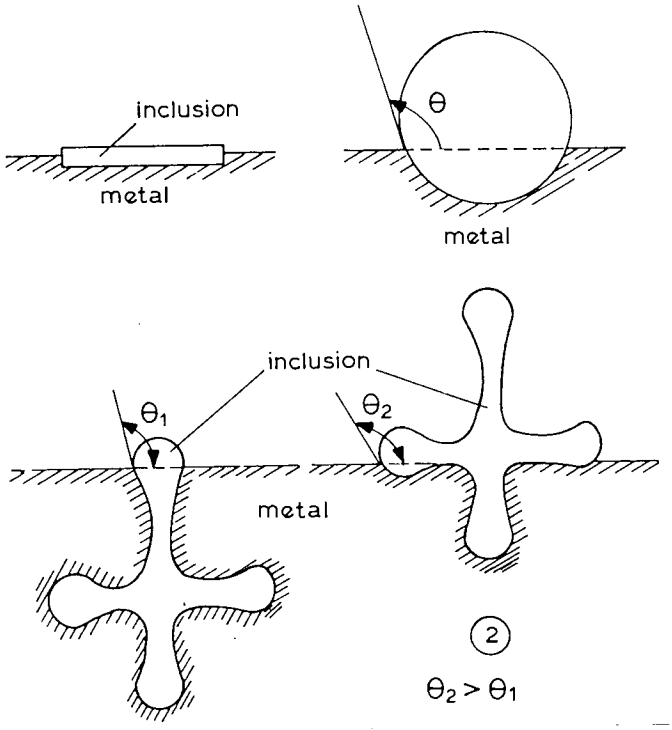

FIG.21 : Stable position of emersion for solid inclusions (16).

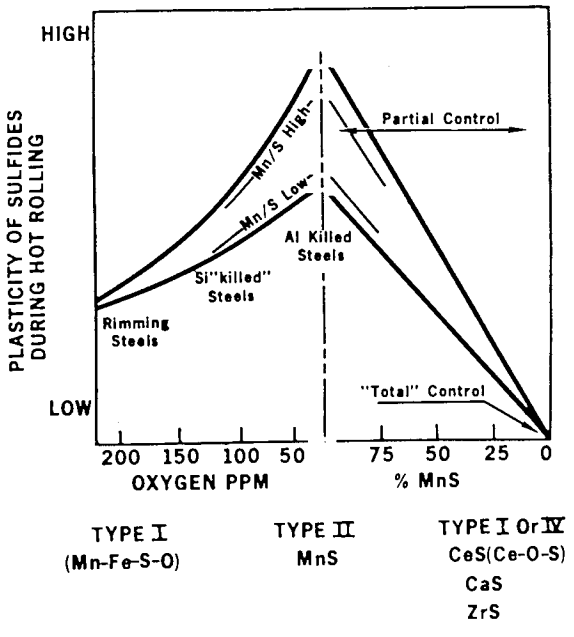

FIG.22 : Effect of oxygen content, manganese to sulphur ratio and sulphide modifier on the plasticity of sulphides during hot rolling (84) .

by the surface tension of the inclusion, itself a function of chemistry and temperature. For the production of aluminium killed calcium treated steels he suggests that solid inclusions and refractories e.g. high alumina, are the most effective means of promoting good separation, whereas liquid inclusions are to be avoided unless a strong chemical affinity between the inclusion and slag/refractory exists. He considered that stirring, by either injection or a porous plug supplying argon, would always be beneficial.

Many other authors have also shown the benefits of refractory, stable ladle linings and argon stirring/calcium silicide injection in the production of clean, aluminium killed low sulphur steels (19,31,34,40,41). The importance of stirring to increase inclusion separation, and generally homogenise the melt during steelmaking is reflected by the numerous conferences (SCANINJECT e.g. (34)) and individual publications (34,40,41,54,56,58) which have appeared on the subject. Details of the various models developed to quantify the process are, however, beyond the scope of this review.

2.1.3.0 INCLUSION SHAPE CONTROL

Deoxidation and desulphurisation are not only important for the control of oxygen and sulphur levels in steel but also they determine the inclusion characteristics in the cast steel e.g.distribution, size, morphology and composition, and after deformation, the shape of the inclusion in the wrought steel, which may affect its resulting mechanical properties (29).

To extend this principle and adapt inclusion characteristics further, the concept of inclusion shape control has been introduced. Originally this practice was aimed at reducing the anistropy of toughness resulting from the elongation of manganese sulphide inclusions in rolled plate without costly desulphurisation (2,85). However, it has subsequently developed

to encompass the control of both oxide and sulphide inclusions (4,24,55,79,94).

An early investigation by LUYCKX et al (84) into sulphide shape control of Al-killed HSLA steels, reported that globular inclusions which do not deform upon rolling can be produced by the control of the steel chemistry. They proposed that this could be accomplished by additions of an element which forms a high melting point sulphide more stable than manganese sulphide and not as readily deformable at hot rolling temperatures. As the concentration of the sulphide modifier increased, so they believed, the amount of elongated MnS formed would gradually decrease until the elongated sulphides became completely replaced by more stable, globular or blocky inclusions. With this explanation they presented a diagram depicting the effect of the Mn/S ratio and oxygen level in the steel upon the inclusion morphology and plasticity during hot rolling showing the resulting reduction of plasticity caused by sulphide shape control (Fig.22). The various elements considered as possible candidates for sulphide shape control were similarly presented diagramatically (Fig.23). The rare earth metals (REM) and calcium were determined to have the greatest potential and a series of experimental melts were made containing sulphur between 0.02 -0.025% to assess the effectiveness of these elements. The results of the calcium experiments were unsatisfactory. This was attributed to its low solubility in steel, and high vapour pressure, which resulted in much of the addition boiling off before it could react. However, the REM when added in such an amount that the cerium (Ce) to sulphur ratio was 1.5 in the final product, resulted in "exclusively" globular rare earth (RE) sulphides, improving the transverse shelf energy almost to that of the longitudinal.

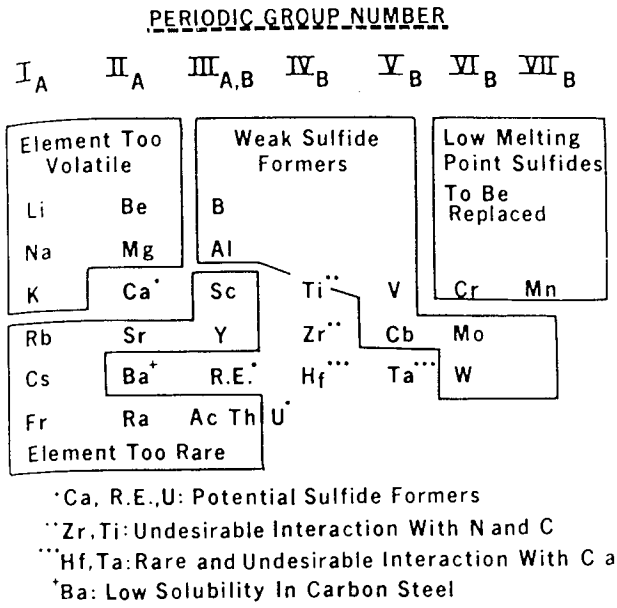

FIG.23 : Potential sulphide formers for HSLA steels (84) .

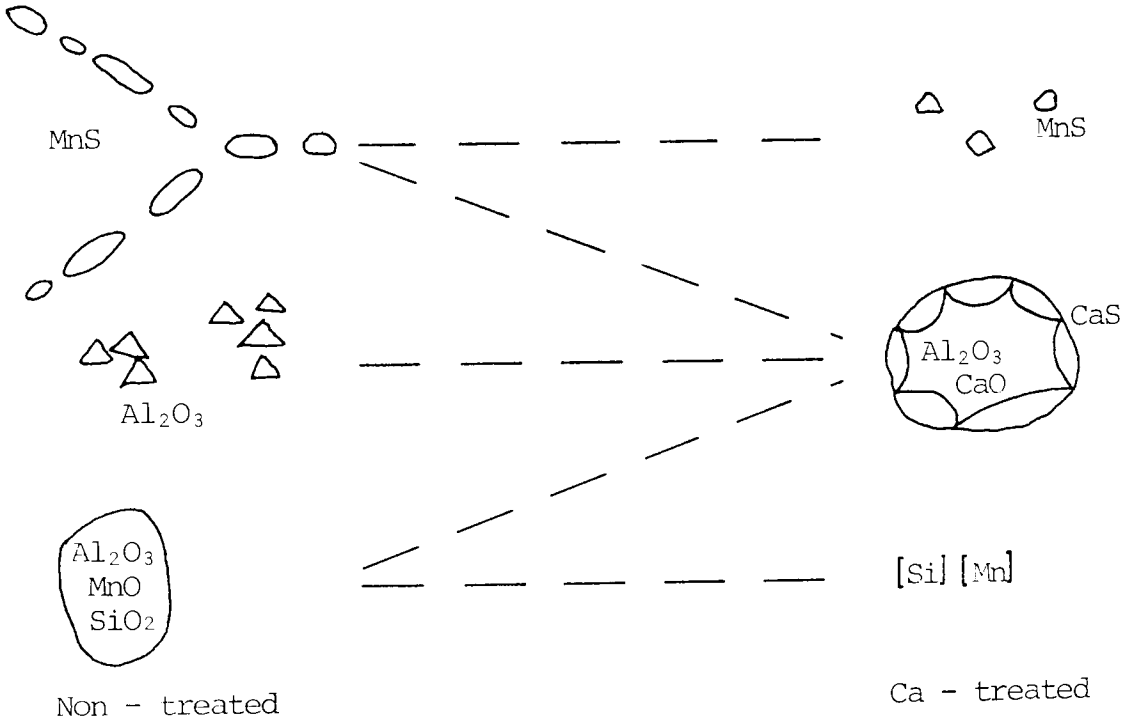

FIG.24 : Modification of inclusions with calcium treatment (55) .

This study highlighted the elements which had the basic property requirements necessary to produce sulphide shape control (Fig.23) and numerous investigators have since carried out further studies into the suitability of calcium (4, 6,37,54,91,92,107), magnesium (31,50,53,90,91), titanium (94,101,107), zirconium (94,96,97) and REM (31,50,53,92,93,103,105,106) and also strontium and barium (50,111). Additionally reviews by PICKERING (4,99) and more recently WILSON and McLEAN (109) have appeared upon inclusion shape control. The latter authors, in agreement with LUYCKX et al (84), considered that sulphide shape control was achieved by the formation of a sulphide solution, containing both manganese and the additive, which produces an inclusion which is non-deformable during hot rolling. However, they also proposed that the formation of a non-metallic inclusion, consisting of a sulphide or oxysulphide of the inclusion controlling element was also responsible. This point has been confirmed in subsequent work (31,36,39,50,51). KIESSLING and LANGE (19) and PICKERING (28) have produced comprehensive studies upon the physical properties, and morphology of inclusions of various compositions found in steel, and the thermodynamic aspects of elements used for inclusion shape control has been discussed by TURKDOGAN (112) and GSCHNEIDNER (113). The physico-chemical properties of the elements commonly used for inclusions shape control are contained within TABLE 2.2 after ABRATIS and LANGHAMMER (70).

The principal element used for inclusion shape control of Al-killed HSLA steel is now calcium. This has occurred for a number of reasons. Zirconium and titanium although found able to control inclusion shape (16,96,97,101,107) have proved to be unsuitable for use in HSLA steels. This is due to their strong affinity for nitrogen and carbon (29), which has been found to have an adverse effect interfering with the other microalloying elements added to control the steel grain size and strength eg. Nb and V (4,29,84,86,94,99,101). Elements such as strontium and

barium have been rejected on the grounds of cost and for health reasons (84). Magnesium although reported to be as successful as calcium in producing sulphide shape control (53,90,95) is not used commercially in HSLA steel production. This, basically, is due to the difficulty found in making the addition, magnesium having a vapour pressure higher than calcium (Mg=17atms Ca=1.8atms 1600° C) (50) and is hence even more volatile. Finally, REM are frequently reported in the literature (31,50,85,92,103) as elements used for inclusion shape control. However, calcium is now used in preference as it is fully integrated with ladle practice i.e. lime alumina slag and calcium phases have been found to separate more effectively than the equivalent RE inclusions as they have a lower density. This situation has only arisen since the introduction of injection metallurgy which allows the successful addition of calcium (56,6). In addition calcium has the advantage of controlling the morphology of oxide inclusions in the ladle, liquid calcium aluminates being produced at steelmaking temperatures (See Fig.8) (a factor which prevents the blockage of continuous casting nozzles (50,55,79), otherwise a problem with ordinary Al killed steels).

PICKERING (4,99) reports that in heavily Al-killed steels alumina inclusions (Al_2O_3) may form as clusters or dendritic masses which may remain in the solidified ingot. These are virtually underformable at all temperatures and tend to fracture and form elongated discontinuous stringers during hot working. When present in sufficient quantity they may cause severe anisotropy of ductility and Charpy shelf energy. These observations have been confirmed by several authors (36,50,78). The addition of calcium results in the transformation of the alumina clusters to globular calcium aluminates. When the calcium addition is sufficient to produce a liquid phase (between 40 and 60% CaO) then oxide shape control is achieved (79). When sulphide shape control is being undertaken with calcium, oxide shape control always occurs as well, due to the greater affinity of calcium for oxygen (26,24) (See section 2.1.2).

The effect of calcium upon inclusion shape is shown schematically in Fig.24 from TAHTINEN et al, (55) and numerous authors (24,36,37,39,55,91,104) have presented X-ray maps using electron probe micro-analysis (EPMA) to show the relative concentrations of elements and their distribution within inclusions in steels which have been injected with CaSi. Fig.25 from IKEDA et al (39) shows typical examples of inclusions found in steel slabs, which contained progressively higher ratios of calcium to oxygen and sulphur (from 25a lowest to 25d highest).

From the analysis of inclusion compositions, several authors have determined the ratio of Ca/S required to produce "perfect" inclusion shape control. A study by SANGBONGI et al (92,93,110) has shown that for Al-killed steels, complete sulphide transformation into globular inclusions can be obtained when the quantity of metallic elements (Ca or REM) that are not combined as oxides is sufficient to react with more than 40% of dissolved sulphur at the start of solidification (Fig.26). They also showed the effect of Ca upon the hardness of MnS inclusions (Fig.27), 5% Ca in substitutional solution will increase the hardness of the MnS considerably.

Similar results to those obtained by SANGBONGI et al (92,93,110) have been reported by IINO et al (115), TAIRA et al (114) and IKEDA et al (39). The latter authors have reviewed much of the earlier literature dealing with inclusion shape control by calcium and have themselves undertaken a comprehensive investigation into the mechanism of inclusion shape control in a number of continuously cast billets and ingot slabs used for the production of linepipe. Fig.25 is from their work and shows typical inclusion compositions that have arisen depending upon the content of Ca, O and S in the melt and during solidification, and Fig 25a shows a comparison between two heats, where the higher oxygen level in heat 1 caused the dirtier steel and also the formation of MnS inclusions

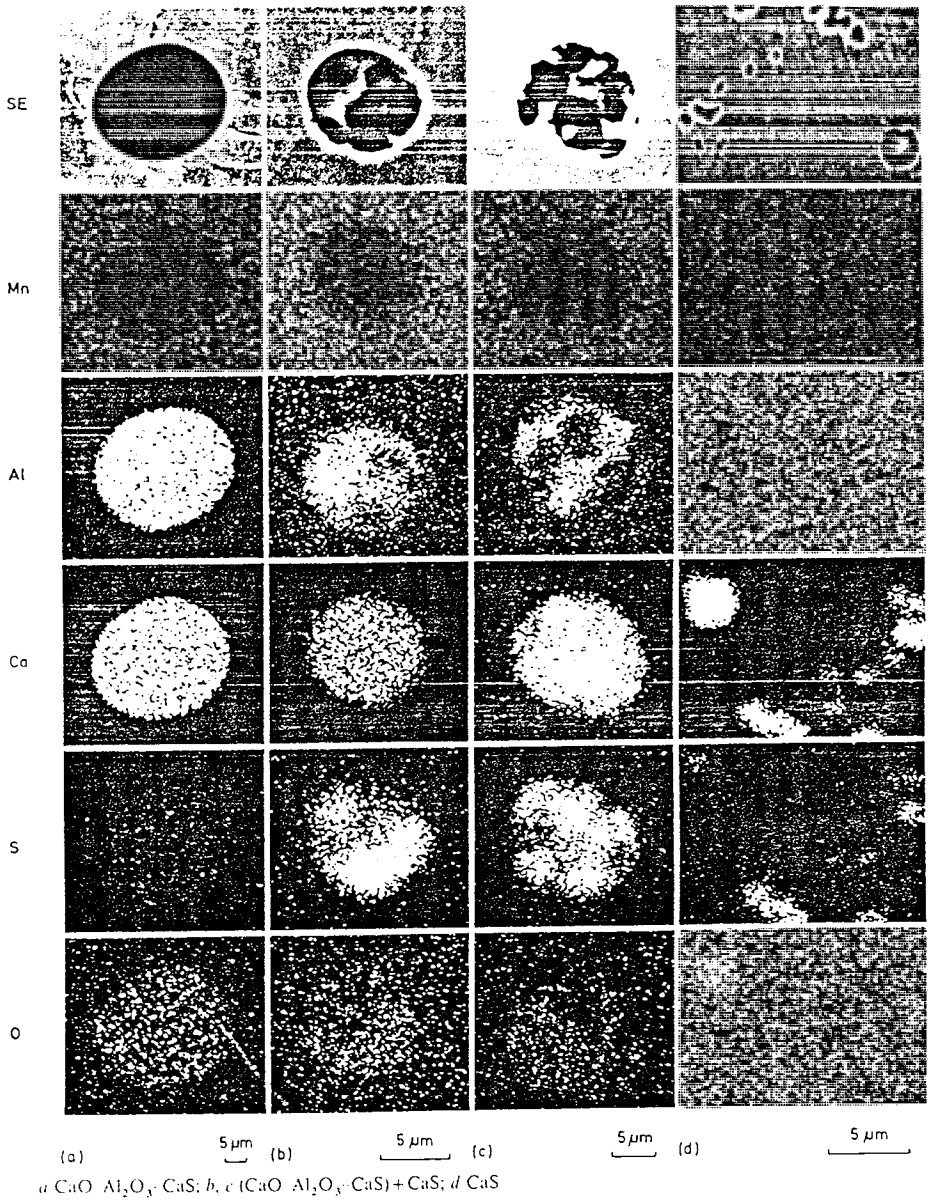

a CaO Al_2O_3-CaS; *b*, *c* (CaO Al_2O_3-CaS)+CaS; *d* CaS

FIG.25 : EPMA images of inclusions in Ca treated steel (39) .

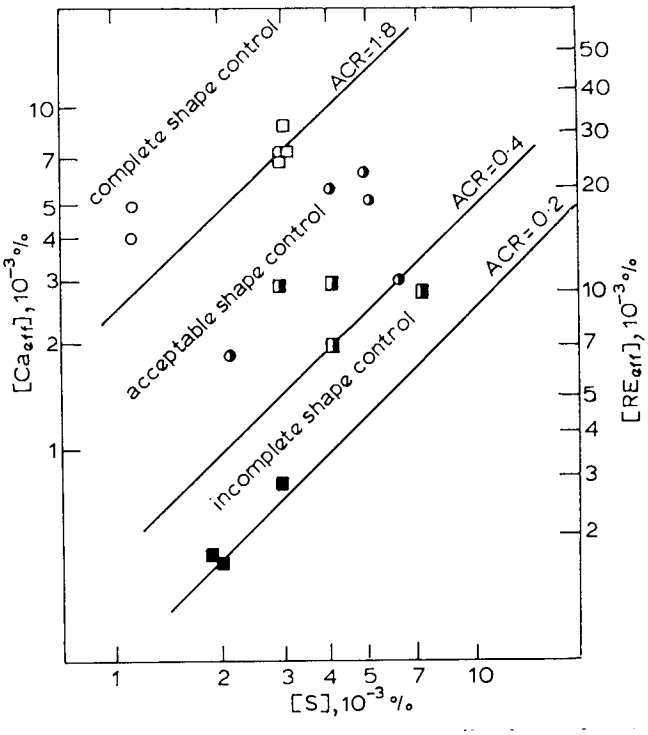

FIG.26 ; Control of morphology and distribution of sulphides in HSLA steel by adding calcium and rare earth elements (16) .

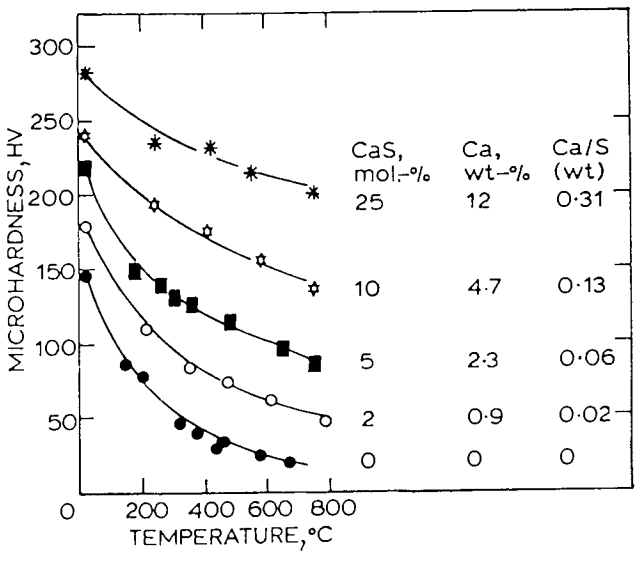

FIG. 27 : Effect of temperature and sulphide composition on microhardness of (CaMn)S solid solutions (16) .

towards the upper surface of the slab. In this case the calcium was combined with oxygen and not sulphur and this is why it appears to be present at a greater concentration than in heat 2; consequently upon solidification with the attendant segregation of manganese and sulphur the formation of MnS has occurred and inclusion shape control was not obtained. Table 2.4 outlines the mechanisms by which they discuss the formation of inclusions in calcium treated steels.

Similarly to SANGBONGI et al (92,93,110), IKEDA et al (39) have found that the amount of calcium in solution at the time of solidification is the critical factor in preventing the precipitation of MnS inclusions from the final liquid to solidify. The correct amount of calcium added ensuring an even distribution of undeformable CaS inclusions in the steel.

TABLE 2.4 Formation mechanism of inclusions in Ca-treated steel (39).

Amount of dissolved Ca	In molten steel	During solid ification
Small (< 1ppm)	$\alpha_{CaS} < 1$ $CaO-Al_2O_3-CaS$ monophase	Ca+S → CaS (in $CaO-Al_2O_3$ CaS) remaining S → MnS or dissolves into iron
Medium (several ppm)	$\alpha_{CaS} = 1$ $CaO-Al_2O_3$CaS + CaS dual-phase	Ca+S → CaS (deposited on $CaO-Al_2O_3$ CaS or precipitates separately)
Large (≃ 10 ppm)	$\alpha_{CaS}= 1$ $CaO(-Al_2O_3)-CaS$ +CaS dual phase	Ca+S → CaS (precipitates alone)

2.2 HYDROGEN INDUCED STEPWISE CRACKING IN LINEPIPE STEELS

INTRODUCTION

The detrimental effect of hydrogen upon the mechanical properties of steel has been recognised for some considerable time e.g. JOHNSON 1875 (116), and in a recent review on the basic aspects of the problems of hydrogen, INTERRANTE (117) comments that there are no highly favourable effects of hydrogen in steel.

The degree of complexity involved in the determination of the effect of hydrogen in steel has been noted by several authors, and BEACHEM (118) comments that "a coherent over-all view of hydrogen damage and its mechanisms continues to remain elusive for several reasons, not the least of which is the number of variables that contribute directly or indirectly to such damage". This view is held by HIRTH (119) who reports that reviews on the subject have been restricted to a discussion from a particular stand point, such as microstructural effects, due to the overwhelming amount of literature on hydrogen effects in steel.

In this section the literature reviewed is primarily concerned with hydrogen stepwise cracking (SWC) in linepipe steels and includes a detailed appraisal of the role that non-metallic inclusions play in this mechanism of hydrogen damage, also a brief review of the role of inclusions in ductile fracture by micro-void coalescence is made.

2.2.1 SERVICE FAILURES

Hydrogen related failures of linepipe, operated in sour environments and resulting in SWC, have been recorded in the literature from as early as 1954 (120). More recently MOORE and WARGA (7) have reported three service "ruptures" which occurred in spirally welded API 5LX* Grade

*API 5LX - AMERICAN PETROLEUM INSTITUTE SPECIFICATION (121) (number afterwards is the yield strength.)

290MPa (42 Ksi) sour gas transmission lines in 1974. Since then MOORE (122) has outlined a number of failures occurring in wet sour crude oil systems and BIEFNER (123) has reviewed six cases, involving sour oil and gas, which had been previously recorded in the literature.

The circumstances of these failures varied widely as follows; strength levels were between 290 and 450 MPa, outside diameters, wall thickness, operating pressure, external environment, hydrogen sulphide (H_2S) content, other gases (CO_2, CH_4), and steel compositions were all different. However, a common feature in all these failures was either blistering or internal cracking, and investigators who made a microscopic examination of the damaged pipe found that the cracks were consistently associated with inclusions, specifically elongated manganese sulphides (MnS).

2.2.1.1 DEFINITION AND APPEARANCE

Stepwise cracking is defined by BRUNO and HILL (124) as a phenomenon occurring in linepipe steels whereby exposure to an aqueous H_2S environment causes cracks to develop in the pipe along the rolling direction that tend to link across the wall thickness. Cracks along parallel planes in the rolling direction are linked by short transverse cracks to form "steps", Fig.28A shows various types of SWC observed in test specimens. If cracking becomes extensive the effective wall thickness of the pipe will be reduced such that the pipe becomes overstressed leading to leaks or complete rupture. This description forms the basis of a standard being considered by the National Association of Corrosion Engineers (NACE) in combination with the test criteria TM-02-84(125) for determining the SWC susceptibility of linepipe steel. A similar test, know as the B.P. or COTTON test has existed for some time (e.g.see Ref. 7) and is essentially the same. The major

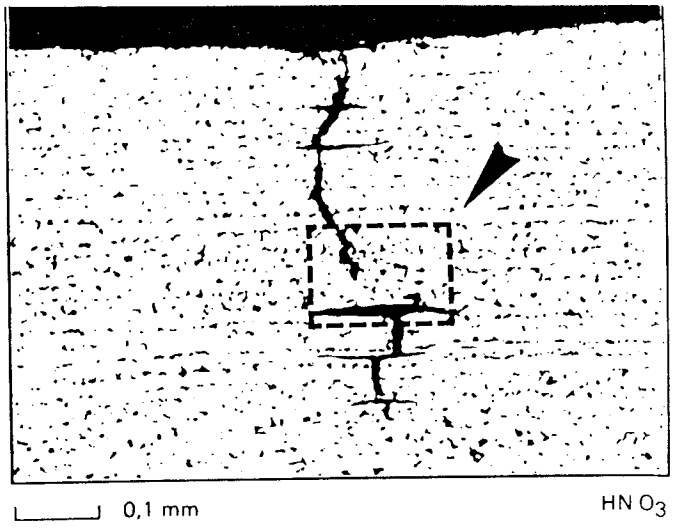

a

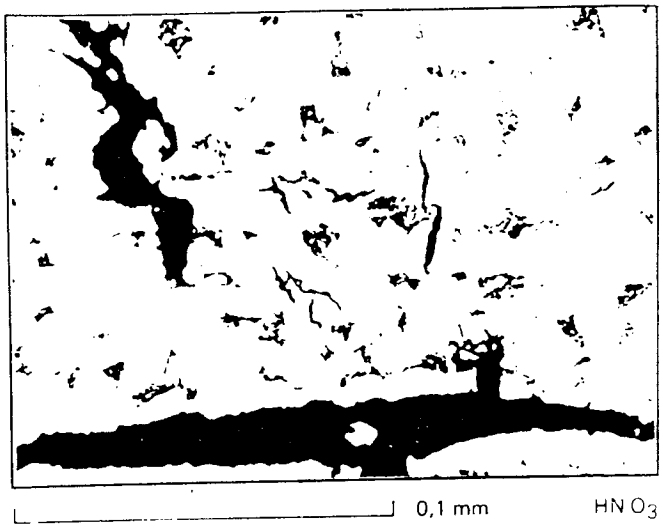

FIG.28B: Stepwise cracking developing in the through-thickness direction (←←←←←tensile stress axis→→→→) (126) .

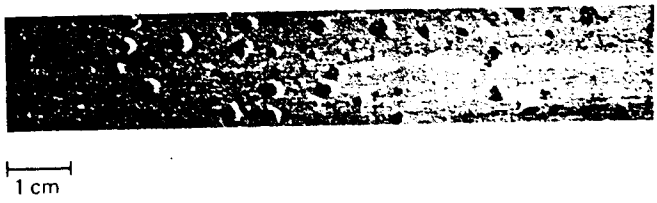

FIG.28C: Example of surface blisters developed after SWC test (126) .

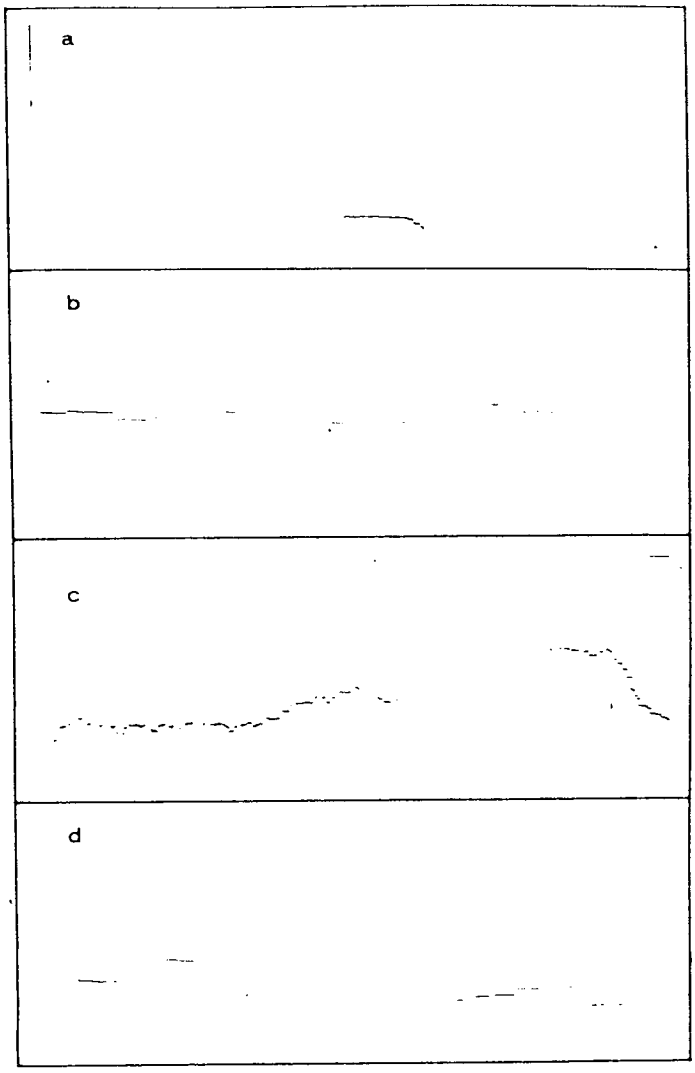

FIG.28A: Various types of stepwise cracks found in test specimens . Unetched 3.5X (124) .

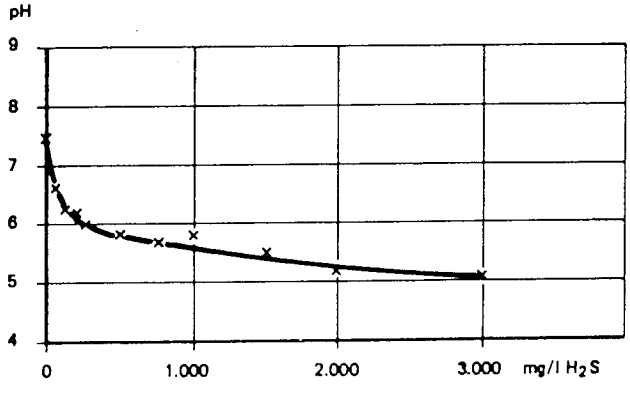

FIG.29 : pH of H_2S containing sea water (126) .

difference between the two tests is the pH level of the solution, which is lower in the NACE test.

Investigators examining SWC in linepipe have used a variety of terms to describe the phenomenon. SWC has alternatively been called; hydrogen induced cracking (HIC), hydrogen induced blister cracking (HIBC), hydrogen induced stepwise cracking (HISC) and type 1 sulphide stress corrosion cracking (SSCC) (123). In this review, to be consistent with the above NACE recommendation cracking due to wet H_2S environments will be termed SWC.

Additionally other forms of damage have been found to occur in pipe subjected to sour conditions. These are; surface blisters (7,124,126,128) and cracks which develop in the through thickness direction of the pipe (8,127,128,129,130,132,133,149), (Fig.28 B and C). The former are considered to be a manifestation of SWC occurring close to the surface of the steel (124,128,132), whereas the latter have only been observed in tests which were carried out under an applied stress, the cracks generally propagating in a direction perpendicular to this stress (126,127,128). This type of crack morphology is regarded as a form of sulphide corrosion cracking (SCC) (134) and has been variously termed in the literature as sulphide stress corrosion cracking (SSCC) (8,133,135), hydrogen induced stress corrosion cracking (HSCC) (126), and sulphide stress cracking (SSC) (123,127,129,130).

To further confuse the issue IINO et al (128,132,137,139) have made no distinctions between cracks whether they occurred in the absence of or under an applied stress, calling them both hydrogen induced cracks i.e. SWC. This again introduces some problems with terminology. Nevertheless one point on which there is common agreement is that the cracking mechanism is a form of hydrogen embrittlement (HE) (128,130,142).

The above situation is clarified further if INTERRANTE's (117) interpretation of SCC is accepted, that is, SCC is caused by anodic dissolution or oxidation whereas HE is caused by the cathodic absorbtion of hydrogen. A similar opinion is held by TROIANO (141). Further, TURN et al (130) reach the conclusion in their study of "SSC" in linepipe steels that corrosion is important only as a source of hydrogen and that the evidence suggests that HE best describes sulphide stress cracking (SSC) of these steels. BIEFNER (123) in his review of SWC in linepipe in sour environments provides the following conclusions as follows; failures by cracking have been observed in linepipe steels under tensile stress in wet H_2S environments, especially when the hardness of the steel was greater than HRC 22 (See NACE standard MR-01-75(1980 REV.) - SULPHIDE STRESS CRACKING RESISTANT MATERIAL FOR OILFIELD EQUIPMENT) (146). When the failure is caused by cracks growing from the surface exposed to the corrosive environment in a direction generally transverse to the applied stress, and sometimes branching, the mechanism is termed SSC. Secondly, some linepipe steels exposed to H_2S environments, whether stressed or unstressed, exhibit internal blisters and delaminations in the rolling plane, often linked by transverse cracks, this is termed SWC.

From these observations it is clear that under an applied stress or not, linepipe steel submitted to a sufficiently hostile sour environment can develop internal cracks, these occur as a result of hydrogen and may propagate in a step-wise manner.

2.2.1.2 ENVIRONMENTAL CONDITIONS

Sour gas or oil, as it is referred to in the literature contains various quantities of hydrogen sulphide (H_2S). Reported levels by MOORE (122) from actual service failures, range from 130 to 350ppm, and evidence from GROENVELD and FESSLER (143) suggests that there is a limiting concentration under which no hydrogen damage will occur. This opinion is

supported by laboratory tests which have found that as the H_2S content increases steels become more susceptible to SWC (144). The NACE standard (14) defines a gas as sour if the H_2S partial pressure exceeds 0.35 kPa.

PARRINI and DE VITO (135) have reported that H_2S may be present in gas as a natural impurity or as a product of the reduction of sulphate ions by bacteria. These organisms normally live in seawater and can be introduced into pipelines either during hydrostatic testing or after water is pumped into submarine gas reservoirs during secondary recovery operations.

In his survey of operational failures MOORE (122) thought it crucial to keep the water, used for hydro-testing, separate from the crude oil, as in his experience failures had been discovered during or soon after. Examination of failed pipe had shown very little general corrosion, however, in his opinion hydrogen cracking occurred due to a critical corrosion rate, which resulted in a critical hydrogen concentration. This he considered could potentially occur when the sour oil came into contact with the residual hydrotest water.

The corrosion of steel in a wet H_2S environment produces cathodic evolution of hydrogen at the steel surface and additionally H_2S has a poisoning effect upon the recombination of hydrogen to its molecular state (142). Hydrogen is released by the reaction (148),

$$H_2S \rightleftarrows H^+ + HS^- \qquad \text{.....22}$$

$$2H^+ \rightleftarrows 2H_{AD} \begin{cases} \rightleftarrows 2H_{AB} & \text{.....23A} \\ \rightleftarrows H_2 & \text{.....23B} \end{cases}$$

$$2HS^- + Fe \rightleftarrows FeS + H_2S + 2e^- \qquad \text{.....24}$$

AB = absorbed

AD = adsorped

The poison effect is believed to be caused by the HS ion, which promotes reaction 23A producing increased hydrogen absorbtion leading to a higher

hydrogen potentials at the steel surface (135,147,148,142).

The rate of hydrogen entry into steels under cathodic polarisation has been reported by ORIANI (149) to be dependent upon many variables, these include; the pH of the solution, its corrosion potential, the chemical composition of the aqueous phase in the near vicinity of the metal and the composition of the metal and of the inclusions in it. He goes on to explain that these all affect the rate of deposition of atomic H upon the steel surface, the rate of recombination of the adsorbed H atoms to form H_2 gas and the rate of the reaction $H_{AD} \rightleftarrows H_{AB}$ transition. The net resultant of these steps determines the rate at which dissolved hydrogen appears at the first subsurface layer of the metal atoms. This rate then determines the hydrogen activity, "a", which sets up the boundary conditions for the diffusion of hydrogen into the bulk metal. A comprehensive review of the environmental factors influencing the SWC susceptibility of linepipe has been made by BIEFNER (123). He found that the pH of the environment and the concentration of H_2S were the main factors affecting the susceptibility of linepipe to SWC. As would be expected, high concentrations of H_2S and low values of pH resulted in an increasing occurrence of SWC. HERBSLEB et al (126) have shown experimentally how the pH of seawater is reduced as the concentration of H_2S is increased (Fig.29).

BIEFNER (123) has also reported that some investigators thought that a threshold H_2S concentration in the environment was necessary for SWC to occur. WILDE et al (150) have considered this point, and determined that the concentration of H_2S may be related to a hydrogen gas fugacity. By a permeation technique they were able to determine, qualitatively, the fugacity of hydrogen generated during corrosion in two solutions of different H_2S concentration. At the same time they carried out SWC cracking tests on a similar steel (GRADE 414 (X60)) in the same solutions. In the test with the high concentration of H_2S (BP. type test

- 2300 - 3500 ppm H_2S) (7) SWC was found to occur in all the steels and the hydrogen fugacity was estimated to be $1.8x10^5$atms, whereas for the lower concentration of H_2S (unspecified) a hydrogen fugacity of $0.8x10^4$ atms was recorded and no SWC was found. In the latter case, there was also a definite decrease in the concentration of absorbed hydrogen. They concluded that the occurrence of SWC was dependent upon the hydrogen input fugacity of the corrosive environment, and that qualitative experiments indicated the existence of a threshold fugacity between 10^4 and 10^5 atms, below which no cracking would initiate.

This is consistent with the work of MOORE (122) above, and PRESSOURYE (155), IINO et al (115) and IKEDA et al (144) who are also of the opinion that a critical hydrogen concentration is responsible for crack initiation, which they believe is dependent upon environmental and metallurgical variables.

2.2.1.3 COMPOSITION AND MICROSTRUCTURAL EFFECTS.

The composition and microstructure of linepipe steel is very much dependent upon property requirements and manufacturing philosophy in addition to specific requirements adopted to limit the occurrence of SWC (1,2,10). An example of the present (1984) range of compositions for steels with fine ferrite/pearlite microstructures is given in TABLE 2.5 (10). It can be seen that for extremely severe sour conditions (NACE test, pH 3.5 (142)) levels of carbon, manganese, phosphorus and sulphur are restricted whilst vanadium, copper, nickel, chromium and inclusion control by calcium treatment is introduced. Investigations into the effect of microstructure and composition upon SWC have occurred in three main areas; i) the effect of alloy additions e.g. copper(Cu) on corrosion resistance and hydrogen absorbtion (110,114,115,131,139,144), ii) the effect of heat treatment and thermomechanical processing (110,135,140,154), and iii) the effect of segregation (7,8,110,131,133,139). These aspects, however, are by no means mutually

%	Sweet; no special requirements	Sweet; special toughness, haz hardness	Sour; pH 5 special toughness, haz hardness	Sour; pH 3.5 special toughness, haz hardness
C	0.08/0.12	0.03/0.07	0.03/0.07	0.05/0.08
Mn	1.25/1.40	1.25/1.40	1.25/1.40	0.75/0.95
Si	0.25/0.35	0.25/0.35	0.25/0.35	0.25/0.35
P	0.025 max	0.025 max	0.020 max	0.020 max
S	0.012 max	0.008 max	0.005 max	0.002 max
Al	0.02/0.06	0.02/0.05	0.03/0.05	0.03/0.05
Nb	0.03/0.045	0.03/0.045	0.03/0.045	0.03/0.045
V	Nil	0.05/0.07*	0.05/0.07*	0.05/0.07*
Cu	Nil	Nil	0.30/0.35	0.30/0.35
Ni	Nil	Nil	0.20/0.25	0.20/0.25
Cr	Nil	Nil	Nil	0.20/0.25*
Ca	Nil	Nil	0.006 max	Ca/S = 2:1 0.006 max

** These elements may be added as an option.*

TABLE 2.5 Typical compositions of linepipe for various service conditions (10) .

exclusive. For example, low temperature transformation products, referred to as "anomalous structure" by MIYOSHI et al (8) have been associated with the segregation of manganese (Mn) and phosphorus (P) by several authors (8,131,144) and either feature is considered detrimental to SWC resistance.

The possibility that certain alloy additions to steel, may improve its resistance to corrosion and hence reduce the amount of hydrogen absorbed has been considered by MOORE and WARGA (7). They found that Cu additions between 0.25 and 0.3% eliminated or significantly reduced SWC and surface blistering in fully killed steels, without impairing other properties, MIYOSHI et al (8) also reported similar results. However, subsequent authors have found that the beneficial effects of copper are only observed in environments where protective films can form (140,144). In steels tested in low pH solutions e.g. pH 3.5 such as in the NACE test, additions of copper have proved ineffective.

This subject has been extensively investigated by IINO et al (115,139). In a series of experiments they recorded the corrosion rate and concentration of absorbed hydrogen (C_H^{45}) of laboratory prepared steel samples containing controlled additions of a number of alloying elements, singularly and in combination. The tests were carried out by immersing the samples in H_2S saturated brine solutions at various values of pH; examples of their results are shown in Fig.30. They reported that the effectiveness of alloy additions, in general, decreased with decreasing pH of the environment. Only nickel(Ni) and some group VIII elements (Pd,Pt) remained effective in reducing the absorbtion of hydrogen at a pH of 4, and no favourable interaction between the elements Ni,Cu,Cr,Mo and W was observed.

Numerous studies have been undertaken to determine the effect of heat treatment upon SWC resistance (114,115,127,135,139,140). It is generally

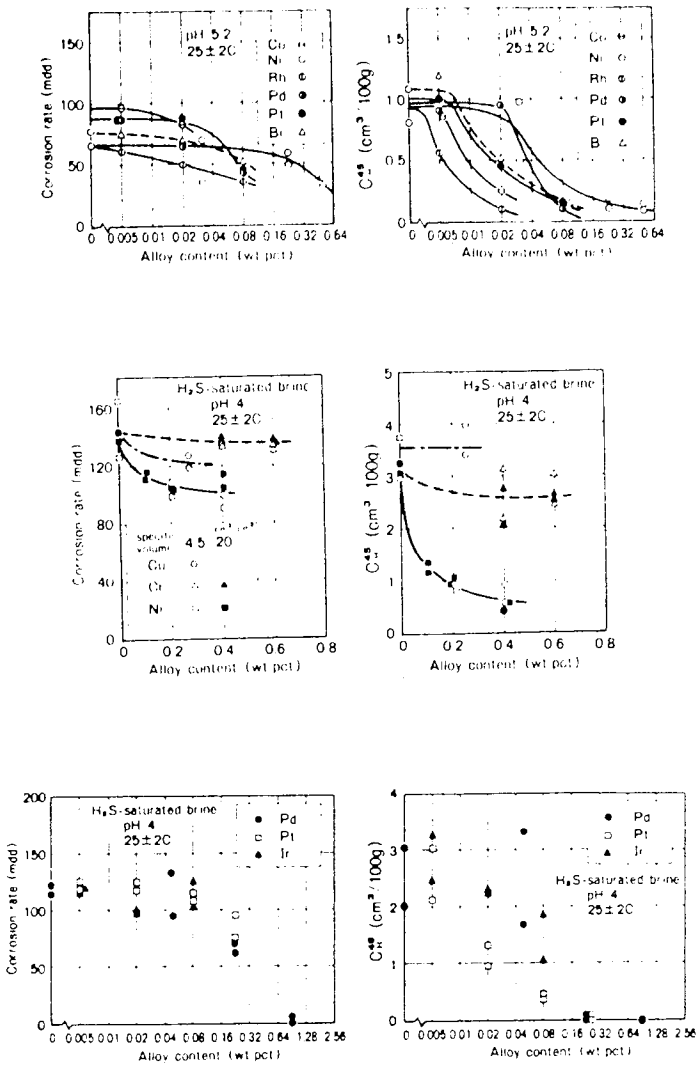

FIG.30 : Corrosion rate and C_H^{45} as influenced by microalloying at various pH levels (115) .

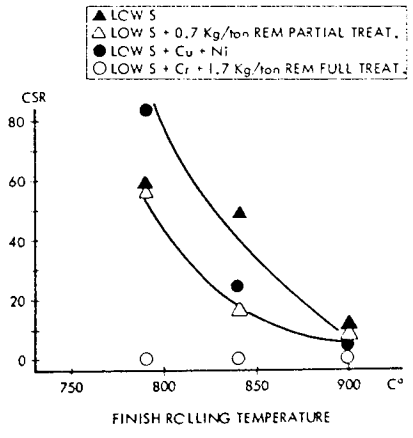

FIG.31 : Influence of finish rolling temperature on cracking suceptibility (135) .

agreed that a homogeneous microstructure is beneficial (163). Normalising, and quench and tempering have been found to be effective. "Anomalous" microstructure such as bainite and martensite (111,114,115,138,140), also banded ferrite/pearlite (128,131,133,163) are considered detrimental to SWC and heat treatments which either remove or reduce these structures have been found to improve SWC resistance.

Quite often, microstructural anomalies such as bainite and martensite, have been associated with areas of segregation (8,128,131,132,141,162,237), particularly manganese and phosphorus, but also, silicon and chromium (144). IINO et al (139) report that vanadium and niobium have been found to segregate whilst TAIRA et al (114) did not observe this. Variability of results in such cases would be expected due to the different manufacturing processes and bulk chemical compositions of steels investigated by the various authors.

A recent study by TAIRA et al (114) on a number of X290 to X483 MPa grade pipes with wall thicknesses between 16 and 25mm and a number of 50Kg laboratory prepared melts (the compositions of which were adjusted to simulate segregation occurring in ingots) revealed the following. Restricting the hardness of the segregation zone to below 300(Hv) in addition to inclusion shape control was found to be essential for the complete elimination of SWC, as hard banded structures containing bainite and martensite were found to be susceptible to hydrogen embrittlement and hence were likely sites for SWC. This is in agreement with the observations of several other authors (131,143,145). However, a study by COLLREN and TITHER (161) has reported that scattered islands of pearlite, bainite and martensite do not promote this type of hydrogen damage, directly conflicting with the above observations.

In explaining their findings TAIRA et al (114) above, reported that the formation of low temperature transformation microstructure depended

principally upon the hardenability of the steel, while the hardness of the low temperature transformation microstructure depends upon carbon content. They proposed that by reducing the manganese content of the steel to below 1%, or reducing the carbon content to below 0.02% significant improvements in SWC resistance could be obtained. Fig.32 from their work shows how heat treatment and tensile strength was found to affect SWC susceptibility. These findings are supported by the work of JONES et al (133). These authors determined the manganese content in the pearlite bands of 29 commercially produced linepipe steels and fitting steels of grade X358 to X552 MPa. By quantitative metallography and EPMA they were able to show that a relationship existed between total inclusion length i.e. projected length (see Appendix B for definition) and the average manganese concentration in the pearlite and segregated bands with SWC as determined by the CLR in the NACE test. An important factor which has been noted by several authors is that pipe which has been heat treated rather than controlled rolled to produce the required mechanical properties is rolled at higher temperatures which reduces the extent of inclusion deformation, a feature which it is generally accepted to significantly affect SWC (152) Fig.31 from PARRINI and De VITO (135) shows the effect of inclusion shape control by REM and rolling temperature upon SWC susceptibility as determined by the crack sensitivity ratio (CSR), (See Appendix A).

Factors concerning inclusion affects in SWC will be considered separately in Section 2.2.3.

Finally, the following comments upon microstructural and compositional factors effecting SWC susceptibility have been made by BIEFNER in his extensive review of the subject: 1)Segregation during casting can produce SWC prone areas in parts of a plate corresponding to the core of the ingot. The effect is particularly severe in large ingots and much less so in small ones. 2)Heavy cold rolling increases SWC but may straighten cracks. 3)Areas of anomalous microstructures, such as bainite and

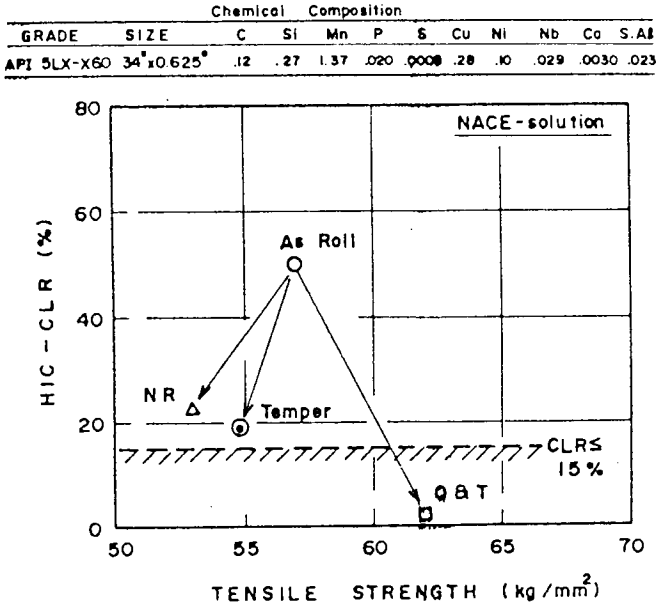

FIG.32 : Effect of heat treatment on SWC resistance (114).

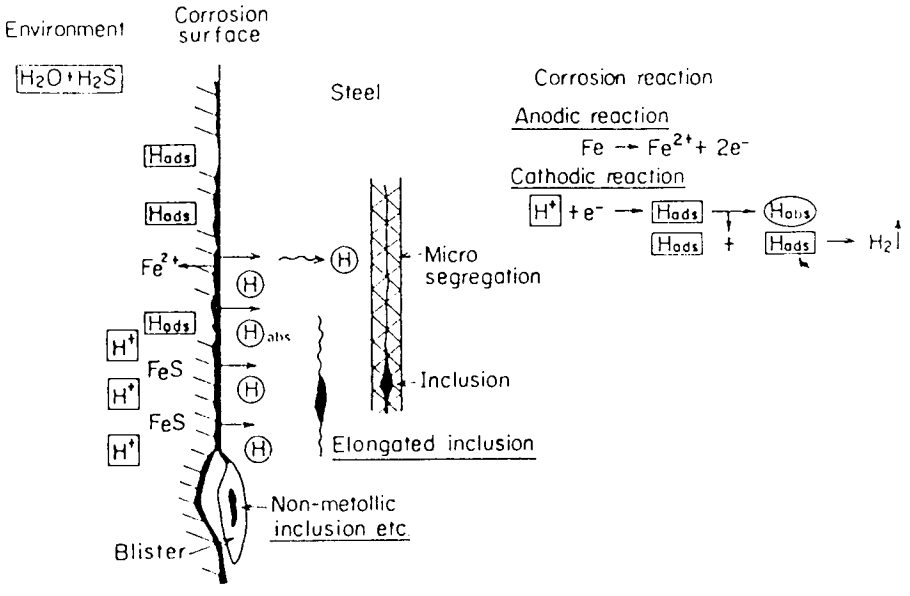

FIG.33 : Mechanisms of stepwise cracking (184) .

martensite are particularly prone to propagating SWC. 4) Quench and tempering and other heat treatments have been shown to improve the resistance of some linepipe steels to SWC and, 5) Copper alloying additions can impart resistance to SWC in mild sour conditions because they form a protective film against corrosion. Additions of chrome, cobalt and nickel may also be beneficial.

2.2.2.0 MECHANISMS OF STEPWISE CRACKING

INTRODUCTION

The mechanism by which SWC occurs is generally held to be hydrogen embrittlement (HE), and although numerous investigations have been undertaken to establish the environmental and metallurgical factors which lead to cracking few authors have examined the HE process per se, although a fairly clear appreciation of the phenomenology of SWC exists. This situation has arisen primarily as a mechanistic explanation for HE is as yet unavailable. (See for example the reviews by INTERRANTE (117), BEACHEM (118), HIRTH (119), ORIANI (149) and THOMPSON and BERNSTEIN (165)).

Presently, one of the most promising develop ments directed towards overcoming this problem is the concept based upon obtaining a critical concentration of hydrogen at microstructural inhomogeneities or "traps". When such a concentration is achieved cracking may then occur. The theory allows that the various mechanisms of hydrogen transport and hydrogen embrittlement, already proposed, may all in fact contribute to the process of cracking at a critical hydrogen concentration. Crack susceptibility is then determined by the microstructure of the alloy and the supply of hydrogen (144,166,167,168,169).

It is the opinion of several authorities (118,119,170,171,192) also, that development and understanding of the mechanisms of fracture in the absence of hydrogen is a prerequisite to defining the problem of failure

by HE. This point is discussed by HIRTH (119) in his review on the effects of hydrogen on the properties of iron and steel. He comments that "although the phenomenology of ductile fracture of low strength steels (which would encompass linepipe) and of crack propagation in high strength steels is being defined,simple mechanisms are not sufficient to rationalise the general degradation in properties produced by hydrogen. Instead a complex process of a number of coupled mechanisms accounts for many of the observed degradation phenomena". A comment which is consistent with the concept of the trap theory of hydrogen embrittlement above.

2.2.2.1 THE PROCESS OF STEPWISE CRACKING

Stepwise cracking of linepipe is generally accepted to result from the absorbtion of nascent hydrogen which then accumulates at discontinuities within steel where it forms molecular hydrogen. The volume increase that accompanies the formation of molecular hydrogen creates internal pressure at the interface of the discontinuities sufficient to cause SWC (8,114,115,118,124,126,128,135,137,150). Fig.33 from IKEDA et al (184) illustrates schematically the cracking process and Fig.34 shows the growth mechanism of SWC. Additionally hydrogen absorbed within the steel matrix is thought to aid the propagation of cracks initiated at discontinuities i.e. HE (135,150,160,132,131).

There is substantial evidence in the literature that the interfaces between non-metallic inclusions (NMI) and the steel matrix, specifically manganese sulphides (MnS), are the preferential sites (discontinuities) within steel where hydrogen collects (trapped) (7,8,126,130,131,137,159,161,172). There is also further evidence that segregation during the solidification of steel results in heterogeneities in inclusion size and distribution, and also steel composition and

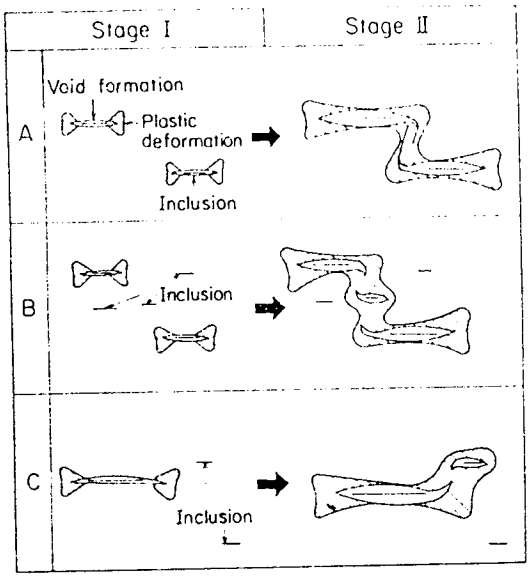

FIG.34 : Schematic representation of stepwise cracking process (184) .

FIG.35 : Small cracks observed on the inner wall of burst pipe (after charging and hydro-testing to failure) (11) .

microstructure, (which is often aggravated during thermomechanical treatments) leading to areas particularly susceptible to SWC (8,110,114,115,126,128,131,160).

2.2.2.2 METALLOGRAPHY AND FRACTOGRAPHY OF CRACKING

An investigation by IINO (128) examined SWC in three X448 MPa grade linepipe steels. Cracking was produced by immersing coupons of steel in an H_2S saturated salt solution (similar to B.P. Test - Appendix A), and by electrolytic hydrogenation for tests carried out under constant load. His results confirmed that internal cracks were initiated at inclusion/matrix interfaces by the precipitation of hydrogen followed by pressurisation. He observed that in the absence of an external stress, fracture developed by a stepwise linkage of the "blister" cracks, which was accompanied by considerable plastic deformation,see Page 55,Fig.28A. For the test carried out at an applied load of 70% of the yield stress, the linking between "blister" cracks took place with the aid of microcracks and was characterised by the absence of large plastic deformation,see Page 54,Fig.28B. Finally in samples loaded at 95% of the yield stress fracture developed by linking hydrogen embrittled cracks generated in slip bands during testing.

Similar observations to these have been made by IKEDA et al (145) and NAKAI et al (11). The latter authors made their observations after full scale burst tests of a range of steels from grade X359 to 414 MPa. The inner surface of 3m long sections of pipe were subjected to corrosive solutions, saturated with H_2S, for periods of up to 2 months, before hydrostatic testing. They also carried out standard immersion tests on steel coupons of the same material (B.P.test). They observed that flakes ("fisheyes") occurred on the fracture surface of all pipes, firstly subjected to the long duration exposure tests, after hydrostatic bursting, even if SWC did not occur in the immersion tests (e.g. Steel G, which contained 0.003 sulphur and .0058 calcium wt%). However, such fracture phenomenon were

not observed in the reference pipes nor the pipes which were subsequently annealed after exposure to the H_2S solutions. Also, many small cracks parallel to the axial direction of the pipes were observed on the inner surface of the fractured parts of burst pipes which contained large amounts of SWC as shown in Fig.35. The appearance of the cross section of these small cracks is shown in Fig.36. The pipe bursting process with SWC based upon these observations is shown schematically in Fig.37. With the evidence from SEM fractography they showed that during hydrostatic burst tests, HE occurs at the tip of SWC where the stress is concentrated, and a new crack propagates toward the inner surface of the pipe perpendicular to the direction of hoop stress. The inner layer of fractured surface showed a "subcleavage" configuration (Fig.37A) which they considered was characteristic of hydrogen embrittlement (similar observations have been made by MIYOSHI et al (8)), whereas the outer layer showed a normal ductile fracture (Fig.37B). They concluded that the least amount of SWC deteriorated the property of the pipes. Several other authors have also used SEM techniques to observe SWC and the fracture modes associated with the propagation of cracks between blisters (114,133,150,173). WILDE et al (150) devised a technique for fracturing specimens containing SWC without destroying the original fracture surface due to hydrogen. This was achieved by welding extension pieces onto the steel with the SWC, introducing a notch (effectively a Charpy specimen) and then fracturing by impact at liquid nitrogen temperature (-196 C),thus ensuring that the material unaffected by hydrogen damage failed by cleavage. Several steels were examined (Grade X298 to 414 MPa) which had various chemical compositions and manufacturing histories. SWC, when it was observed, was predominantly found to initiate at inclusions, particularly elongated MnS, and propagation occurred in the plane parallel to the plate surface by a fracture mode they described as "feathery", and also in a step-wise manner. Both fracture morphologies were considered to occur by a hydrogen assisted mechanism.

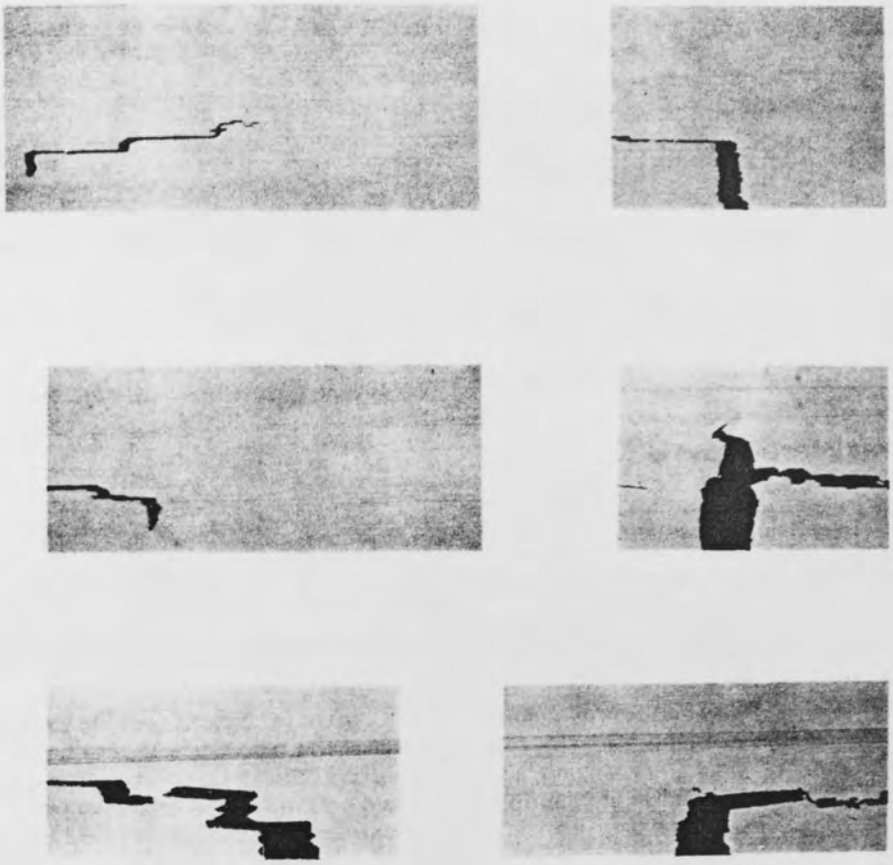

FIG.36 : Typical cracks observed in the cross sections of burst pipes (11) .

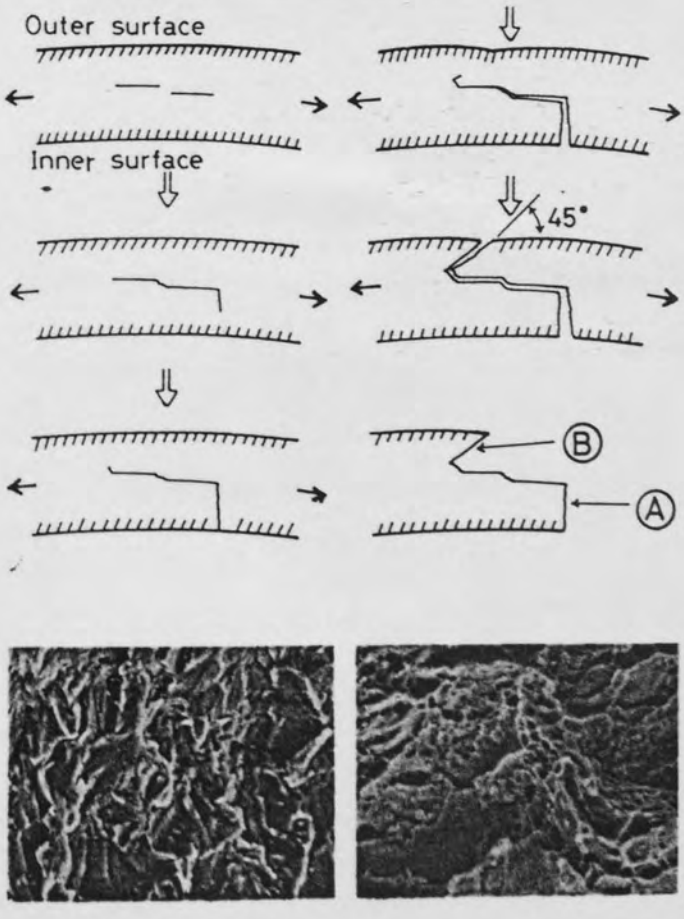

FIG.37 : Illustration of burst process of pipe with SWC (11) .

In a similar investigation JONES et al (133) observed SWC by fracturing specimens which had previously been subjected to the NACE test and then immersed in liquid nitrogen. They found that following initiation at non-metallic inclusions, cracks grew in the plane parallel to the surface of the plate (Fig.38a) and in a step-wise manner (Fig.38b) by quasi-cleavage (Fig.38a), also, step-wise cracks were found to occur by a local shearing mechanism (Fig.38c), even within the same steel. When SWC occurred extensive local deformation was often found.

From these observations it is clear that the fracture appearance due to hydrogen embrittlement cannot be simply defined, and may vary depending upon the conditions, both metallurgical and environmental, under which it was produced. Stress appears to have a strong influence upon the fracture mode.

2.2.2.3 MECHANISMS OF HYDROGEN EMBRITTLEMENT

As noted beforehand (2.2.2.0) HE is believed to be responsible for SWC, however, few authors have expanded on this assertion. The concept of internal pressurisation, originally proposed by ZAPFFE and SIMS (174), is one mechanism of HE which is sometimes referred to in studies on SWC (128), however, general reviews dealing with the effects of hydrogen upon iron and steel comment on at least five individual mechanisms which may be responsible for HE (one of which is internal pressurisation) (119,120,149,170,175). In these reviews there is general agreement that none of the mechanisms proposed to explain HE is in fact general enough to account for all the the cases which have been observed and PRESSOURYE (155) has commented "rather it now seems that several if not all of the proposed mechanisms of HE may be active at the same time, depending upon the experimental conditions".

FIG.38(a): SWC propagating by quasi-cleavage (133).

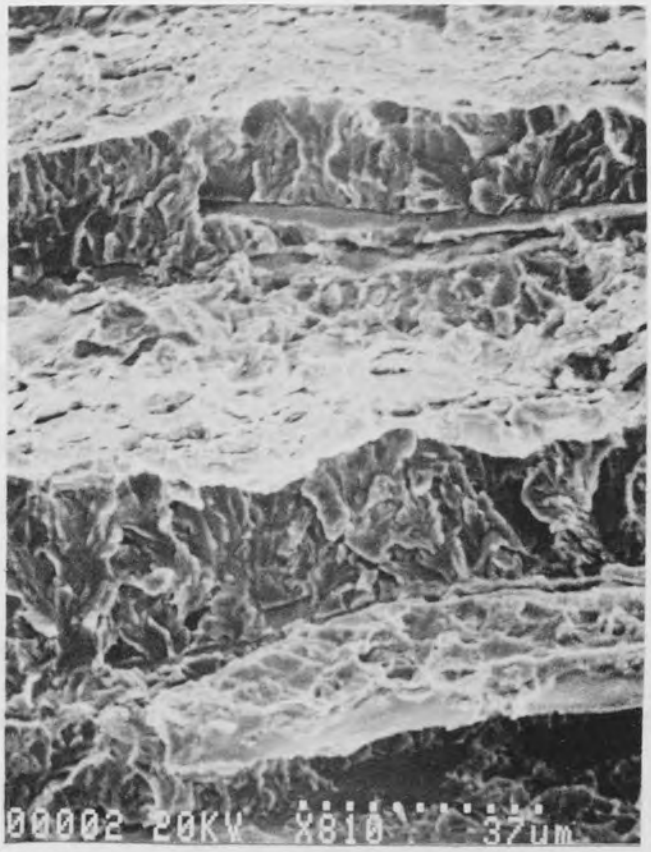

FIG.38(b): Step produced by a quasi-cleavage mechanism (133) .

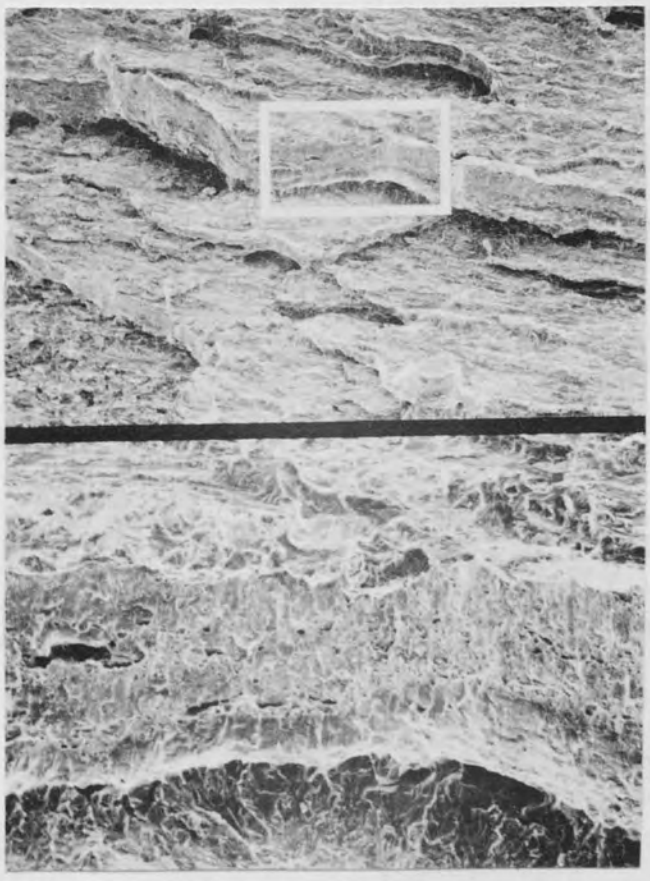

FIG.38(c): Step produced by a local shearing process (40X & X200) (133) .

The mechanisms of hydrogen embrittlement currently considered as capable of causing damage in steel are briefly outlined below after LOUTHAN and McNITT (170), and INTERRANTE (117);

1. Precipitation of hydrogen gas at internal defects. The pressure developed by this precipitation is added to the applied stress and thus lowers the apparent fracture stress. This mechanism was originally proposed by ZAPFFE and SIMS (174).

2. Interaction of dissolved hydrogen to reduce the cohesive strength of the lattice. This model was proposed by TROIANO (176) and modified by ORIANI (149,177).

3. The adsorption theory, which assumes that hydrogen is adsorbed at the crack tip and changes the surface energy of the crystal lattice, thereby lowering fracture resistance. This theory was first proposed by PETCH (178).

4. Absordtion of hydrogen to increase the ease of dislocation motion or generation or both. This mechanism, proposed by BEACHEM (179) differs in general from the previous models in that hydrogen is assumed to enhance plasticity locally rather than truly embrittle the lattice and,

5. Association of hydrogen with dislocations either to restrict dislocation mobility or to provide localised hydrogen accumulations and thereby embrittle the lattice. The dislocation-hydrogen association was proposed by BASTIEN and AZOU (180) and has been developed by TIEN (181,182).

The authors responsible for the original theories have been referred to above and the majority of these papers are to be found in a METAL SCIENCE SOURCE BOOK on HYDROGEN DAMAGE edited by BEACHEM (118). Additionally extensive discussion, of these mechanisms, and information from subsequent publications is contained in the introduction section of this compendium by BEACHEM (118) and also in the review papers by HIRTH (119), TYSON (175) and INTERRANTE (117).

Although no direct reference is made in the above reviews to SWC in linepipe steels a number of points are discussed which are relevant to the process of hydrogen migration and concentration at discontinuities within steel i.e. inclusions and hence to crack formation.

Both HIRTH (119) and ORIANI (149) report that crack growth resulting from internal pressurisation of cavities by hydrogen is possible only when a sufficiently severe external environment is available to produce the necessarily high hydrogen fugacity. Blister formation in the absence of an external stress (as frequently observed for linepipe steels subjected to sour conditions (124,126) (Fig. 28B)) is cited by HIRTH (119) as evidence. ORIANI (149) further adds that the growth of these cavities is associated with plastic deformation, and that initiation may be assisted by the decohesioning effect of dissolved hydrogen at points of large stress produced by dislocation interactions or by plastic incompatibilities at second phase particles and at regions of enriched solute concentration.

The concentration of hydrogen within steels as affected by stress state has been reviewed recently by LOUTHAN et al (183), and INTERRANTE (117) discusses the factors affecting the solubility and diffusivity of hydrogen in steel. These mechanisms are regarded by HIRTH (119), however, only as a means of transporting sufficient quantities of hydrogen to regions within the steel where cracking may initiate.

BEACHEM (118) also discusses crack formation as a result of hydrogen concentrating at "weak zones" within the steel, (which might be an inclusion or grain boundary) in the absence of an applied stress. He considers that once a plastic zone has developed as a result of hydrogen pressurisation, the plasticity is further aided by hydrogen, which in turn aids the entry of hydrogen into the cracking zone.

This directly conflicts with ORIANIs' (149) theory above i.e. cracking is assisted by the decohesioning affect of hydrogen. The problem lies in determining whether hydrogen assists decohesion i.e. "perfect cleavage", or deformation i.e. plasticity which at present is still undecided. To add further conflict to this problem, several authors (185,186,187,188) have postulated that cleavage and plasticity (dislocation emission) may in fact occur concurrently in some situations, and a recent investigation by VEHOFF and NEUMAN (189) of cracking in an iron -2.6% silicon single crystal in a hydrogen gas atmosphere, using an in situ SEM technique, has produced evidence of just this.

To return to SWC and hydrogen damage, two similar studies by IINO (128) and IKEDA et al (184) have analysed the effect of stress state and hydrogen transport phenomena upon the concentration of hydrogen and the occurrence of SWC. The study by IINO (128) considered the stress state arising around a cavity which was internally pressurised and the effect of an externally applied stress upon this stress distribution. Areas of high hydrogen concentration in the vicinity of the cavity were considered to occur by dislocation and/or stress induced diffusion transport mechanisms. Tensile and negative hydrostatic stresses were expected to enhance hydrogen concentration by diffusion, and shear stresses were expected to affect the transport of hydrogen by dislocations; this was in agreement with the comments made by LOUTHAN et al (183) in their aforementioned review. The results of the stress analysis were said to be consistent with the observations of SWC in steel specimens which contained cracks produced in the absence of an applied stress and also with applied loads. IKEDA et al (184) presented their results schematically for the case of internal crack growth for an unstressed Grade 359 MPa pipe charged with hydrogen (Fig.34).

Finally, a synthesis of the five HE mechanisms has been incorporated into a solution to the problem of hydrogen in steels and SWC by PRESSOURYE et

al (160). This is based on the trap theory of HE. The premise is that, whatever the mechanism(s) operating, a crack will be initiated or assisted by hydrogen whenever the sum of the applied and residual stress plus the effect of hydrogen (σ_T^H), exceeds the cohesive strengths of the matrix plus the effect of hydrogen (σ_C^H) Fig.39. This corresponds to a critical value (Ck) of the amount of hydrogen (Ch) trapped on the pre-existing defect. The important parameters acting upon both Ch and Ck are schematically shown in Fig.40, this gives some idea of the complexity of the problem. PRESSOURYE (155,159,168,190,191) has published several reviews dealing with these parameters. Although this approach does not identify a specific HE mechanism, if there is indeed one, it does offer a compromise.

2.2.2.4.0 FRACTURE AND HYDROGEN EMBRITTLEMENT (HE)

It was stated in Section 2.2.2.0 that although several mechanisms of HE have been proposed no single mechanism is considered sufficiently comprehensive to totally explain the phenomenon. As a result, in the course of discussing mechanisms of HE, several workers have expressed the opinion that it would be expedient to identify and understand the mechanisms of fracture in the absence of hydrogen as a preliminary to establishing the factors leading to hydrogen assisted failure (118,119,149,165,169,171,175,192,201).

THOMPSON and BERNSTEIN (171,192,204,206,207,209,236) have repeatedly advocated this approach, and have commented that by obtaining detailed data on microstructure/fracture interactions "an accurate physical description of hydrogen effects on fracture" and "a rigorous test of the ability of any mechanism(s) to describe the varying manifestations of HE" can then be determined (165).

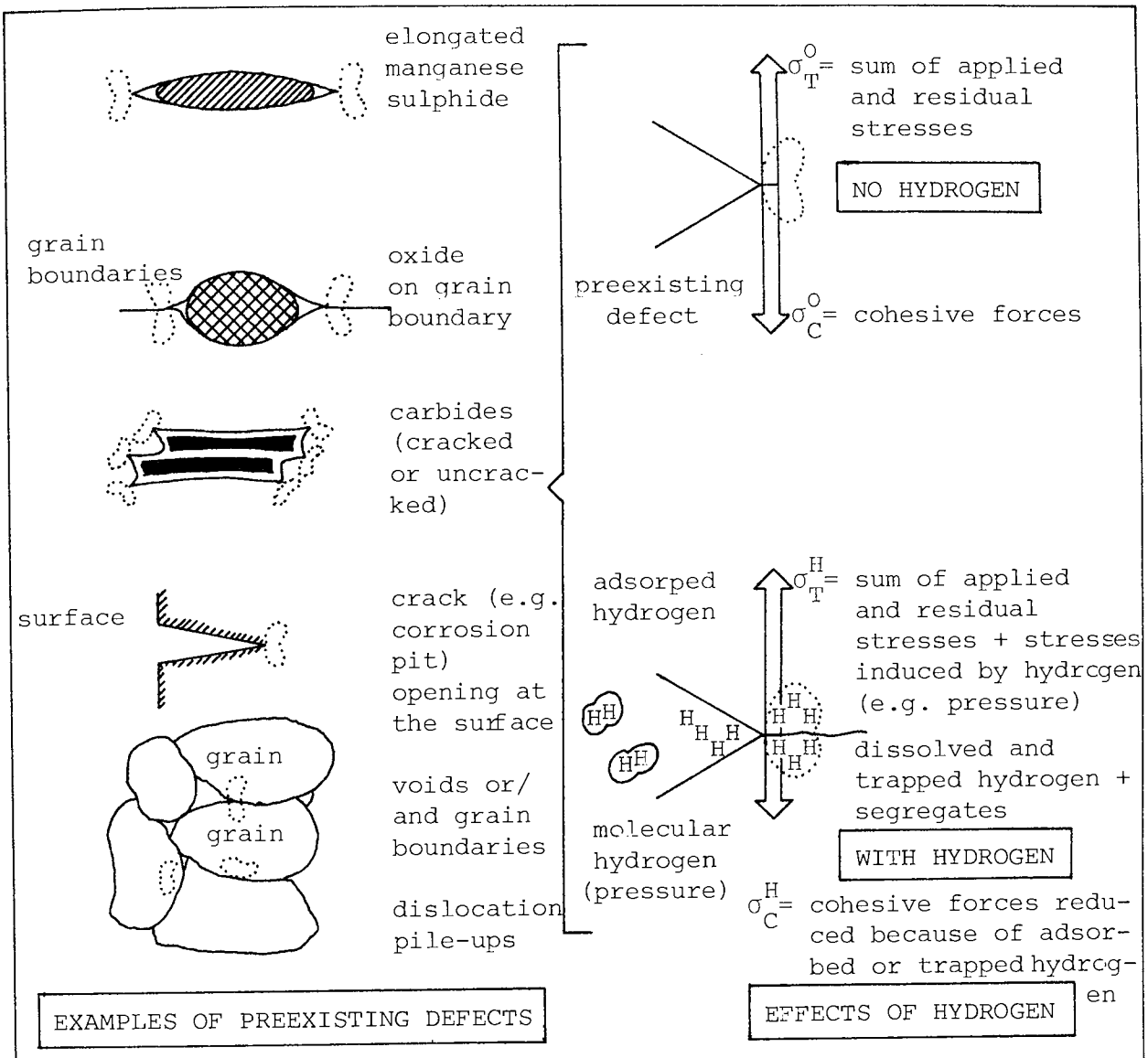

FIG.39 : Important parameters acting upon both C_K and C_H (see text for explanation) (155) .

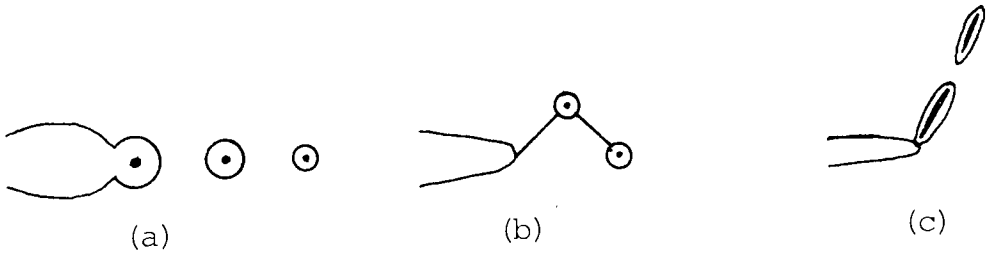

FIG.41 : (a) 'Normal' ductile fracture . (b) Shear decohesion . (c) Delamination . (218)

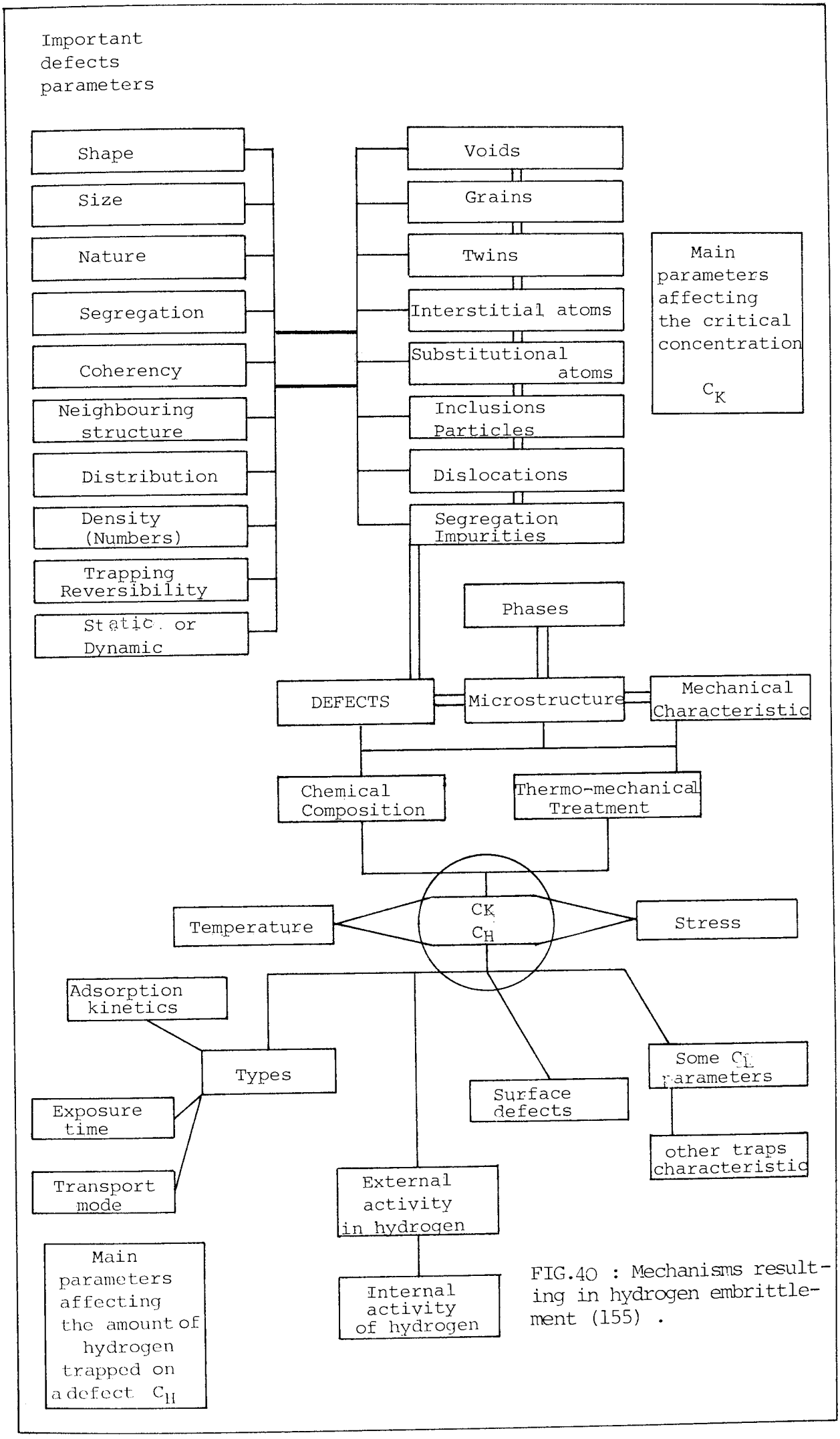

FIG.40 : Mechanisms resulting in hydrogen embrittlement (155) .

A problem which is universally recognised, however, is that the microstructural origins of fracture are not fully known despite a considerable amount of phenomenological knowledge.

BEACHEM (118), in his introductory commentary upon hydrogen assisted failure, acknowledges this problem and has attempted to clarify the situation firstly by establishing basic fracture concepts. In a general discussion he outlines developments in the mechanistic aspects of fracture and the important factors which influence these mechanisms, such as stress state and strain localisation. (see also Ref.237 also by BEACHEM). On this foundation he then addresses the effect(s) of hydrogen upon failure.

THOMPSON and BERNSTEIN (165,171,192,236) have likewise classified fracture modes, described their microstructural origins and facture appearances. They considered microvoid coalescence (MVC), cleavage, quasi-cleavage (QC), intergranular fracture (IG), and ductile tearing (TTS) and also the possibility that any number of these fracture modes may appear together i.e. mixed mode. In treating the influence of hydrogen upon fracture they determined that particle effects, microvoid growth affects, plasticity effects and impurity effects were the most significant parameters. These they believe either interact with hydrogen to change the normal fracture process without greatly influencing the fracture mode or may completely change it.

In further publications THOMPSON and BERNSTEIN (209,169) discuss how careful fractography and metallography may be usefully applied to observe and determine the interaction of hydrogen with microstructure and the effect upon fracture. In this work are numerous examples collected from the literature (e.g.CIALONE and ASARO (202,203), HIRTH (119), see also FRENCH et al (208) and ORIANI et al (205)) illustrating how comparative studies i.e. fracture with and without hydrogen have been used to obtain

information upon microstructural/hydrogen interactions and the resulting fracture process. The majority of the studies reported were concerned with the effect of hydrogen upon (normal) fracture by MVC, as this represents the most common fracture mode observed in ductile materials (118,119,165).

However, as far as the author is aware no such comparative studies have been undertaken in steels with compositions and microstructures similar to linepipe. Nevertheless, the fracture modes in the absence of hydrogen and with hydrogen have been studied on an individual basis in these steels. The metallography and fractography of cracking in linepipe exposed to sour conditions i.e. hydrogen charged, has already been discussed in SECTION 2.2.2.2. and the ductile fracture of these steels, as generally observed during tensile testing, is reviewed briefly below.

It is, at this point, germane to note that several investigators (13,14,15) have studied the microstructural origins of fracture and the fracture topography of steels charged with hydrogen, that have a slightly higher alloy content and strength level i.e. 700 -1000 MPa than that normally found in linepipe. These steels were either tested to failure under constant load and charging conditions (NACE TM-01-77 (142)) or charged with hydrogen and then immediately tested in tension.

These investigators found "fisheyes" or areas of flat fracture, whose appearance was predominantly associated with NMI at the point(s) of fracture initiation. Also this fracture phenomenon has been observed by some of the investigators noted above (e.g CIALONE and ASARO (202,203), FRENCH et al (208)) who undertook comparative investigations in spheroidised carbon steels.

The observation of this type of fracture phenomenon is significant as they appear to have very similar characteristics to the "fisheye"

fractures, reported in the study by NAKAI et al (11), (See SECTION 2.2.2.2.). In this study "fisheyes" or "flakes" resulted after hydrostatic burst tests of linepipe which had previously been exposed to a sour environment for some considerable time.

2.2.2.4.1 DUCTILE FRACTURE

The ductile fracture of steels has been studied by many authors, and a detailed discussion is well beyond the scope of this work. Much relevant information is contained, however, within several very comprehensive reviews on ductile fracture by ROSENFIELD (217), WILSDORF (218), VAN STONE et al (211), HOWARD and WILLOUGHBY (219), LESLIE (220) and EMBURY (221).

It is now well established that ductile fracture in steels with compositions and microstructures similar to linepipe occurs by void initiation at second phase particles, followed by void growth and coalescence i.e. MVC (211,218,219, 220,271), where it is agreed that non-metallic inclusions play the predominant role in the process and greatly influence the fracture appearance and the total ductility of the steel (211,220,221). In keeping with the rest of this review the following discussion will be restricted to the effects of inclusions upon ductile fracture.

BAKER et al (173,197,198) were probably the first authors to make a comprehensive study into the effect of inclusion parameters upon toughness anisotropy of steels. They found that inclusion volume fraction, dispersion and morphology i.e. shape had a combined effect upon steel toughness. Anisotropy, a characteristic of hot rolled structural steels, was reduced and an overall improvement in ductility was found for low inclusion volume fractions, homogeneous inclusion dispersions and

globular inclusion morphologies that were resistant to deformation during hot rolling. These observations have since been confirmed by numerous workers (211,212,220,225).

In brief, ductile fracture is initiated by void formation at inclusions either by particle cracking or the decohesion of the particle/matrix interface. GOODS and BROWN (227) who have made an extensive review of the subject comment that the interface between the inclusion and matrix plays an important role in the process and note that interface chemistry can significantly affect the tendency for void formation, and impurities at the interface can reduce the strain necessary for void initiation. Interestingly, FISHER and GURLAND (232) have discussed this point in their study of void formation in spheroidised carbon steels. They note that solute segregation to particle interfaces may encourage void formation and may be a contributing factor to the reduced ductility observed in cases of HE.

Other factors influencing void formation are the size of inclusions and their shape with respect to the testing direction (227). Generally, large inclusions have been observed to nucleate voids at lower strains than small ones (211), whilst the effect of inclusion shape upon initiation has been found to be dependent upon testing direction (227). BEREMIN (225) has observed that void initiation occurs by decohesion in rolled steels containing elongated MnS inclusions when tensile tests were carried out in the through-thickness direction, whereas, particle cracking was the predominant void forming mechanisms in longitudinal tests. The formation of voids by decohesion occurred at lower strains than that required for particle cracking. This factor was believed to explain, partly, why the ductility i.e. the reduction in area (RA) was lower in the through-thickness direction. The possibility that some particles are decohered during hot rolling and thus void initiation has

effectively occurred at this stage has also been suggested by some authors (197,198).

After cavities have been formed, continued deformation causes void growth and finally coalescence (211). HOWARD and WILLOUGHBY (219) have shown that growth and coalescence may develop in several ways (Fig.41), as follows; Firstly "Normal" ductile rupture (Fig.41A) proceeds as a result of necking between voids, like in small tensile specimens. Secondly, shear decohesion (Fig.41B) commonly occurs when deformation becomes highly localised onto shear bands between voids, such as in materials of low work hardening capacity or where the capacity for work hardening has been exhausted (212). Finally (Fig.41c) delamination, which typically occurs in materials with a low resistance to tearing, and is found for example in steels with highly elongated inclusions i.e. RA in through-thickness tensile tests (212).

The variables effecting ductile fracture are numerous and WILSDORF (218) has compiled a table (Table 2.6) of the many features found to influence ductile fracture mechanisms involving second-phase particles. A very important feature listed is the stress state during fracture which is significantly affected by the geometry of the test specimen. For example, a number of investigators (222,223,224) using simple tensile tests have shown that the introduction of a notch can have a great effect upon ductility. The stress triaxiality (hydrostatic tension) resulting from the notch has been found to localise plastic strain, and decrease ductility by promoting void initiation, growth and plastic instability (222).

The decrease in steel ductility with an increasing volume fraction of inclusions has been accepted for sometime (217). So too has the anisotropy of ductile fracture occurred as a result of inclusion elongation and reorientation during hot rolling (229). These factors

Shape of specimen	Cylindrical
	Sheet
	Others
Particles	Volume fraction
Type of particle	Inclusion
	Precipitate
	Dispersion
Particle shape	Spherical
	Elongated
Particle size	<10 nm; 0.05-1 μm; $>1\mu$m
Particle location	Matrix
	Grain boundary
	Spacing between particles
	Orientation
Grain structure of matrix	Size
	Shape
	Preferred orientation
	Grain boundaries
Free surface energy	Matrix
	Particle
	Matrix-particle
State of stress	Uniaxial
	Triaxial
	Hydrostatic
	Normal
Strain	Magnitude
	Rate
Stress	Yield stress
	Flow stress
	Fracture stress
Work hardening	Dislocation cell structure
	Deformation mode due to stacking fault energy

TABLE 2.6 Variables used in ductile fracture mechanisms involving second-phase particles (218) .

have been investigated by many workers for hot rolled low C-Mn steel plate (212,213,214,215,225,229,230,231,233,234,235). Fig.42 shows the effect, typically observed, of sulphur content (e.g. inclusion volume fraction) and testing direction upon the RA for a number of hot rolled Mn-Nb plate steels (212).

SPITZIG, in a series of publications (213,231,234,235) has presented similar data for a number of hot-rolled C-Mn steels. In these investigations the steels studied contained carbon at 0.1 and 0.2% and sulphur levels of 0.004, 0.013 and, 0.013% rare earth treated. He has also shown that inclusion shape and volume fraction may be characterised by a single parameter, inclusion projected length (see Appendix B), which was correlated to the fracture strain (and Charpy shelf energy) regardless of testing direction and sulphur content of these steels (Fig.43). The projected inclusion length parameter was originally introduced by BAKER and CHARLES (197) in a study of the effect of inclusions upon short transverse toughness. SPITZIG (234), as noted above, has developed this and produced a general formula such that the projection parameter can be evaluated for the three principal testing directions. He defined that the projected length of inclusions per unit area on a plane parallel to the fracture plane was proportional to the volume fraction of inclusions and inversely proportional to the inclusion dimensions perpendicular to the fracture plane (231). Additionally he determined a similar parameter the projected area (235) and also evaluated the mean free distance and the nearest-neighbour distance between inclusions (231,235). These were all found to correlate with the fracture strain regardless of the amount or shape of inclusions or the test direction.

Several workers (211,212,214,231) in their investigations of ductile fracture have made studies of fracture appearance for the three principal testing directions using SEM. Fig.44 from VAN STONE et al (211) shows a

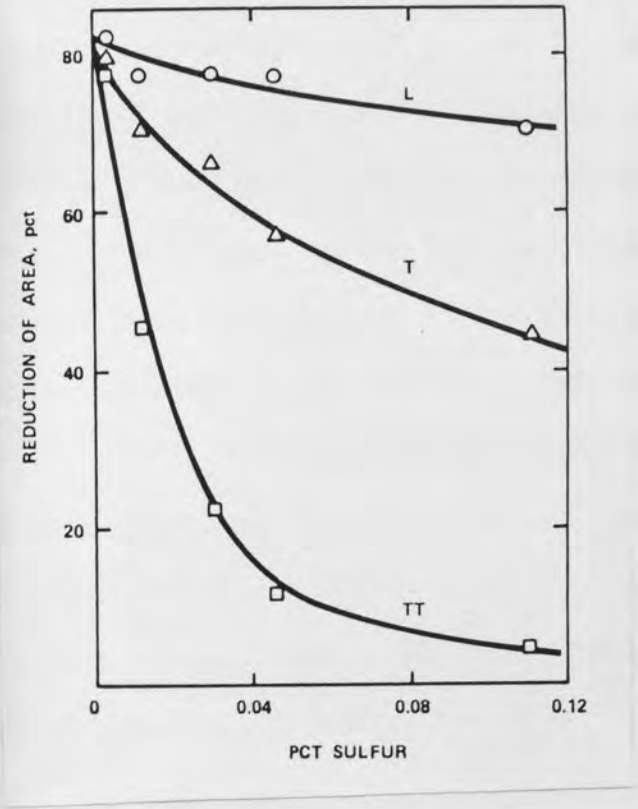

FIG.42 : Effect of sulphur content on reduction in area in straight-way rolled Mn-Nb steels (212) .

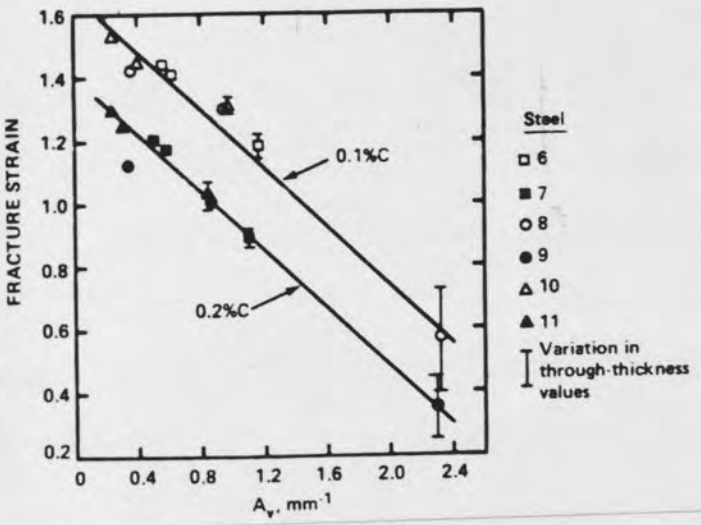

FIG.43 : Effect of inclusion projected area per unit volume, Av, on a plane perpendicular to the tensile direction on the longitudinal, transverse and through-thickness fracture strain of the 0.1 and 0.2 pct carbon steels (235).

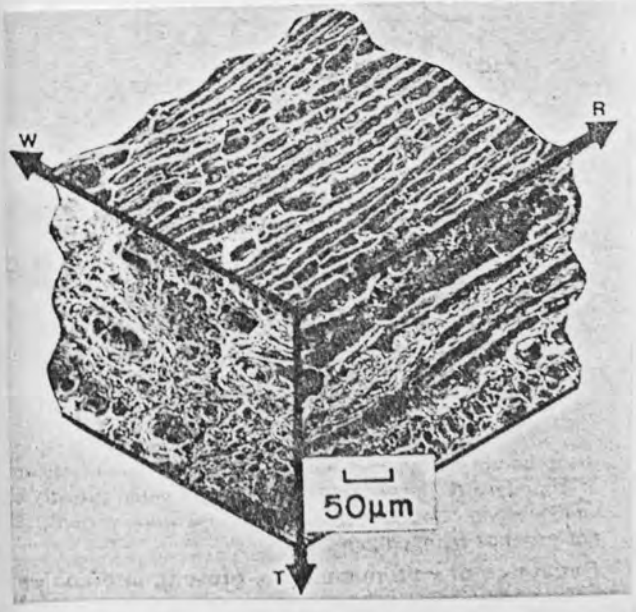

FIG.44 : Fracture surfaces on the three mutually perpendicular planes - R(rolling) longitudinal W(width) transverse and T(thickness) short-transverse direction respectively (211) .

typical isometric presentation of the three fracture surfaces for a 0.2C-1Mn-0.4Cr-0.03Mo (wt.%) steel with a relatively high (but unspecified) sulphur content. This serves to show the effect of inclusion anisotropy upon the resulting fracture appearances. The low ductilities found with specimens tested in the through-thickness direction (See Fig.42) are a direct result of the large effective area of inclusions found on this fracture surface (See Fig.44 - testing direction T). A study by TAKADA et al (215) has in fact determined that the tensile ductility of a series of hot-rolled C-Mn steels containing different inclusion volume fractions and shapes can be related to the inclusion area fraction on the fracture surface, regardless of the testing direction.

The shape of inclusions, (as a result of hot rolling) size and distribution greatly influences the shape, size and population of dimples upon the resulting fracture surface. As can be seen in Fig.44, long flat inclusions oriented in the rolling direction, produce a terrace type fracture on the through-thickness fracture surface. However, when testing is carried out in the longitudinal direction, the inclusion nucleated voids are considerably smaller and equiaxed. The transverse direction represents the intermediate case.

The fracture appearance of the longitudinal and transverse specimens in Fig.44 also show a second population of smaller dimples. In lower S steels (<0.013%) this secondary population of voids has been observed to occur for all three testing orientations (204). The secondary population of voids is believed to arise through the formation of cavities at other second phase particles i.e. carbides.

A number of workers have made observations of the void formation and growth process by sectioning tensile specimens through their axis in the direction of testing to reveal the extent of cavitation (212,214,231).

MELANDER and STENINGER (214) in particular, have observed void formation at inclusions and pearlite nodules in specimens tested in the longitudinal and through-thickness direction, by straining specimens to different amounts and observing the occurrence of cavitation. The material they investigated was a hot rolled 0.2% C -0.025% niobium microalloyed steel. In the longitudinal specimens voids were observed at some equiaxed particles, prior to straining, otherwise void formation at MnS inclusions was found to occur by particle cracking (in agreement with the findings of BEREMEN (225) noted earlier) and at strains of the order of 0.2 to 0.5. Void nucleation at pearlite nodules occurred by decohesion and particle cracking but at much higher strains i.e. 1.1. Void initiation in the specimens tested in the through-thickness direction occurred by particle decohesion and was observed at the minimum increment of strain applied 0.08. Fracture was believed to develop in regions containing higher than average concentrations of sulphides, oxides and pearlite.

SPEICH and DABKOWSKI (212) who conducted a similar investigation in a series of low C-Mn steels with sulphur contents of 0.003 to 0.11% observed that final fracture developed from the centre of the necked tensile specimen, where the hydrostatic stress component was greatest. This stage of fracture was characterised by rapid void growth, resulting from the coalescence of smaller voids or localised shearing, that produced large holes, finally leading to fracture.

Finally, the case has been put recently (221,228), that void initiation is a statistical process, which is dependent upon the distribution of particles capable of forming voids under the given conditions of stress, plastic strain and work hardening. Hence the mechanism of ductile fracture as presented here is somewhat oversimplified to facilitate presentation. In reality void initiation would be expected to proceed

in combination with the growth of any previously initiated void population, as the deformation proceeded.

2.2.3 THE EFFECT OF NON-METALLIC INCLUSIONS UPON STEPWISE CRACKING

INTRODUCTION

The detrimental effects of non-metallic inclusions (NMI) on the SWC susceptibility of steels used for linepipe is now well established (7,8,123,126,127,128,133,135,137,150,154,161), and a number of investigators have considered the problem in detail (126,133,137,150,159,160,161).

From these studies it has become clear that the inclusion dispersion, as represented by volume fraction (sulphur and oxygen levels), size, distribution and the resulting shape of inclusions after thermomechanical processing significantly influences the resistance of pipe to SWC. These features are in turn inherently controlled by inclusion composition and morphology which is determined by steel making practice and has been reviewed in Section 2.1.

2.2.3.1 INCLUSION MORPHOLOGY AND COMPOSITION

In an investigation of the factors influencing the hydrogen cracking sensitivity (SWC) of pipeline steels, MOORE and WARGA (7) concluded that the most important feature was manganese sulphide (MnS) morphology. They commented that elongated Type II MnS stringers render the steel very crack sensitive, where as ellipsoidal shape, Type I, MnS inclusions are much less harmful. They also reported that since all fully killed steels except those treated with rare earth metals (REM) necessarily contain Type II MnS inclusions, they are inherently more susceptible to SWC than semi-skilled steels. Since this report, numerous investigators have confirmed that Type II MnS inclusions are commonly associated with SWC (34,110,123,135,149) and that inclusion morphology as affected by

steelmaking chemistry, particularly inclusion shape control using REM and calcium, can be effective in improving the steels resistance.

However, at the same time it has been found that Type II MnS inclusions are not exclusively responsible for the initiation of SWC. A number of investigators having discovered other inclusion compositions and morphologies, and also large carbide and nitride particles were also associated with SWC.

COLDREN and TITHER (161) made an in situ SEM study of SWC on two hot rolled Grade X448 linepipe steels, where they found rare earth sulphides and aluminium, silicon and calcium containing phases associated with cracks as well as MnS inclusions. They concluded that inclusions were the only structural features consistently associated with SWC. TAIRA et al (127) have also reported SWC at alumina (Al_2O_3) clusters and massive niobium carbonitrides in a number of Grade X 320 to 483 MPa linepipes in addition to MnS inclusions. Similar observations have been made by NAKASUGI et al (194). These authors report that no cracking was observed at calcium sulphide (CaS) inclusions even under the severe conditions imposed by the NACE test. However, a more recent investigation by TAIRA et al (114) reports that SWC has been observed at clusters of CaS inclusions in steels. The formation of these clusters, they believe, occurs as a result of excessively high calcium additions. To avoid the occurrence of such harmful clusters and prevent the formation of MnS inclusion they have determined that a critical Ca/S ratio exists (Fig.45) for maximum SWC resistance. (This is essentially the same as the examples given in Section 2.1.3 on inclusion shape control (92,93)). Observations of SWC in REM treated steels have also been associated with inclusion clusters.

PRESSOURYE and ZMUDZINSKI (159) have made an extensive study on the influence of inclusions on hydrogen embrittlement, showing examples of

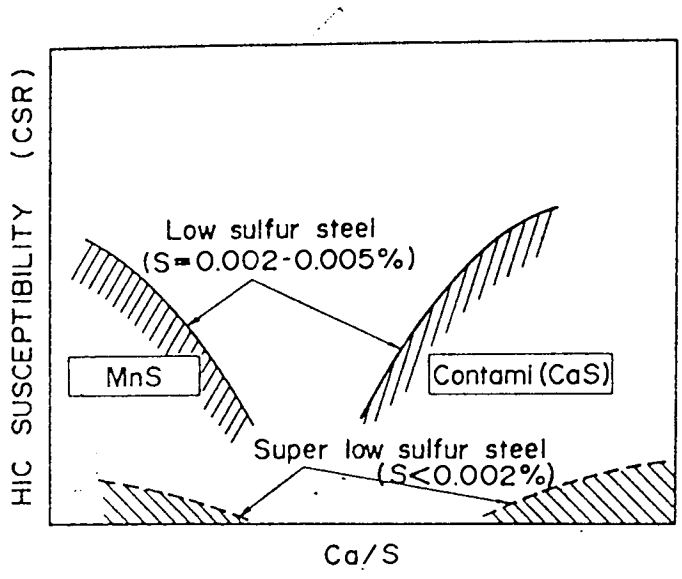

FIG.45 : Effect of Ca/S ratio on SWC resistance (114) .

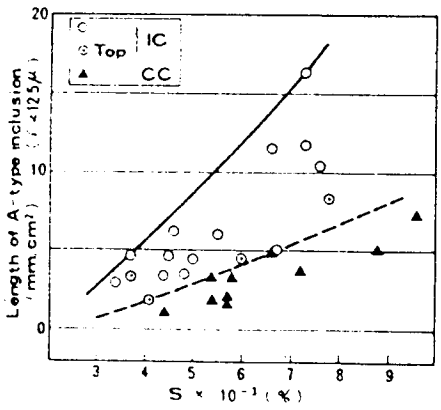

FIG.46 : Relationship between S content and SWC suceptioility (162).

crack formation upon MnS inclusions and calcium aluminates in pearlitic steels, cathodically charged with hydrogen. They also comment that crack initiation was observed upon titanium carbides, titanium nitrides and alumina inclusions. They conclude that crack formation was found more frequently upon the sharpest extremities of inclusions (e.g. MnS) and that careful inclusion control should benefit SWC resistance.

HERBSLEB et al (126) draw similar conclusions from their study of SWC in a number of low alloy pipeline steels. They comment that the geometrical shape of the inclusions was more important than their chemical composition in promoting SWC initiation. However, at the same time they acknowledge that the chemical composition was responsible for the original inclusion morphology. By example they noted that sulphides were generally more deformable than oxides during hot rolling leading to innocuous geometrical shapes. However, oxides occurring as clusters were considered to be equally deterimental to SWC when they formed planar arrays or stringers during rolling.

Finally IINO et al (115,139) experimented with titanium and REM, and calcium and titanium additions to steel in order to control the inclusion morphology and prevent any tendency towards clustering. Their results showed that titanium nitride inclusions, which formed in the melt, acted as preferential sites for inclusion nucleation. This proved to successfully disperse the inclusions in the steel and prevent the formation of MnS inclusions which would have otherwise formed as a result of segregation during solidification. Steels treated this way had an improved resistance to SWC.

In summary, Type II MnS inclusions have been found to be more detrimental to SWC than other inclusions, primarily due to their tendency to elongate during rolling. Inclusion shape control, which is brought about by compositional changes, if carefully managed, can result in inclusions

with a globular morphology that do not deform during hot rolling leading to an improvement in SWC resistance.

2.2.3.2 INCLUSION VOLUME FRACTION (SULPHUR AND OXYGEN CONTENT)

The volume fraction of inclusions has very seldomly been reported in studies of SWC, normally the susceptibility of steels has been related to total sulphur (8,123,137) and sometimes oxygen and sulphur levels (115,139), as these can be determined more conveniently than inclusion volume fraction. However, VANDER VOORT (195) reports that numerous image analysis studies, to determine volume fraction, have shown that calculations of the weight percent of sulphur or oxygen in the inclusions based on image analysis measurements agrees well with the sulphur and oxygen content determined by traditional analytical techniques. Thus it would seem that inclusion volume fraction is satisfactorily characterised by sulphur and oxygen levels in steel in relation to SWC susceptibilty.

The literature (123) reports some disagreement, however, as to the effect of sulphur content upon SWC and the data is often associated with a great deal of scatter. This is not surprising, since the steels examined were produced by different steelmaking methods (continuously or ingot cast) which results in different solidification patterns and hence segregation. Also the inclusion morphologies and compositions were often different, this may influence the results for steels with essentially similar sulphur contents (see last Section 2.2.3.1).

MIYOSHI et al (8) have examined the SWC susceptibility of a number of linepipe steels with strengths from 393 to 641 MPa. For specimens extracted from the less segregated parts of the ingot resistance to SWC increased with decreasing sulphur content, whereas, for specimens from the more segregated parts of the ingot, SWC was independent of sulphur level.

A study by FUJII et al (162) compared the occurrence of SWC in a Grade X 359 MPa seamless linepipe produced via ingot casting and continuous casting. Their results are presented in Fig.46. Clearly SWC resistance is improved in the continuously cast steel. This, they believed, was a direct result of the reduced segregation produced by this casting method.

To determine the extent of segregation and the effect of inclusion shape control upon SWC resistance, NAKAI et al (110) made an extensive investigation of SWC in a Grade X448 MPa linepipe produced by the ingot route. The degree of SWC was measured by ultrasonic scanning, and specimens were extracted from various positions corresponding to the original ingot. Their results are shown schematically in Fig.47, the atomic concentration ratio (ACR) reflects the quantities of calcium or REM added to obtain inclusion shape control (See Fig.26 and Text in Section 2.1.3). They concluded that a remarkable decrease in the occurrence of SWC is observed in steels when the ACR ratio exceeded 1.8. This was believed to be due to the removal of "V" and "A" segregates through treatment by calcium or REM.

A study by IINO (137) investigated the influence of sulphur content on the SWC resistance of a number of linepipe steels. The steels were prepared (Grade X449MPa) by laboratory melting and controlled rolling. Additionally, the effect of applied stress on the amount of hydrogen evolved after electrolytic charging was examined. The sulphur content of the steel specimens was 0.001, 0.007, 0.0121 and 0.025 wt%. The steel containing 0.007% S was found to be the most susceptibile to SWC. IINO (137) concluded that this result occurredas the time required to attain a critical level of hydrogen for cracking was the least for this steel at the hydrogen charging rate used in the experiment, the hydrogen

FIG.47 : Comparison of the suceptibility of SWC between low S steel and rare earth or Ca treated steel (110) .

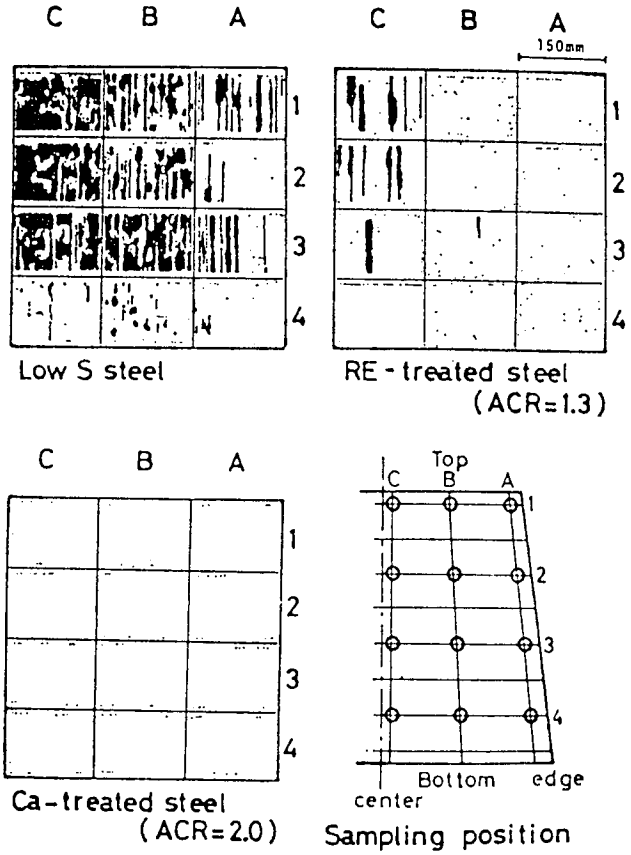

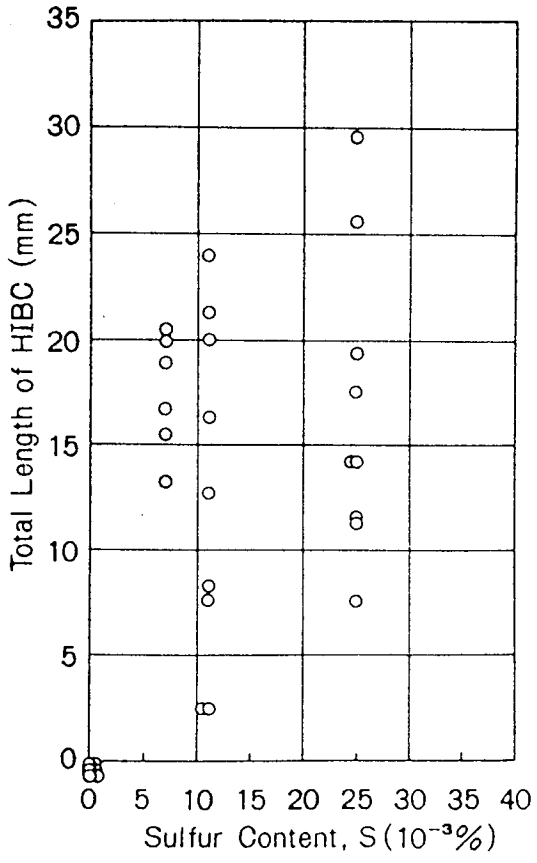

FIG.48 : Total length of HIBC (SWC) in immersion test (132) .

supply rate was believed to be influenced by the charging conditions and stress state. Consequently, he proposed that if the hydrogen charging rate was increased then the dependence upon sulphur level would be eliminated. Such a result was found when the charging current was increased, resulting in an increased hydrogen supply.

In a subsequent paper HILL and IINO (132) have shown that for long term immersion tests (NACE test) the extent of cracking increases with increasing sulphur content (Fig.48). In discussing the previous results above (137), and the results of the long term immersion tests they concluded that SWC resistance could change depending on the stress state, the range of sulphur content and the strength level of the steel.

The concept of a critical hydrogen concentration requirement, necessary to cause cracking has been developed by PRESSOURYE et al (155,168,193) and a model to determine the SWC resistance of linepipe steels has been produced for a range of sulphur contents (16). The following observations were considered to significantly affect SWC resistance; A large density i.e. volume fraction, of homogeneously distributed inclusions was believed to be beneficial to SWC resistance because the amount of hydrogen trapped on an inclusion at a given time (C_H) (See Fig.39 and 40 for an explanation of C_K and C_H) increased slowly. However, this only offered a temporary solution as a critical concentration of hydrogen (C_K) could eventually be reached. This is in agreement with IINO'S observations above. PRESSOURYE et al (160) further commented that heterogeneous distributions of inclusions would be deleterious to SWC resistance as the effects of hydrogen would be concentrated and facilitate cracking such as observed in areas of segregation. A low inclusion density would naturally be advantageous to SWC resistance. The model presented by PRESSOURYE et al (160) made the following assumptions; 1) the shape of inclusions would become rounder as the sulphur content decreased, 2) the inclusion interparticle spacing

would increase as the sulphur content decreased and, 3) inclusions were considered to get smaller the lower the sulphur content. The results are shown schematically in Fig.49. According to their premise cracking would start when the hydrogen at an inclusion (n_H^{ip}) exceeded the critical concentration for cracking (nc), where the parameters of inclusion size (di), interparticle spacing (x) and sulphur content were extrapolated from results collected from the literature (196). It was concluded that the model predicted behaviour in agreement with the results of SWC tests from the literature. SWC either increasing continuously with increasing sulphur content (Fig.49 - CURVE A) or reaching a maximum at a certain sulphur level (Fig.49 - CURVE B) depending upon the rate of hydrogen supply.

To confirm these results PRESSOURYE et al (160) carried out SWC tests (NACE test) upon 30 industrial heats of normalised steels with a wide range of sulphur contents. They also determined various inclusion parameters using a QUANTIMET 720 image analyser, these were; average inclusion length and thickness, aspect ratio, the interparticle spacing and the number of inclusions per unit area (mm^2). The results of this investigation found that as the sulphur level decreased the length and aspect ratio of the inclusions decreased and the interparticle spacing at the 90% probability level i.e. the probability of finding another inclusion at a given distance with 90% confidence, increased. The results of the SWC tests are shown in Fig.50, from these it can be seen that a maximum susceptibility occurs at a sulphur level of 0.003%, and then recedes until a sulphur level of 0.012% when susceptibility increases again continuously with sulphur content. To explain these results they determined that four ZONES existed (Fig.51),

ZONE 1 - 0.002%S - no cracking occurs as the value of hydrogen trapped per particle (n_H^{ip}) is less than the critical concentration required (nc).

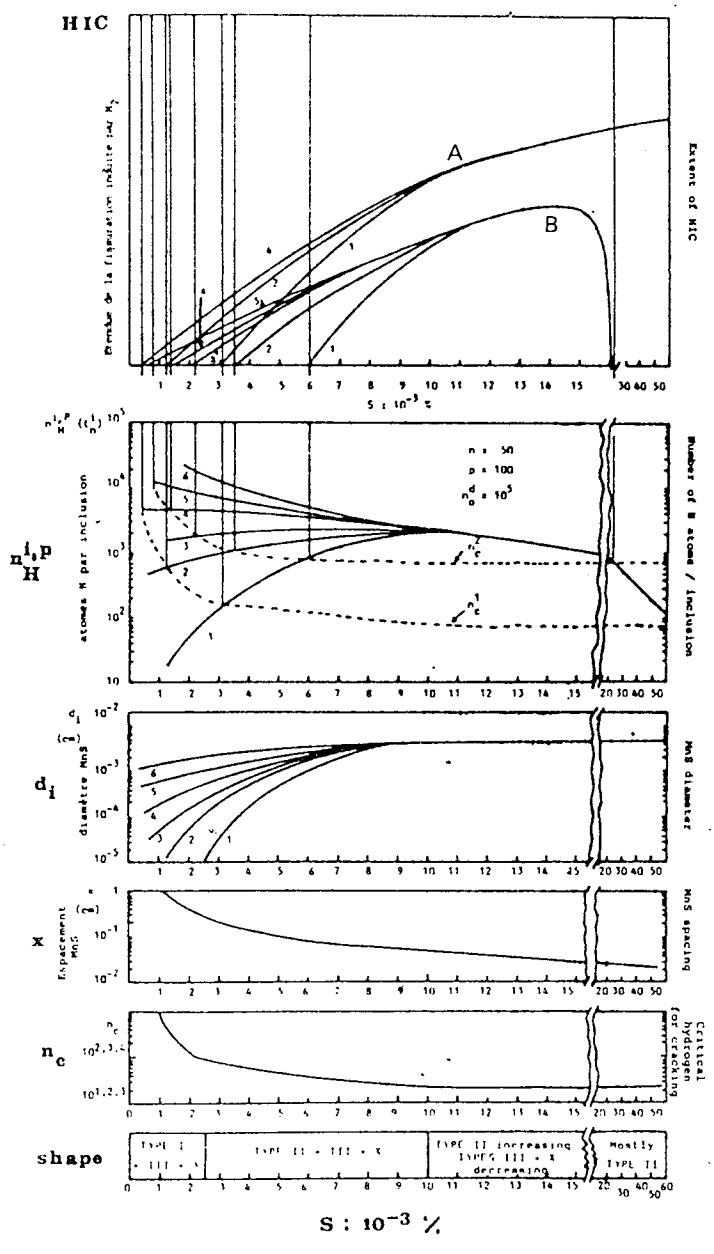

FIG.49 : Model of hydrogen embrittlement to determine the SWC(HIC) resistance of steels with different sulphur contents (160) .

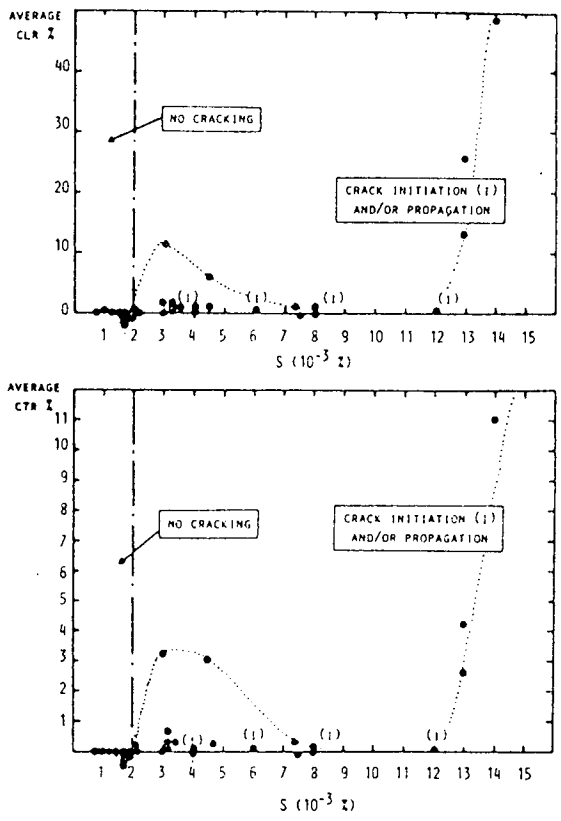

FIG.50 : SWC occurring in 30 industrial heats of steel with various sulphur contents (160) .

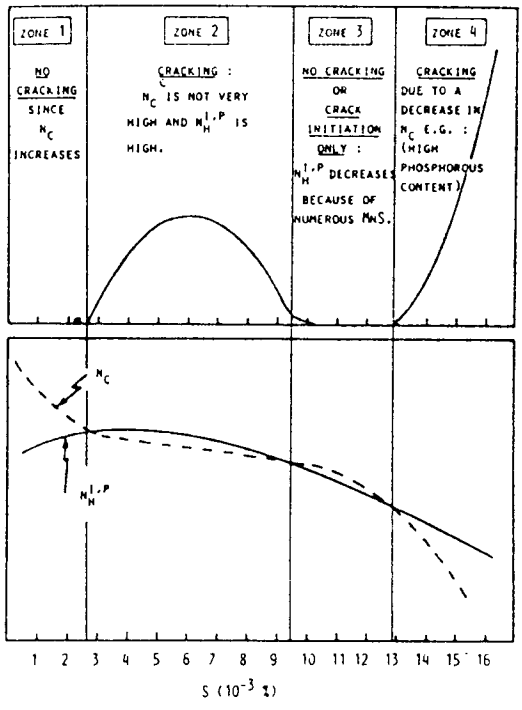

FIG.51 : Schematic determination of SWC suceptibility (160) .

ZONE 2 - cracking occurs as Nc is not high enough and/or n_H^i P not low enough.

ZONE 3 - where cracking does not or is just initiated, due to a beneficial effect of the numerous inclusions present.

ZONE 4 - where cracking restarts due to a drop in Nc (high sulphur and segregated ZONES containing phosphorus and high carbon equivalent leading to anomalous microstructure).

In conclusion they determined that steels free of SWC can be produced if the sulphur level is below 0.002% and the phosphorus content low (< 0.007%). These levels were shown to be related to the fact that below these critical values, sulphides get rounder, finer, and more homogeneously distributed, with less microsegregation at the interface and in the neighbouring structure. Above these amounts SWC was found to occur versus sulphur content with or without maxima. This was shown to be related to the phosphorus content and other microstructure characteristics of the steel (e.g. carbon equivalent) Fig.52. In addition it was stated that oxide inclusion would become important in controlling SWC susceptibility at low sulphur levels.

2.2.3.3 SIZE,SHAPE AND DISTRIBUTION OF INCLUSIONS

Large inclusions, regardless of their composition and morphology, are generally held to be detrimental to the SWC resistance of steels (115,159). However, the shape of inclusions is regarded by many authors to be the parameter principally affecting the steels susceptibility (115,123,126,135,150,160). Hence, numerous investigators have reported improved SWC resistance with inclusion shape control (See Section 2.2.3.1), which also has the effect of reducing segregation of sulphur and oxygen and thereby producing a more homogeneous distribution of inclusions in the steel.

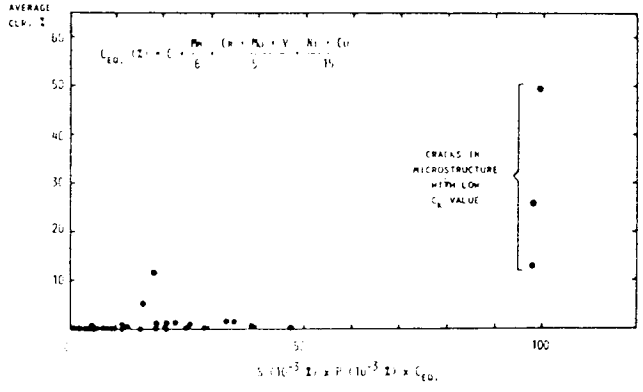

FIG.52 : Step-wise cracking as determined by the crack length ratio (CLR) versus the sulphur ,phosphorus and carbon equivalent (160) .

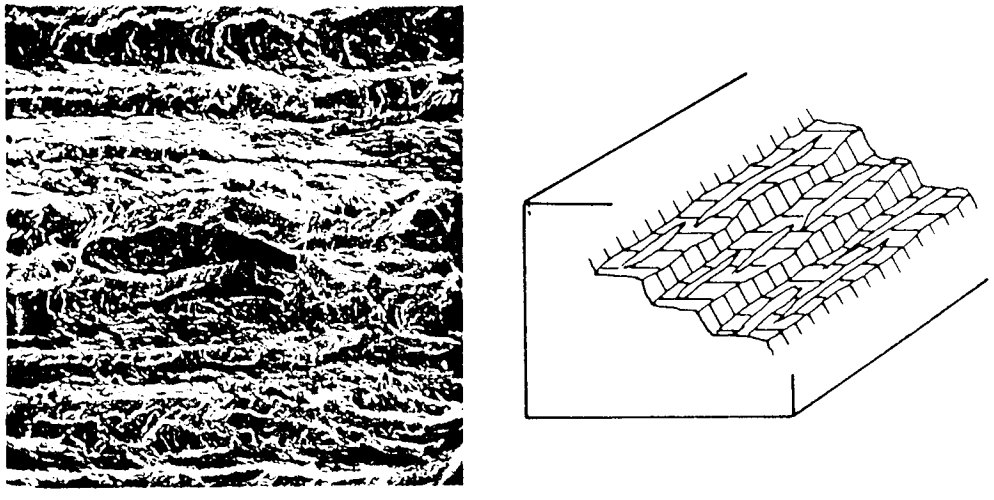

FIG.53 :SEM fractograph of linepipe showing regions of stepwise crack propagation - Mag. X500 . Sketch shows inclusions in relation to steps (150).

In a study of SWC in a number of linepipe steels of Grade X290 to X552 MPa, submitted to the B.P. immersion test, PARRINI and DE VITO (135) concluded that lowering the sulphur content was a necessary but not sufficient means for improving SWC resistance,in as much as the shape of the inclusions - as much or more than quantity - was the most important factor.

IINO et al (115) reported that SWC occurred when hydrogen became trapped at the interfaces of "crack like flat sulphides and the matrix". When the width of these sulphides exceeded about 10 microns SWC nuclei would occur. A nuclei, once formed, would become pressurised with hydrogen gas to form a crack. Growth would then be facilitated by stress induced diffusion to the crack tip region, promoted by pressurisation of the cavity. Around a globular inclusion, on the other hand, no stress induced hydrogen diffusion would take place because of the lack of any triaxial stress concentration. This, IINO et al (115) concluded, was the very reason why inclusion shape control is essential for improvements in the SWC resistance of linepipe steels.

The propagation of SWC, has been reported by WILDE et al (150) to be dependent upon the location and distribution of the inclusions which incubate hydrogen blisters. They considered that the step width was related to the number of inclusions in that plane which blistered, whereas the step height was governed by the distance between such planes and the stress distribution associated with the crack. This is shown schematically in Fig.53.

HERBSLEB et al (126) have likewise attributed cracking to be influenced by the location, geometrical shape and population of non-metallic inclusions. They proposed that continuously cast steels, which produced a more favourable distribution of inclusions than ingot cast (See FUJII

et al (162) Section 2.2.3.2), and low sulphur contents leading to a reduction in the number of inclusions would improve SWC resistance.

MIYOSHI et al (8) investigated the effect of rolling, and inclusion elongation upon SWC susceptibility. They determined the inclusion plasticity in an Al-killed steel of composition 0.22C, 0.97Mn, 0.016S, 0.04Nb and .03V (wt%) which was given a 60% reduction at various rolling temperatures. Their results were presented as the distribution of inclusion lengths (Fig.54). Lower finishing temperatures, with the exception of the sample rolled at 650°C, were found to increase the number of elongated inclusions. As the inclusions were reported to be of Type II and III MnS these results are in agreement with investigations of the deformability of inclusions carried out by BAKER et al (197,198). The authors then determined the SWC susceptibility of these steels and related this to the (total) projected length of inclusions (Fig.55), it can be seen from this that regardless of the finishing temperature, the crack length tends to be enlarged with increasing total inclusion length. However, they also report that similar shape change is also observed in extremely low sulphur steels, but the amount of inclusions in these steels is much reduced, total inclusion lengths being very small. Consequently they concluded that shape change of inclusions cannot dominate SWC in the extremely low sulphur steels produced by controlled rolling.

A study by JONES et al (133) evaluated the projected length of inclusions and the SWC susceptibility (NACE test) of 29 commercially produced linepipe and fitting steels of yield strength between 358 and 552 MPa. No correlation was found between SWC resistance and projected length nor for that matter sulphur content. They did find, however, that SWC initiation was controlled to a large extent by the non-metallic inclusions, which they considered to be most adequately described by the measurement of projected length. However, the microsegregation of Mn was

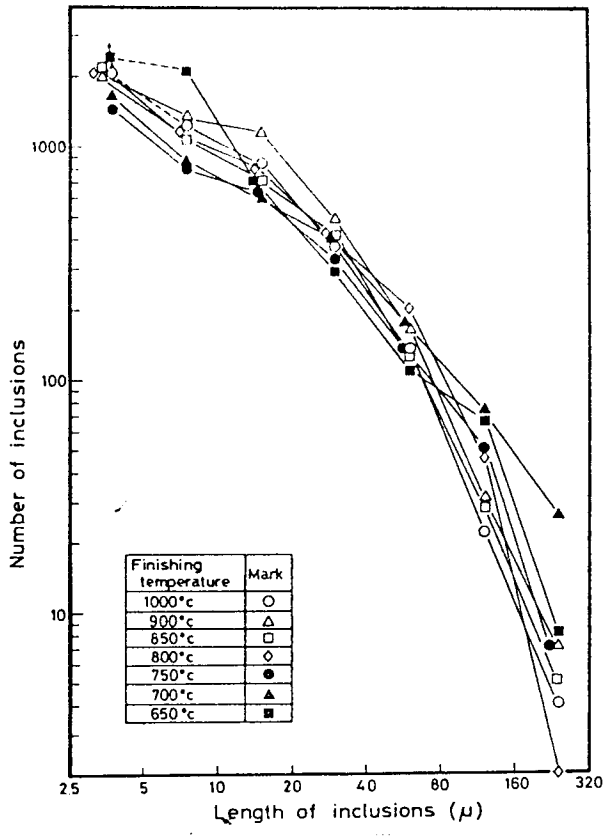

FIG.54 : Influence of finishing temperature on the size distribution of inclusions (8) .

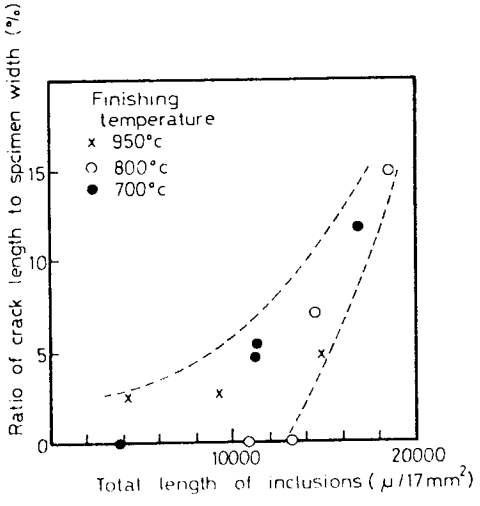

FIG.55 : Relation between ratio of crack length to specimen width and total length of inclusions in steel (8) .

also felt to be important, since cracking was observed in the segregated bands of the low sulphur steels (<0.002) that had completely modified inclusions. A fairly good correlation was obtained between SWC resistance as expressed by the crack length ration (CLR) if both the projected length of the inclusions and the average Mn content in the pearlite bands and segregation zones was determined. This was expressed by the formula below, see Fig.56,

$$C_S = Mn + 0.23\Theta$$

where, Cs= the index of SWC susceptibility Θ = total projected length of non metallic inclusions mm/mm^2 .

It was considered that the projected length of inclusions was a useful parameter as it gave an estimate of the number, size and shape of the inclusions. However, no attempt was made to determine the interparticle spacing as this was found to be extremely difficult to measure. Therefore, the through thickness crack susceptibility (as measured by CTR or CSR) was not related to the inclusion parameters since the inter-inclusion spacing would be critical in the analysis.

Returning to the model proposed by PRESSOURYE et al (16) based upon a critical hydrogen concentration for SWC (Previous Section 2.2.3.2. and Section 2.2.2.3), these authors commented upon several factors concerning inclusion size, shape and distribution as they affect SWC resistance:-

Size large inclusions were considered deleterious, even if round in shape, because of the higher probability that they will lie in a microstructural region which has a low resistance to cracking (low CK value - see Fig.40) to SWC (159),

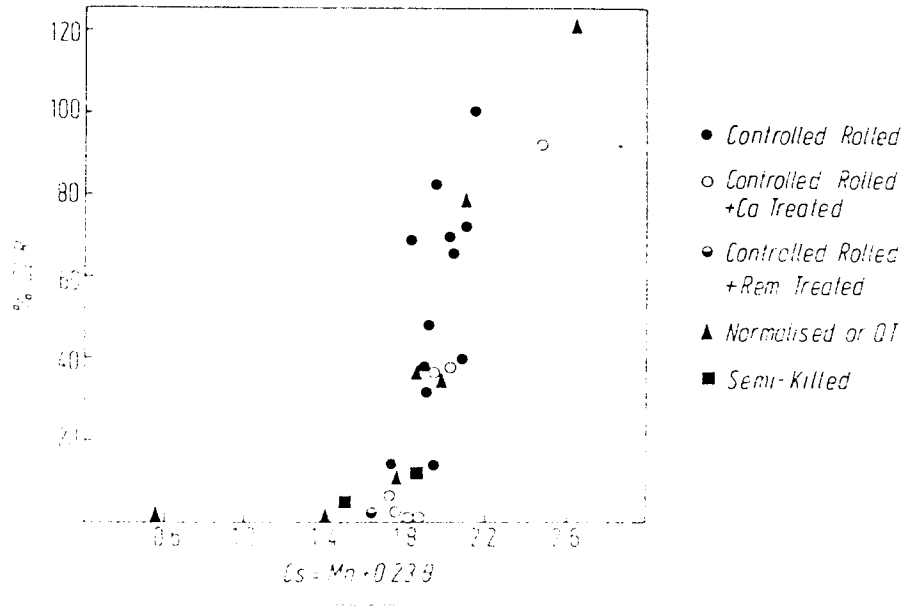

FIG.56 : Plot of CLR versus the index of HIC suceptibility, Cs (133).

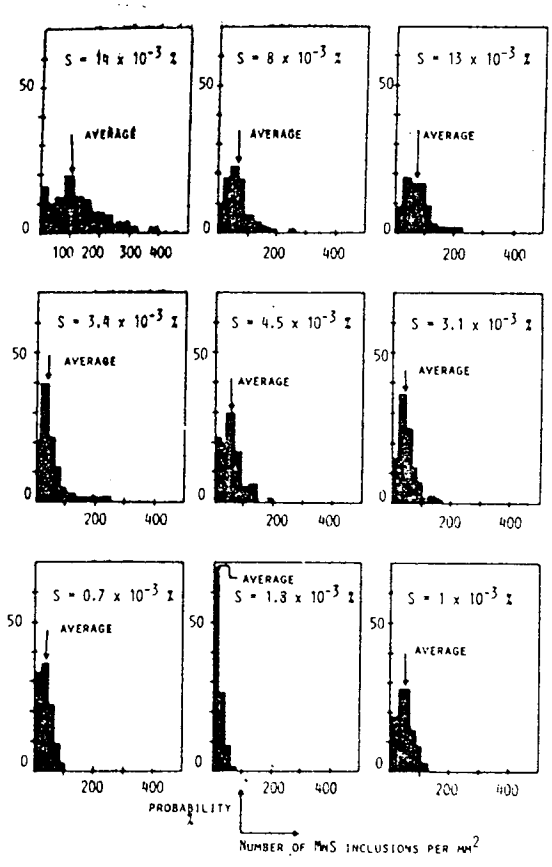

FIG.57 : The distribution of sulphide inclusions for steels of various sulphur contents (160) .

Shape — shape will influence the final pressure developed at the inclusion interface (199), the stress system around the particle (200) and the diffusion of hydrogen towards the particle (201). All the data they collected pointed toward the disadvantageous effect of elongated shapes, hence, round shapes were considered beneficial and,

Distribution — heterogeneous distributions of inclusions (oxides or sulphides) were considered bad, as high local concentrations of hydrogen could collect (with concomittent decohesion and stress concentration).

In their study of the SWC susceptibility of 30 normalised commercial steels PRESSOURYE et al (160) determined the distribution of sulphide inclusions for steels with high, medium and low sulphur contents using a QUANTIMET 720. As the sulphur content decreased the probability of observing a large number of inclusions per mm decreased (Fig.57) and the distribution became more closely centred around the mean. This was taken to be evidence of the sulphide distribution becoming more homogeneous as the sulphur content decreased and another reason (apart from shape, size etc.) why the critical hydrogen concentration for SWC should increase.

3.0 EXPERIMENTAL PROCEDURE

INTRODUCTION

The experimental programme was designed to produce a number of steels, by small-scale melting (18kg), the compositions of which were controlled to obtain the higher levels of inclusion volume fraction (sulphides) and manganese found in the segregated zones of commercially manufactured linepipe steels. These areas are known to be particularly susceptible to SWC(123).

In the production of the experimental melts, oxygen levels were controlled by aluminium deoxidation i.e. to produce a killed steel. To vary the inclusion dispersion between steels, calcium silicide injection was carried out. Four steels with different inclusion characteristics were finally produced for experimentation.

The resulting cast ingots were sectioned and hot rolled at various temperatures. The plates were then themselves sectioned for the purpose of quantitative metallography, mechanical testing, and wet hydrogen sulphide immersion tests i.e. hydrogen charging. The latter tests were carried out upon unstressed steel coupons, and notched tensile specimens, which were immediately pulled to failure after charging.

Scanning electron microscopy and quantitative metallography was undertaken to investigate the interaction of inclusions and hydrogen. Observations were made of any cracking in the unstressed steel coupons and changes in the fracture appearance between the uncharged and charged tensile specimens.

3.1 MATERIAL PREPARATION

3.1.0 EXPERIMENTAL MELTS

Melting was carried out using a RADYNE 60kw, 3kHz induction furnace. The unit was contained within a sindanyo box i.e. coilbox, that could be tilted hydraulically to facilitate casting. The furnace layout, refractories and argon supply are shown in Fig.58A and B. The furnace was designed to minimise reoxidation, by maintaining an argon atmosphere throughout melting and during casting. Highly stable refractory materials e.g. alumina were used throughout its construction. It was anticipated that these factors in combination with the stirring effect produced by the induction would allow control of the melting conditions.

The crucibles used for melting were of high alumina and had a capacity for 30kg of molten steel. The top section of the crucible was cemented into the coilbox with a high alumina cement. This was cast as one continuous piece and was moulded to form the lower half of the pouring spout as well. A tightly fitting mild steel lid, which was lined with alumina, was manufactured so that an argon atmosphere could be maintained within the furnace during melt out and melt conditioning. This lid also served to reduce excessive heat loss, it was sealed in position using a refractory putty. Contained within the lid was a series of discharge vents through which argon was supplied and also a charging hatch. The hatch was manufactured from graphite and had a central hole through which the refractory lance was passed during calcium silicide injection. It was also used as an observation port, for making alloy additions, and taking temperature readings. Whilst this port was not in use it was sealed with a tightly fitting graphite plug. Graphite was used to construct the charging hatch as it offered a method of oxygen control by

60 KW - 3 KHz INDUCTION FURNACE

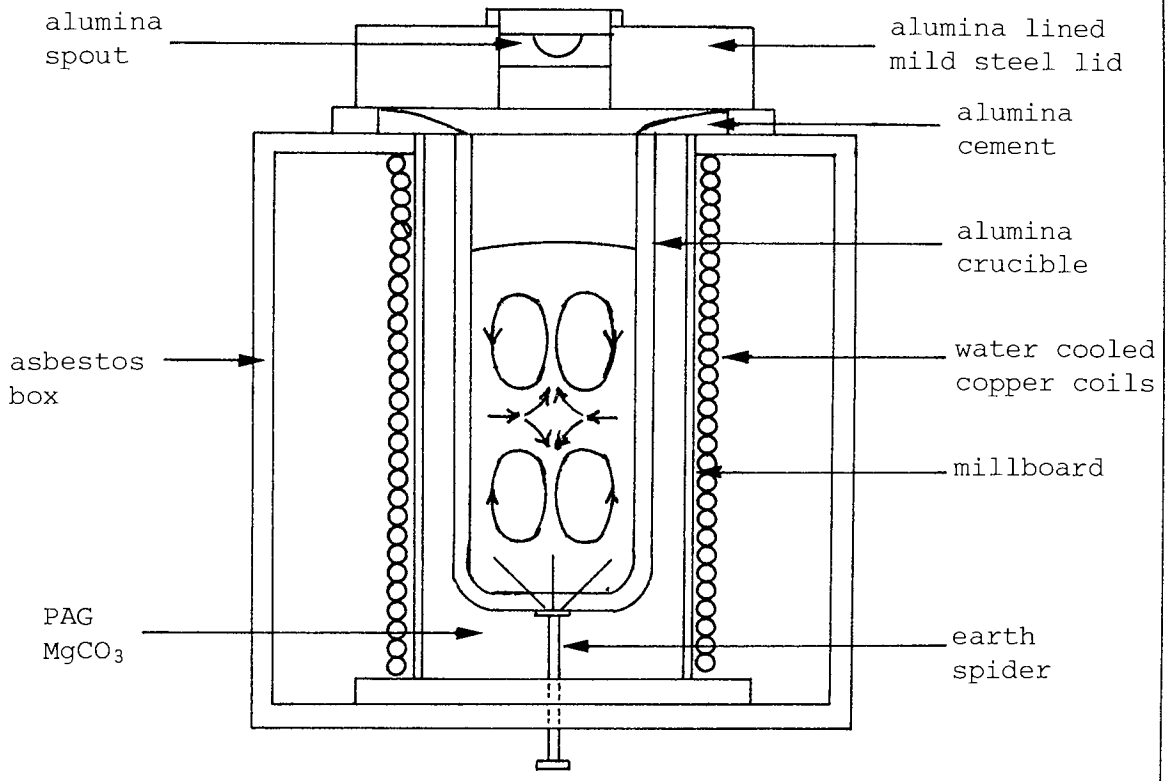

FIG.58A : Front view - showing refractories .

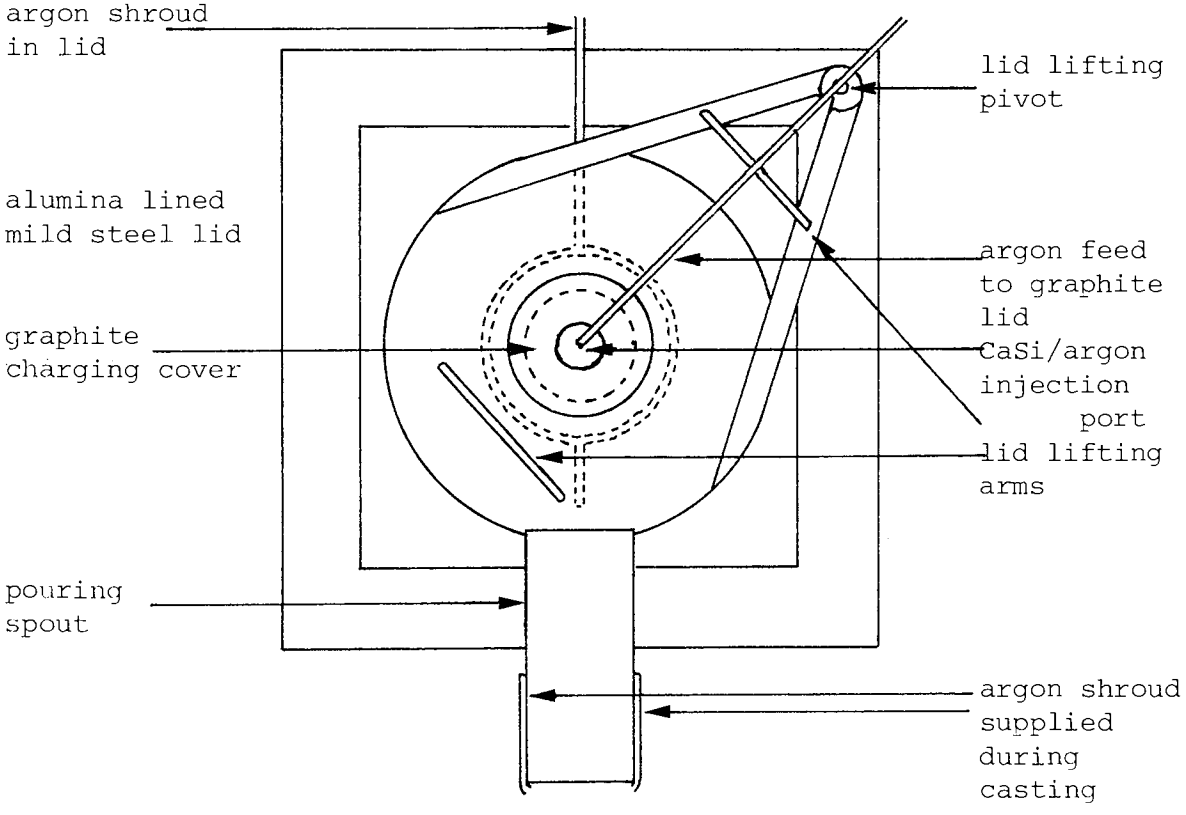

FIG.58A and 58B : Furnace layout, refractories and argon supplies .

reacting with any air ingressed into the furnace. Argon was also supplied to the graphite cover to prevent oxidation.

The pouring spout was shielded from the atmosphere by a moulded alumina cover, which was fixed in place and sealed with refractory putty resulting in maximum protection for the molten steel when casting against reoxidation. At the end of the pouring spout were attached two jets which supplied argon during casting. This assured an argon shroud around the molten steel stream when it was poured into the ingot mould.

3.1.1 MELTING PROCEDURE

Prior to producing a melt in a new crucible a wash melt was always carried out in order to ensure that the refractory cement and the unit as a whole was free from moisture.

The casts were produced using a charge of 18kg of low carbon mild steel scrap of nominal composition:

C	Si	Mn	P	S	Cr	Mo	Ni	Al	Cu	Sn	O	N	Ca	H wt%
.06	.05	.39	.015	.019	.04	.01	.09	.001	.03	.009	.007	.0065	.0002	.0001

A low sulphur melt was also produced using a charge of electrolytic iron of nominal composition:

C	Si	Mn	P	S	Cr	Mo	Ni	Al	Cu	Sn	O	N	Ca	H
.01	.01	.01	.01	.01	T	T	T	.005	T	T	.065	ND	T	ND

T = trace, ND = not determined

The majority of the charge was packed into the crucible, and any remaining metal was added through the charging hatch after the initial charge had melted out.

After charging, the lid and pouring spout cover were sealed into position and the argon flow started. The furnace power was then switched on and maintained at a maximum (60KW) during melt out.

As melting proceeded the whole furnace unit was tilted occasionally in order to assist the downward movement of the charge, and prevent "bridge" formation. In the development of a reproducible melting technique the problem of "bridge" formation was repeatedly encountered. A total of twenty-seven melts were made before four ingots of acceptable composition were obtained. "Bridge" formation occurred as a result of temperature gradients within the material charged to the furnace, these resulted from an unbalanced power supply. The furnace power coupled strongly into the charge in the lower half of the crucible and melted the steel there, whilst the material above fused across the crucible adhering to the side and forming a "bridge", this was then unable to fall into the molten steel beneath. The increased density of steel in the bottom of the furnace, as a result of melting, caused the power to be concentrated to an even larger extent in this region, further unbalancing the power supply, and super heating this liquid.

In these circumstances, if the furnace was left on full power, in an attempt to melt the bridge, but not tilted, the temperature generated in the molten steel at the bottom of the crucible and the intense stirring power of the induction eroded the crucible usually resulting in earth leakage causing the furnace to cut out (spider at the base of the crucible - see Fig. 58A). Careful tilting of the furnace, under power, was found to be the only method capable of overcoming this problem. The molten metal in the bottom of the crucible was used to melt through one side of the "bridge", by careful tilting, which then allowed it to fall into the melt when the furnace was tilted back to its normal position.

This, however, could not be achieved without removing the graphite lid, and hence opening the furnace to the atmosphere.

Once melt out had been achieved and all of the steel charged, the power supply was turned down (≃25kW) and the temperature of the melt maintained at 1600°C.

Temperature readings were taken using a platinum/platinum-13% rhodium thermocouple, protected by a silica sheath attached to the end of a stainless steel probe. The silica sheath containing the thermocouple was placed into the centre of the molten bath to a depth of about 20cm (with the power off) and held until the temperature reading stabilised. The readout was taken directly from a calibrated digital recorder.

3.1.2 DEOXIDATION AND ALLOY ADDITIONS

Deoxidation was carried out entirely by aluminium. Levels of residual aluminium aimed for in the cast steel were 0.04%. At this quantity of aluminium the soluble oxygen content would be expected to be less than 5ppm according to recent equilibrium data (35). The levels of manganese and silicon aimed for in the steel were 1.6% and 0.25% respectively. Adjustments to carbon levels were also necessary, the carbon content aimed for was 0.1% except for one melt where a low carbon content was desired (≃0.02%).

The melt additions for the four steels used for further experimentation are shown in Table 3.1 below, the steels are identified as casts F, L, K and M.

TABLE 3.1 DETAILS OF STEEL MAKING - 18Kg MELT

Steel Code	Additions - grammes					Injection Time (Min)	Flow Rate	Cast Temp C	Comments
	Al	Mn	Si	C	CaSi				
F	40	245	48	-	-	-	-	1580	0.02S
L	40	245	48	10	-	-	-	1600	0.02S
K	50	252	-	8	65	1.5		1600	High S 0.02 Ca injected
M	62	330	-	25	65	1.0		1610	Low S 0.01 - charge, electrolytic Fe

NOTE: Melt out took between 35 and 50 min. i.e. stabilised temperature 1600°C.

The amount of aluminium, manganese, silicon and carbon that was added was based upon previous melting experience gained during the development of the melting technique.

Deoxidation was carried out immediately after the temperature of the molten bath had stabilised at 1600°C. The addition was made through the charging port. Commercial grade aluminium as fine turnings was contained within a crimped shim-steel cartridge, the cartridge was attached to a mild steel plunging rod, which was immersed into the molten steel.

The alloy additions were made two minutes after deoxidation. Crushed, electrolytic manganese flakes, lump silicon and graphite (<1mm) were used. These were added using the same method as for the aluminium addition.

3.1.3 CALCIUM SILICIDE INJECTION

The injection of calcium silicide powder was carried out using an apparatus provided by Foseco Limited, Birmingham. The powder used was an alloy of 30%Ca/70%Si.

The injection unit (Fig.59) consisted of a two compartment perspex cylinder which was uniformly pressurised by argon. The upper compartment contained the calcium silicide charge and this was metered into the lower section by a motorised screw feed. There the powder was fluidised with the argon gas and injected, (via a short length of connecting plastic tube) through the refractory lance (silicon carbide) into the melt.

The screw feed had a variable speed, which was operated at its maximum, i.e. 60rpm during injection. The unit was capable of delivering 100g of calcium silicide in 2.5 minutes.

The whole apparatus was attached to an arm, which could be swung around and moved up and down on an upright support. The depth to which the lance was immersed into the melt was about 100mm from the bottom of the crucible. The level was predetermined before the furnace was charged and the correct position was controlled by a "stop" on the upright support.

The amount of calcium silicide injected was limited by the quantity of silicon required for alloying i.e. 0.25%. Therefore, a maximum addition of 65 g could be made for an 18kg melt, which was equivalent to 19.5 g of calcium in total or 1.08g Ca/kg steel (1.08kg/tonne).

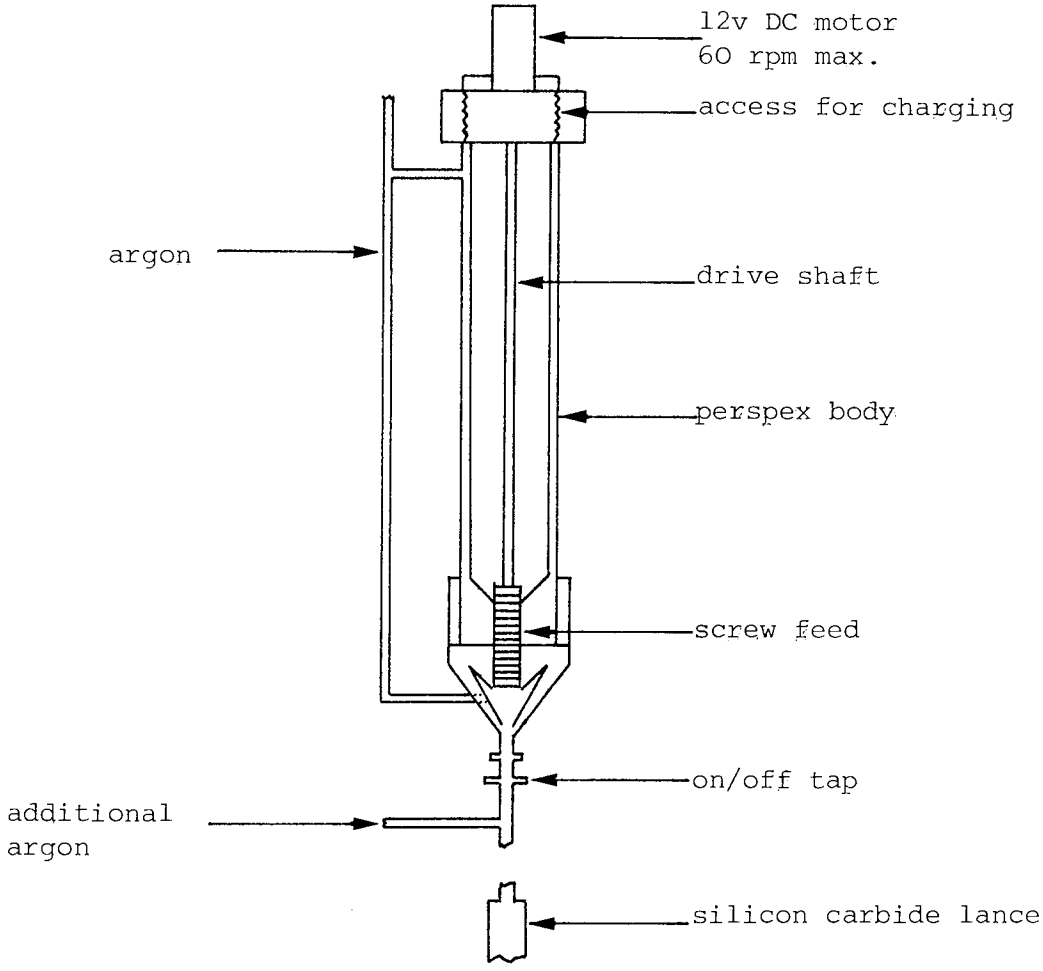

FIG.59 : Calcium silicide injection apparatus .

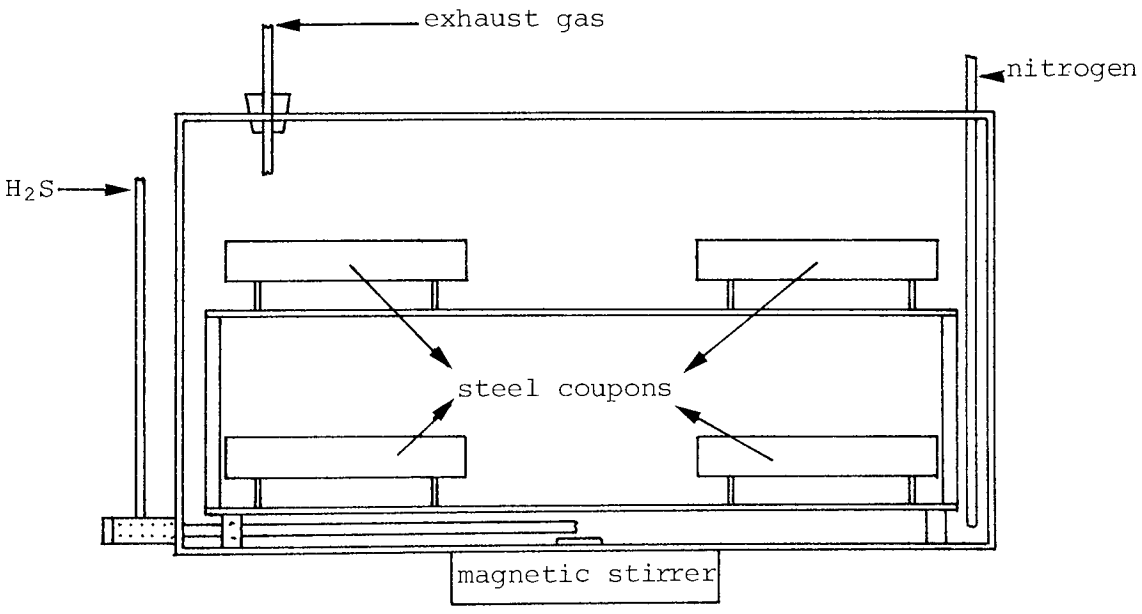

FIG.62 : Hydrogen sulphide test cell .

Injection was carried out two minutes after the addition of the alloying elements (see Table 3.1 for details).

3.1.4 CASTING

Casting was carried out two minutes after the final addition (either calcium silicide or alloying elements), and during this time a final temperature reading was taken. Just prior to casting, the argon flow rate to the furnace was increased and the argon supply to the pouring spout (see Fig.58A) was turned on.

A square sectioned cast iron ingot mould was used for casting which measured 300mm high and had a minimum cross section of 80 x 80mm, this was positioned on a steel base plate. Before use, both the ingot mould and base plate were coated with a refractory wash, and baked in an electric furnace at 500°C to ensure they were free from moisture.

The ingot mould and base plate were removed from the drying furnace a few moments before casting, and positioned directly below the pouring spout. The distance between the pouring spout and the top of the ingot mould was kept to a minimum.

The mould was purged with argon just before casting. Casting took only a few seconds. Immediately after casting the ingot was covered with a proprietary hot top (FOSECO-FEDEX 3). The mould and ingot were allowed to cool to room temperature before the ingot was removed.

3.1.5 INGOT SECTIONING AND IDENTIFICATION

The top section of the ingot was cut off and discarded, leaving an ingot of dimension 250 x 80 x 80mm. The ingot was then cut longitudinally to produce a billet 250 x 80 x 43mm. This was divided into four equally

sized sections for hot rolling, each section was identified by the temperature at which it was hot rolled i.e. the top section of each ingot was rolled at 1100°C and this was labelled 1 (see Fig.60). Thus the plate resulting from ingot M rolled at 1100°C was identified as M1, at 1000°C M0, at 900°C M9 and at 750°C M75. The sections used for hot rolling measured 80 x 56 x 43mm. The section height, 43mm, was the maximum height (roll gap) accepted by the rolling mill used. Three slices were taken from the ingot at the top, middle and bottom positions for chemical and metallographic analysis (Fig.60).

3.1.6 HOT ROLLING

Rolling was carried out using a two high mill by courtesy of Birmingham University, Department of Metallurgy and Materials. The roll diameters were 460mm and the rolling speed was 65.5m/min.

The mill settings were determined such that approximately 10% reduction was obtained for each of the first two passes, then 20% reduction per pass after that, until the final pass, when another 10% reduction was made to give a total reduction of 70% and a final plate thickness of 12.5mm, (see Table 3.2. below).

TABLE 3.2 ROLLING SCHEDULE

Pass Number	Entry Height (mm)	Exit Height (mm)	%R	ε	Mill Screw Down (mm)
1	42	37.5	10	.11	4.3
2	37.5	34	10	.1	3.7
3	34	27	20	.22	6.2
4	27	21.5	20	.23	5.5
5	21.5	17.5	20	.22	4.3
6	17.5	14	20	.22	3.5
7	14	12.5	10	.09	1.2
TOTAL			70	1.19	

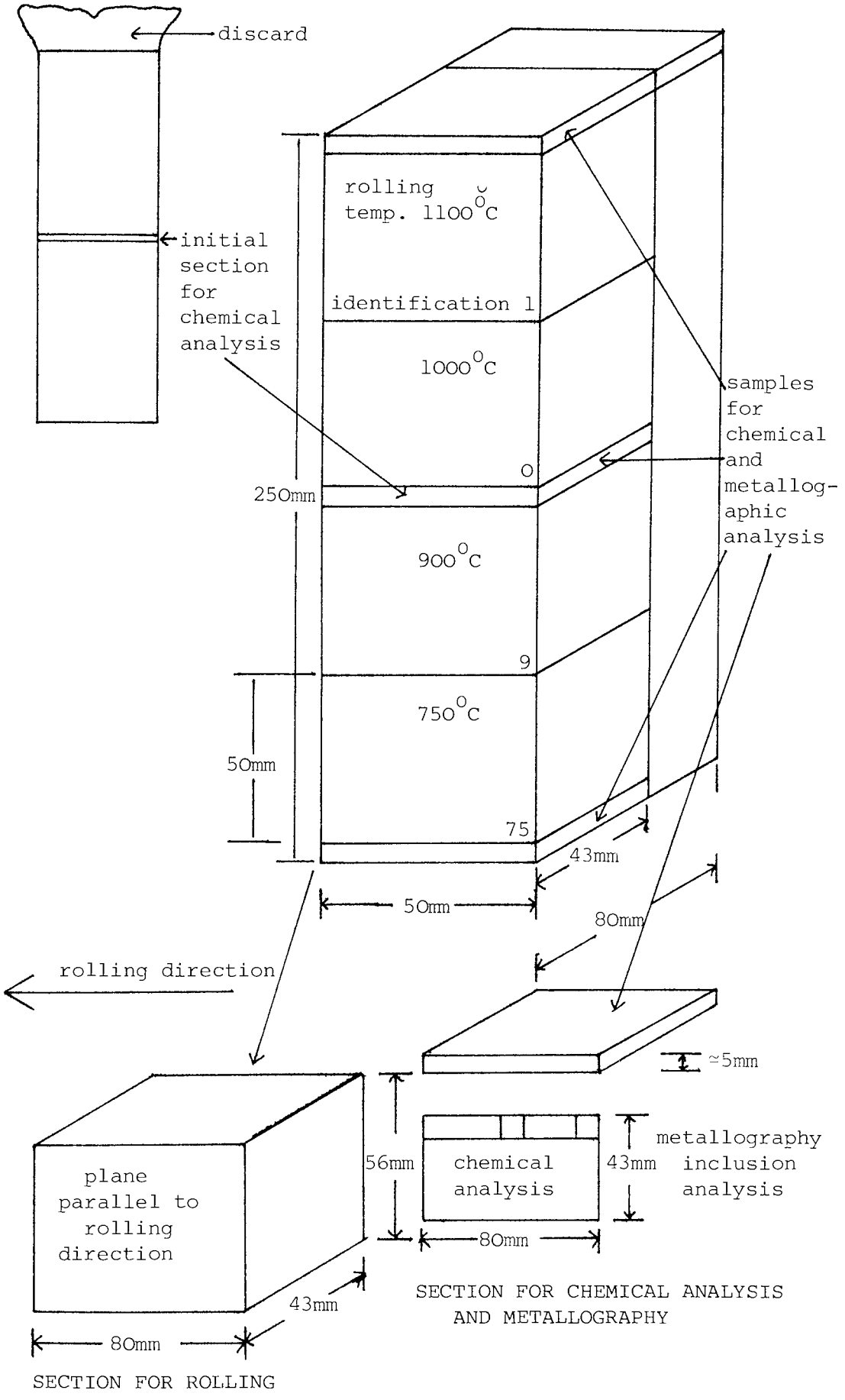

FIG.60 : Section of the as cast ingot .

The steel sections for rolling were heated in a gas-fired furnace. Four rolling temperatures were chosen to reflect the ranges of hot rolling found in commercial practice i.e. 750/900/1000 and 1100°C. Rolling schedules and the typically large reductions used in commercial practice (e.g. controlled rolling) could not be used as: (a) the maximum roll gap and hence the initial material thickness was 43mm, and (b) reductions any greater than 70% would have resulted in a steel plate insufficiently thick to allow any reasonable mechanical tests to be carried out.
The steel sections themselves were heated in a specially designed, mild steel, furnace box. This could contain four specimens at any one time. There were several advantages of using this method: i) better temperature control, ii) the box could contain a controlled atmosphere to restrict oxidation (95%N_2, 5% H_2) and iii) moving the specimens in and out of the furnace for reheating after each pass was easier.

The box had two steel tubes welded onto both sides of it which extended out of the furnace. These acted as handles, which allowed it to be moved in and out, and also one was used to supply the controlled atmosphere, whilst the other contained the thermocouple. The temperature within the box was monitored continuously. The sections were all preheated for one hour prior to the first rolling pass, after which they were returned to the furnace to reheat (approx. 10 min) between passes. After rolling was completed the steel plates were allowed to air-cool.

3.1.7 SECTIONING OF THE ROLLED PLATE

The plates were all grit-blasted to remove any adhering oxide films and then sectioned using an upright bandsaw (with a coolant), as shown in Fig.61.

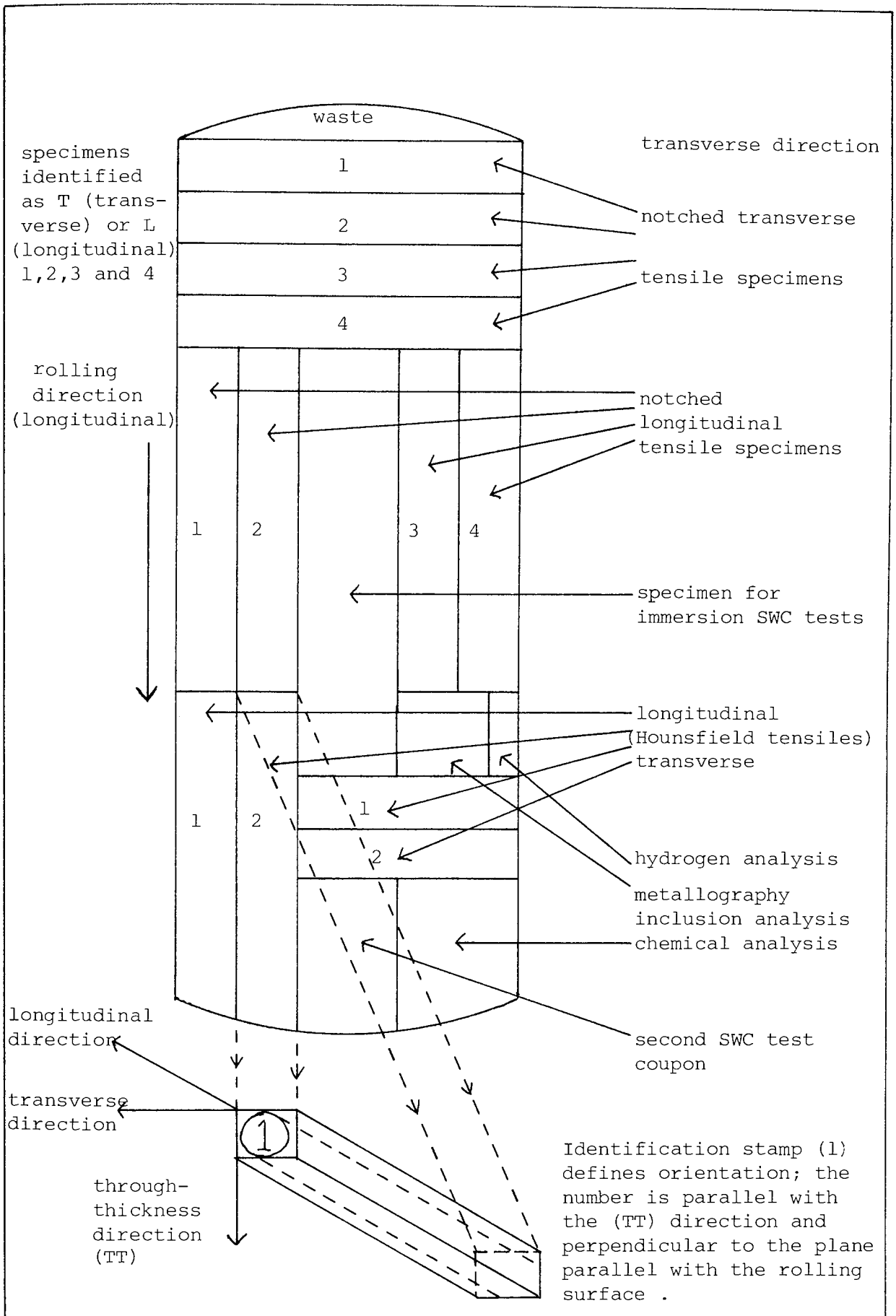

FIG.61 : Sectioning of the rolled plate .

From each plate the following specimen blanks were extracted: 1) four transverse and four longitudinal notched tensile specimens; 2) two transverse and two longitudinal Hounsfield No.14 specimens; and 3) coupons for SWC test. Additionally specimens for chemical analysis and metallography were taken. It should be noted that each specimen was stamped for identification, the stamp was made at the end such that the section perpendicular to the plate surface (see Fig.61) could be recognised after the specimens had been turned down to a tensile specimen.

3.2 MATERIAL TESTING

3.2.0 HYDROGEN SULPHIDE EXPOSURE TESTING

These tests were carried out using the NACE standard test solution TM-01-77(142) and SWC was determined in accordance with the NACE standard test method for evaluating the stepwise cracking resistance of linepipe steels, TM-02-84(125).

A test cell, manufactured from perspex, was designed to contain the test solution and specimens, using the guide-lines contained in the above standard (TM-02-84) (see Fig.62, Page 118). This had a capacity for 10 litres of test solution.

3.2.1 TEST SOLUTION

The solution was prepared from Analar reagents and the hydrogen sulphide (H_2S) gas used for the experiments was 99.9% purity. Ten litres of solution were made up as follows: 500g of sodium chloride and 50g of glacial acetic acid (48ml) were dissolved in 9450g of distilled water. The initial pH of the solution was approximately 3.

3.2.2 TEST PROCEDURE

The solution was transferred to the test cell and the specimens for exposure were equally spaced out on a perspex rack in the solution (see Fig.62). The unit was then sealed from air and purged with nitrogen for one hour to de-aerate the solution, after which it was saturated with H_2S. The initial H_2S flow-rate was 200cc per minute for one hour and then 10cc per minute thereafter. The solution was continuously agitated throughout the duration of the test by a magnetic stirrer, H_2S was introduced at the base of the cell just above the stirrer which ensured its even dispersion in the solution. The tests were conducted for 96 hours (after the initial 1-hour saturation period) at room temperature 25+ or $-3^{o}C$.

At the end of the test the specimens were removed from the solution, rinsed under cold water and cleaned of any corrosion debris using a nylon brush, they were then washed in acetone and dried. The pH at the end of the test was measured.

3.2.3 STEPWISE CRACKING TESTS

3.2.3.0 SPECIMEN PREPARATION

The specimens extracted from the rolled plates were machined and surface ground, the final dimensions were 100 x 20 x 10.2mm, the final surface finish was obtained using 320 grit paper (dry). The coupons were then ultrasonically cleaned in acetone, dried and immediately placed in the solution in the test cell. They were positioned on their long narrow sides.

3.2.2.1 SPECIMEN EXAMINATION

3.2.2.1.0 SURFACE BLISTERS

After cleaning both broad faces of the coupons were photographed. Then an analysis of the blistering on these surfaces was made using a Reichart Polyvar microscope fitted with an eyepiece graticule. The distribution of blister sizes by area was measured. As a large range of blister sizes was observed the measurements were grouped using a geometric scale to the power of 2.

3.2.3.1.1 ANALYSIS OF STEPWISE CRACKING

SWC was evaluated in accordance with the NACE standard TM-02-84(125). The steel coupons were sectioned transversely at 25, 50 and 75mm (see Fig.63A). The pieces were then mounted in conductive bakelite and given standard metallographic preparation (see Section 3.4.0). The sections were examined at a magnification of X100. Cracks were measured as illustrated in Fig.63B, cracks separated by less than 0.5mm were considered as single cracks, those which occurred at up to 1mm below the steel surface were not included in the analysis. When necessary, higher magnifications, light etching and interference contrast were used to distinguish between cracks and small inclusions, scratches or other discontinuities.

The following ratios were calculated for each section and for the average of each coupon:

$$\text{Crack sensitivity ratio, (CSR)} = \frac{(a \times b)}{W \times T} \times 100\%$$

$$\text{Crack length ratio, (CLR)} = \frac{a}{W} \times 100\%$$

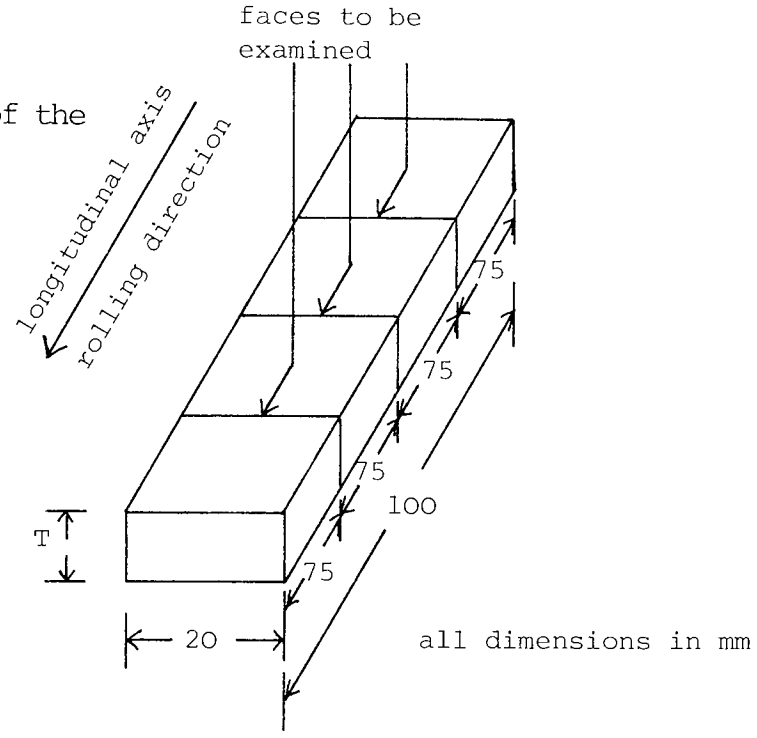

FIG.63A: Sectioning of the SWC coupon .

FIG.63B: Measurement of SWC .

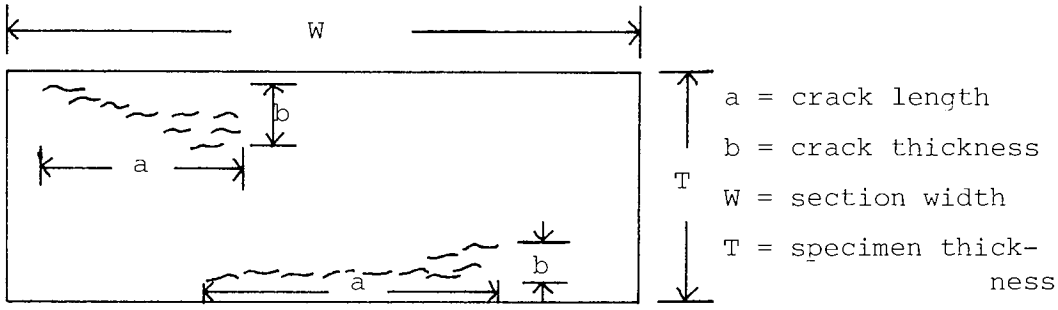

FIG.63C: Small size SWC specimens .

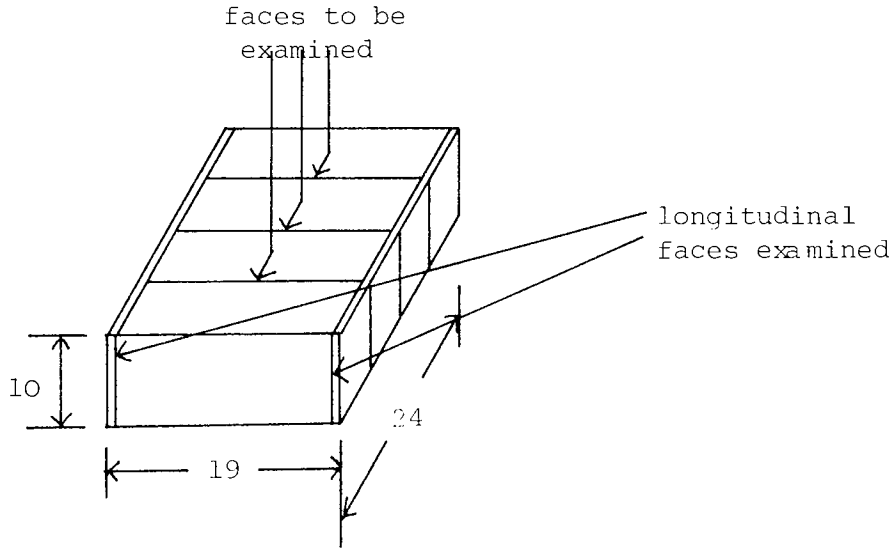

FIG.63 : Evaluation of stepwise cracking .

Crack thickness ratio, (CTR) $= \frac{b}{T} \times 100\%$

Where: a = crack length

b = cracking thickness

W = section width

T = specimen thickness (see Fig.63B)

3.2.4 FURTHER SWC TESTS

The results of the full size SWC tests proved somewhat inconclusive and therefore, a second test was carried out using smaller coupons of steel measuring 24 x 19 x 10mm. These were prepared in exactly the same way as in the previous SWC test (Section 3.2.3.0), but the duration of the tests was doubled to 192 hours.

The method of evaluating the extent of SWC was again as before (Section 3.2.2.1.1). However, the coupons were sectioned at 6, 12 and 18mm. Additionally, before sectioning, the long-side faces of each coupon were milled back 1mm and polished (see Fig.63C), the extent of cracking upon the longitudinal section was then observed. No examination of the blistering was made in this case.

3.2.5 HYDROGEN ANALYSIS

For both tests (full size and small SWC test) specimens from each steel plate measuring 10 x 10 x 20mm were prepared in the same way as the large coupons and immersed in the test solution at the same time. After the test was completed these were immediately washed and cleaned with a nylon brush in cold water, swilled in acetone, dried and then put in a large flask of liquid nitrogen. These were then sent for hydrogen analysis (see Section 3.3 Chemical Analysis).

3.2.6 NOTCHED TENSILE TESTS

From each steel plate, four transverse and four longitudinal circumferentially notched tensile specimens were machined. The dimensions and design of which are shown in Fig.64. Two from each orientation were tested after hydrogen charging and two were tested in the absence of hydrogen.

A notched rather than an ordinary tensile specimen was used for several reasons:

1 It has been shown (223) that the strain along the axis of a notched tensile specimen reduces with distance from the minimum cross-section at the notch.

By preparing metallographic axial cross-sections of fractured specimens it is then possible to measure the population and area fraction of voids at various distances along the axis. From these measurements a qualitative determination of the extent of void formation with decreasing strain (position along the axis) can then be carried out.

2 The continuous measurement of the change in notch diameter with load can be accurately determined using a clip gauge, with knife edges which fit into the notch. From this data the effective stress and effective plastic strain across the notch can be calculated and presented as a flow curve.

3 Finally, it was intended to produce through-thickness specimens, so that the notch ductility in this orientation could be measured and

related to inclusions parameters. As the thickness of the plate produced was only 12.5mm this would have necessitated the attachment of extension stubs by, for example, friction welding. The notch would then ensure that the failure occurred in the parent metal and was not influenced by the welding process. However, due to restrictions of time, this work was not realised.

3.2.6.0 HYDROGEN CHARGED NOTCHED TENSILES

To observe the effect of hydrogen upon the notched tensile properties, two of the longitudinal and two of the transverse notched specimens were tested after hydrogen charging by immersion in the NACE (142) solution for 96 hours (Section 3.2.1).

These were prepared, after machining, by ultrasonic degreasing in acetone, after which both threaded ends were protected with electro-platers stop-off lacquer.

After 96 hours exposure specimens were removed from the test solution successively (batches of 16 were tested at any one time), brushed free of any corrosion debris under cold water with a nylon brush, and then immersed in acetone to remove the stop-off lacquer. The specimens were then pulled to failure, the time elapsed between removing the specimen from the test cell to commencing tensile testing was five minutes in each case. The testing of 16 specimens, therefore, took 80 minutes (while a specimen was being tested another could be prepared), during this time the flow of H_2S to the remaining specimens in the test cell was maintained. Each time a specimen was removed (they were all individually attached to nylon fishing line, such that removal took no more than a few seconds) the cell was resealed. It was believed that for such a long period of charging and the small volume of the test pieces that the

difference in exposure times between the first and last specimens would not result in any significant variation in the results. The specimens, upon removal from the solution, would be saturated with hydrogen, and the triaxiality produced by the notch effect would also be expected to strongly concentrate hydrogen in the area of the notch (117, 183).

3.2.6.1 TESTING PROCEDURE

The notched tensile tests were carried out using a MAND precision tensile testing machine. The cross-head speed was 0.2mm/min. The change in notch diameter with load was measured using an electronic clip gauge, the knife edges of which were designed to fit into the vertex of the notch. The load versus the change in notch diameter were continuously recorded throughout the test on an x-y chart recorder. The load was calibrated on the y-axis of the chart recorder to show 2.5 tonnes full scale deflection, and the change in notch diameter as measured by the clip gauge was calibrated with a micrometer on the x-axis.

A spring loaded clip was used to hold the clip gauge in position around the notch during the test, and to ensure that it accurately followed the contraction in the notch diameter.

Additionally, two Hounsfield No.14 tensile specimens were machined from both the longitudinal and transverse directions of each steel plate. These were tested on a 50 tonne INSTRON at a cross head speed of 0.5mm/min. The uniaxial yield strength, ultimate tensile strength and the fracture strain was measured for each specimen.

For both the notched tensile specimens and the Hounsfield specimens the initial and final cross-sectional diameters were measured using a shadowgraph at 50x magnification.

3.2.6.2 STRESS AND STRAIN MEASUREMENTS

From the load versus change in notch diameter recorded by the chart recorder, the effective stress and effective plastic strain at the notch cross section were calculated using the following formulae:

$$\varepsilon_p = 2\ln(do/di) \quad \ldots . 1$$

$$\sigma_p = P/Ai \quad \ldots . 2$$

$$Ai = \pi di^2/4 \quad \ldots . 3$$

where: ε_p = effective plastic strain

σ_p = effective stress

do = initial notch diameter

di = instantaneous notch diameter

P = load (kN)

Ai = instantaneous cross sectional area

To draw the effective stress versus effective plastic strain curve (flow curve) a TEKTRONICS 4042 computer with a digitising tablet was used to digitise the load versus change in notch diameter recorded by the chart recorder. Points were digitised, beginning at the yield point, at strain increments of 0.02 representing a movement by the strain gauge of 0.05mm and 5mm on the chart recorder. A simple programme was then written using the formulae given above to convert the digitised information into effective stress and strain.

3.2.7 HARDNESS TESTING

For each steel plate Vickers pyramidal hardness was measured using a 10kgf load. Three measurements were taken on each occasion, on a flat, metallographically prepared specimen.

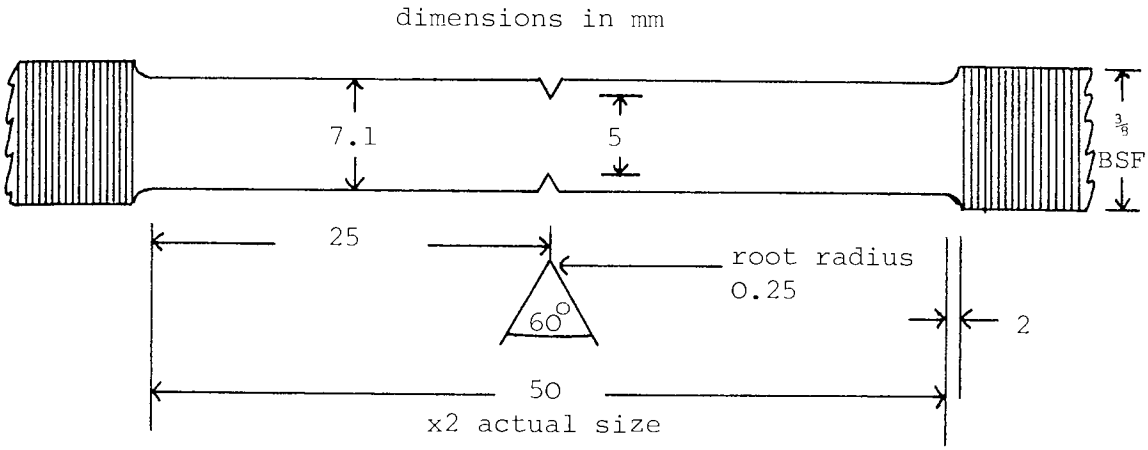

FIG.64 : Design of notched tensile .

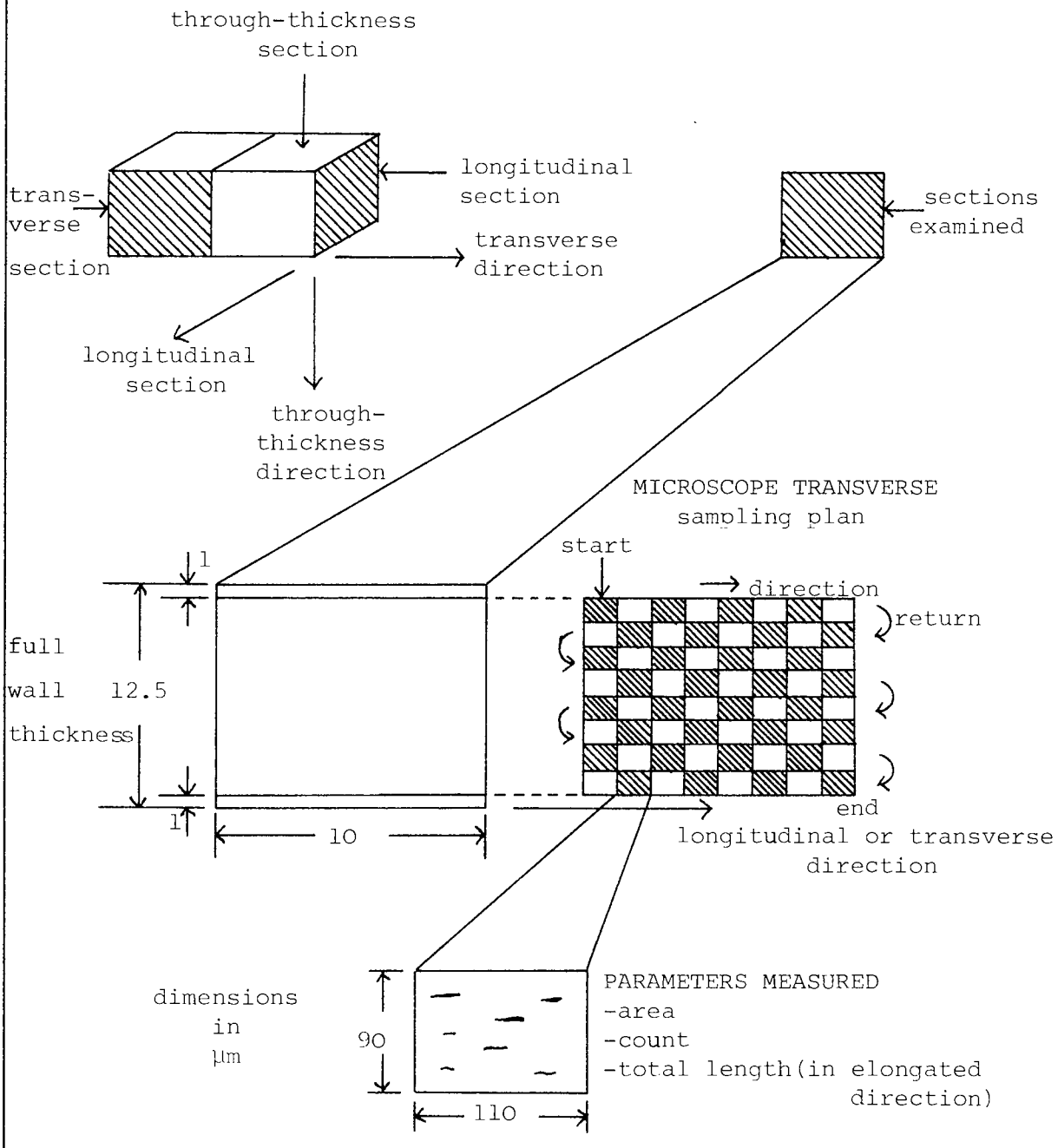

FIG.65 : Specimen orientation and sampling scheme for image analysis.

3.3 CHEMICAL ANALYSIS

All chemical analysis was undertaken at Round Oak Laboratories of Brierly Hill, West Midlands. Analysis was carried out on the as-cast ingots from the mid-section samples (see Fig.60) and the samples as shown in Fig.61 for the rolled plate.

Oxygen content was measured by hot vacuum extraction (Balzer), hydrogen was similarly determined by vacuum extraction (mercury diffusion pump) at 800°C. Sulphur and carbon contents were determined using hot fusion apparatus (LECO) and calcium was measured by atomic absorption. All other elements were measured on a Quantovac.

3.4 METALLOGRAPHY AND FRACTOGRAPHY

3.4.0 GENERAL METALLOGRAPHIC PREPARATION

All specimens for optical and scanning electron microscopy were mounted in conducting bakelite and ground and polished using automatic polishing equipment (Lecovari Pol Vp50). Wet grinding, was to 600 grit, followed by ultrasonic cleaning in Inhibisol. Final polishing was done using 6μm and 1μm diamond cloths. Etchants used were 2% Nital and 4% Picral.

3.4.1 INGOT STRUCTURE

To obtain some idea of the solidification pattern and segregation in the cast ingot, a typical ingot, of composition 0.04C - 1.6Mn - 0.25Si - 0.01S wt% was cut longitudinally through the centre. The two sections were milled flat and then finished by grinding. A sulphur print was made on one half of the ingot, whilst the other half was swabbed with a solution of ammonium persulphate (20%) to reveal the macro-structure.

3.4.2.0 IMAGE ANALYSIS

All image analysis was carried out using Analytical Measuring Systems (AMS) Vids II and III equipment, coupled to a Nikon Labophot microscope, courtesy of Birmingham University, Department of Metallurgy and Materials.

The microscope objective used for all the inclusion analyses was 40X, this had a theoretical resolution of 0.42μm and a depth of focus of 1.2 μm. The instrument was calibrated using a graticule, one pixel (square shaped) measured 0.625μm. Hence the resolution of the microscope was better than the detection limits of the instrument and this then set the lower limit of size detection, i.e. 0.625μm. The area of each field measured was 0.038mm^2.

Quanti→tative metallography i.e. grain size and pearlite area fraction, was carried out using a 20X objective. This had a theoretical resolution of 0.69μm and a depth of focus of 1.4μm, one pixel measured 1.633μm and the total field area was 0.257mm^2. Hence again the detection limits were established by the size of the pixel.

3.4.2.1 SPECIMEN PREPARATION FOR INCLUSION ANALYSIS

For the analysis of inclusions, reproducibility and consistency of metallographic preparation was considered essential to obtain accurate results. Therefore, specimen preparation was carried out following the recommendations for "Improving Metallographic Sample Preparation for Inclusion Analysis by Automatic Methods" by NELSON and BLANN (238), and as outlined in the ASTM standard E768-80, "Preparing and evaluating Specimens for Automatic Inclusion Assessment in Steel".

Specimen preparation was achieved using automatic polishing equipment (see Section 3.4.0). However, the load, platen speed and timing were in this case controlled so that each specimen received the same amount of preparation.

The final 1μm diamond polishing stage was carried out using diamond paste suspended in glycerin, instead of a water based lubricant, to prevent dissolution of calcium inclusions. Final ultrasonic degreasing was done in Inhibisol. Just prior to examination each specimen was briefly hand polished on an unnapped, 0.05μm alumina (suspended in methanol) cloth, and then finally with selvyt.

Specimens polished by these techniques were examined under the microscope using interference contrast, and dark field illumination to observe the quality of the preparation. This method was considered to produce a consistent and reproducible finish.

3.4.2.2.0 INCLUSION ANALYSIS

3.4.2.2.1 AS CAST INGOT

For each ingot an analysis of inclusion size distribution, by maximum horizontal chord was carried out. Specimens for analysis were extracted from the same position in each ingot, as shown in Fig.60. The inclusions were grouped in sizes of less than 2μm, 2 to 4μm ....14 to 16μm any inclusions exceeding 16μm were measured manually and recorded. A minimum of 2000 individual inclusions was measured upon each section.

3.4.2.2.2 ROLLED PLATE

For each plate, inclusion analysis was made on specimens extracted from the position shown in Fig.61. Full plate thickness transverse and longitudinal sections were observed, the sampling scheme and the specimen

orientations are shown in Fig.65. The inclusion features measured were area, total inclusion length and count, per field i.e. individual inclusion features could not be measured with this equipment. The number of inclusions observed for each sample was a minimum of 2000 or 100 fields, whichever condition was satisfied first. These numbers were necessarily a compromise between accuracy and time (see Appendix C, part 1).

3.4.2.3 MICROSTRUCTURAL ANALYSIS

After the inclusion analysis, ferrite grain size and pearlite area fraction were measured on the same specimens. To measure pearlite fraction the specimens were etched in picral, for ferrite grain size measurements etching was done by nital. In both cases care was taken to ensure each specimen was etched for the same period of time, to obtain equivalent contrast between specimens. The grain size measurements were carried out upon the longitudinal section in the through-thickness and longitudinal direction and on the transverse section in the transverse direction so as to account for the anisotropy of the grain shape. The pearlite area fraction was determined upon the longitudinal face. For both grain size and pearlite fraction 10 fields were observed i.e. 2.57mm^2 in total.

3.4.3 NOTCHED TENSILE SPECIMENS

To observe the effect of microstructure and hydrogen on deformation and void formation a number of notched tensile specimens were sectioned along their central axis. The cut was made on the plane parallel to the through-thickness direction (see Fig.66A), which had been marked during machining (see Fig.61). These were then mounted in conductive bakelite and polished (see Section 3.4.0 and 3.4.2.1).

The change in notch profile as a result of tensile testing, was measured using a digitising tablet and the Vids II AMS image analysis equipment. Comparisons were then made between the original notch cross-section and the section produced after testing to give an indication of the strain in the notch region.

The area, count and total length of voids (inclusions + voids) was measured along the central axis of the specimen (length was measured in the direction of applied stress). Three fields were measured at each point along the axis as shown in Fig.66B.

Finally specimens were etched and examined by optical and scanning electron microscopy.

3.4.4.0 SCANNING ELECTRON MICROSCOPY (SEM)

A Cambridge Instruments Microscan 150 fitted with a Link System 860 energy dispersive analysis (EDA) unit was used for electron microscopy and microanalysis. All specimens (mounted in bakelite or fracture surfaces) were given a sputtered carbon coat prior to examination to prevent non-conducting particles e.g. inclusions from charging up during examination.

3.4.4.1 IN-SITU INCLUSION ANALYSIS

Specimens from the mid-section of the cast ingot at the central and edge positions (see Fig.60) were used to determine inclusion composition. For each ingot a minimum of 50 inclusions was examined on a flat polished specimen.

Analysis was carried out using the semi-quantitative facility of the energy dispersive analyser, aluminium, silicon, sulphur, calcium, mangan-

ese and iron were measured, additionally the inclusion size was recorded. Quantitative analysis was not used, as the majority of the inclusions examined were less than 5μm and analysis of such small particles would have inevitably resulted in beam penetration, causing unrealistically high iron peaks, which would have made quantitative analysis ineffective.

3.4.4.2 MICROSCOPY AND FRACTOGRAPHY

Selected specimens from the step-wise cracking tests and sectioned tensile specimens were etched and examined optically and in the SEM. Any micro-analysis was done using the same method as above. Additionally line composition profiles (line-scans) and X-ray maps were carried out on some specimens using the Link Systems analyser.

Examination of fracture surfaces, of the Hounsfield and hydrogen charged and uncharged notched tensile specimens was done by SEM. In order that a satisfactory comparison between fracture surfaces could be made, a systematic approach to specimen examination was adopted. To begin with the whole fracture surface was viewed macroscopially i.e. 20X to observe any significantly large fracture features. Then a region from the edge to the centre of the specimen was observed at successively higher magnifications (see Fig.67).

This was believed to offer an acceptable approach for an axisymmetric tensile specimen. Because of the number of individual fracture surfaces produced i.e. 192 in total, and the time involved in observing an individual specimen (plus the limited availability of SEM facilities) only the specimens rolled at 900 and 1100°C were examined.

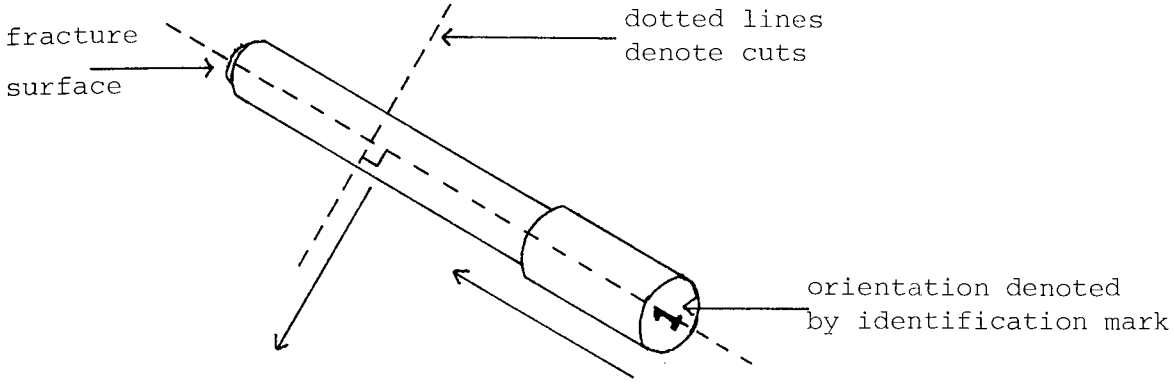

FIG.66A: Cross-sectioning of tensile specimens .

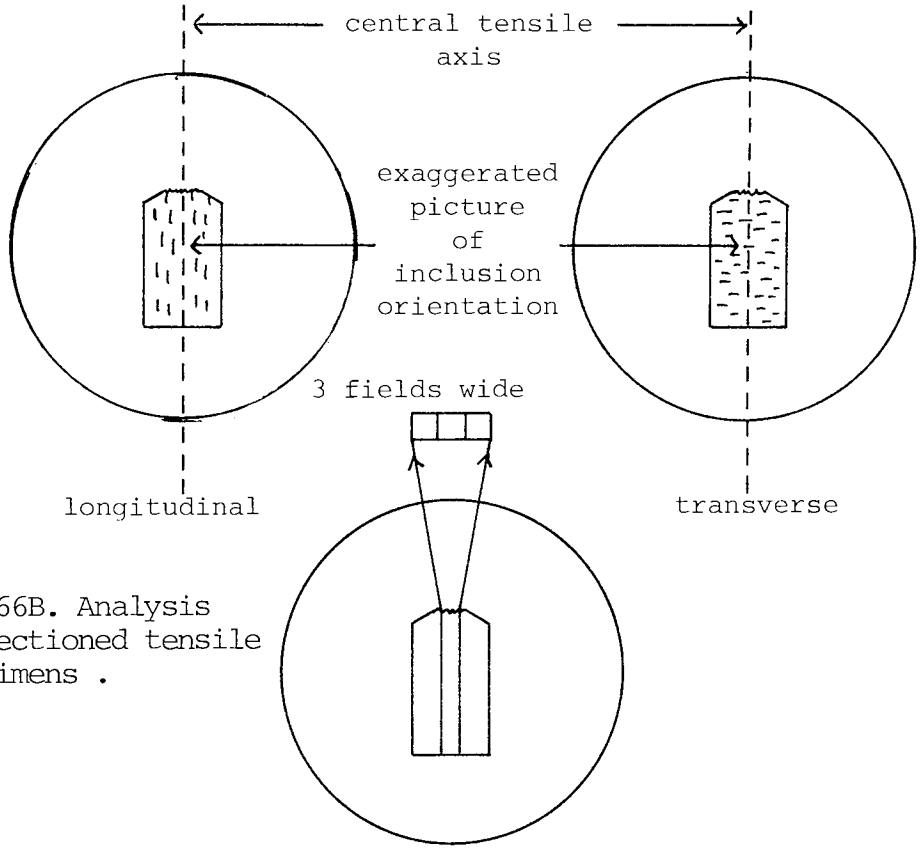

FIG.66B. Analysis of sectioned tensile specimens .

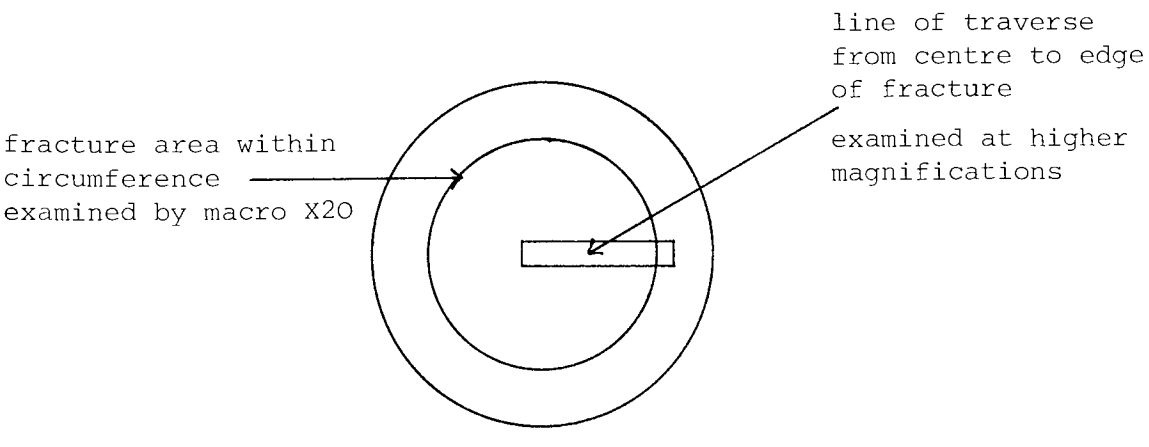

FIG.67 : Examination of fracture surfaces by SEM .

Once again micro-analysis was carried out using EDA. Additionally the cleavage fracture surface of a number of specimens was observed, these were produced by fracturing specimens after immersion in liquid nitrogen by impact.

4.0 EXPERIMENTAL RESULTS

4.1 CHEMICAL ANALYSIS

4.1.0 INGOT

Presented in Table 4.1 below are the results of the chemical analysis of the 4 as cast ingots.

TABLE 4.1 CHEMICAL ANALYSIS OF AS CAST INGOTS

STEEL CODE	C	Si	Mn	P	S	Al	Ca	N	O
L	0.07	0.23	1.6	0.015	0.019	0.08	0.0002	0.006	0.0049
F	0.02	0.27	1.58	0.019	0.019	0.017	0.0002	"	0.0044
K	0.08	0.29	1.57	0.016	0.009	0.043	0.0002	"	0.0025
M	0.13	0.31	1.62	0.005	0.003	0.076	0.0002	"	0.0018

All values in wt.%, balance iron.

4.1.1 ROLLED PLATE

Table 4.2 below gives the chemical analysis of the steel plates, showing the rolling temperatures and respective positions from the cast ingot.

TABLE 4.2 CHEMICAL ANALYSIS OF STEEL PLATES

POSITION FROM INGOT	STEEL CODE	C	Mn	P	S	Al	O (ppm)	Ca (ppm)
TOP	L1	0.08	1.42	0.013	0.02	0.08	26	ND
	F1	0.02	1.6	0.02	0.016	0.021	26	ND
ROLLING TEMP 1100°C	K1	0.08	1.59	0.015	0.01	0.04	22	40
	M1	0.12	1.61	0.003	0.004	0.084	17	34
	LO	0.07	1.42	0.014	0.019	0.081	35	ND
	FO	0.02	1.62	0.019	0.017	0.025	42	ND
ROLLING TEMP. 1000°C	KO	0.07	1.6	0.015	0.01	0.043	23	35
MIDDLE	MO	0.13	1.62	0.004	0.004	0.083	20	24
	L9	0.08	1.4	0.012	0.02	0.08	33	ND
	F9	0.02	1.61	0.018	0.016	0.023	45	ND
ROLLING TEMP. 900°C	K9	0.07	1.6	0.016	0.011	0.041	27	36
	M9	0.13	1.59	0.003	0.004	0.085	18	24
	L75	0.07	1.43	0.017	0.018	0.083	48	1
	F75	0.02	1.63	0.023	0.015	0.021	49	3
ROLLING TEMP. 750°C	K75	0.07	1.6	0.017	0.01	0.045	25	38
BASE	M75	0.12	1.62	0.003	0.004	0.079	18	24

ND = not determined, all values in wt%, balance iron.

4.2 INGOT ANALYSIS

4.2.0 MACRO-STRUCTURE AND SULPHUR PRINT

Plate 1 shows a sulphur print and Plate 2 the macro-etched structure of a typical ingot used in this study. From these it can be seen that the ingots are completely sound.

A fine grained chill layer (from 7.5 to 15mm thick) is visible around the perimeter of the ingot which develops into a region of columnar crystal growth towards the centre. The central area is typically equiaxed and the upper sections of the ingot appear to have a slightly more heterogeneous sulphur distribution than the lower.

4.2.1 METALLOGRAPHIC EXAMINATION

For steels L and F the inclusion dispersion was characterised by networks of type II MnS inclusions, these appeared light grey in colour under bright field illumination and were translucent. Plate 3 (from steel F) shows a typical example of the type of large inclusion cluster observed, it is possible to see the internal reflected light (which appears as areas of lighter colour within the inclusion matrix) for some of the inclusions. Also on this plate in the top right hand corner is a darker inclusion (presumably alumina (Al_2O_3)) surrounded by MnS, this was also characteristic of both steels L and F. Plate 4 (steel L) shows a further example, note that the Al_2O_3 inclusions are angular in shape, they were also quite often larger than the MnS.

The most frequently observed inclusion phase in steels L and F was MnS the shape of which varied from spherical to ellipsoidal to "cigar

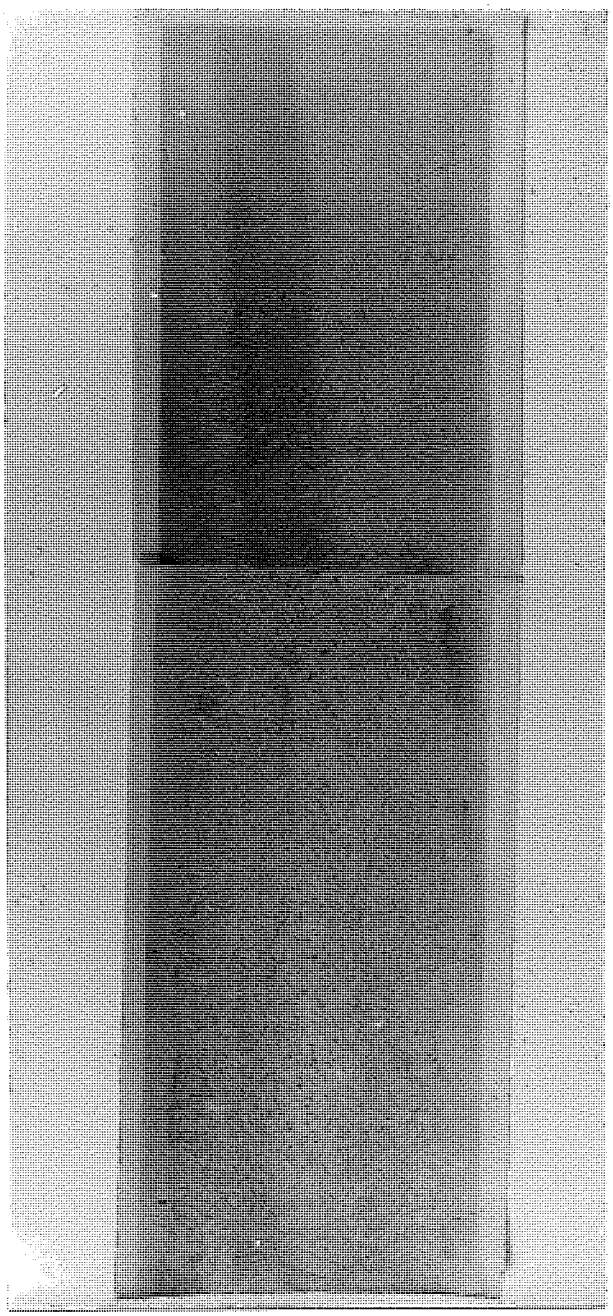

PLATE 1 : Sulphur print of typical as cast ingot .

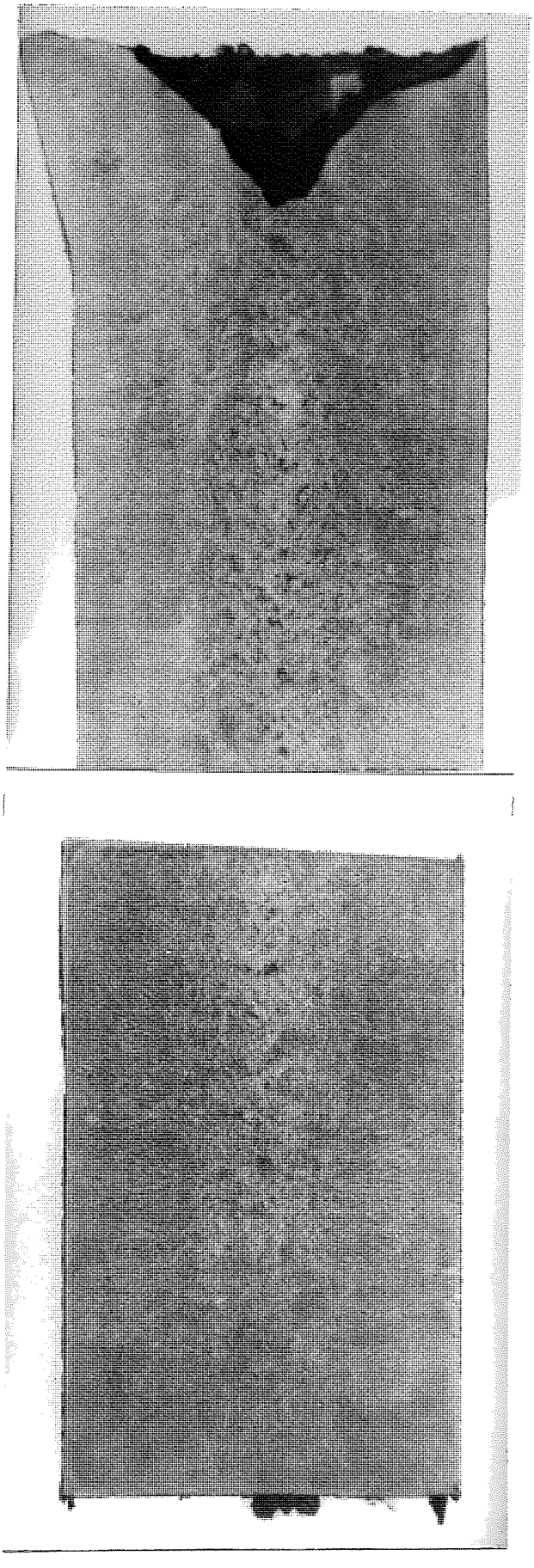

PLATE 2 : Macro-etch of typical as cast ingot .

shaped". Rarely were individual inclusions greater than 5μm observed but clusters whose total length was in excess of 40μm were not uncommon. Observations of etched as cast samples of steel L revealed many of the MnS clusters to be preferentially situated in areas of ferrite, the MnS inclusions in etched samples of steel F (which contained 0.02%C) appeared fairly evenly dispersed and slightly less numerous than in steel L.

The inclusions in steels K and M (which were calcium treated) were of similar appearance and typical examples are shown in Plates 5 (steel K) and 6 (steel M). Under bright field illumination the colour of the inclusions was grey, and some appeared to be translucent as internal reflections were observed (Plate 5). However, a number of inclusions were observed, for both steels, which contained a second phase (Plate 6) that was darker in colour, this was possibly alumina or calcium aluminate. In both steels the inclusions appeared uniformly dispersed, observations of etched specimens revealed that none were preferentially situated in either areas of ferrite or pearlite. The inclusion shape was generally spherical, with sizes predominantly below 5μm in diameter.

The density of inclusions decreased from steel L,F,K to M.

4.2.2 INCLUSION SIZE ANALYSIS

The results of the inclusion size analysis are given in Appendix D in Tables D1,D2,D3 and D4. Also included in these tables are the total number of inclusions measured, the inclusion % area fraction (AF) (calculated by assuming that the inclusions were spherical) and the total inclusion projected length per unit area (given by the sum of all the inclusion diameters divided by the area of the specimen examined (see section 4.3.2.2)

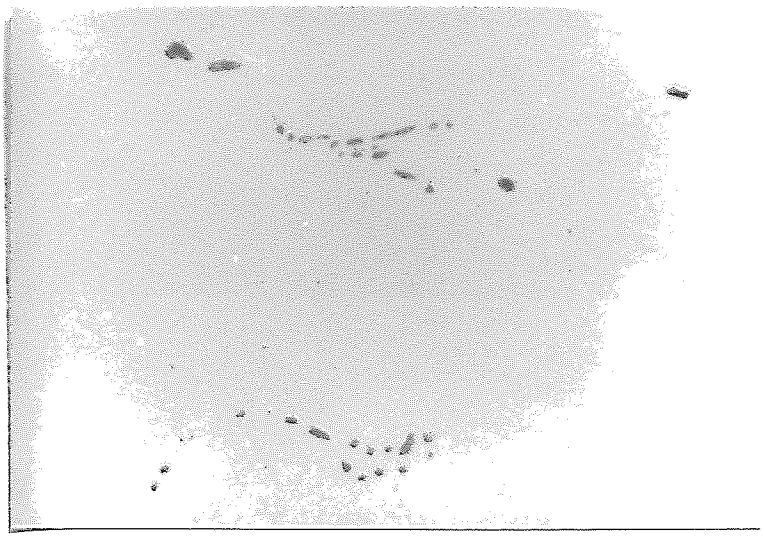

PLATE 3 : Steel F as-cast . Typical example of MnS networks and an Al_2O_3 inclusion surrounded by MnS (top right hand corner) . Mag. X840 .

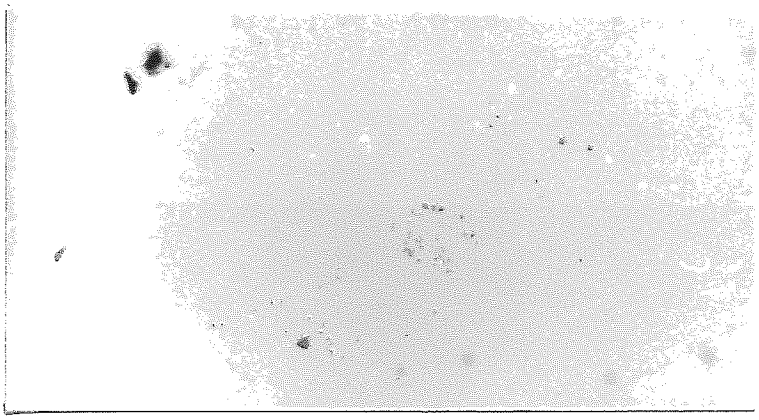

PLATE 4 : Steel L as-cast . Example of area with high density of MnS clusters and larger (black) angular Al_2O_3 inclusions surrounded by rims of MnS . Mag.X420 .

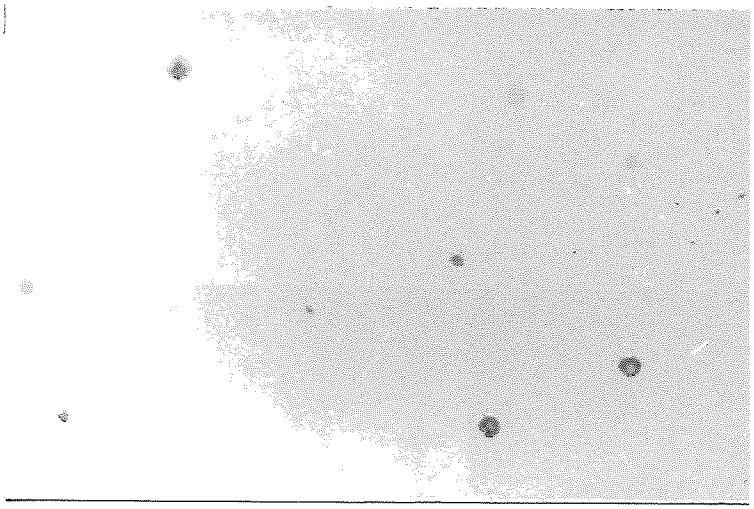

PLATE 5 : Steel K as-cast . Sulphide inclu-tions showing internal reflections . Mag.X840.

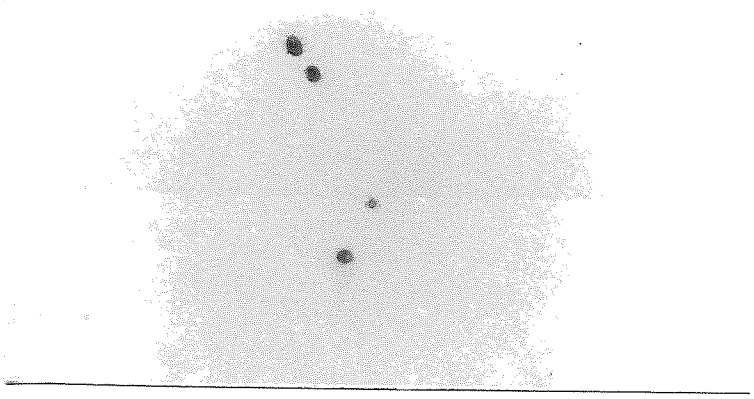

PLATE 6 : Steel M as-cast . Example of two-phase inclusions . Darker possibly oxide rich centres surrounded by a sulphide envelope Mag. X840 .

To allow a comparison to be made between the inclusion size distributions between steels and the three sampling positions within an ingot i.e. top, middle and base, the data given in the tables above was normalised to give the number of inclusions greater than a given size found in an area $10mm^2$. These results are also tabulated in the above tables and plotted in Figs. 68,69,70 and 71, for steels L,F,K and M respectively.

The distribution of inclusion sizes is widely reported to be log-normal (240,241) and an analysis using the method of moments (Appendix C Part 2) was undertaken to determine if the inclusion distributions in this study were also. The results of this analysis are given in Table D5 in Appendix D together with the normal and log-normal means and standard deviations (S.D.) for each distribution. Fig. 72 shows the resultant log-normal probability graph of the inclusion size distribution for the samples taken from the mid-section of each ingot.

4.2.3 INCLUSION COMPOSITIONS

The as cast inclusion compositions are given in Tables D6,D7,D8 and D9 in Appendix D. From these tables it can be observed that a high iron level has been recorded for all the inclusions analysed. This has arisen as a result of matrix excitation because the electron beam has penetrated the generally small (<5μm) inclusions found in the steels. (There is also the possibility that the concentration of manganese in the inclusions has also been influenced as the matrix managanese level was ≃ 1.6%). The variation of iron in inclusions with inclusion size is shown in Fig. 73 this represents the data for all inclusions analysed in all 4 ingots. Due to the above effect and in order to obtain a better idea of the relative proportions of Al, Mn, S and Ca in the inclusions the data was normalised by recalculating the amount of each element assuming 100% in

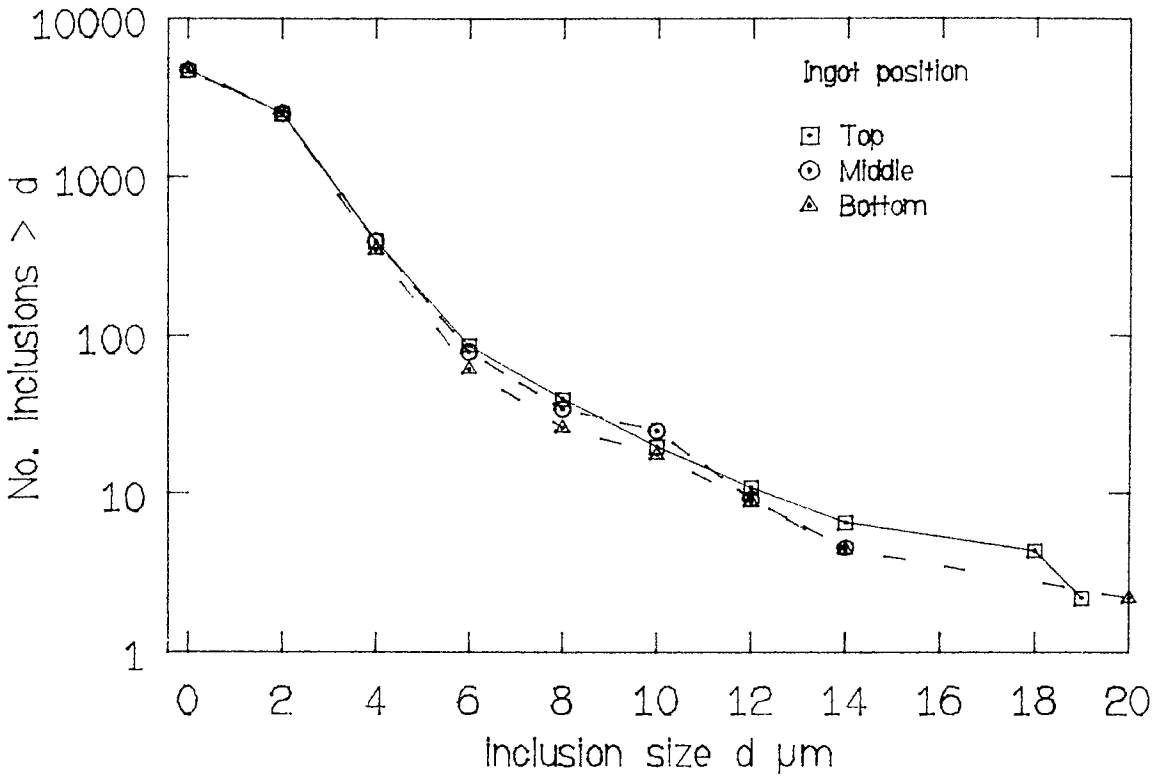

FIG.68 : Inclusion size distribution , steel L as cast .

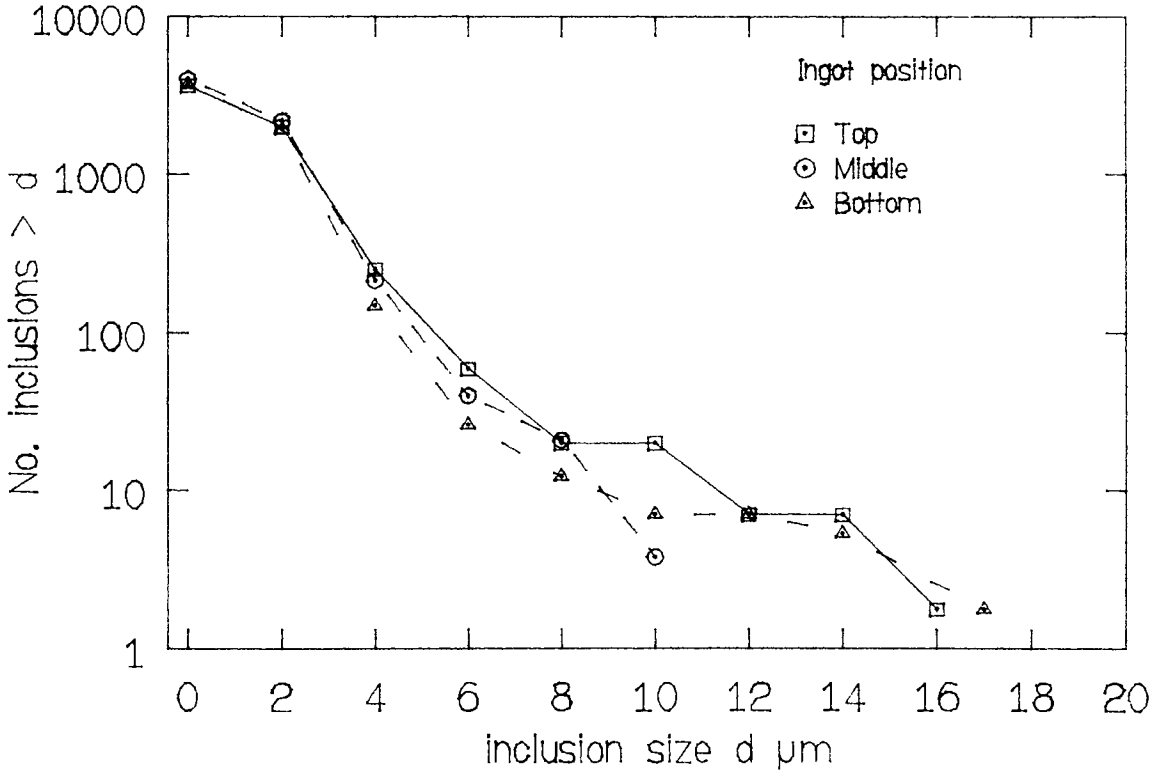

FIG.69 : Inclusion size distribution , steel F as cast .

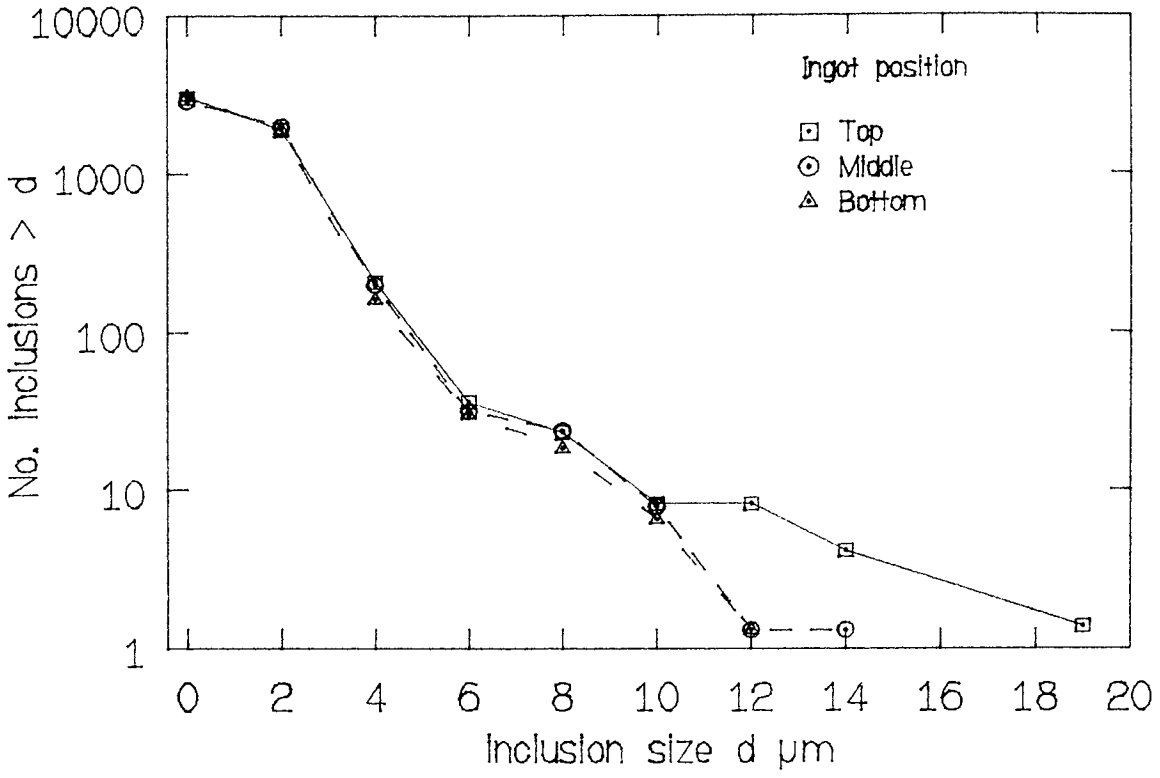

FIG.70 : Inclusion size distribution , steel K as cast .

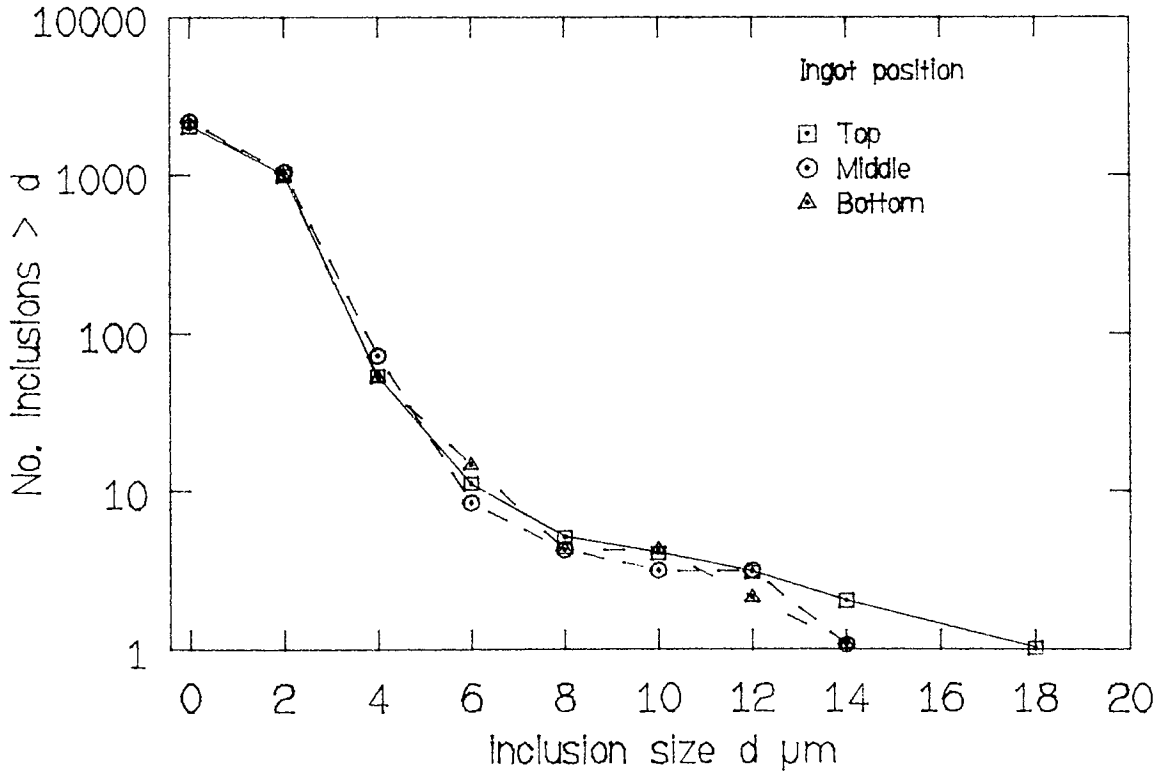

FIG.71 : Inclusion size distribution , steel M as cast .

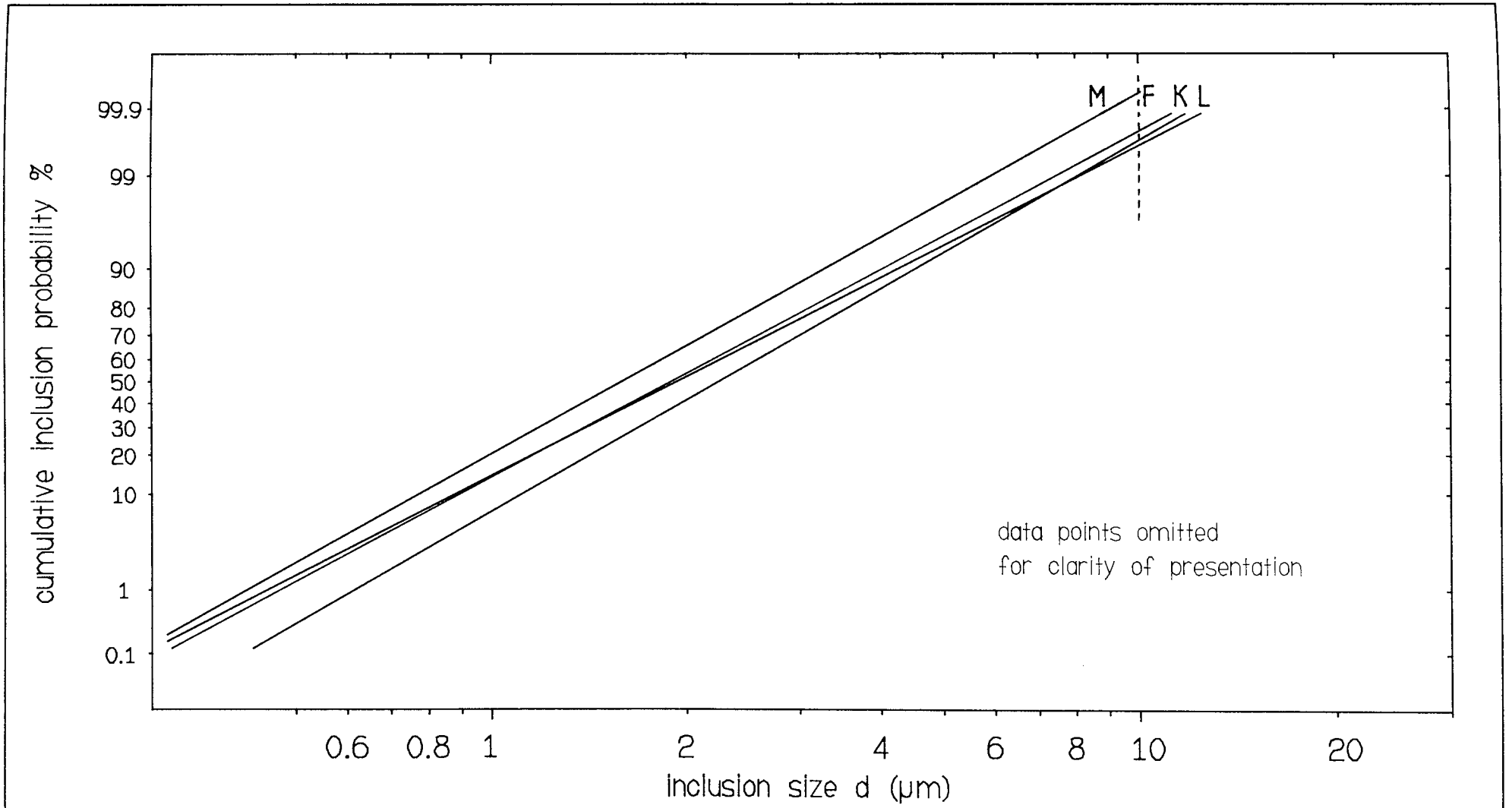

FIG.72 : Log-normal probability graph of the as cast inclusion size distribution . Size analysis from the mid-section of ingots .

the absence of iron. Graphs of the normalised inclusion compositions against inclusion size are then shown for steels L,F,K and M in Figs. 74, 75,76 and 77 respectively. Also tabulated below (Table 4.3) are the mean inclusion compositions for both the data given in Tables D6, D7, D8 and D9 and the normalised results and a classification of inclusion types according to composition.

Additionally Plates 7, a,b,c,d,e, and f (steel K) and Plates 8a, b,c, and d (steel F) show X-ray maps of the element distributions for typical inclusions observed in these steels.

4.3 ROLLED PLATE

4.3.0 METALLOGRAPHY

4.3.0.0 MICROSTRUCTURAL OBSERVATIONS

Observations of the longitudinal (L), transverse (T) and through-thickness (T/T) sections of the rolled plates, after nital etching, revealed pearlite/ferrite microstructures for all steels rolled at 900,1000 and 1100°C. The steels rolled at 750°C had a microstructure of ferrite and partially spheroidised bands of cementite.

Plates 9a,b, 10a,b, 11a,b, 12a,b, 13a,b, and 14a,b show isometric projections of typical examples of the microstructures observed, where the subscript "a" represents a low magnification (42X) and "b" a higher magnification (420X).

The microstructures of the steels rolled at 1000 and 1100°C were very similar in each steel i.e. L,F,K and M, as were the microstructures of steels K and L (which both contained $\simeq$ 0.08%C) at equivalent rolling temperature.

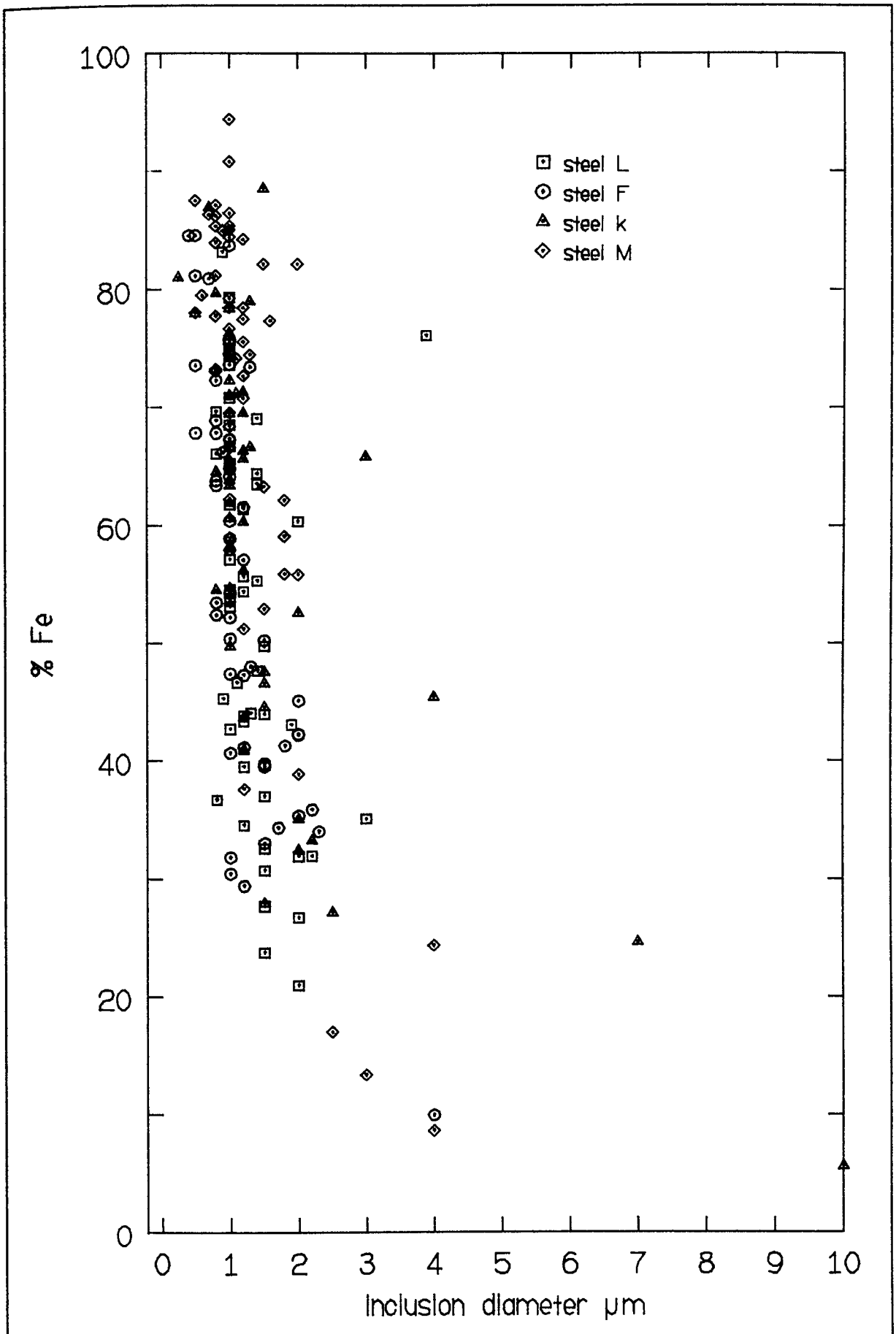

FIG.73 : Increases in inclusion iron content with decreasing inclusion size due to beam penetration .

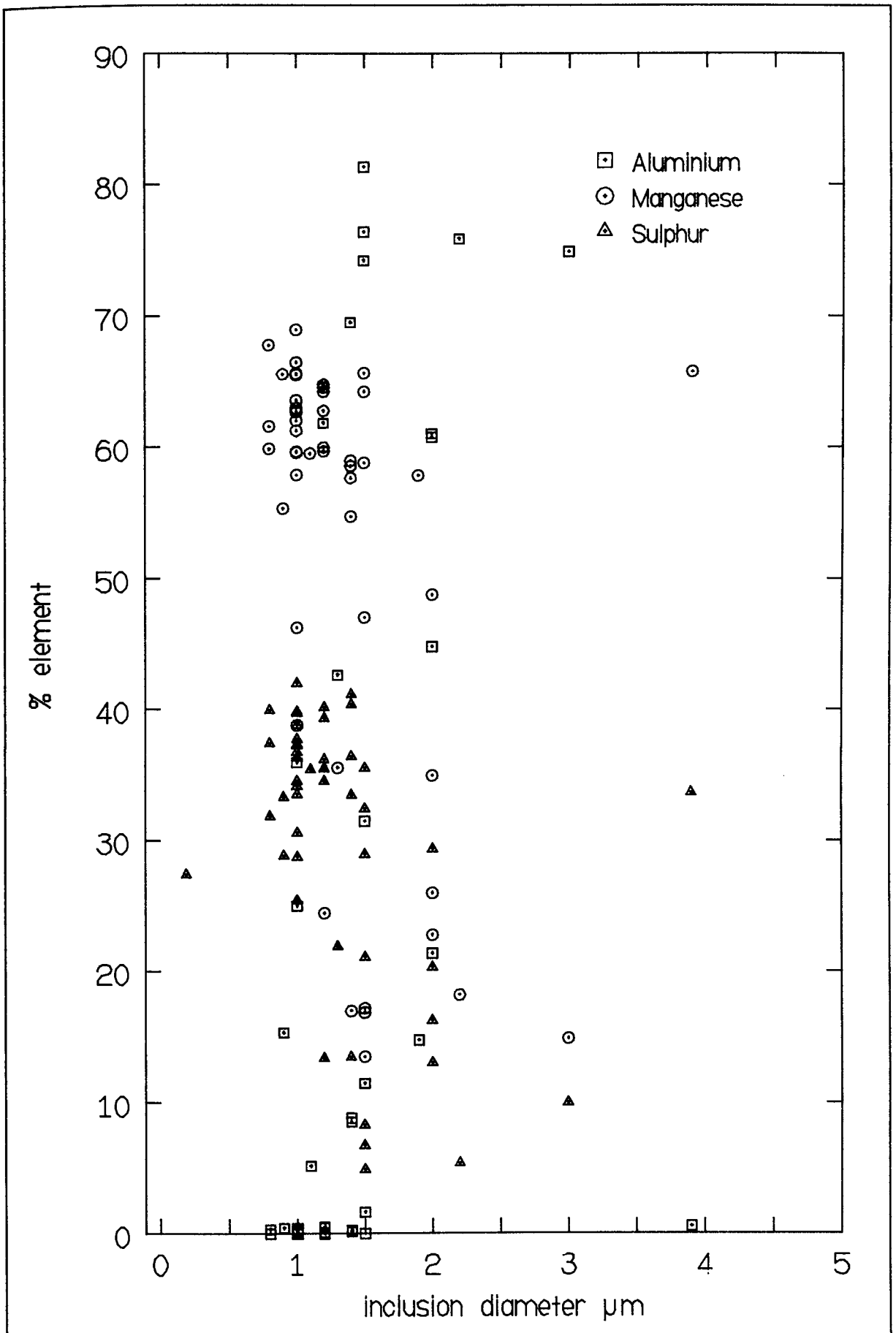

FIG.74 : Variation of inclusion composition with inclusion size . Steel L as cast .

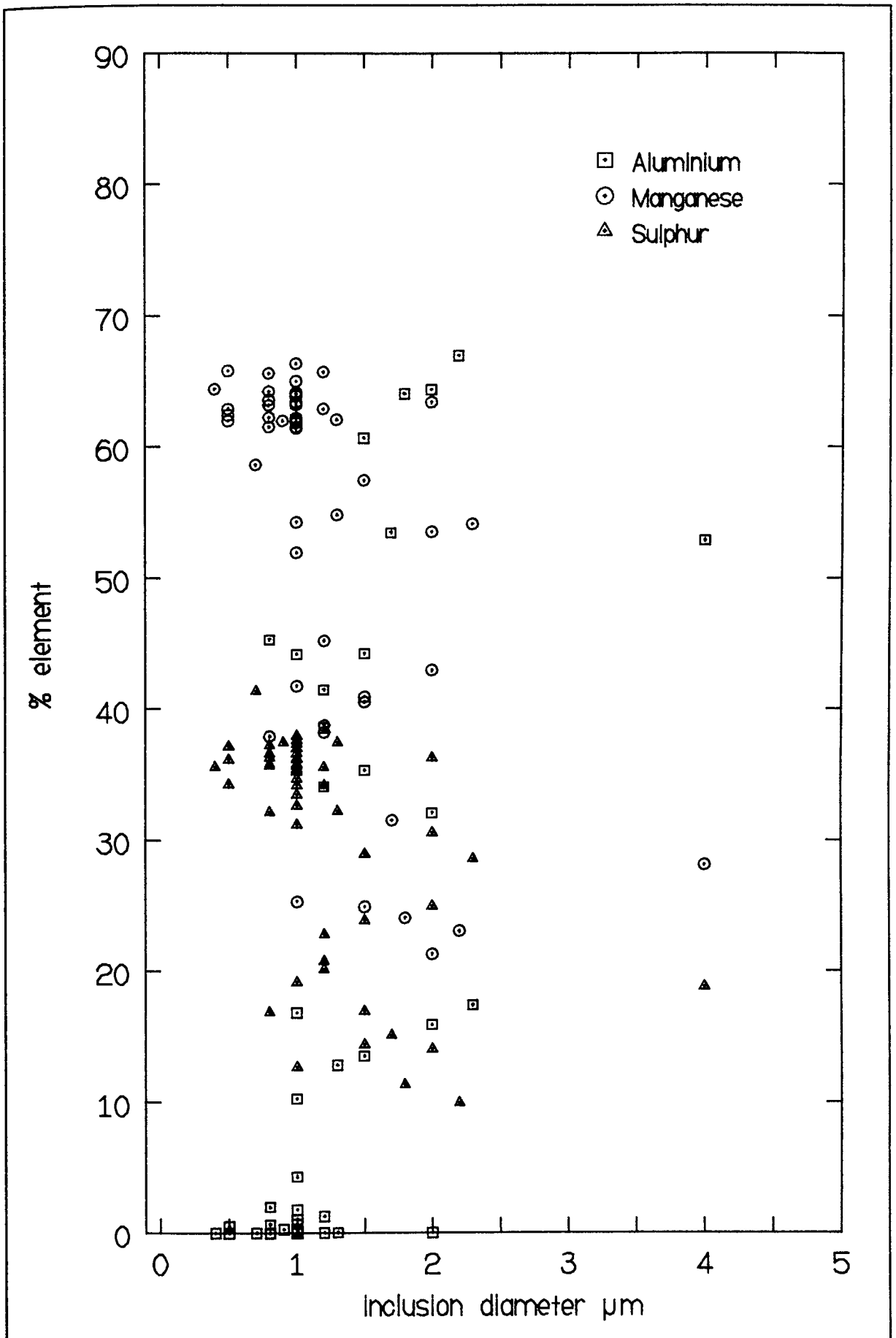

FIG.75 : Variation of inclusion compositions with inclusion size Steel F as cast .

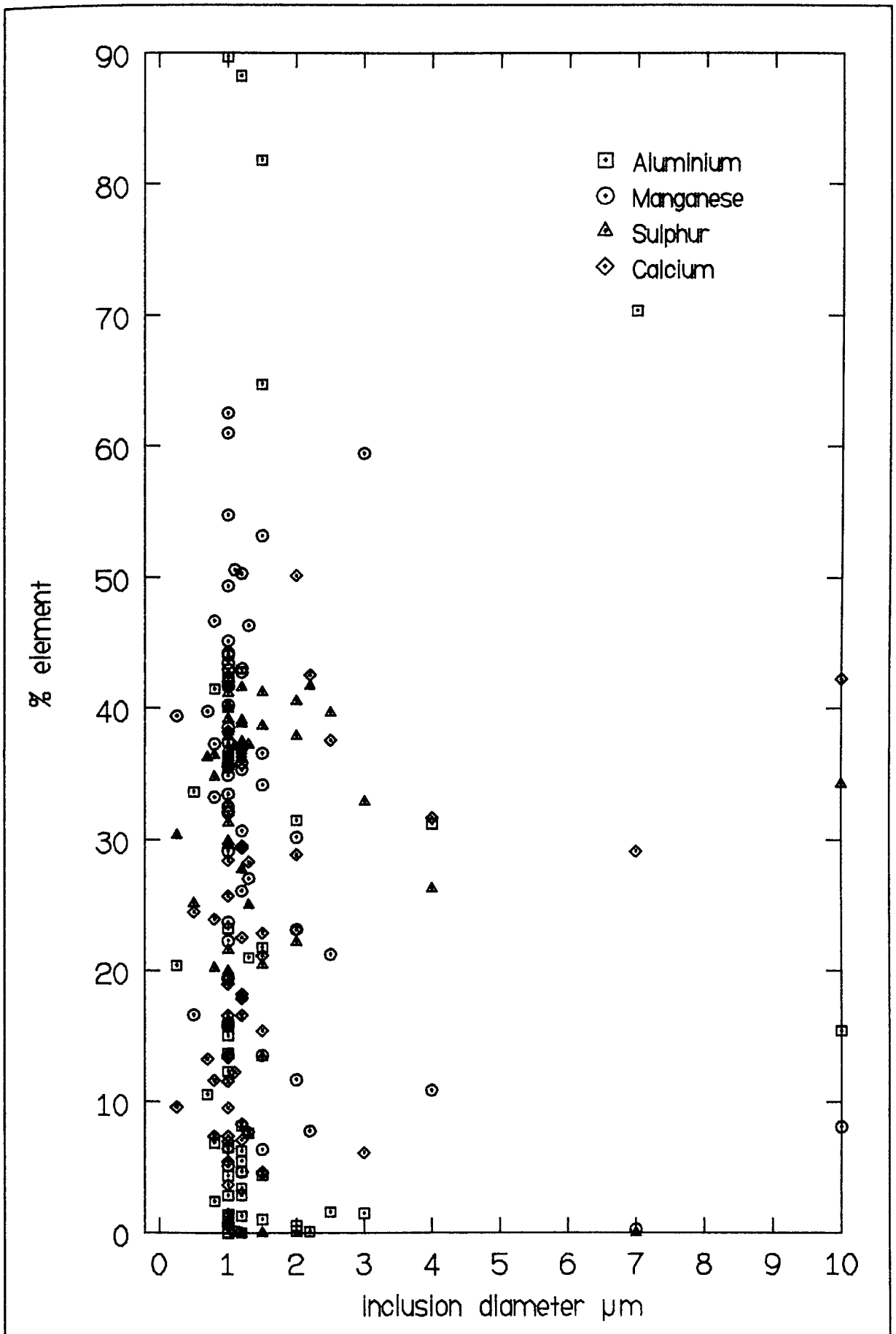

FIG.76 : Variation of inclusion composition with inclusion size . Steel K as cast .

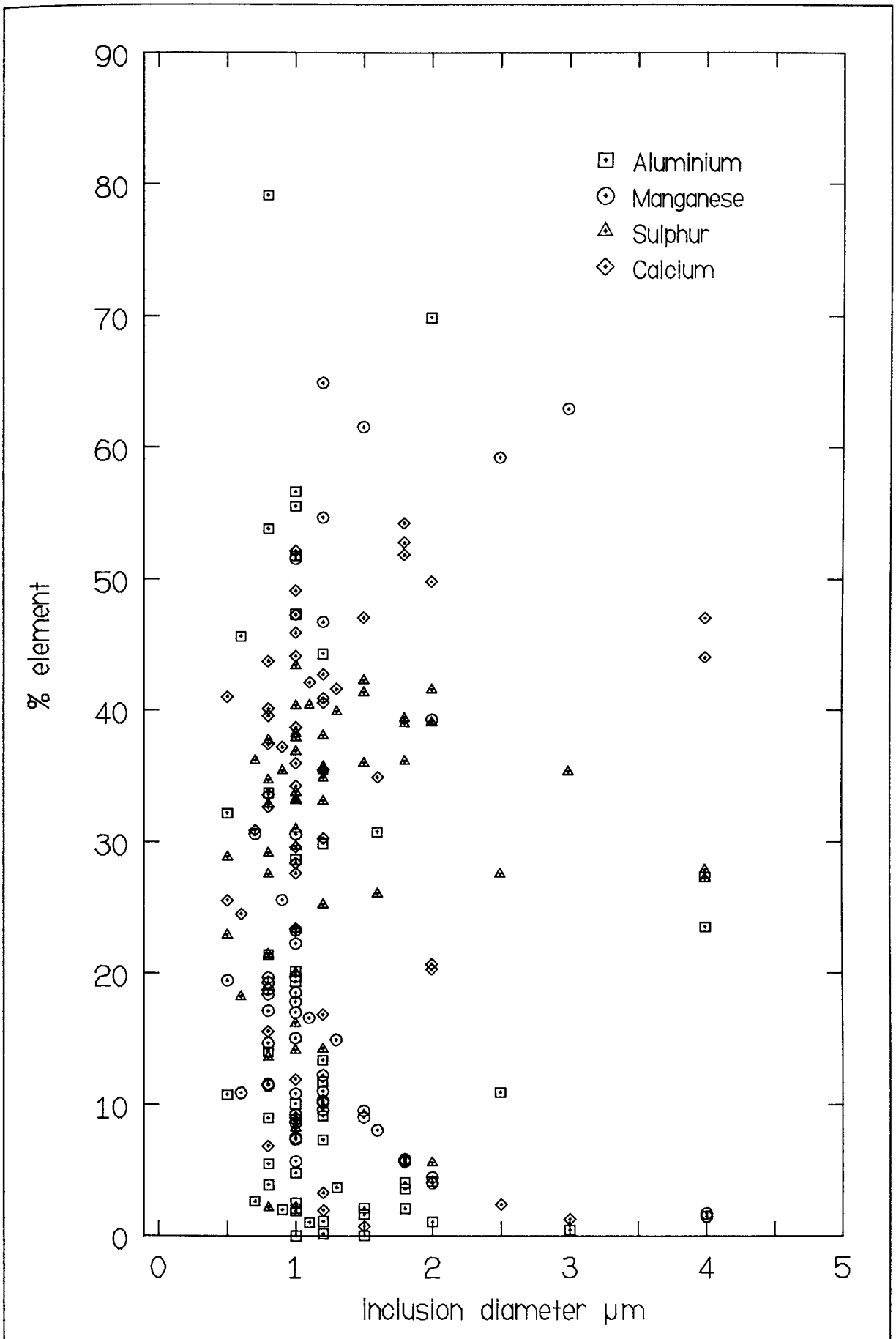

FIG.77 : Variation of inclusion composition with inclusion size . Steel M as cast .

TABLE 4.3 AS CAST INCLUSION COMPOSITIONS - SUMMARY

	Al	S	Mn	Si	Ca	Fe
STEEL L						
MEAN ANALYSIS	11.41	13.15	23.35	T	T	51.97
NORMALISED	23.76	27.38	48.61	T	T	-

T = Trace — All values in per cent

CLASSIFICATION OF INCLUSION TYPES: (Normalised data)

22%	ALUMINIUM RICH
20%	ALUMINIUM/SULPHUR/MANGANESE
58%	MANGANESE SULPHIDE

	Al	S	Mn	Si	Ca	Fe
STEEL F						
MEAN ANALYSIS	9.47	12.33	22.36	T	T	55.8
NORMALISED	21.42	27.39	50.59	T	T	-

CLASSIFICATION OF INCLUSION TYPES: (Normalised data)

21.15%	ALUMINIUM RICH
19.23%	ALUMINIUM/SULPHUR/MANGANESE
59.62%	MANGANESE SULPHIDE

	Al	S	Mn	Si	Ca	Fe
STEEL K						
MEAN ANALYSIS	6.13	12.89	12.6	T	8.6	59.49
NORMALISED	15.13	31.8	31.09	T	21.22	-

CLASSIFICATION OF INCLUSION TYPES: (Normalised data)

1.82%	CALCIUM ALUMINATE
5.45%	Al RICH (70%) + (Ca, Mn, S)
58.18%	Ca, Mn, S
29.09%	Ca, Mn, S, Al (10%Al)
3.64%	Mn, S
1.82%	Ca, S (10% Al + +Mn)

	Al	S	Mn	Si	Ca	Fe
STEEL M						
MEAN ANALYSIS	4.23	9.79	7.18	T	9.42	69.34
NORMALISED	13.8	31.93	23.42	T	30.72	-

CLASSIFICATION OF INCLUSION TYPES: (Normalised data)

NONE	CALCIUM-ALUMINATE
5.78%	Al RICH (70%) + (Ca, Mn, S)
36.54%	Ca, Mn, S
42.31%	Ca, Mn, S, Al (10%Al)
5.77%	Mn, S
9.62%	Ca, S (10%Al + Mn)

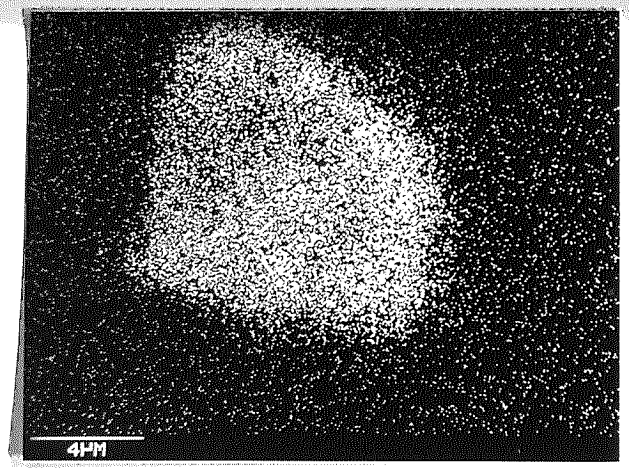

a. Ca X-ray (39.86%)

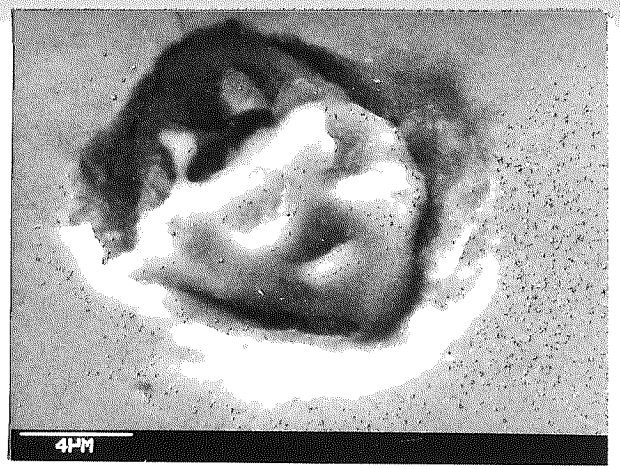

b. secondary image

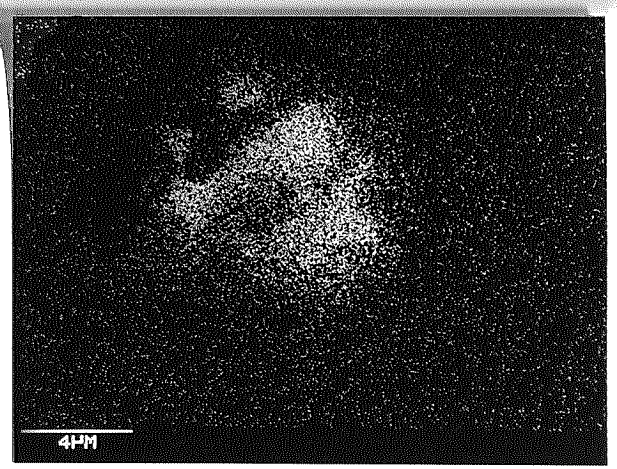

c. Al X-ray (14.56%)

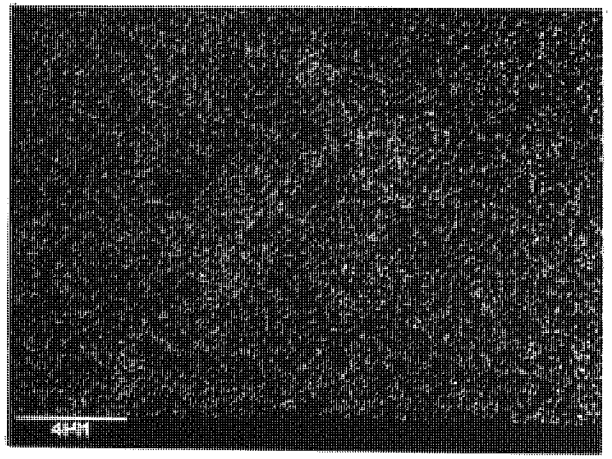

d. Mn X-ray (7.64%)

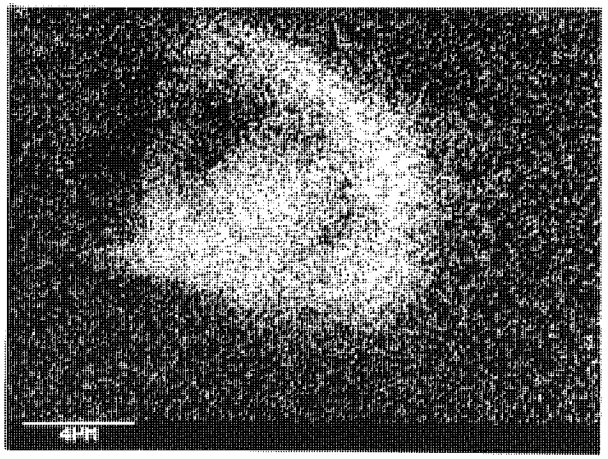

e. S X-ray (32.32%)

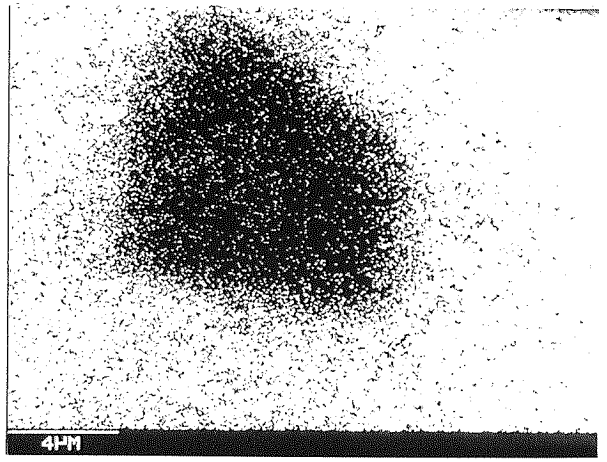

f. Fe X-ray (5.61%)

PLATE 7a,b,c,d,e and f : X-ray maps and secondary image of an inclusion from steel K as cast . Spot analysis (as a %) from the centre of the inclusion is given for each element .

PLATE 8a,b,c and d : X-ray maps and secondary image of an inclusion from steel F as-cast . Percentages are the result of spot analysis obtained at the mid-section of the inclusion .

←←←←

a. secondary image

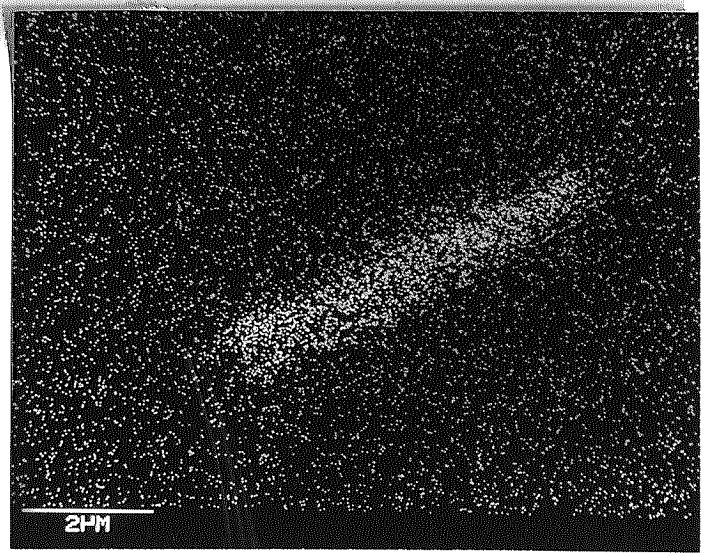

→→→→

b. Mn X-ray (30.24%)

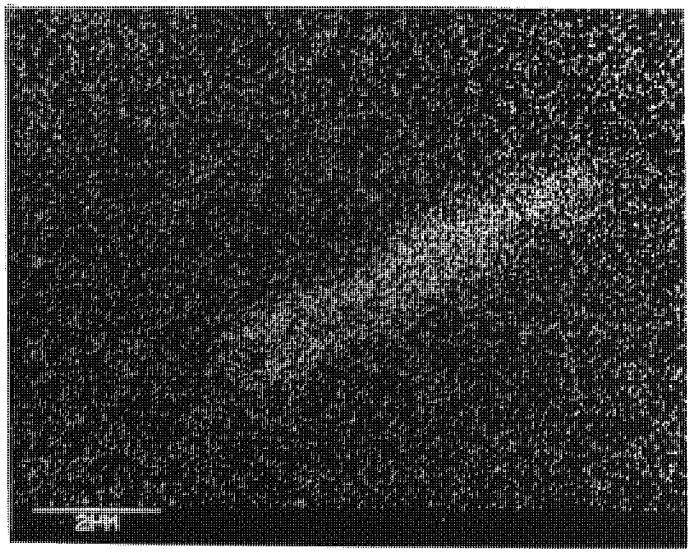

←←←←

c. S X-ray (12.76%)

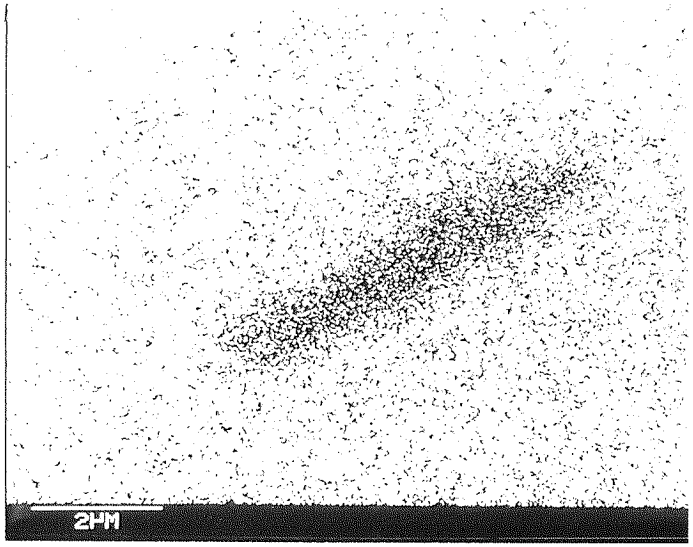

→→→→

d. Fe X-ray (46.18%)

As the carbon content of the steels increased i.e. from F (0.02%C) to K and L to M (0.14%C), so did the proportion of pearlite (cementite for the steels rolled at 750°C) whilst the ferrite grain size decreased (see Plates 12 and 13). Increases in the rolling temperature produced an increase in the resulting ferrite grain size (see Plates 11 and 14).

Pearlite banding (or cementite - 750°C) and elongation of ferrite grains in the direction of rolling was observed in steels L,K and M. This decreased, however, with increasing rolling temperature (see Plates 11,12 and 14). The elongation of ferrite grains was particularly pronounced in all steels rolled at 750°C (see Plates 9a and 9b). Steel F contained only a very small amount of pearlite which appeared evenly distributed throughout the matrix. In all the steels grain boundary cementite was observed (see Plates 11,12,13, and 14).

4.3.0.1 QUANTITATIVE METALLOGRAPHY

Table 4.4 gives the results of the quantitative analysis of microstructure obtained by image analysis. The mean grain diameters in the longitudinal, transverse and through-thickness directions are recorded together with the equivalent volume diameter (assuming the grains can be simply modelled as triaxial ellipsoids) and the ASTM grain size. Pearlite % area fraction (equivalent to % volume fraction (240)) is also tabulated.

4.3.1.0 INCLUSIONS

4.3.1.1 METALLOGRAPHIC OBSERVATIONS

For steels K and M there appeared to be little change in the inclusion dispersion and shape from that observed in the as cast state, and certainly there was no obvious difference betwen the shape and morphology

of inclusions observed in the steel plates rolled at the four different temperatures i.e. 750, 900, 1000 and 1100°C. A very small number of isolated elongated inclusions were observed on the longitudinal section of steel K, these were light grey in colour, presumably MnS and up to about 10μm in length.

Close observation of individual inclusions in steels K and M using interference contrast and high magnification (840X) revealed no decohesion between the inclusions and the matrix or cracks within inclusions. This result was confirmed during SEM investigations.

In steels F and L, as for steels K and M above, any inclusion deformation was difficult to determine visually, however, reorientation of the networks of MnS inclusions observed in the as cast state had occurred. This resulted in linear arrays ('strings of pearls') of closely associated, small (<5μm) inclusions in both the longitudinal and transverse planes (e.g. Plate 15). Again as observed in steel K above, only infrequently were elongated inclusions observed for both steels and these were seldomly greater than 10μm in length. The total length of inclusion arrays, however, was often in excess of 40μm and approached 80μm in some observations on the longitudinal planes of steel L and F.

High magnification optical and SEM observations revealed no decohesion at the inclusion/matrix interface or cracking within the inclusions for both these steels.

An array of MnS inclusions is shown in the centre of the transverse section in Plate 13b, which is steel F rolled at 1000°C, and individual

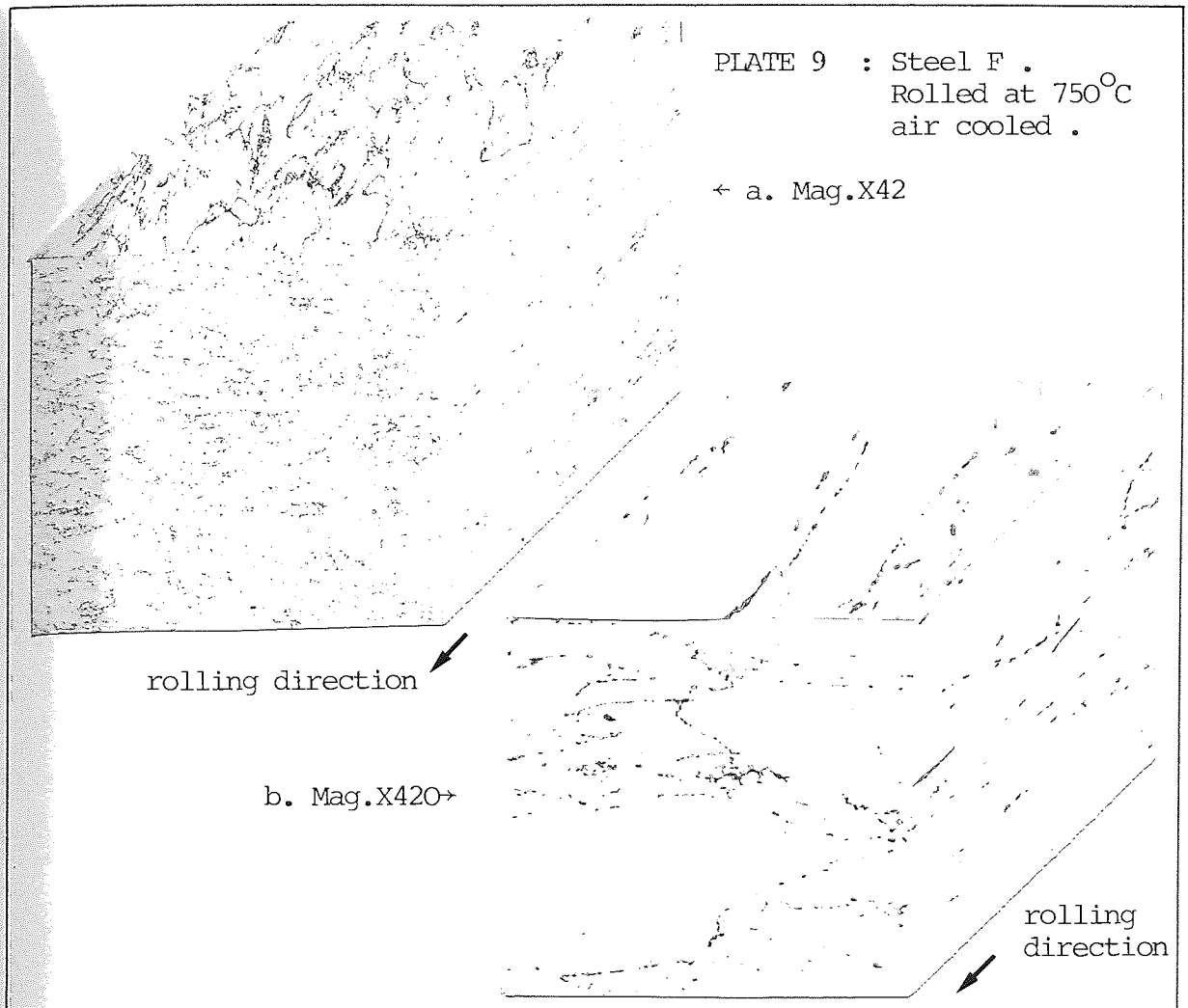

PLATE 9 : Steel F .
Rolled at 750°C
air cooled .

← a. Mag.X42

b. Mag.X420→

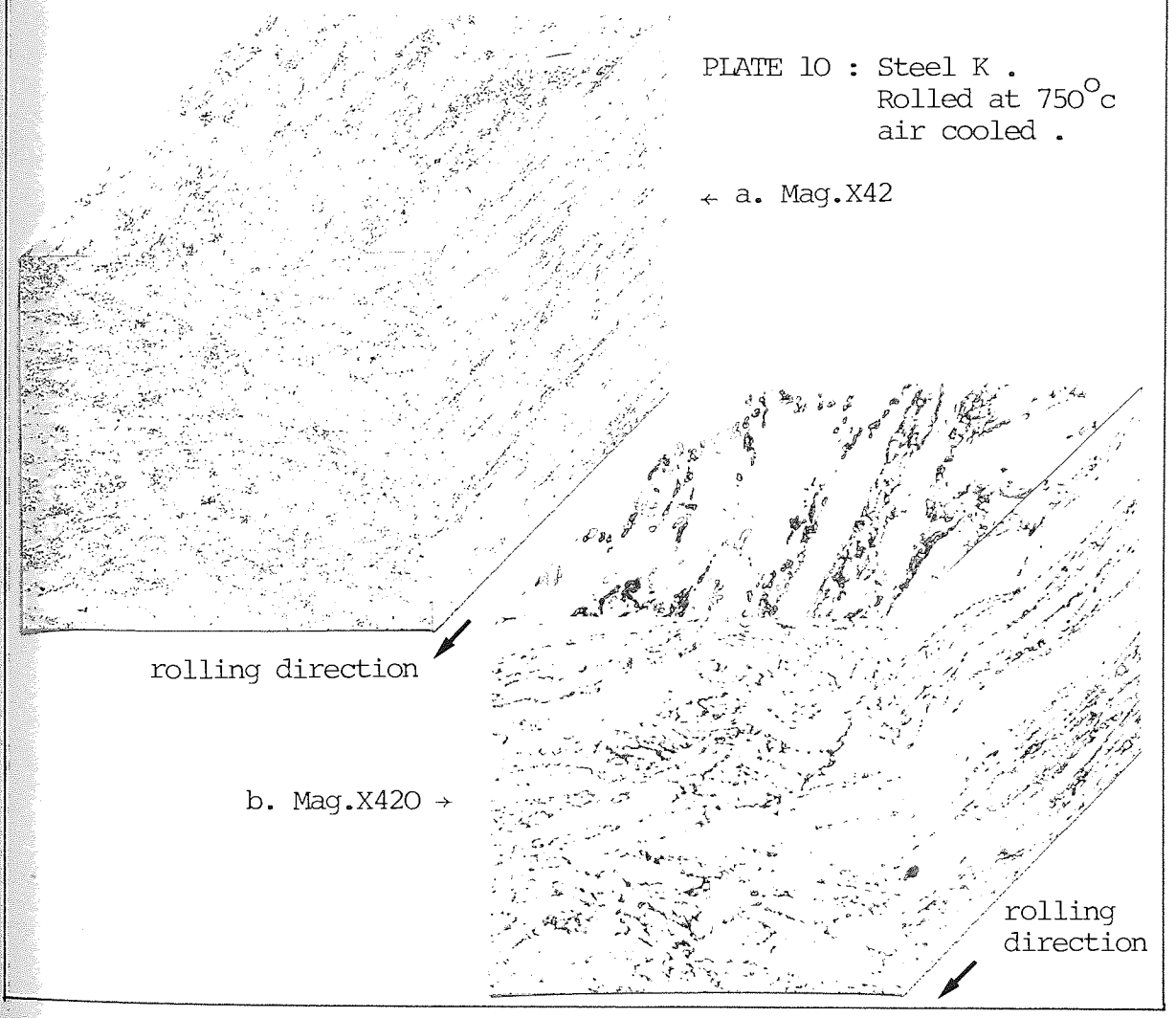

PLATE 10 : Steel K .
Rolled at 750°c
air cooled .

← a. Mag.X42

b. Mag.X420 →

PLATE 11 : Steel M .
Rolled at 900°C
air cooled .

← a. Mag.X42

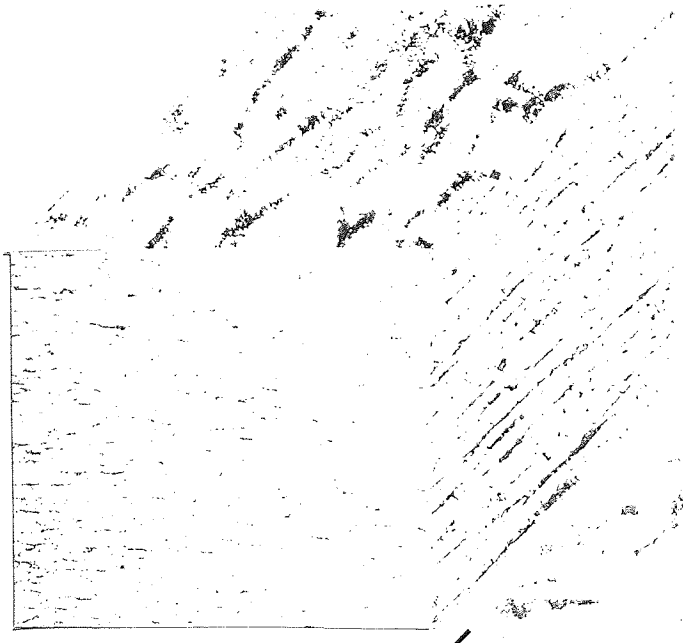

rolling direction

b. Mag.X420 →

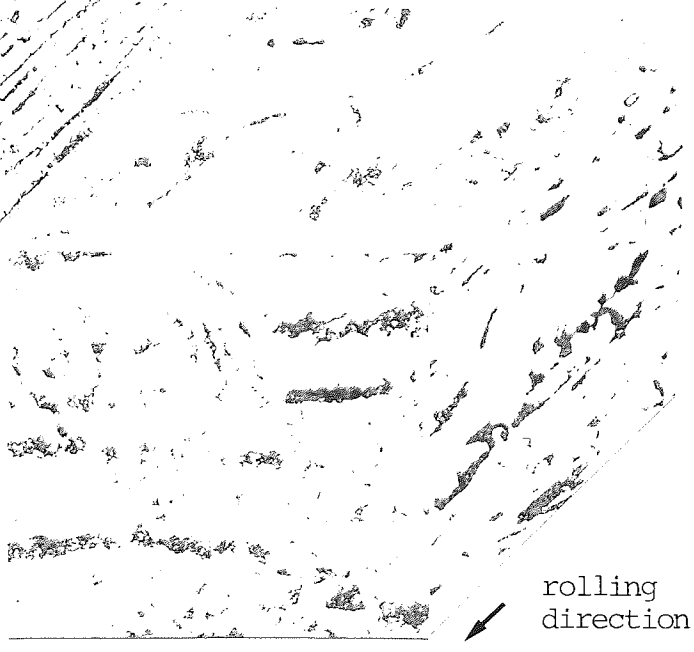

rolling
direction

PLATE 12 : Steel L .
Rolled at 900°C
air cooled .

← a. Mag.X42

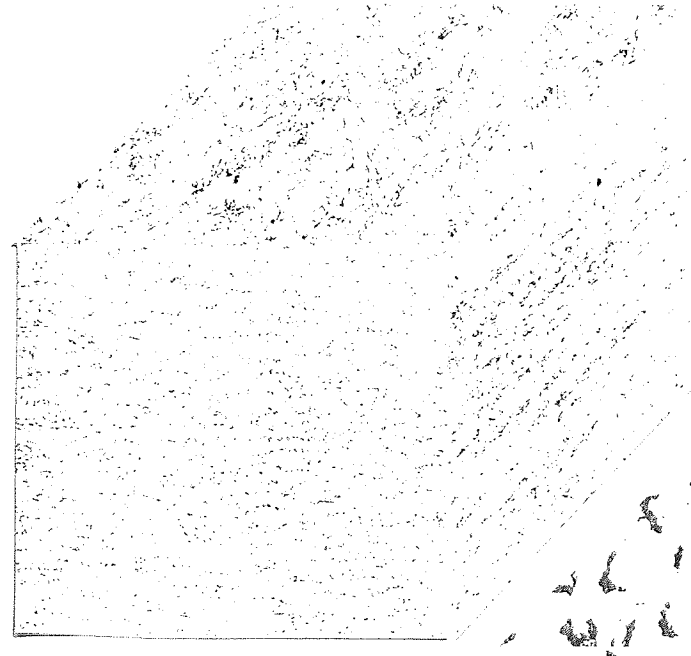

rolling direction

b. Mag.X420 →

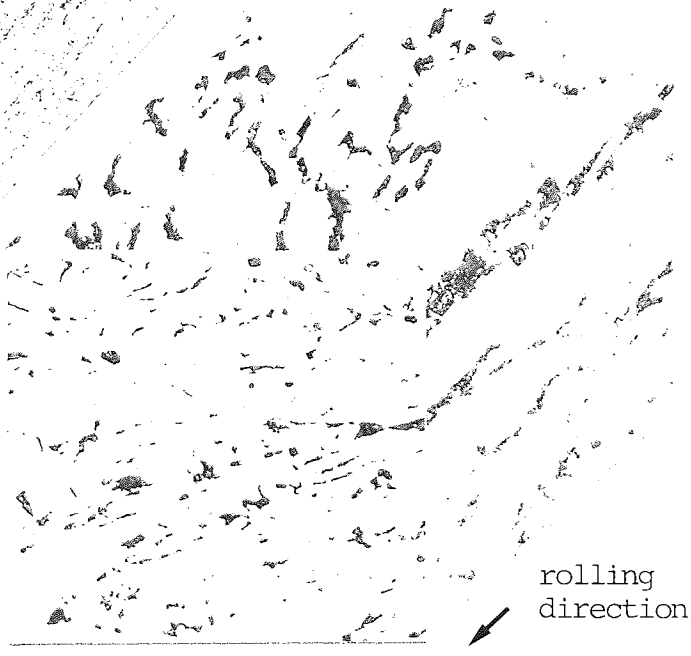

rolling
direction

PLATE 13 : Steel F .
Rolled at 1000°C
air cooled .

← a. Mag.X42

rolling direction

b. Mag.X420 →

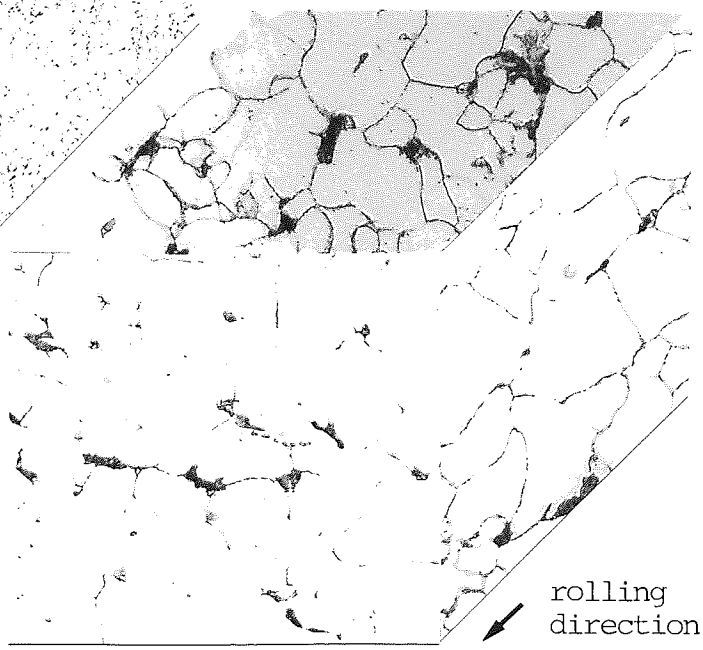

rolling
direction

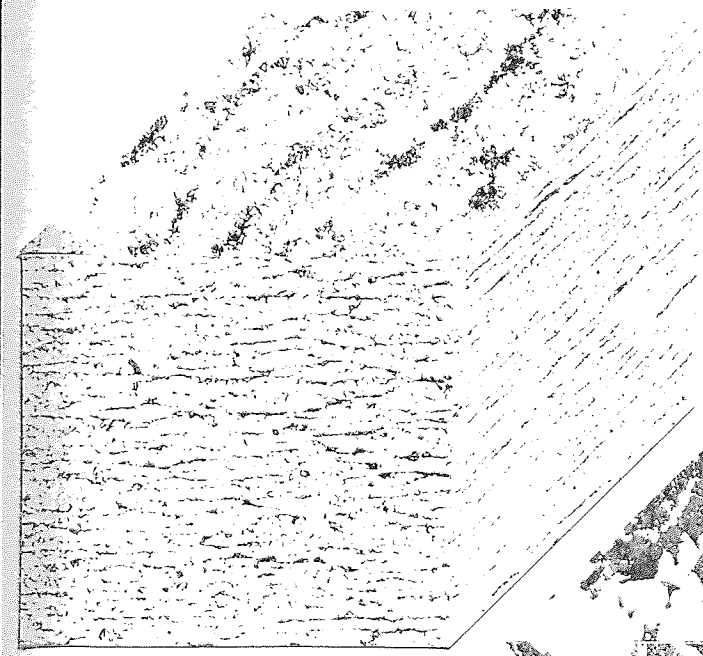

PLATE 14 : Steel M .
Rolled at 1100°C
air cooled .

← a. Mag.X42

rolling direction

b. Mag.X420 →

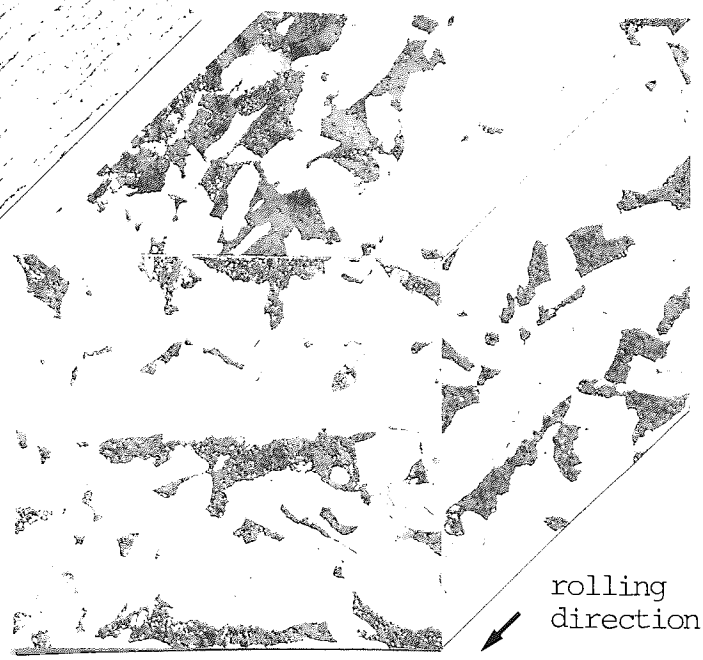

rolling
direction

TABLE 4.4 GRAIN SIZE (DIAMETERS μm AND ASTM) AND % PEARLITE

STEEL CODE	LONG SECTION: ROLLING DIRECTION				LONG SECTION: THROUGH THICKNESS DIRECTION			TRANSVERSE SECTION - AND DIRECTION			Equivalent Volume Diameter (μm)
	GRAIN SIZE			Pearlite Area %	GRAIN SIZE						
	Mean (μm)	S.D.	ASTM		Mean (μm)	S.D.	ASTM	Mean (μm)	S.D.	ASTM	
L9	13.17	0.47	9.19	8.7	11.3	0.32	9.63	12.59	0.6	8.89	12.95
L0	16.65	0.45	8.51	8.1	15.36	0.28	8.74	16.09	0.28	8.61	16.02
L1	16.87	0.71	8.47	8.2	15.31	0.30	8.75	15.6	0.41	8.7	15.91
F9	13.55	0.55	9.11	1.1	9.84	0.22	10.03	11.85	0.26	9.47	11.65
F0	17.67	0.61	8.34	0.6	16.26	0.32	8.58	16.49	0.55	8.54	16.8
F1	25.2	0.86	7.32	0.8	24.24	1.2	7.43	24.08	0.77	7.45	24.5
K9	11.9	0.26	9.48	9.7	10.63	0.17	9.8	14.41	0.57	8.93	12.2
K0	16.8	0.48	8.48	9.4	15.25	0.35	8.7	16.48	0.24	8.54	16.16
K1	18.0	0.35	8.28	9.3	16.78	0.42	8.49	18.2	0.75	8.26	17.65
M9	10.8	0.39	9.69	19.9	9.2	0.28	10.1	11.1	0.35	9.55	10.33
M0	16.04	0.35	8.62	19.4	14.61	0.28	8.89	16.22	0.32	8.58	15.61
M1	17.22	0.39	8.41	18.6	15.58	0.51	8.7	16.8	0.44	8.48	16.5

elongated inclusions are shown in Plate 9b on the longitudinal section of steel F rolled at 750°C.

4.3.1.2 INCLUSION RELATIVE PLASTICITY

As a measurement of the extent of inclusion deformation relative to that of the matrix the inclusion relative plasticity index "ν" has been calculated, using the formulae given by BAKER and CHARLES (253), at the four rolling temperatures for each steel.

The relative plasticity "ν" is given by,

$$\nu = \frac{\log Pi - \log Po}{\log H}$$

where

P = the mean inclusion projected length per unit area (see below for explanation)

o = cast steel

i = rolled steel

H = steel true strain = $\ln \frac{ho}{h}$ e.g. $\ln \frac{43}{12.5}$

ho = initial height = 43mm

h = final height = 12.5mm

The inclusion aspect ratio "λ" may also be calculated by $(Pi/Po)^2$. The results of the relative plasticity calculations are given in Table 4.5 below and are also shown graphically in Fig.78. The as cast inclusion projected lengths are contained in Tables D1,D2,D3 and D4 in Appendix D and the inclusion projected lengths after rolling are taken from Tables D12 in Appendix D. These were obtained by dividing the mean total inclusion length recorded upon the longitudinal section (in the longitudinal direction - see Appendix B Eqa. B4) by the field area ($0.038mm^2$).

TABLE 4.5 INCLUSION RELATIVE PLASTICITY

STEEL CODE	Pi mm^{-1}	Po mm^{-1}	Relative Plasticity	Aspect Ratio
L75	1.97	1.09	0.49	3.27
L9	2.23	1.1	0.58	4.11
L0	1.97	1.1	0.48	3.21
L1	1.81	1.08	0.43	2.81
F75	1.39	0.8	0.49	3.02
F9	1.54	0.89	0.49	2.99
F0	1.48	0.89	0.46	2.77
F1	1.53	0.85	0.52	3.24
K75	0.96	0.75	0.22	1.64
K9	0.89	0.74	0.17	1.45
K0	1.06	0.74	0.32	2.05
K1	0.96	0.73	0.25	1.73
M75	0.41	0.43	-0.04	1
M9	ND	0.44	ND	ND
M0	0.44	0.44	0.00	1
M1	0.48	0.42	0.13	1.31

ND = not determined.
The results are also shown graphically in Fig.78. Page 170.

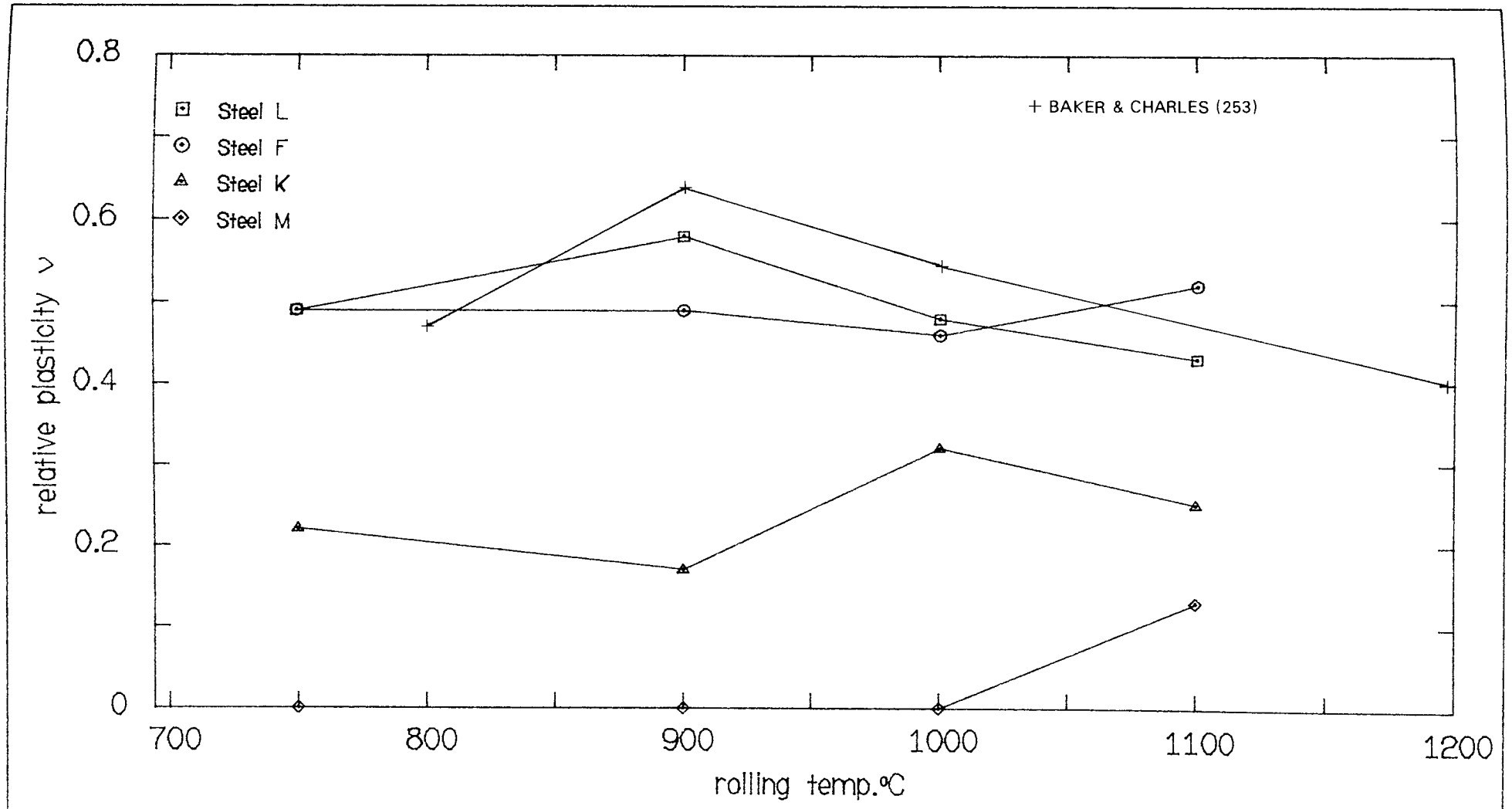

FIG.78 : The effect of rolling temperature upon inclusion relative plasticity .

The projected lengths were calculated in this manner to be consistent with the determination of the inclusion projected lengths for the as cast steels. These were calculated by multiplying the number of particles in each size group by the dimension of the class mean, summing these totals and dividing the grand total by the number of fields observed and the field area. NOTE: The projected lengths determined from the mid-sections of the as cast ingots were used to calculate the inclusion relative plasticities for the steels rolled at 900 and 1000°C.

4.3.2.0 QUANTITATIVE ANALYSIS OF INCLUSIONS

4.3.2.1 DATA FROM IMAGE ANALYSIS

The inclusion area, count (number) and total length obtained from image analysis are set out in Tables D10, D11 and D12 in Appendix D. The tabulation gives the number of fields observed, the mean value, standard deviation (S.D.), coefficient of variance (C. of V.), maximum value (Max), minimum value (Min) and range for the longitudinal and transverse sections of each steel. Additionally, from this data the average inclusion area, average inclusion major axis, minor axis and aspect ratios have been calculated for each field observed, collated and presented in Tables D13, D14, D15 and D16 in Appendix D. These were subsequently used to calculate the inclusion parameters as defined in Section 4.3.2.2. These features are given as follows (inclusion shape is assumed ellipsoidal)

a_1 or a_2 = average inclusion area (μm^2)
= $\frac{\text{AREA PER FIELD}}{\text{NUMBER PER FIELD}}$

d_1 or d_2 = average inclusion major axis (μm)
= $\frac{\text{TOTAL INCLUSION LENGTH PER FIELD}}{\text{NUMBER PER FIELD}}$

d_3 = average inclusion minor axis = $\frac{4ai}{di}$

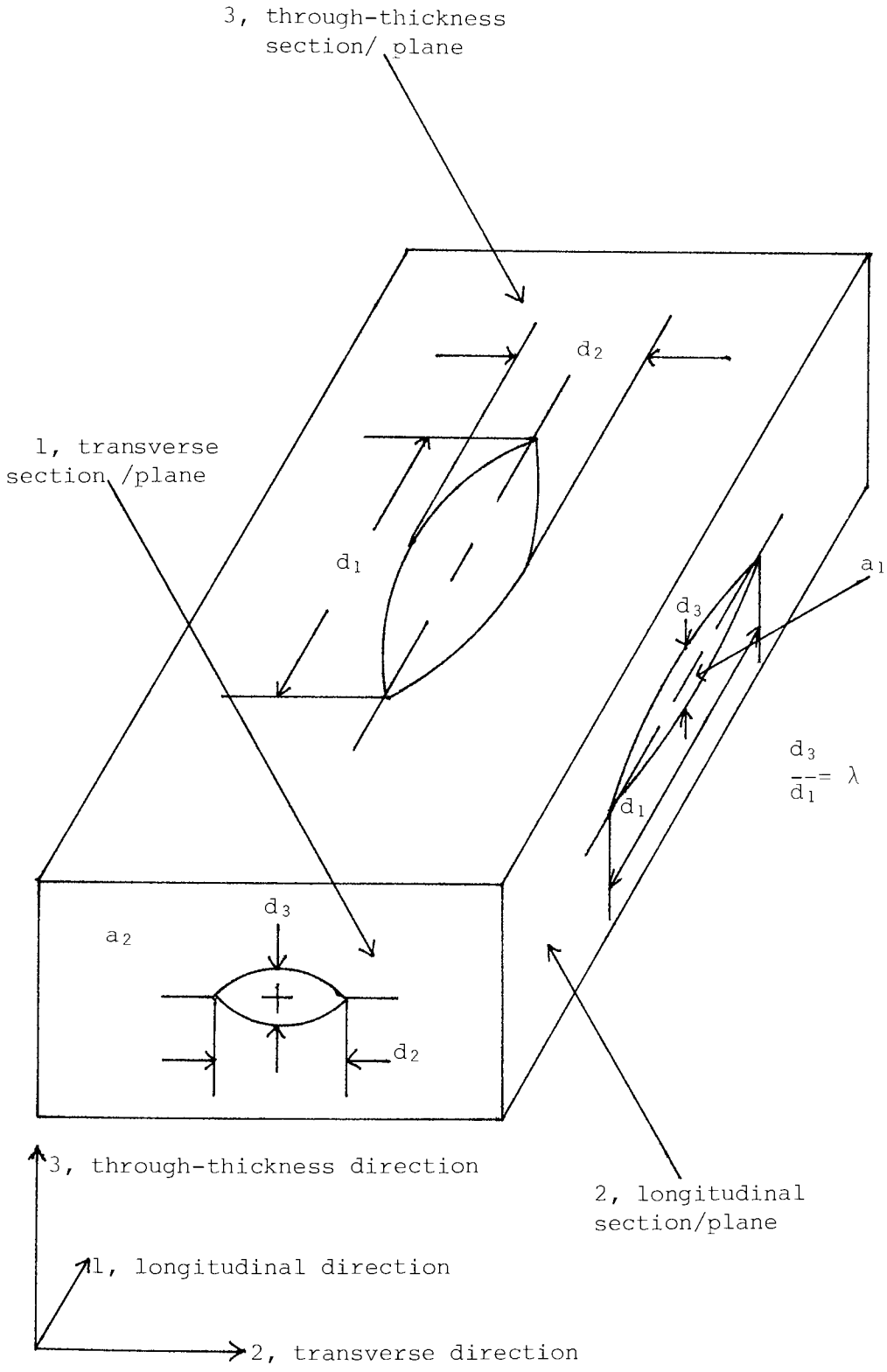

FIG.79 : Diagram showing planes, directions and inclusion dimensions.

$$i = 1, 2 \text{ or } 3$$

$$\text{aspect ratio} = \frac{di}{d_3}$$

For a complete description of inclusion dimensions/notation see Fig.79.

4.3.2.2 INCLUSION PARAMETERS

Using the above data obtained from the image analysis the following inclusion parameters have been derived,

$\%A_F$ - percent area fraction = $\frac{\text{AREA}}{\text{FIELD AREA}} \times 100$
(equivalent to % volume fraction, %Vv)

P_{Li} - the projected (total) length of inclusions per unit area (mm/mm^2) in the longitudinal (L), transverse (T) and through-thickness (T/T) directions,

P_{Ai} - the projected area of inclusions per unit volume (mm^2/mm^3) in the L,T and T/T directions.

MFD_i - the mean free distance (mm) i.e. the average edge to edge distance between an inclusion and all its neighbours, in the L,T and T/T directions and the,

NND_i or Δi - the nearest neighbour distance (mm) i.e. the average centre-to-centre distance between an inclusion and its closest neighbour, on the L, T or T/T plane.

The parameters P_L, P_A, MFD and Δ are derived in Appendix B. The equations used to determine P_L, P_A, MFD and Δ in this study were Eqns. B8, B11, B15 and B22 respectively. Each parameter was calculated

for each field analysed so that the frequency distribution for each parameter could be determined. These were calculated for the longitudinal, transverse and through-thickness directions for P_L, P_A and MFD and planes for Δ. The data resulting from these calculations was then analysed statistically (see next Section 4.3.2.3) the results of which are given in Tables D17, D18, D19, D20 and D21 in Appendix D.

4.3.2.3 STATISTICAL ANALYSIS OF INCLUSION PARAMETERS

As the parameters A_F, P_L, P_A, MFD and Δ can be usefully correlated with the steels mechanical properties (see Section 4.4.1) the calculation of confidence limits, probabilities and the relative accuracy of the analysis was required. However, it was found that the frequency distribution of these parameters was not normal i.e. normally distributed and as such any of the above statistical estimates calculated from the data as it stood would be invalid. Figs. 80, 81, 82, 83 and 84 show histograms of typical frequency distributions for A_F, P_L, P_A, MFD and Δ which are representative of the type of distributions which were observed. The data can be seen to be skewed (positive skew and kurtosis) and the normal curves which have been fitted to the data under estimate the extreme values at the right of the distributions and over estimate those to the left. It is important that these extreme values are accounted for as they often significantly affect mechanical properties.

Therefore, the original data was transformed using logarithms (base 10), to normalise it, producing the familiar log-normal distribution. This type of transformation has been successfully applied by several other workers investigating inclusion parameters (245, 246, 248, 249). The distribution of counts was found to be best described by a Poisson distribution i.e. random and a square-root transformation was appropriate

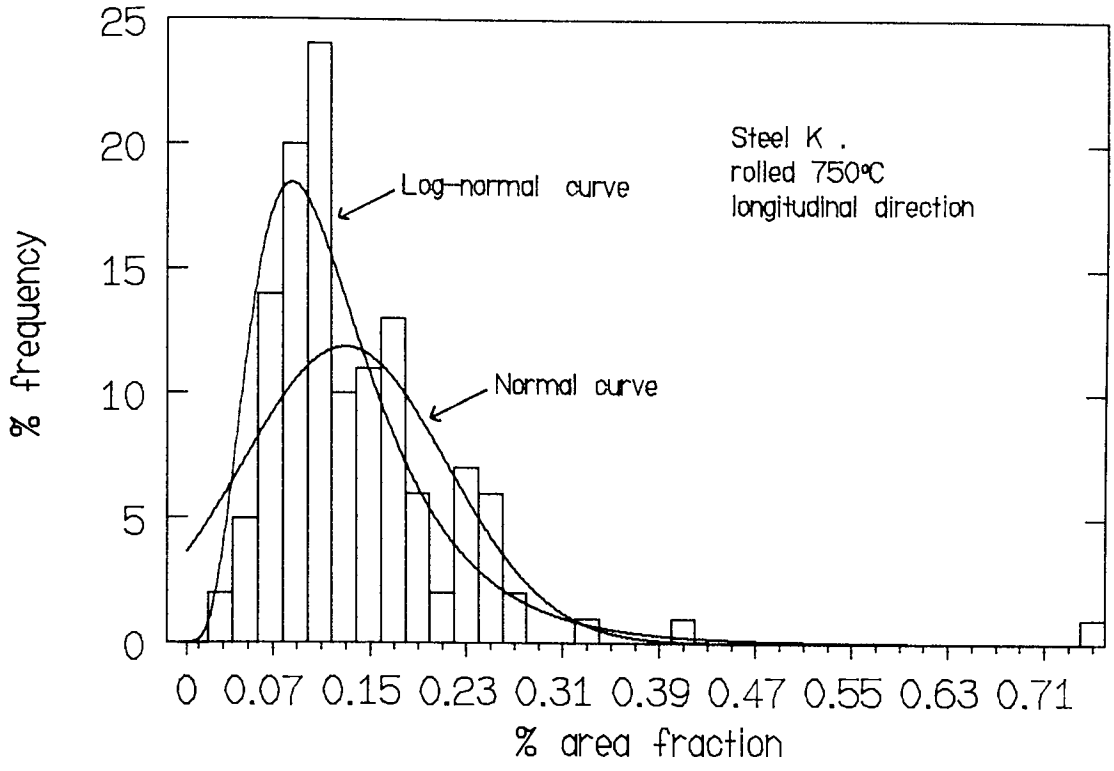

FIG.80 : Histogram of the frequency distribution of % area fraction .

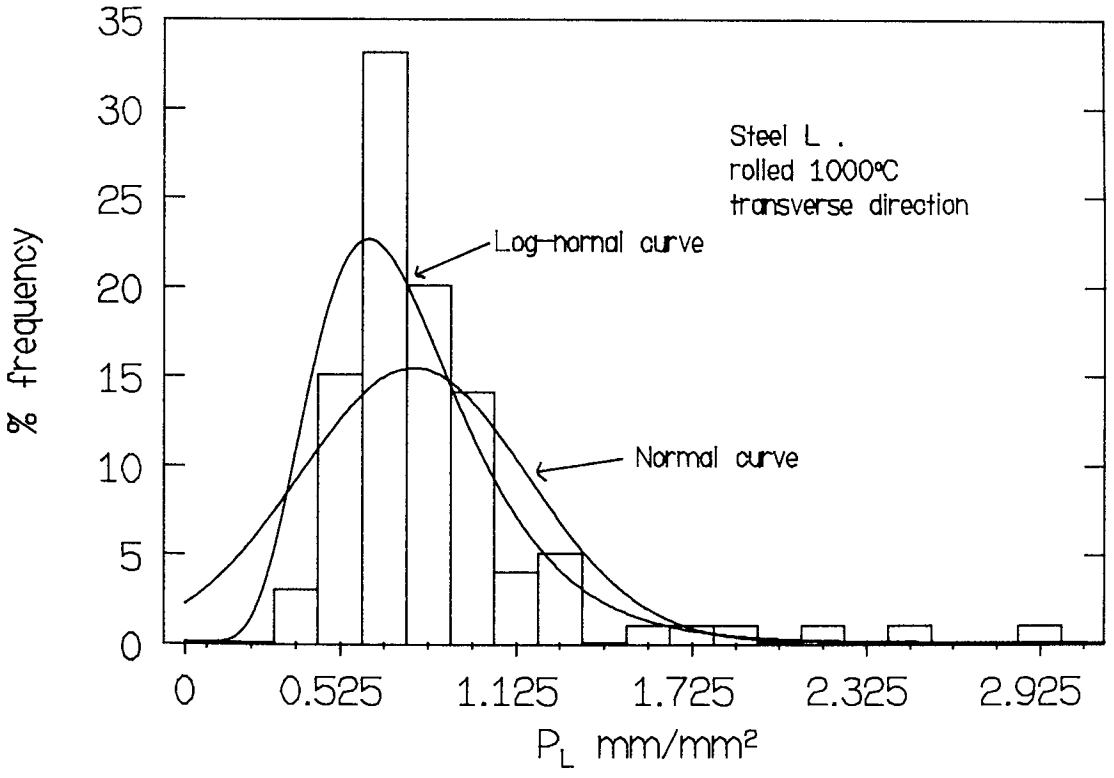

FIG.81 : Histogram of the frequency distribution of inclusion projected length per unit area .

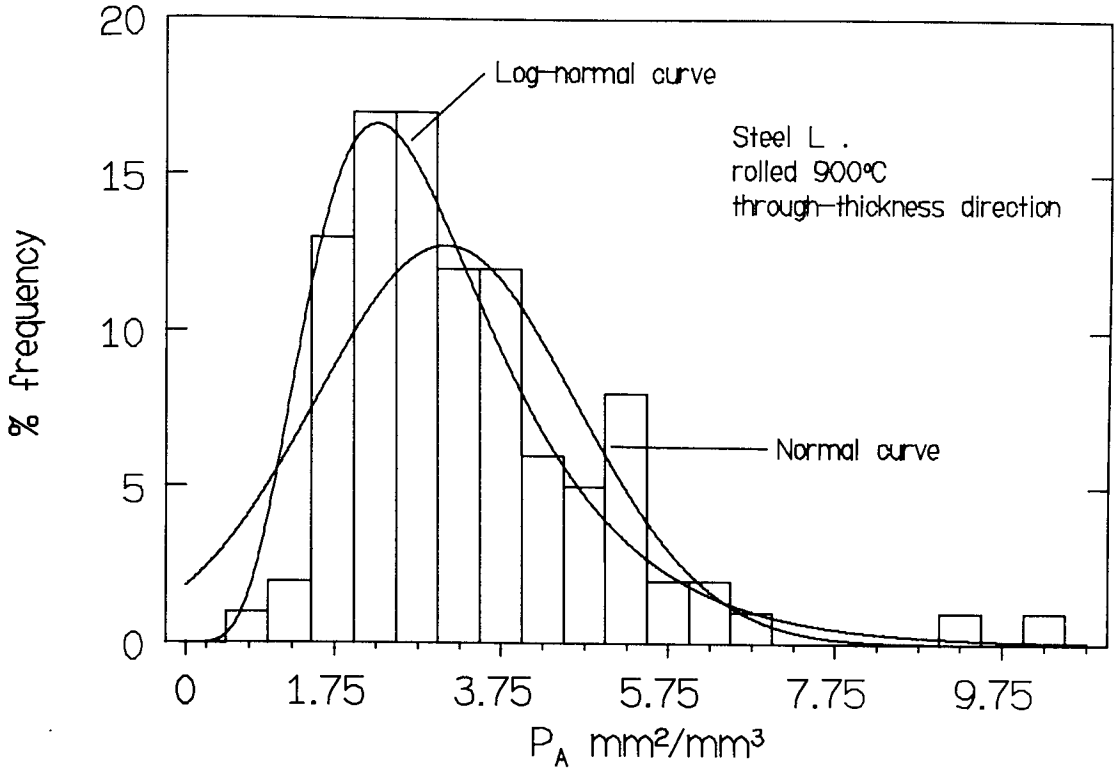

FIG.82 : Histogram of the frequency distribution of inclusion projected area per unit volume .

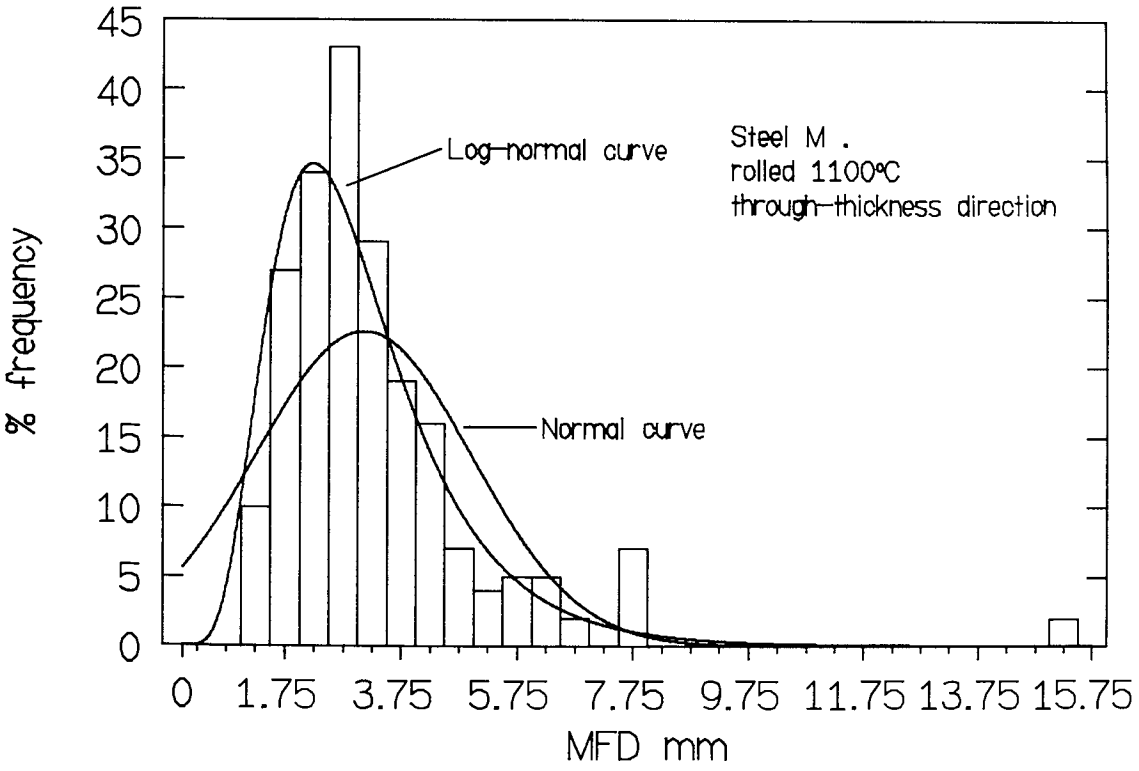

FIG.83 : Histogram of the frequency distribution of the mean free distance between inclusions .

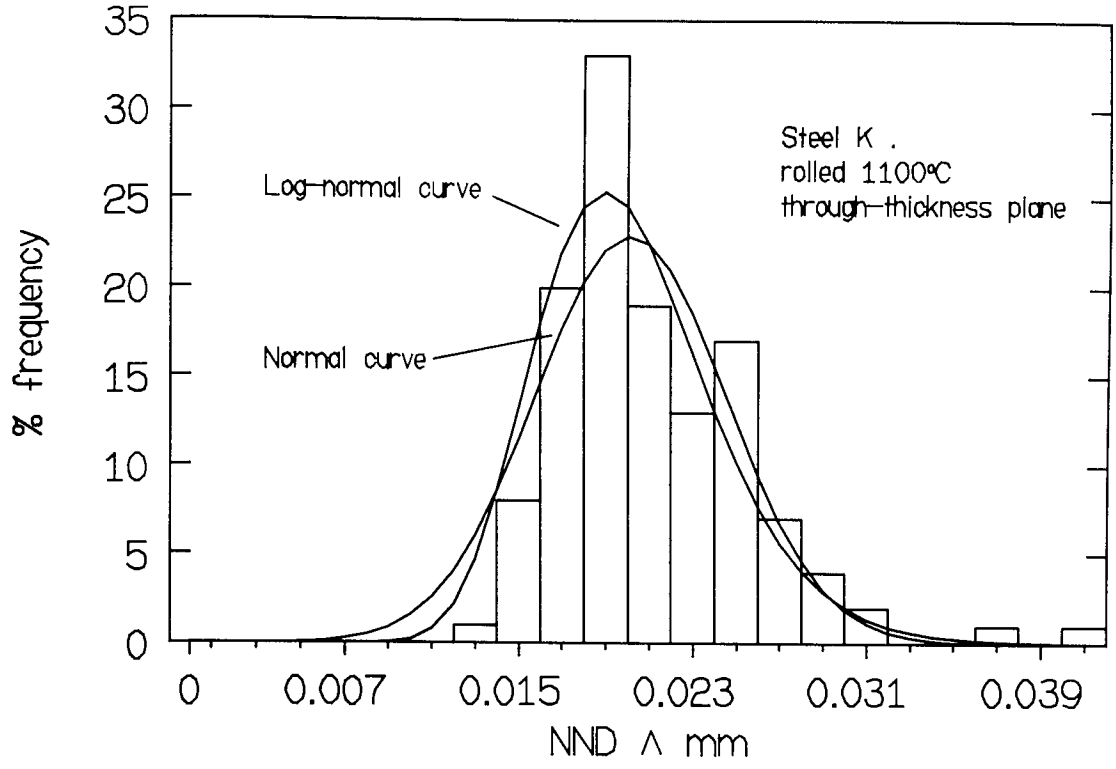

FIG.84 : Histogram of the frequency distribution of the inclusion nearest-neighbour distance .

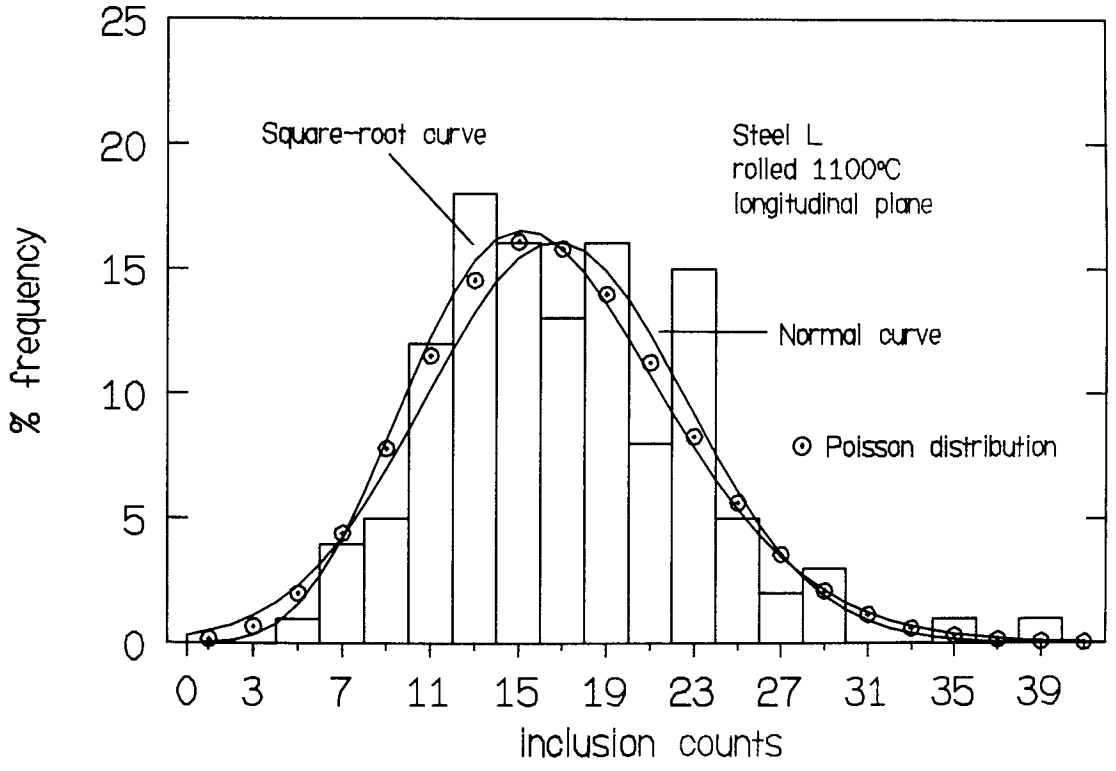

FIG.85 : Histogram of the frequency distribution of inclusion counts .

in this case (247, 251). Fig. 85 shows a typical example of the distribution of counts together with the normal, Poisson and transformed curves for comparison). The log-normal curves are also shown in Figs. 80, 81, 82, 83 and 84, and can be seen to be a far more satisfactory description of the data.

To test more rigorously whether the transformation adequately satisfies the conditions of normality the method of moments was used. This method is considered more suitable than the Chi-squared goodness of fit test as the latter test often requires additional grouping at the extremes of the range (252). The method of moments are described in Appendix C Part 2 and the results are presented for both the untransformed and transformed data. The following inclusion parameters were analysed; the data from the image analysis i.e. area, count and total length and the derived inclusion parameters P_L, MFD, and Δ, these are tabluated in Appendix D in Tables D22 to D27.

NOTE: The results obtained for % area fraction are the same as for area and similarly the results for P_A are the same as P_L, the reason for this is that both parameters were calculated from the other by a constant, therefore to prevent repetition only the results of area and P_L have been reproduced.

For a normal distribution the moment coefficient of skewness (B1) should be equal to zero (the closer to zero the better and the data conforms to a normal distribution) and the moment coefficient of kurtosis (B2) should be equal to three and not greater than five. Extreme values are indicated if the value of the statistic (Ev) exceeds 1.32 (see Appendix C Part 2)(195).

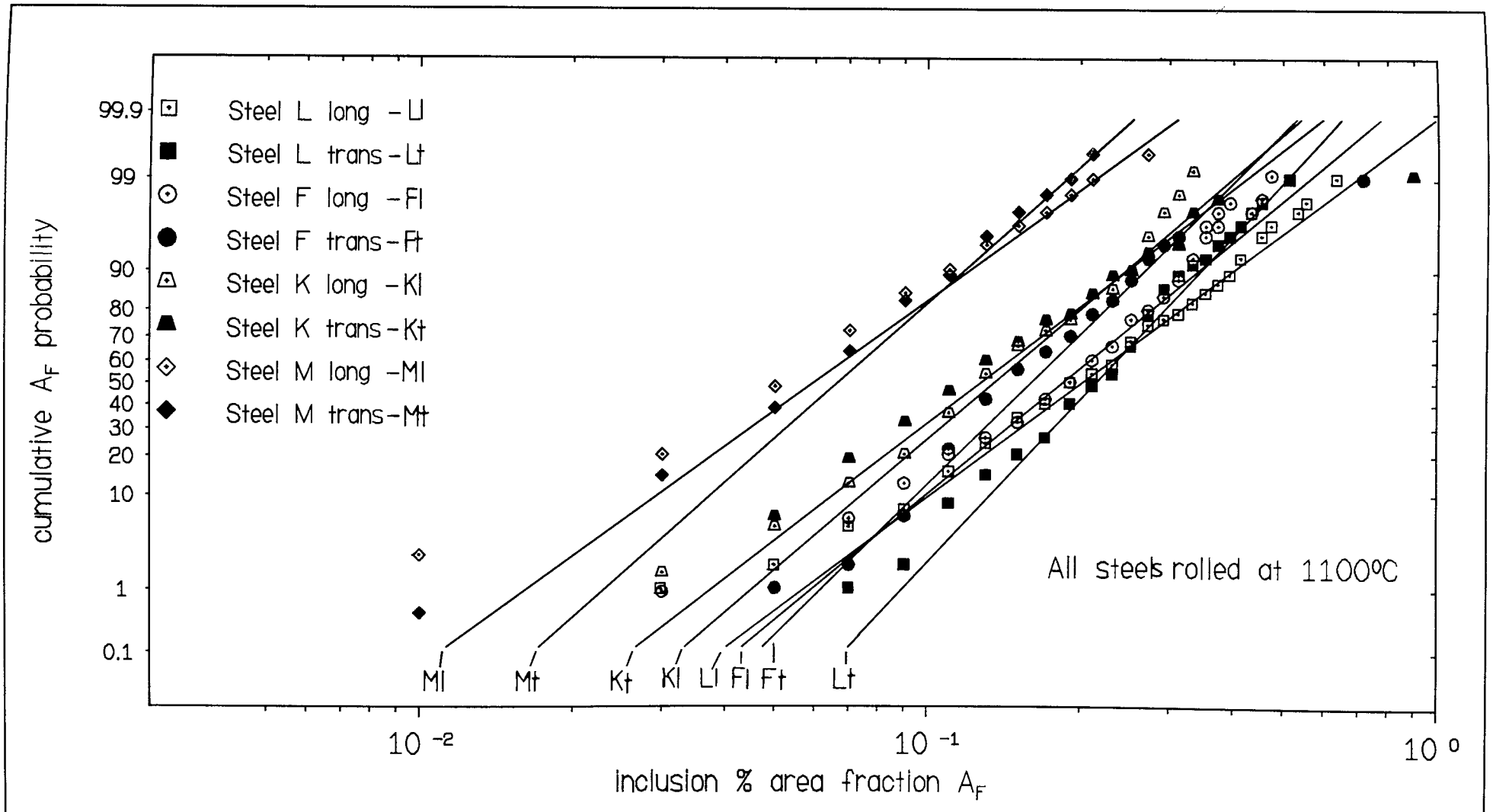

FIG.86 : Log-normal probability graph of the inclusion % area fraction distribution on the longitudinal and transverse planes .

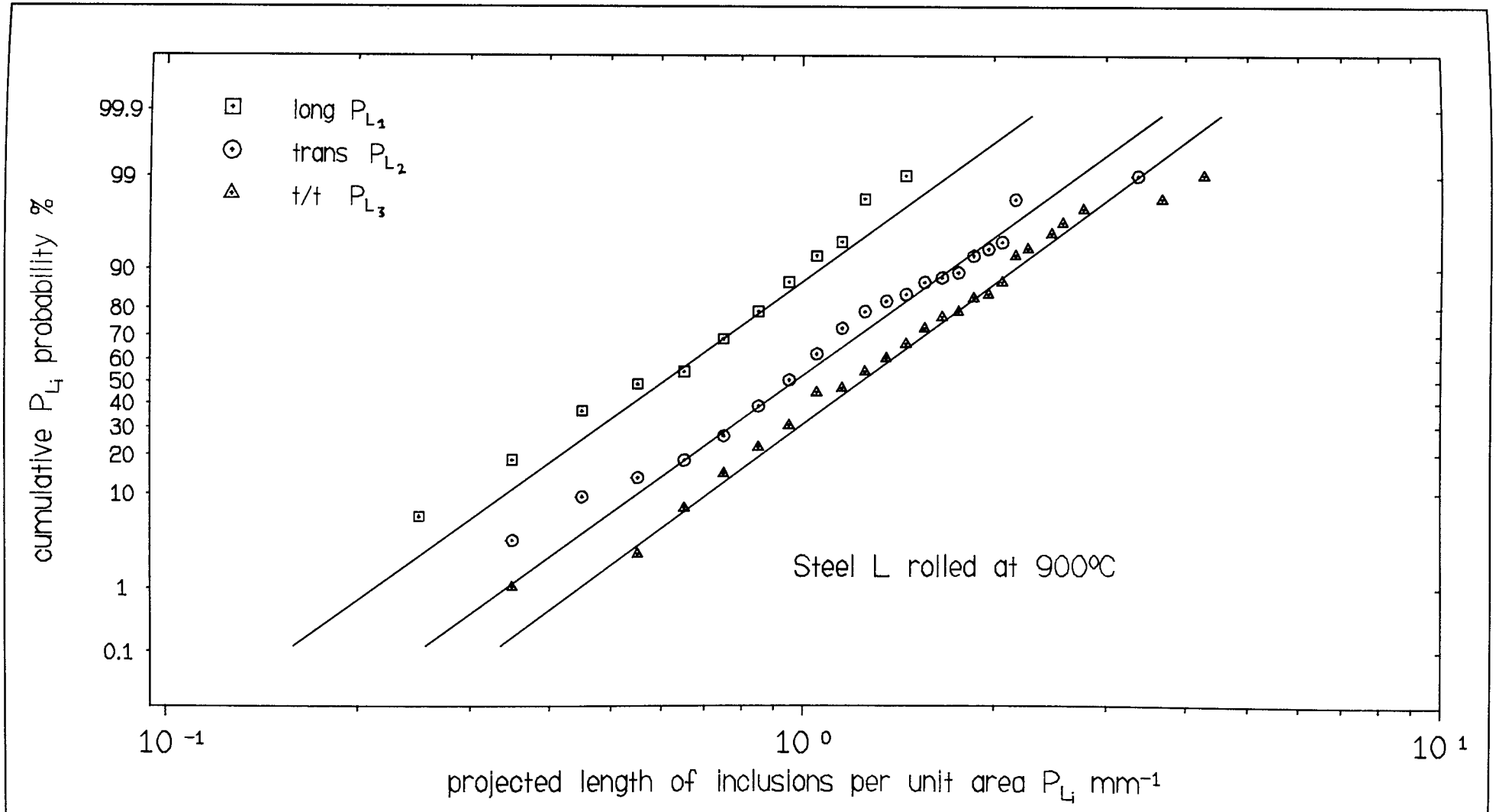

FIG. 87 : Log-normal probability graph of the inclusion projected length distribution in the longitudinal (P_{L_1}) ,transverse (P_{L_2}) and through-thickness (P_{L_3}) directions .

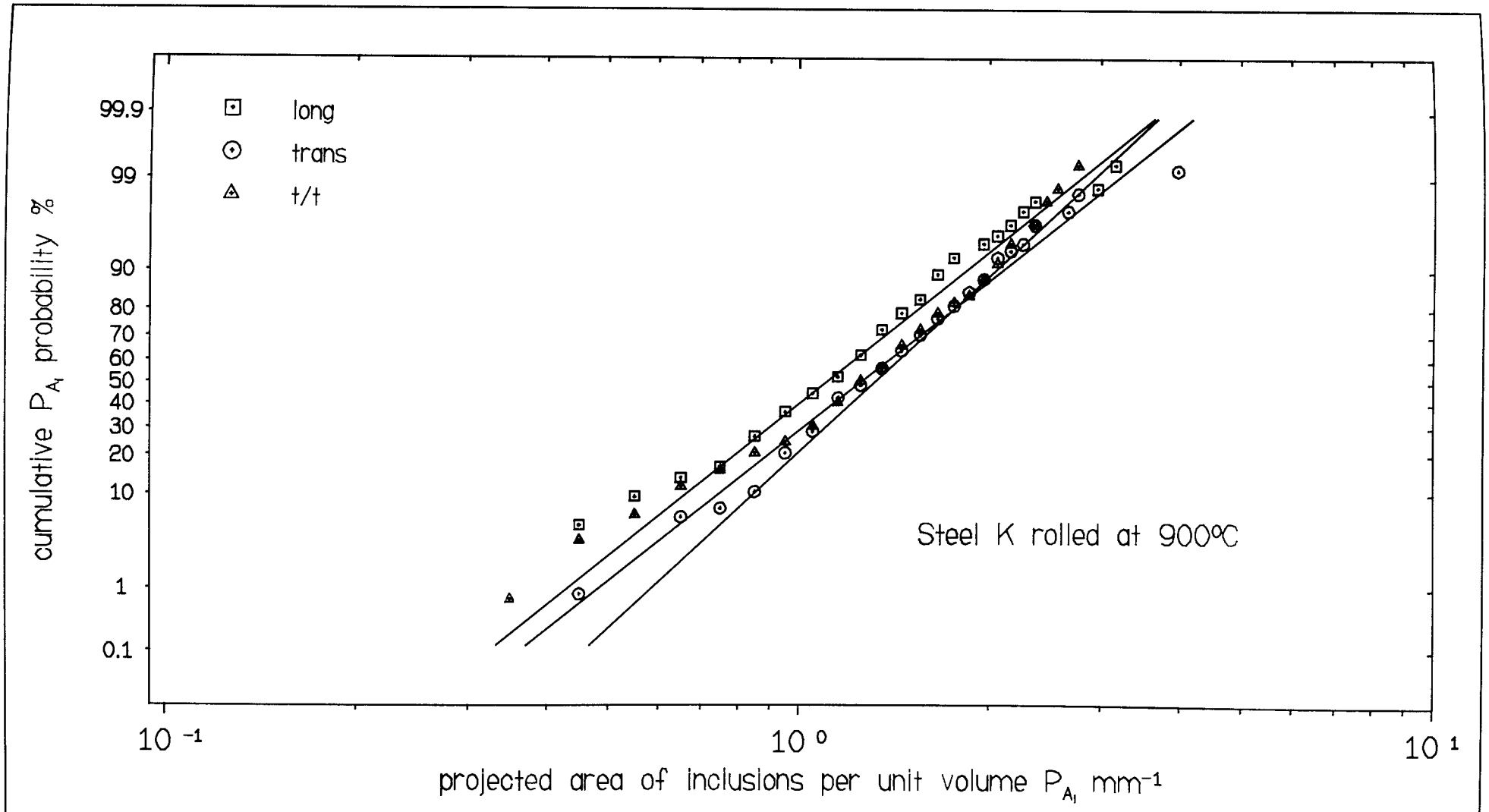

FIG.88 : Log-normal probability graph of the inclusion projected area distribution in the longitudinal (P_{A_1}) ,transverse (P_{A_2}) and through-thickness (P_{A_3}) directions .

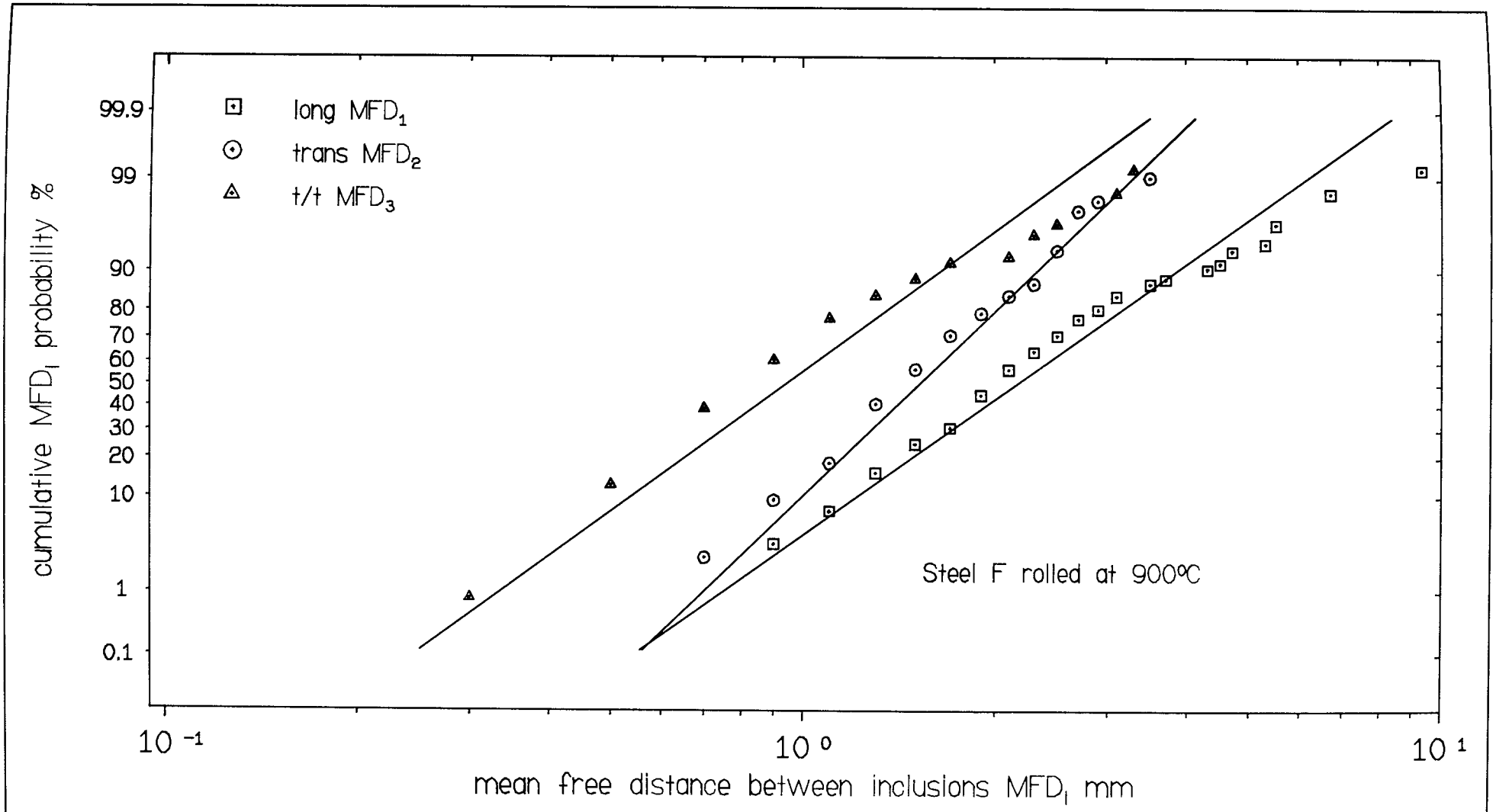

FIG.89 : Log-normal probability graph of the distribution of mean free distances between inclusions in the longitudinal (MFD_1) ,transverse (MFD_2) and through-thickness directions .

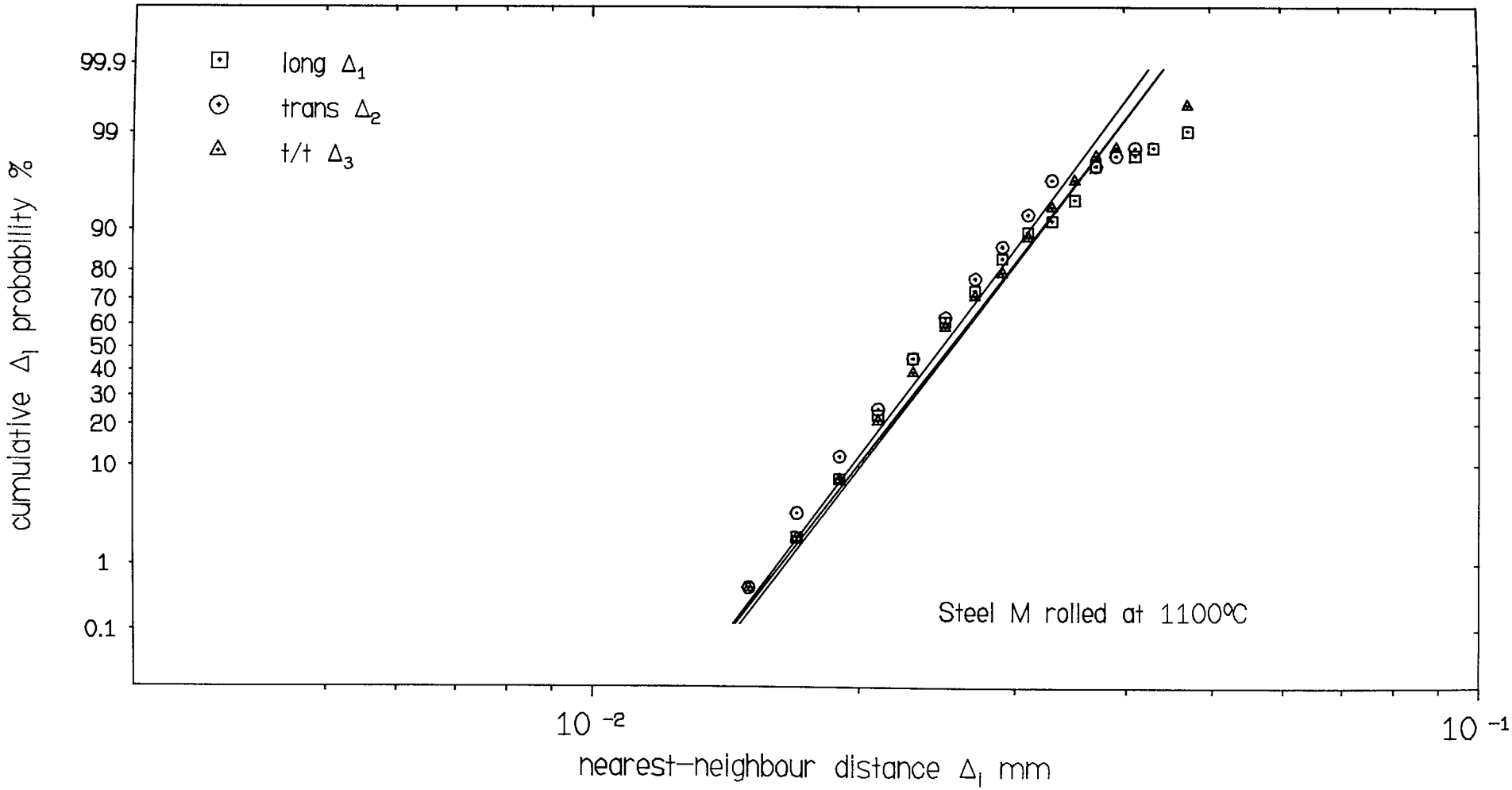

FIG.90 : Log-normal probability graph of the distribution of nearest-neighbour distances between inclusions on the longitudinal (Δ_1) ,transverse (Δ_2) and through-thickness planes .

Further evidence of log-normality is shown in Figs. 86, 87, 88, 89 and 90 which are graphs of the cumulative inclusion parameters (e.g. % A_F, P_A, P_L, MFD and Δ) on log-normal probability paper. The data is linearised, and also allows a comparison between the different sets of data e.g. the difference in inclusion $\%A_F$ between the four steels L, F, K and M rolled at 1100°C may be seen in Fig.86.

With the data satisfactorily normalised; confidence limits, relative accuracy and probabilities can be calculated using normal statistical methods. These calculations are shown in Appendix C Part 3 for the transformed data. Hence the tables of results referred to in the previous section (Tables D17 to D21 in Appendix D) for $\%A_F$, P_L, P_A, MFD and Δ are presented as follows:

i) anti-log of the transformed mean (geometric)

ii) the transformed standard deviation

iii) 95% confidence limits (95% C.L.) about the normal mean

iv) the minimum and maximum values

v) the % relative accuracy (% RA)

vi) the number of fields observed.

4.3.2.4 COMPUTER APPLICATION

Due to the large amount of data, calculations and statistical analysis involved in the above determinations a programme was developed to handle all the information, to assist in analysing the results and to plot graphs, the basic data from the image analysis being accessed from files. A simplified flow diagram of the programme developed for this purpose is shown in Fig.91.

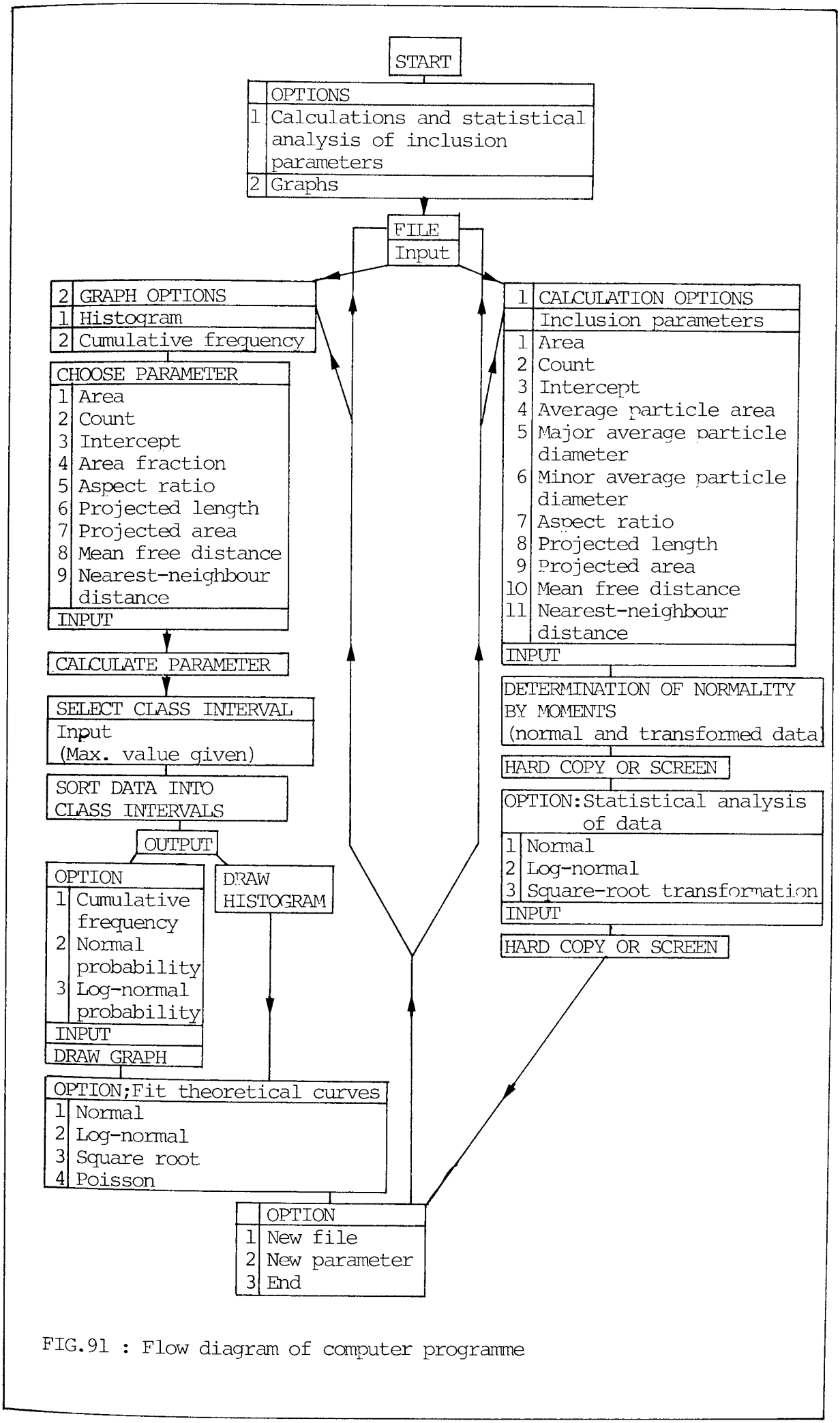

FIG.91 : Flow diagram of computer programme

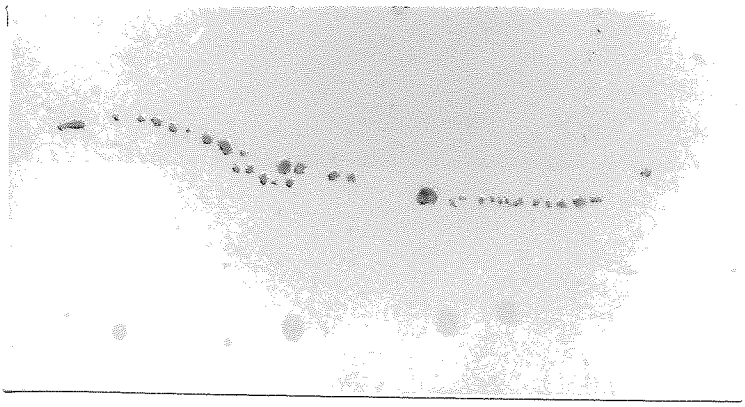

PLATE 15 : Typical example of a MnS network which has been reoriented and strung out after hot rolling . Steel L rolled at 900°C . Also note the darker alumina inclusion situated within the largest single inclusion in the string . Mag.X840 .

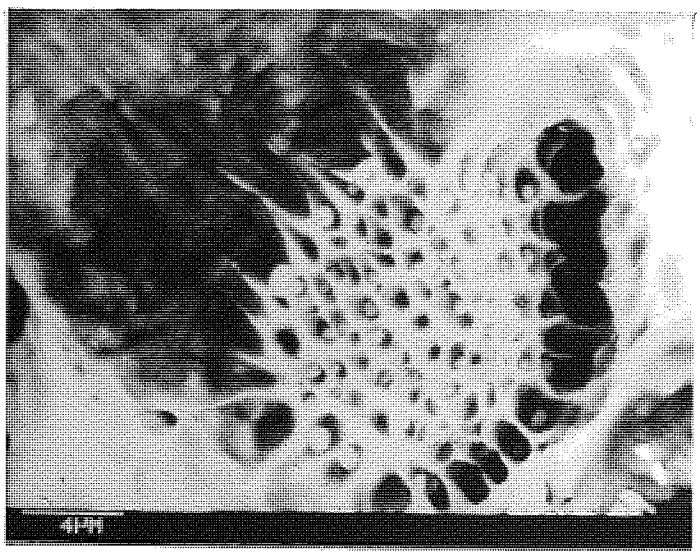

PLATE 16 : Cluster of inclusions (MnS) which have acted collectively to form a single void . Smaller voids exist around the individual inclusions themselves . Steel F rolled at 1100°C . Hounsfield tensile specimen .

4.4 MECHANICAL TESTS

4.4.0 HOUNSFIELD TENSILE TESTS

The results of the Hounsfield tensile tests are given in Table D28 in Appendix D. The values reported are yield stress (YS), ultimate tensile stress (UTS) and fracture strain. The data in these tables show that the YS and UTS increased in the order F, L, K and M reflecting the increasing level of carbon found in these steels. The YS and UTS was a maximum for the steels rolled at 750°C, whereas the levels of YS and UTS were quite similar for the steels rolled at 900,1000 and 1100°C. There was no systematic difference in the YS and UTS for the steels tested in either the longitudinal or transverse directions, nor the fracture strain for steels K and M. However, the fracture strain decreased in the transverse testing direction for steels L and F.

The fracture strains have then been plotted against a number of inclusion parameters including the A_F in Fig.92, the projected length of inclusions on a plane parallel to the fracture plane in Fig 93, and the reciprocal of the mean free distance between inclusions in a direction parallel to the tensile direction in Fig.94. The numbering on the graphs represents the temperature at which the steels were rolled.

In addition the inclusion data for nearest-neighbour distance (Table D21 Appendix D) and average inclusion size (Table D14 and D15 Appendix D) has been used in a model for ductile fracture. The model is based on a previously proposed criterion for the linkage of voids nucleated at second phase particles by LEROY et al (254), which has been adapted by SPITZIG (235) to account for inclusion anisotropy. The model assumes

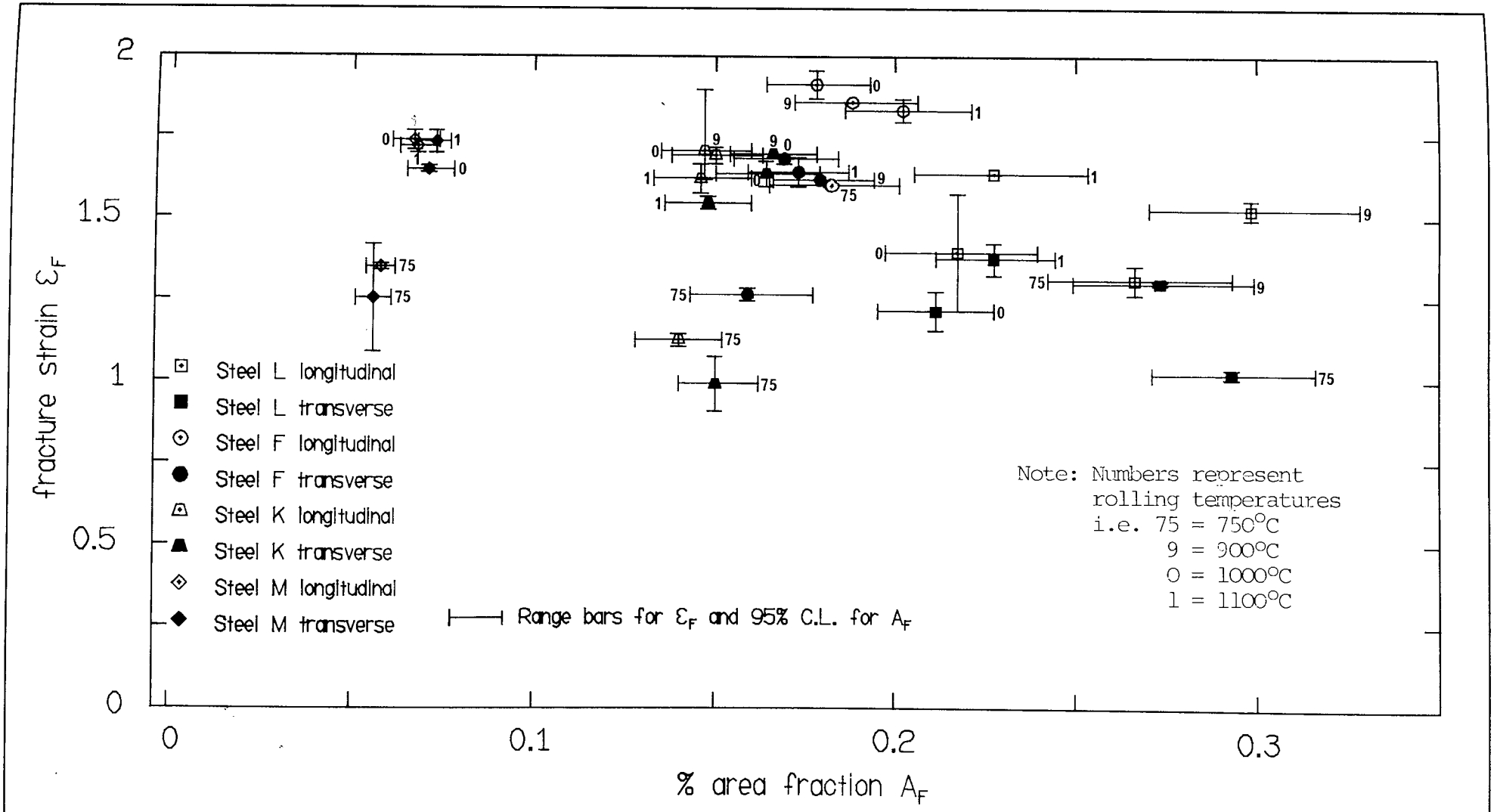

FIG.92 : Effect of inclusion % area fraction upon fracture strain in the transverse and longitudinal directions . Hounsfield specimens .

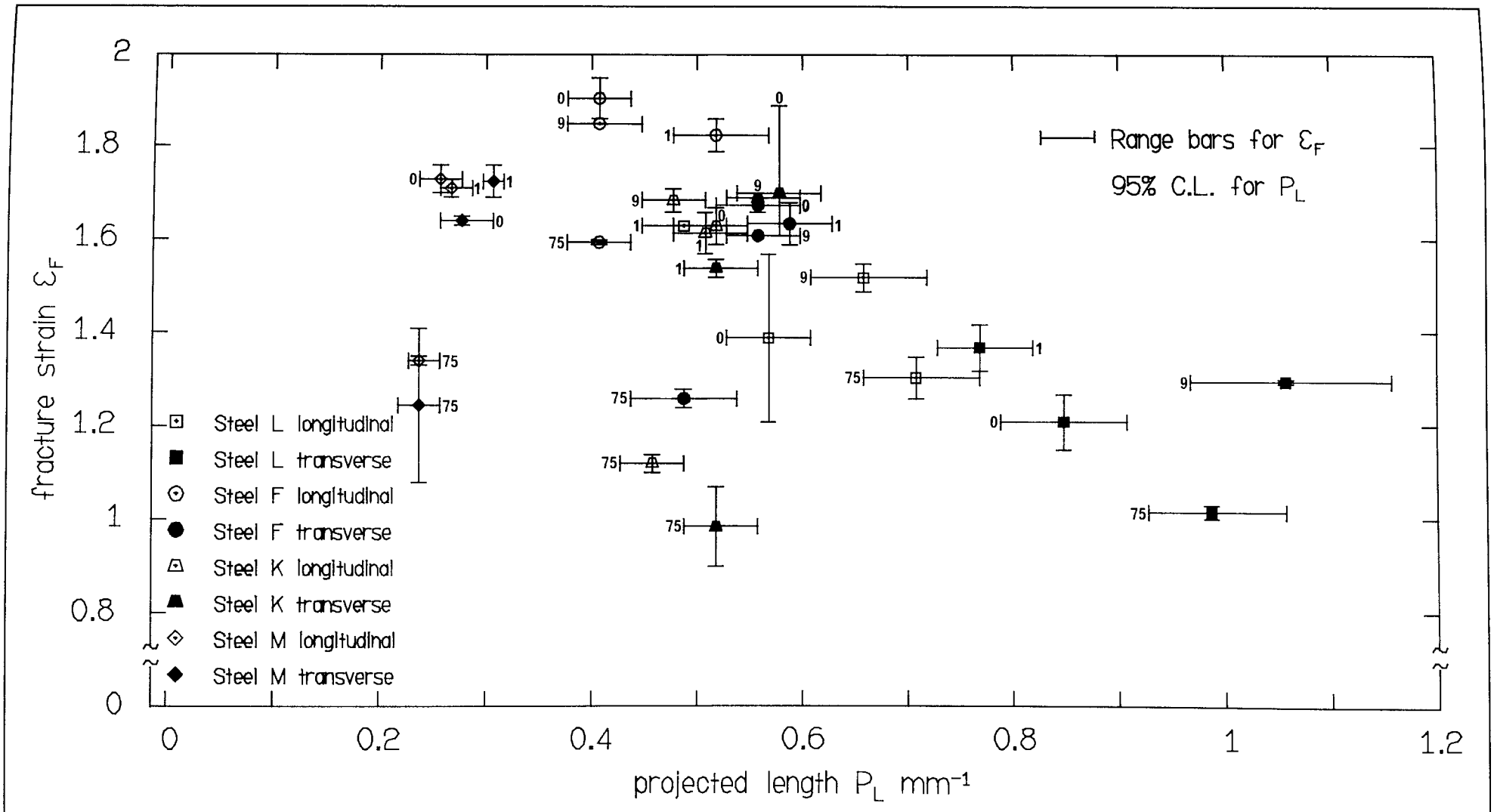

FIG.93 : Effect of inclusion projected length per unit area on a plane parallel to the fracture plane vs the fracture strain in the longitudinal and transverse directions . Hounsfield specimens .

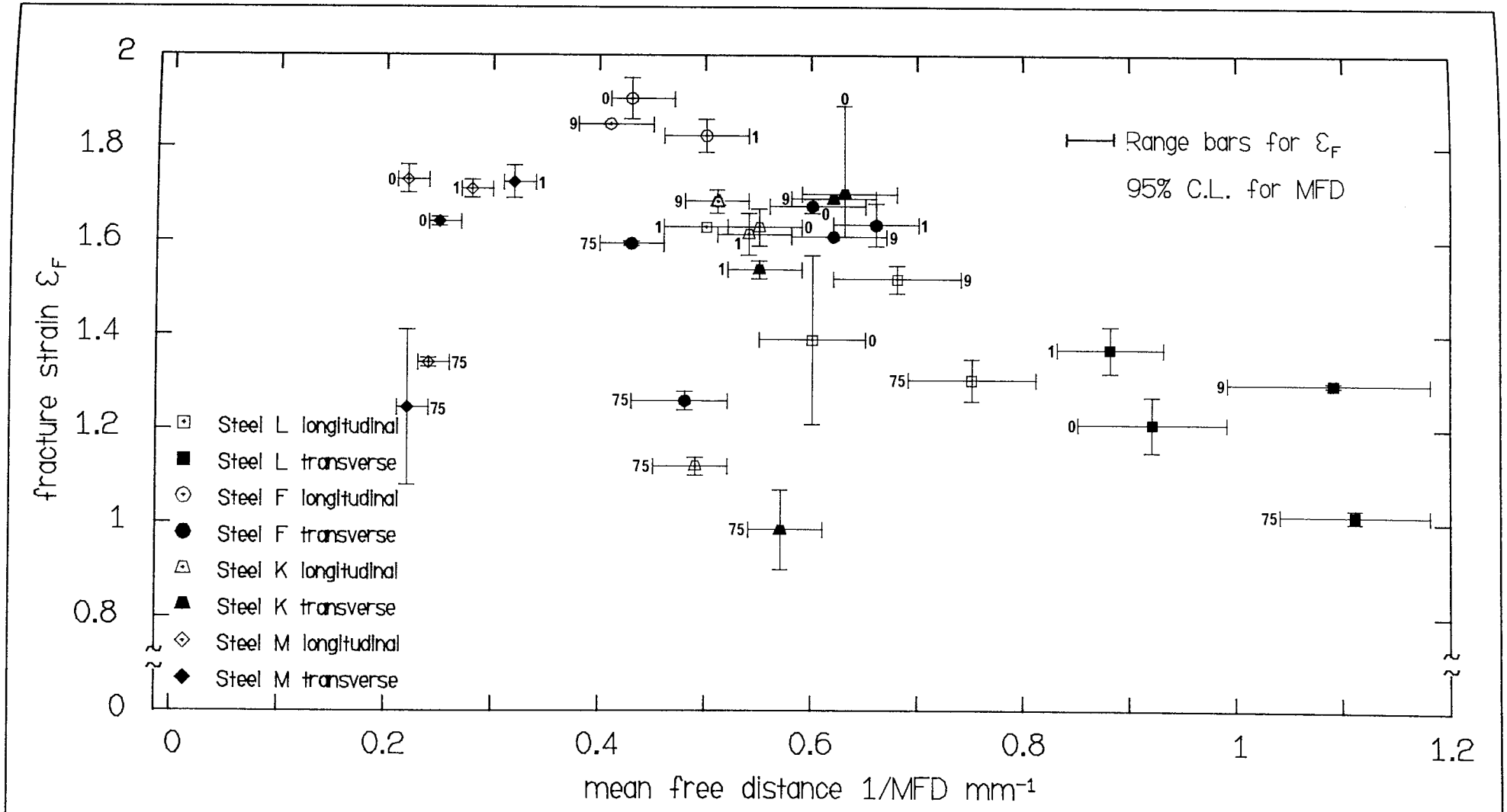

FIG.94 : Effect of mean free distance between inclusions in a direction parallel to the tensile direction on the fracture strain in the longitudinal and transverse directions .Hounsfield specimens .

that fracture occurs when voids nucleated at second phase particles coalesce when the spacing between voids in the tensile direction becomes equal to some multiple of the particle spacing in the fracture plane. The conditions for fracture are found when the spacing between voids on a plane parallel to the tensile direction Λi, at a tensile strain, e,

$$\Lambda i = \Delta j - dj\ (1+Ae) \qquad \ldots\ i$$

becomes a multiple of the inclusion spacing on the plane perpendicular to the tensile direction Λk, which is given by,

$$\Lambda k = \Delta m - dm \qquad \ldots ii$$

where, i = 1,2,3 for the longitudinal, transverse and through-thickness planes,

Δj = the smallest nearest-neighbour distance on a plane parallel to the tensile direction,

dj = inclusion dimension on the plane Δj, and is taken as the diameter of a circle of area equivalent to that of the elliptical inclusion,

Δm = the nearest-neighbour distance on the plane perpendicular to the tensile direction,

dm = the diameter of a circle of area equivalent to that of the elliptical inclusion on the plane Δm,

A = a constant that accounts for the possibility that the voids elongate at a rate different from the rate of extension of the specimen.

It is assumed that voids do not grow significantly in the plane perpendicular to the tensile direction and that void initiation occurs immediately upon straining. Also, although movement of inclusions will occur during straining the average nearest-neighbour spacing is found not to change for a random distribution of particle centres (250).

Thus by combining Eqs. i and ii and introducing a factor B into Eq. ii, which is an empirical constant of proportionality (that accounts for any lateral void growth and the effect of necking), fracture is predicted when,

$$\Delta j - dj\ (1 + Ae) = B(\Delta m - dm) \qquad \ldots \text{ iii}$$

by rearranging Eq. iii the true strain to fracture is given by,

$$\varepsilon Fi = In \frac{(\Delta j - B(\Delta m - dm) + (A-1)\ dj)}{Adj} \qquad \ldots \text{ iv}$$

for the longitudinal and transverse specimen orientations,

i = 1 (LONGITUDINAL) $\Delta j = \Delta 1, \Delta m = \Delta 2, dm = d_2 d_3\ dj = d_1 d_3$

i = 2 (TRANSVERSE) $\Delta j = \Delta 2, \Delta m = \Delta 1, dm = d_3 d_1\ dj = d_2\ d_3$

The constants A and B used by SPITZIG (235) in his study of a 0.1%C and 0.2%C (1% Mn) hot rolled pearlitic steel were 2 and 0.3 and 3 and 0.3 respectively. However, these values were considered as adjustable parameters chosen to give agreement between observed and predicted values, where the constant A primarily reflected differences in the matrix properties.

The results of this analysis are plotted in Fig.95, the values of the constants used in the calculation and the predicted and observed fracture strains are given in Table 4.6 below.

TABLE 4.6 FRACTURE MODEL, DATA AND RESULTS

STEEL CODE	CONSTANTS A	CONSTANTS B	LONGITUDINAL OBSERVED	LONGITUDINAL PREDICTED	TRANSVERSE OBSERVED	TRANSVERSE PREDICTED
L75	1.5	0.3	1.31	1.25	1.02	1.13
L9	1.0	0.3	1.52	1.45	1.3	1.54
L0	1.0	0.3	1.39	1.59	1.21	1.7
L1	1.0	0.3	1.63	1.56	1.37	1.63
F75	1.5	0.3	1.6	1.39	1.26	1.53
F9	1.0	0.3	1.85	1.6	1.61	1.73
F0	1.0	0.3	1.91	1.67	1.68	1.76
F1	1.0	0.3	1.83	1.65	1.64	1.73
K75	2.5	0.3	1.12	1.19	0.99	1.21
K9	1.5	0.3	1.69	1.6	1.69	1.51
K0	1.5	0.3	1.63	1.53	1.7	1.62
K1	1.5	0.3	1.62	1.59	1.54	1.65
M75	3.5	0.3	1.34	1.4	1.25	1.37
M9	ND	ND	ND	ND	ND	ND
M0	2	0.3	1.73	1.81	1.64	1.66
M1	2	0.3	1.71	1.73	1.73	1.7

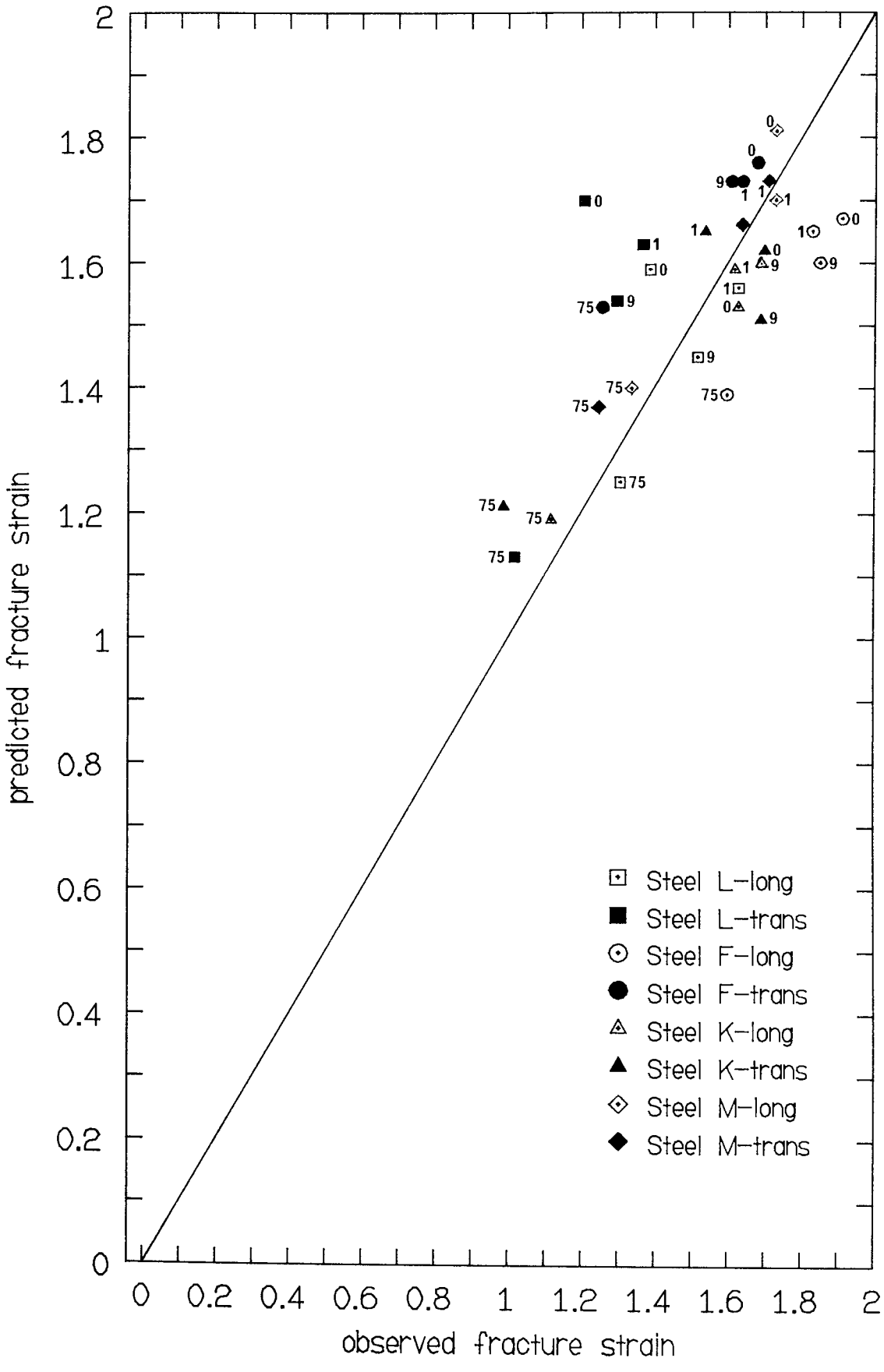

FIG.95 : Comparison of the observed and predicted fracture strains calculated from model for ductile fracture (Spitzig) .

4.4.1 NOTCHED TENSILE TESTS

The results of the uncharged and hydrogen charged notched tensile tests are given in Tables D29 and D30 respectively in Appendix D. The data tabulated is average yield stress (YS) and range, average ultimate tensile stress (UTS) and range and average fracture strain and range.

For the uncharged notched tensile specimens the data given in the above tables follows similar trends to that reported for the Hounsfield tensile specimens in Section 4.4.0. However, the introduction of the notch has increased the YS and UTS and lowered the fracture strain in all cases.

There was no systematic change in the YS between the hydrogen charged and uncharged tensile specimens although the UTS was consistently lower in the hydrogen charged specimens.

The fracture strain has been greatly reduced in all the hydrogen charged specimens and the influence of testing direction found in the uncharged specimens for steels F and L has not occurred.

Typical effective stress vs effective plastic strain curves are reproduced in Figs.96, 97, 98 and 99 which show the effect of hydrogen upon the shape and extent of the flow curves compared to the uncharged steels.

In Figs.100 and 101 the relationship between the uncharged and H-charged fracture strains versus the inclusion projected length per unit area on a plane parallel to the fracture plane are shown and in Figs. 102 and 103 the reciprocal of the mean free distance between inclusions in a

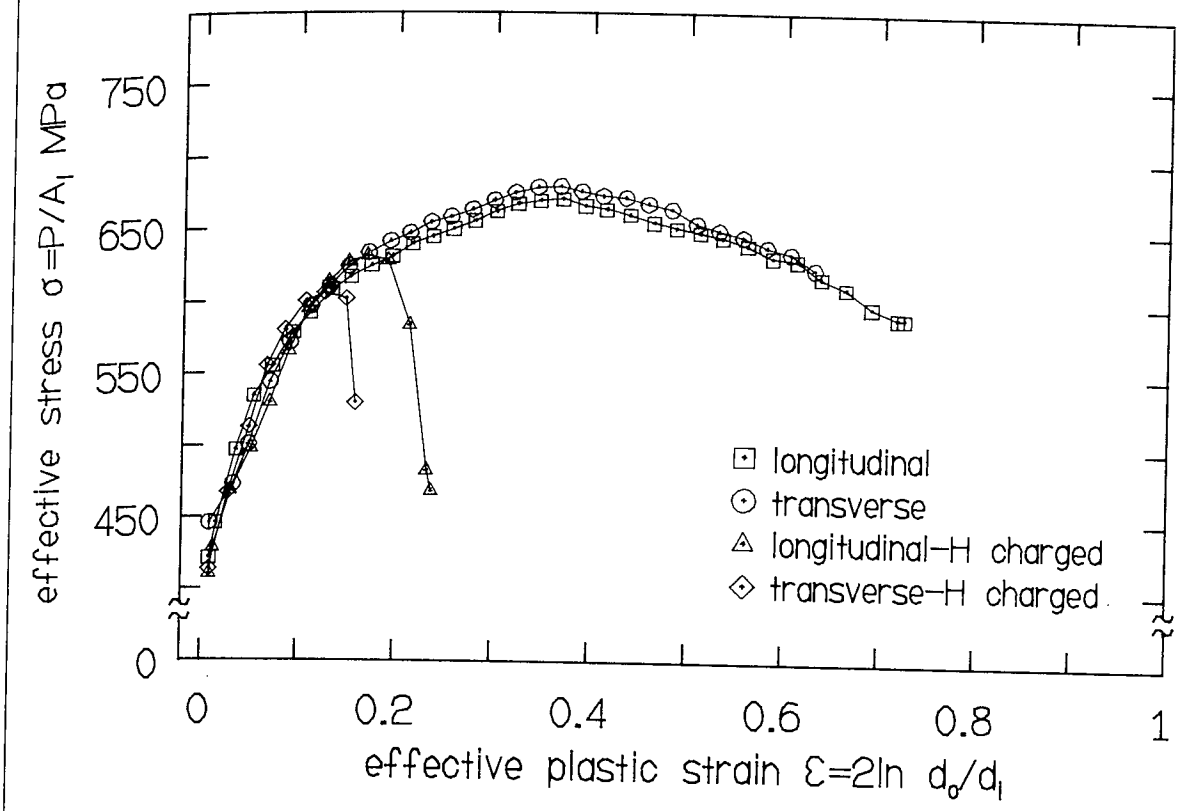

FIG.96 : Effective stress vs effective plastic strain , notched tensile specimens . Steel F rolled at 1000°C .

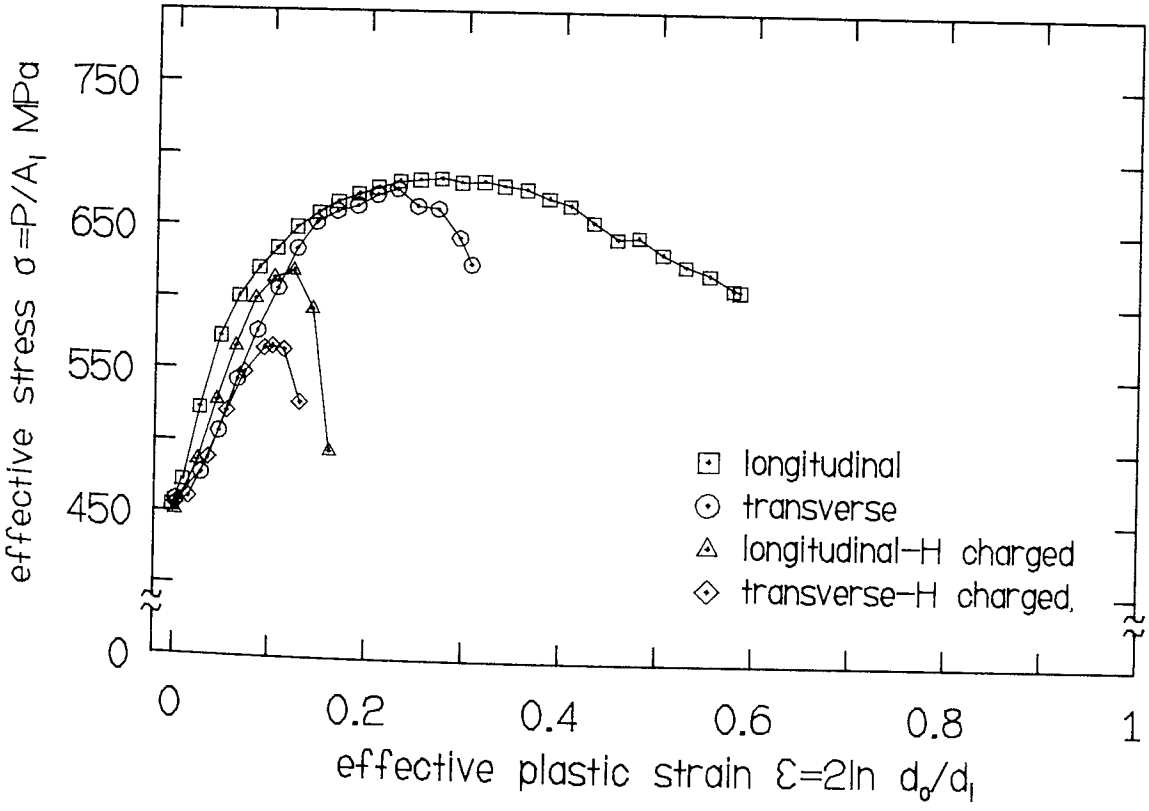

FIG.97 : Effective stress vs effective plastic strain , notched tensile specimens . Steel L rolled at 1100°C .

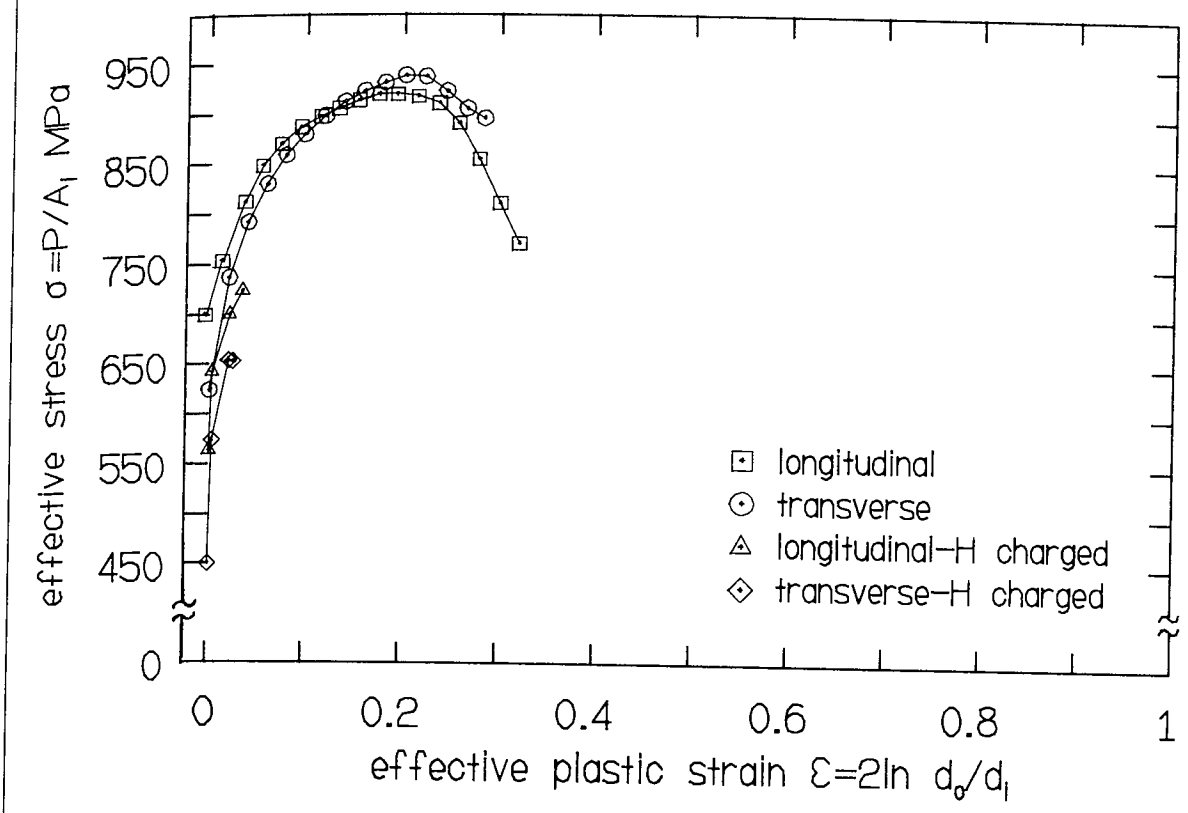

FIG.98 : Effective stress vs effective plastic strain , notched tensile specimens . Steel K rolled at 750°C .

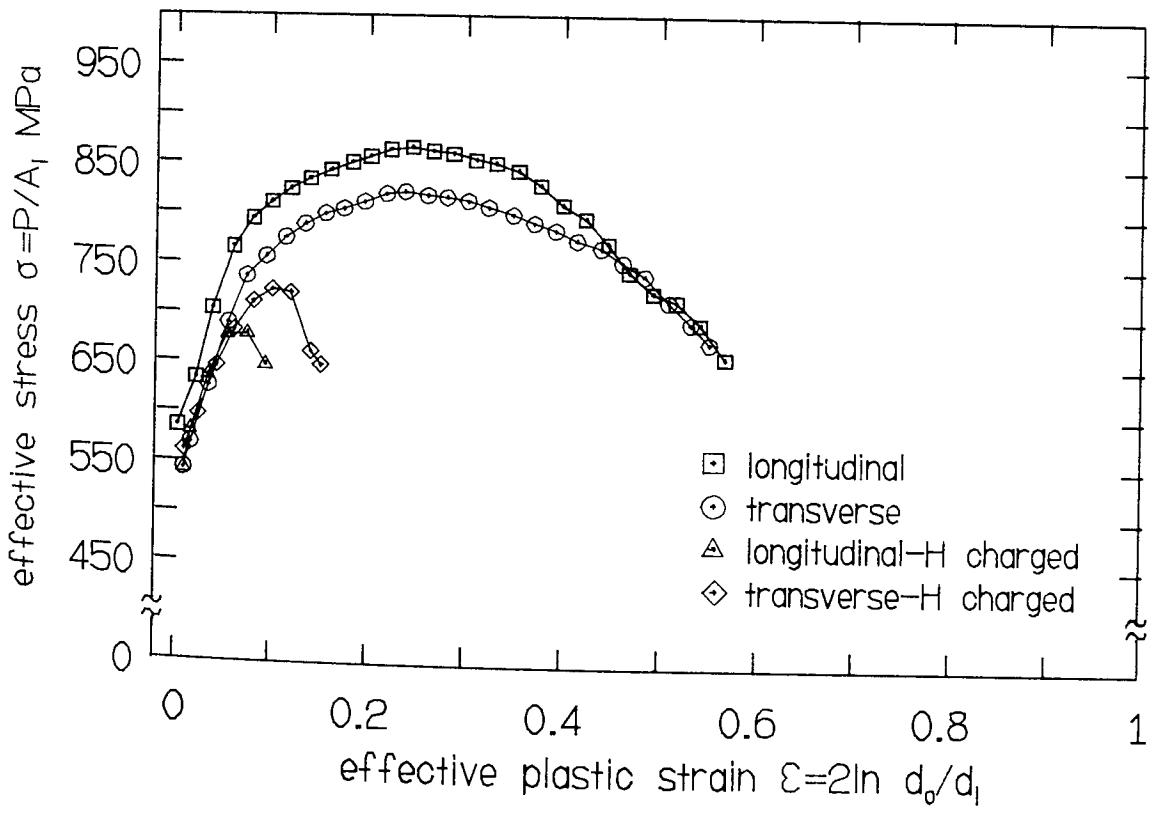

FIG.99 : Effective stress vs effective plastic strain , notched tensile specimens . Steel M rolled at 900°C .

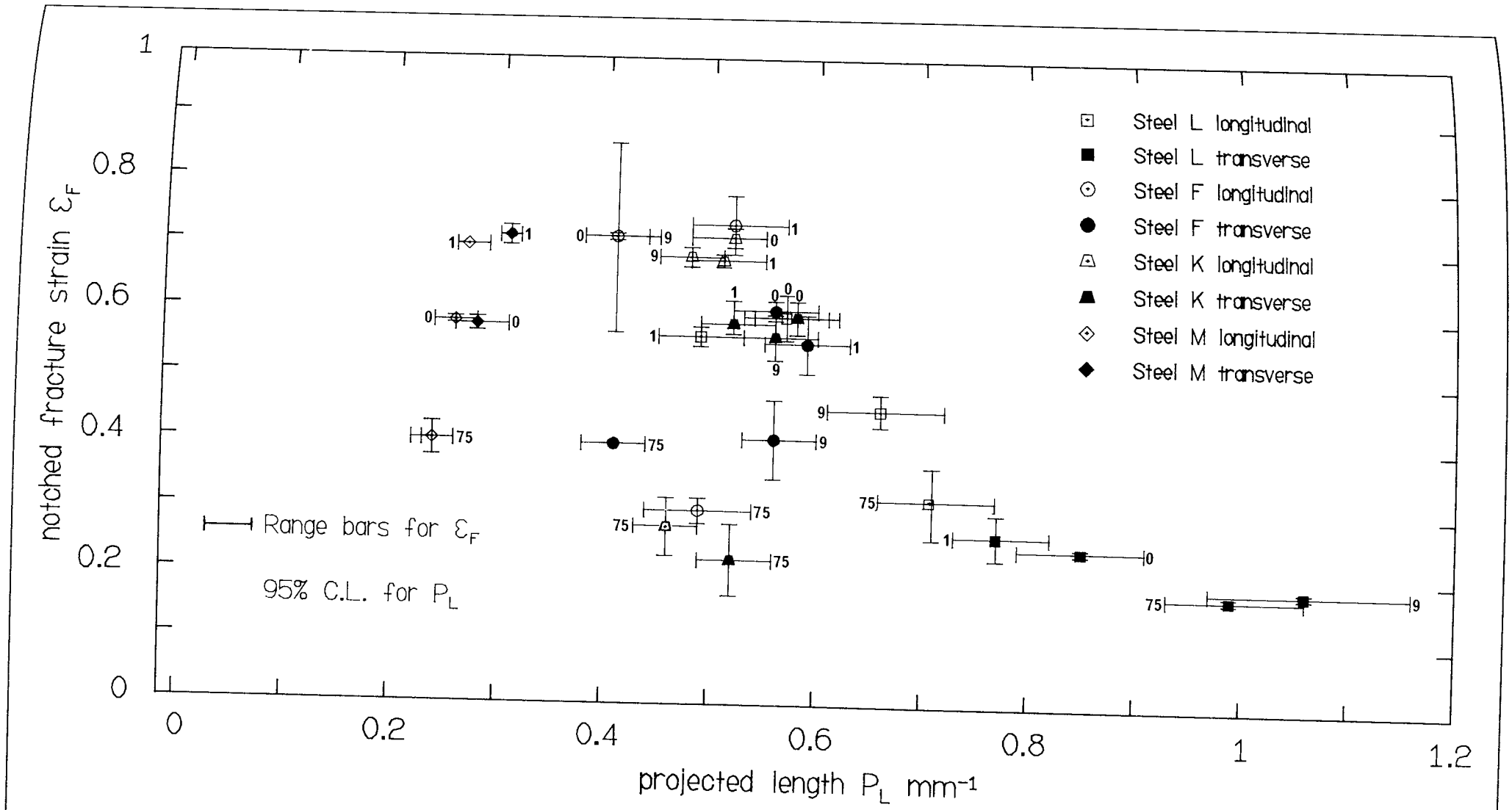

FIG.100: Effect of inclusion projected length per unit area on a plane parallel to the fracture plane vs the fracture strain in the longitudinal and transverse directions . Notched specimens , no hydrogen .

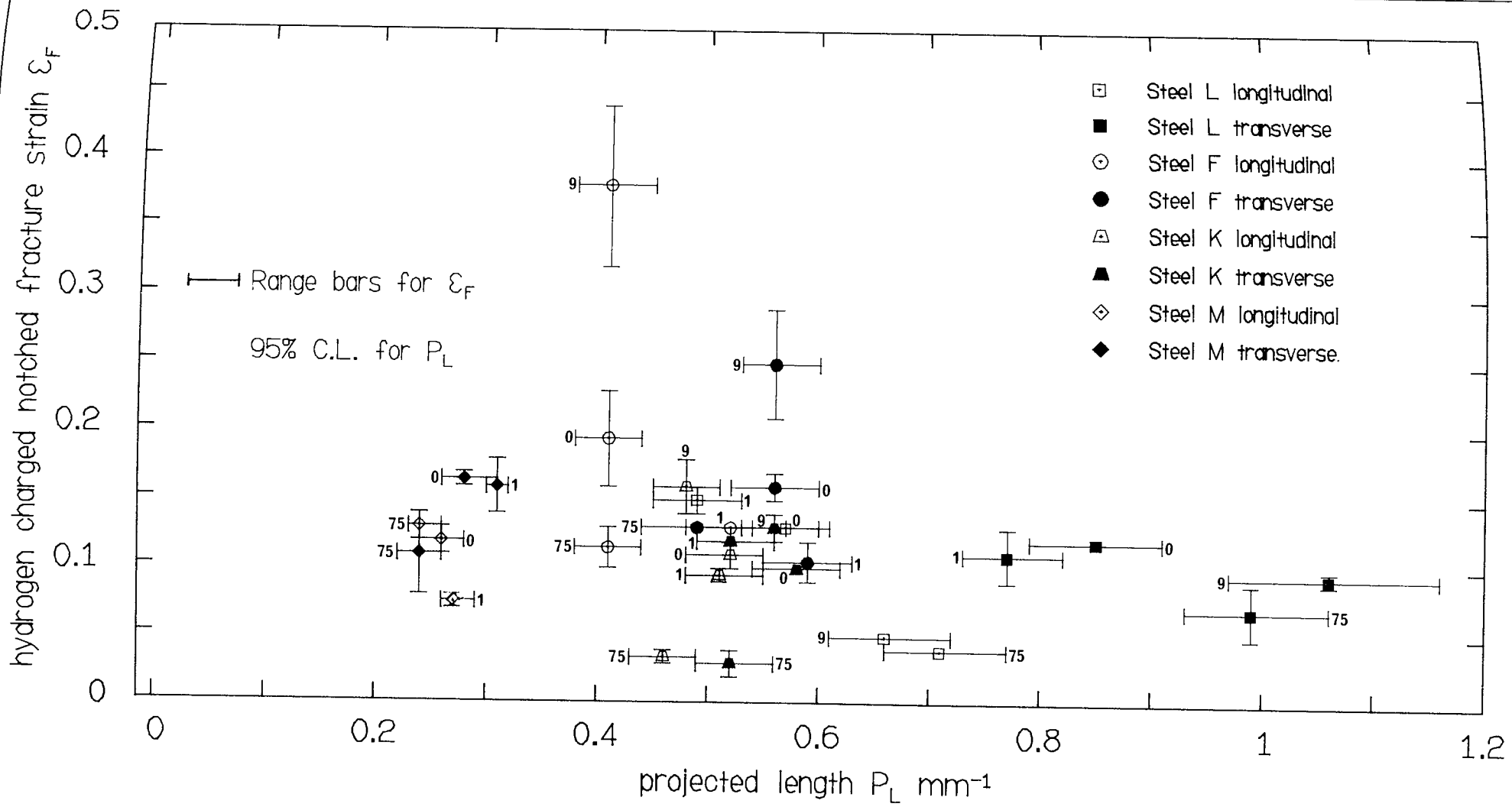

FIG.101: Effect of inclusion projected length per unit area on a plane parallel to the fracture plane vs the fracture strain in the longitudinal and transverse directions . Notched specimens , hydrogen charged .

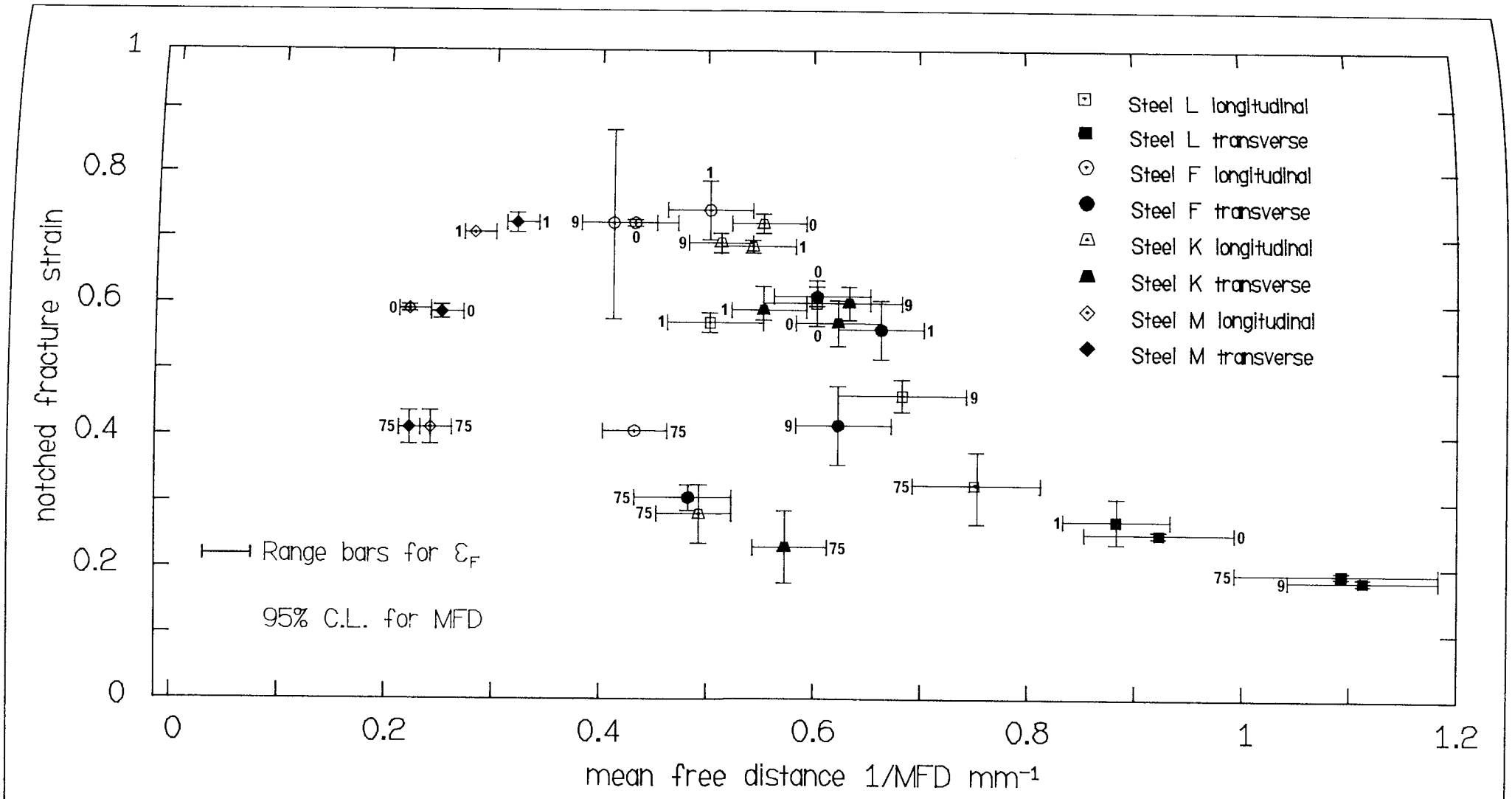

FIG.102: Effect of mean free distance between inclusions in a direction parallel to the tensile direction versus the fracture strain in the longitudinal and transverse directions . Notched specimen .

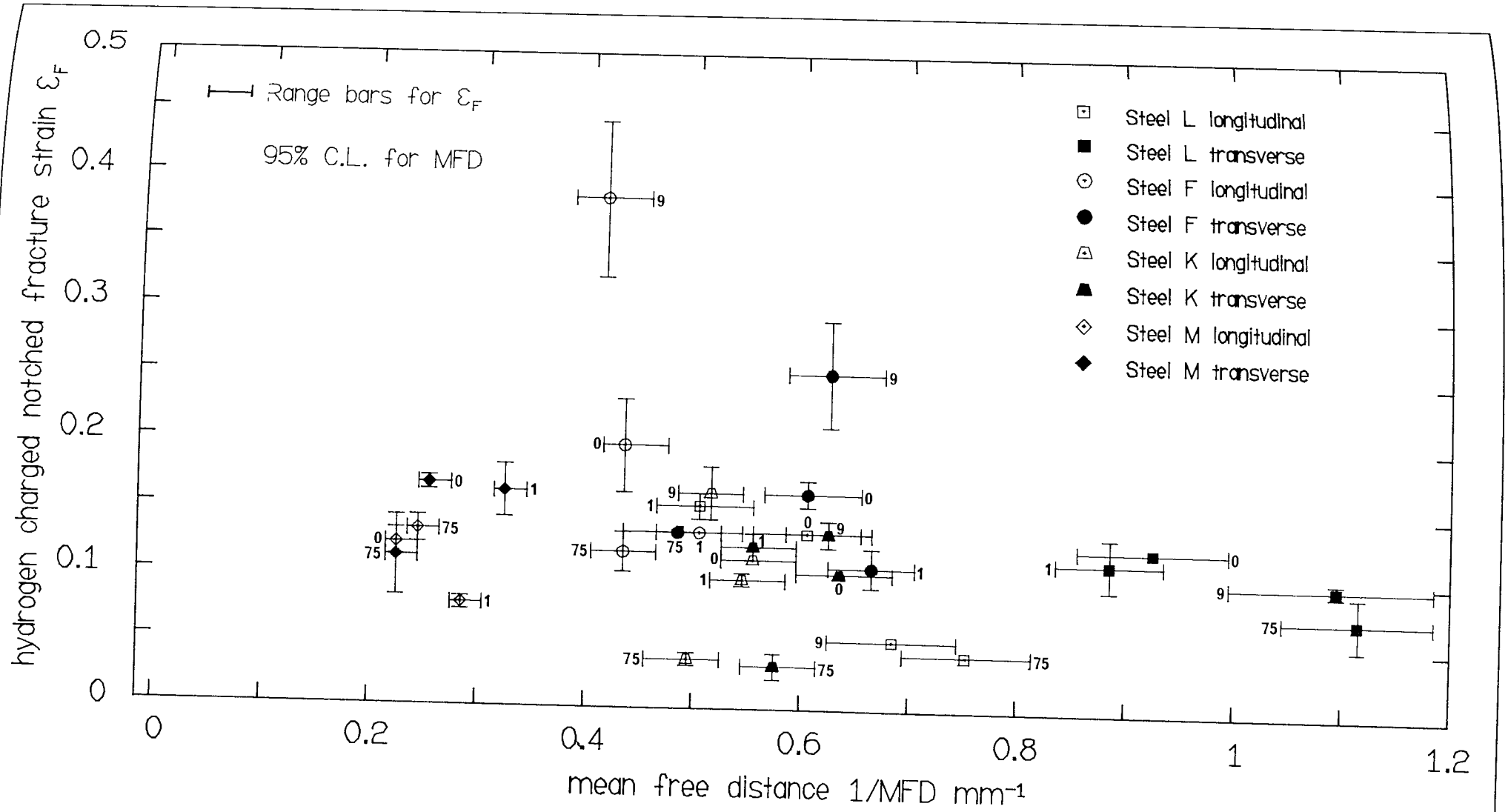

FIG.103: Effect of mean free distance between inclusions in a direction parallel to the tensile direction vs. the fracture strain in the longitudinal and transverse directions . Notched specimens hydrogen charged .

direction parallel to the tensile direction is plotted against the uncharged and H-charged fracture strain. Also shown in Figs. 104 and 105 is the percentage loss in fracture strain between the Hounsfield and notched uncharged specimens and the notched uncharged and notched H-charged specimens given below, versus the inclusion projected length on a plane parallel to the fracture plane (numbering on the graphs represents the temperature at which the steels were rolled).

$$\% \text{ FL} = \frac{\text{FA} - \text{FB}}{\text{FA}} \times 100$$

where % FL = percentage loss in fracture strain

FA = either the Hounsfield fracture strain or notched uncharged fracture strain

FB = either the notched uncharged fracture strain or the notched charged fracture strain.

4.4.2 FRACTOGRAPHY AND METALLOGRAPHY

Plate 20 shows a typical SEM macrograph of the type of fracture surface observed for the Hounsfield specimens. This example (Steel L rolled at 1100°C) was tested in the longitudinal direction, a classical "cup and cone" type fracture has resulted (see also Plate 17A), this type of fracture was found for all the steels tested, Plates 21 to 26 show details of the fracture surface at higher magnifications (the positions from which these were observed are indicated).

The fracture surfaces which were observed for the Hounsfield specimens displayed many characteristics in common with the uncharged (UC) notched tensile specimens (NTS). Therefore, to prevent repetition in describing these and to concentrate upon the principal aim of the fractographic

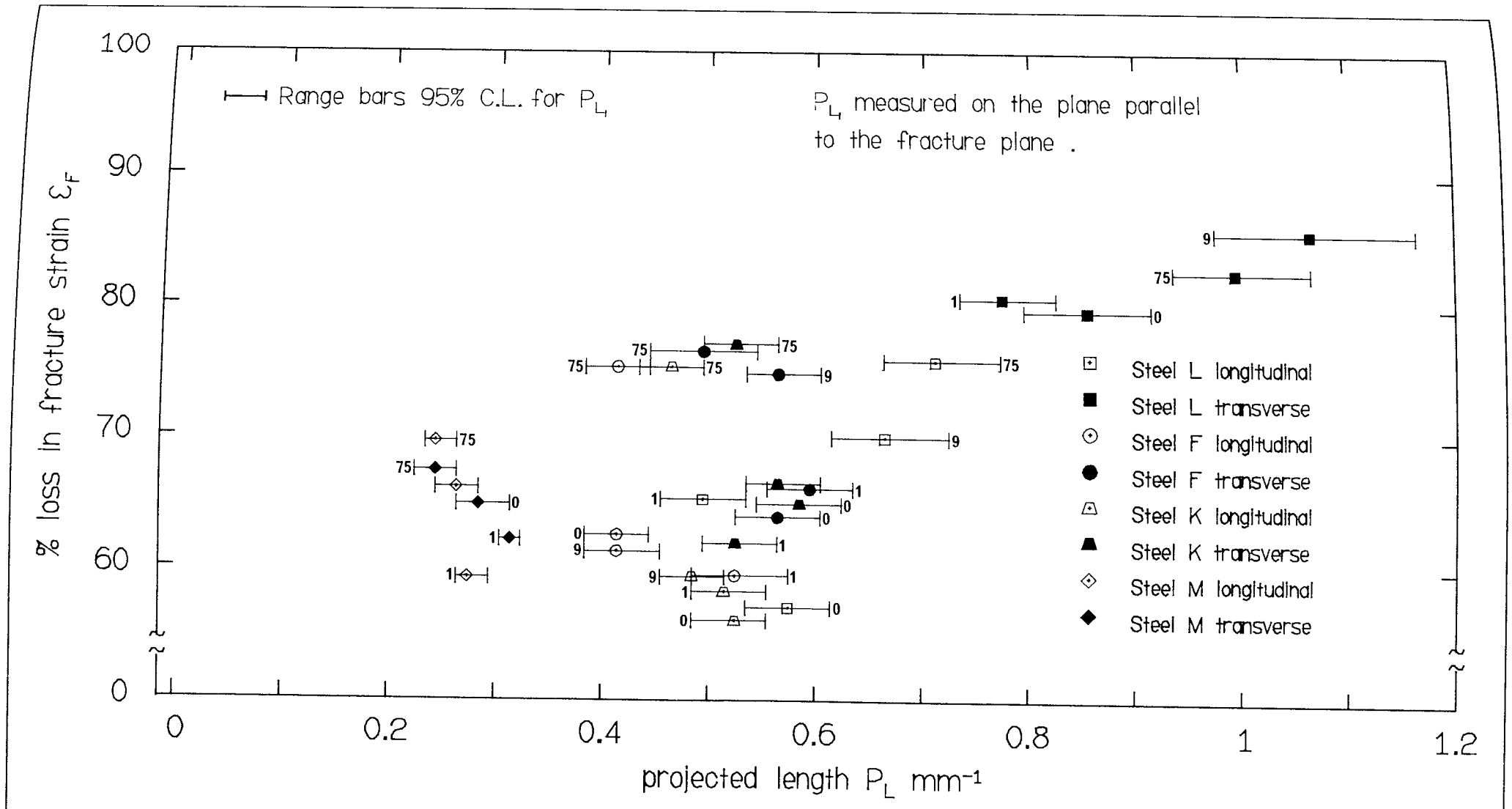

FIG.104: Percentage loss in fracture strain between Hounsfield and notched (uncharged) tensile specimens versus the projected inclusion length per unit area in the longitudinal and transverse directions .

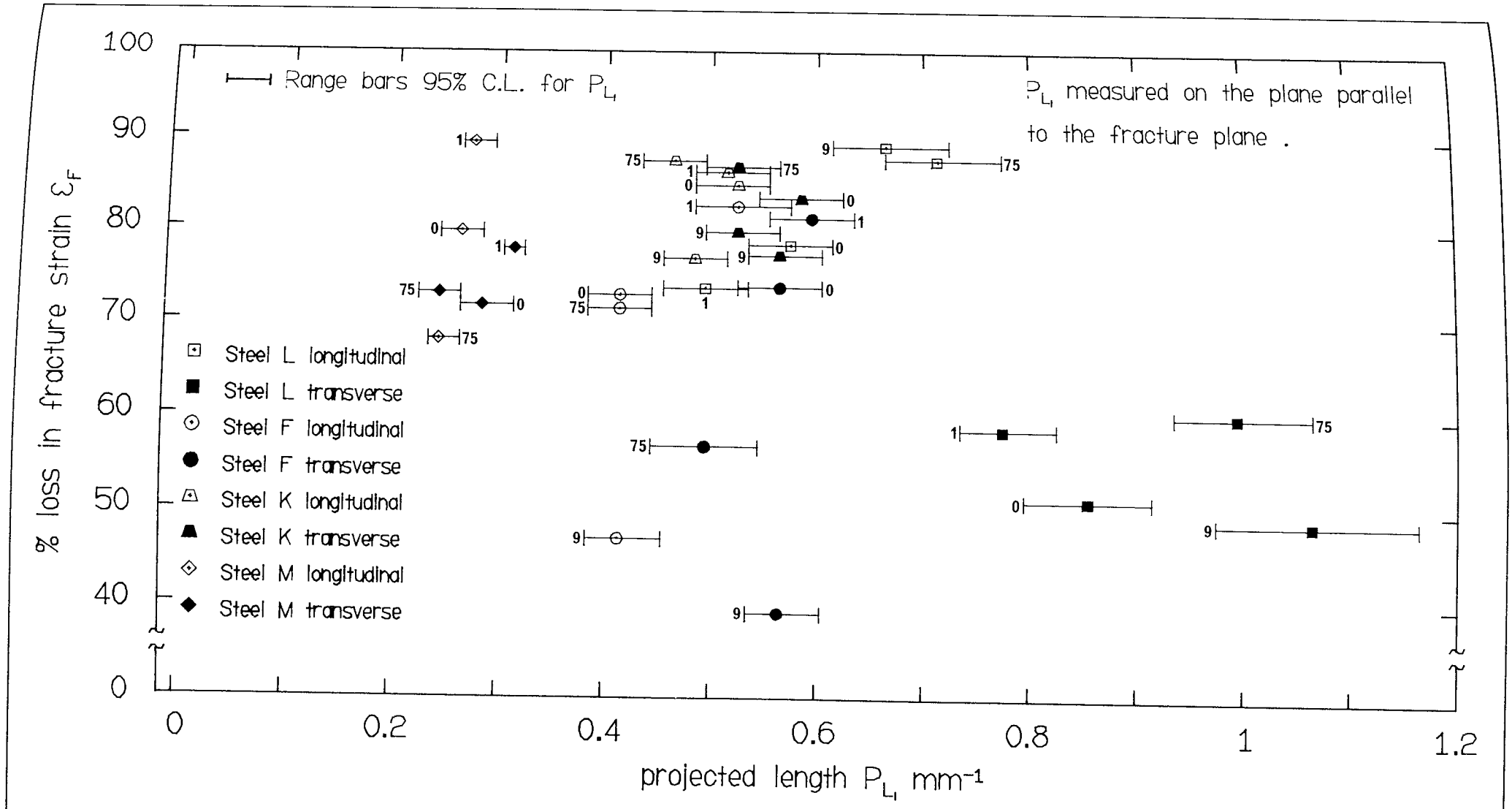

FIG.105: Percentage loss in fracture strain of notched tensile specimens due to hydrogen charging versus the projected inclusion length per unit area in the longitudinal and transverse directions .

study i.e. to compare the fracture appearance between UC-NTS and hydrogen charged (HC) - NTS further descriptions of the fracture surfaces for the Hounsfield specimens will not be made.

For all the steels tested in the absence of hydrogen fracture occurred by micro void coalescence (MVC).

Observations of the dimples upon the fracture surfaces of UC-NTS for steels F and L show that they contained the remains of broken up MnS inclusions, this was particularly so for specimens tested in the longitudinal direction. The dimples occurring upon the longitudinal sections were also markedly deeper than those upon the transverse sections, these dimples were more ellipsoidal in shape. Upon the transverse sections dimples quite often contained unfractured inclusions. The inclusions which had broken up during fracture appeared, originally, to have been "ribbon" like in morphology, Plate 41, whereas the inclusions which remained intact were more "pancake" like, Plate 44. In some cases the fracture surface was found to be covered with, very small, but apparently undeformed inclusions, Plate 61, or clusters of small inclusions, Plate 16, which appeared to have been responsible collectively for the formation of a single dimple.

In steels L and F there was a distinctive difference between the fracture surfaces in the longitudinal and transverse directions. A terraced type fracture occurring in the latter case, Plate 28, whereas a more equiaxed dispersion of dimples was observed for the former, Plate 27.

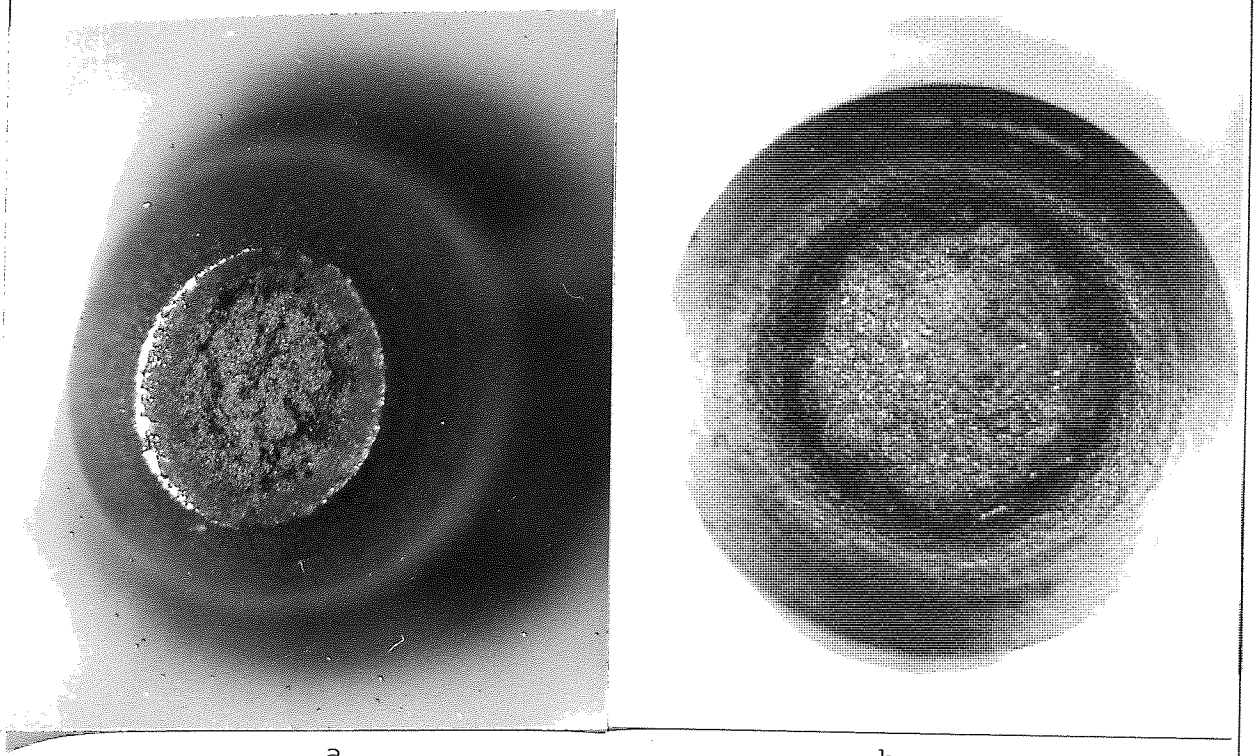

a b

PLATE 17a and b : Macros' of typical fracture surfaces for Hounsfield (17a) and notched (17b) tensile specimens . Steel L rolled at 1100°C ,Mag X10.

18 19

PLATE 18 and 19 : Macros' of notched hydrogen charged tensile specimens . "Fisheyes" can be observed in both cases .
Plate 18 is steel K rolled at 1100°C and tested transversely Mag X10.5 .
Plate 19 is steel M rolled at 1000°C and tested longitudinally Mag X9.5 .

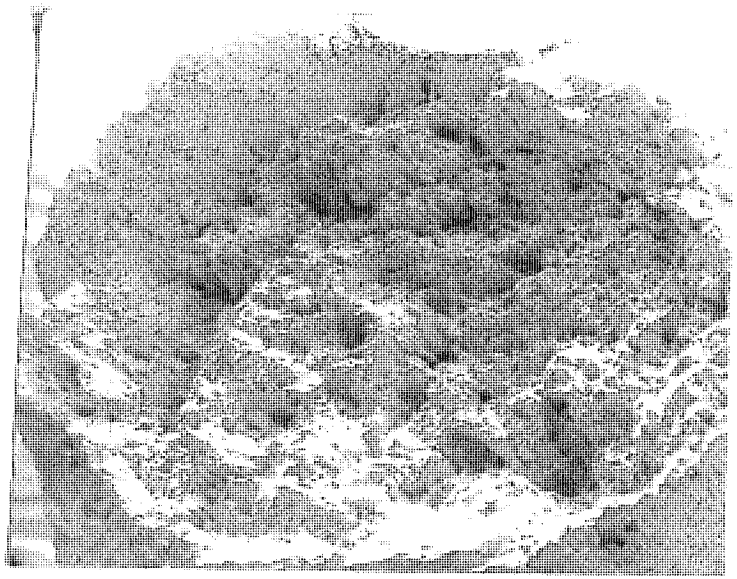

PLATE 20 : SEM macro of Hounsfield tensile specimen . Mag X20 .

Specimen details for plates 20, 21,22,(following page) 23,24,25 and 26 .
Steel L rolled at 1100°C and tested longitudinally .

PLATE 21 →→

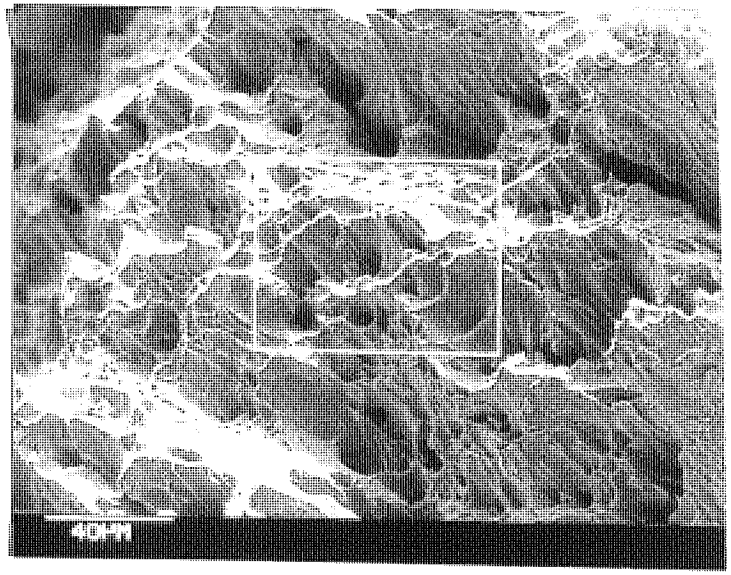

PLATE 22 →→

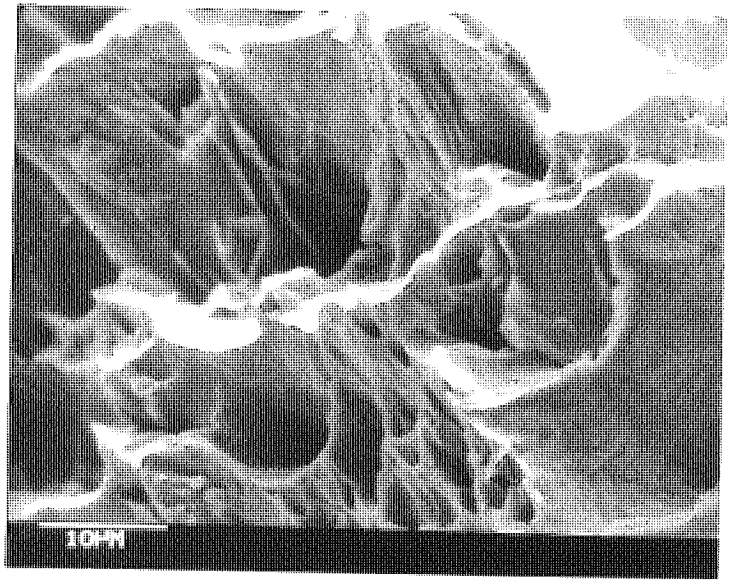

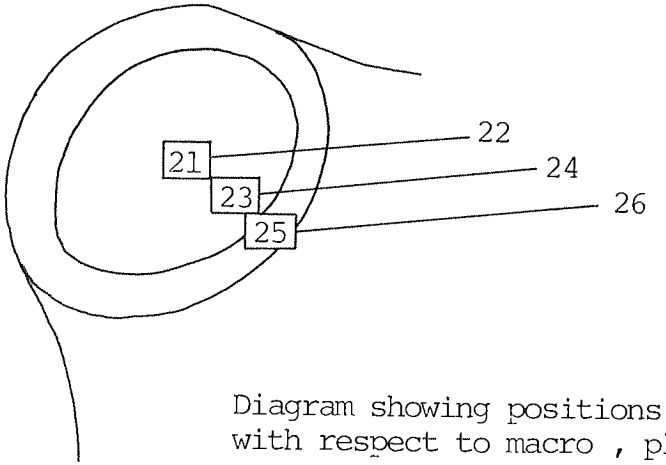

Diagram showing positions of plates 21 to 26 with respect to macro , plate 20 above .

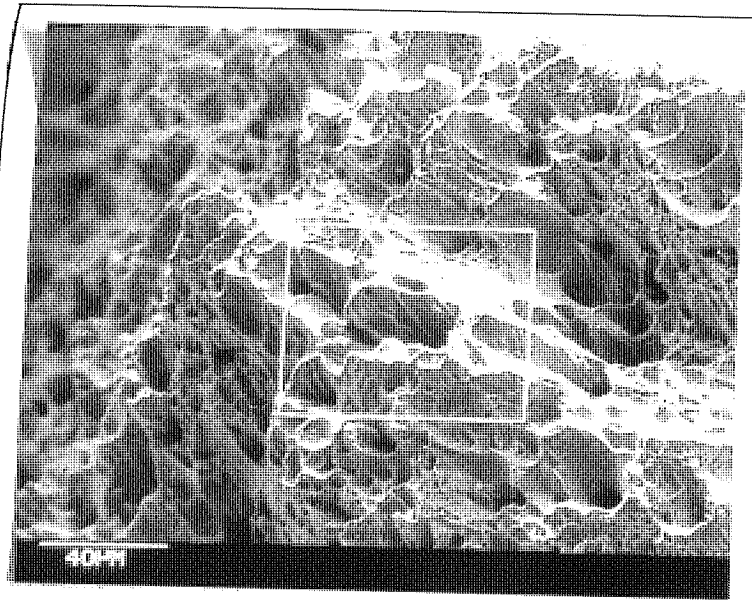

PLATE 23 :
←←←←←

PLATE 24 :
→→→→→

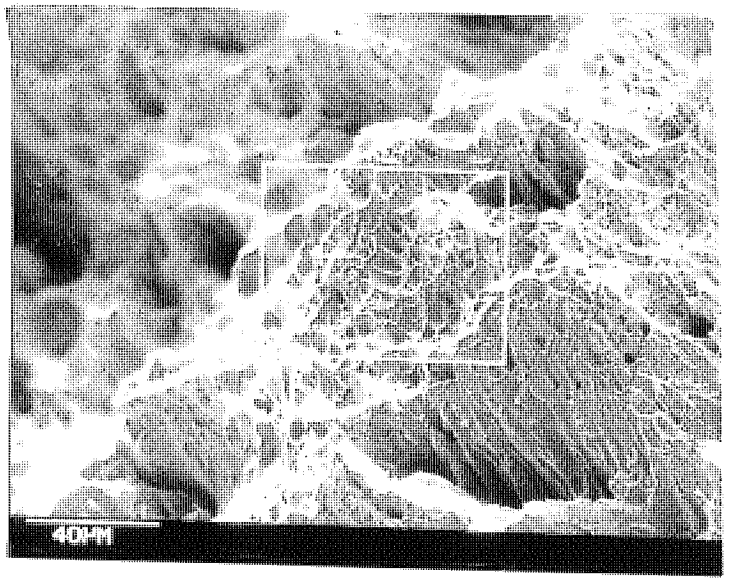

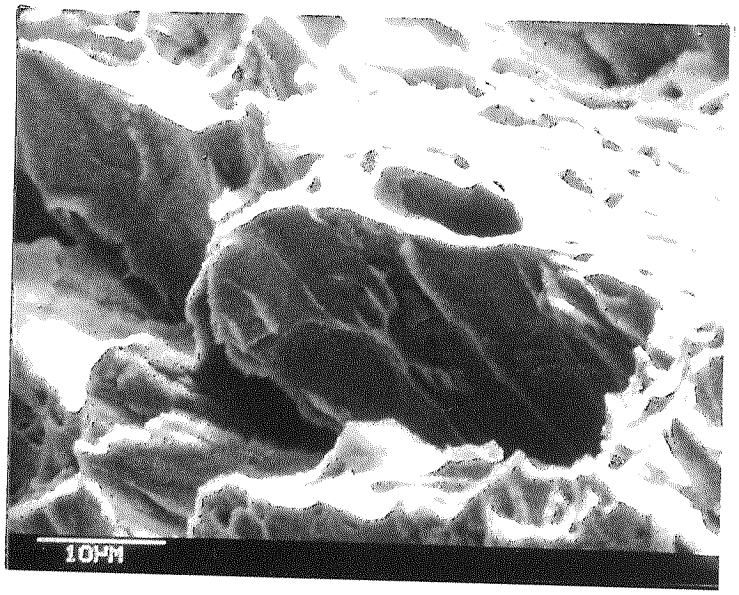

PLATE 25 :
←←←←←

PLATE 26 :
→→→→→

Details of fracture surface for Hounsfield tensile specimen . See previous page for further information .

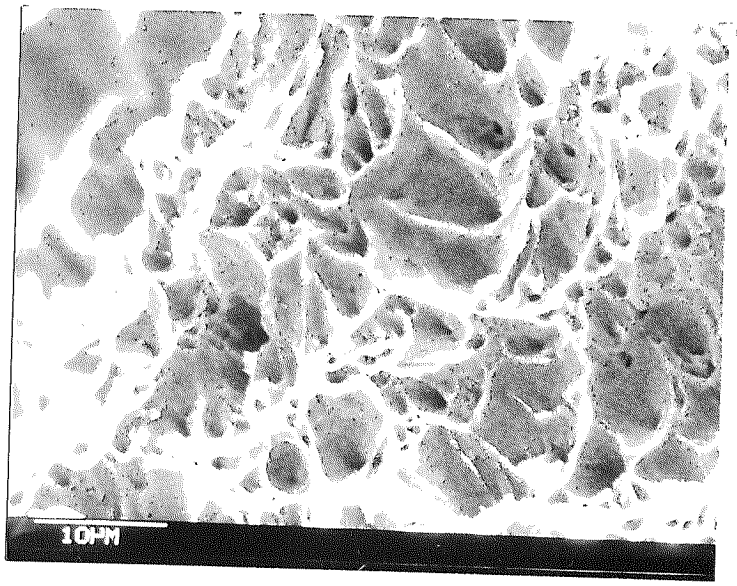

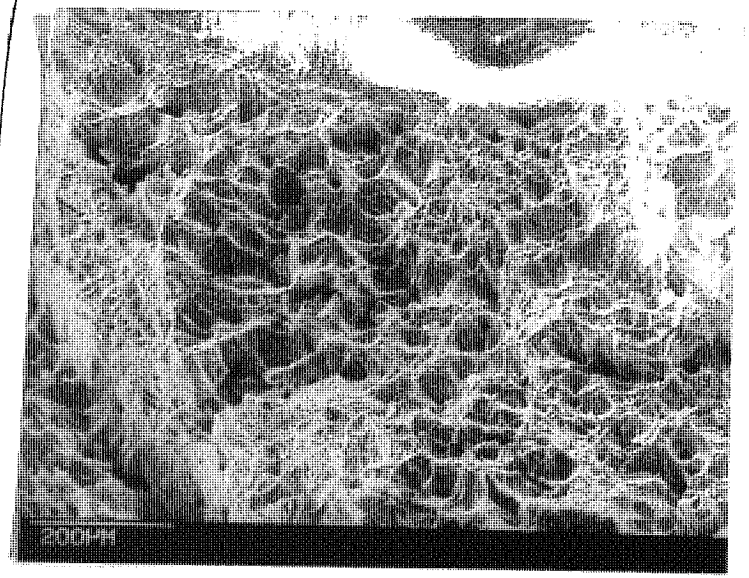

Plates 27,28,29 and 30 comparison of fracture surfaces between hydrogen charged and uncharged notched tensile specimens . Steel L rolled at 1100°C .

←←←←←

PLATE 27 : Longitudinal .

←←←←←←UNCHARGED→→→→→→

PLATE 28 : Transverse .

→→→→→→

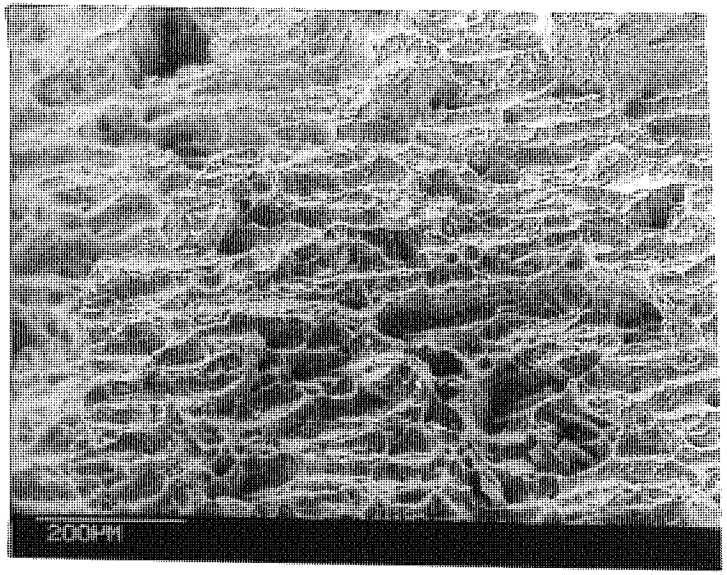

SEM Fractographs

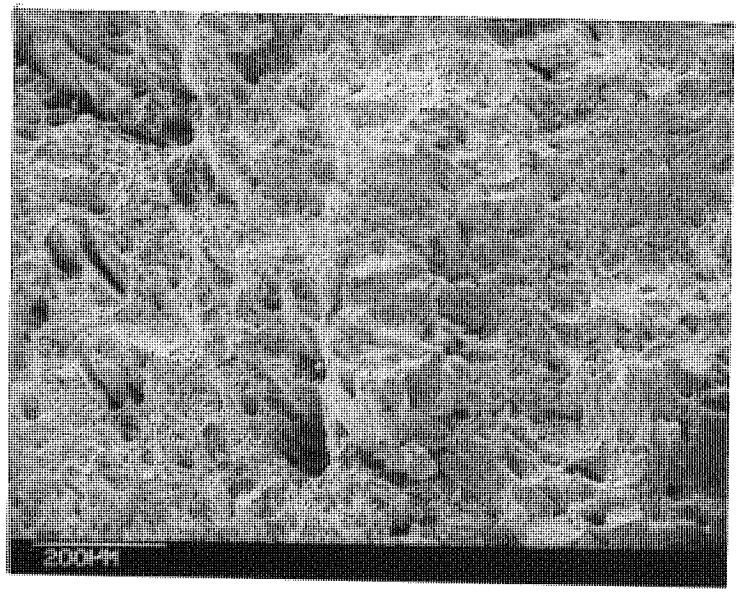

←←←←←

PLATE 29 : Longitudinal .

←←←←←HYDROGEN CHARGED→→→→→→

PLATE 30 : Transverse .

→→→→→→

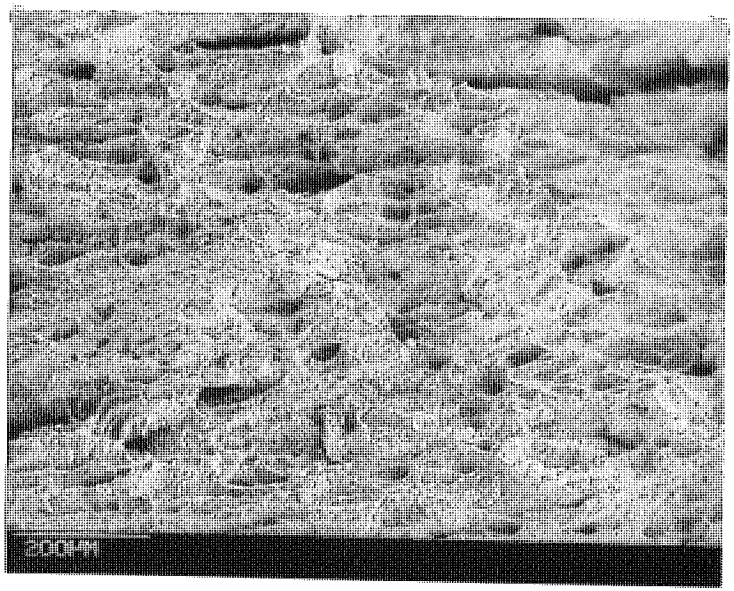

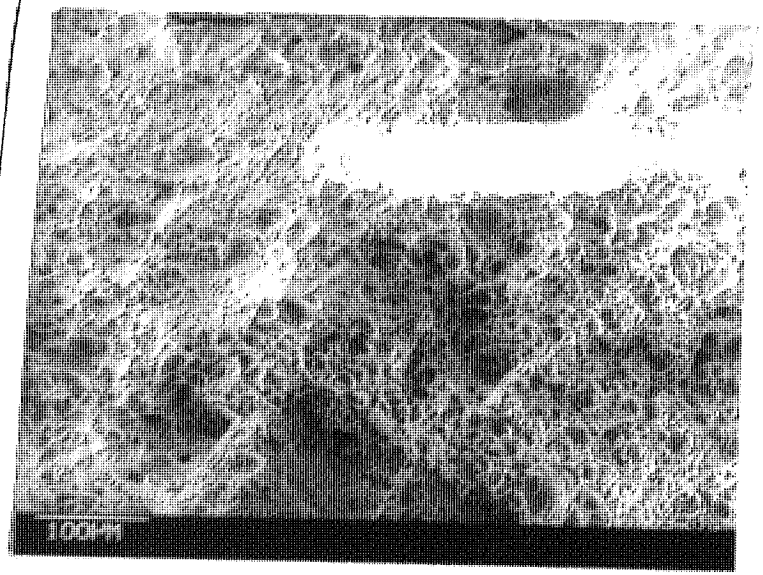

Plates 31,32,33 and 34 comparison of hydogen charged and uncharged notched tensile specimens . SEM fractographs . Steel M rolled at 900°C transverse specimens .

←←←←←←←

PLATE 31 : Typical micro-void coalescence . Uncharged .

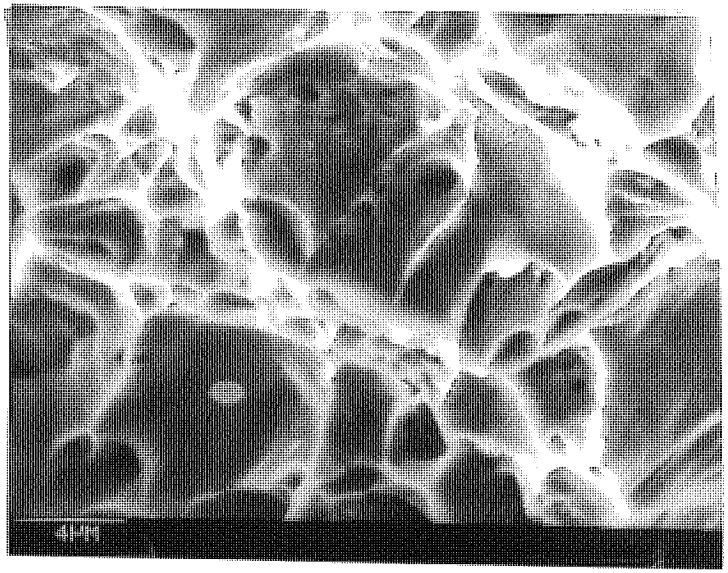

→→→→→→→

PLATE 32 : Inclusion associated with void . Higher magnification of central area of Plate 31 .

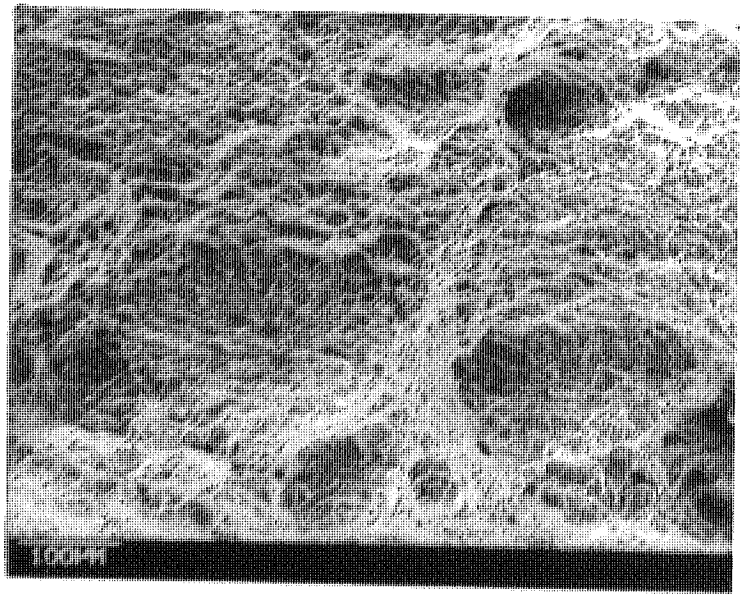

←←←←←←←

PLATE 33 : Hydrogen charged note areas of "flat" fracture .

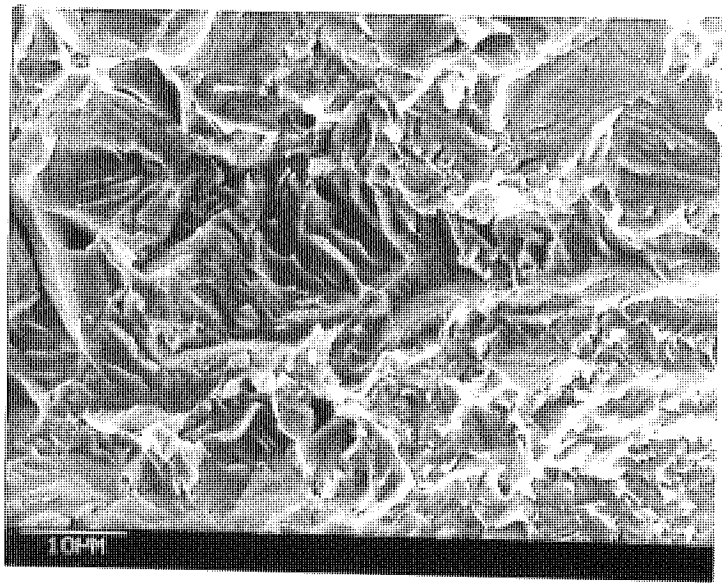

→→→→→→→

PLATE 34 : Higher magnification of area of "flat" fracture in Plate 33 . Quasi-cleavage fracture appearance, note also absence of inclusions on fracture surface .

Plates 35,36,37,38 and 39 comparison of hydrogen charged and uncharged notched tensile specimens . SEM fractograph . Steel K rolled at 900°C longitudinal specimens .

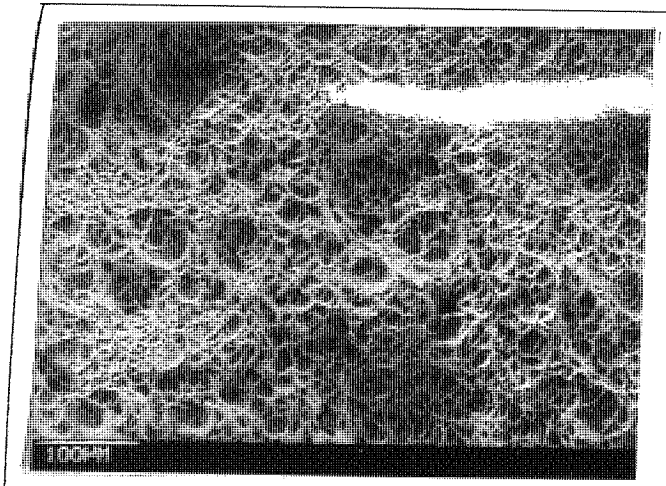

PLATE 35 : Uncharged , typical micro-void coalescence .

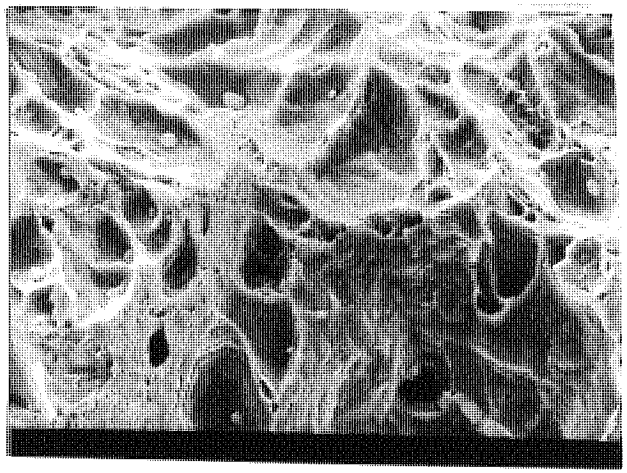

PLATE 36 : Inclusions associated with voids . Higher magnification of central area in Plate 35 .

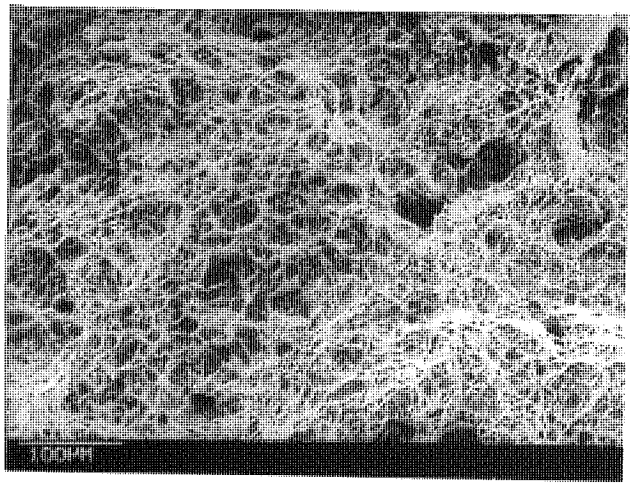

PLATE 37 : Hydrogen charged .

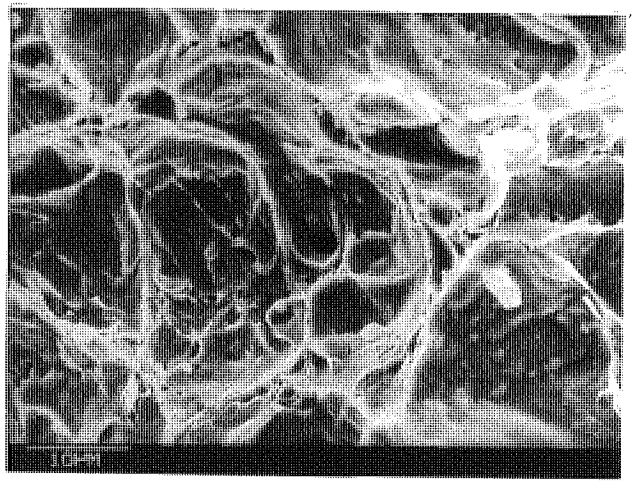

PLATE 38 : Higher magnification of Plate 37 .

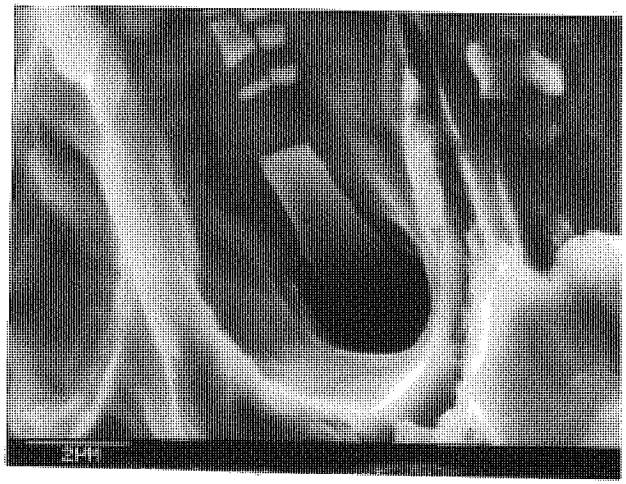

PLATE 39 : Detail of Plate 38 showing cracked elongated MnS inclusion within void .

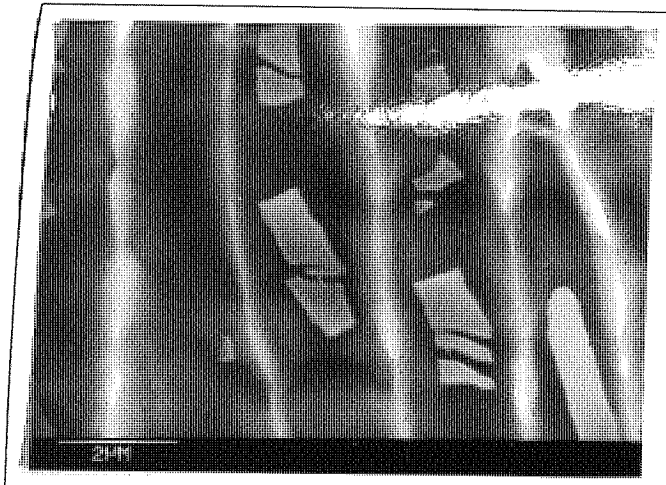

PLATE 40 : Detail of Plate 41 showing cracked MnS inclusions . Uncharged longitudinal specimen .

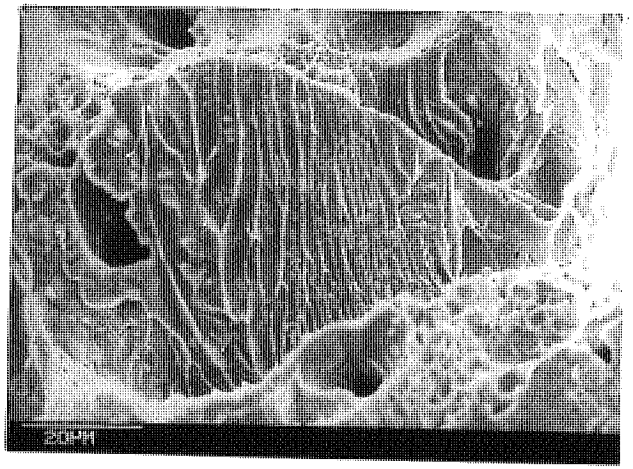

PLATE 41 : Elongated networks of MnS inclusions .Uncharged longitu- specimen .

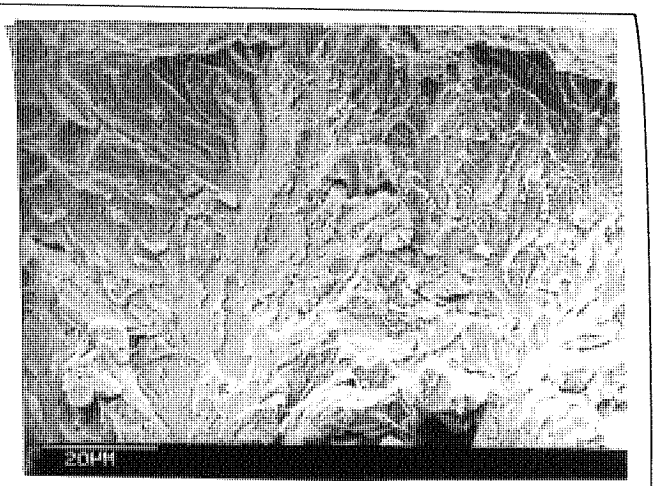

PLATE 42 : Hydrogen charged, area of "flat" fracture, note absence of inclusions . Longitudinal specimen .

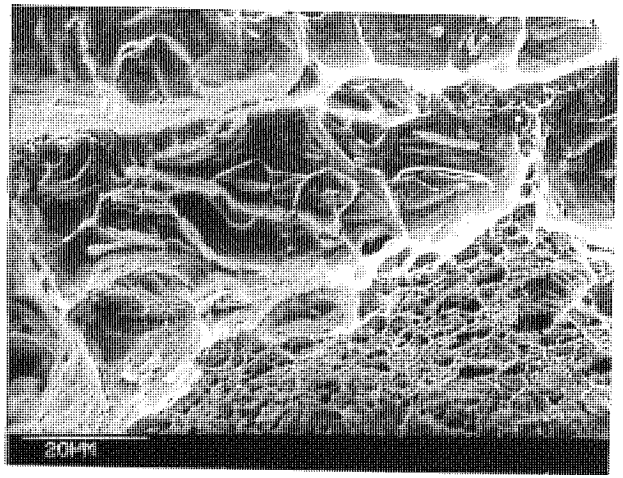

PLATE 43 : Flattened MnS inclusion producing large voids . Uncharged transverse specimen .

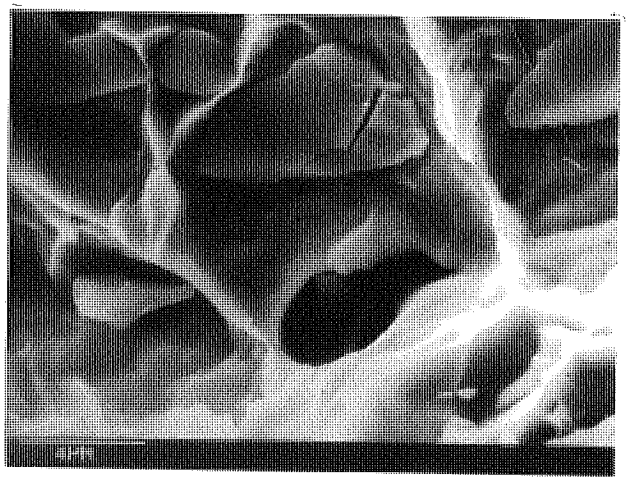

PLATE 44 : Detail of Plate 43 show- pancake shaped inclusions, voids mainly formed by decohesion .

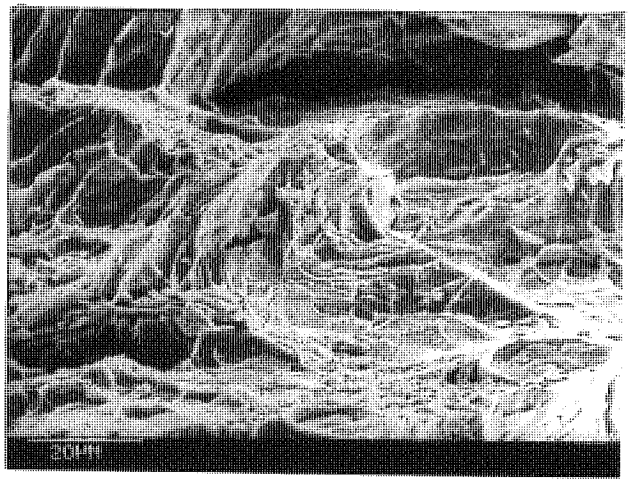

PLATE 45 : Hydrogen charged, large gaping cracks often associated with inclusions . Transverse specimen .

Plates 40,41,42,43,44 and 45 steel L rolled at 900°C, comparison of hydrogen charged and uncharged specimens . SEM fr'graph.

The anisotropy of fracture appearance found for steels F and L, appeared to have resulted due to the orientation of inclusions and hence their shape in respect of the testing direction, this was not found in steels K and M, where both transverse and longitudinal fracture surfaces were similar, Plates 31 and 35. In these steels little inclusion cracking was observed, although steel K contained a number of "ribbon" like MnS inclusions, Plate 37 and 39, which had fractured during testing. The majority of inclusions in steels M and K which remained within the dimples after fracture were globular in shape.

The difference in fracture appearance between the HC and UC-NTS was very pronounced and was quite visible on a macroscopic level, Plates 17B, 18 and 19. Typically, the fractures of the HC-NTS were planar, and light reflective (such as might be observed at the lower shelf in a charpy impact test for a mild steel) in contrast to the dull appearance of the UC-NTS. Often "fisheye" type fractures were observed, some of which were visible to the unaided eye, Plate 19, whilst others were microscopic Plates 33 and 53. This was a common observation for all the steels examined.

Plates 27 to 47 contrast the fracture appearance between the HC and UC-NTS for each steel investigated i.e. L, F, K and M. These attempt to characterise the differences which were typically found.

As a general observation if the fracture mode did not change from MVC as a result of hydrogen charging i.e. no fisheyes occurred, then the resulting fracture appearance was more "feathery" i.e. a qualitative appraisal of the dimple size would suggest they had become finer, and more numerous

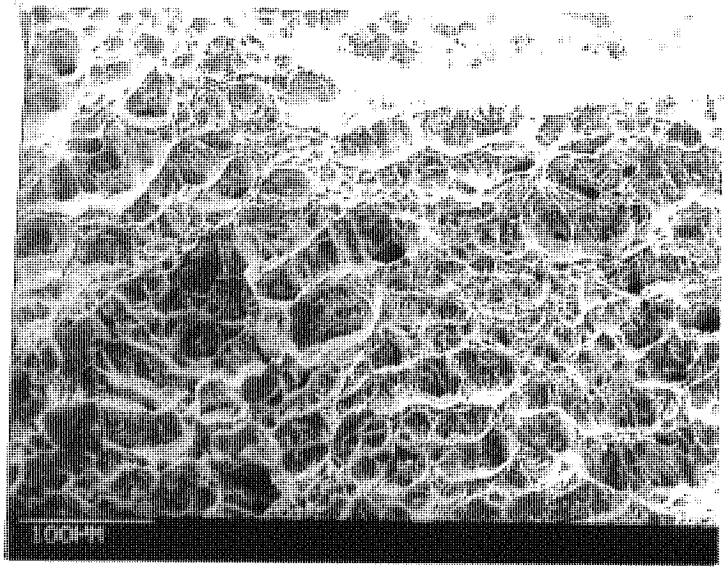

PLATE 46 : Steel L rolled at 1100°C longitudinal specimen, uncharged .

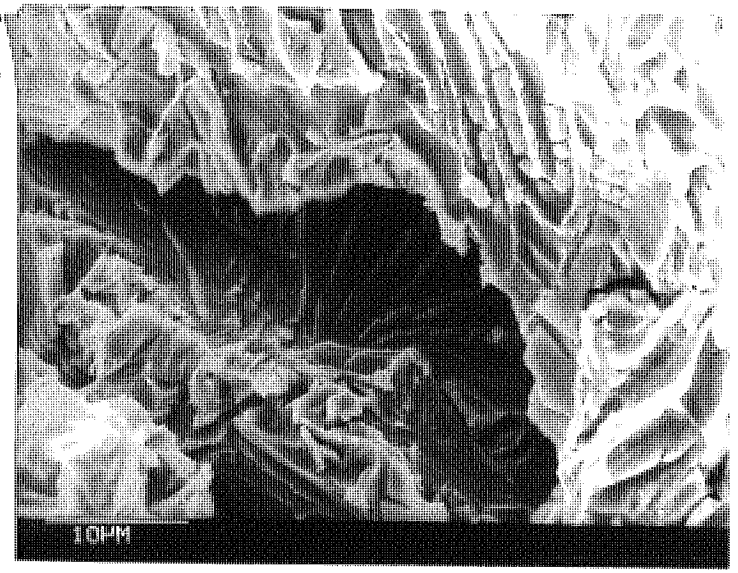

PLATE 48 : Steel L rolled at 1100°C . Detail of Plate 49 showing inclusions lying in the mouth of the crack .

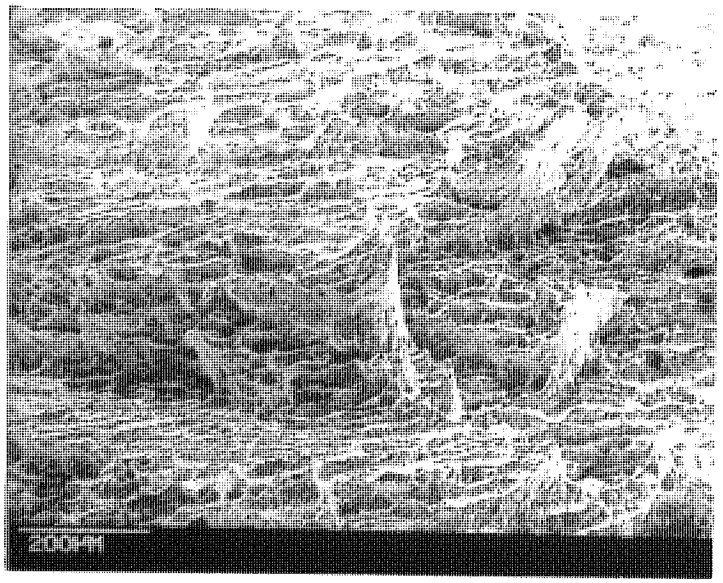

PLATE 47 : Steel L rolled at 1100°C, transverse specimen, uncharged .

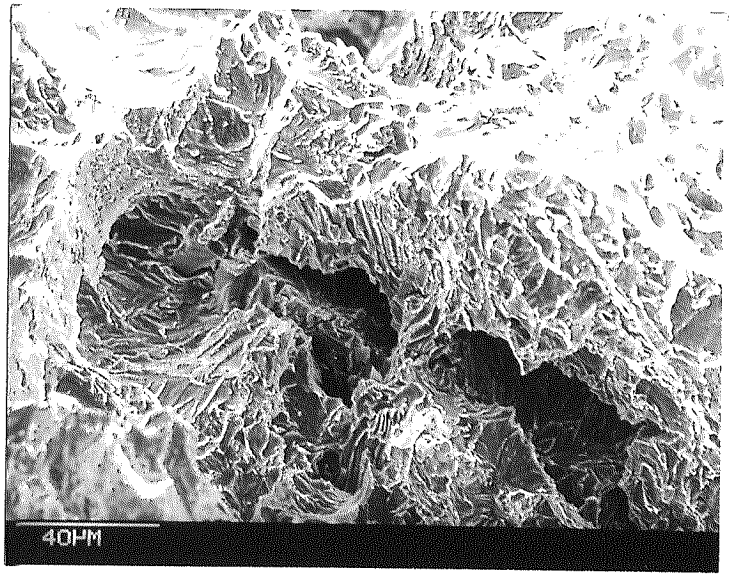

PLATE 49 : Steel L rolled at 1100°C, hydrogen charged, longitudinal specmen . Gaping crack opened up transverse to tensile direction associated with inclusions

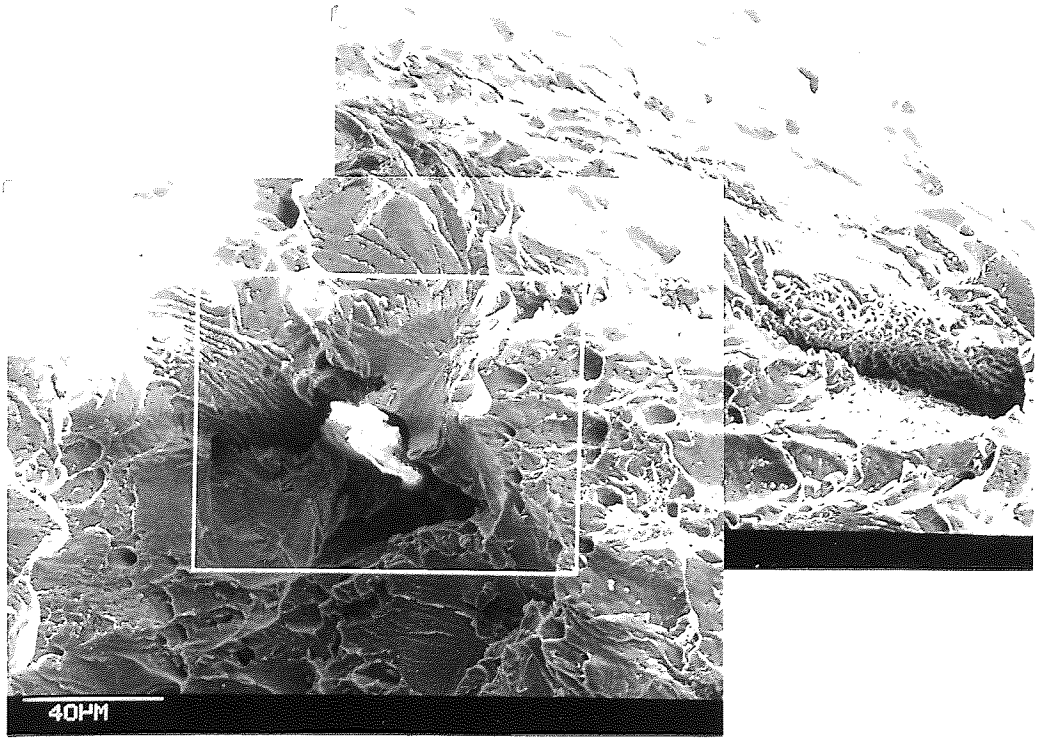

PLATE 50 : Steel F rolled at 1100°C, longitudinal specimen, hydrogen charged . Left hand crack has arisen from large silicate inclusion (white) but is also associated with MnS networks . Whereas right hand crack has developed from a network of very closely associated MnS inclusions .

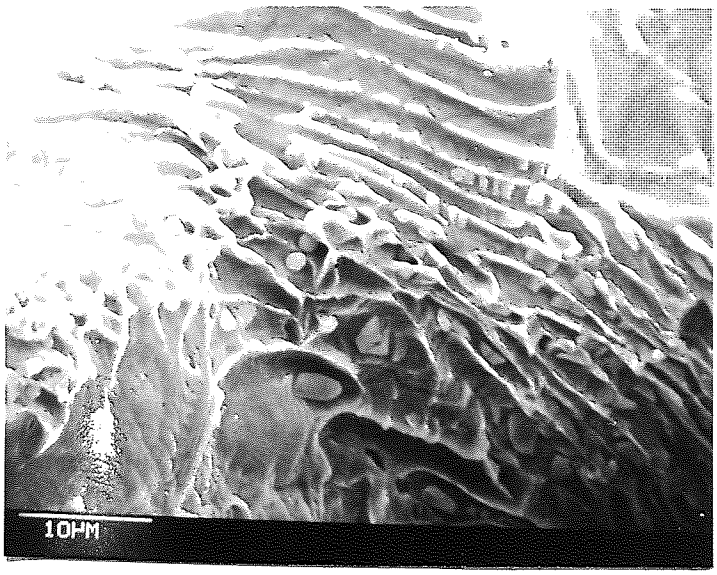

PLATE 51 : Detail of Plate 50 above showing MnS network .

PLATE 52 : Detail of Plate 50 above, note absence of inclusions and ripples (beach marks) on the fracture surface .

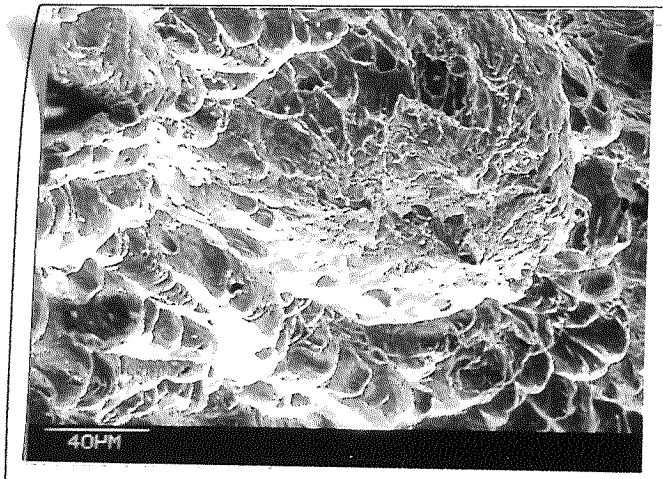

PLATE 53 : Typical example of "flat" fracture phenomenon .

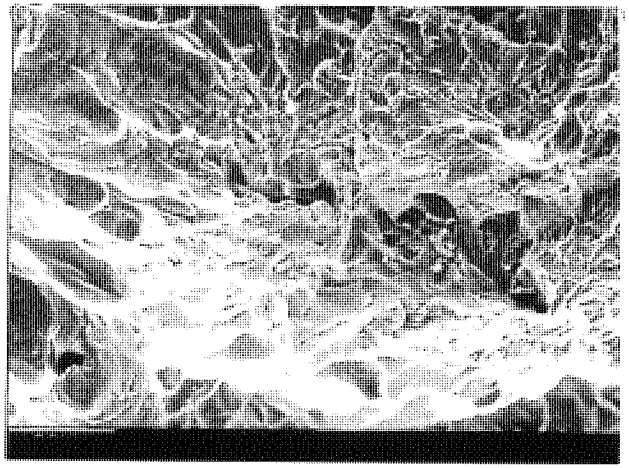

PLATE 54 : Detail of central area in Plate 53 (bar 20µm) showing region scanned in Plates 55,57 and 58 .

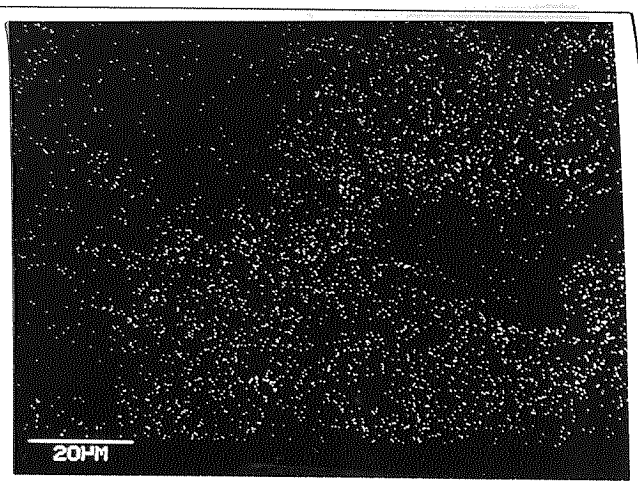

PLATE 55 : Sulphur X-ray map of Plate 54 .

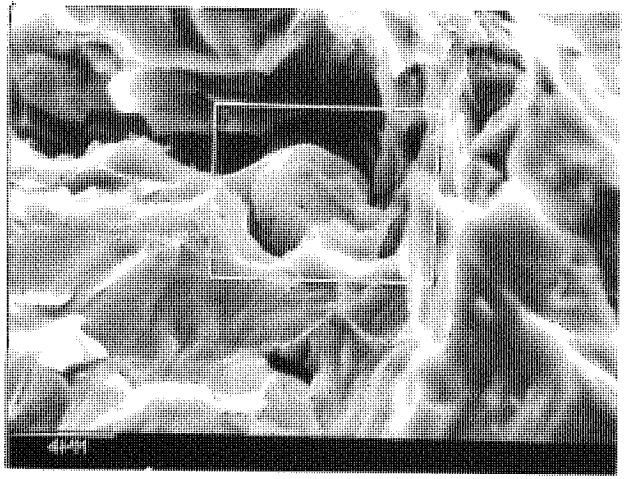

PLATE 56 : Detail of Plate 54 .
Spot analysis Al 74.67, S 5.76, Mn 11.13 and Fe 8.29 (%) of inclusion

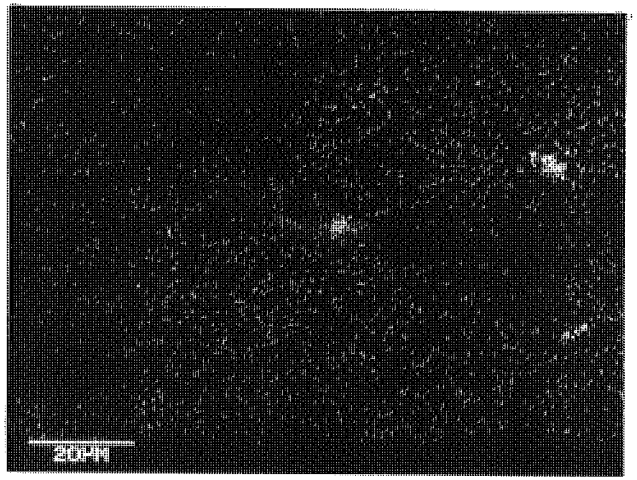

PLATE 57 : Aluminium X-ray map of Plate 54 .

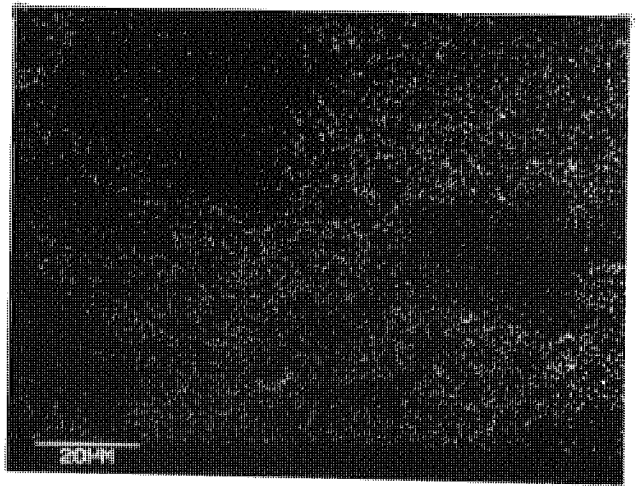

PLATE 58 : Manganese X-ray map of Plate 54 .

Plates 53,54,55,56,57 and 58 steel F rolled at 900^{o}C, hydrogen charged, longitudinal specimen.

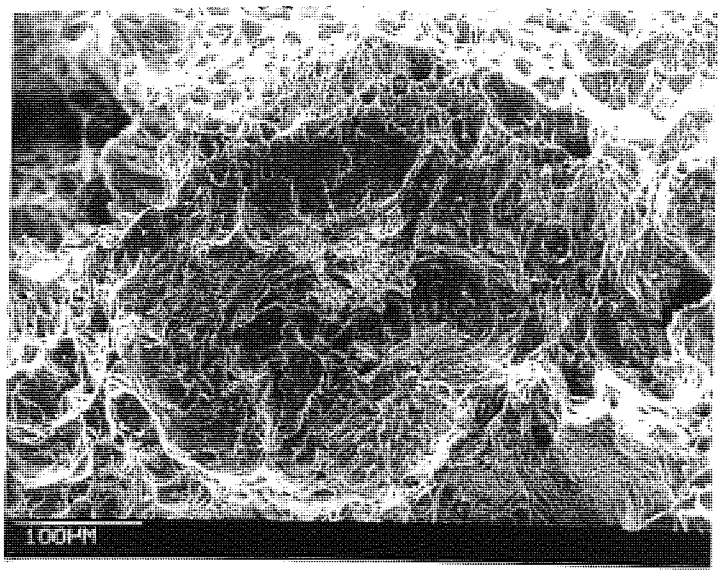

PLATE 59 : "Fisheye" type fracture associated with MnS networks and Al_2O_3 clusters . Steel F rolled at 900°C .

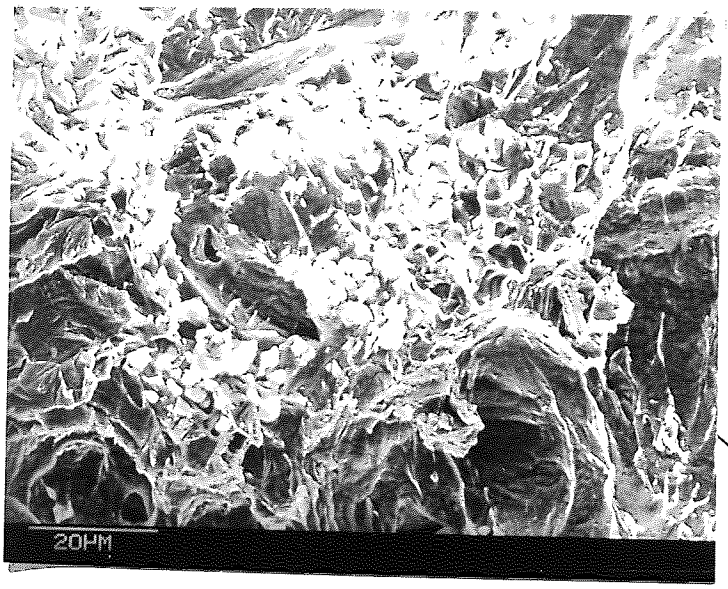

PLATE 60 : Detail of Plate 59 above showing cluster of Al_2O_3 inclusions in the centre of "fisheye" .

PLATE 59 →→→

60

61

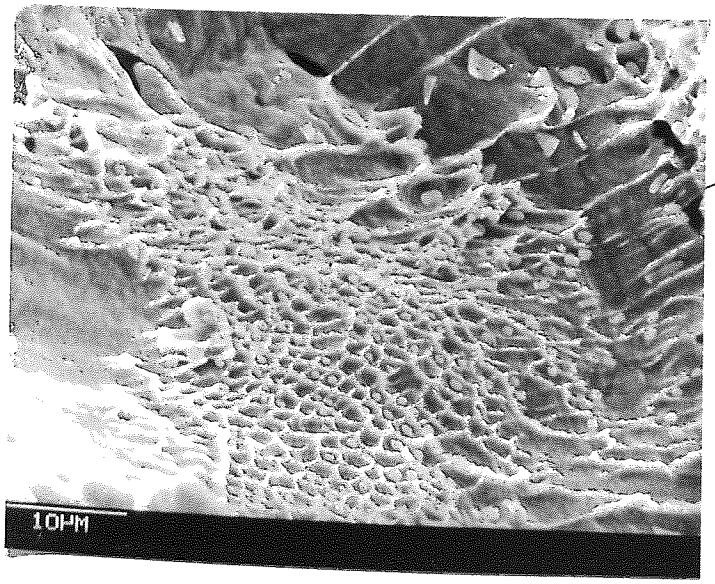

PLATE 61 : Detail of Plate 59 showing network of closely associated MnS inclusions at the edge of the "fisheye" .

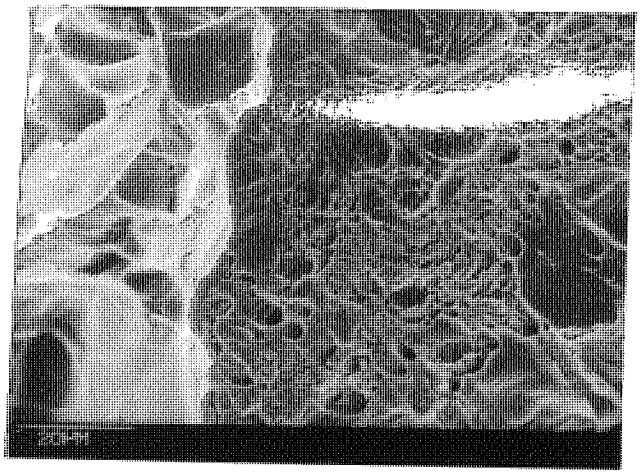

PLATE 62 : Detail of Plate 63 showing rim of plateau, on the left is the edge of the "fisheye" .

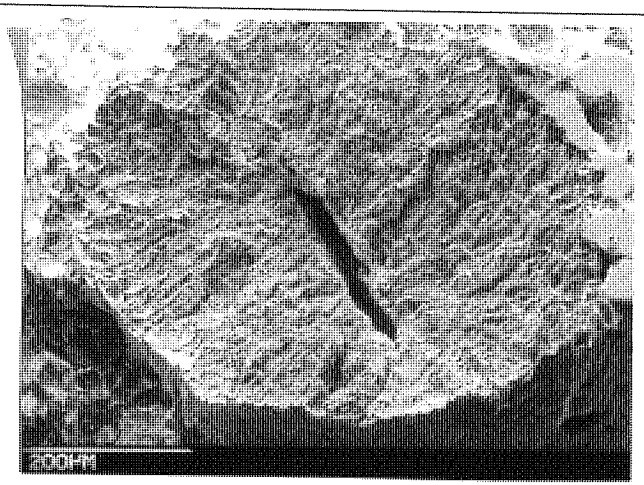

PLATE 63 : Example of "fisheye" fracture . Steel M rolled at 1100°C and tested transversely .

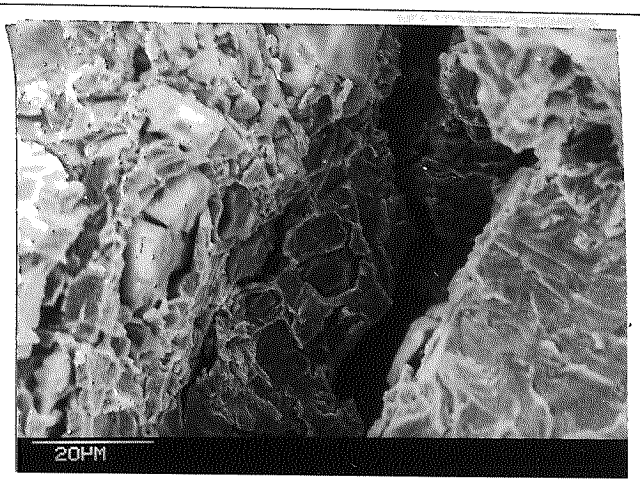

PLATE 64 : Detail of Plate 62 showing Al_2O_3 inclusions and Ca, Mn and S containing phases in the crack mouth .

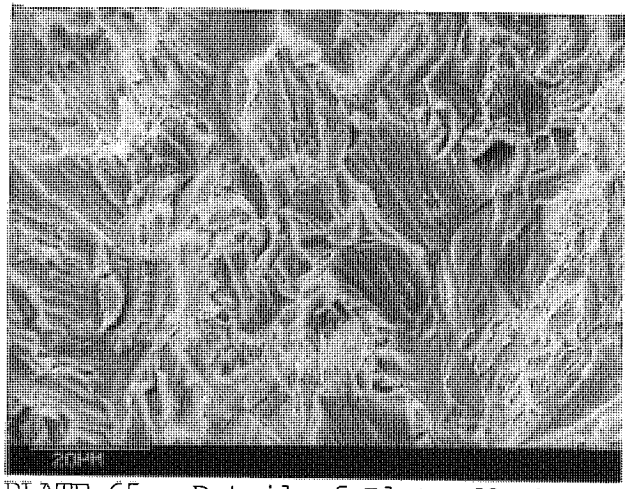

PLATE 65 : Detail of Plate 63 showing fracture surface of "fisheye", the area observed was just above the tip of the crack .

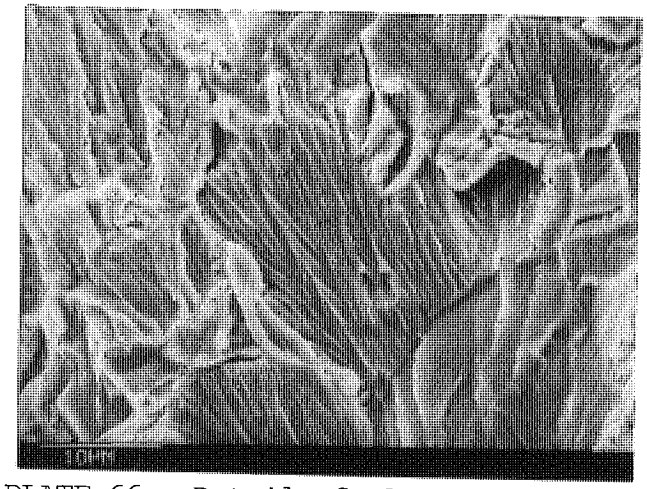

PLATE 66 : Detail of Plate 65 showing tear ridges and localised plasticity . Note the absence of inclusions .

PLATE 67 : Detail of Plate 66 showing orientated tear ridges on the fracture surface, probably as a result of fracture across a pearlite colony .

in comparision to the UC-NTS. This is shown by comparison of Plates 27 and 29, 28 and 30, and 35 and 37.

The variety of fracture morphologies observed for the HC-NTS upon a single fracture surface, however, cannot be overstated. In many cases inclusions appeared to be involved with the fracture process, particularly the distinctive "fisheye" phenomenon. A more detailed study of this type of fracture is shown in Plates 48 to 67. A very common feature of this fracture was the occurrence of larger (often 10μm) inclusions, or closely associated clusters of inclusions (Al_2O_3, MnS and also Ca and Si containing phases) either in the crack opening Plates 48, 49, 50, 56 and 64 or upon the surrounding fracture surface, Plates 59, 60 and 61.

Finally, Plates 68 to 89 are axial cross sections of UC and HC-NTS. These show, for the UC-NTS, the extent of void formation at inclusions and also pearlite colonies and grain boundary carbides near the fracture surface and also some distance away. Very close to the fracture surface, where extensive deformation has taken place (as shown by the elongation of ferrite grains in the tensile direction, Plates 68, 69 and 82) voids have occurred at inclusions, grain boundary carbides and around and within pearlite colonies, Plates 69, 70, 78, 80 and 81. Whereas further away from the fracture surface void formation has only occurred at inclusions. For steels L and F this has mainly resulted in particle cracking for specimens tested longitudinally, Plate 72, whereas decohesion was also observed for the specimens tested in the transverse direction. In steels K and M decohesion was the principal void forming mechanism in both the longitudinal and transverse directions, Plate 83.

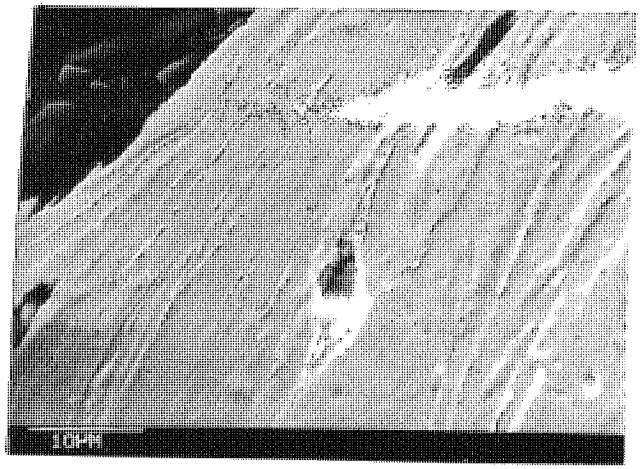

PLATE 68 : Heavily deformed area from the edge of the fracture .

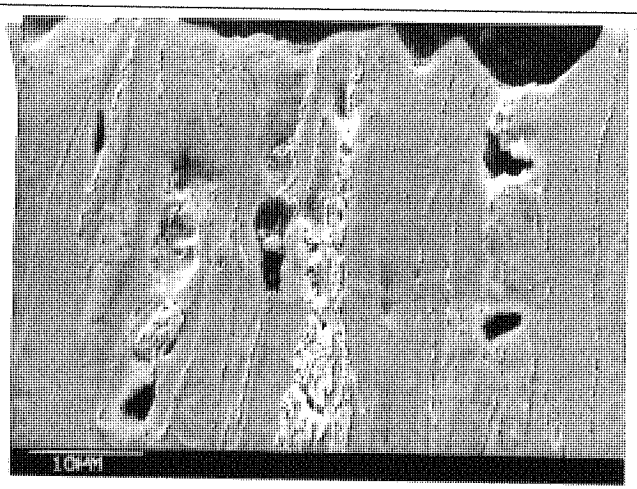

PLATE 69 : Void formation at inclusions and carbide particles (within pearlite colonies) .

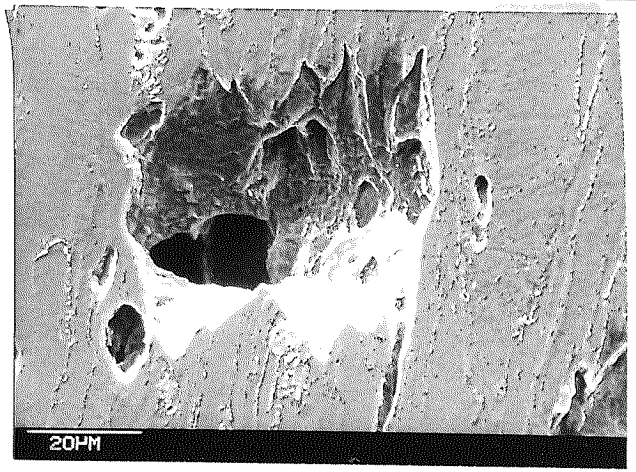

PLATE 70 : Void coalescence just below the fracture surface .

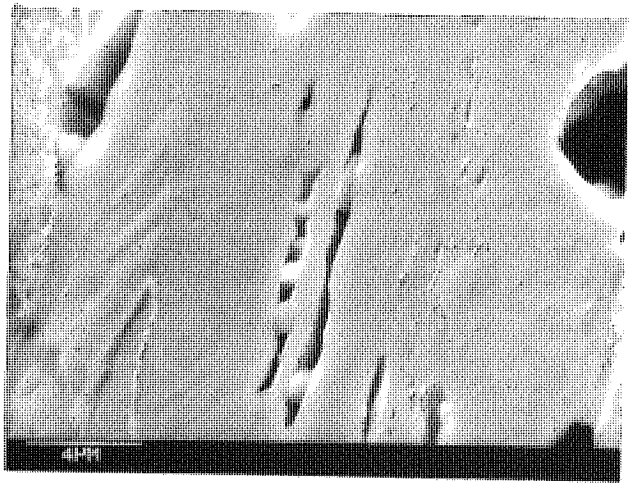

PLATE 71 : Voids formed at MnS inclusions mainly by inclusion cracking .

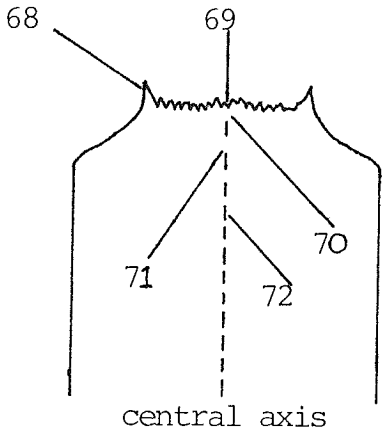

Void formation occurring at positions shown in diagram above

PLATE 72 : Cracking and decohesion at MnS inclusion .

Plates 68,69,70,71 and 72 SEM micrographs of axial cross sections of steel F, rolled at 900^{o}C, notched longitudinal tensile

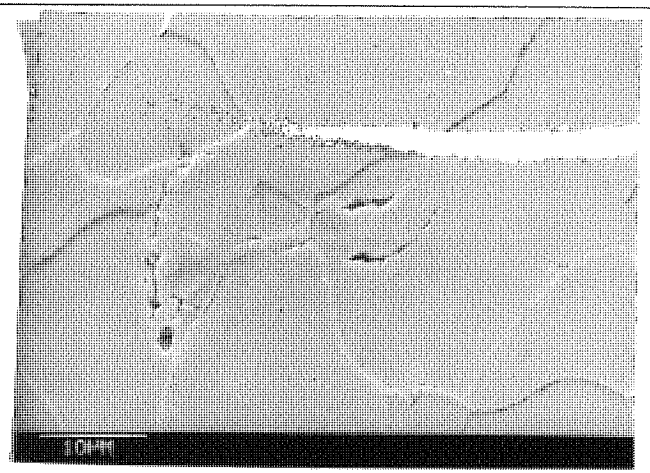

PLATE 73 : Voids formed by decohesion at MnS inclusions just below fracture surface .

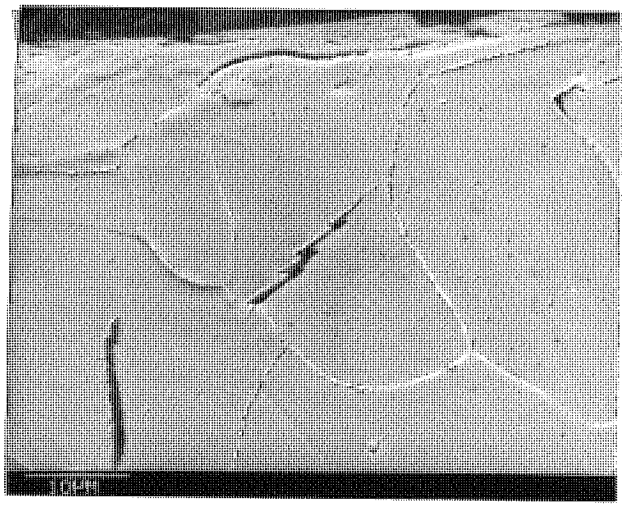

PLATE 74 : Heavily deformed region adjacent to fracture surface giving way to undeformed matrix containing transgranular cracks . Note partial decohesion of Al_2O_3 inclusion at bottom of Plate .

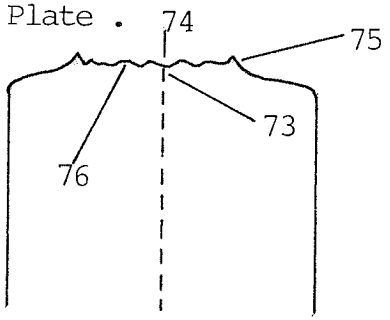

Cracking and void formation occurring at positions shown in diagram above

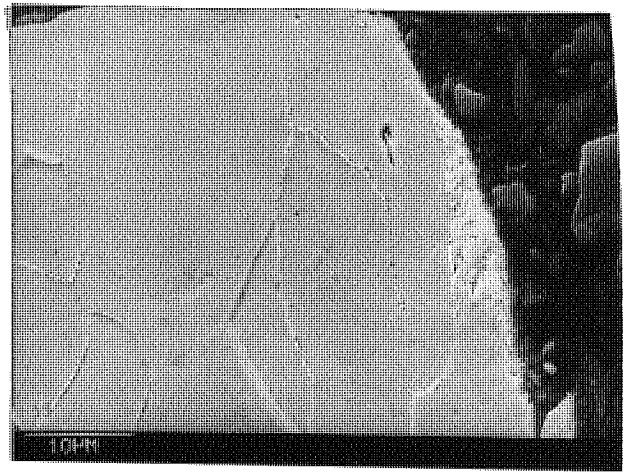

PLATE 75 : Void formation by decohesion at MnS inclusion at the edge of the specimen, note minimal deformation .

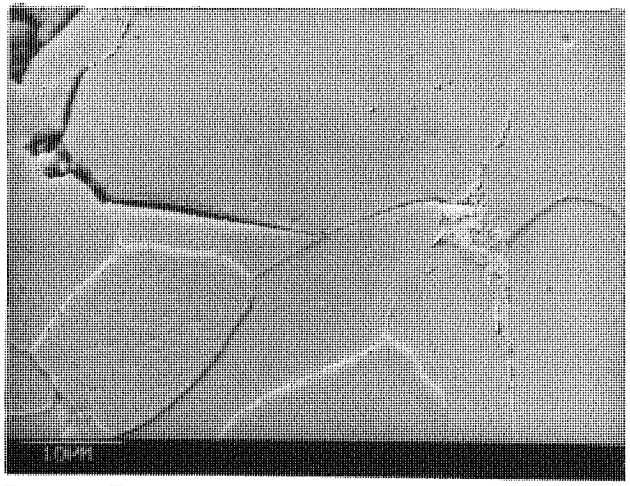

PLATE 76 : Transgranular and intergranular cracks emanating from Al_2O_3 inclusion next to fracture surface .

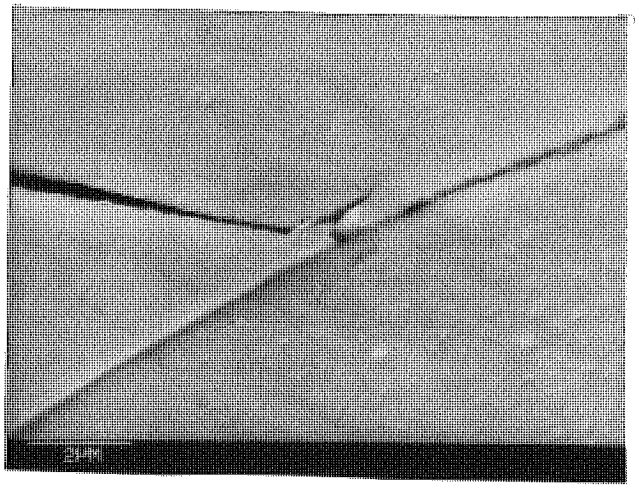

PLATE 77 : Detail of Plate 76 showing sub-micron particle associated with two converging cracks .

Plates 73,74,75,76 and 77 SEM micrographs of axial section of steel F, rolled at 900^{o}C, notched longitudinal tensile

PLATE 78 : Detail of Plate 80 below .

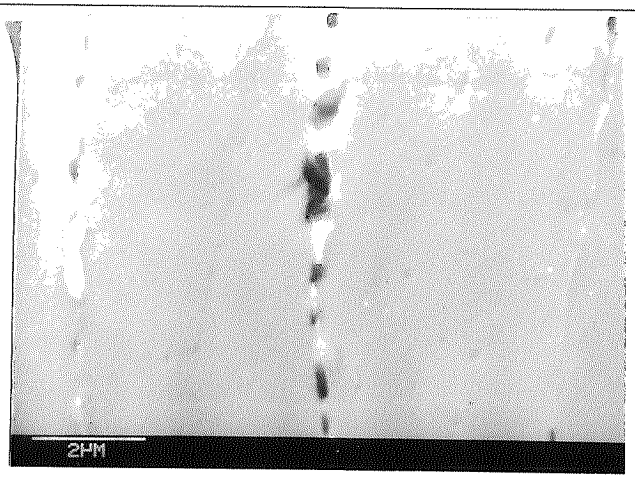

PLATE 79 : Void formation by cracking of grain boundary carbides .

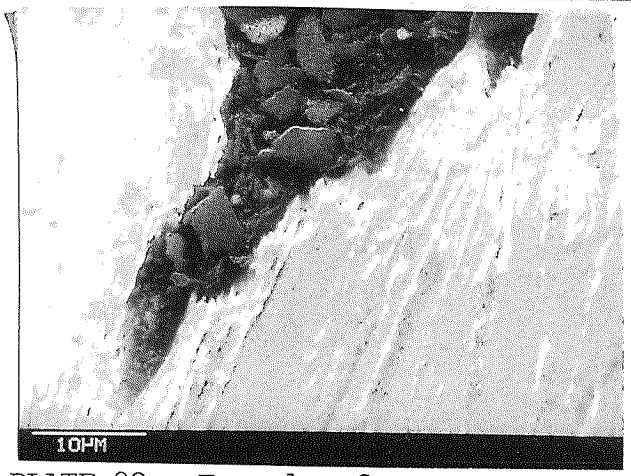

PLATE 82 : Example of cross section through fracture surface showing cusps formed from pearlite colonies .

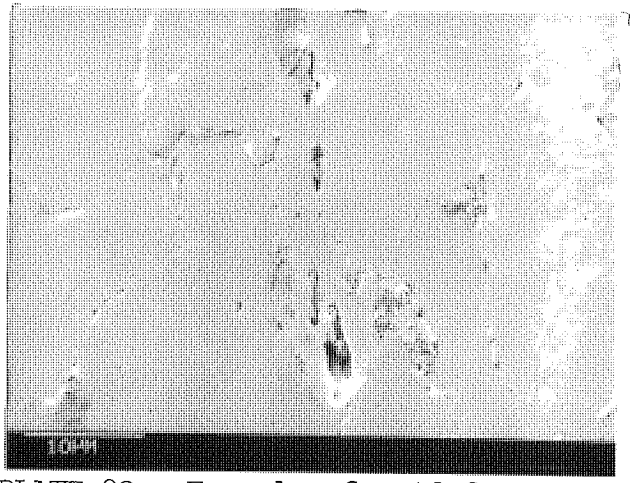

PLATE 80 : Example of void formation at MnS inclusions and pearlite colonies and grain boundaries .

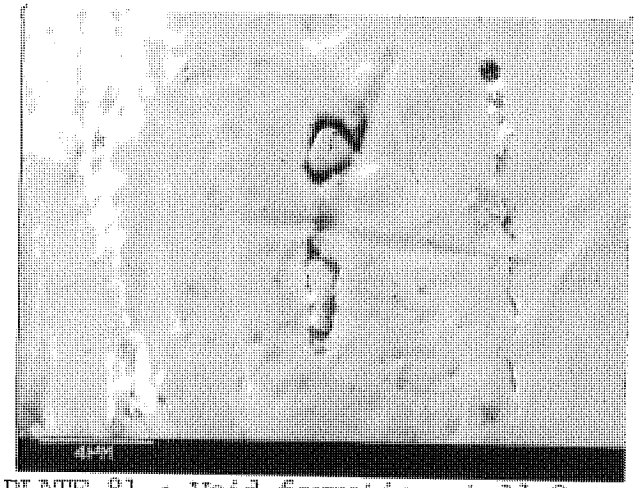

PLATE 81 : Void formation at Al_2O_3 inclusions and at grain boundary carbides .

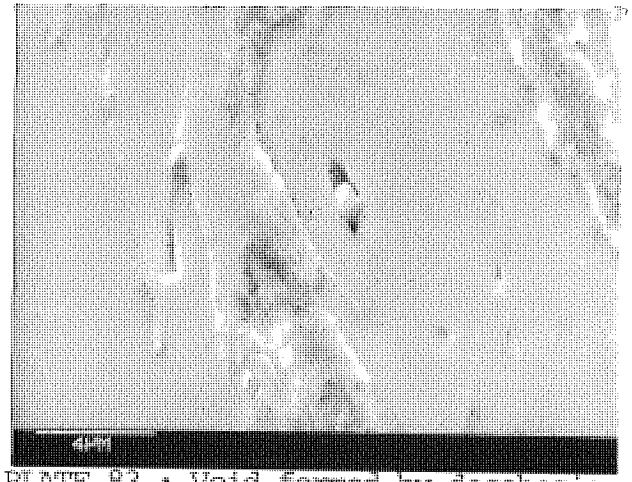

PLATE 83 : Void formed by decohesion at CaAlS containing inclusion .

Plates 78 to 80 steel L rolled at 1100°C tested longitudinally uncharged .

Plates 82 and 83 steel K rolled at 900°C tested longitudinally uncharged .

In contrast, very little deformation was observed in the HC-NTS and cracks, rather than voids, were found to have occurred adjacent to, (Plates 74, 76, 84, 85 and 87), and some distance from, (Plate 88) the fracture surface. Decohesion, rather than particle cracking (Plates 73, 75 and 86) was observed at inclusions. However, cracks were not always found to be associated with inclusions, nor for that matter at any particular microstructural feature, although in steel M, planar cracks, propagating in a direction perpendicular to the tensile direction were often found to be associated with pearlite bands, Plates 88 and 89.

The only area where evidence of extensive deformation was found in the HC-NTS was in narrow bands directly adjacent to the fracture surface, Plates 74 and 89, however, planar fractures were also observed in these areas, Plate 84 where no evidence of deformation could be detected. Little variation in the characteristics of the axial cross-sections was observed for all the HC-NTS in either testing direction.

4.4.3 QUANTITATIVE ANALYSIS

The results of the image analysis undertaken upon the axial cross-sections of the notched hydrogen charged and uncharged specimens (steels L, F, K and M) rolled at 1100^{o}C are given in Tables D31 to D33 in Appendix D. The values recorded were the number of voids per unit area (area density), the % area fraction of voids and the total length of voids (in the direction of applied stress) against the distance Z(mm) from the minimum section of the specimen. These have also been presented graphically in Figs.106 to 117. The attempt to measure the change in the axial cross-section of the neck as a result of deformation proved unsuccessful.

Plates 84 to 87, steel K rolled at 1100°C tested longitudinally and hydrogen charged .

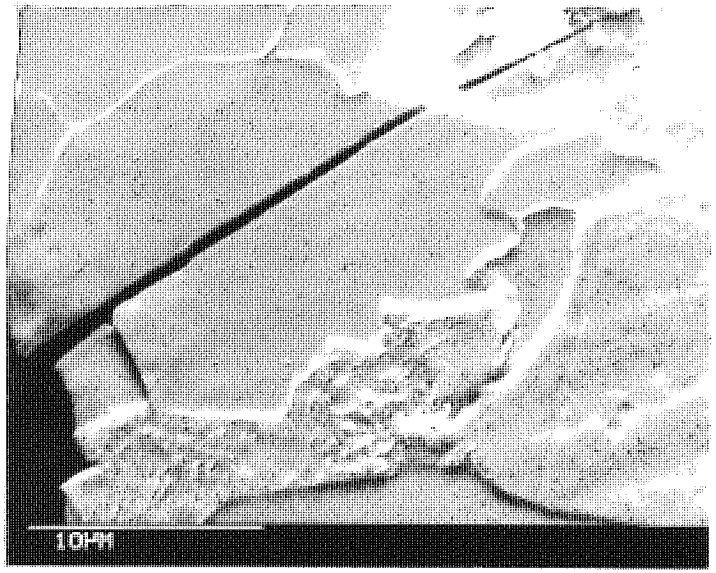

←←←←←

PLATE 84 : Transgranular cracks adjacent to fracture surface .

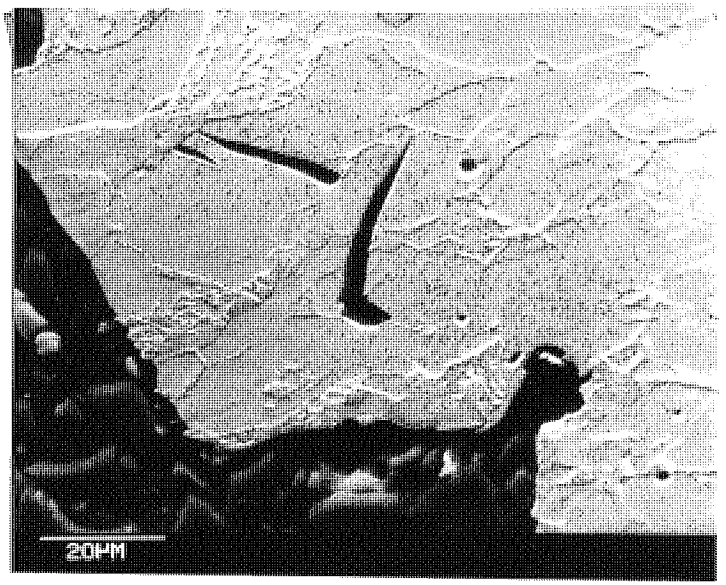

PLATE 85 : As Plate 84 above . Note absence of deformation .

→→→→→

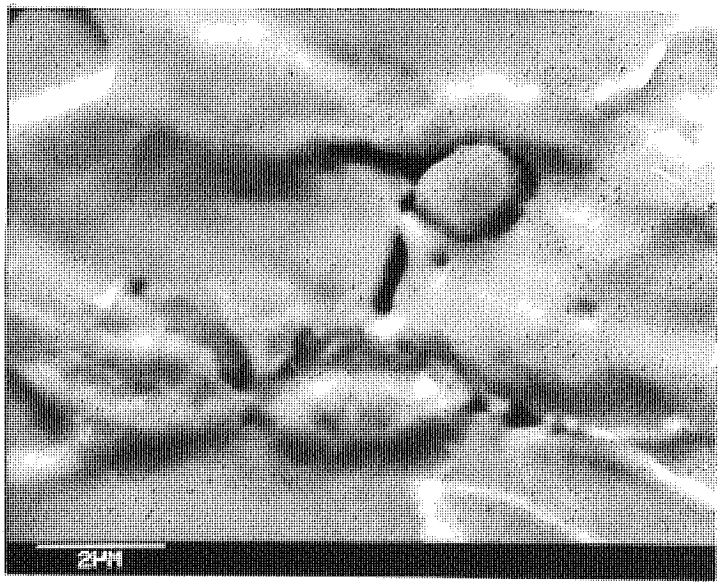

PLATE 86 : Void formed by decohesion at CaS inclusion and at grain boundary - propagation of void from inclusion .

←←←←←

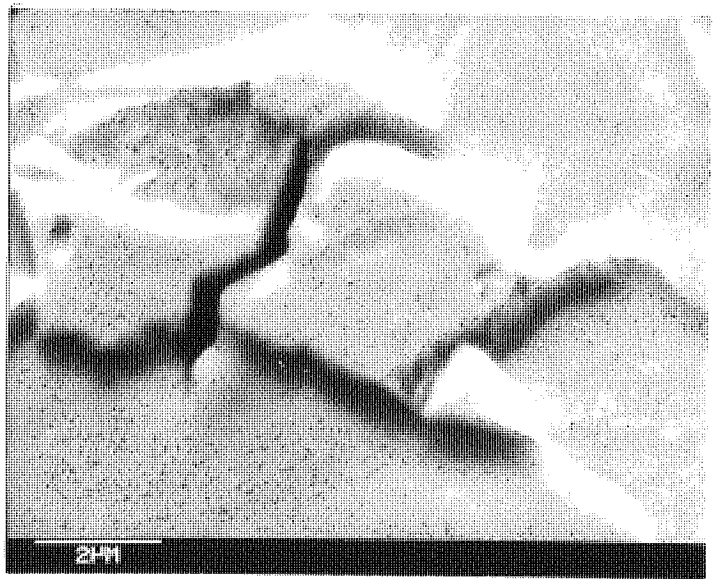

PLATE 87 : Crack developed in massive carbide particle .

→→→→→

PLATE 88 : Example of cracks occurring predominantly in the pearlite bands and running perpendicular to the tensile axis . Mag.X420 .

PLATE 89 : Evidence of plasticity adjacent to the fracture surface . Mag.X420 .

Plates 88 and 89 steel M rolled at 1100^{o}C tested longitudinally hydrogen charged .

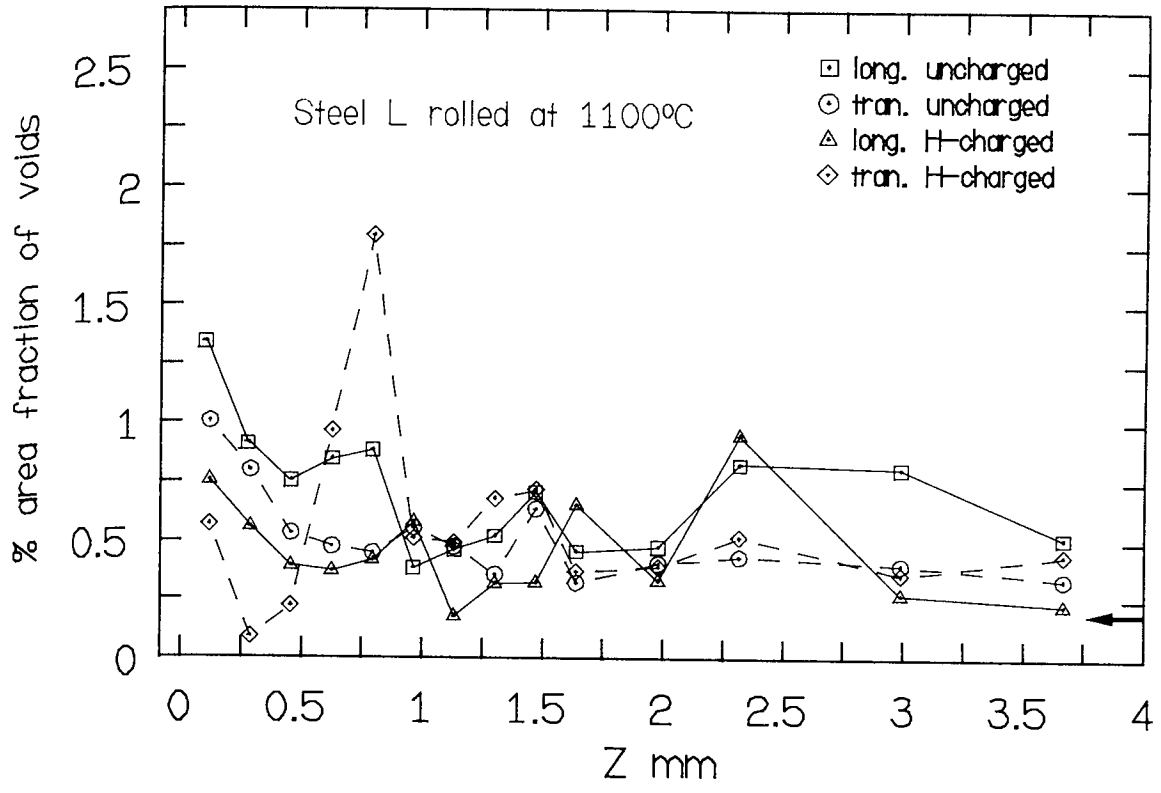

FIG.106: The area fraction of voids vs the vertical distance from the minimum section of the neck (Z) .

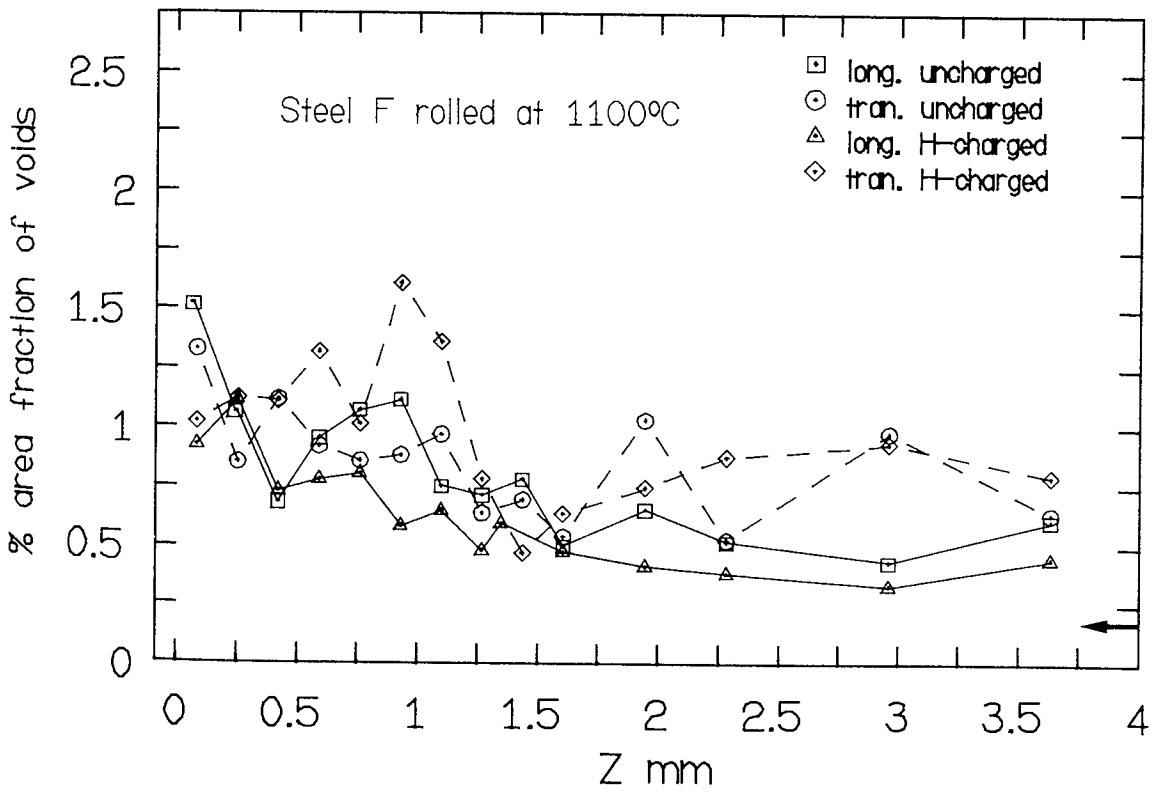

FIG.107: The % area fraction of voids vs the vertical distance from the minimum section of neck (Z) .

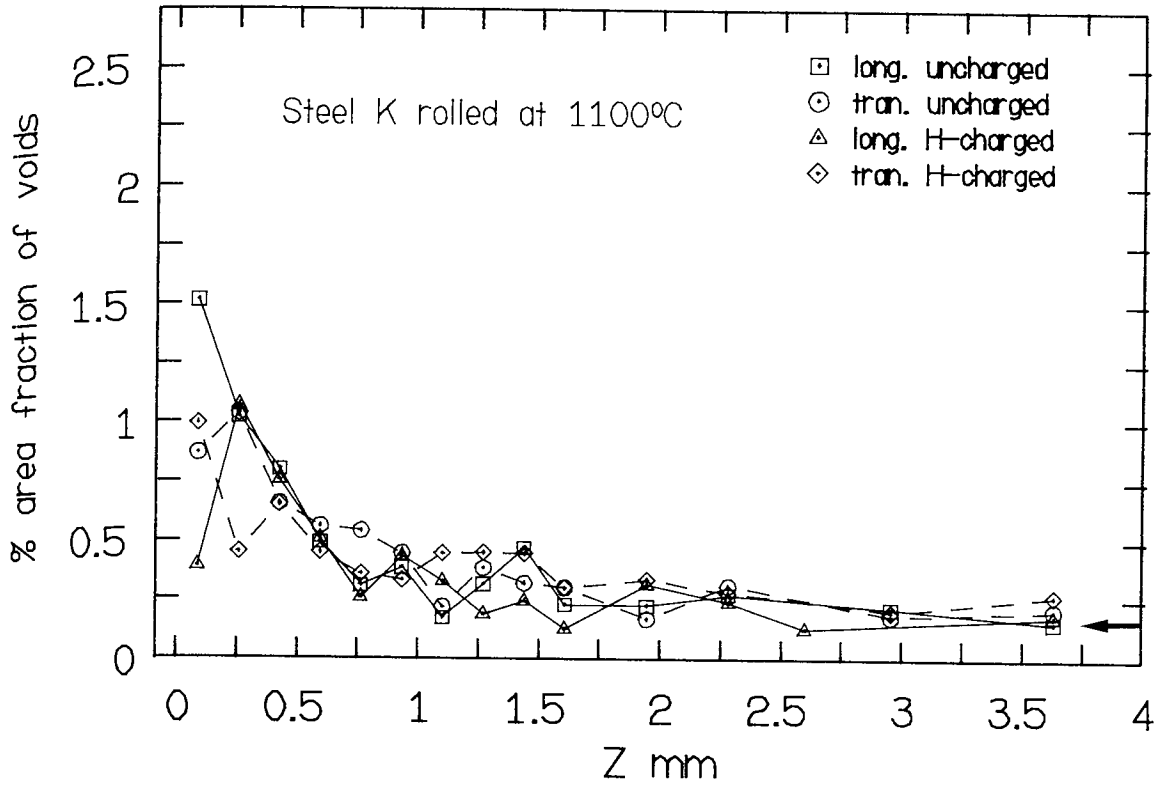

FIG.108: The % area fraction of voids vs the vertical distance from the minimum section of the neck (Z) .

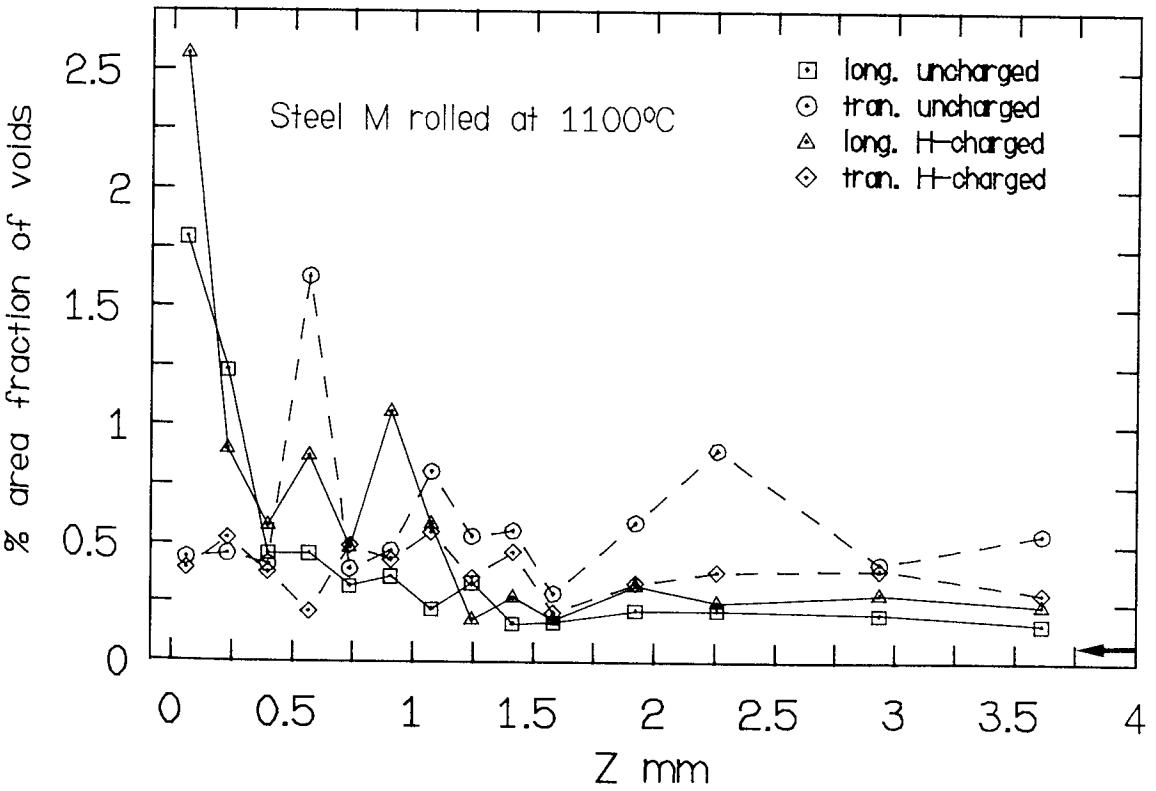

FIG.109: The % area fraction of voids vs the vertical distance from the minimum section of the neck (Z) .

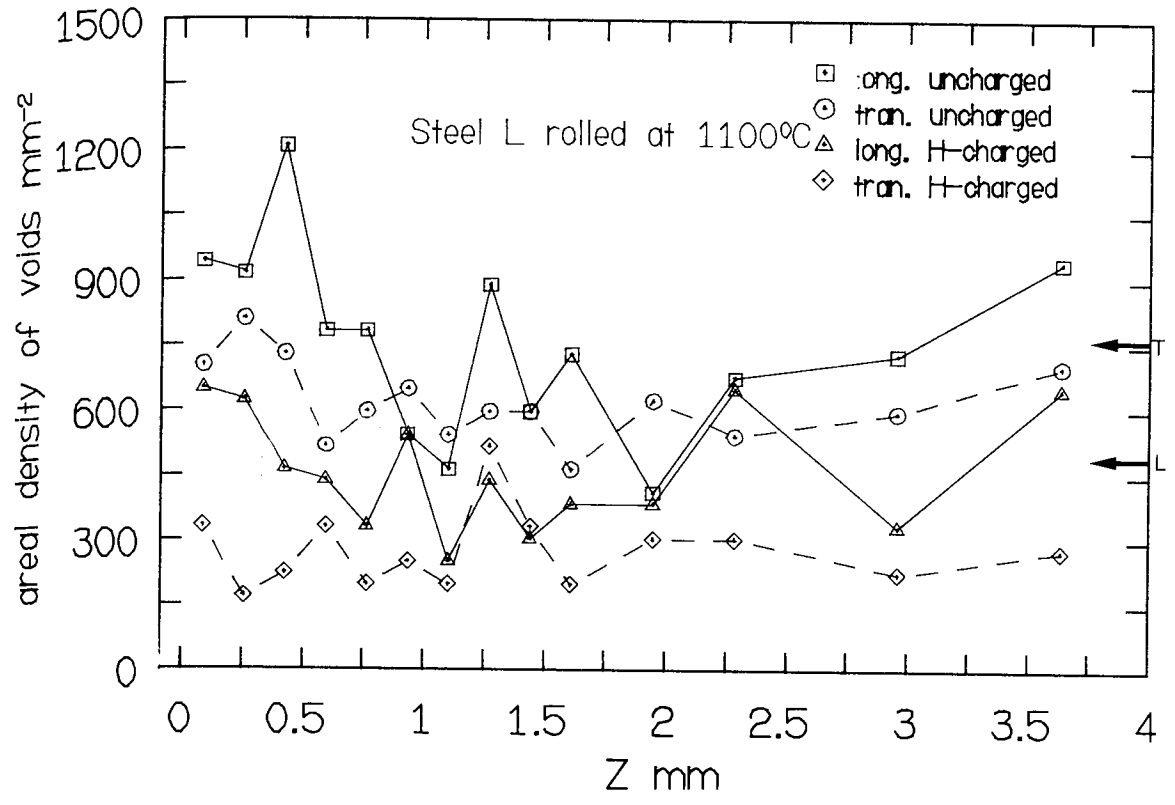

FIG.110: Areal density of voids vs the vertical distance from the minimum section of neck (Z) .

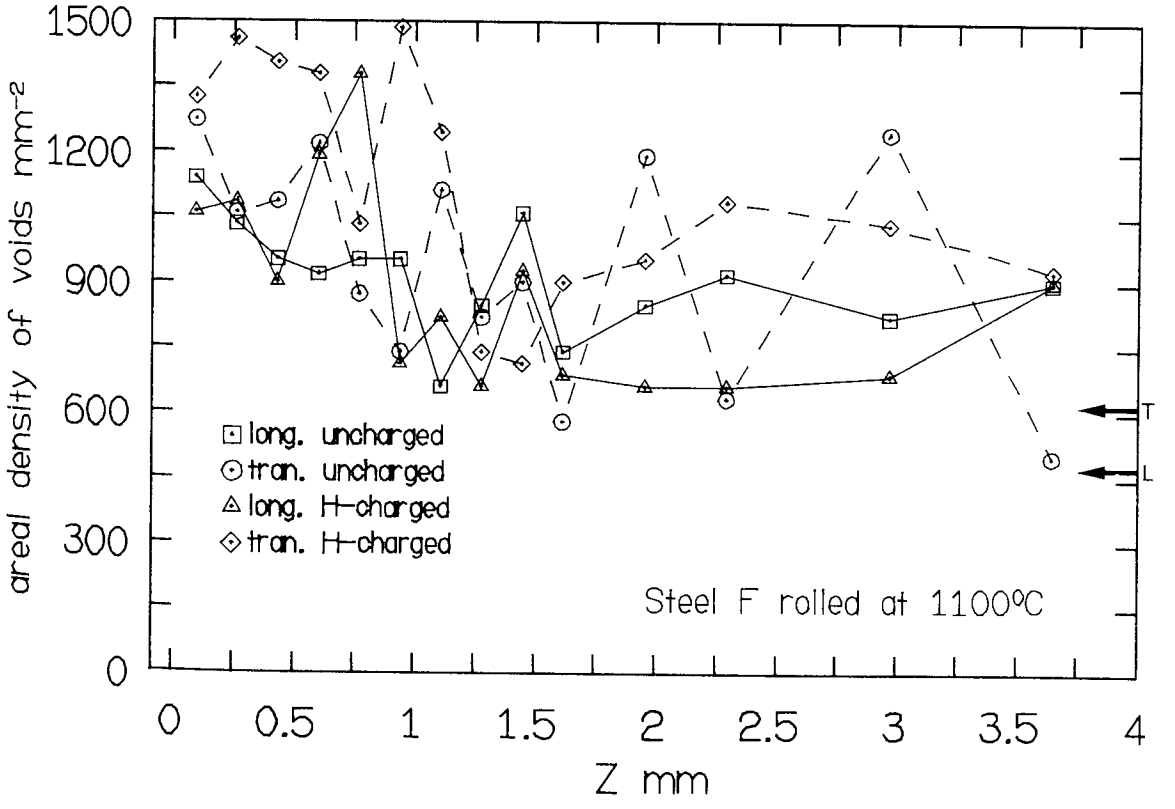

FIG.111: Areal density of voids vs the vertical distance from the minimum section of neck (Z) .

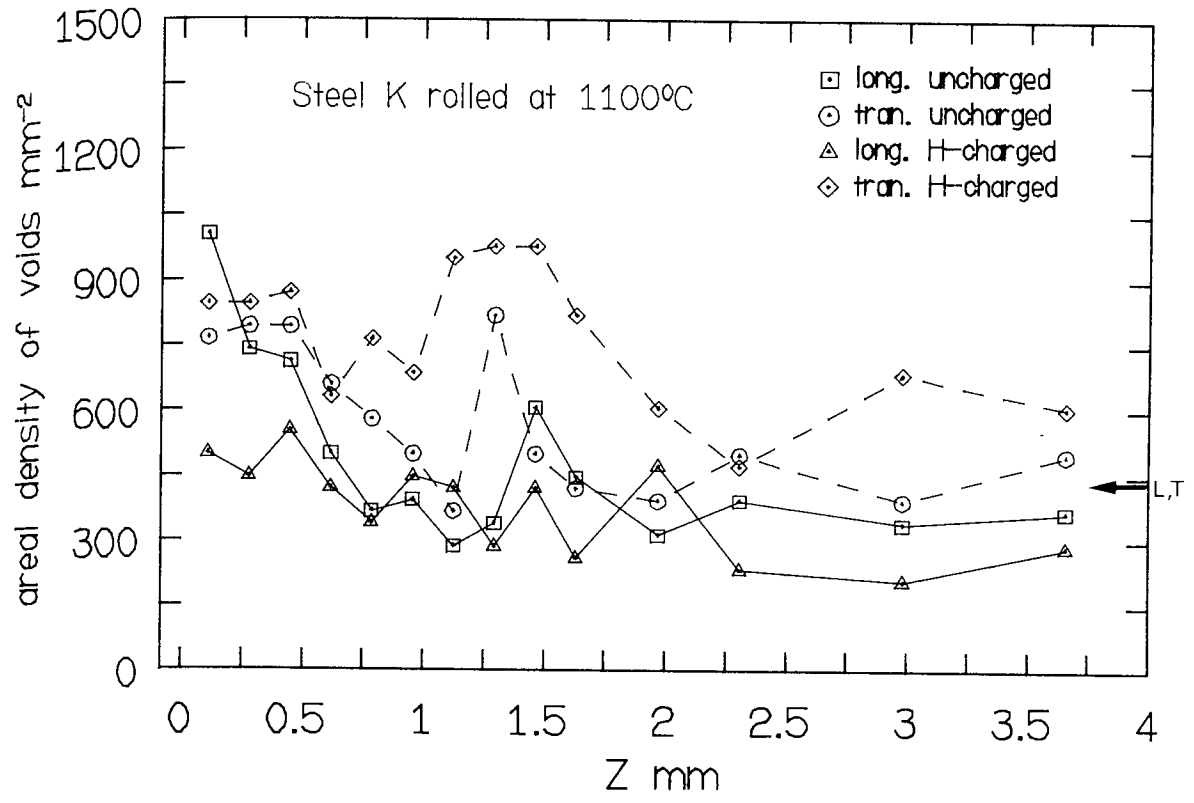

FIG.112: Areal density of voids vs the vertical distance from the minimum section of neck (Z) .

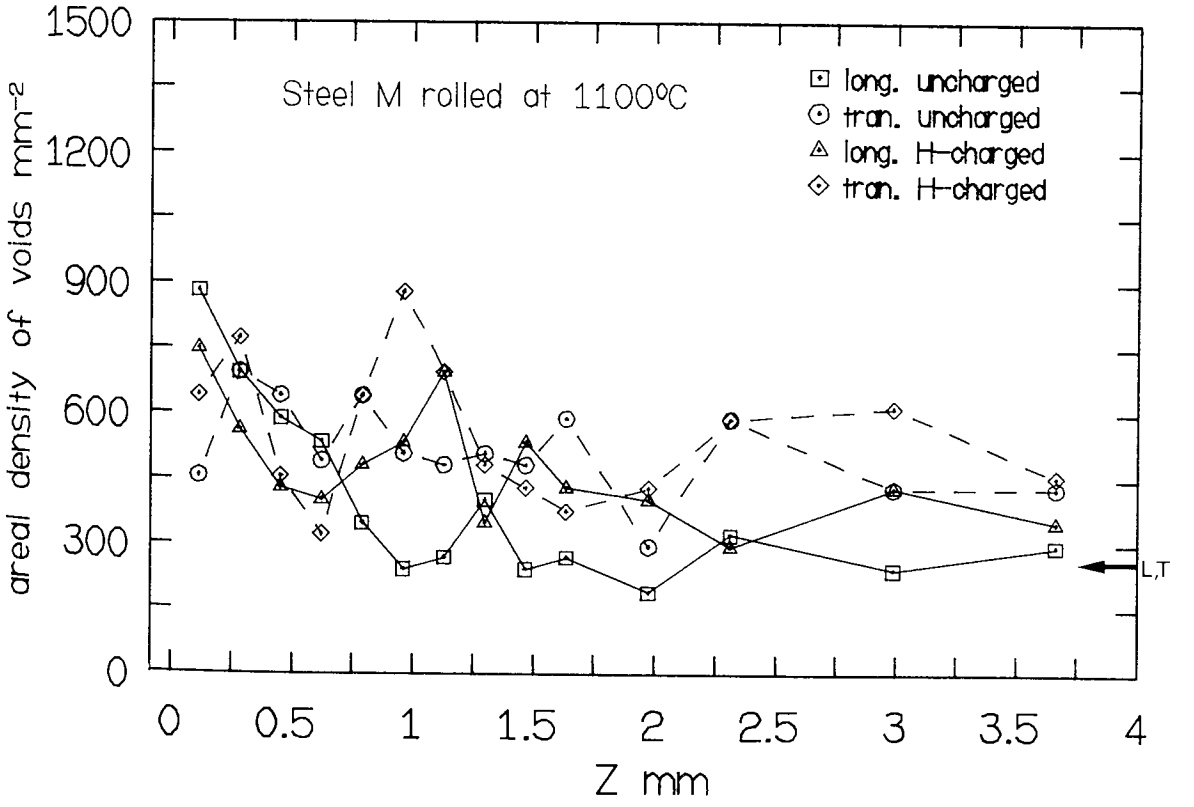

FIG.113: Areal density of voids vs the vertical distance from the minimum section of the neck (Z) .

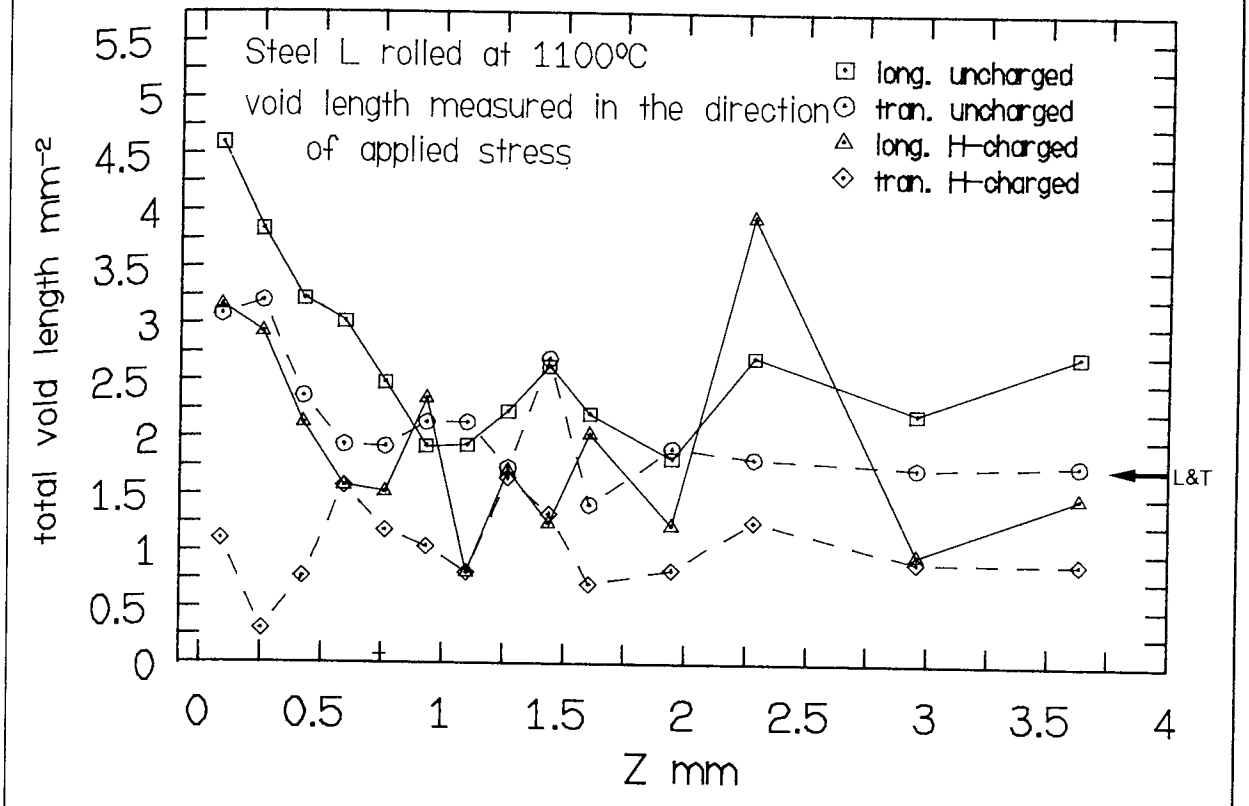

FIG.114: Total void length per unit area vs the vertical distance from the minimum section of the neck (Z) .

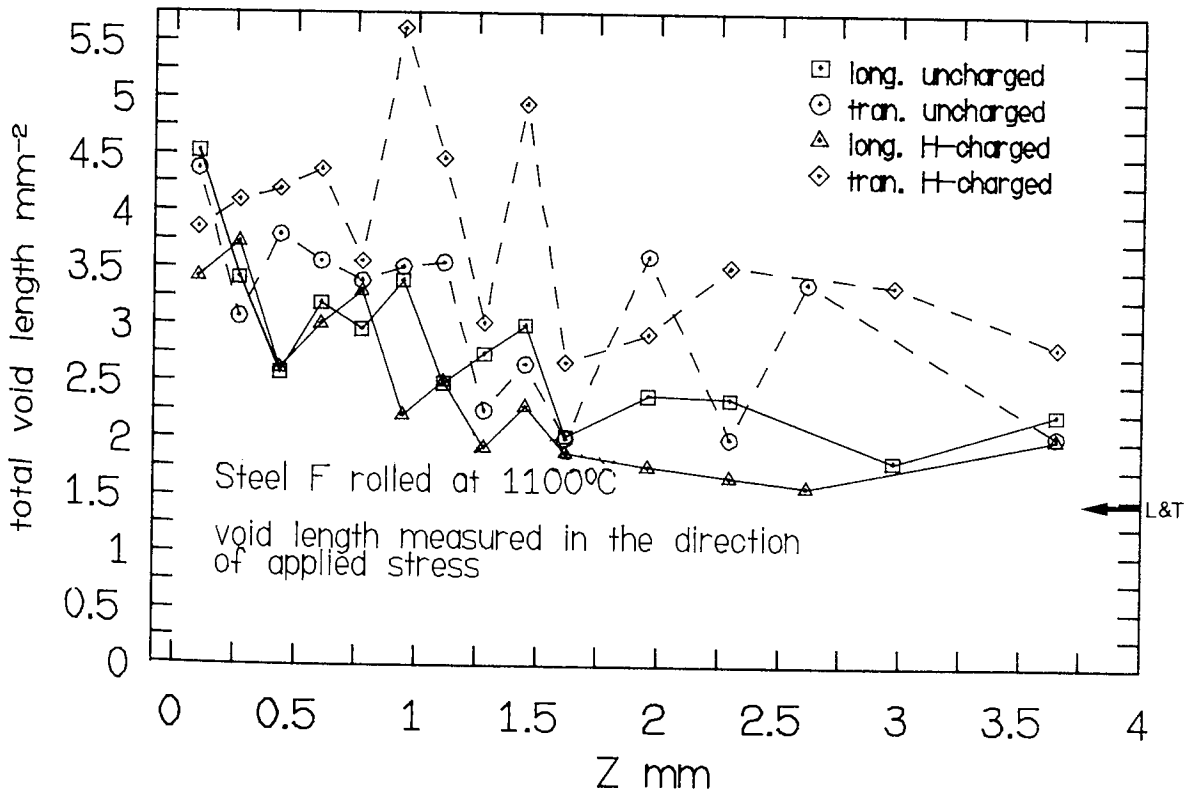

FIG.115: Total void length per unit area vs the vertical distance from the minimum section of neck (Z) .

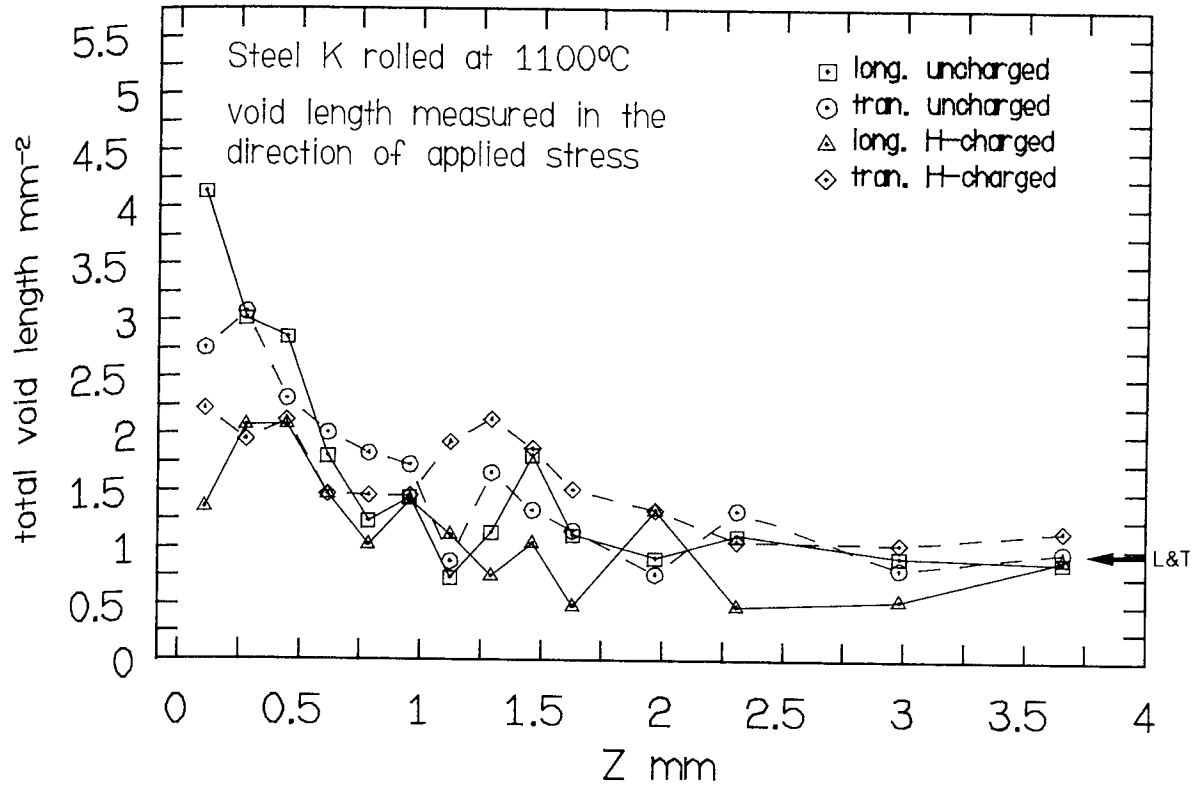

FIG.116: Total void length per unit area vs the vertical distance from the minimum section of neck (Z) .

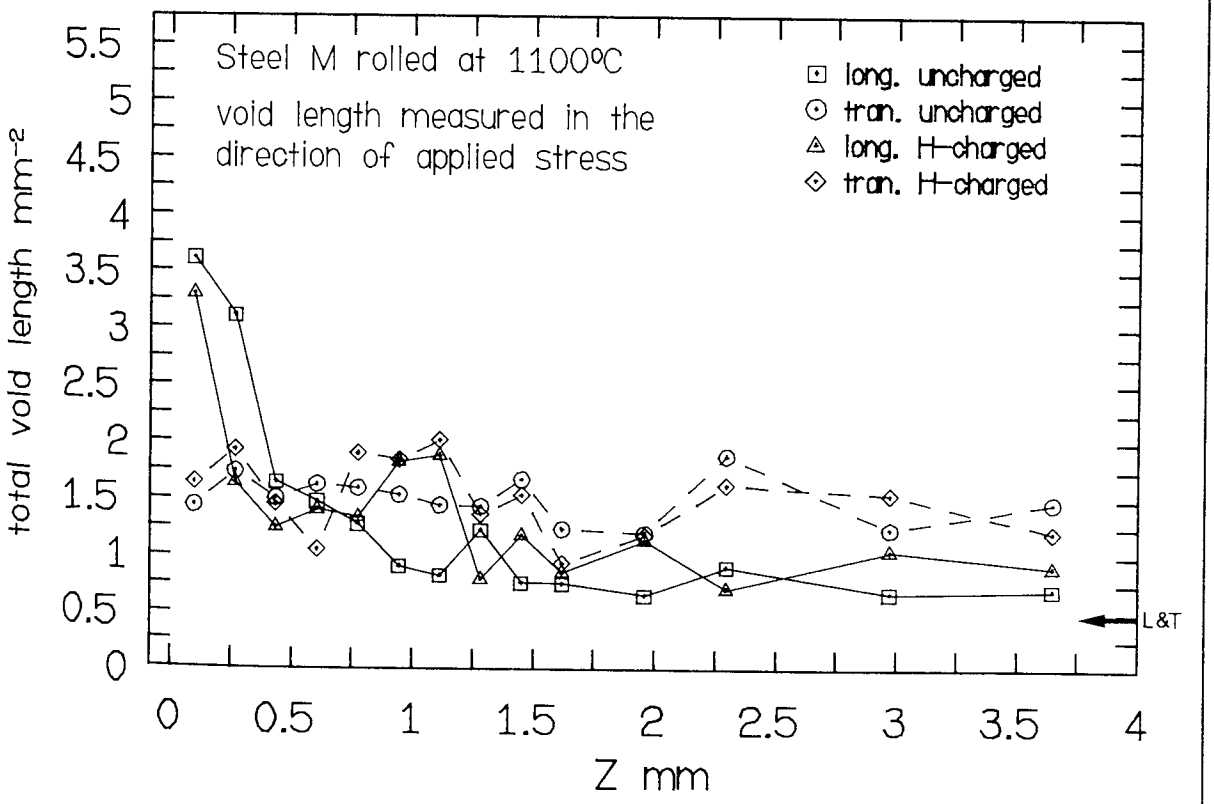

FIG.117: Total void length per unit area vs the vertical distance from the minimum section of the neck (Z) .

4.4.4 VICKERS HARDNESS

The results of the Vickers hardness for each steel are tabulated in Table 4.7 below.

TABLE 4.7 VICKERS PYRAMIDAL HARDNESS (VPH)

STEEL CODE	VPH	STEEL CODE	VPH	STEEL CODE	VPH	STEEL CODE	VPH
L75	172	F75	163	K75	206	M75	198
L9	151.5	F9	141.5	K9	168	M9	174
L0	150.5	F0	145.5	K0	166	M0	167
L11	149.5	F11	139.2	K11	171	M11	172

4.5.0 STEPWISE CRACKING TESTS

The results of both SWC tests (full size Test 1 and reduced size Test 2) are reported in Tables 4.8 and 4.9 below. These record the number of individual cracks measured (upon each section examined) and the CLR, CTR and CSR and the mean value of these parameters for all the three faces examined. The amount of hydrogen in the steels before and after charging is also recorded. Table 4.10 gives the results of the analysis of cracking found upon the side faces of the small specimens (Test 2) in terms of the CLR, CTR and CSR on each section and the average value for both sections.

TABLE 4.8 RESULTS OF STEP-WISE CRACKING - TEST 1, FULL SIZE COUPONS - 96HRS - (Dash - no crack observed)

STEEL CODE	SECTION 1				SECTION 2				SECTION 3				MEAN VALUES			HYDROGEN (ppm)	
	CLR	CTR	CSR	No. of CRACKS	CLR	CTR	CSR	No. of CRACKS	CLR	CTR	CSR	No. of CRACKS	CLR	CTR	CSR	BASE	AFTER CHARGING
L75	30.65	11.86	3.64	1	9.1	6.86	0.62	1	32.55	10.98	3.57	1	24.1	9.9	2.61	0.11	1.4
L9	-	-	-	-	-	-	-	-	-	-	-	-	-	-	-	"	1.6
L0	-	-	-	-	-	-	-	-	-	-	-	-	-	-	-	"	1.3
L1	-	-	-	-	-	-	-	-	-	-	-	-	-	-	-	"	1.0
F75	-	-	-	-	2.2	1.47	0.03	1	-	-	-	-	0.73	0.49	0.01	0.15	0.9
F9	54.54	9.8	5.34	1	-	-	-	-	-	-	-	-	18.18	3.27	1.78	"	0.8
F0	-	-	-	-	-	-	-	-	-	-	-	-	-	-	-	"	0.9
F1	4.85	3.24	0.16	1	-	-	-	-	-	-	-	-	1.62	1.08	0.05	"	0.7
K75	-	-	-	-	-	-	-	-	-	-	-	-	-	-	-	0.25	1.8
K9	-	-	-	-	-	-	-	-	1.65	0.69	0.01	1	0.55	0.23	0.00	"	1.2
K0	11.05	4.41	0.49	1	-	-	-	-	1.57	6.27	0.99	1	8.95	6.5	0.49	"	1.1
K1	6.5	1.08	0.07	1	10.5	3.24	0.34	2	-	-	-	-	5.67	1.44	0.14	"	1.2
M75	-	-	-	-	-	-	-	-	-	-	-	-	-	-	-	0.2	1.1
M9	-	-	-	-	-	-	-	-	-	-	-	-	-	-	-	"	1.0
M0	-	-	-	-	-	-	-	-	-	-	-	-	-	-	-	"	0.7
M1	-	-	-	-	-	-	-	-	-	-	-	-	-	-	-	"	1.2

TABLE 4.9 RESULTS OF STEP-WISE CRACKING - TEST 2, SMALL COUPONS - 192 HRS - (Dash - no cracks observed)

STEEL CODE	SECTION 1				SECTION 2				SECTION 3				MEAN VALUES			HYDROGEN (ppm)	
	CLR	CTR	CSR	No. of CRACKS	CLR	CTR	CSR	No. of CRACKS	CLR	CTR	CSR	No. of CRACKS	CLR	CTR	CSR	BASE	AFTER CHARGING
L75	-	-	-	-	31.47	16.6	5.22	1	-	-	-	-	10.49	5.53	0.02	0.11	10.1
L9	22.79	11.1	2.53	1	-	-	-	-	-	-	-	-	7.6	3.7	0.84	"	8.8
L0	27.00	17.9	4.83	1	-	-	-	-	30.26	39.8	12.04	1	19.09	19.23	5.62	"	8.5
L1	-	-	-	-	-	-	-	-	-	-	-	-	-	-	-	"	9.1
F75	-	-	-	-	-	-	-	-	3.74	1.7	0.06	1	1.25	0.57	0.02	0.15	7.5
F9	-	-	-	-	-	-	-	-	4.86	3.87	0.19	1	1.62	1.29	0.06	"	4.3
F0	19.68	2.8	0.55	1	-	-	-	-	-	-	-	-	0.66	0.93	0.18	"	3.8
F1	-	-	-	-	-	-	-	-	13.38	5.3	0.71	1	4.46	1.77	0.24	"	3.1
K75	-	-	-	-	-	-	-	-	22.63	7.08	1.6	1	7.54	2.36	0.53	0.25	5.2
K9	-	-	-	-	2.56	3.64	0.09	1	-	-	-	-	0.85	1.21	0.03	"	5.4
K0	-	-	-	-	1.37	1.1	0.02	1	-	-	-	-	0.46	0.37	0.01	"	5.6
K1	-	-	-	-	-	-	-	-	1.89	0.6	0.01	1	0.63	0.2	0.00	"	4.0
M75	-	-	-	-	-	-	-	-	13.61	13.1	1.78	1	4.54	4.37	0.59	0.2	8.0
M9	18.00	17.7	3.19	1	-	-	-	-	-	-	-	-	6.00	5.9	1.06	"	3.2
M0	10.37	2.8	0.29	1	-	-	-	-	-	-	-	-	3.46	0.93	0.1	"	5.6
M1	2.45	0.6	0.01	1	-	-	-	-	-	-	-	-	0.82	0.2	0.00	"	6.5

TABLE 4.10 RESULTS OF STEP-WISE CRACKING TEST 2, OBSERVATIONS UPON SIDE FACES

STEEL CODE	SIDE 1			SIDE 2			MEAN VALUES		
	CLR	CTR	CSR	CLR	CTR	CSR	CLR	CTR	CSR
L75	92.75	42.6	39.51	99.88	49.9	49.84	96.31	46.25	44.68
L9	70.42	49.7	35.00	49.17	24.0	11.8	59.79	36.85	23.4
L0	45.42	22.8	10.36	33.58	27.6	7.34	39.5	25.2	8.85
L1	-	-	-	-	-	-	-	-	-
F75	40.88	10.47	4.28	6.58	1.45	0.1	23.73	5.96	2.19
F9	18.23	10.5	1.91	7.58	6.9	0.52	12.91	8.7	1.22
F0	9.04	3.88	0.35	-	-	-	4.52	1.94	0.18
F1	14.46	11.1	1.6	2.54	6.1	0.04	8.5	8.6	0.82
K75	29.33	13.2	3.87	48.58	14.3	6.95	38.96	13.75	5.41
K9	4.92	1.6	0.08	15.13	5.0	0.76	10.02	3.3	0.42
K0	4.92	4.6	0.23	1.13	2.7	0.01	3.02	3.65	0.12
K1	1.42	2.5	0.04	1.42	0.6	0.01	1.42	1.55	0.03
M75	47.25	20.6	9.73	21.08	50.6	3.2	34.17	35.6	6.47
M9	29.17	38.0	11.08	15.83	12.0	0.15	22.5	25.0	5.62
M0	15.63	11.3	1.77	14.46	0.32	0.05	15.04	5.81	0.91
M1	9.04	6.2	0.56	-	-	-	4.52	3.1	0.28

The following inclusion parameters have then been plotted against the CLR and/or CTR for both tests 1 and 2; the % area fraction Fig. 118, the projected length of inclusions on a plane parallel to the plane of cracking i.e. CLR vs P_{L3} and CTR vs P_{L2} Fig.119 the projected length of inclusions on a plane parallel to the plane of cracking for the cracks measured upon the side faces of test 2 i.e. CLR vs PL_3 and CLT vs PL_2, Fig. 120. Also the probability of exceeding a projected length of 1.4 mm/mm^2 on a plane parallel to the fracture plane against the CLR and CTR has been plotted in Fig.121. The lettering on the graphs identifies the steel and the temperature at which it was rolled.

4.5.1 SURFACE BLISTERS

The analysis of the blister size distribution is reported in Table 4.11. The distribution of the log (transformed) of the blister size distribution was also examined using the method of moments described in Appendix C Part 2, to see if it followed a log-normal type distribution. The results of this analysis are given in Table 4.12 below, included in this table is the total number of blisters observed, the % area fraction of blisters, the mean blister size and standard deviation, for each steel coupon.

4.5.2 METALLOGRAPHY AND FRACTOGRAPHY

A typical example of the blistering which occurred on the surface of the steel coupons is shown in Plate 90A and a single blister at higher magnification in Plate 90B. Plate 91 shows a section through a blister, where the blister has actually grown out of the coupon at the side face.

For all the steels examined when cracking was observed as a result of immersion in the NACE solution it followed the familiar "stepwise"

pattern which has been consistently reported in the literature, Plates 98, 107 and 108. Large "blister"-like cracks are linked together by fissures in the matrix which itself appeared to have deformed plastically, Plates 107 to 110. Very often the blister like cracks were associated with (large) non-metallic inclusions Plates 101 and 108, however, smaller cracks were observed which had initiated at non-metallic inclusions but which had not propagated to any great extent, Plates 114 to 118. When cracks did propagate the crack path was found not to be preferentially associated with any particular microstructural features (that is except for the joining up of blister cracks which had developed from inclusions).

An attempt was made to crack open some of the coupons, at liquid nitrogen temperature, after SWCs had been produced by immersion in the NACE solution, so that any intervening matrix would fail by cleavage. Plates 92 to 94 show typical cleavage fractures for the steels examined and Plates 95 to 97 show the resulting fracture surface after immersion in the NACE solution and cracking at liquid nitrogen temperature. It can be seen that a terraced type fracture has occurred where the areas associated with the internal blisters appear to have failed in a quasi-cleavage type mode. Inclusions were often found to be associated with these areas of fracture.

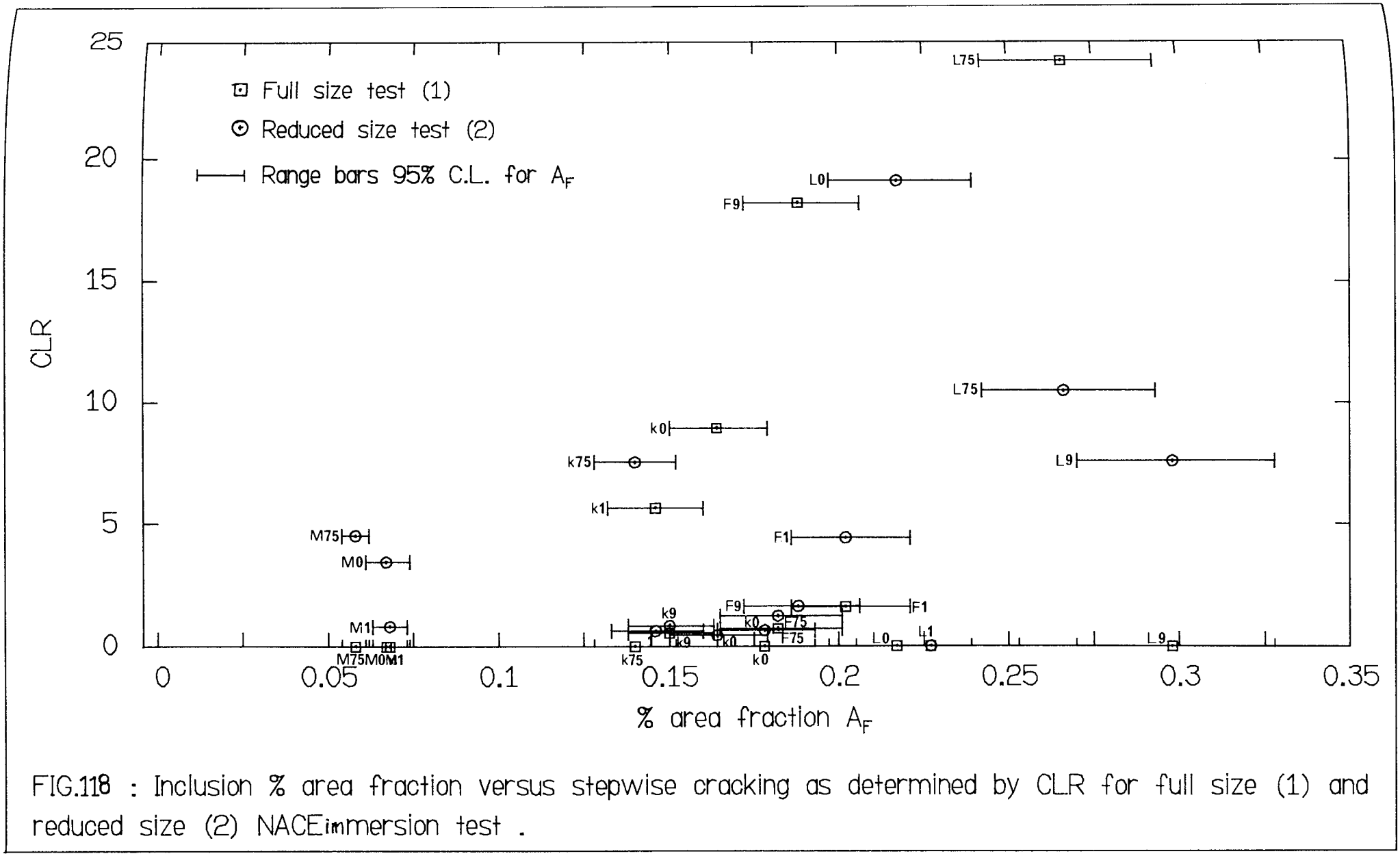

FIG.118 : Inclusion % area fraction versus stepwise cracking as determined by CLR for full size (1) and reduced size (2) NACEimmersion test .

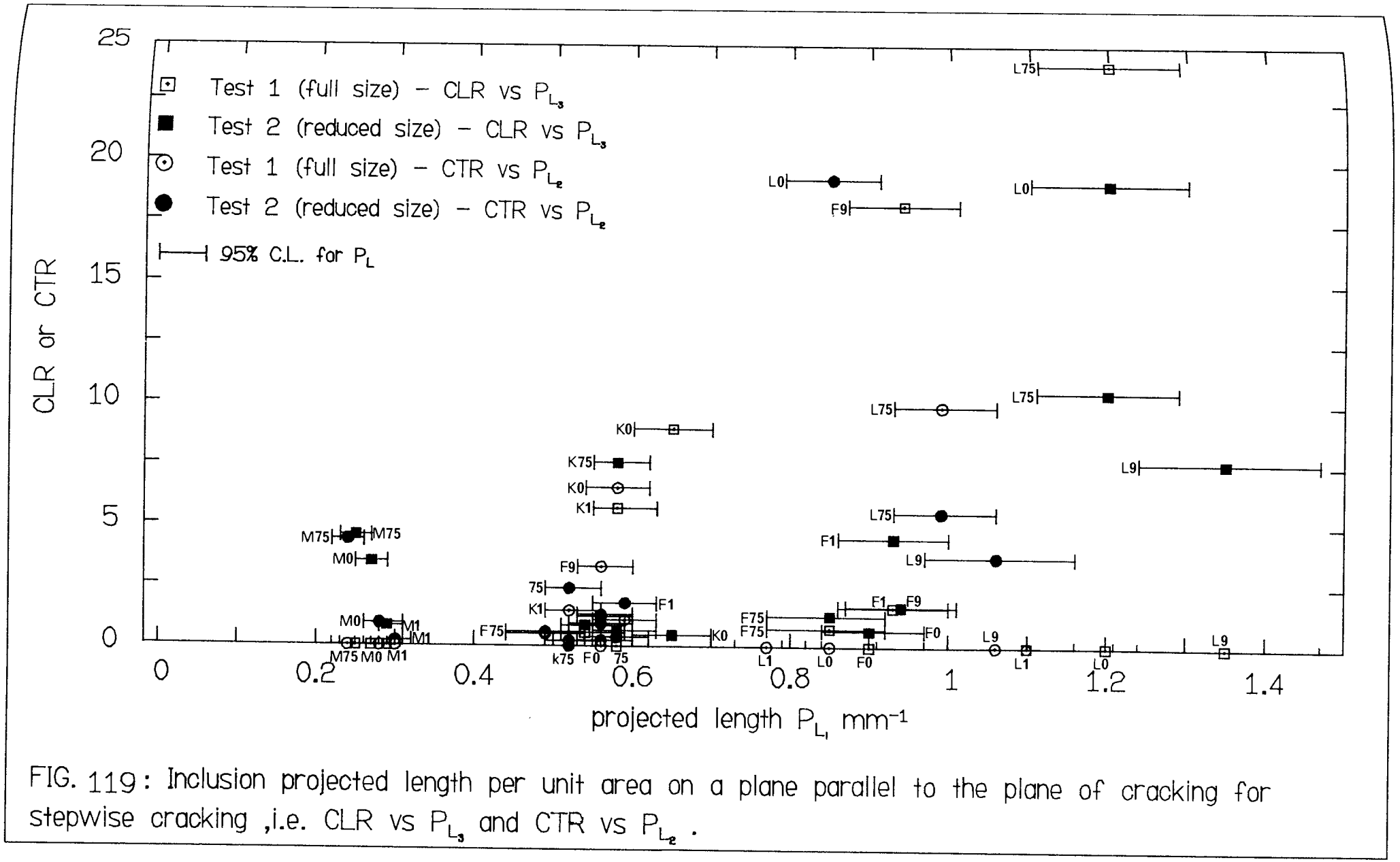

FIG. 119 : Inclusion projected length per unit area on a plane parallel to the plane of cracking for stepwise cracking ,i.e. CLR vs P_{L_3} and CTR vs P_{L_2} .

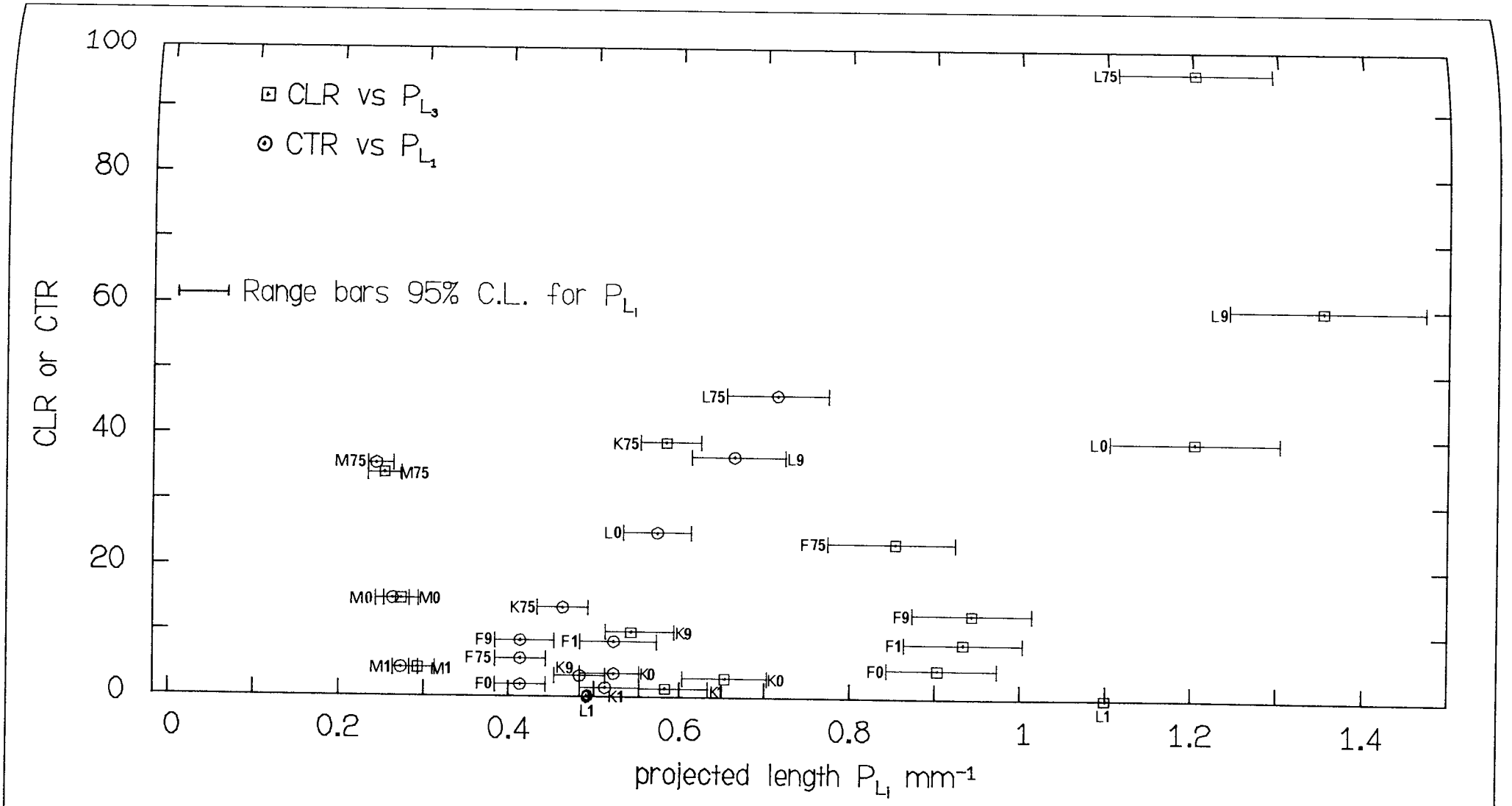

FIG.120: Inclusion projected length per unit area on a plane parallel to the plane of cracking for stepwise cracking . Test 2 (reduced size), measurements made on longitudinal plane .

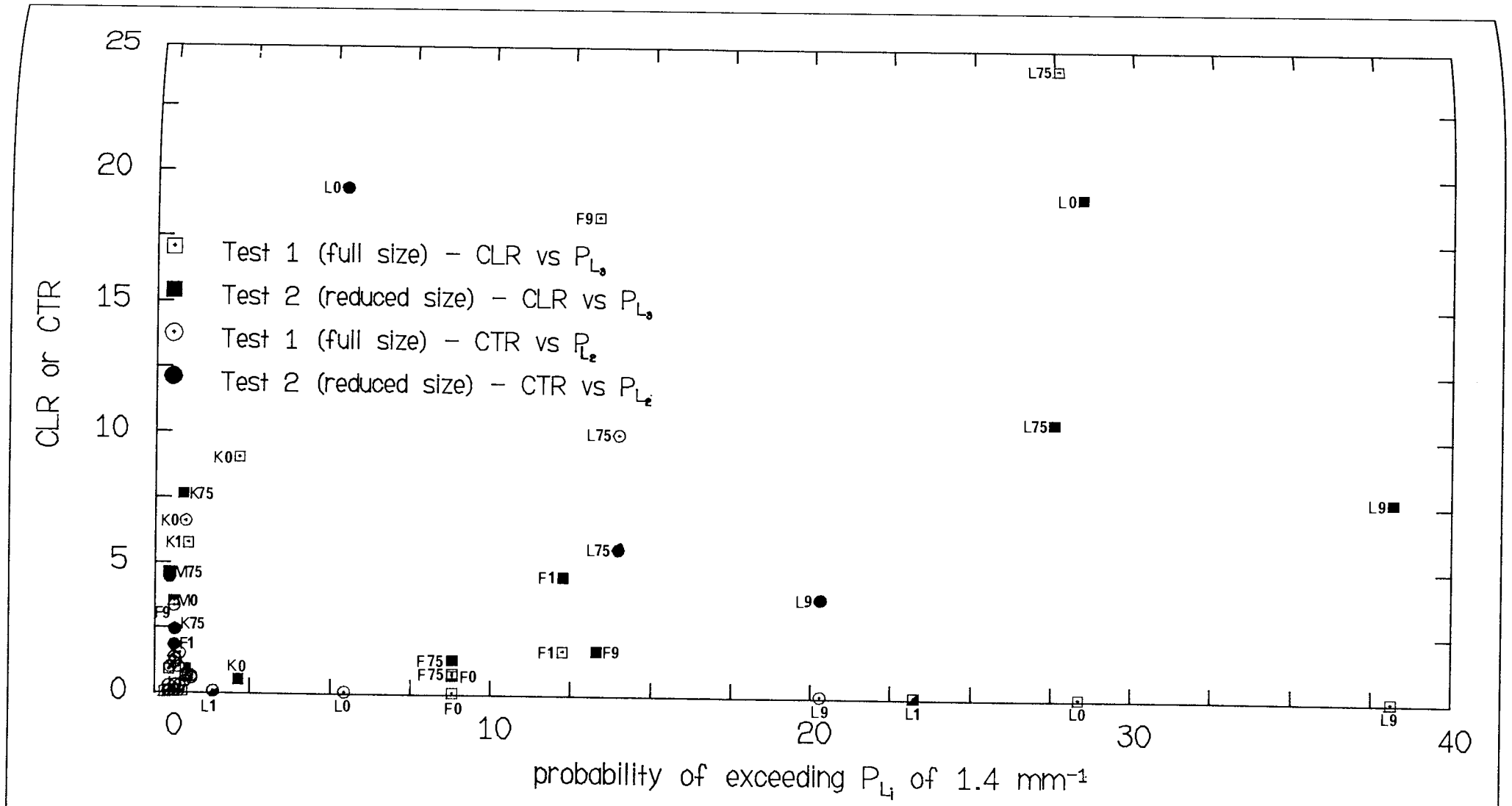

FIG.121: Probability of exceeding a projected length per unit area of 1.4 mm^{-1} versus stepwise cracking as determined by the CLR and CTR .

TABLE 4.11 BLISTER SIZE DISTRIBUTION - STEELS L AND F

SIZE RANGE mm	CLASS MID	L75		L9		L0		L1		F75		F9		F0		F1	
		COUNT	C.F. %	COUNT	C.F. %	COUNT	C.F. %	COUNT	C.F. %	COUNT	C.F. %	COUNT	C.F. %	COUNT	C.F. %	COUNT	C.F. %
0-0.01	0.005	3	1.84	10	7.14	-	-	-	-	-	-	-	-	-	-	-	-
0.01-0.02	0.015	39	25.77	19	20.71	1	2.27	4	5.33	-	-	-	-	-	-	-	-
0.02-0.04	0.03	52	58.02	64	66.91	6	21.88	6	15.91	12	21.33	2	9.09	-	-	1	3.23
0.04-0.08	0.06	21	70.55	13	75.71	7	43.75	9	36.36	5	28.00	5	31.82	1	4.76	2	9.68
0.08-0.16	0.12	31	89.57	19	89.29	7	65.63	8	52.27	28	65.33	4	50.00	3	19.05	8	35.48
0.16-0.32	0.24	4	92.02	4	92.14	2	71.88	3	63.64	6	73.33	-	-	5	42.86	1	38.71
0.32-0.64	0.48	4	94.48	3	94.29	4	84.38	7	77.27	10	86.67	3	63.63	3	57.14	10	70.97
0.64-1.28	0.96	2	95.71	4	97.14	-	-	2	81.82	5	93.33	2	72.72	3	71.43	4	83.87
1.28-2.56	1.92	2	96.93	1	97.86	3	93.75	-	-	2	96.00	3	86.36	3	85.71	3	93.55
2.56-5.12	3.84	2	98.16	2	99.29	-	-	4	90.91	1	97.33	2	95.45	1	90.48	1	96.77
5.12-10.24	7.68	2	99.39	-	-	1	96.88	3	97.73	1	98.67	-	-	-	-	-	-
10.24-20.48	5.36	-	-	-	-	-	-	-	-	-	-	-	-	1	95.24	-	-

TABLE 4.11 (Cont'd) BLISTER SIZE DISTRIBUTION - STEELS K AND M

SIZE RANGE mm	CLASS MID	K75		K9		K0		K1		M75		M9		M0		M1	
		COUNT	C.F. %	COUNT	C.F. %	COUNT	C.F. %	COUNT	C.F. %	COUNT	C.F. %	COUNT	C.F. %	COUNT	C.F. %	COUNT	C.F. %
0-0.01	0.005	-	-	1	0.88	-	-	-	-	-	-	-	-	-	-	-	-
0.01-0.02	0.015	-	-	-	-	-	-	-	-	1	5.26	-	-	-	-	-	-
0.02-0.04	0.03	3	5.17	13	12.28	6	17.14	1	5.0	1	10.53	7	10.14	7	14.89	3	5.77
0.04-0.08	0.06	3	10.34	8	19.3	1	20.00	1	10.00	-	-	5	17.39	2	19.15	1	7.69
0.08-0.16	0.12	21	46.55	48	61.4	14	60.00	4	30.00	9	57.89	15	39.13	15	51.06	20	46.15
0.16-0.32	0.24	7	58.62	17	76.32	3	68.57	5	53.00	-	-	6	47.93	4	59.57	6	57.69
0.32-0.64	0.48	5	67.24	17	91.23	4	88.57	4	75.00	3	73.68	13	66.67	7	74.47	14	84.62
0.64-1.28	0.96	10	84.48	3	93.86	1	82.86	-	-	1	84.42	7	76.8	5	85.11	4	92.31
1.28-2.56	1.92	5	94.74	3	96.49	5	97.06	4	95.00	2	89.47	12	94.2	6	97.87	2	96.15
2.56-5.12	3.84	2	96.49	3	99.12	-	-	-	-	1	94.74	3	98.55	-	-	-	-
5.12-10.24	7.68	1	98.08	1	98.25	-	-	-	-	-	-	-	-	-	-	1	98.08
10.24-20.48	15.36	-	-	-	-	-	-	-	-	-	-	-	-	-	-	-	-

TABLE 4.12 STATISTICAL ANALYSIS OF BLISTER SIZE DISTRIBUTIONS. UNITS mm

STEEL CODE	TOTAL NUMBER OF BLISTERS	% AREA FRACTION	MEAN BLISTER AREA	S.D	LOG-TRANSFORMED DATA SKEWNESS	KURTOSIS
L75	162	4.44	0.24	0.959	2.4	6.18
L9	139	2.06	0.152	0.501	1.35	5.19
L0	31	1.46	0.558	1.41	0.86	3.23
L1	43	3.85	1.072	2.104	0.48	2.44
F75	74	3.08	0.412	1.015	0.29	3.23
F9	21	1.87	0.84	1.162	0.67	1.63
F0	20	3.41	1.545	3.3	0.39	2.98
F1	30	1.85	0.653	0.799	0.00	2.29
K75	57	4.45	0.727	1.242	0.19	2.4
K9	113	3.7	0.41	0.953	0.36	4.34
K0	34	1.64	0.445	0.64	0.2	2.34
K1	19	0.98	0.598	0.696	0.02	2.35
M75	18	1.22	0.623	0.969	0.07	2.53
M9	68	5.24	0.754	0.88	0.00	1.92
M0	46	2.54	0.495	0.651	0.02	1.98
M1	51	2.68	0.51	1.09	0.28	3.74

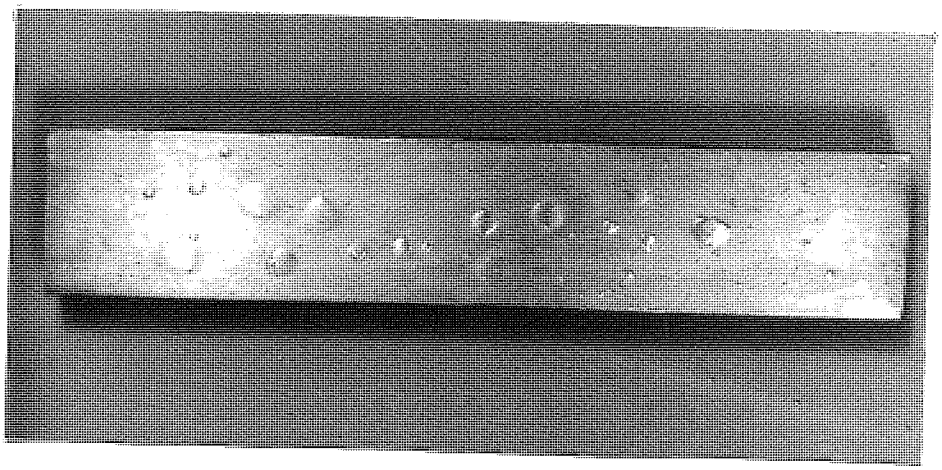

PLATE 90A: Example of typical coupon after immersion in NACE test solution for 96 hours .Appro. actual size .

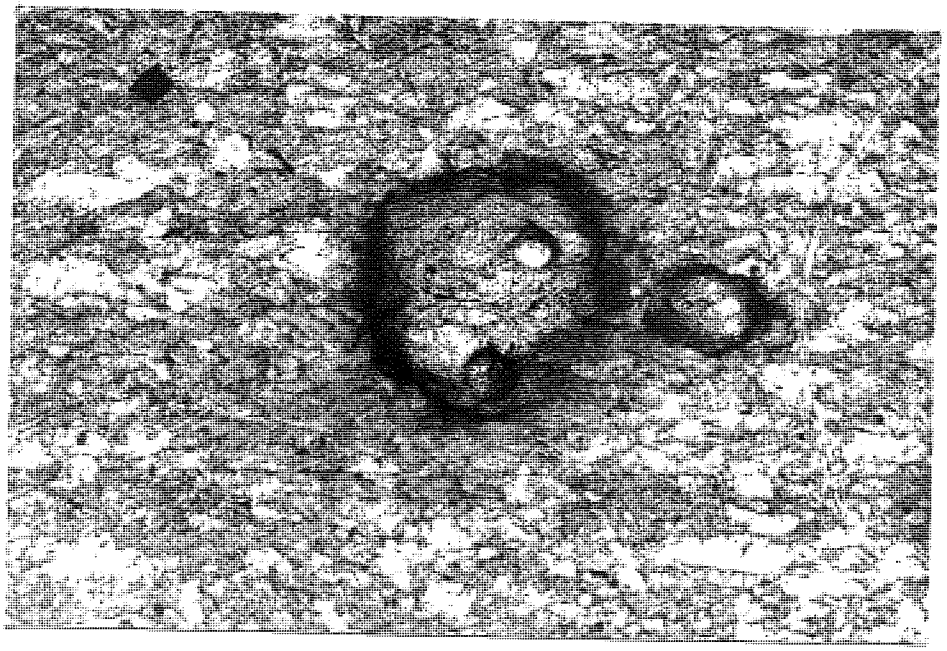

PLATE 90B: Typical example of blisters at higher Mag. (as above) showing smaller blisters which have developed in association with large central blister . Mag.X10 .

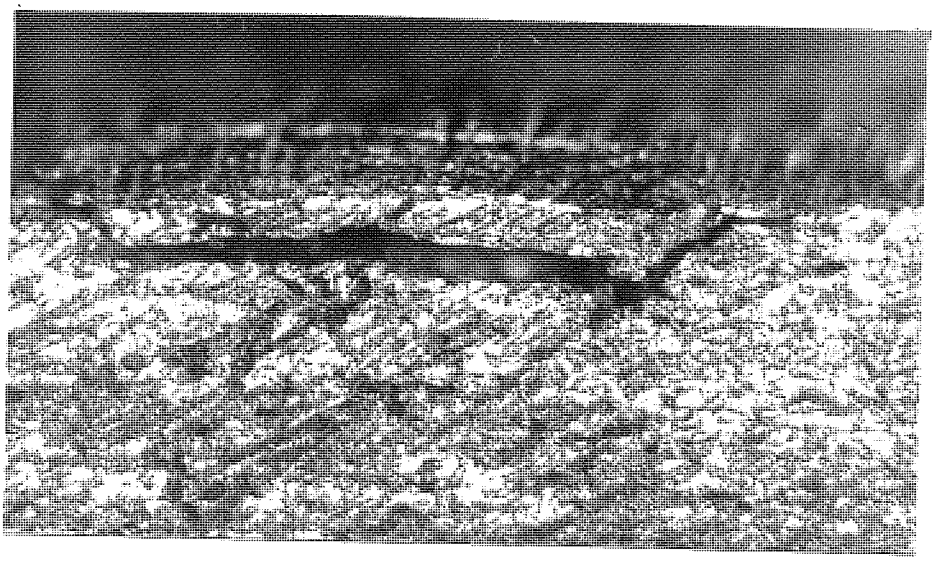

PLATE 91 : Section through blister which developed at the side of a coupon . Mag.X20 .

Plates 92 to 94 typical cleavage fracture surfaces . Steel K rolled at 1100°C and fracture at liquid nitrogen temperature .

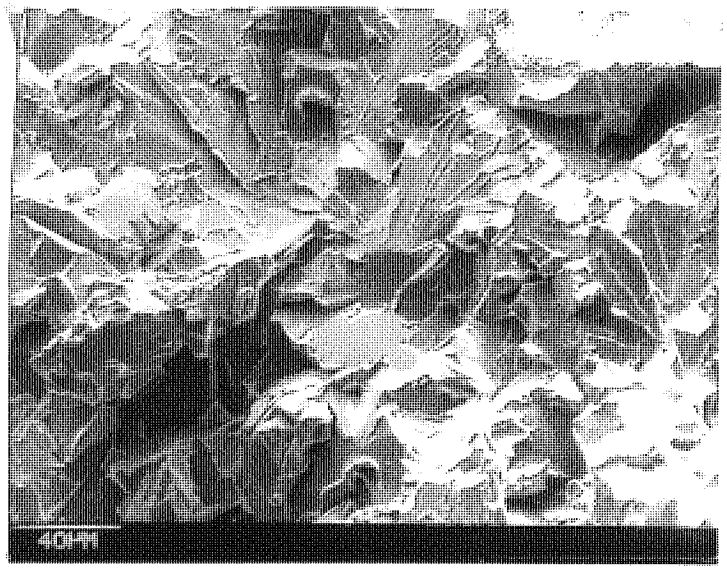

←←←←←←

PLATE 92 :

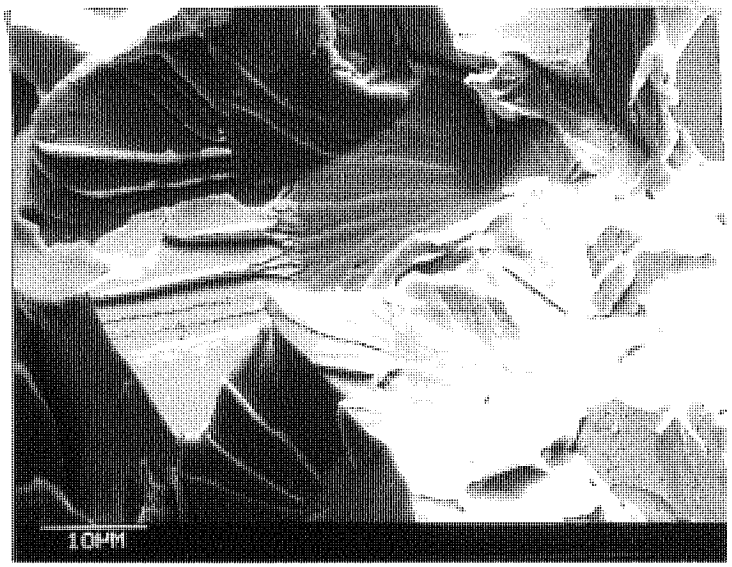

→→→→→→

PLATE 92a:

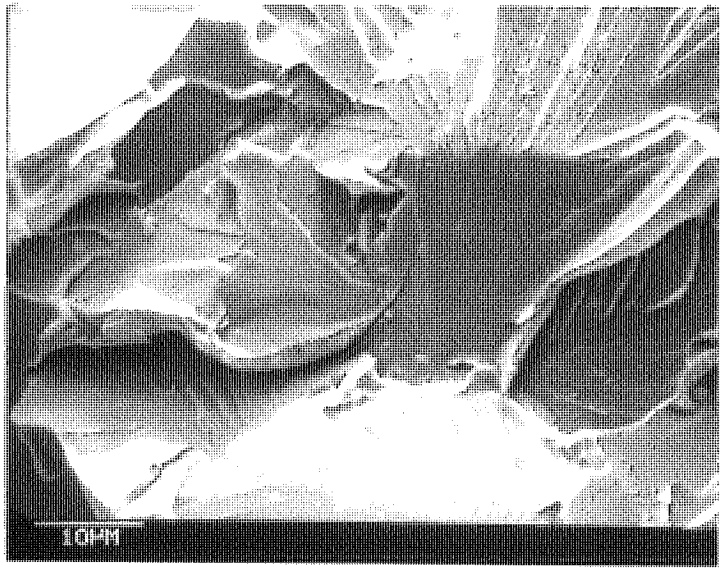

PLATE 93 :

←←←←←

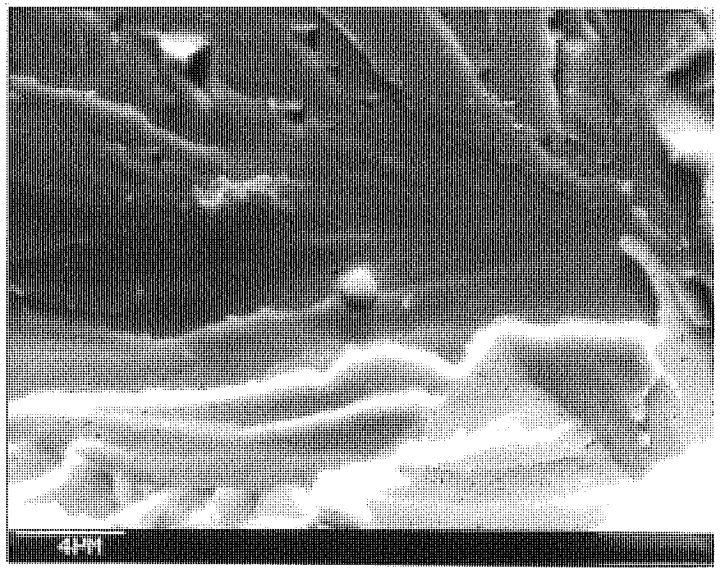

PLATE 94 :

→→→→→

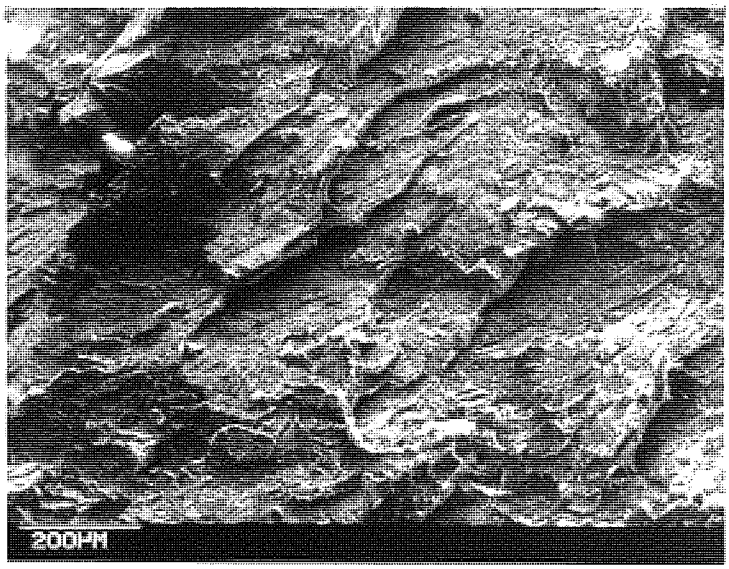

PLATE 95 : SEM fractograph of stepwise cracking .

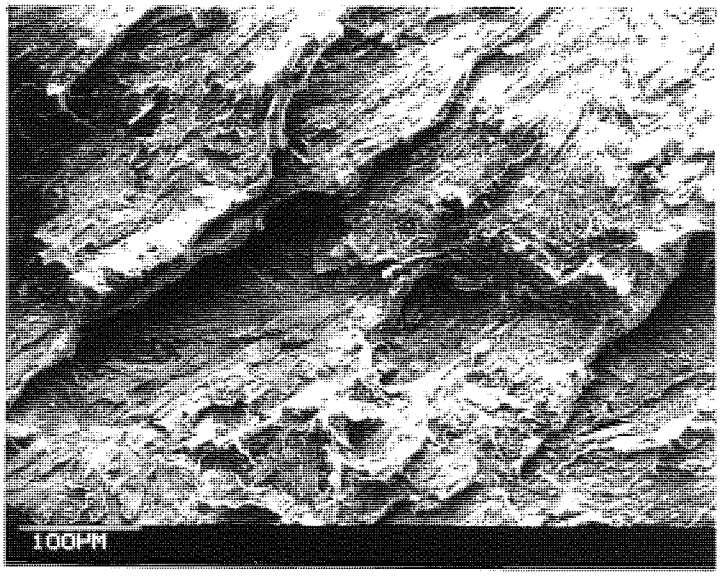

PLATE 96 : Detail of Plate 95 above .

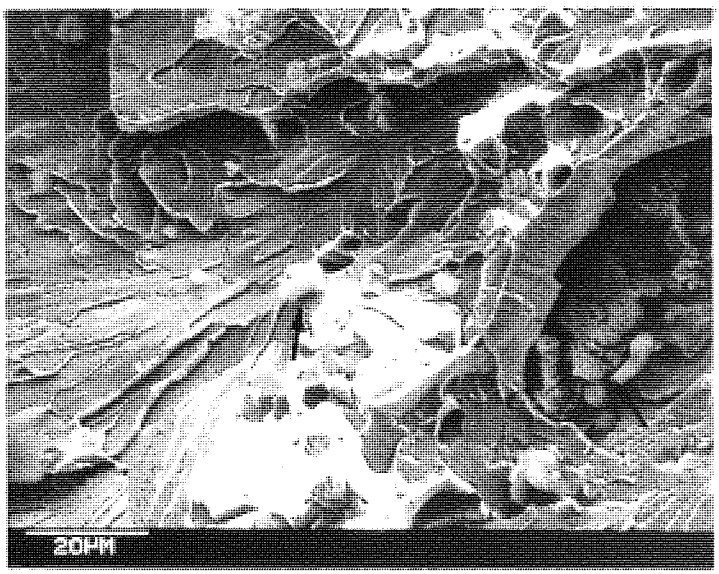

PLATE 97 : Detail of Plate 96 above, inclusion debris situated in cavity at right hand side of photograph →

Plates 95 to 97 steel L rolled at 900^{o}C, immersed for 96 hours in NACE solution and then fractured at liquid nitrogen temperature to reveal fracture surface associated with SWC .

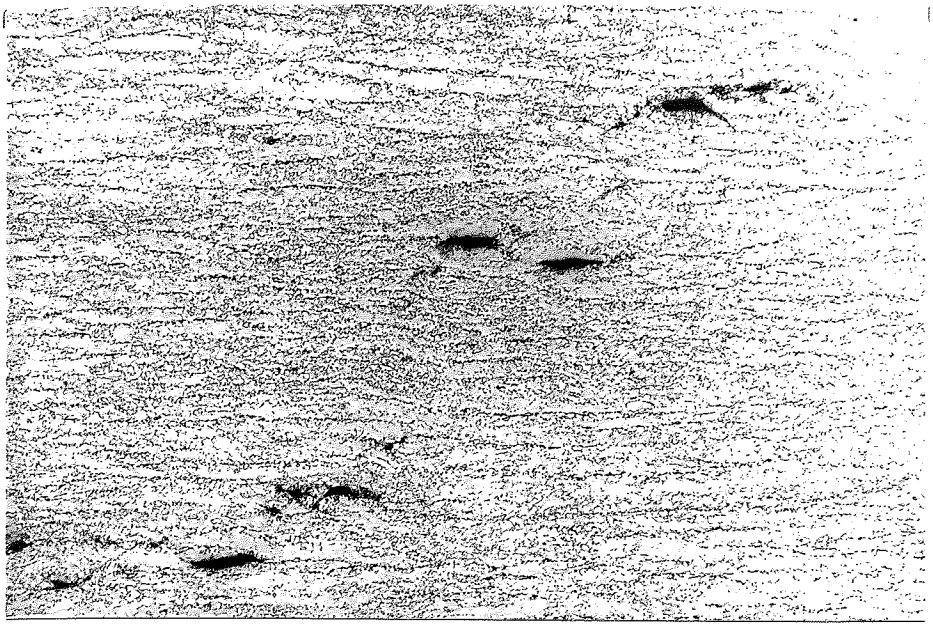

PLATE 98 : Typical example of stepwise cracking . Mag.X42 .

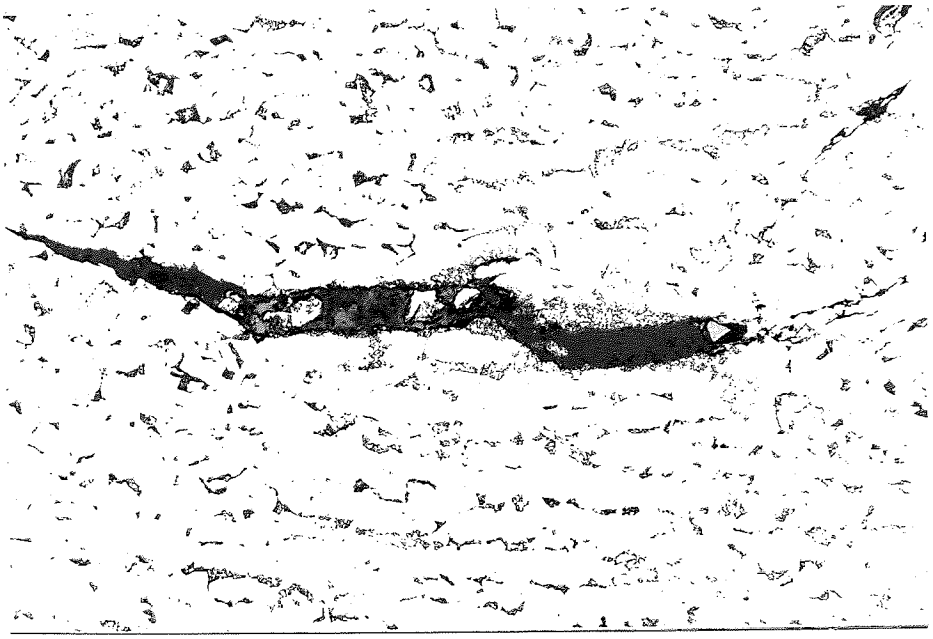

PLATE 99 : Crack associated with large silicate inclusion. .
See Plates 101 to 106 for further detail . Mag.X168 .

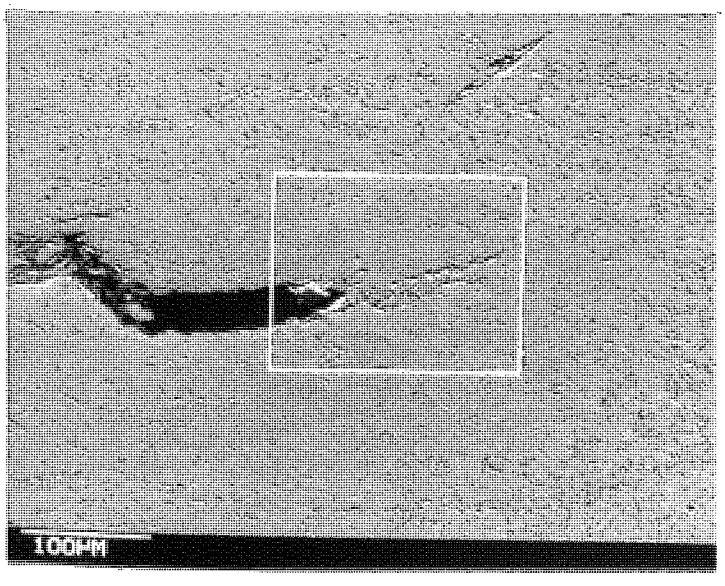

PLATE 100: SEM micro-
graph of Plate 99 above.

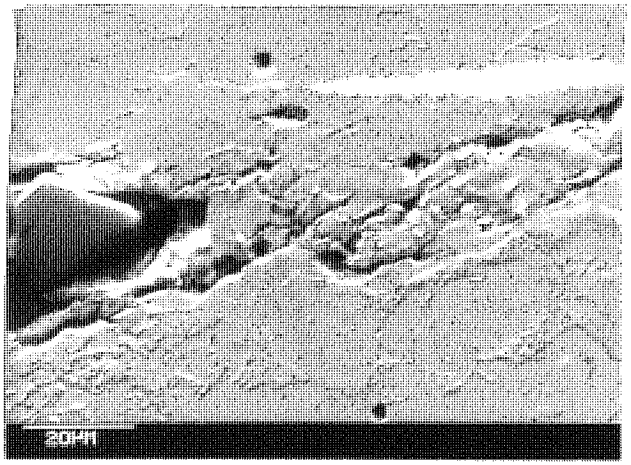

PLATE 101: SEM image of silicate inclusion in stepwise crack .

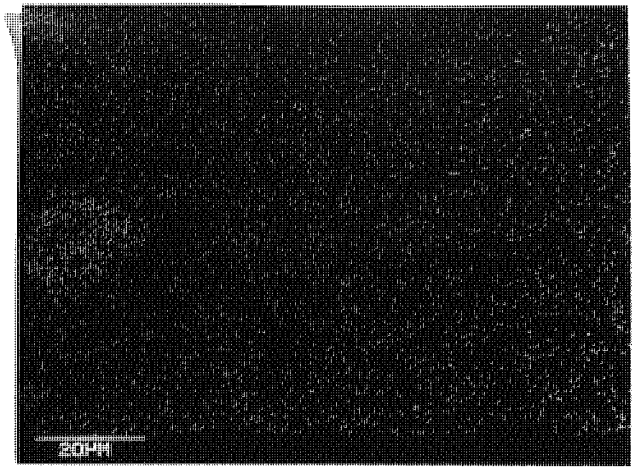

PLATE 102: Al X-ray map .

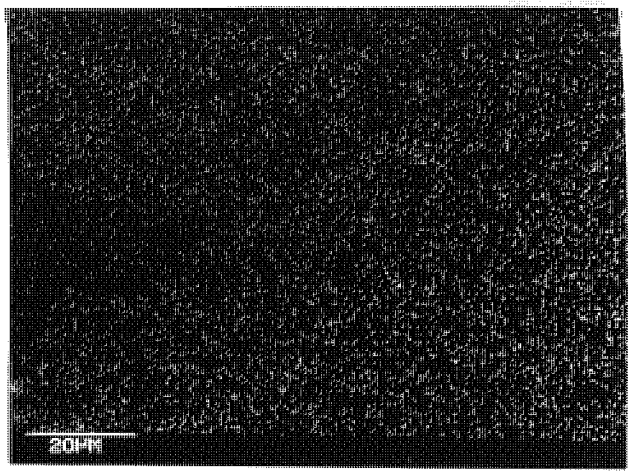

PLATE 103: Mn X-ray map .

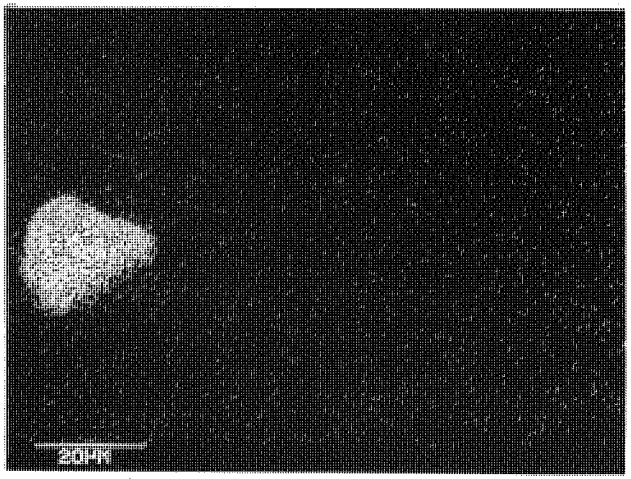

PLATE 104: Si X-ray map .

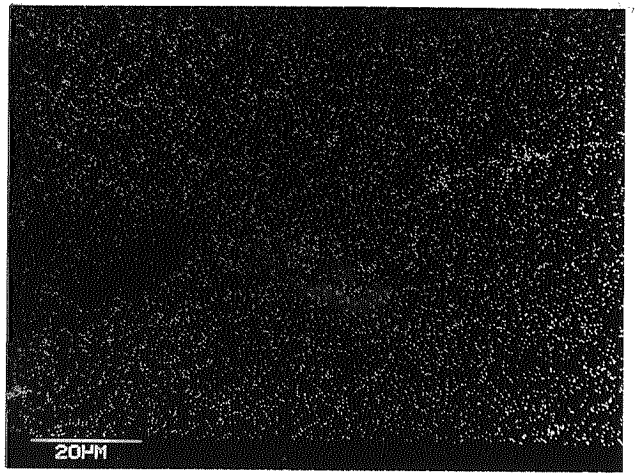

PLATE 105: S X-ray map, note increase of S concentration in front of crack .

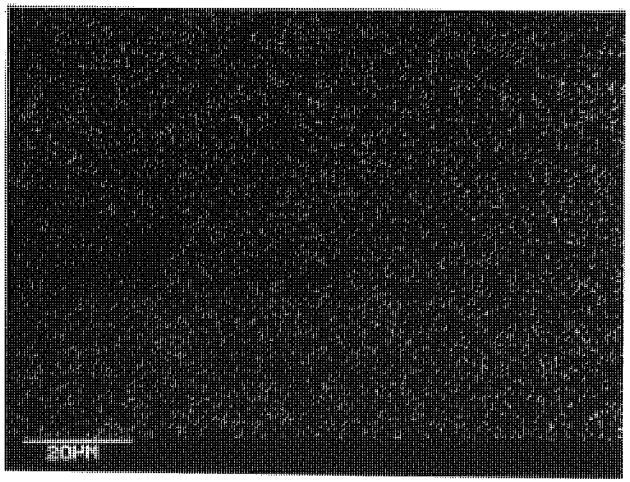

PLATE 106: Ca X-ray map .

Plates 101 to 106 steel K rolled at 1100^{O}C NACE test 96 hours (see also Plates 99 and 100)

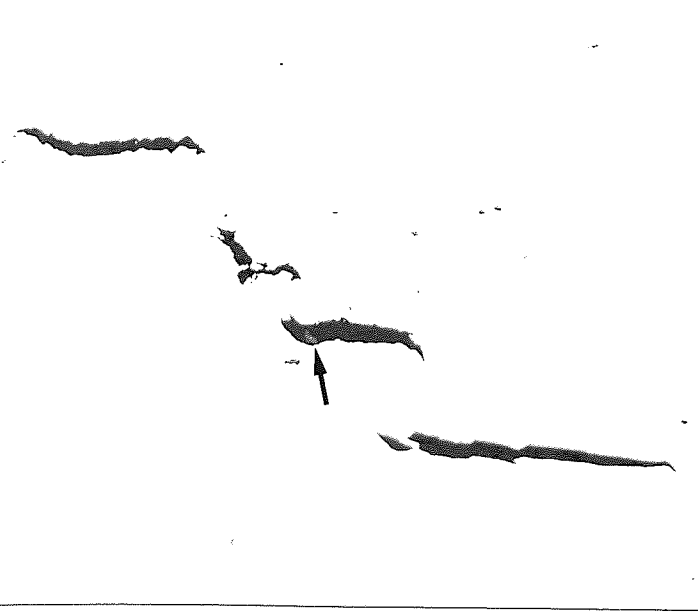

PLATE 107: Typical example of stepwise cracking . Steel F rolled at 750°C NACE test 96 hours as polished . Mag.X270 .

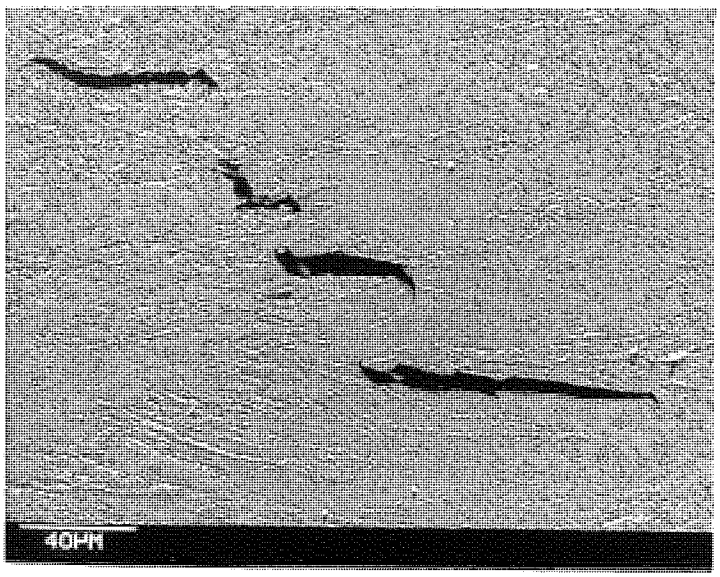

PLATE 108: SEM micrograph of Plate 107 above . Nital etch .

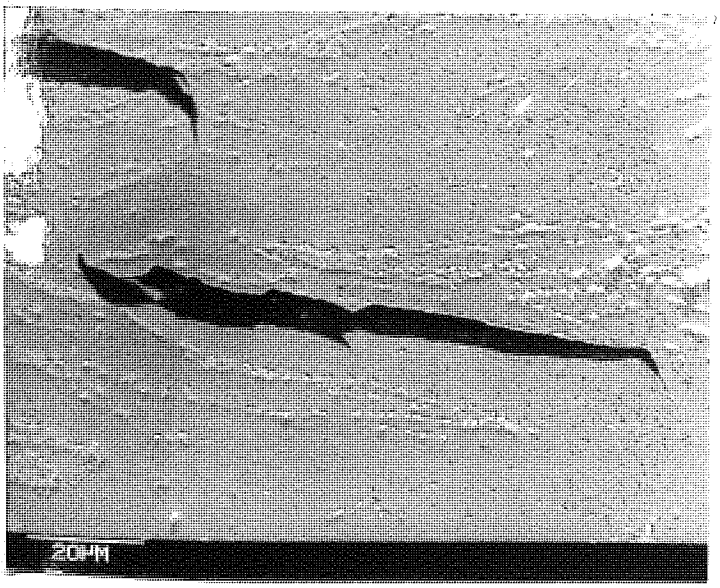

PLATE 109: Detail of Plate 108 above .

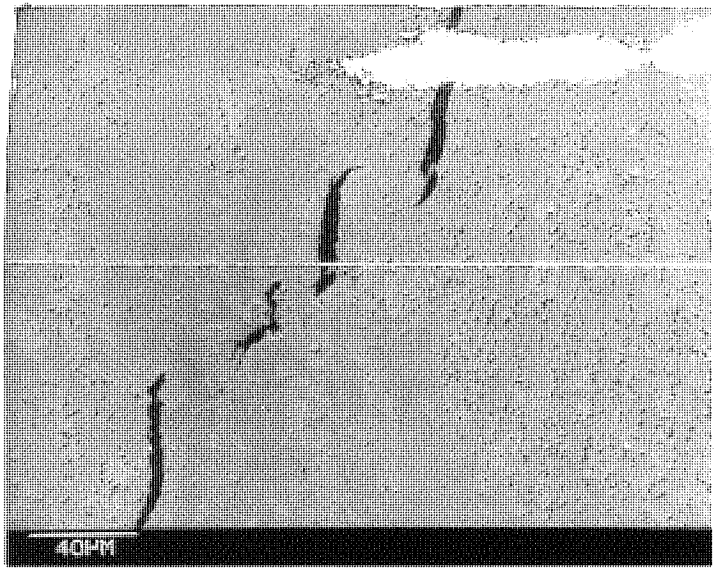

Plates 110 to 113 X-ray line scans (scan line shown on plate 109) across area of stepwise cracking, see Plates 107 to 109 for further details . Mn and S peaks coincide with MnS inclusion visible just below scan line .

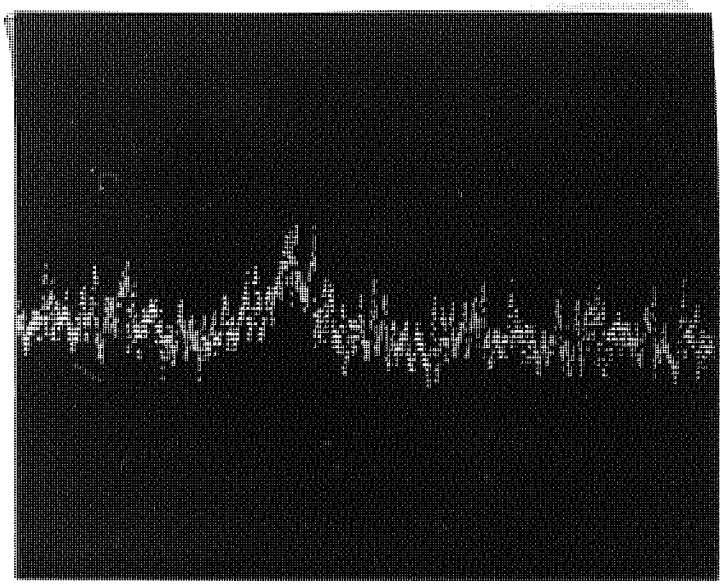

←←←←←←

PLATE 110: SEM micrograph of SWC .

→→→→→→

PLATE 111: S X-ray line scan.

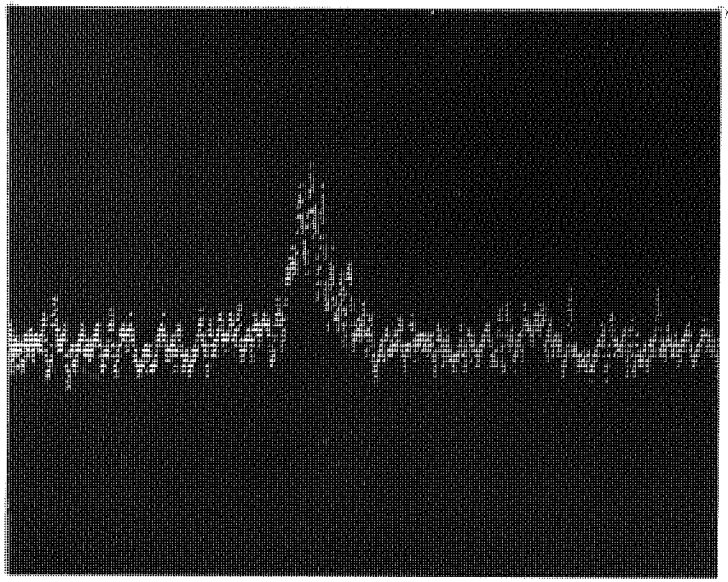

←←←←←←

PLATE 112: Mn X-ray line scan .

PLATE 113: P X-ray line scan .

→→→→→→

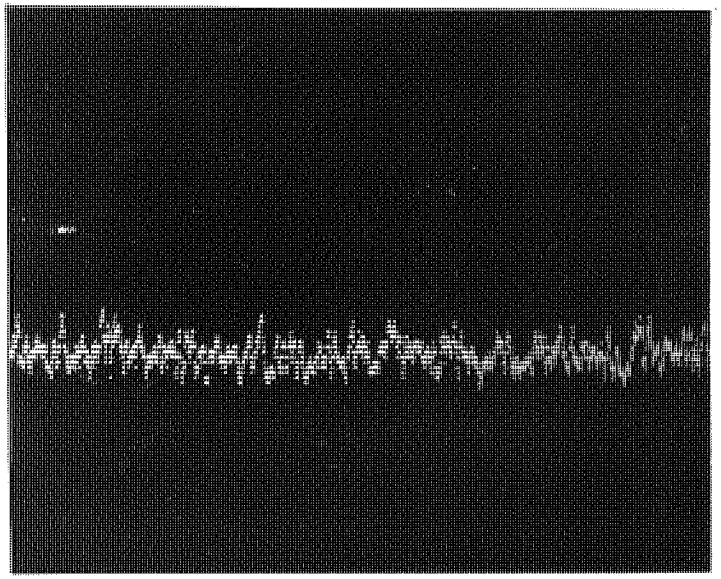

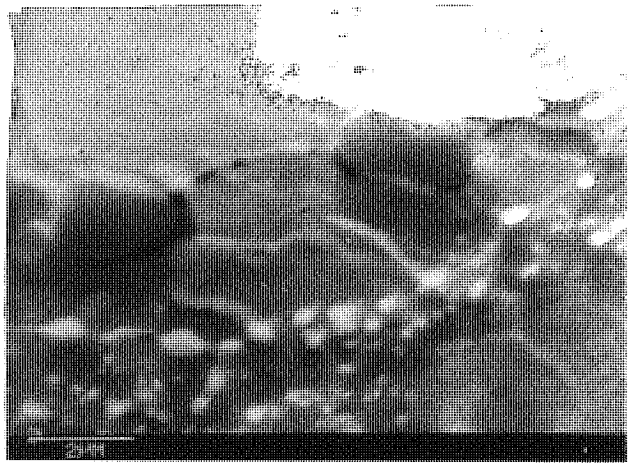

PLATE 114: SEM micrograph of decohesion at inclusions after NACE test .

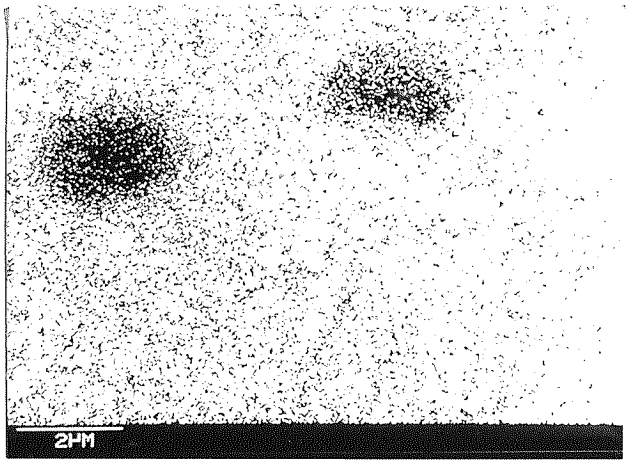

PLATE 115: Fe X-ray map .

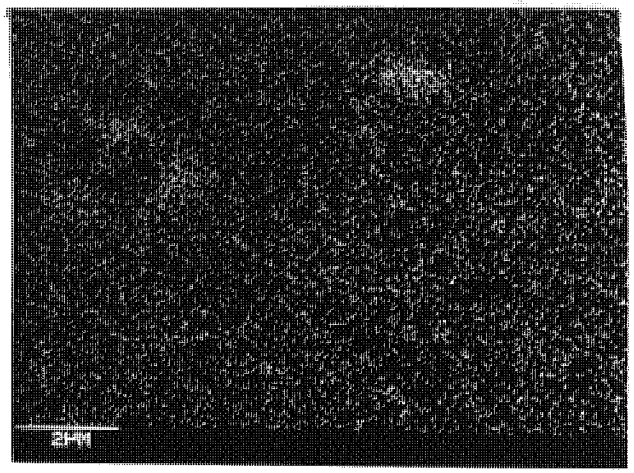

PLATE 116: Mn X-ray map .

Plates 114 to 118 two closely associated alumina inclusions and trace of MnS which are partly decohesed and crack running along sub-grain boundary between them . Steel F rolled at 700^{O}C NACE test 96 hours nital etch .

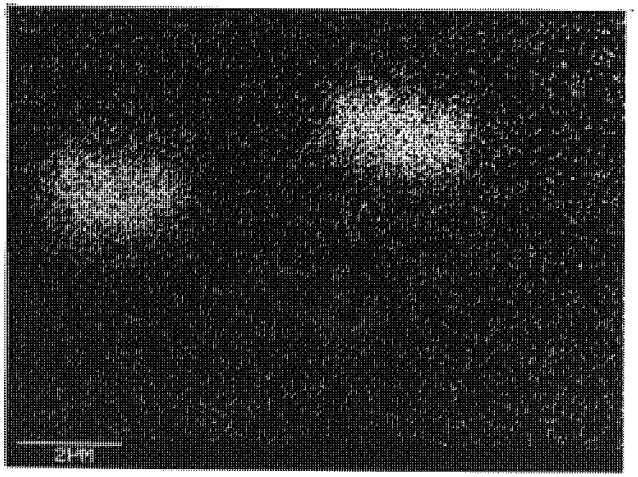

PLATE 117: Al X-ray map .

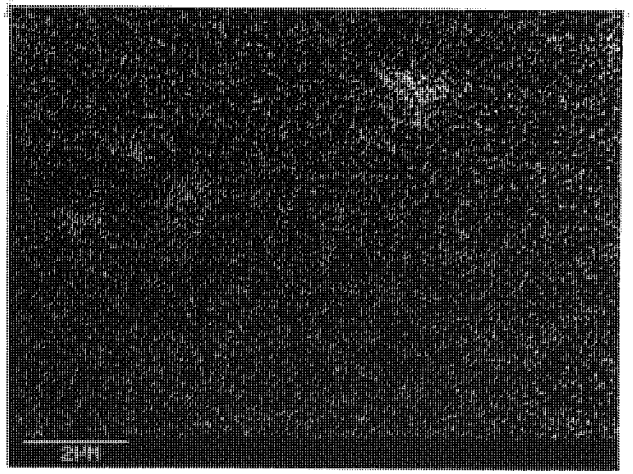

PLATE 118: S X-ray map .

5.0 DISCUSSION OF RESULTS

5.1 INTRODUCTION TO DISCUSSION OF RESULTS

The purpose of this investigation was to identify the role of non-metallic inclusions in the process of stepwise cracking (SWC). To achieve this a study was designed which compared the resistance of a number of steels, with different inclusion characteristics, to SWC. The steelmaking process was envisaged to be the stage which would have the greatest influence over inclusions. The control of the physical and chemical conditions within the molten steel determined these characteristics in the cast ingot and subsequently, the inclusions resistance to deformation during hot rolling.

The initial observations in this discussion are, therefore, directed at characterising the inclusions in the four ingots produced for experimentation. The effectiveness of steelmaking is considered and its influence upon steel cleanness, inclusion size distribution and morphology.

Subsequently, the effect of hot rolling upon the inclusion (and steel microstructure) is examined. Specifically to identify if this has altered the inclusion characteristics from their as-cast condition.

Further discussion is then aimed at identifying the influence of inclusions upon tensile ductility and correlating inclusion parameters with fracture strain. This was carried out in order to provide a reference point for discussing the influence of inclusions and hydrogen upon ductility.

An attempt is then made to correlate SWC with the inclusion parameters found to describe ductile fracture and a discussion of the factors causing SWC is undertaken.

Finally the implications of steelmaking and thermo-mechanical treatments upon linepipe steels is considered in the light of the above comments with the objective of identifying how SWC may be reduced through inclusion control.

5.2 PRODUCTION OF CAST INGOTS

5.2.0 FACTORS AFFECTING MELTING AND INCLUSION CONTROL

5.2.1 MELT OUT

Probably one of the most significant features of induction melting is the electromagnetic stirring produced in the melt (the intensity of which is determined by the frequency and power supplied to the coils). In fact, induction facilities are incorporated in some commercial ladle systems (ASEA-SKF(57)) to produce this effect, as it offers the opportunity to stir the melt in either vacuum or a controlled atmosphere.

The advantages of such a system are several; compositional and temperature gradients are reduced, alloy additions are quickly and effectively incorporated into the melt and, of more importance to this study, the formation and separation of primary inclusions is promoted(64, 68). In general the melt is effectively homogenised and "cleansed" through stirring.

The furnace used in this investigation was rated at 3kHz with a power capability of 60kW which at full power created an intense stirring in the melt. This, unfortunately, led to problems during melt-out, i.e. bridge formation (see Section 3.1.1, Page 113).Tilting the furnace, which was necessary to remove the bridge, produced a large surface area of intensely stirred hot metal which could react with air (oxygen) aspirated

through the open top of the furnace (a complete argon atmosphere could not be maintained during this activity) resulting in oxidation. The extent to which this occurred was unpredictable, i.e. the soluble oxygen content of the melt could not be measured before deoxidation and this caused the variations in the amount of aluminium (Al) consumed during deoxidation and the steel compositions that are discussed below.

5.2.2 DEOXIDATION AND THE REMOVAL OF PRIMARY INCLUSIONS

Deoxidation was carried out immediately after melt-out and, although the residual Al levels in the cast steels, Table 4.2(Page143), were found difficult to control, the quantities were sufficient in all melts to ensure that the steels were fully killed. According to PALMAERS et al (32) if the soluble Al content exceeds 0.008% then pure Al_2O_3 inclusions will occur in molten steel.

The effectiveness of deoxidation, despite the problems at melt-out was good, and the steels produced had low total oxygen levels (Table 4.2) (the total oxygen level may be considered equivalent to the oxygen combined as oxide inclusions i.e. the soluble oxygen contents of the steels at these levels of residual Al are negligible (4)), and would, therefore, be classified as "clean" in terms of oxide inclusions for this type of steel (9).

Upon deoxidation, the power supply to the furnace was reduced to 25kW in order to maintain the melt temperature at 1600°C, this also had the effect of reducing the stirring intensity. Nevertheless, it was still sufficiently strong to remove any reaction products i.e. primary oxides which emerged at the surface of the melt to the sides of the crucible. Consequently, this meant that the surface of the melt was always in contact with the furnace atmosphere and not, as in the majority of steel-

making situations, covered by a slag. It was believed, however, that during this stage of the melting the argon introduced into the furnace chamber to protect the melt from aspirated air was far more effective, resulting in little reoxidation (the furnace was at that time completely sealed).

Because of this situation, i.e. no slag formation, the only means by which primary inclusions could be removed from the melt was by separation to the crucible walls and this appeared to occur. Inspection of the crucibles, after casting, found a build-up of material sintered to the walls just below the melt line, which thinned out towards the base of the crucible. Evidently this build up of material was caused by the accumulation of deoxidation products (and desulphurisation products for steels K and M) which had separated from the melt.

To obtain an indication of how much Al_2O_3 formed in the molten steel and was subsequently separated to the crucible walls (considering only steels L and F, as steels K and M were Ca treated, which altered the chemistry as well as the physical conditions within the molten steel (Section 5.2.3)) it is possible to estimate the volume fraction of Al_2O_3 produced assuming that the Al consumed during deoxidation was all oxidised in the melt and then separated to the crucible walls viz:

STEEL L Al consumed during deoxidation is the difference between the amount added and the residual level remaining in the melt = 0.143%. This combines with $0.161\%O_2$ to form alumina, i.e. 0.143 x 54/48, ratio of Al to O_2 in Al_2O_3.

The volume fraction of Al_2O_3 formed with $0.161\%O_2$ may then be estimated as follows (21):

$$O_2 wt\% = \frac{MO}{MI} \times \frac{di}{dm} \times Vv(\%) \quad \ldots (1)$$

where: MO = weight of oxygen in a mole of inclusion

MI = molar weight of inclusion

di = inclusion density - Al_2O_3 = 3.96 (19)

dm = matrix density - Fe = 8.87

Vv(%) = volume fraction of oxide

Rearranging Eq.1 above gives:

$$Vv(\%) = wt\%O_2 \times \frac{MI}{MO} \times \frac{dm}{di} \quad \ldots (2)$$

hence the amount of alumina produced in steel L was approximately 0.68% by volume. A similar calculation for steel F (Al consumed = 0.2%) gives a volume fraction of Al_2O_3 of 0.95%.

It is interesting to note that the oxygen consumed in producing Al_2O_3 i.e. steel L = 0.161% and steel F = 0.225% is approaching that found in equilibrium with liquid iron at 1600°C i.e. 0.23% $\underline{O}$ (21), and this does not account for any $\underline{O}$ which may have reacted with carbon and was thus permanently removed from the melt as carbon monoxide, which emphasises further the large amount of oxidation which occurred during melt-out.

The calculations above give some idea of the substantial amount of primary oxide produced during deoxidation, nearly 1% by volume in steel F and the effectiveness of stirring (the time between deoxidation and casting was only 4 minutes) in removing inclusions from the melt and hence, why deposits were clearly visible upon the crucible wall.

The fact that the major proportion of deposited material was just below the melt line suggests that the inclusions in the melt and those which emerged at the surface are brought into contact with the crucible wall at this position primarily as a result of the stirring pattern produced in the molten steel (see Fig.58a, Page 112, Ref. 225).

The physical separation of inclusions from liquid steels has been shown by several workers (16, 18, 81) to be strongly influenced by the interfacial forces between the melt and the inclusion phase. Conditions favouring the emergence of inclusions at the surface of the melt and removal by attachment to refractory surfaces (as well as inclusion growth by collisions) are:

(i) a high interfacial tension between the melt and inclusions γ_{sm};

(ii) a high melt surface tension γ_m, and

(iii) a low inclusion surface tension γ_s.

More generally these factors influence the contact angle between the inclusion phase and the melt (see Fig.21, Page 42), an angle of $> 90^{o}$ favouring adhesion between contacting inclusions, between inclusions and refractory and the emergence of inclusions at the metal/gas interface.

Investigations have shown that the contact angle between Al_2O_3 and liquid iron is about 140^{o}(80) and studies have found that Al_2O_3 inclusions readily agglomerate and adhere to the sides of Al_2O_3 crucibles (62, 63, 78) particularly when the melt is agitated (68), which was the situation in this study. In addition the soluble oxygen levels

produced by deoxidation will have increased the surface tension of the melt γm (see above) further encouraging inclusion separation (see Fig.20, Page 36).

Other factors controlling deoxidation and inclusion separation, particularly deoxidant solution and inclusion nucleation, were difficult to analyse systematically due to the dynamic conditions within the melt. However, in accordance with opinions expressed in the literature (20, 66, 73, 77) stirring has proved beneficial to the steel cleanliness, and these stages do not appear to have limited the formation and separation of primary inclusions in the steels investigated.

5.2.3 CALCIUM SILICIDE INJECTION

Calcium silicide injection was undertaken in steels K and M to reduce the volume fraction and alter the morphology of MnS inclusions. This was successfully achieved (Plates 5, 6, (Page 148), 7, (Page 160) and Tables 4.2, (Page 143), 4.3, (Page 159) and D17 (Appendix D)).

The ability of Ca to desulphurise fully killed steel has been well documented in the literature over recent years (6, 24, 36, 39, 55, 56, 57, 58) a low soluble oxygen level being a pre-requisite (thermodynamically) for effective desulphurisation. It is evident in this study that the levels of soluble oxygen in both melts K and M were sufficiently low to allow desulphurisation to occur (Table 4.2, Page 143).

A calculation based upon the equilibrium constant for the reaction

$(CaO) + \underline{S} = (CaS) + \underline{O}$ can be used to determine the soluble oxygen levels required to achieve the sulphur levels which resulted in steels K (0.01%S) and M(0.004%S) (59) viz:

$$\log K = \frac{-5150}{T} + 1.191 = \frac{a\underline{O}}{a\underline{S}}$$

For steel M it is 1.1ppm and steel K equals 2.8ppm of oxygen. However, if the level of Al necessary to obtain these oxygen levels (using the equilibrium constant given in Table 2.1, Page 16) is calculated the result is 0.074% Al for steel K and 0.3% Al for steel M, and it can be seen that the actual Al levels in steels K (0.046%Al) and M (0.08% Al) were insufficient. The fact that such low sulphur levels were produced may be explained as follows;

Upon the addition of Ca to an Al killed steel calcium aluminate phases are produced (e.g. 18,. 24, 31, 36, 37) and it has been shown that the net effect of this reaction is to lower the soluble $\underline{O}$ level. This has been found to occur as a result of the formation of a mixed oxide (AlCaO) which has a lower activity in comparison to equivalent amounts of either CaO or Al_2O_3 existing separately (see Fig.6, Page 19)(18, 25, 53, 85). Such mixed phases were found in both steels K and M (Table 4.3, Page 159) and this explains why low sulphur levels resulted.

The above explanation also indicates why a larger amount (relatively) of S was removed from steel K (50% ≡ 0.01% total) compared to steel M (40% ≡0.006% total). As more Ca was consumed in steel M in forming calcium aluminate phases sufficient to reduce the soluble $\underline{O}$ to a level low enough to allow a final S content of 0.004%, i.e. 1.1ppm for steel M compared with 2.8ppm for steel K.

The lower % volume fraction of inclusions (increased deoxidation and desulphurisation) in steels K and M compared to steels L and F shows the effectiveness of the Ca injection process in aiding the elimination of inclusions from these steels. In addition to the comments made for primary deoxidation (Section 5.2.2) the following factors will have influenced inclusion elimination in these steels;

Firstly, calcium in liquid iron at 1600°C reduces the solubility of both oxygen and sulphur resulting in the precipitation of oxides, sulphides and/or oxysulphides in the melt (24, 31, 37, 39, 76). Secondly, as previously discussed the surface tension of liquid iron increases with a decrease in the level of soluble oxygen, this will have been further increased in steels K and M because both the soluble $\underline{O}$ and $\underline{S}$ will have been reduced as a result of Ca treatment, $\underline{S}$ having a similar effect upon the surface tension of iron as oxygen (see Fig.2[illegible], Page 36). Thirdly, the stirring intensity in the melt will have been further increased (under full argon protection) as a result of argon injection and violent Ca vaporisation.

This combination of factors will have contributed to the improved "cleanness" of steels K and M compared to steels L and F; Inclusions forming in the melt will have had a greater opportunity to escape, hence the lower %volume fraction of inclusions in steels K and M (see Table D17). The increase in the surface tension of the melt will have encouraged the attachment of inclusions to the refractory crucible walls, to each other and to emerge at the surface and hence to separate, i.e. by an increase in contact angle. This implies that the contact angle of the sulphide phases produced in steels M and K was sufficiently high to allow effective separation from the melt i.e. similar to alumina. Finally, the increased stirring intensity and the possibility of inclusions

becoming attached to rising gas bubbles (argon and calcium vapour) will have promoted collisions and the rise of inclusions to the surface of the melt, by flotation, again assisting separation. Similar observations to these have been made by other authors investigating calcium silicide injection of Al killed steels(24, 31, 37), and the results of this study show clearly that the process creates very favourable physical and chemical conditions in the melt for inclusion control.

5.2.4 STEEL COMPOSITIONS

The steel compositions aimed for in this study were chosen to reflect the composition of the segregated zones found in commercially produced ingots. This approach was adopted as previous investigators(114, 123) who had studied SWC in steel plates manufactured from small laboratory melts discovered that their resistance to SWC was surprisingly good. These results were believed to be due to the reduced segregation of both alloying elements and inclusions which occurred in the small ingots.

From the results of the chemical analysis of the cast ingots (Table 4.1) and steel plates (Table 4.2) it can be seen that variations between the proposed and actual steel compositions have occurred. This has arisen primarily through the problems associated with melt-out, i.e. bridge formation (reported in Section 3.1.1 and initially discussed in Section 5.2.1) and a significant variation between steel compositions has occurred particularly for the strong deoxidising elements carbon (C) and Al. The cause of these variations, however, may be simply explained.

During melt-out the furnace was tilted in order to melt through the bridge, whilst this operation was carried out it was not possible to maintain an argon atmosphere, hence any aspirated air caused oxidation. The extent of oxidation was then dependent upon the time required to melt

through the bridge and completely melt-out all the steel charge. As oxidation progressed the elements with a high affinity for oxygen reacted to form their respective oxides, in the order Al, C, Si, Mn and finally Fe (see Fig.4, Page 12). From the compositions of the charge material (Section 3.1.1., Page 113) it can be seen that the Al content was negligible (0.001%). Therefore, the original Al would have been consumed by oxidation quickly, further $\underline{O}$ would have then resulted in the melt, producing CO and permanently removing C from the steel. However, oxidation of Si, Mn or Fe would not necessarily result in a total loss of these elements as upon Al deoxidation their oxides would be reduced by Al, returning Si, Mn and Fe to the melt.

Under these variable conditions the extent of oxidation could not be determined. The amount of C lost during melt-out could not be compensated for accurately by an alloy addition after deoxidation and similarly the amount of Al necessary for deoxidation (leaving 0.04% as residual) could not be evaluated. The result is that steels L, K and M have C contents of 0.08%, 0.08% and 0.13% respectively, whereas the level aimed for was 0.1%C and steels F, L and M have Al contents of 0.02%, 0.08% and 0.08% when the level aimed for was 0.04% (Table 4.2, Page 143).

Consequently, the microstructures of the four steels produced are dissimilar (see Table 4.4 (Page 167) and Plates 9 to 14 (Pages 164 to 166)) at comparable rolling temperatures, which has meant that the properties of the steels (ductility and SWC resistance) cannot be evaluated purely in terms of differences in inclusion characteristics. This has complicated the interpretation of results.

It is noted that variations in matrix composition from one part of an ingot to another (Table 4.2) are not significantly different, i.e. macro

segregation appears to have been absent probably as a result of rapid solidification.

5.3 INCLUSIONS IN THE AS-CAST INGOTS

5.3.0 SIZE DISTRIBUTION

A common factor for all four ingots was that the majority of inclusions observed were less than 10 μm in size, (Tables D1 to D4, Appendix D). Before examining the inclusion size distributions on an individual ingot basis a number of general points are germane to explaining this result.

1 Generally, the larger inclusions found in commercially cast ingots are from a primary source(89) (exluding exogenous inclusions), these can often be identified by their composition e.g. Al_2O_3 inclusions in Al-killed steels(24). The number of such inclusions which become entrapped in solidified ingots is determined by the success of separation operations, e.g. argon stirring during ladle steelmaking, after which any large inclusions which are carried over during casting can only separate whilst the steel is still molten. Examination of Figs.68 to 71(Pages 150 and 151) reveals that no inclusions greater than 20μm in diameter were observed in any of the ingots and Fig.72(Page152), which is the data from the mid-section of each ingot plotted on log- normal probability paper (the fit to which is given in Table D5 in Appendix D) shows that only 1% of inclusions observed were greater than 10μm and about 8% greater than 5μm. These results further emphasise the effectiveness of primary inclusion separation in all four steels which was discussed in the previous Sections.

2 Solidification - As the ingots produced were small, solidification was fairly rapid (even though the ingot moulds were pre-heated) and

this has inhibited the formation and growth of secondary and tertiary inclusions. Upon casting several factors will have affected the final size distribution of inclusions in the solidified steel. These are:

(i) the size and number of primary inclusions carried over

(ii) the level of soluble oxygen and sulphur in the melt prior to casting

(iii) reoxidation

(iv) the solubility of oxygen and sulphur (and other elements notably Mn)

(v) the rate of solidification

These factors will have interacted dynamically during solidification and effectively influenced the availability of reactive elements capable of forming inclusions and/or promoting inclusion growth. Because the decrease in temperature during solidification was rapid, macrosegregation (Section 5.2.4) was practically absent (unlike in industrial practice (24, 31, 38)) and thus rejection of elements from the solidification front would be restricted, homogenising the composition of the ingots. Microsegregation, i.e. interdendritic probably did occur, the type II MnS networks occurring in steels L and F are evidence (Plates 3 and 4, Page 148). However, these were not always inter-connected as shown in Plate 16(Page 186) which again indicates that solidification was rapid. The mechanisms by which secondary and tertiary inclusions could have formed was either by homogeneous nucleation or, more likely, heterogeneously on existing primary inclusions (Plates 4 and 6). Whichever mechanism occurred, the potential for growth would be greatly reduced as the rapid solidification would restrict movement of nuclei in the melt

and hence the possibility of growth by collision and also, as a result of limited segregation, diffusional growth would be dependent upon the concentration of reacting elements surrounding the nucleated inclusion. In any case previous evidence has found that inclusion growth by diffusion adds little to inclusion size beyond 2μm(68, 77). These factors explain why the inclusion size range was small in all the ingots analysed regardless of the inclusion composition.

3 Shape - Inclusion size distribution was measured by maximum horizontal chord. This method only measures the inclusion dimension horizontally at its maximum cross-section at the given orientation of the specimen. In the as-cast steels specimen orientation was chosen arbitrarily as no directionality was observed. For steels L and F which contained Type II MnS inclusions the results may be in error as it is well documented that the morphology of such inclusions is not represented accurately by polished micro-sections(109, 128, 173). The network-like morphology of this phase appearing as a collection of closely associated small inclusions on a planar section (see above). The number of small inclusions therefore was probably overestimated and the number of large inclusions underestimated. Furthermore, it was assumed that inclusions were spherical in shape which was not always the case in steels L and F (Plates 3, 4 and 8, Pages 148 and 161). The random orientation of the section used for measurement may have averaged this effect out to some extent, certainly in steels K and M where the majority of inclusions were spherical little error would be introduced (Plates 5 and 6, Page 148).It is encouraging however, that the % area fraction of inclusions calculated, assuming that they were all spherical in shape, are in fair agreement with % area fractions in the rolled

materials, which were measured directly by image analysis (compare Tables D1 to D4 to D17 in Appendix D).

In comparing the inclusion size distributions for the four ingots (Figs.68 to 71, Pages 150 and 151), the immediate difference between each can be seen to be one of scale. These distributions follow a similar pattern, but the number of inclusions observed in each size range decreases in the order L, F, K and M. Taking into account the previous general comments it appears that decreases in the S and O levels are reflected by a decrease in the number of inclusions in each size group regardless of inclusion composition. The probability of finding a large inclusion in a steel with a low S and O content is therefore expected to be less than a steel with a higher S and O content and this appears to be the case (see Fig.72(Page 152) and compare steel M with L).

What this does not show, but which is clear from inspection of the polished microsections (Plates 3 to 6), is that in steels L and F inclusions were often more closely associated in clusters (Type II MnS) whereas in steels K and M there is an even dispersion.

The more homogeneous dispersion of inclusions in steels K and M has resulted from calcium treatment. Apart from reducing the bulk S and O levels the effect of Ca (in conjunction with Al) in solution is to lower the solubility of S and O in the steel at a given temperature compared to a similar steel without Ca. Hence, inclusions form at an earlier stage (note their spherical shape which is indicative of formation in the molten state) and the removal of oxygen and sulphur from the melt at this time means that there is then less opportunity for segregation of these elements which in steels that have not been Ca treated (L and F) would

otherwise lead to the formation of inclusions from the last liquid to solidfy, producing a heterogeneous dispersion.

5.3.1 INCLUSION COMPOSITION AND MORPHOLOGY

Consistent with previous studies of Al-killed steels the inclusions in casts L and F were Type II MnS and Al_2O_3(24, 36, 37). The effect of Ca treatment, in steels K and M, has been to alter the morphology of the Type II MnS networks as observed above and has also prevented the formation of angular Al_2O_3 inclusions, the majority of inclusions observed being spherical.

In steels L and F three distinct inclusion types were identifiable (Table 4.3, Page 159):

(i) alumina rich

(ii) containing alumina, sulphur and manganese, i.e. 2-phase, MnS precipitated upon primary Al_2O_3; and

(iii) manganese sulphides.

The normalised ratios of the three phases given in Table 4.3 show that they were present in very similar proportions in both steels.

The inclusions in steels K and M contained varying degrees of calcium, (Tables D8 and D9 in Appendix D) only a small proportion of the inclusions observed contained no calcium, i.e. 6%. It is clear that for steel K complete inclusion shape control was not achieved, evidence for this is shown in Plates 38 and 39(Page 211) and is discussed further in Section 5.5 "Deformation of Inclusions During Hot Rolling". Whereas for steel M which, on average, had a 10% higher Ca content than steel K complete inclusion shape control was produced (see Section 5.5 and 5.6).

It has been reported in the literature(50) that for low alloy steels, the control of sulphides begins when the ratio of Ca/S in the steel exceeds 0.8. In this study the ratio of Ca/S in steel K was 0.37 and steel M 0.88 and would appear to confirm the observation above. A more detailed investigation, which was directed at controlling inclusion shape as a means to preventing stepwise cracking(110) finds that for full inclusion shape control in commercially sized ingots (shape control in the V and A segregated areas of the ingot) an atomic concentration ratio (ACR) of Ca to S of 1:8 and above is necessary (see Fig.27, Page 50).

ACR was calculated as follows:

$$ACR = \frac{32\ [\%Ca\ eff]}{40\ \ [\%S]}$$

Where %Ca eff = [% Ca total]. [1 - 0.98[%O total]

Using the data in Table 4.2 (averaged for the four sections) the ACR for steel K = 0.3 and steel M = 0.53. Examination of Fig.27(Page 50) shows that steel K lies in the region of incomplete inclusion shape control whereas steel M is acceptable. The evidence in the following section and the results of the mechanical tests, Section 5.6, suggest that the inclusion shape control, particularly in steel M, was successful i.e. no anistropy. It is possible that due to the absence of macrosegregation in the small ingots used in this study compared to the large ingots used in the industrial investigation (23 to 26 tonne ingots) complete inclusion shape control was obtained at a lower ACR.

5.4 STATISTICS, IMAGE ANALYSIS AND INCLUSION PARAMETERS IN THE ROLLED STEELS

The developments in micro-computer based image analysis systems in recent years has allowed the collection of microstructural information on a greatly increased scale as compared to previous labour intensive and

subjective manual methods. To make practical use of such large amounts of data it becomes necessary to use statistical methods to estimate parameters which may be usefully applied to describe the data and which can subsequently be related to the microstructure and/or material properties under investigation.

In this study great care was taken to ensure that all the specimens were prepared to the same standard of finish(238) and the equipment was set up using the same procedures, each time, to avoid experimental inaccuracies.

In a similar manner sampling and the determination of the inclusion parameters was carried out to satisfy statistical requirements such that any variability within the data could be satisfactorily estimated (Appendix C).

It has been noted recently by several authorities(244, 245, 246) that microstructural data has been used in a number of studies without statistical justification, making the conclusions of these studies somewhat dubious (primarily data has been used either with insufficient numbers to warrant parametric methods of analysis or data which was not normally distributed has been treated as such).

A number of previous workers investigating inclusion parameters have found that they are distributed log-normally(240, 245, 246, 248, 249) with the exception of inclusion counts (numbers) which have been found to follow a Poisson or random distribution(240, 250). Such was the case in this study (Tables D22 to D27 in Appendix D and Figs.80 to 90, Pages 175 to 183) and the inclusion parameters mean free distance and nearest-neighbour distance were also shown to be log normally distributed (Tables

D27 and D28 Appendix D). The author is unaware of any previous study which has identified this.

Fitting the data to the distribution was carried out by the method of moments (Appendix C, part 2). This method has been used previously by VAN DER VOORT(195) in a study of inclusion %area fraction in a number of steels with sulphur levels from 0.02% to 0.2%. In this work data was collected together in sets, i.e. a set consisted of a number of field measurements, the means of these sets were then calculated and these were tested by the method of moments for normality (application of the central limit theory). A 10% relative accuracy was aimed for, (see Appendix C, part 1, eqa. C1). In the majority of cases this was achieved, however, over 1000 individual field measurements were required.

In the present study, using transformed data, considerably less effort (max of 240 fields) was required to obtain a similar relative accuracy to the study above, whilst still ensuring that the data conformed to a normal (log- normal) distribution. This method, therefore, offers savings in analysis time without compromising statistical accuracy.

Having established that the inclusion parameters follow the log-normal distribution it is possible to estimate extreme values, i.e. fields containing large numbers/sizes of inclusions. The ability to calculate such values is a criterion which is seen as becoming more important in defining steel cleanness and predicting structure property relationships, primarily as large inclusions with irregular geometrical shape are in many cases detrimental to steel properties(259).

In this study only field parameters have been recorded (except as cast size distribution Section 5.3.0) that is, individual inclusion area,

shape and size were not measured directly these were determined by calculating the average inclusion area, shape and size from the field data, assuming that the inclusions were shaped as ellipsoids (Tables D13 to D15, Appendix D). Therefore the reported maximum (extreme) values of these parameters in the above tables will tend to underestimate the true values.

This does not mean that the parameters of projection, mean free distance, and nearest-neighbour distance are inaccurate, as it is assumed when calculating these parameters that all the inclusions are the same size and ellipsoidal in shape (see Appendix B)(240). However, clearly in steels L and F (Type II MnS) this was not the case and some error may have been introduced when calculating the above parameters for these steels.

It is nevertheless encouraging, to see that similar correlations to those found by SPITZIG(234, 235, 249), in his studies on ductility and inclusions, have been obtained. Particularly as he used a far more sophisticated SEM based image analysis system (see following Section 5.6)

5.5 DEFORMATION OF INCLUSIONS DURING HOT ROLLING

Nearly all modern line-pipe steels are manufactured via controlled rolling. This process has been adopted by steel producers as it offers a method of increasing the strength and toughness of steel plate without the need for costly alloy additions or heat treatments. The improvement in properties is primarily achieved by grain refinement(257). It has been found, however, that to produce the required increases in toughness and more specifically strength, very low finish rolling temperatures are necessary. Such low finishing temperatures (between 600 and 800^{o}C)

have caused pronounced anisotropy of ductility and toughness in the finished plate. This has been related to increased inclusion deformation and alignment of inclusion clusters (Al_2O_3 and the Type II MnS networks) in the rolling direction as the temperature of rolling decreases(8).

To combat anisotropy and the clustering of inclusions calcium treatments have been introduced(6, 56). The effectiveness of calcium in reducing sulphur/oxygen levels and controlling inclusion morphology has already been discussed in Section 5.3.1. This Section considers the influence of calcium upon the subsequent deformation of inclusions during hot rolling.

As stated in Section 3.1.5 - Experimental Procedure (Page 119), the maximum capacity of the rolling mill used in this study was for a billet 43mm high. Any attempt to simulate a controlled rolling schedule under these circumstances would have produced a steel plate (sheet) of insufficient thickness to carry out practical mechanical tests. However, in commercial practice, once the billet has been broken down, the final passes in controlled rolling normally make a reduction of at least 60%(5, 10). A 70% reduction of the billet in this study produced a plate with a final thickness of about 12.5mm which was adequate for carrying out mechanical tests and suitably simulated the last and possibly most significant stages of controlled rolling in terms of inclusion deformation. Assuming that the inclusion characteristics were equivalent in each section of each billet i.e. L, F, K and M, a comparison of inclusion deformation at a range of rolling temperatures and for different inclusion compositions/morphologies was possible.

From metallographic observations, described in the results (Section 4.3.1.1, Page 162), it was reported that few inclusions appeared to have become highly elongated during rolling in all steels, but that the networks of Type II MnS inclusions appeared to have been strung-out and reorientated in the rolling direction in steels L and F. Inspection of Table D16 in Appendix D which gives the average inclusion aspect ratios for each steel on the longitudinal and transverse sections would tend to confirm that only a limited amount of inclusion deformation has occurred. This interpretation must be treated with some caution, however, as the original shape of the inclusions was assumed to be spherical and deformation was presumed to create an ellipsoidal inclusion, which was certainly not the case for the Type II MnS inclusions in steels L and F.

Probably a better description of inclusion deformation and one which has been rigorously investigated in the past(253) is the inclusion relative plasticity (RP), which evaluates the amount of inclusion deformation in comparison to the matrix. An RP of zero implying no deformation, at one the deformation would be to the same extent as the matrix and values above one suggest that inclusion deformation has occurred to a larger extent than that occurring for the matrix.

RP was determined for each steel at the four different rolling temperatures the results of which are shown in Fig.78 (Page 170). The advantages of measuring the inclusion RP as described in Section 4.3.1.2. (Page 168) are several:

(i) measurements can be made on a field basis rather than having to measure individual inclusions, which allows the measurement of larger numbers of inclusions;

(ii) such measurements are efficiently carried out by image analysis; and

(iii) a true indication of inclusion deformation is obtained as measurements are made in the as-cast condition before deformation and in the rolled plate afterwards.

The disadvantages of this method are that it results in a mean inclusion RP and, therefore, gives no indication of differences in inclusion deformation with size. Also no distinction is made between oxide and sulphide inclusions which are known to deform to different amounts during hot rolling(99).

For purposes of comparison in this study Fig.78 clearly shows the effect of calcium upon inclusion RP and hence on inclusion deformability. In steel M, in which the inclusions contained the highest average calcium content (31%) (Table 4.3, Page 159) practically no inclusion deformation occurred, whereas in steel K in which the inclusion contained slightly less calcium (21%) some deformation occurred at all of the rolling temperatures examined. For both steels L and F inclusion deformation resulted, which is in agreement with previous studies upon similar steels(253).

A number of points require further comment as they have more general implications:

1 Inclusion Size - Other investigators(213, 253, 256) have found that RP increases with increasing inclusion size, it is generally accepted that the surface area on which frictional forces can operate is less for small inclusions than for large ones, and so the total deforming forces are also less.

A point to note is that the technique used to roll the steels in this study, i.e. reheating between passes, has been shown to cause spheroidisation of inclusions between passes particularly at high reheating temperatures and for those inclusions less than 5 μm in size (213, 256). It is possible that the RP recorded in this study underestimated inclusion deformation because of the small size distribution and it should not be compared to results from commercial practice without bearing this in mind.

2 Matrix composition - In this study and previous investigations(253), the matrixes in which the inclusions have been deformed were not identical. The significance of this factor is the difference in matrix flow stresses between steels of varying compositions. This may restrict comparison of data. It has been reported recently that strengthening of the matrix, by whatever process, increases the RP of MnS(219).

3 Type II MnS - Previous investigators have not measured the RP of steels containing Type II MnS inclusions(198, 253), although they agree that the deformation of these types of inclusion is similar to that occurring in Types I and III, the reason being the difficulty found in accurately measuring this type of morphology.

The results of this study in comparison to previous investigations must be considered with the above comments in mind. From Fig.78, however, it can be seen that the data from BAKER and CHARLES(253), which was measured for a steel of similar matrix composition to steel L but which contained a higher sulphur content (larger as-cast inclusions) and Type I MnS, that the results agree fairly well. Steel F, which had a very similar

inclusion dispersion/ morphology and composition to steel L but a lower RP then provides further evidence in confirmation of the comment above (219) that an increase in matrix strength increases the RP of MnS, steel L having a higher carbon content than steel F and hence a higher matrix strength at equivalent rolling temperatures. (The RP of inclusions in steel F at 1100°C appears to slightly rise again which is counter to the result expected, it is difficult to determine why this occurred).

In summary, the RP of inclusions in the calcium treated steels (steels K and M) has decreased in comparison to ordinary Al-killed steels containing Type II MnS inclusions (steels L and F). In agreement with other workers(39, 92, 93, 110, 114, 115) it appears that there is a critical amount of calcium needed to produce complete inclusion shape control. In this study complete inclusion shape control has occurred when the calcium content of the inclusions (normalised data Table 4.2) was about 30% (steel M) at 22% calcium (steel K) incomplete inclusion shape control has occurred.

5.6 INCLUSIONS, ANISOTROPY AND TENSILE DUCTILITY

The results of the tensile tests for both the Hounsfield and uncharged (UC) notched tensile specimens (NTS) are consistent with previous studies upon ductile fracture in similar steel(6, 198, 212, 213, 214, 215, 230, 231, 234, 235).

NOTE: The % area fraction and % volume fraction of inclusions have been shown to be equivalent(240, 241). Therefore, in discussing ductile fracture any reference to % volume fraction of inclusions implies the % area fraction of inclusion the results of which are recorded in Table D17 in Appendix D. Similarly it has been shown

(195) that the levels of oxygen and sulphur in steels are fairly well characterised by the inclusion % volume fraction.

The tensile ductility of the steels, as described by the fracture strain, decreased as the % volume fraction of inclusions increased, i.e. in the order (decreasng ductility) steels M, K, F and L. Fig.92 (Page 188) shows this for the Hounsfield specimens and similar results were obtained for the UCNTS,(Table D29, Appendix D).

Anisotropy of tensile ductility was found in steels L and F, whereas, steels M and K were practically isotropic. This was due to the differences in inclusion morphology and inclusion shape and orientation with respect to the testing direction for these steels. As discussed previously, for steels K and M, calcium treatment had produced essentially spherical inclusions which were homogeneously distributed. Hot rolling had caused no inclusion deformation in steel M and only minor changes of inclusion shape in steel K (Fig.78, Page 170). Whereas in steels L and F the MnS networks, identified in the as-cast ingot, were deformed and reorientated in the rolling direction.

The isotropy of tensile ductility, found in steels M and K, therefore, further confirms that the calcium treatment has effectively controlled the inclusion morphology in these steels and prevented inclusion shape change during hot rolling.

Inspection of Plates 27 and 28 (Page 209) shows typical fracture surfaces for the longitudinal and transverse testing directions for steel L (the fracture surfaces examined for steel F displayed very similar features). The elongated void shapes on the transverse fracture surface, correspond to the shape of inclusions (and reorientation effects) produced as a

result of hot rolling. This is not observed for the longitudinal fracture surface, as the shape of the inclusions and hence the resulting void shapes in relation to the testing direction, were effectively equiaxed. In contrast the transverse fracture appearance of the calcium treated steels was unchanged in comparison to the longitudinal fracture appearance (Plates 31 and 35, Pages 210 and 211) as the inclusions remained spherical in shape and were homogeneously distributed (Plate 32, Page 210).

From the evidence above it is clear that in all cases fracture was by micro-void coalescence (MVC). This fracture mode was observed for all the Hounsfield and UCNTS investigated. The effect of the notch in the UCNTS was to reduce the fracture strain in all cases in comparison to the Hounsfield specimens (see Tables D29 and D30). It can be observed by comparing Plates 17a and 17b (Page 206) that the amount of shear fracture occurring in the UCNTS was less than that for the Hounsfield specimens, i.e. that associated with the 'cone' region for the Hounsfield specimens. These results are in agreement with previous investigations (222, 224, 225, 226) and confirm that increases in stress concentration and triaxiality, caused by a notch, localise plastic strain, promoting void initiation and growth in the notch region. Plastic instability then occurs earlier. This has lead to the lower levels of fracture strain recorded for the UCNTS in comparison to the normal Hounsfield specimens(222).

The axial cross-sections of steel F (longitudinal (Plates 68 to 72, Page 220)) typify the processes involved in MVC. Plate 72 shows void formation (by cracking and decohesion) at a MnS inclusion in an area of low strain. Plate 71 shows void growth at inclusions towards the neck of the specimen where the strain is higher, and Plate 70 shows void coalescence just below the fracture surface. In the regions of high strain

(Plates 68 and 69) void formation has also occurred at pearlite colonies.

In Fig.92 (Page 188) it can be observed that the % volume fraction of inclusions does not adequately describe changes in fracture strain in the longitudinal and transverse testing directions for steels L and F. The fracture strain being consistently lower for the transverse testing direction in comparison to the longitudinal at the same level of inclusion % volume fraction. This is a result of inclusion anisotropy, as described above, and has been noted by numerous workers(211, 212, 214, 215) investigating the effect of inclusion deformation upon the ductility of steels tested at different orientations (this effect has been shown to an even greater extent for steels tested in the through-thickness direction, which regrettably was not possible in this study, see Fig.42, Page 89, for example).

In order to account for anisotropy of fracture a number of inclusion parameters have been developed, using stereological relatioships, to relate the inclusion characteristics, i.e. shape, size and number as well as % volume fraction to fracture strain (and also CVN) regardless of testing direction (see Appendix B)(8, 195, 197, 220, 231, 233, 234, 235, 240, 241, 243, 246, 248, 250).

Possibly the most commonly used parameter is the inclusion projected length although others include the projected inclusion area, the mean free distance and nearest-neighbour distance between inclusions.

Figs.93(Page 189) and 100(Page 198) show the relationship between the inclusion projected length on a plane parallel to the fracture plane versus the fracture strain in both the longitudinal and transverse testing directions for the Hounsfield and UCNTS respectively, a fairly good

correlation is observed (except for the steels rolled at 750°C: this point is discussed below). Similarly the reciprocal of the mean free distance between inclusions in a direction parallel to the tensile direction proves to correlate with fracture strain, Figs.94(Page 190) and 102(Page 200). This is in agreement with work carried out by SPITZIG(231, 243) and emphasises that it is the inclusion shape with respect to the testing direction (as well as the % volume fraction of inclusions) and, therefore, the distance between inclusions perpendicular to the direction of applied stress which influence the fracture strain. When either an increase in the inclusion % volume fraction or a decrease in the inclusion dimensions in the direction of testing or a combination of both occurs the fracture strain decreases, i.e. an increase in the inclusion projected length or a decrease in the MFD between inclusions.

Examination of Fig.104(Page 203) shows the % loss in fracture strain between the Hounsfield and UCNTS versus the inclusion projected length. It would appear, that the notch effect is enhanced as the projected length of inclusions increases. This is possibly the result of triaxiality promoting lateral void growth of the already deformed inclusions.

In Figs.93, 94, 100 and 102 there appears to be no clear indication that rolling temperature has had any influence upon fracture strain, that is with the exception of steels rolled at 750°C. The lower fracture strains observed in these specimens cannot be accounted for by any significant change in inclusion characteristics particularly for steels M and K, (Tables D10 to D12, Appendix D). The difference between these steels and those rolled above 900°C was the matrix microstructure, e.g. Plates 9 and 10, compared to Plates 11 and 12(Pages 164 and 165). In the latter case, i.e. all steels rolled above 900°C ferrite/pearlite microstructures resulted, whereas at 750°C ferrite and partially

spheroidized cementite was produced, due to the repeated reheating and rolling in the transition region i.e. $\gamma + \alpha$. Previous investigators have commented on this effect in commercially manufactured plate which was finished at low rolling temperatures(258) and found that such microstructures resulted in an increase in steel strength (YS and UTS) at the expense of toughness, which was found in this study (see Tables D30 and D31 in Appendix D). The dislocation sub-structure produced in these steels was considered to cause these changes in mechanical properties(258).

A further feature which is not explained by inclusion characteristics alone is the high fracture strain in the longitudinal specimens of steel F compared to the fracture strains in all testing directions in steels K and more obviously steel M which both had a lower P_L and higher MFD. This is due to the influence of carbides, i.e. pearlite, upon fracture (effectively carbon content). In Table 4.4(Page 167) the % area fraction (equivalent to volume(240)) of pearlite is reported. It is practically absent in steel F, at a similar levels in steels K and L (9%) and considerably higher in steel M (19%). In the original design of the experiment the variation in carbon levels was not intended, the levels aimed for were 0.1% (except for steel F). However, this was not achieved in any of the steels, the reasons for this have already been discussed in Section 5.2.4.

It is now firmly established that second phase particles (collectively) influence fracture strain (e.g. 213, 214, 217, 218, 219, 220, 229) and inclusions, in structural steels, have generally been found to have the major influence.Void formation occurring at such particles at the early stages of straining leading to void growth and final failure at lower fracture strains. This has been found to be particularly true for MnS

inclusions, in comparison to either pearlite colonies or individual carbides. The latter types of second phase become involved in the fracture process when sufficient strain has occurred, either to crack the particles or cause decohesion(214). If there is a large amount of pearlite or carbides then the voids formed upon these particles can dominate those produced at inclusions at the later stages of straining, particularly when there is a low % volume fraction of inclusions, as in steel M, and hence, influence the fracture strain.

Considering the above it is found, not surprisingly, that there is a fairly good correlation between fracture strain and either projected length or MFD for steels L and K (see Figs.93,94,100 and 102) as they both contained very similar pearlite volume fractions. In steels M and F the fracture strains differ to those of K and L at the same inclusion projected length or MFD as a result of the respectively higher and lower pearlite volume fractions (see Table 4.4) in these steels. Comparing steels F and L, which both contained similar inclusion morphologies, shape and dispersion, the influence of pearlite and carbides is further emphasised.

One other aspect which may have influenced the fracture strains of the steels is grain size (GS). Because of the range of values found in the different steels and other microstructural variables, i.e. pearlite, it is difficult to determine whether this has had a major influence (Table 4.4). It is, however, generally accepted in the literature that a decrease in grain size will increase toughness (and strength)(257, 258).

Finally, an attempt was made to relate the inclusion parameters of size, shape and nearest-neighbour distance (NND) to the fracture-strain in the Hounsfield specimens using a model of ductile fracture which was develo-

ped in a study upon similar steels by SPITZIG(235). The model is described in Section 4.4.0(Page 187) and the results are given in Table 4.6(Page 193) and reproduced in Fig.95(Page 194). This exercise was carried out to determine if the inclusion parameters calculated from the image analysis data were capable of describing fracture in accordance with the SPITZIG(235) model and to emphasise the influence of other microstructural effects such as those described above i.e. pearlite and GS, which were accounted for by adjusting the constant A in this model (see Table 4.6). This point is made in preparation for the discussion upon SWC as it will be seen that variations in microstructure are significant to the interpretation of hydrogen induced damage of steels.

Fig.95 shows a reasonable correlation between the predicted and observed fracture strains. This is encouraging considering that the model actually applies to the growth of pre-existing voids assuming that void initiation at inclusions occurs at zero strain. Also the NNDs on a polished plane are thought to be larger than on a fracture surface as a result of necking during tensile testing (235).

Clearly there are numerous factors to consider apart from the inclusion characteristics when studying ductile fracture. But in this study it has been found that inclusions are the microstructural components which have the greatest influence upon fracture by MVC. The results show that it is a combination of inclusion %volume fraction and shape with respect to the testing direction which determine fracture strain primarily by influencing the amount of matrix which must separate to produce fracture. Within this matrix the various other microstructural components will additionally assist or restrict fracture.

5.7 THE INFLUENCE OF HYDROGEN UPON TENSILE DUCTILITY AND ANISOTROPY (NOTCHED SPECIMENS)

All of the tensile specimens charged with hydrogen and subsequently pulled to fracture failed at a lower true stess and strain than comparable uncharged specimens, compare Tables D30 and D31 in Appendix D. This is in agreement with numerous other studies which have investigated the influence of hydrogen upon steels of a wide range of compositions, microstructures and mechanical properties (.e.g. 12, 14, 15, 171, 175, 180).

Figs.96 to 99(Pages 196 and 197), which are typical flow curves for both the uncharged (UC) and hydrogen charged (HC) notched tensile specimens (NTS) show that upon loading little difference between these curves can be detected. However, a loss of load bearing capacity (instability) occurred in the HC specimens at a considerably earlier stage than in the UC specimens, and failure then ensued fairly rapidly, in some cases catastrophically, without further extension, Fig.98.

Plotting the fracture strains of these tests against the projected length of inclusions on a plane parallel to the fracture plane and the reciprocal of the MFD between inclusions in the testing direction, (Figs.101 and 103 respectively, Pages 199 and 201) reveals no correlation with these inclusion parameters unlike that found for the UCNTS (see Figs.100 and 102, Pages 198 and 200). This suggests that there is no (obvious) influence of inclusions upon the hydrogen charged fracture strain as described by the parameters of projected length and MFD, i.e. % volume fraction and shape of inclusions, nor does there appear to be any influence of testing direction upon fracture strain. The results are in fact best described as scattered.

Inspection of Fig.105(Page 204) which shows the % loss in fracture strain between the UC and HC NTS against the inclusion projected length does not provide any further clarification other than highlighting the rather random way hydrogen has reduced the fracture strains for all the steels tested.

Examining the fracture appearance of the HC NTS and comparing the axial cross-sections of the HC and UC specimens (undertaken for steels rolled at 1100°C) provides some evidence to explain why no such correlation has occurred.

The occurrence of, what has previously been termed 'fisheyes' and areas of 'flat fracture' (e.g. 11, 12, 13, 14, 15) upon the fracture surfaces of the HC specimens immediately distinguished them from the UC specimens. These features were frequently observed regardless of the steel composition, microstructure or testing direction and varied in size from less than 20 microns to over 2000 microns in cross-section, (see Plates 19, Page 206, 50 to 52, Page 215, and 59 to 61, Page 217). The fracture mode often associated with these features was quasi-cleavage (Plates 34 and 42, Pages 210 and 212).

In the absence of fisheyes or flat fracture the HC specimens failed by MVC. However, comparing this to the MVC which occurred for the UC specimens (Plates 27 to 30, Page 209), there is clearly a difference. In the HC specimens the fracture surface was covered with a finer and more numerous population of dimples, regardless of the testing direction, and the influence of inclusion shape (and reorientation steels L and F) upon the dimple shape was less pronounced. Failure however, was still clearly plastic in nature, and inclusions were observed upon the fracture

surface, unlike the fracture surface of the fisheyes, where, except for the central areas inclusions were not observed.

The occurrence of inclusions in the central regions of fisheyes or flat fractures was a common characteristic of this fracture. Various inclusion compositions were found to be associated with either the central crack for the fisheye or clustered (often centrally but not exclusively) for the areas of flat fracture (Plates 63 and 64, Page 218 and 50 to 61, Pages 215 to 217, respectively). No particular inclusion composition was found to be predominantly associated with either fracture, rather the criteria for such fractures was either inclusion size i.e. large or density i.e. clusters of inclusions . Often a gaping crack (see Plate 63) perpendicular to the fracture plane was associated with the fisheye fractures.

Further to the above observations upon fracture appearance, in comparing axial cross-sections of HC and UC specimens (Plates 68 to 89, Pages 220 to 225) it can be seen that deformation, in the body of the HC specimen is negligible whereas considerable evidence of plasticity is found in the UC specimens i.e. elongation of grains/pearlite colonies in the tensile direction. Plates 68 to 72(Page 220) show the typical sequence of events leading to fracture by MVC in the UC specimens. Void initiation - by decohesion and particle cracking - has occurred at both inclusions and pearlite colonies followed by void growth, primarily in the direction of principal stress and finally coalescence (see Plate 70) and failure. In contrast, in the HC specimen (Plates 73 to 77, Page 221) inspection of axial cross-sections finds limited void formation at inclusions (which has occurred by decohesion) and no evidence of plasticity, except in narrow bands adjacent to the fracture surface, i.e. highly localised. The most striking features are cracks, which have occurred within the

body of the matrix, but these do not appear to be specifically related to any microstructural feature. Plate 76 shows an example of such a crack which has originated at an inclusion.

The results of the quantitative analysis of the axial cross-sections (Tables D31 to 33 in Appendix D) i.e. the change in void (inclusion plus void) % area fraction, areal fraction and total length measured in the direction of applied stress (and reproduced graphically in Figs.106 to 117, Pages 226 to 231) were extremly difficult to interpret due to the large amount of scatter.

In general terms all three parameters decreased from a maximum at the minimum notch cross-section back towards the original inclusion level, regardless of testing direction or hydrogen charging (the original inclusion levels are indicated by the arrows on Figs.106 to 117). However, the magnitude of these parameters was nearly always higher in the longitudinal testing direction for the UC steels in comparison to the transverse and lower in the HC specimens in comparison to the UC for both testing directions as the minimum cross-section of the neck was approached, i.e. as Z approached zero.

These results tend to confirm the previous observations that the process of void formation, growth and coalescence is restricted in the hydrogen charged specimens. In fact plasticity appears to have been virtually absent, except for the regions adjacent to the fracture surface and cracks rather than voids have appeared within the matrix. It is probable that some of the anomalous results recorded in the quantitative analysis represent cracks which have occurred within the matrix in the HC specimens. For example in Fig.106(Page 226) there is a peak in the % area fraction of voids found at about 0.75mm behind the minimum cross-

section, this does not correspond to an increase in the areal density of voids in this position (Fig.110, Page 228) nor an increase in the total length of voids in the direction of applied stress (Fig.114). It must be concluded, therefore, that this represents a crack running perpendicular to the direction of applied stress, similar to that shown in Plates 88 and 89(Page 225).

To summarise, there appears to be no relationship between the hydrogen charged fracture strains in all the steels examined and the inclusion parameters as was previously discovered (Section 5.6) for the specimens tested in the absence of hydrogen. However, fracture phenomenon known as fisheyes and areas of flat fracture were often found upon the fracture surface of hydrogen charged specimens and were associated with either large singular inclusions or clusters of inclusions. Fracture in the hydrogen charged specimens in the absence of the above fracture phenomenon occurred by MVC which appeared to be 'finer' than that occurring for the uncharged specimens. Plasticity was observed to be virtually absent in axial cross-sections of hydrogen charged specimens and cracks were found within the matrix. The only plasticity observed was very localised at the fracture surface. With these points in mind the following sequence of events is proposed.

Prior to tensile testing the specimens were subjected to the NACE SWC test. Considering the effects of such a test (which are reported in Tables 4.8 and 4.9 and discussed in the following Section) it would be anticipated that similar cracks (hydrogen damage) had already been created in these specimens before tensile testing. Assuming that this is the case, and ignoring for the moment that hydrogen may also have influenced the plastic response of the steel during loading, the HCNTS effectively already contained defects in addition to their inclusion population i.e.

SWC (which probably initiated at inclusions and propagated into the matrix). Therefore, the original inclusion parameter of % volume fraction, shape and number will not represent the major microstructural defects, (as they were previously shown to describe for normal fracture by MVC) now SWCs, from which the process of void initiation, growth and coalescence proceeded. Under these circumstances it is not surprising that there is no correlation between the inclusion parameters, projected length or MFD, and hydrogen charged fracture strain as they no longer characterise the defects within the steels from which fracture developed.

It is not unreasonable, either, to suggest that the cracks observed on the axial cross-sections of the hydrogen charged specimens are the SWC originally introduced into the material by hydrogen charging and which have opened up to some extent during testing. The fisheyes and flat fractures themselves represent SWC which were situated within the notch region and were sufficiently large to influence the fracture process, and subsequently become revealed upon the surface of the fractured specimens. It is possible that the combined effect of the notch and large SWC in the notch region were sufficient to raise the stress in this area to trigger cleavage (quasi-cleavage) fracture mechanisms extending the original SWC/fisheyes in size. Upon crack propagation the removal of constraint would have resulted in stress relief, and subsequent failure of the regions between the internal cracks (which were not necessarily situated within the minimum cross-section) probably occurred by a highly localised (shear type) plastic mechanism. The result was the 'fine' micro voids observed on the fracture surface of specimens charged with hydrogen in the absence of fisheyes or flat fractures and the very localised plasticity observed adjacent to the fracture surface on the axial cross-sections.

Considering the influence of hydrogen on the above sequence of events in terms of the proposed mechanisms of hydrogen embrittlement, the following possibilities arise:

(i) the initial cracks (SWC) have probably resulted from internal hydrogen pressurisation(117, 119, 174) which, from the evidence in this study, has predominantly occurred at inclusions (SWC is discussed further in the following Section),

(ii) crack propagation by a cleavage type mechanism may have been promoted by hydrogen becoming adsorped onto the surface of (internal) cracks (178) lowering the stress required to propagate this type of fracture and/or the decohesion of particles (inclusions or carbides) from the matrix may have been promoted in a similar manner. This may account for the more numerous and 'finer' dimples found for the HC specimens where void initiation (by decohesion) has been able to occur at a greater number of particles,

(iii) the cohesive strength of the matrix may have been reduced as a result of hydrogen dissolved in the lattice (76,177), again possibly promoting cleavage type fracture mechanisms,

(iv) the ease of dislocation movement may have been restricted by hydrogen contained within the lattice causing high (local) stresses favouring cleavage fracture mechanisms or alternatively dislocation movement may have been enhanced encouraging plasticity and MVC.

Whichever of the above mechanisms was operative is difficult to determine. However, it is clear that either closely associated inclusions or large inclusions have acted as focal points for triggering hydrogen damage in the steels examined in this study and this has led to the changes in fracture appearance and reductions in fracture strain.

5.8 THE ROLE OF INCLUSIONS IN HYDROGEN STEPWISE CRACKING

Stepwise cracking tests were carried out upon standard size steel coupons for 96 hours (Test 1) and reduced size coupons for 192 hours (Test 2). The standard NACE solution MR-01-77(142) was used in both cases. The. results of these tests are given in Tables 4.8 and 4.9(Pages 233 and 234)

In Test 1, for steels F, L and K, SWC appeared to occur arbitrarily regardless of rolling temperature or inclusion content. Steel M, on the other hand, was completely resistant to SWC at all rolling temperatures and contained the lowest inclusion % volume fraction. Observation of Fig.118 shows that there was a tendency for the magnitude of SWC to increase with an increase in the % inclusion volume fraction.

As the results of Test 1 were inconclusive a second test was carried out (Test 2) with the prime objective of causing cracks in the steels, i.e. by effectively increasing the bulk hydrogen concentration of the matrix, (it is very unlikely that linepipe would be subjected to these conditions in service.) Inspection of Table 4.9 shows that higher matrix concentrations of hydrogen were achieved but the resulting analysis of SWC did not prove to clarify the situation any further than was found in Test 1.If anything it was further confused as the magnitude of SWC in a number of steels was less than had originally been detected in Test 1. Also steel M, which was resistant to SWC in Test 1 was found to be more susceptible in Test 2 in comparison to steels K and F, and steel L1(L $1100^{o}C$) in both tests was completely resistant to SWC whereas the susceptibility of steel L at other rolling temperatures was poor. It is

difficult to explain why this result occurred, particularly as the microstructure of the steel and the inclusion parameters were not significantly different for steel L when rolled at 900 and 1000°C.

From the results of both tests it can be observed that the tendency for SWC to occur is greater in steels which contain a higher % volume fraction of inclusions which happens to be the steels (L and F) which were not calcium treated. Consequently it would appear that the reduction in the % volume fraction of inclusions through calcium injection does increase SWC resistance. However, it must be remembered that calcium has also affected the morphology and distribution of inclusions. At the same time, it is acknowledged that SWC need not necessarily occur in any of these steels (or possibly be detected by the NACE test procedure TM-02-84(125). This trend is shown in Fig.118(Page 238) for both tests.

To determine if the SWC susceptibility of steels was influenced by inclusion shape/morphology (as well as % volume fraction) the results of the SWC tests were plotted against the inclusion projected length. Using this parameter it was possible to plot the CLR and CTR against the projected length of inclusions on a plane parallel to the direction of cracking (in the same way that the projected length was plotted against fracture strain, i.e. parallel to the fracture plane). This is shown in Fig.119(Page 239) and it can be seen that similar to the above, the susceptibility of a steel to SWC increases as the projected length of inclusions on a plane parallel to the fracture plane increases. This result is confirmed in Fig.120(page 240), which shows the CLR and CTR, i.e. the length of crack per unit area measured on the longitudinal sections of Test 2 versus the inclusion projected length on a plane parallel to the crack plane. It would appear therefore that both inclusion shape and % volume fraction influence SWC resistance.

Other workers (8, 133) who have tried to relate the inclusion projected length to the CLR have either similarly found that SWC susceptibility increases with increasing projected length or reported that no correlation was observed. In the latter study, correlation was only found when the influence of manganese segregation was combined with the inclusion projected length, implying that both inclusions and the matrix composition surrounding the inclusion influences SWC susceptibility. A similar conclusion was drawn by PRESSOURYE et al(180) in their study of SWC.

Recalling the previous Section (Section 5.7) there was strong evidence suggesting that either large inclusions or clusters of inclusions were responsible for causing the 'fisheye' or 'flat' type fractures on the surface of hydrogen charged tensile specimens. It was assumed that such fracture phenomenon had originated from SWC initiated during hydrogen charging. Inspection of Plates 95 to 118(Pages 247 to 252) confirms this observation, showing the occurrence of cracks in association with inclusions. The evidence in this case is not overwhelming as finding the initiating source of SWC was dependent upon sectioning the specimen. This effectively samples a smaller area of crack than a fracture surface. However, the number of inclusions actually found to be associated with SWC, as for example, shown by the above Plates, strongly supports this assertion.

A further attempt to confirm this point was undertaken by fracturing specimens with visible SWC by impact after they had been cooled to minus 196^{o}C in liquid nitrogen. Examples of the results are shown in Plates 95 to 97(Page 247). Although inclusions were observed upon the fracture surfaces the point of crack initiation could not be determined. Terraced type fracture surfaces occurred (see Plate 95) similar to those produced in the study by WILDE et al (150).

Nevertheless, in agreement with many other workers (e.g. 7, 8, 114, 115, 123, 130, 131, 133) inclusions were found to be the microstructural component most commonly associated with SWC, and for the majority of cases cracks were associated with large inclusions.

As this finding implies that inclusion size is the critical factor influencing SWC initiation (and also clusters of closely associated inclusions, i.e. those revealed upon the fracture surface after tensile testing of specimens containing SWC's) a plot of the probability of finding an inclusion projected length greater than 1.4mm/mm^2 versus the CLR and CTR was made (Fig.121, Page 241). A projected length of 1.4mm/mm^2 was chosen in order that all the steels tested could be compared. A larger size would have resulted in steel M having a zero probability of exceeding this length and a smaller one would have approached the mean projected length for steel L, this was necessarily a compromise to some extent. The result of this analysis confirms that the tendency for large SWCs increases with the probability of finding a steel containing inclusions with a high projected length and shows that as a result of reductions in the inclusion % volume fraction, and inclusion shape control (due to calcium treatment in steels M and K) SWC resistance was improved. It must be remembered, that the projected length is a field parameter and therefore tends to normalise the influence of any one large inclusion in a single field, it does however, adequately describe clusters of inclusions in a single field. It is anticipated that a better correlation could have been made if the size of individual large inclusions was determined. It is further believed, as commented in Section 5.7, that after a crack has initiated at an inclusion its size becomes dependent upon other factors, such as the surrounding microstructural features and the supply of hydrogen, as well as the influence of other inclusions, and therefore the crack becomes

unrelated to such inclusion parameters. Rather this infers that if a crack does initiate in a steel which contains inclusions with a higher mean projected length or probability of exceeding a given projected length it then has the potential to become larger.

The analysis of blisters which formed upon the surface of the steel coupons after testing (reported in Tables 4.11 and 4.12, Pages 242 to 244) did not prove to reveal any systematic variation in blister size distribution, number or % area fraction with steel type or rolling temperature.

Previous authors have reported that blisters are nucleated at inclusions and/or large carbides near the surface of steels which have been subjected to a high hydrogen input fugacity (12, 124, 126, 260) and although microsections of blisters were not examined in this study, considering that SWC (internal blisters) were found to have commonly occurred in association with inclusions it would seem reasonable to conclude that the majority of blisters also initiated at inclusions.

It is interesting to note that the distribution of blister sizes was found to be described by the log-normal distribution in all but 2 cases (Table 4.12) as was the distribution of inclusion sizes. This may indicate some correspondence between the two distributions, however, at the same time it must be stated that other microstructural features, e.g. grain size have been reported to conform to this distribution(240).

A further point of relevance is the bulk hydrogen levels recorded for each steel. In the first instance these must be regarded as best estimates as the levels of hydrogen recorded in the steels are very low (approaching the limits of detectability) and may be influenced by such

factors as blister formation, i.e. which had often ruptured releasing trapped hydrogen (see Plate 90B, Page 245).

A comparison of Tables 4.8 and 4.9(Pages 233 and 234) shows that the levels of hydrogen were higher in Test 2 than in comparison to Test 1 and this was to be expected considering the charging time and surface to volume ratio for the different specimens in each test. Steel F had the lowest H concentration in both tests, whereas for steels L, M and K it is difficult to determine precisely which steels contained the highest or lowest H levels. It should be noted that steels rolled at 750°C appeared on average to contain higher H levels than those rolled at 900°C and above.

It is interesting to find that the levels of hydrogen reported in steels K and M before charging were higher than steels L and F. This is believed to have occurred as these steels were injected with CaSi and argon. Such increases of H in steels have been reported in the literature in commercial ladle injection processes, see for example Fig.12(Page 25), and are believed to result from moisture associated with the CaSi or hydrogen in the argon gas which is picked up by the steel during injection.

An overall explantion of the above results with respect to inclusions may be considered as follows.

It is widely accepted that a mechanistic explanation of hydrogen embrittlement (HE) is as yet unavailable(117, 119) and presents a formidable challenge to investigators in many fields of science. However the, interaction of hydrogen with microstructure is becoming clearer(155) and it is now fairly well accepted that regardless of the actual mechanism of

HE, when a sufficient concentration of hydrogen collects at a microstructural inhomogeneity, i.e. a trap fracture may result and any number of the proposed mechanisms of HE may be involved. The possible mechanisms involved have already been highlighted in Section (5.7) where their influence on fracture was considered.

From the evidence in this study (Section 5.7 and 5.8) it is the author's opinion that inclusions are the principal microstructural traps, i.e. focal points for hydrogen concentration and initiation of SWC.

Very persuasive evidence supporting this assertion has been produced in a recent study by TUYEN and WILDE(172). By using an autoradiographic technique they were able to show that hydrogen (tritium) was associated with inclusions at higher concentrations than in comparison to the surrounding matrix, the steel investigated was a HSLA steel similar in composition to the steels investigated in this study.

To discuss the interaction of hydrogen with microstructure and subsequently highlight the factors which it is believed will influence the concentration of hydrogen at inclusions, a number of key factors which influence the diffusion and concentration of hydrogen in steel must be outlined, these are:

(i) its limited solubility/concentration in the matrix;

(ii) adsorption of hydrogen onto both external and internal surfaces;

(iii) absorbtion into the steel lattice;

(iv) transport of hydrogen by;

(a) diffusion,

(b) dislocations;

(v) the localisation of hydrogen at internal sites in the bulk steel by -

(a) adsorption of hydrogen atoms on surfaces, i.e. internal interfaces,

(b) precipitation of molecular hydrogen at voids producing an internal gas pressure, and

(c) in solution at interstitial sites.

Upon placing a steel coupon in the charging environment a corrosion reaction is set up which produces nascent hydrogen, this either recombines to molecular H_2 or is adsorped upon the steel surface and may then become absorbed into the matrix. It has been shown that H_2S environments poison the recombination process in favour of H adsorption (142) and as the H_2S concentration of the charging medium increases and the pH decreases, the fugacity of hydrogen produced at the steel surface increases(150). For the purposes of this discussion it is assumed that the fugacity of hydrogen produced by immersing the steel coupons in the NACE solution was the same for all the steels in the study. The fugacity of hydrogen at the steel surface effectively determines; the rate of hydrogen supply to the matrix by diffusion by creating a gradient (chemical potential) and, the equilibrium concentration of hydrogen within the matrix, i.e. through SIEVERT's Law $C_H=K(pH_2)^{\frac{1}{2}}$.

Further to this, diffusion of hydrogen is influenced by temperature (constant in this case) and elastic stress fields which are tensile in nature(117). These may either be on a macroscopic scale, i.e. notches in tensile specimens, or on a microscopic scale, i.e. the elastic stress field of dislocations or solute atoms. In areas which are stressed

triaxially the flow of hydrogen to these regions will be greater than that occurring by diffusion alone due to a chemical potential, and the concentration of hydrogen in these regions will exceed the level determined by the hydrogen fugacity produced by the corrosion reaction. INTERRANTE(117) calls such areas "regions of locally increased solubility".

As hydrogen diffuses into the matrix it encounters various microstructural inhomegeneities (many of which are necessary components of the steel introduced to obtain the required mechanical properties). These all effectively compete for hydrogen and eventually a crack initiates on the feature which traps a sufficiently high concentration, the concentration of hydrogen at the particular inhomogeneity being influenced by one or more of the above mechanisms.

At the same time the other features which trap hydrogen but do not hold sufficient amounts to initiate a crack, effectively remove hydrogen from the system. Therefore, either a possible crack initiating site is potentially such a strong hydrogen trap that hydrogen collects at this point regardless of other traps, or, the other competing traps gradually fill up with hydrogen until the driving force for diffusion ceases for these locations and subsequent hydrogen is then diverted to the potential crack initiation site i.e. the site which remains a hydrogen sink. In practice, it would be expected that a synergy arises between the various microstructural components within the steel, influencing the distribution and concentration of hydrogen.

PRESSOURYE(155) has in fact categorised many microstructural traps and determined that two distinct types can be identified, 'attractive traps' and 'physical traps'. An attractive trap is a region of the crystal

lattice where hydrogen atoms are subjected to a drawing force, which pulls the atoms to the centre of the region. A physical trap is a modification of the ideal crystal lattice which results in an energetically more favourable site for hydrogen to stay in, e.g. incoherent particle/matrix interfaces and voids. Inclusions are generally believed to act as physical traps.

Why inclusions should act as the principal focus for hydrogen concentration in these types of steel can be determined by considering how they influence diffusion and concentration of hydrogen to a larger extent than the other microstructural features within the steel. The following points are relevant.

Inclusions are distributed throughout a steel in various sizes and shapes (after hot rolling) and their density is best described by % volume fraction (as we have seen in previous Sections of this study, Appendix D Table D17). Volume fraction is dependent upon steelmaking practice. On an individual basis inclusions may be considered to trap hydrogen as follows:

(i) actually within the inclusion lattice,
(ii) at the inclusion/matrix interface,
(iii) at a void between the inclusion and matrix, and
(iv) in the matrix immediately surrounding the inclusion.

It is important to appreciate that all inclusions, i.e. as described by % volume fraction will to some extent influence hydrogen concentration within the matrix as well as at other microstructural features, but as has been found in this study either large inclusions, or clusters of inclusions apparently act as initiating sites, i.e. principal hydrogen

traps, for SWC. Trapping of hydrogen at inclusions with respect to the points above may be influenced by the following factors;

(i) For hydrogen to actually reside in the inclusion lattice the interface between the inclusion and matrix must be intact to allow hydrogen to diffuse across. It has been postulated by CIALONE and ASARO(201) that if hydrogen were to concentrate within the inclusion lattice it could do so to a larger extent than the iron lattice since the tetrahedral interstices are some 35% larger by volume for MnS inclusions. According to data published by KIESSLING and LANGE(19) this would also be true for calcium aluminates and alumina phases. If a crack subsequently initiated the inclusion could then act as a source of hydrogen to a greater extent than the matrix.

(ii) A number of investigators have found that segregation of impurities to inclusion/matrix interfaces can lead to a reduction in fracture strain(219, 227, 232). This only applies to inclusions which are coherently bonded and may not necessarily apply for MnS inclusion for the reasons which are given below in (iii). Evidence from the autoradiographic study by TUYEN and WILDE(172) discussed above found hydrogen at interfaces between the inclusions (various compositions) and the matrix. The possibility arises that segregation of solute elements in the last liquid to solidify leading to inclusion precipitation may also produce a region surrounding the inclusion which contains a high concentration of tramp elements i.e. Sn, As etc. creating distortion in the lattice at and adjacent to the interface of the matrix and inclusion. The general distortion in the lattice surrounding the inclusion may then

trap hydrogen; consequently reducing the concentration of hydrogen required in comparison to the matrix in general, at which fracture i.e. decohesion, could occur, adding to the effect of impurities in reducing the fracture strain. Once such decohesion occurs, effectively a void has been produced which leads to point (iii).

(iii) A number of workers investigating hydrogen cracking have proposed that at sufficiently high hydrogen fugacities and with sufficient time, hydrogen can collect at a void and recombine to its molecular state. This results in an increase in the gas volume producing an internal pressurisation which may then exceed the yield stress of the steel, hence causing crack growth(137, 174, 219, 260).

Voids occurring at inclusions purely as a result of the difference in the coefficient of thermal expansion between the matrix and the inclusions, during solidification and cooling to room temperature, have been investigated by BROOKSBANK and ANDREWS(261). They have calculated that for MnS inclusions voids could arise (particularly for large inclusions). Otherwise, during the deformation process (controlled rolling) voids may be introduced either from differences in inclusion and matrix plasticity or from inclusion cracking. If such cracks are present they would act as a physical hydrogen trap from which the above pressurisation could develop.

(iv) On the other hand if the inclusion coefficient of thermal expansion is such that upon solidification it is too big for the hole it is residing in, then residual tensile stresses,

which dilate the lattice adjacent to the inclusion may arise. These could create regions having a locally increased solubility for hydrogen. BROOKSBANK and ANDREWS(261)have calculated that Al_2O_3 and CaAlO phases have a lower coefficient of thermal expansion than iron and would thus be expected to cause this effect. Apparently CaS is neutral, i.e. it has very nearly the same coefficient of thermal expansion as iron.

Further, if hydrogen precipitates at a void between the inclusion/matrix interface any resulting pressurisation could also create tensile stresses adjacent to the inclusion in the matrix. If such pressurisation causes plastic deformation, dislocation as well as diffusion transport modes could contribute to hydrogen concentration.

With the above factors influencing the interaction of hydrogen and inclusions, it can be appreciated that large inclusions (in comparison to other microstructural features) or clusters of closely associated inclusions effectively amplify the possibility of any of these interactions and , therefore, hydrogen concentration, as they would have;

1 a larger capacity for storing hydrogen,

2 a larger inclusion matrix interface,

3 for a single large inclusion, the possibility of a greater misfit due to the thermal coefficient of expansion between inclusions and matrix, and

4 particularly for clusters of inclusions, interaction of the above mechanisms which could further increase hydrogen concentrations within the matrix.

Hence it would appear that such factors could either singularly or in combination cause a sufficient amount of hydrogen to collect at inclusions, rather than any other microstructural component, and exceed the critical concentration required for cracking.

Reconsidering the results of this study with the above factors in mind a number of points may be explained:

a) Bulk hydrogen levels of the charged specimens: this is probably a reflection of the ability of each steel to trap hydrogen. Steel F having on average the lowest hydrogen concentration presumably because the low carbon content of this steel resulted in a low volume fraction of carbides (as shown in Table 4.4, Page 166) which even in combination with a higher inclusion volume fraction compared to steels K and M resulted in a decrease in its ability to store hydrogen. In a similar way the steels rolled at 750°C had a different microstructure to those rolled above 900°C. Regardless of carbon or inclusion content the change in microstructure has resulted in a higher hydrogen concentration. As with the lower fracture strains reported for these steels previously this may have arisen due to the creation of dislocation substructures during rolling which has produced a greater capacity for storing hydrogen in these steels.

b) In considering the SWC resistance of the steels in this study with regard to inclusions there are probably two main reasons why cracking did or did not occur:

- the microstructure was capable of containing the hydrogen absorbed during the NACE test primarily as it contained a sufficiently large number of innocuous traps to prevent the critical concentration occurring, and

- an inclusion or group of inclusions within the steel was a sufficiently strong hydrogen trap, for the reasons given above, that the critical concentration of hydrogen was exceeded and cracking occurred regardless of other micro-structural traps.

The actual process of cracking can in itself produce a physical hydrogen trap which will concentrate hydrogen and maintain cracking at the expense of other hydrogen traps. It may then become such a strong trap that hydrogen residing at other areas within the matrix is diverted to it causing internal pressurisation and creating internal stresses at this point. The resulting stress may then trigger cracking at other nearby inclusions i.e. by lowering the critical concentration of hydrogen required to produce cracking at these regions, hence producing step-wise cracking. In fact, once sufficient hydrogen concentration has occurred to produce cracking, any hydrogen stored in the near vicinity of the inclusion (particularly as described in point (iv) above) may be freed (as a result of crack growth and stress relaxation).

Several possibilities then arise; the sudden high concentration of hydrogen now existing within the unstressed matrix i.e. not now having "a locally increased solubility" as it would have had whilst under stress, may be sufficient to cause secondary cracking. This may either occur within the matrix or at other microstructural inhomogeneities e.g.

carbides or smaller inclusions, wherever the critical hydrogen concentration is exceeded. Otherwise the hydrogen released may diffuse to the newly formed crack, which now has a increased capacity for hydrogen as its interface area and volume have increased, promoting further crack growth. At this stage the crack path will be greatly influenced by the proximity of other inclusions and the intervening microstructure (see Plates 101, Page 249, 108 and 109, Page 250 and 114, Page 252).

The great number of microstructural and environmental variables which may influence cracking are shown schematically in Figs.39(Page 80) and 40(Page 81) after PRESSOURYE (155). From these diagrams and the foregoing discussions it may be appreciated that in order to limit a steels resistance to SWC not only careful inclusion control is required but microstructural control also. And it is now considered, by several investigators (155,169), that this approach offers a more pragmatic solution to the problem of hydrogen embrittlement e.g. SWC than in comparison to previous controls which imposed limits on hardness and/or on a strength criteria e.g.NACE TM-01-77 (142).

5.9 STEP-WISE CRACKING (SWC) IN LINEPIPE STEELS - IMPLICATIONS

This study attempted to identify the role of inclusions in SWC by producing a number of steels having similar compositions and microstructures but varying inclusion characteristics.

From the results it was found that SWC, as identified by the NACE test, initiated primarily at large inclusions or at clusters of inclusions and propagated between these sites.

It would appear therefore, that the principal objective, during commercial steelmaking, is to limit the number of large inclusions and the

formation of inclusion clusters so as to reduce a steel's susceptibility to SWC. At the same time the results have shown that the inclusion % volume fraction, inclusion morphology and composition must be controlled; a low % volume fraction of homogeneously distributed spherical inclusions (as described by the projected length or MFD) reducing the probability of SWC occurring.

In terms of inclusion characteristics the above description could provide a framework specification for a SWC resistant steel. However, it would be inappropriate to specify figures drawn from this study, i.e. % volume fraction, as in defining the property requirements of a commercial linepipe, other factors such as general mechanical properties, severity of environment and financial implications would need consideration. A full specification would then be a compromise between guaranteed immunity from SWC, adequate mechanical properties and economic viability.

From this work it is clear that the injection of calcium silicide to control inclusions, offers a practical approach to obtaining such a specification and this is why it has been generally adopted by commercial steel manufacturers.

Calcium silicide injection in itself, however, is not sufficient, rather it is the continuous control of the physical and chemical conditions within the melt, through real time data acquisition and dynamic adjustment of the conditions in the liquid steel, up to the time of casting, which will dictate the quality of steel produced; calcium silicide, along with temperature control, highly refractory ladel linings, argon stirring, atmospheric protection (clearly demonstrated in this study) etc., only offer a means of obtaining this control. A combination of these factors should allow control over the steelmaking process and

provide 'clean' liquid steels containing low levels of primary inclusions, and solute elements e.g. O and S.

Beyond ladle steelmaking the casting stage has a significant effect upon the homogeneity of the finished product. Due to the inherent problem of segregation either solute elements e.g. O, S and Mn must be removed to such levels that, concentration in the last liquid to solidify does not result in the precipitation of inclusions or, methods of preventing segregation are introduced, e.g. rapid solidification. Both mechanisms are aimed at preventing either large inclusions or clusters of inclusions forming during solidification.

Finally, through the control of composition, the inclusion itself must be resistant to deformation and cracking during controlled rolling.

Consideration and close control of the above steelmaking processes offers a practical approach to restricting SWC in linepipe steels.

Further to the steelmaking process it becomes necessary to test the steel in question for SWC resistance. To determine this resistance on the basis of detecting large inclusions or clusters of inclusions represents a general problem which is also experienced in predicting fatigue and fracture resistance (233, 245, 259).

It is somewhat ironic that hydrogen, introduced into steel by the NACE test has the capability of revealing such inclusion features through cracking. However, as an alternative to the NACE test it should be possible to characterise a steel's resistance to SWC through inclusion counting. The results of this study have shown that, through image analysis and transformed data, sufficient inclusion data can be collected

to satisfy statistical requirements, and some correlation has been shown between the inclusion parameters and SWC. This is encouraging since the image analysis was only capable of measuring field parameters, i.e. not individual inclusions, and the steel microstructures studied were somewhat varied.

It is believed, that in a commercial situation, where the control of the steelmaking process (as described above) is carried out effectively, it would be possible to statistically characterise the inclusion population in the finished pipe and from this predict the probability of either large or clusters of inclusions occurring and hence the possibility of SWC initiating. This method, would offer a considerably more efficient means of evaluating a steel's resistance to SWC during manufacture as automated image analysis could be used to establish the distribution of inclusion features and from this predict SWC susceptibility rather than the time consuming NACE test.

It is noted, that in the first instance, it would be necessary to calibrate the inclusion parameter e.g. P_L against SWC by a number of initial NACE tests. This approach may require a more careful appraisal of cracks which have occurred at inclusions, as the procedure for measuring cracks in the NACE test, only does so at a relatively low magnification, i.e. X100. Plate 114(Page 252) shows an example of crack (void) formation at inclusions at a scale which would not be detected or reported in the NACE test.

Finally, it must be remembered that the NACE test is only designed to evaluate the SWC resistance of steels under static (no load) conditions, whereas, in practice this is obviously not the case. A linepipe in service experiences three principal load conditions; unpressurised,

service pressure and hydrostatic test pressure, and studies have shown (128, 145, 199, 200) that the extent of stress and the distribution of stress associated with inclusions (modelled in various geometries) varies with the applied load. By inference, this may then mean, that the distribution and concentration of hydrogen associated with an inclusion (as described in the previous Section 5.8) may also change.

The implication of the above comment is, that during service, hydrogen may diffuse and collect at inclusions within the steel lattice but not reach a critical concentration. However, as a result of stress redistribution, through depressurisation or hydrostatic testing (or mechanical damage), sufficient hydrogen may become concentrated to cause SWC. The point is, if this was to occur during hydrostatic testing, the embrittlement which has clearly been demonstrated to occur in this study, for the hydrogen charged notched tensile specimens (Section 5.7), could be triggered, the consequences of which are self-evident. Whilst suggesting that this could happen - evidence of hydrogen related failure during hydrostatic burst testing of pipe previously subjected to the NACE test, and where SWC was not detected, having already been produced, Nakai et al(11) - it is recognised that this study did not duplicate the stress states of pipe found in practice, nevertheless, there is the possibility of such a situation arising.

6.0 CONCLUSIONS

1 The intense stirring caused by induction, combined with refractory alumina crucibles, produced conditions during melting which were very favourable for primary inclusion separation and the production of clean steels. The low % volume fraction of inclusions which resulted in the cast steels confirm this point (particularly when the large amount of oxidation which occurred during initial melt-out is taken into account).

2 Calcium silicide injection led to a further reduction of the % volume fraction of inclusions in steels M and K, in comparison to steels L and F (which were not calcium treated); both oxygen and sulphur levels were reduced. This result is believed to have occurred through a combination of calcium silicide injection and the factors cited in 1 above. Calcium acted by reducing the solubility of oxygen and sulphur in the melt. This led to the formation of primary oxy- sulphide inclusions in the melt together with an increase in the surface tension of the liquid steel. In combination with the turbulence caused by injection, these factors promoted inclusion formation and separation giving rise to very clean steels.

3 The size distribution of inclusions in all four as-cast steels was greatly influenced by the rapid solidification which occurred in the small ingots used. The majority of inclusions observed, regardless of whether the steel was calcium treated or not, were less than 20 microns.

4 The principal differences between the inclusions in the as-cast plain aluminium killed steels and the calcium treated steels was composition and morphology. The inclusions contained in the plain aluminium killed steels were alumina and networks of type II manganese sulphides, whereas, in the calcium treated steels, the inclusions were of a mixed calcium manganese oxy-sulphide composition, and were essentially spheriodal in shape.

5 Complete inclusion shape control, through calcium treatment, was achieved in steel M but not in steel K. The transition from a deformable to an underformable inclusion (measured as an average calcium level in the inclusion) occurred at a calcium level between 22 and 30%. This is in general agreement with results given in the literature for commercial steels (50, 110).

6 The inclusion parameters calculated from image analysis were found to follow the log-normal distribution (except inclusion counts which followed a Poisson distribution) in agreement with previous investigations (240, 245, 246, 248, 249). The parameters of mean free distance and nearest-neighbour distance were also identified as being log-normally distributed. The author is unaware of any previous study which has identified this.

7 Transformed inclusion data (log-normal) proved to allow a considerable saving in the number of fields requiring analysis to obtain a given statistical accuracy (in this study 10% was aimed for) in comparison to a similar study which used a grouping method to normalise the data (195).

8 The inclusion relative plasticity measurements confirmed that inclusion shape control was achieved in steel M (see conclusion 5) and were in general agreement with a previous study (253), which examined the plasticity of manganese sulphide inclusions, as found in steels L and F.

9 The morphology, and shape of inclusions (as affected by hot rolling), proved to influence the tensile ductility of the steels. The fracture strains in the longitudinal and transverse directions for steel M were isotropic, whereas, steel K exhibited some anisotropy and steels L and F had a marked anisotropy.

10 Inclusions were the microstructural components which most significantly affected fracture strain. All fractures in the absence of hydrogen were by microvoid coalescence.

11 A fairly good correlation was achieved between fracture strain and a number of inclusion parameters (i.e. inclusion projected length P_L, mean free distance between inclusions (MFD) and the nearest neighbour distance between inclusions (NND). It was found that an increase in the inclusion % volume fraction or an increase in the mean inclusion dimension measured on a plane parallel to the fracture plane (or a combination of both) led to a decrease in fracture strain.

12 Fracture strain was considerably less in the hydrogen charged notched tensile specimens in comparison to the uncharged specimens. No correlation was found between fracture strain, in the hydrogen charged notched tensile specimens, and the inclusion parameters P_L

or MFD, as had previously been established for the uncharged specimens.

13 Inclusions were observed to be associated with distinctive fracture phenomenon upon the fracture surface of the hydrogen charged specimens. These had previously been referred to in the literature as "fisheyes" or areas of "flat fracture" (13, 14, 15). The criteria for fracture at these phenomenon was inclusion size i.e. large, or numbers i.e. clusters (morphology). Composition, per se, did not appear to be important.

14 It was believed that the above fracture phenomenon resulted from stepwise cracks introduced into the notched tensile specimens during the NACE test. Upon the application of a load, the SWC's within the notched region became the principal defects from which fracture ensued. It was considered that, any number of the mechanisms proposed to cause hydrogen embrittlement, may have assisted failure. However, it was not possible to identify any one mechanism specifically. Because the cracks were the principal defects in the steel and not the inclusions this explained why no correlation was found between fracture strain and P_L or MFD.

15 In the absence of "fisheyes" or "flat fracture" failure in the hydrogen charged notched tensile specimens was by microvoid coalescence, however, this was on a finer scale than that observed for the uncharged specimens. Axial cross-sections of specimens showed that plasticity in the hydrogen charged specimens was extremely localised in narrow regions adjacent to the fracture surface.

16 Stepwise cracks were, in the majority of cases, found associated with inclusions and in corroboration of conclusion 13, size and density (clusters), rather than any other inclusion characteristic appeared to be the prerequisite for cracking.

17 A limited correlation was found between the inclusion projected length and SWC (as described by the crack length and thickness ratios, CLR and CTR). As the projected length of inclusions increased the possibility of large SWCs occurring increased.

18 It was believed that SWC initiated principally at large inclusions or clusters of closely associated inclusions because the critical concentration of hydrogen required for cracking occurred at such microstructural sites (traps) in preference to others.

19 It was proposed that hydrogen could be trapped at inclusion in the following ways:

(i) actually within the inclusion lattice,
(ii) at the inclusion/matrix interface,
(iii) at a void between the inclusion and matrix, and
(iv) in the matrix immediately surrounding the inclusion.

20 It was proposed that the following factors may have influenced trapping of the critical concentration of hydrogen at inclusions:

(i) the possibility that inclusions could contain larger concentrations of hydrogen than the steel lattice,

(ii) the segregation of tramp elements, e.g. Sn, As during solidification around inclusions, causing lattice distortion and produ-

cing regions having a "locally increased solubility" for hydrogen,

(iii) the formation of voids at inclusions during hot rolling through particle cracking or differences in the matrix and inclusion plasticity or, due to differences in the coefficient of thermal expansion between the matrix and the inclusion during solidification, where the inclusion becomes smaller than the hole it is residing in e.g. MnS. The void acting as a physical trap for hydrogen allowing precipitation of molecular hydrogen and leading to internal pressurisation,

(iv) the formation of stress fields around inclusions, again through differences between the inclusion and matrix coefficients of thermal expansion. Where in this case the inclusion is too large for the hole it is residing in, e.g. alumina, resulting in areas surrounding the inclusion which are stressed in tension and have a "locally increased solubility" for hydrogen.

21 It was believed that either large inclusions or clusters of closely associated inclusions would amplify the factors proposed in 19 and 20 above and hence lead to the critical concentration of hydrogen occurring at such inclusions in preference to other microstructural sites.

22 Once SWC had initiated the proximity of other inclusions, the intervening microstructure and the further accumulation of hydrogen was considered to dictate the crack path and extent of crack propagation.

23 To reduce SWC in commercial steelmaking the principal objective was considered to be the limitation of the number of large inclusions or clusters of closely associated inclusions which occurred. Further, the possibility of using automatic image analysis and transformed data to characterise the inclusion population of a steel was considered to offer a means of predicting whether it satisfied a specification and had adequate SWC resistance, rather than carrying out the time consuming NACE test.

7.0 SUGGESTIONS FOR FURTHER WORK

- The production of steels which contain a minimal amount of micro-structural and compositional variation. Either very simple iron base alloys, having carefully controlled levels of oxygen (using solid electrolyte sensor) and sulphur to which gradual increases in alloy additions are made, or, the use of one specific alloy composition where oxygen and sulphur levels can be accurately controlled. In both cases a sophisticated laboratory steel-making apparatus would be required; including vacuum facilities, the capability of operating under an inert atmosphere, heating of the steel under quiescent and agitated conditions, continuous temperature and oxygen monitoring at different regions in the melt, injection facilities for argon, Ca-Si and other alloying elements and casting under inert gas.

- More sophisticated image analysis; preferably SEM based to identify inclusion compositions simultaneously and an ability to accurately measure and record the size, shape and position (with regard to a reference position) of the inclusions. The data analysis should be simultaneous with data aquisition so that statistical accuracy can be monitored, further flexibility should be incorporarted to allow the addition of specific software (for data manipulation) to the basic data handling programs.

- Analysis of inclusions in situ or extracted on replicas, via bromo-ethane etching. Revealing morphology (SEM) and removing the background iron peak, when measuring compositions, for small inclusions (less than 10 μm) (TEM with energy dispersive analysis).

- Pattern analysis of inclusion distributions in cast ingots; this is a standard statistical method for determining whether a pattern i.e. segregation of inclusions exists within the ingot. Being able to identify such a pattern (if one exists) within a commercial steel would then mean that specimens from the segregated areas of the ingots could be extracted. Testing could then be confined to such areas i.e. the areas most suceptible to SWC.

- A more thorough examination of void formation and growth at various increments of strain, preferably in simple iron based alloys whose inclusion parameters have been characterised previously. Requiring a standard specimen geometry and mechanical testing facilities whereby stress and strain increments can be accurately controlled either by pre-programming or direct control from sensors (clip gauge) on the specimen. SEM based computer controlled image analysis to measure voids; this system would have the advantage over optical systems due to resolution, depth of focus and insitu chemical analysis facilities, enabling it to differentiate between inclusions and voids.

- A test facility, which could simulate the stress states of linepipe which occur in service, whilst being charged with hydrogen.

- Permeability tests of simple iron based alloys which have had their microstructure quantitatively analysied. Enabling a picture, to be drawn up, of the trapping ability of known alloys. Combined with a system to detect internal cracking (SWC) (acoustic emission ?) and thereby estimate the critical concentration of hydrogen required for cracking in such a steel.

APPENDICES

		Page
Appendix A	Stepwise cracking tests	322
Appendix B	Inclusion parameters	323
Appendix C	Statistical analysis	328
Appendix D	Tables	332

APPENDIX A

STEPWISE CRACKING TESTS

As with the various terms used in the literature to describe SWC (Section 2.2.1.1) authors investigating its occurence have carried out numerous different tests and measured the resulting cracks in different ways. Table A1 list the conditions under which immersion SWC tests have been carried out.

Table A1. H_2S SATURATED SOLUTIONS USED IN IMMERSION SWC TESTS

SOLUTION	pH	SEVERITY OF ENVIRONMENT	INVESTIGATOR	MEASUREMENT
Synthetic seawater, ASTM D1141 without heavy metal ions B.P.Solution NACE Tm-02-84	5-1 to 5-4	INCREASING ↓	MIYOSHI et al(8)	CLR, CTR
			TURN et al (130)	CSR
			WILDE et al (4)	CSR
			NAKAI et al (110)	CLR, CSR
			TAIRA et al (127, 114)	CLR,,CSR
			IKEDA et al (144)	CLR
			MOORE & WARGA (7)	CSR
			PARRINI & DE VITO (135)	CLR,CRT,CSR
Pure Water	4.6	SEVERITY	TAIRA et al (144)	CLR
0.5% acetic acid	3.0		IKEDA et al (145, 144)	CLR
0.5% acetic acid 5% sodium Chloride (NACE Tm-01-77)	3.5 to 2.8		FUJII et al (162)	CLR
			TAIRA et al (127, 114)	CSR,CLR
			JONES et al (133)	CLR,CSR,CTR
			IKEDA et al (145, 144)	CLR

Measurements:

$$CSR = \frac{\Sigma(axb)}{WxT} \times 100\%$$

$$CLR = \frac{\Sigma a}{W} \times 100\%$$

$$CTR = \frac{\Sigma b}{T} \times 100\%$$

Some authors (135) have defined CSR as $\frac{\Sigma a \times \Sigma b}{W \times T}$

APPENDIX B

INCLUSION PARAMETERS

PROJECTED LENGTH - P_L mm/mm^2

The projected (total) inclusion length per unit area was introduced by BAKER and CHARLES (197) in their studies of the influence of deformed inclusions on the short transverse ductility of hot-rolled steels. In this work they showed that P_L was derived from the inclusion variables %Vv, size and shape. Subsequently it has been used by a number of other workers investigating inclusion/property relationships in steels (8, 133, 220, 234). More recently SPITZIG (248), in his study of the effect of inclusions on the tensile ductility and Charpy shelf energy (CVN) of hot-rolled C-Mn steels, has shown that a good correlation exists between tensile ductility and P_L when the P_L is determined on a plane parallel to the fracture plane i.e. perpendicular to the tensile direction, for the longitudinal, transverse and through-thickness testing directions.

The following analysis is similar to that presented by SPITZIG (234,231), and determines the inclusion P_L in the three principal directions Fig. 79 gives details of the notation used in the analysis.

The following assumptions were made; inclusions were taken to be shaped as triaxlialellipsoids and were of equal shape and size. The axes of the ellipsoids are labelled $\bar{d}_1$, $\bar{d}_2$ and $\bar{d}_3$ and these represent the average inclusion lengths in the longitudinal ($\bar{d}_1$), transverse ($\bar{d}_2$) were through-thickness ($\bar{d}_3$) directions. The average dimensions of the ellipsoids $\bar{d}_1$, $\bar{d}_2$ and $\bar{d}_3$ are related to the measured (image analysis) average inclusion dimension by the following formulae (240),

$$\bar{d}i = \frac{\Pi}{2}\,\bar{d}i \qquad \text{.....(B1)}$$

where i = 1,2 or 3.

(the factor $\Pi/2$ is introduced to account for section errors)

N_A = the number of inclusions per unit area

N_V = the number of inclusions per unit volume

V_V = the volume fraction of inclusions (equivalent to the area fraction A_F (240)),

where,

$$N_{Ai} = N_V \bar{d}i \qquad \ldots\ldots(B2)$$

and $$N_V = \frac{6\,V_V}{\bar{d}_1\,\bar{d}_2\,\bar{d}_3} \qquad \ldots\ldots(B3)$$

The projected length of inclusions per unit area is given by,

$$P_L = N_A d \qquad \ldots\ldots(B4)$$

for spherical inclusions all of the same size. However, as a result of deformation the inclusions are assumed to deform into triaxial ellipsoids. For this case the projected length of inclusions on a plane parallel to the fracture plane may be defined as follows for the three testing directions,

longitudinal - $P_{L_1} = N_{A_3}\, d_2$ .....(B5)

transverse - $P_{L_2} = N_{A_3}\, d_1$ .....(B6)

and through-thickness - $P_{L_3} = N_{A_2}\, d_1$ .....(B7)

By substituting Eqs. B1,B2 and B3 into Eqs. B5,B6 and B7 results in,

$$P_{L_1} = \frac{24V_V}{\Pi^3 d_1}, \quad P_{L_2} = \frac{24V_V}{\Pi^3 d_2} \text{ and } P_{L_3} = \frac{24V_V}{\Pi^3 d_3}$$

or the general formulae $$P_L i = \frac{24V_V}{d_i\,\Pi^3} \qquad \ldots\ldots(B8)$$

PROJECTED AREA - P_A mm^2/mm^3

The projected area of inclusions per unit volume may be determined, like P_L, for the three principal directions. In general terms and again following SPITZIG (235) (with the same assumption and relationships used previously for P_L) $P_A i$ is given as,

$$P_A i = 2N_V \bar{a}i \qquad \ldots\ldots(B9)$$

where,

$\bar{a}$ = the mean cross sectional area of the particles on planes normal to i,

and, $$\bar{a} = \frac{\Pi}{4}\,\bar{d}j\,\bar{d}k \qquad \ldots\ldots(B10)$$

where,

$\bar{d}j$ and $\bar{d}k$ = the apparent principal inclusion dimensions on a plane

normal to i, i.e. on the longitudinal plane $\bar{d}j = \bar{d}_1$ and $\bar{d}k = \bar{d}_3$.

By substituting Eqs. B1,B3 and B10 into B9 gives,

$$P_A i = \frac{6Vv}{\Pi \, di} \qquad \ldots\ldots(B11)$$

It may be observed here that $P_A i$ and $P_L i$ are related by the factor $4/\Pi^2$ such that $P_L i = \frac{4}{\Pi^2} P_A i$

In addition the total inclusion interface area per unit volume, Sv, may be estimated from $P_L i$(234),

$$Svi = \sqrt{2} \, \Pi \, P_L i \qquad \ldots\ldots(B12)$$

All three parameters P_L, P_A, Sv may be observed to be proportional to the Vv of inclusions and inversely proportional to the inclusion dimensions in the direction of projection.

MEAN FREE DISTANCE (MFD) mm

The mean free distance is the average edge to edge distance between an inclusion and all its neighbours and may be defined as (235,241,242,250)

$$MFD = \frac{1 - Vv}{N} \qquad \ldots\ldots(B13)$$

where (240,241) $N_L = \frac{1}{2} P_A$ $\ldots\ldots(B14)$

as P_A may be determined for the three principal directions so too can the MFD by using the appropriate value of $P_A i$.

Hence by substituting Eqs. B14 and B11 into Eq. B13 gives

$$MFDi = \frac{\Pi}{3} \frac{(1-Vv)}{Vv} \, di \qquad \ldots\ldots(B15)$$

This then accounts for the inclusion anisotropy such that the MFD may be evaluated in the longitudinal (1), transverse (2) and through-thickness (3) directions.

Note: In the calculation of $P_L i$, $P_A i$ and MFDi the inclusion variables observed on the longitudinal plane (2) have been used to determine P_{L_1}, P_{L_3}, P_{A_1}, P_{A_3} and MFD_1, MFD_3, whilst the variables measured upon the transverse plane (1) have been used to determine P_{L_2}, P_{A_2} and MFD_2.

NEAREST-NEIGHBOUR DISTANCE (NND) - Δ mm

The nearest-neighbour distance has been evaluated for a random distribution of a low volume fraction of points, however, it has also been shown to adequately describe a random distribution of particles in which either the particle size and/or the particle volume fraction is small (235,241,250).

Accepting this condition the Δ may be evaluated in the volume Δv or on a plane Δ_A viz.(235,240,241,250),

$$\Delta v = 0.554\ N\bar{v}^{1/3} \qquad \ldots\ldots(B16)$$

$$\Delta_A = 0.5\ N_A^{-1/2} \qquad \ldots\ldots(B17)$$

As with the MFD it is then possible to calculate the Δ on a plane taking into account the inclusion anisotropy by using the following stereological relations (235),

$$Nv = \frac{Vv}{V} = 0.703\ \frac{N_A^2}{N_L} \qquad \ldots\ldots(B18)$$

$$V = \frac{\Pi}{6}\ (dj\ dk^2) \qquad \ldots\ldots(B19)$$

$$dk = \frac{Vv}{1.56\ N_L} \qquad \ldots\ldots(B20)$$

Solving Eqs. B18,B19, and B20 for N_A produces

$$N_A = \frac{2.06\ N_L}{\sqrt{dj\ dk}} \qquad \ldots\ldots(B21)$$

and substituting Eq. B21 into Eq.B17 gives the Δ on a plane,

$$\Delta i = 0.5 \left(\frac{\sqrt{dj\ dk}}{2.06\ N_{Lk}} \right)^{1/2} \qquad \ldots\ldots(B22)$$

e.g. $$\Delta_1 = 0.5 \left(\frac{d_1\ d_3}{1.03\ P_{A_3}} \right)^{1/2}$$

Note: The data given in Table D21 of Appendix D for the Δ on the transverse plane Δ_2 and the through-thickness plane Δ_3 were both determined from the inclusion data collected from the transverse plane (1). This is because no image analysis was undertaken upon the through-thickness plane, so therefore the mean value of d_1, recorded upon the accompanying longitudinal plane 2) was used in conjunction with the data from the transverse plane to evaluate Δ_3

i.e. $\Delta_3 = 0.5\left(\frac{\sqrt{d_1 d_2}}{1.03 P_{A_2}}\right)^{\frac{1}{2}}$

Also the average Δv may be calculated by substituting Eqs.B4 and B2 into B15 giving,

$$\Delta v = 0.554\left(\frac{48Vv}{\Pi^4 d_1 d_2 d_3}\right)^{-\frac{1}{3}} \qquad \ldots\ldots(B23)$$

CALCULATIONS BY COMPUTER

In using a computer to calculate the various inclusion parameters rounding up was carried out upon the final values i.e. the results given in the tables in Appendix D. Hence small variations may be found in the results when calculating certain inclusion parameters using the basic inclusion data in Appendix D which has itself been rounded up.

APPENDIX C

STATISTICAL ANALYSIS

PART 1. SAMPLING REQUIREMENTS - NUMBER OF FIELDS OR INCLUSIONS

This problem has been examined by several authors (195,240,243,244,247) a number of whom have developed formulae to enable the calculation of either the number of fields or the number of individual inclusions that need to be observed in order to obtain a given relative error(accuracy) at a set level of confidence e.g. 95%.

An example of the former (number of fields) is given by VANDER VOORT (242), who used the method suggested by DEHOFF (240),

$$N = \left(\frac{200}{\%RA} \; \frac{S}{\bar{x}} \right)^2 \qquad \ldots\ldots (C1)$$

N = number of fields

% RA = percent relative accuracy

$\bar{x}$ = mean value of the inclusion parameter

s = standard deviation

VANDER VOORT considered a 10% relative accuracy at 95% C.L. as satisfactory for most cases. The problem with this method is that the data must be normally distributed, otherwise the result will be incorrect.

Other authors (240,243,247) have preferred the latter method (number of inclusions). This requires the measurement of individual inclusion feature where the dispersion of these features is assumed to be random (POISSON) and a factor must be determined which accounts for the geometry of the features. Hence it is inappropriate when field parameters are determined as in this study, and only suitable when individual inclusions are measured.

In his review of the application of statistical methods to quantitative microscopy NICHOLSON (244) commented that "an 'appropriate' sampling design will involve many sections, more sections per specimen and more specimens than the stereologist would like. This is just the way it

is!. The characterisation of variability in embedded structure is expensive". A view which is held by several other authors (242,244,246). Under these circumstances a compromise between time, cost and accuracy is neccesary.

Because of these restrictions an initial estimate of the number of fields required was undertaken based upon steel M using the method described by VANDER VOORT (242) in Eq.C1 above. Steel M was chosen as it was believed to contain the lowest inclusion density and thus would be expected to display the largest degree of variability between determinations, and require the highest number of field measurements to obtain a given level of accuracy (in this case a 10% RA was adopted). The observation that variability increases with decreasing inclusion density has been discussed by VANDER VOORT (242). As an additional bench mark a minimum of 2000 individual inclusions were observed for each steel, which is the figure PICKERING (243) has calculated (using the "number of inclusions" method) sufficient to obtain a 10% relative accuracy at 95% C.L.
Calculations of the % RA using the methods above proved satisfactory and either a minimum of 100 fields or 2000 individual inclusions was adopted for the rest of the analyses. Subsequent determinations of the %RA calculated from the transformed data proved to give the desired level of accuracy (See APPENDIX D Tables D17 to D21).

PART 2 MEASURE OF DATA NORMALCY BY MOMENTS

The four moments about zero are calculated as follows,

$$\bar{x}^r = \frac{x_1^r + x_2^r + \ldots\ldots + x_n^r}{N} = \sum \frac{x^r}{N}$$

where, r = 1,2,3 or 4 i.e. the four moments

$\bar{x}^r$ = the four moments about zero

x_n^r = the individual values

N = the total number of values

where $\bar{x}^1$ = the arithmetic (or (log-trans.)geometric)mean

$\bar{x}^2$ = second moment etc.

The moments about the mean are then calculated viz,

$U_2 = \overline{x^2} - (\overline{x^1})^2$ - 2nd moment about the mean

$U_3 = \overline{x^3} - 3.\overline{x^1}.\ \overline{x^2} + 2\ (\overline{x^1})^3$ - 3rd moment about the mean

$U_4 = \overline{x^4} - 4\ \overline{x^1}\ \overline{x^3} + 6\ (\overline{x^1})^2\ \overline{x^2} - 3(\overline{x^1})^4$ - 4th moment about the mean.

The skewness (B1) is then given by,

$B1 = \frac{U_3 . |U_3|}{(U_2)^3}$ - the closer B1 is to zero, the better the data conforms to a normal distribution,

and kurtosis (B2),

$B2 = \frac{U_4}{(U_2)^2}$ - B2 approaches 3 for a normal distribution, values greater than 5 indicate non-normalcy.

A further statistic Ev can be evaluated which indicates any abnormally high values in the distribution, this is calculated by,

$Ev = \frac{(\overline{x^4})^{\frac{1}{4}}}{(\overline{x^2})^{\frac{1}{2}}}$ - a value exceeding 1.32 indicates fields containing abnormally high values.

Also for a POISSON distribution the moment coefficient of skewness, B1 = $1/\sqrt{\overline{x}}$ and kurtosis, B2, = $3 + 1/\overline{x}$.

PART 3. CONFIDENCE LIMITS FOR TRANSFORMED DATA

The mean derived from the transformed data will always be lower than the original arithmetic mean. It is, therefore, more correct to use the arithmetic mean of the sample but, unfortunately, there is no simple method for estimating confidence limits for the arithmetic mean from a contagious distribution i.e. the log-normal distribution (247). One compromise is to use the factor derived from the transformation and apply this to the arithmetic mean of the sample as follows,

log - normal data (Base 10)

$\overline{y}$ = mean of the transformed data

sy = standard deviation of the transformed data

$\overline{x}$ = arithmetic mean

t95= table of Students, t distribution with n' degrees of freedom

$n' = (N-1)$ i.e. $n' = 60$ $t = 2$, $n' = 120$ $t = 1.98$ and

$n' = \infty$ $t = 1.96$

N = number of determinations

95% C.L. = anti log $\frac{(t.sy)}{(N-1)}$

and the true population mean x lies between $\bar{x}$ x 95% C.L. and $\bar{x}$/95% C.L. The confidence limits are then not necessarily equal on both sides of the mean i.e. + ve and - ve (unlike normal data), this reflects the skewness of the original untransformed data.

Part 4. PERCENTAGE RELATIVE ACCURACY (%RA)

From the transformed confidence limits the %RA can then be determined viz,

$$\%RA = \frac{95\% \text{ C.L.}}{\bar{x}} \times 100$$

This was calculated using the largest C.L. recorded.

PART 5. PROBABILITIES

Given a normally distributed variate the probability of exceeding a given value can be expressed (1 - tailed test) as,

$$F(z) = \frac{x - \bar{x}}{s}$$

x = value to be exceeded

$\bar{x}$ = sample mean

s = sample standard deviation

$F(z)$ = areas under the tail of a standard normal curve e.g. Ref.(239) Table 3.

For transformed data the calculation is simply,

$$F(z) = \frac{\log x - \bar{y}}{sy}$$

APPENDIX D

TABLES

TABLE: D1

INCLUSION SIZE DISTRIBUTION STEEL L AS CAST INGOT

SIZE RANGE d(μm)		TOP		MIDDLE		BOTTOM	
		No. Inclusions	No. Inclusions > d/10mm^2	No. Inclusions	No. Inclusions > d/10mm^2	No. Inclusions	No. Inclusions > d/10mm^2
0	2	955	4651.5	904	4680.2	1016	4795.3
2	4	957	2538.2	947	2592.9	996	2547.7
4	6	151	420.4	143	406.4	127	343.0
6	8	23	86.3	18	76.2	16	62.0
8	10	6	35.4	5	34.6	4	26.6
10	12	5	22.1	6	23.1	4	17.7
12	14	2	11.1	2	9.2	2	8.9
14	16	1	6.6	2	4.6	1	4.4
16		0	6.6	0	0	0	4.4
17		0	6.6	0	0	0	4.4
18		1	4.4	0	0	0	4.4
19		1	2.2	0	0	0	4.4
20		0	0	0	0	1	2.2

Total No. of Inclusions	: 2120	Total No. of Inclusions	: 2027	Total No. of Inclusions	: 2167
Total Area of Inclusions	: 0.0132mm^2	Total Area of Inclusions	: 0.0124mm^2	Total Area of Inclusions	: 0.0123mm^2
No. of Fields	: 120	No. of Fields	: 115	No. of Fields	: 120
% Area Fraction	: 0.292	% Area Fraction	: 0.287	% Area Fraction	: 0.273
Projected Length	: 1.08mm^{-1}	Projected Length	: 1.1mm^{-1}	Projected Length	: 1.09mm^{-1}

TABLE: D2

INCLUSION SIZE DISTRIBUTION STEEL F AS CAST

SIZE RANGE d(um)		TOP		MIDDLE		BOTTOM	
		No. Inclusions	No. Inclusions > d/10mm^2	No. Inclusions	No. Inclusions > d/10mm^2	No. Inclusions	No. Inclusions > d/10mm^2
0	2	940	3699.8	936	3977.6	993	3713.9
2	4	1009	2035.8	1047	2202.2	1021	1956.1
4	6	108	249.6	93	216.2	69	148.7
6	8	21	58.4	10	39.8	8	26.6
8	10	8	21.2	9	20.9	3	12.4
10	12	0	21.2	2	3.8	1	7.1
12	14	3	7.1	0	0	0	7.1
14	16	0	7.1	0	0	2	5.3
16		1	1.8	0	0	0	5.3
17		0	0	0	0	1	1.8
18		0		0	0	0	0
19		0	0	0	0	0	0
20		0	0	0	0	0	0

Total No. of Inclusions	: 2090	Total No. of Inclusions	: 2097	Total No. of Inclusions	: 2098
Total Area of Inclusions	: 0.0119mm^2	Total Area of Inclusions	: 0.0111mm^2	Total Area of Inclusions	: 0.0105mm^2
No. of Fields	: 150	No. of Fields	: 140	No. of Fields	: 150
% Area Fraction	: 0.21	% Area Fraction	: 0.211	% Area Fraction	: 0.186
Projected Length	: 0.85mm^{-1}	Projected Length	: 0.89mm^{-1}	Projected Length	: 0.8mm^{-1}

TABLE: D3 . INCLUSION SIZE DISTRIBUTION STEEL K AS CAST

SIZE RANGE d(um)		TOP		MIDDLE		BOTTOM	
		No. Inclusions	No. Inclusions $>d/10mm^2$	No. Inclusions	No. Inclusions $>d/10mm^2$	No. Inclusions	No. Inclusions $>d/10mm^2$
0	2	810	3045.4	643	2861.1	879	3073.6
2	4	1219	1913.4	1375	2007.4	1315	1906.5
4	6	124	209.6	112	181.9	98	160.6
6	8	9	36.3	7	33.2	9	30.5
8	10	11	23.8	12	23.9	9	18.6
10	12	3	8.4	5	8.0	4	6.6
12	14	0	8.4	0	8.0	1	1.3
14	16	2	4.2	1	1.33	0	0.0
16		0	4.2	0	0.0	0	0.0
17		0	4.2	0	0.0	0	0.0
18		0	4.2	0	0.0	0	0.0
19		1	1.4	0	0.0	0	0.0
20		0	0.0	0	0.0	0	0.0

Total No. of Inclusions : 2179	Total No. of Inclusions : 2155	Total No. of Inclusions : 2315
Total Area of Inclusions: $0.0137mm^2$	Total Area of Inclusions: $0.0141mm^2$	Total Area of Inclusions : $0.0133mm^2$
No. of Fields : 190	No. of Fields : 200	No. of Fields : 200
% Area Fraction : 0.191	% Area Fraction : 0.187	% Area Fraction : 0.176
Projected Length : $0.75mm^{-1}$	Projected Length : $0.74mm^{-1}$	Projected Length : $0.73mm^{-1}$

TABLE: D4 INCLUSION SIZE DISTRIBUTION STEEL M AS CAST

SIZE RANGE d(um)		TOP		MIDDLE		BOTTOM	
		No. Inclusions	No. Inclusions > d/10mm^2	No. Inclusions	No. Inclusions > d/10mm^2	No. Inclusions	No. Inclusions > d/10mm^2
0	2	1027	2053.9	1058	2171.2	1059	2134.1
2	4	932	1005.0	918	1047.4	901	1009.1
4	6	41	53.1	60	72.2	35	52.1
6	8	6	11.23	4	8.5	10	14.9
8	10	1	5.1	1	4.3	2	4.3
10	12	1	4.1	2	3.2	0	4.3
12	14	1	3.1	0	3.2	1	2.1
14	16	1	2.0	1	1.1	1	1.1
16		0	2.0	0	0.0	0	0.0
17		0	2.0	0	0.0	0	0.0
18		1	1.0	0	0.0	0	0.0
19		0	0.0	0	0.0	0	0.0
20		0	0.0	0	0.0	0	0.0

Total No. of Inclusions	: 2011	Total No. of Inclusions	: 2044	Total No. of Inclusions	: 2009
Total Area of Inclusions	: 0.0092mm^2	Total Area of Inclusions	: 0.009 mm^2	Total Area of Inclusions	: 0.0088mm^2
No. of Fields	: 260	No. of Fields	: 250	No. of Fields	: 250
% Area Fraction	: 0.094	% Area Fraction	: 0.096	% Area Fraction	: 0.093
Projected Length	: 0.42mm^{-1}	Projected Length	: 0.44mm^{-1}	Projected Length	: 0.43mm^{-1}

TABLE: D5 STATISTICAL ANALYSIS OF THE AS CAST INCLUSION SIZE (DIAMETER) DISTRIBUTION - UNITS MICRONS

Steel Code	Ingot Position	Mean Size	S.D.	Log-Transformed Data Mean	S.D.	Skewness	Kurtosis
L	TOP	2.35	1.58	-2.7153	0.2721	0.03	1.79
	MID	2.34	1.52	-2.7126	0.2694	0.01	1.72
	BASE	2.26	1.47	-2.7276	0.2657	0.03	1.7
F	TOP	2.4	1.42	-2.6937	0.2605	-0.01	1.72
	MID	2.25	1.3	-2.7217	0.2573	0.00	1.5
	BASE	2.17	1.31	-2.738	0.2546	0.01	1.55
K	TOP	2.45	1.41	-2.6819	0.255	-0.04	1.84
	MID	2.58	1.3	-2.6482	0.2397	-0.25	2.17
	BASE	2.38	1.29	-2.6898	0.2502	-0.05	1.68
M	TOP	2.06	1.25	-2.7594	0.2505	0.04	1.52
	MID	2.04	1.18	-2.7619	0.2508	0.26	1.59
	BASE	2.93	1.0	-2.559	0.1623	-2.42	7.084

TABLE: D6. COMPOSITION OF INCLUSIONS IN STEEL L AS CAST

Aluminium %	Sulphur %	Manganese %	Silicon %	Calcium %	Iron %	Size (µm)
51.67	3.64	12.37	0.00	0.4	31.92	2.2
0.13	8.02	15.69	0.00	0.00	76.15	3.9
8.38	15.57	30.27	0.00	0.33	45.25	0.9
3.94	14.95	25.78	0.02	0.07	55.28	1.4
0.00	9.21	15.8	0.02	0.06	74.9	1.0
0.07	5.6	11.03	0.03	0.11	83.17	0.9
1.11	21.83	44.29	0.03	0.21	32.55	1.5
0.00	20.15	42.9	0.00	0.28	36.68	0.8
56.63	6.28	13.09	0.05	0.22	23.72	1.5
8.47	11.63	19.34	0.04	0.19	60.33	2.0
55.3	4.87	12.19	0.00	0.00	27.64	1.5
0.00	7.72	12.97	0.00	0.00	79.31	1.0
8.4	15.59	32.95	0.00	0.00	43.05	1.9
6.42	16.23	32.97	0.00	0.45	43.93	1.5
2.63	11.25	16.94	0.00	0.15	69.03	1.4
48.23	12.84	17.98	0.00	0.00	20.95	2.0
0.23	17.42	26.6	0.00	0.1	55.65	1.2
0.00	18.18	28.74	0.00	0.00	53.08	1.0
36.41	7.03	8.88	0.00	0.05	47.63	1.4
37.42	8.09	14.78	0.00	0.24	39.47	1.2
30.49	13.81	23.78	0.03	0.00	31.89	2.0
0.07	13.22	18.23	0.00	0.00	68.49	1.0
0.05	17.07	25.6	0.00	0.2	57.08	1.0
0.09	15.01	21.38	0.00	0.02	63.49	1.4
0.05	14.37	21.01	0.06	0.15	64.37	1.4
48.67	6.47	9.66	0.00	0.16	35.05	3.0
8.33	9.58	15.42	0.00	0.02	66.64	1.0
0.00	10.99	18.11	0.08	0.0	70.82	1.0
0.1	10.49	15.74	0.09	0.01	73.58	1.0
0.00	9.3	16.32	0.05	0.00	74.33	1.0
0.00	23.22	42.27	0.00	0.00	34.52	1.2
23.84	12.26	19.86	0.01	0.00	44.03	1.3
0.11	12.68	20.91	0.04	0.23	66.04	0.8
0.00	15.55	30.87	0.02	0.00	53.56	1.0
0.03	16.48	28.65	0.08	0.4	54.36	1.2
0.00	15.49	23.04	0.08	0.00	61.39	1.2
0.18	19.53	37.61	0.00	0.00	42.68	1.0
21.78	14.61	32.57	0.00	0.33	30.7	1.5
51.28	3.06	8.49	0.02	0.17	36.97	1.5
2.74	18.88	31.76	0.00	0.00	46.62	1.1
0.00	15.94	30.29	0.00	0.00	53.76	1.0
0.00	17.83	32.31	0.00	0.15	49.71	1.5
0.00	16.94	28.49	0.02	0.02	54.53	1.0
12.48	8.83	13.47	0.00	0.00	65.22	1.0
0.27	19.39	36.41	0.01	0.14	43.78	1.2
0.00	20.07	36.38	0.00	0.2	43.36	1.2
0.00	14.12	31.9	0.02	0.24	53.73	1.0
44.56	9.55	19.03	0.00	0.17	26.7	2.0
0.00	14.42	24.01	0.02	0.00	61.72	1.0
0.00	12.12	18.17	0.08	0.00	69.63	0.8

TABLE: D7. COMPOSITION OF INCLUSIONS IN STEEL F AS CAST

Aluminium %	Sulphur %	Manganese %	Silicon %	Calcium %	Iron %	Size (μm)
0.00	11.95	20.24	0.00	0.00	67.8	0.5
0.00	7.89	11.19	0.02	0.00	80.91	0.7
0.08	5.77	9.96	0.02	0.00	84.57	0.5
0.00	12.95	23.27	0.02	0.00	63.76	0.8
0.00	9.05	17.4	0.00	0.00	73.55	0.5
0.00	5.5	9.96	0.00	0.01	84.53	0.4
0.00	11.79	20.34	0.07	0.00	67.79	0.8
0.00	6.99	11.77	0.09	0.00	81.14	0.5
0.00	9.22	16.3	0.00	0.00	74.49	1.0
0.00	9.88	17.26	0.07	0.18	72.26	0.8
37.65	6.66	14.13	0.04	0.3	41.23	1.8
0.05	9.18	15.3	0.01	0.07	75.4	1.0
0.00	12.74	22.25	0.00	0.22	64.79	1.0
36.71	8.68	15.06	0.05	0.00	39.5	1.5
0.09	12.66	20.96	0.00	0.11	66.18	0.9
0.03	13.12	22.74	0.00	0.00	64.12	1.0
11.48	18.7	35.76	0.00	0.11	33.96	2.3
0.00	18.24	34.23	0.00	0.18	47.35	1.0
0.00	9.09	14.88	0.00	0.23	75.8	1.0
0.2	11.58	19.16	0.06	0.15	68.84	0.8
0.9	25.09	44.4	0.08	0.14	29.39	1.2
0.00	12.41	20.09	0.06	0.17	67.27	1.0
17.56	11.87	20.37	0.00	0.00	50.2	1.5
21.55	8.03	18.03	0.00	0.00	52.39	0.8
1.05	20.88	38.04	0.01	0.00	40.62	1.0
0.71	22.23	45.26	0.00	0.00	31.8	1.0
0.18	9.75	16.3	0.06	0.07	73.64	1.0
14.81	8.75	14.89	0.01	0.00	61.54	1.2
6.66	16.74	28.51	0.09	0.00	47.99	1.3
47.62	16.89	25.3	0.00	0.23	9.96	4.0
0.01	9.94	16.5	0.00	0.13	73.42	1.3
0.00	18.02	34.68	0.00	0.08	47.22	1.2
0.00	20.94	36.65	0.01	0.18	42.22	2.0
43.22	8.79	17.59	0.00	0.00	30.4	1.0
17.79	8.64	16.4	0.01	0.11	57.06	1.2
2.13	16.59	30.8	0.00	0.18	50.31	1.0
0.00	8.66	15.59	0.02	0.05	75.69	1.0
4.06	14.02	21.5	0.04	0.02	60.36	1.0
0.91	14.94	30.56	0.05	0.14	53.41	0.8
35.41	9.91	20.69	0.00	0.00	34.27	1.7
0.04	5.73	10.44	0.03	0.05	83.71	1.0
0.00	14.72	26.34	0.08	0.01	58.84	1.0
10.26	19.75	34.62	0.05	0.00	35.32	2.0
9.04	19.4	38.5	0.00	0.08	32.98	1.5
25.65	10.2	24.41	0.01	0.00	39.72	1.5
7.69	14.27	23.77	0.03	0.01	54.22	1.0
21.12	9.14	19.96	0.03	0.00	52.75	1.0
35.37	7.69	11.68	0.02	0.15	45.08	2.0
43.0	6.36	14.78	0.04	0.00	35.83	2.2
0.00	13.29	23.29	0.06	0.00	63.36	0.8
20.05	12.22	26.61	0.00	0.00	41.11	1.2
18.54	14.41	24.83	0.05	0.00	42.17	2.0

TABLE: D8. COMPOSITION OF INCLUSIONS IN STEEL K AS CAST

Aluminium %	Sulphur %	Manganese %	Silicon %	Calcium %	Iron %	Size (μm)
53.05	0.01	0.21	0.17	21.94	24.62	7.0
0.02	13.85	13.88	0.05	6.73	65.47	1.0
35.89	7.43	3.54	0.07	8.56	44.52	1.5
0.00	14.2	13.9	0.00	5.3	66.61	1.0
0.5	14.44	15.52	0.05	5.67	63.82	1.0
0.00	12.72	9.92	0.05	7.84	69.47	1.0
1.71	24.55	15.4	0.00	17.42	40.93	1.2
26.08	0.42	1.49	0.04	1.06	70.91	1.0
1.6	13.27	13.69	0.00	6.08	63.35	1.0
0.56	22.01	19.53	0.05	11.3	46.55	1.5
4.7	13.73	13.56	0.03	6.13	61.86	1.0
35.02	0.00	1.85	0.00	2.82	60.31	1.2
3.72	16.39	20.89	0.1	10.58	40.81	1.2
15.72	14.76	38.32	0.04	3.29	27.88	1.5
9.37	0.00	1.55	0.00	0.53	88.55	1.5
9.55	5.55	8.97	0.01	1.65	74.27	1.0
1.57	10.36	10.26	0.04	6.45	71.33	1.2
14.56	32.32	7.64	0.0	39.86	5.61	10.0
0.51	11.23	20.33	0.04	2.09	65.8	3.0
17.05	14.36	5.93	0.00	17.29	45.37	4.0
0.14	7.73	13.5	0.06	0.17	78.4	1.0
0.00	9.06	14.46	0.08	0.13	76.27	1.0
0.11	25.59	7.91	0.11	33.86	32.42	2.0
1.09	9.41	9.58	0.00	4.81	75.1	1.0
7.01	8.35	15.46	0.00	2.58	66.6	1.3
0.74	21.85	17.26	0.00	16.51	43.64	1.2
1.14	12.59	14.37	0.00	5.57	66.34	1.2
2.49	11.12	11.26	0.05	5.54	69.53	1.2
8.0	14.99	11.17	0.02	16.12	49.72	1.0
14.91	10.51	10.97	0.06	10.97	52.58	2.0
0.09	27.84	10.37	0.07	28.4	33.23	2.2
1.38	4.74	5.19	0.01	1.73	86.93	0.7
3.88	5.78	7.5	0.06	1.83	80.95	0.25
4.16	8.65	12.23	0.00	2.64	72.32	1.0
0.58	17.51	12.13	0.00	11.85	58.28	1.0
2.38	13.35	15.89	0.04	4.98	63.36	1.0
4.8	11.46	14.69	0.02	4.06	64.97	1.0
6.83	10.49	15.59	0.03	2.47	65.58	1.0
0.36	26.32	19.58	0.00	18.71	35.03	2.0
2.06	16.11	22.04	0.00	3.66	56.13	1.2
0.00	15.43	19.43	0.00	4.55	60.59	1.0
0.37	15.17	22.49	0.05	3.03	58.9	1.0
0.04	10.68	14.56	0.00	3.53	71.19	1.1
2.44	12.32	16.53	0.04	4.12	64.54	0.8
2.3	20.26	17.9	0.00	11.99	47.55	1.5
0.01	13.42	14.78	0.00	6.16	65.62	1.2
7.41	5.54	3.66	0.07	5.39	77.95	0.5
1.2	14.84	9.94	0.00	16.03	57.99	1.0
1.09	16.57	16.95	0.00	10.88	54.5	0.8
1.6	7.81	5.67	0.00	5.93	79.0	1.3
5.56	7.17	8.02	0.04	3.2	76.01	1.0
8.42	4.1	6.75	0.01	1.05	79.67	0.8
0.14	16.16	20.43	0.00	8.58	54.69	1.0
1.15	28.88	15.44	0.04	27.32	27.17	2.5
12.27	5.79	9.28	0.07	1.58	71.01	1.0

TABLE: D9. COMPOSITION OF INCLUSIONS IN STEEL M AS CAST

Aluminium %	Sulphur %	Manganese %	Silicon %	Calcium %	Iron %	Size (μm)
9.35	3.88	2.23	0.04	5.02	79.48	0.6
4.34	6.67	3.24	0.00	7.3	78.44	1.0
0.00	1.86	1.71	0.02	2.01	94.4	1.0
2.97	12.66	2.49	0.00	15.34	66.54	1.0
0.27	10.43	4.28	0.00	10.87	74.15	1.1
2.36	6.32	4.27	0.02	9.01	78.01	0.5
4.02	2.86	2.43	0.01	3.19	87.49	0.5
0.91	17.38	2.58	0.00	23.29	55.84	1.8
9.8	4.14	1.91	0.03	4.84	79.27	1.0
1.35	14.77	2.15	0.00	19.63	62.1	1.8
1.05	15.5	3.61	0.01	21.94	57.89	1.0
6.97	2.24	1.73	0.05	4.76	84.24	1.2
20.64	20.54	1.13	0.08	33.29	24.33	4.0
10.9	0.3	1.59	0.04	0.94	86.23	0.8
0.8	5.07	2.82	0.08	5.87	85.35	0.8
0.94	10.17	3.8	0.02	10.61	74.46	1.3
0.78	15.17	3.49	0.04	17.28	63.24	1.5
0.66	23.87	24.01	0.02	12.61	38.84	2.0
8.07	2.52	3.62	0.00	1.4	84.4	1.0
0.4	30.58	54.53	0.00	1.1	13.39	3.0
9.03	22.8	49.17	0.03	1.98	16.99	2.5
0.3	5.32	3.84	0.01	5.59	84.95	0.9
1.99	7.3	4.16	0.01	8.8	73.03	0.8
9.08	5.77	3.08	0.00	9.04	73.03	0.8
1.66	14.77	2.3	0.01	22.21	59.03	1.8
21.45	25.41	1.57	0.00	42.93	8.64	4.0
0.36	4.95	4.18	0.00	4.22	86.3	0.7
0.68	11.02	5.54	0.01	15.43	67.31	1.0
0.54	17.28	22.81	0.02	8.19	51.15	1.2
3.06	9.02	15.71	0.05	2.66	69.5	1.0
1.8	3.74	2.52	0.00	4.8	87.14	0.8
0.00	3.51	2.04	0.1	3.55	90.81	1.0
3.43	4.41	2.95	0.04	5.23	83.94	0.8
0.29	7.55	1.61	0.04	8.4	82.12	1.5
9.04	7.36	6.22	0.05	8.96	68.38	1.0
0.72	16.37	2.14	0.02	18.55	62.2	1.0
8.32	2.11	2.77	0.00	1.78	85.01	1.0
12.48	0.99	0.71	0.06	3.61	82.14	2.0
6.71	5.66	2.15	0.04	7.97	77.49	1.2
2.86	8.71	2.98	0.00	9.91	75.54	1.2
0.1	20.62	40.51	0.00	1.2	37.56	1.2
2.13	10.17	15.96	0.00	0.96	70.78	1.2
7.68	1.11	0.99	0.05	3.74	86.43	1.0
2.84	4.86	2.61	0.03	4.34	85.32	1.0
0.01	16.91	28.98	0.00	0.33	52.9	1.5
1.04	10.1	3.92	0.04	11.71	73.2	0.8
10.12	2.55	3.22	0.01	2.92	81.18	0.8
6.95	5.89	1.82	0.09	7.9	77.35	1.6
1.96	8.19	2.17	0.03	9.2	78.45	1.2
1.82	18.35	1.97	0.05	22.0	55.8	2.0
3.65	9.7	2.8	0.05	11.17	72.64	1.2
1.12	9.41	2.52	0.02	10.29	76.64	1.0

TABLE: D10. AREA OF INCLUSIONS (μm^2) PER FIELD

Steel Code	No. of Fields.	Mean	S.D.	C.ofV. %	Min. Value	Max. Value	Range
L75L	100	100.13	45.67	0.46	18.16	241.40	223.24
L75T	100	110.26	40.94	0.37	31.64	244.63	212.99
L9L	100	112.05	60.64	0.54	24.11	457.61	433.5
L9T	100	102.76	50.57	0.40	29.59	383.2	353.61
L0L	100	81.65	39.41	0.48	13.47	228.8	215.33
L0L	100	79.32	44.5	0.56	34.86	345.11	310.25
L1L	100	86.64	44.51	0.52	13.47	240.82	227.35
L1T	100	86.52	30.65	0.36	29.59	189.25	159.66
F75L	131	68.6	40.46	0.59	11.71	215.53	203.52
F75T	100	59.85	38.51	0.64	16.01	208.2	192.19
F9L	125	70.95	34.88	0.49	12.5	217.57	205.07
F9T	100	67.51	27.81	0.41	24.6	174.21	149.61
F0L	120	67.0	29.85	0.45	13.67	200.39	186.72
F0T	102	63.56	29.24	0.46	19.92	173.82	153.9
F1L	120	76.23	33.41	0.44	13.28	177.73	164.45
F1T	100	64.99	32.06	0.49	20.70	267.18	246.48
K75L	125	52.58	31.67	0.6	9.38	280.07	270.69
K75T	125	56.55	21.72	0.38	14.93	127.73	112.80
K9L	150	56.39	35.3	0.63	16.11	328.13	312.02
K9T	126	62.44	27.39	0.44	17.28	193.65	176.37
K0L	125	61.92	29.44	0.48	9.38	158.49	149.11
K0T	115	55.46	24.77	0.45	9.96	152.34	142.38
K1L	120	54.89	37.11	0.68	16.11	336.61	320.5
K1T	126	55.66	24.3	0.44	9.67	127.44	117.77
M75L	240	21.75	13.35	0.61	2.63	112.79	110.16
M75T	220	21.11	14.69	0.71	0.88	113.38	112.5
M9L	NOT DETERMINED						
M9T	NOT DETERMINED						
M0L	233	25.28	16.88	0.67	0.58	97.26	96.68
M0T	200	26.76	15.84	0.59	0.6	106.63	106.34
M1L	210	25.67	14.45	0.56	2.34	103.42	101.08
M1T	202	27.39	12.4	0.45	6.73	82.03	75.3

TABLE: D11. NUMBER OF INCLUSIONS PER FIELD (COUNTS)

Steel Code	No. of Fields	Mean	S.D.	C.ofV. %	Min. Value	Max. Value	Range
L75L	100	26	8.5	0.3	9	50	41
L75L	100	36.6	10.7	0.3	14	59	45
L9L	100	24.3	9.2	0.4	8	45	37
L9T	100	41.7	15.0	0.4	13	88	75
L0L	100	25.4	9.4	0.4	9	58	49
L0T	100	36.6	14.1	0.4	17	113	96
L1L	100	18.8	7.1	0.4	5	42	37
L1T	100	29	7.4	0.3	11	48	37
F75L	131	15.8	5.4	0.3	5	39	34
F75T	100	18.9	9.9	0.5	5	62	57
F9L	125	16.7	6.0	0.4	5	38	33
F9T	100	21.4	5.5	0.3	11	36	25
F0L	120	16.9	6.0	0.4	6	34	28
F0T	102	22.9	6.4	0.3	9	38	29
F1L	120	17.7	6.0	0.3	5	39	34
F1T	100	23.6	5.9	0.3	10	43	33
K75L	125	16.1	5.3	0.3	7	35	28
K75T	125	16.8	4.7	0.3	7	29	22
K9L	150	14.6	4.7	0.3	5	24	19
K9T	126	16.9	4.8	0.3	6	31	25
K0L	125	16.6	5	0.3	5	30	25
K0T	115	18.6	5	0.3	7	31	24
K1L	120	17.0	4.8	0.3	16	30	24
K1T	126	16.2	5.7	0.4	3	33	30
M75L	240	8.7	3.3	0.4	2	19	17
M75T	220	9.3	3.4	0.4	2	21	19
M9L	NOT DETERMINED						
M9T	NOT DETERMINED						
M0L	233	8.6	4	0.5	1	25	24
M0T	200	10.1	3.5	0.3	1	24	23
M1L	210	9.8	3.2	0.3	2	19	17
M1T	202	10.4	3.7	0.4	3	28	25

TABLE: D12 TOTAL LENGTH OF INCLUSIONS (μm) PER FIELD
(direction of measurement indicated by suffix)

Steel Code	No. of Fields	Mean	S.D.	C.ofV. %	Min. Value	Max. Value	Range
L75L	100	74.03	26.39	0.36	21.87	157.5	135.63
L75T	100	82.65	27.04	0.33	27.5	150.62	123.12
L9L	100	83.82	39.28	0.47	22.5	261.25	238.75
L9T	100	82.04	28.64	0.35	30.62	153.12	122.5
L0L	100	74.04	32.01	0.43	13.12	193.12	180.0
L0T	100	69.01	27.05	0.4	31.25	227.5	196.25
L1L	100	68.04	34.5	0.51	16.25	223.12	206.87
L1T	100	65.63	20.78	0.32	28.12	126.87	98.75
F75L	131	52.36	24.18	0.46	15.63	140.63	125.0
F75T	100	46.75	25.64	0.55	14.06	141.1	127.34
F9L	125	58.13	22.66	0.39	14.48	129.69	114.85
F9T	100	51.96	14.62	0.28	26.56	111.71	85.15
F0L	120	55.83	20.00	0.36	10.15	121.09	110.94
F0T	102	54.49	16.42	0.31	21.09	96.09	75.0
F1L	120	57.48	22.35	0.39	10.19	123.44	113.25
F1T	100	52.16	16.61	0.32	22.65	134.38	111.73
K75L	125	36.18	12.66	0.35	11.25	78.75	67.5
K75T	125	36.81	11.35	0.31	14.37	66.87	52.5
K9L	150	33.63	12.43	0.37	9.37	68.75	59.38
K9T	126	37.72	11.73	0.31	10.62	75.62	65.0
K0L	125	40.08	16.18	0.4	10.62	99.37	88.75
K0T	115	35.61	11.63	0.33	8.75	71.87	63.12
K1L	120	36.24	14.07	0.39	15.0	85.0	70.0
K1T	126	34.72	12.62	0.36	6.25	68.75	62.5
M75L	240	15.51	7.04	0.45	3.12	44.37	41.25
M75T	220	15.87	7.15	0.45	1.98	42.4	40.42
M9L	NOT DETERMINED						
M9T	NOT DETERMINED						
M0L	233	16.64	9.25	0.56	0.62	49.37	48.75
M0T	200	18.84	7.7	0.41	0.66	51.01	50.35
M1L	210	18.25	7.61	0.42	3.31	47.7	44.39
M1T	202	19.22	7.32	0.38	5.62	51.87	46.25

TABLE: D13 AVERAGE INCLUSION AREA (μm^2) PER FIELD

Steel Code	No. of Fields	Mean	S.D.	C.ofV. %	Min. Value	Max. Value	Range
L75L	100	3.89	1.44	0.37	1.3	10.16	8.86
L75T	100	3.03	0.75	0.25	1.43	5.56	4.13
L9L	100	4.78	2.02	0.42	1.54	12.71	11.71
L9T	100	2.46	0.77	0.31	1.32	7.37	6.05
L0L	100	3.33	1.39	0.42	1.35	8.17	6.82
L0T	100	2.2	0.99	0.45	1.11	10.45	9.34
L1L	100	4.64	1.96	0.42	1.22	12.52	11.3
L1T	100	2.96	0.79	0.27	1.3	5.39	4.09
F75L	131	4.43	2.41	0.54	1.2	17.94	16.74
F75L	100	3.2	1.22	0.38	1.41	8.62	7.21
F9L	125	4.28	1.53	0.36	1.63	12.82	11.19
F9T	100	3.18	1.15	0.36	1.48	8.3	6.82
F0L	120	4.15	1.82	0.44	1.62	16.7	15.08
F0T	102	2.8	1.17	0.42	1.33	9.15	7.82
F1L	120	4.46	1.5	0.34	1.9	8.38	6.48
F1T	100	2.74	0.98	0.36	1.45	8.1	6.65
K75L	125	3.37	2.12	0.63	1.17	20.0	18.83
K75T	125	3.37	1.02	0.3	1.49	6.92	5.43
K9L	150	4.06	3.62	0.89	1.32	41.02	39.7
K9T	126	3.76	1.35	0.36	1.52	8.37	6.85
K0L	125	3.67	1.22	0.33	1.33	4.34	3.01
K0T	115	2.96	0.96	0.32	1.17	6.09	4.92
K1L	120	3.18	1.57	0.49	1.19	13.46	12.27
K1T	126	3.53	1.26	0.36	1.31	8.1	6.79
M75L	240	2.53	1.17	0.46	0.88	8.69	7.81
M75T	220	2.25	1.56	0.69	0.44	15.23	14.79
M9L	NOT DETERMINED						
M9T	NOT DETERMINED						
M0L	233	2.89	1.46	0.51	0.53	10.04	9.51
M0T	200	2.62	1.26	0.48	0.29	9.38	9.09
M1L	210	2.61	1.16	0.44	0.68	8.62	7.94
M1T	202	2.69	1.01	0.38	0.91	9.11	8.2

TABLE: D14 AVERAGE INCLUSION MAJOR AXIS (μm) PER FIELD

Steel Code	No. of Fields	Mean	S.D.	C.ofV %	Min. Value	Max. Value	Range
L75L	100	2.89	0.69	0.24	1.56	5.56	4.0
L75T	100	2.27	0.39	0.17	1.35	3.36	2.10
L9L	100	3.6	1.33	0.37	1.33	8.75	7.42
L9T	100	2.0	0.37	0.18	1.27	3.05	1.78
L0L	100	2.96	0.79	0.27	1.31	6.07	4.76
L0T	100	1.91	0.33	0.17	1.28	3.31	2.03
L1L	100	3.68	1.37	0.37	1.48	9.43	7.95
L1T	100	2.27	0.47	0.21	1.31	3.71	2.4
F75L	131	3.34	1.09	0.33	1.61	6.56	4.95
F75T	100	2.5	0.62	0.25	1.62	6.09	4.47
F9L	125	3.53	0.82	0.23	1.82	6.25	4.43
F9T	100	2.44	0.4	0.16	1.72	3.58	1.86
F0L	120	3.41	0.9	0.26	1.69	7.23	5.54
F0T	102	2.31	0.46	0.2	1.63	3.86	2.23
F1L	120	3.31	0.92	0.28	0.39	6.74	6.35
F1T	100	2.21	0.42	0.19	1.56	4.07	2.51
K75L	125	2.29	0.6	0.26	1.33	5.63	4.3
K75T	125	2.2	0.39	0.18	1.44	3.36	1.92
K9L	150	2.33	0.63	0.27	1.19	5.23	4.04
K9T	126	2.27	0.49	0.22	1.42	4.37	2.95
K0L	125	2.39	0.55	0.23	1.33	4.34	3.01
K0T	115	1.92	0.36	0.19	1.21	3.0	1.79
K1L	120	2.12	0.54	0.25	1.19	4.47	3.28
K1T	126	2.18	0.45	0.21	1.18	3.48	2.3
M75L	240	1.8	0.48	0.27	0.9	4.02	3.12
M75T	220	1.69	0.47	0.28	0.88	4.26	3.38
M9L			NOT DETERMINED				
M9T			NOT DETERMINED				
M0L	233	1.91	0.58	0.3	0.62	4.73	4.11
M0T	200	1.87	0.46	0.25	0.66	3.81	3.15
M1L	210	1.86	0.46	0.25	0.74	3.83	3.09
M1T	202	1.87	0.4	0.21	0.97	3.61	2.64

TABLE: D15. AVERAGE INCLUSION MINOR AXIS (μm) PER FIELD

Steel Code	No. of Fields	Mean	S.D.	C.ofV. %	Min. Value	Max. Value	Range
L75L	100	1.68	0.32	0.19	0.98	3.06	2.08
L75T	100	1.68	0.2	0.12	1.35	2.34	0.99
L9L	100	1.68	0.24	0.14	1.04	2.55	1.51
L9T	100	1.55	0.32	0.21	1.15	4.04	2.89
L0L	100	1.41	0.35	0.25	0.84	2.52	1.68
L0T	100	1.44	0.37	0.26	1.1	4.6	3.56
L1L	100	1.6	0.3	0.19	1.01	2.69	1.68
L1T	100	1.64	0.17	0.1	1.25	2.20	0.77
F75L	131	1.61	0.4	0.25	0.86	4.23	3.37
F75T	100	1.59	0.32	0.25	0.97	2.37	1.4
F9L	125	1.52	0.26	0.17	0.96	2.61	1.65
F9T	100	1.63	0.37	0.23	1.05	3.94	2.89
F0L	120	1.51	0.28	0.19	0.92	2.94	2.02
F0T	102	1.5	0.33	0.22	0.98	3.18	2.2
F1L	120	1.76	1.3	0.74	1.13	15.57	6.74
F1T	100	1.54	0.28	0.18	1.1	2.53	1.43
K75L	125	1.78	0.51	0.29	1.06	4.53	3.47
K75T	125	1.92	0.3	0.16	1.24	2.78	1.54
K9L	150	2.08	0.83	0.4	1.17	9.98	8.81
K9T	126	2.06	0.4	0.19	1.35	3.5	2.15
K0L	125	1.92	0.3	0.16	1.12	2.97	1.85
K0T	115	1.93	0.33	0.17	1.07	2.98	1.91
K1L	120	1.84	0.49	0.27	1.07	5.32	4.25
K1T	126	2.02	0.33	0.16	1.09	2.96	1.87
M75L	240	1.73	0.37	0.21	0.84	3.34	2.5
M75T	220	1.59	0.48	0.3	0.57	5.32	4.75
M9L			NOT DETERMINED				
M9T			NOT DETERMINED				
M0L	233	1.83	0.44	0.24	0.76	2.95	2.19
M0T	200	1.72	0.44	0.26	0.56	4.77	4.21
M1L	210	1.73	0.35	0.2	0.9	3.26	2.36
M1T	202	1.79	0.3	0.17	1.05	3.21	2.16

TABLE: D16. AVERAGE INCLUSION ASPECT RATIO PER FIELD

Steel Code	No. of Fields.	Mean	S.D.	C.ofV. %	Min. Value	Max. Value	Range
L75L	100	1.74	0.39	0.22	1.04	3.23	2.19
L75T	100	1.35	0.2	0.15	0.94	2.02	1.08
L9L	100	2.17	0.83	0.38	0.9	5.74	4.84
L9T	100	1.31	0.28	0.21	0.57	2.34	1.77
L0L	100	2.17	0.65	0.3	1.0	4.44	3.44
L0T	100	1.36	0.24	0.18	0.61	1.92	1.31
L1L	100	2.36	0.94	0.4	1.02	5.57	4.55
L1T	100	1.38	0.24	0.17	0.96	2.06	1.10
F75L	131	2.09	0.57	0.27	1.17	4.32	3.15
F75T	100	1.59	0.36	0.23	1.0	3.38	2.38
F9L	125	2.36	0.57	0.24	1.29	4.67	3.38
F9T	100	1.54	0.24	0.16	0.68	2.11	1.43
F0L	120	2.28	0.55	0.24	0.99	3.71	2.72
F0T	102	1.56	0.26	0.17	0.95	2.21	1.26
F1L	120	2.03	0.6	0.3	0.03	5.18	5.15
F1T	100	1.45	0.22	0.15	0.86	2.12	1.26
K75L	125	1.32	0.26	0.2	0.78	2.31	1.53
K75T	125	1.15	0.2	0.17	0.83	2.02	1.19
K9L	150	1.16	0.26	0.22	0.52	2.4	1.88
K9T	126	1.11	0.22	0.2	0.71	2.07	1.36
K0L	125	1.25	0.26	0.21	0.73	1.98	1.25
K0T	115	1.0	0.14	0.14	0.68	1.48	0.8
K1L	120	1.18	0.26	0.22	0.61	2.43	1.82
K1T	126	1.08	0.14	0.13	0.78	1.95	1.17
M75L	240	1.06	0.24	0.23	0.6	2.39	1.79
M75T	220	1.08	0.2	0.19	0.53	1.82	1.29
M9L			NOT DETERMINED				
M9T			NOT DETERMINED				
M0L	233	1.06	0.24	0.23	0.52	2.71	2.19
M0T	200	1.10	0.17	0.15	0.43	1.94	1.51
M1L	210	1.08	0.2	0.19	0.62	2.0	1.38
M1T	202	1.05	0.16	0.15	0.62	1.81	1.19

TABLE: D17. % AREA FRACTION OF INCLUSIONS ON LONG (L) AND TRANS (T) PLANES

Steel Code	Transformed Mean	S.D.	95% C.L. about Normal Mean	Min. Value	Max. Value	% R.A.	No. of Fields
L75L	0.239	0.21	$^{+0.027}_{-0.024}$	0.048	0.641	10.05	100
L75T	0.273	0.167	$^{+0.023}_{-0.022}$	0.084	0.65	7.23	100
L9L	0.264	0.213	$^{+0.03}_{-0.028}$	0.064	1.215	10.18	100
L9T	0.246	0.197	$^{+0.026}_{-0.024}$	0.079	1.018	9.41	100
L0L	0.194	0.214	$^{+0.022}_{-0.02}$	0.036	0.608	10.27	100
L0T	0.193	01.67	$^{+0.016}_{-0.016}$	0.093	0.916	7.92	100
L1L	0.199	0.23	$^{+0.026}_{-0.022}$	0.036	0.639	11.08	100
L1T	0.213	0.16	$^{+0.017}_{-0.016}$	0.079	0.503	7.56	100
F75L	0.155	0.251	$^{+0.019}_{-0.017}$	0.031	0.572	10.42	131
F75T	0.136	0.235	$^{+0.018}_{-0.016}$	0.043	0.553	11.33	100
F9L	0.167	0.224	$^{+0.018}_{-0.016}$	0.033	0.578	9.44	125
F9T	0.166	0.17	$^{+0.015}_{-0.013}$	0.065	0.463	8.05	100
F0L	0.162	0.19	$^{+0.015}_{-0.014}$	0.036	0.532	8.22	120
F0T	0.153	0.194	$^{+0.015}_{-0.014}$	0.053	0.462	9.16	102
F1L	0.182	0.208	$^{+0.019}_{-0.016}$	0.035	0.472	9.03	120
F1T	0.158	0.173	$^{+0.014}_{-0.014}$	0.055	0.709	8.23	100

TABLE: D17. CONT.

Steel Code	Transformed Mean	S.D.	95% C.L. about Normal Mean	Min. Value	Max. Value	% R.A.	No. of Fields
K75L	0.123	0.216	0.14 +0.012 -0.012	0.025	0.744	9.11	125
K75T	0.139	0.182	0.15 +0.012 -0.01	0.04	0.399	7.61	125
K9L	0.13	0.229	0.15 +0.013 -0.012	0.043	0.871	8.81	150
K9T	0.152	0.179	0.166 +0.012 -0.012	0.046	0.514	7.45	126
K0L	0.146	0.221	0.164 +0.015 -0.014	0.025	0.421	9.32	125
K0T	0.133	0.201	0.147 +0.013 -0.012	0.026	0.405	8.93	115
K1L	0.126	0.224	0.146 +0.014 -0.013	0.043	0.894	9.75	120
K1T	0.134	0.2	0.148 +0.012 -0.012	0.026	0.338	8.4	126
M75L	0.049	0.249	0.058 +0.004 -0.004	0.007	0.3	7.51	240
M75T	0.045	0.3	0.056 +0.005 -0.005	0.002	0.301	9.57	220
M9L			NOT DETERMINED				
M9T			NOT DETERMINED				
M0L	0.052	0.335	0.067 +0.007 -0.006	0.002	0.258	10.41	233
M0T	0.06	0.286	0.071 +0.007 -0.006	0.001	0.283	9.56	200
M1L	0.059	0.239	0.068 +0.005 -0.005	0.006	0.275	7.73	210
M1T	0.066	0.194	0.073 +0.004 -0.005	0.018	0.218	6.36	202

TABLE: D18. PROJECTED LENGTH PER mm^2 IN THE LONG(L) TRANS(T) AND THROUGH-THICKNESS(T/T) DIRECTIONS

Steel Code	Transformed Mean	S.D.	95% C.L. about Normal Mean	Min. Value	Max. Value	% R.A.	No. of Fields
L75L	0.66	0.176	0.71 +0.06 -0.05	0.24	1.5	8.36	100
L75T	0.99	0.14	0.99 +0.07 -0.06	0.33	1.88	6.58	100
L75T/T	1.12	0.163	1.2 +0.09 -0.09	0.35	2.54	7.72	100
L9L	0.6	0.192	0.66 +0.06 -0.05	0.22	1.48	9.14	100
L9T	0.97	0.191	1.06 +0.1 -0.09	0.34	3.4	9.12	100
L9T/T	1.23	0.187	1.35 +0.12 -0.11	0.36	4.22	8.92	100
L0L	0.52	0.175	0.57 +0.04 -0.04	0.18	1.41	8.3	100
L0T	0.79	0.155	0.85 +0.06 -0.06	0.39	2.9	7.31	100
L0T/T	1.09	0.191	1.2 +0.1 -0.1	0.21	3.12	9.12	100
L1L	0.45	0.188	0.49 +0.04 -0.04	0.17	0.95	8.95	100
L1T	0.74	0.126	0.77 +0.05 -0.04	0.3	1.4	5.92	100
L1T/T	0.98	0.212	1.1 +0.11 -0.1	0.26	0.36	10.17	100
F75L	0.38	0.178	0.41 +0.03 -0.03	0.09	0.98	7.26	131
F75T	0.43	0.209	0.49 +0.05 -0.05	0.11	1.75	9.99	100
F75T/T	0.76	0.197	0.85 +0.07 -0.08	0.25	2.27	8.08	131
F9L	0.38	0.195	0.41 +0.04 -0.03	0.09	0.98	8.2	125
F9T	0.53	0.144	0.56 +0.04 -0.03 +0.09	0.23	1.34	6.76	100

TABLE: D18. CONT.

Steel Code	Transformed Mean	S.D.	95% C.L. about Normal Mean	Min. Value	Max. Value	% R.A.	No. of Fields
F9T/T	0.86	0.19	+0.09 0.94 -0.07	0.24	2.09	7.96	125
F0L	0.38	0.165	+0.03 0.41 -0.03	0.14	0.82	7.12	120
F0T	0.52	0.157	+0.04 0.56 -0.04	0.02	1.16	7.37	102
F0T/T	0.84	0.164	+0.07 0.9 -0.06	0.16	1.95	7.08	120
F1L	0.45	0.203	+0.05 0.52 -0.04	0.13	6.53	8.81	120
F1T	0.56	0.136	+0.04 0.59 -0.04	0.26	1.35	6.39	100
F1T/T	0.85	0.187	+0.07 0.93 -0.07	0.16	1.99	8.09	120
K75L	0.43	0.17	+0.03 0.46 -0.03	0.14	1.99	8.09	120
K75T	0.5	0.154	+0.04 0.52 -0.03	0.16	0.91	6.41	125
K75T/T	0.55	0.155	+0.04 0.58 -0.03	0.18	1.27	6.44	125
K9L	0.45	0.173	+0.03 0.48 -0.03	0.18	1.29	6.56	150
K9T	0.53	0.148	+0.04 0.56 -0.03	0.2	1.59	6.15	126
K9T/T	0.5	0.175	+0.04 0.54 -0.03	0.15	1.11	6.42	150
K0L	0.49	0.165	+0.03 0.52 -0.04	0.15	1.04	6.87	125
K0T	0.55	0.158	+0.04 0.58 -0.04	0.16	1.29	6.96	115
K0T/T	0.6	0.182	+0.05 0.65 -0.05	0.17	1.6	7.65	125
K1L	0.47	0.168	+0.04 0.51 -0.03	0.18	2.15	7.26	120

TABLE: D18. CONT.

Steel Code	Transformed Mean	S.D.	95% C.L. about Normal Mean	Min. Value	Max. Value	% R.A.	No. of Fields
K1L	0.47	0.168	+0.04 0.51 -0.03	0.18	2.15	7.26	120
K1T	0.49	0.169	+0.04 0.52 -0.03	0.13	1.1	7.02	126
K1T/T	0.54	0.165	+0.05 0.58 -0.03	0.24	1.37	7.1	120
M75L	0.22	0.199	+0.02 0.24 -0.01	0.03	0.84	5.97	240
M75T	0.21	0.23	+0.02 0.24 -0.02	0.02	0.69	7.25	220
M75T/T	0.23	0.202	+0.02 0.25 -0.01	0.05	0.72	6.08	240
M9L	NOT DETERMINED						
M9T	NOT DETERMINED						
M9T/T	NIT DETERMINED						
M0L	0.22	0.258	+0.02 0.26 -0.02	0.02	0.72	7.93	233
M0T	0.25	0.224	+0.03 0.28 -0.02	0.01	1.08	7.42	200
M0T/T	0.23	0.266	+0.02 0.27 -0.02	0.01	0.8	8.19	233
M1L	0.25	0.182	+0.02 0.27 -0.01	0.04	0.63	5.84	210
M1T	0.28	0.159	+0.01 0.3 -0.02	0.08	0.82	5.19	202
M1T/T	0.27	0.192	+0.02 0.29 -0.01	0.05	0.77	6.16	210

TABLE: D19. PROJECTED AREA PER mm^2 ON A PLANE PARALLEL TO THE LONG(L) TRANS (T) AND THROUGH-THICKNESS (T/T) TESTING DIRECTIONS

Steel Code	Transformed Mean	S.D.	95% C.L. about Normal Mean	Min. Value	Max. Value	% R.A.	No. of Fields
L75L	1.62	0.176	+0.15 1.75 -0.13	0.59	3.7	8.36	100
L75T	2.33	0.14	+0.16 2.45 -0.15	0.82	4.63	6.58	100
L75T/T	2.76	0.163	+0.23 2.95 -0.21	0.87	6.27	7.72	100
L9L	1.49	0.192	+0.15 1.63 -0.13	0.54	3.65	9.14	100
L9T	2.39	0.191	+0.24 2.63 -0.22	0.84	8.38	9.12	100
L9T/T	3.04	0.187	+0.3 3.34 -0.28	0.9	10.41	8.92	100
L0L	1.29	0.175	+0.12 1.4 -0.11	0.43	3.49	8.3	100
L0T	1.95	0.155	+0.16 2.09 -0.14	0.96	7.15	7.31	100
L0T/T	2.69	0.191	+0.27 2.95 -0.25	0.52	7.69	9.12	100
L1L	1.1	0.188	+0.11 1.2 -0.1	0.43	2.35	8.95	100
L1T	1.83	0.126	+0.11 1.9 -0.11	0.75	3.46	5.92	100
L1T/T	2.41	0.212	+0.28 2.71 -0.25	0.65	8.89	10.17	100
F75L	0.93	0.178	+0.07 1.01 -0.07	0.22	2.41	7.26	131
F75T	1.06	0.209	+0.12 1.2 -0.11	0.26	4.31	9.99	100
F75T/T	1.89	0.179	+0.16 2.09 -0.16	0.62	5.6	8.08	131
F9L	0.93	0.195	+0.08 1.02 -0.08	0.21	2.41	8.2	125
F9T	1.31	0.144	+0.09 1.39 -0.09	0.57	3.3	6.76	100

+0.38

TABLE: D19. CONT.

Steel Code	Transformed Mean	S.D.	95% C.L. about Normal Mean		Min. Value	Max. Value	% R.A.	No. of Fields
				+0.38				
F9T/T	2.13	0.19	2.32		0.59	5.17	7.96	125
				-0.18				
				+0.08				
F0L	0.94	0.165	1.0		0.34	2.02	7.12	120
				-0.06				
				+0.1				
F0T	1.29	0.157	1.37		0.5	2.86	7.37	102
				-0.09				
				+0.16				
F0T/T	2.08	0.164	2.22		0.4	4.82	7.08	120
				-0.14				
				+0.11				
F1L	1.1	0.203	1.28		0.32	16.12	8.81	120
				-0.1				
				+0.1				
F1T	1.38	0.136	1.46		0.64	3.33	6.39	100
				-0.09				
				+0.19				
F1T/T	2.1	0.187	2.29		0.41	4.92	8.09	120
				-0.17				
				+0.08				
K75L	1.05	0.17	1.13		0.34	2.53	7.09	125
				-0.07				
				+0.08				
K75T	1.22	0.154	1.3		0.39	2.24	6.41	125
				-0.08				
				+0.09				
K75T/T	1.36	0.155	1.44		0.45	3.14	6.44	125
				-0.09				
				+0.07				
K9L	1.1	0.173	1.19		0.43	3.18	6.56	150
				-0.08				
				+0.08				
K9T	1.31	0.148	1.39		0.5	3.93	6.15	126
				-0.08				
				+0.09				
K9T/T	1.24	0.175	1.34		0.37	2.74	6.42	150
				-0.08				
				+0.09				
K0L	1.2	0.165	1.28		0.36	2.56	6.87	125
				-0.08				
				+0.1				
K0T	1.35	0.158	1.44		0.4	3.18	6.96	115
				-0.09				
				+0.12				
K0T/T	1.47	0.182	1.6		0.42	3.9	7.65	125
				-0.12				
				+0.09				
K1L	1.17	0.168	1.26		0.44	5.29	7.26	120
				-0.08				

TABLE: D19. CONT.

Steel Code	Transformed Mean	SD	95% C.L. about Normal Mean	Min. Value	Max. Value	% R.A.	No. of Fields
K1T	1.2	0.169	1.29 +0.09 -0.09	0.31	2.71	7.02	126
K1T/T	1.34	0.165	1.44 +0.11 -0.09	0.6	3.39	7.1	120
M75L	0.54	0.199	0.6 +0.03 -0.04	0.09	2.06	5.97	240
M75T	0.53	0.23	0.59 +0.05 -0.04	0.05	1.69	7.25	220
M75T/T	0.56	0.202	0.62 +0.04 -0.04	0.05	0.72	6.08	240
M9L			NOT DETERMINED				
M9T			NOT DETERMINED				
M9T/T			NOT DETERMINED				
M0L	0.55	0.258	0.64 +0.05 -0.05	0.05	1.78	7.93	233
M0T	0.63	0.224	0.7 +0.05 -0.05	0.02	2.66	7.42	200
M0T/T	0.56	0.266	0.66 +0.06 -0.05	0.02	1.97	8.19	233
M1L	0.62	0.182	0.68 +0.04 -0.04	0.11	1.56	5.84	210
M1T	0.69	0.159	0.74 +0.04 -0.04	0.21	2.03	5.19	202
M1T/T	0.66	0.192	0.73 +0.04 -0.05	0.13	1.9	6.16	210

TABLE: D20. MEAN FREE DISTANCE BETWEEN INCLUSIONS MFD (mm) IN THE LONG(L), TRANS(T) AND THROUGH-THICKNESS(T/T) DIRECTIONS

Steel Code	Transformed Mean	S.D.	95% C.L. about Normal Mean		Min. Value	Max. Value	% R.A.	No. of Fields
L75L	1.23	0.177	1.34	+0.11 -0.1	0.54	3.39	8.38	100
L75T	0.86	0.14	0.9	+0.06 -0.05	0.43	2.45	6.6	100
L75T/T	0.72	0.163	0.78	+0.06 -0.06	0.32	2.29	7.74	100
L9L	1.34	0.192	1.48	+0.14 -0.12	0.54	3.68	9.17	100
L9T	0.84	0.192	0.92	+0.09 -0.07	0.24	2.38	9.14	100
L9T/T	0.66	0.188	0.72	+0.07 -0.06	0.19	2.23	8.95	100
L0L	1.54	0.175	1.68	+0.14 -0.13	0.57	4.6	8.31	100
L0T	1.02	0.155	1.09	+0.08 -0.08	0.28	2.08	7.33	100
L0T/T	0.74	0.192	0.83	+0.07 -0.07	0.26	3.83	9.14	100
L1L	1.82	0.188	2.0	+0.18 -0.17	0.85	4.66	8.97	100
L1T	1.09	0.126	1.14	+0.07 -0.06	0.58	2.67	5.93	100
L1T/T	0.83	0.213	0.94	+0.09 -0.09	0.22	3.09	10.2	100
F75L	2.15	0.178	2.35	+0.18 -0.16	0.83	9.12	7.29	131
F75T	1.88	0.209	2.1	+0.21 -0.19	0.46	7.6	10.01	100
F75T/T	1.06	0.197	1.18	+0.09 -0.09	0.36	3.21	8.1	131
F9L	2.16	0.195	2.41	+0.2 -0.19	0.83	9.36	8.21	125

TABLE: D20. CONTINUED

Steel Code	Transformed Mean	S.D.	95% C.L. about Normal Mean		Min. Value	Max. Value	% R.A.	No. of Fields
F9T	1.52	0.144	1.61	+0.1 -0.11	0.6	3.52	6.77	100
F9T/T	0.94	0.19	1.04	+0.09 -0.07	0.38	3.38	7.97	125
F0L	2.13	0.166	2.3	+0.16 -0.15	0.99	5.83	7.13	120
F0T	1.55	0.158	1.66	+0.12 -0.12	0.7	4.02	7.38	102
F0T/T	0.96	0.165	1.04	+0.07 -0.07	0.41	4.95	7.09	120
F1L	1.82	0.203	2.01	+0.18 -0.16	0.12	6.29	8.82	120
F1T	1.44	0.136	1.51	+0.1 -0.09	0.6	3.1	6.41	100
F1T/T	0.95	0.187	1.05	+0.09 -0.08	0.4	4.91	8.1	120
K75L	1.9	0.17	2.05	+0.15 -0.13	0.79	5.91	7.1	125
K75T	1.63	0.154	1.75	+0.11 -0.11	0.89	5.08	6.42	125
K75T/T	1.47	0.155	1.57	+0.11 -0.09	0.63	4.46	6.45	125
K9L	1.82	0.173	1.97	+0.13 -0.12	0.62	4.6	6.58	150
K9T	1.53	0.149	1.62	+0.1 -0.1	0.51	4.04	6.16	126
K9T/T	1.61	0.175	1.75	+0.12 -0.11	0.73	5.36	6.66	150
K0L	1.67	0.165	1.81	+0.12 -0.12	0.78	5.58	6.88	125
K0T	1.48	0.159	1.59	+0.11	0.63	4.95	6.98	115

E

TABLE: D20 CONTINUED

Steel Code	Transformed Mean	S.D.	95% C.L. about Normal Mean	Min. Value	Max. Value	% R.A.	No. of Fields
K0T/T	1.36	0.183	+0.12 1.49 -0.1	0.5	4.73	7.66	125
K1L	1.71	0.169	+0.13 1.84 -0.12	0.37	4.59	7.27	120
K1T	1.67	0.169	+0.13 1.81 -0.12	0.74	6.38	7.03	126
K1T/T	1.49	0.165	+0.11 1.6 -0.11	0.59	3.35	7.11	120
M75L	3.71	0.199	+0.25 4.16 -0.24	0.97	23.39	5.97	240
M75T	3.8	0.23	+0.33 4.51 -0.3	1.18	44.36	7.25	220
M75T/T	3.59	0.202	+0.24 4.03 -0.23	1.13	16.09	6.08	240
M9L	NOT DETERMINED						
M9T	NOT DETERMINED						
M9T/T	NOT DETERMINED						
M0L	3.66	0.258	+0.36 4.5 -0.33	1.12	42.15	7.94	233
M0T	3.19	0.224	+0.29 3.95 -0.27	0.75	89.75	7.42	200
M0T/T	3.55	0.266	+0.37 4.53 -0.35	1.01	80.98	8.19	233
M1L	3.2	0.182	+0.21 3.53 -0.19	1.28	18.59	5.84	210
M1T	2.9	0.16	+0.17 3.1 -0.15	0.98	9.71	5.2	202
M1T/T	3.01	0.192	+0.21 3.35 -0.19	1.05	15.17	6.16	210

TABLE: D21. NEAREST NEIGHBOUR DISTANCE BETWEEN INCLUSIONS (mm) ON A LONG(L), TRANS(T) AND THROUGH-THICKNESS PLANE

Steel Code	Transformed Mean	S.D.	95% C.L. about Normal Mean	Min. Value	Max. Value	% R.A.	No. of Fields
L75L	0.0138	0.0707	0.014 +0.0004 -0.0005	0.0097	0.0234	3.27	100
L75T	0.0123	0.0671	0.0124 +0.0004 -0.0003	0.0092	0.0194	3.12	100
L75T/T	0.0163	0.0699	0.0165 +0.0005 -0.0005	0.0118	0.0266	3.24	100
L9L	0.0138	0.0802	0.014 +0.0005 -0.0005	0.0088	0.0204	3.73	100
L9T	0.0117	0.0721	0.0119 +0.0004 -0.0004	0.0082	0.0187	3.34	100
L9T/T	0.0165	0.1	0.0169 +0.0008 -0.0007	0.0091	0.0305	4.67	100
L0L	0.0134	0.0911	0.0137 +0.0005 -0.0006	0.0083	0.0247	4.24	100
L0T	0.0123	0.0656	0.0125 +0.0004 -0.0004	0.0069	0.0178	3.05	100
L0T/T	0.0172	0.0806	0.0184 +0.0007 -0.0006	0.0096	0.0246	3.47	100
L1L	0.0153	0.09	0.0157 +0.0006 -0.0006	0.0086	0.0303	4.19	100
L1T	0.0136	0.0592	0.0138 +0.0003 -0.0004	0.0101	0.021	2.73	100
L1T/T	0.0195	0.065	0.0197 +0.0006 -0.0005	0.015	0.0314	3.01	100
F75L	0.017	0.08	0.0173 +0.0005 -0.0006	0.0101	0.0294	3.21	131
F75T	0.0169	0.0959	0.0173 +0.0008 -0.0007	0.0092	0.0294	4.46	100
F75T/T	0.0255	0.105	0.0263 +0.0013 -0.0012	0.125	0.0589	4.9	131
F9L	0.0161	0.0849	0.0164 +0.0006 -0.0005	0.0108	0.0286	3.47	125
F9T	0.0155	0.0566	0.0156 +0.0004 -0.0004	0.0112	0.0213	2.62	100

TABLE: D21. CONT.

Steel Code	Transformed Mean	S.D.	95% C.L. about Normal Mean	Min. Value	Max. Value	% R.A.	No. of Fields
F9T/T	0.0232	0.0706	0.0235 +0.0009 -0.0007	0.015	0.0355	3.27	125
F0L	0.0161	0.08	0.0164 +0.0005 -0.0006	0.0111	0.032	3.39	120
F0T	0.0149	0.0616	0.0151 +0.0004 -0.0004	0.0117	0.024	2.84	102
F0T/T	0.0229	0.0764	0.0233 +0.0008 -0.0008	0.0156	0.0362	3.51	120
F1L	0.0162	0.0825	0.0166 +0.0005 -0.0006	0.0108	0.0384	3.49	120
F1T	0.0149	0.0548	0.015 +0.0004 -0.0003	0.011	0.022	2.54	100
F1T/T	0.0217	0.0659	0.0219 +0.0007 -0.0006	0.0155	0.0337	3.05	120
K75L	0.0187	0.0686	0.019 +0.0005 -0.0005	0.0124	0.0288	2.82	125
K75T	0.0188	0.0632	0.019 +0.0005 -0.0005	0.144	0.0283	2.6	125
K75T/T	0.021	0.0762	0.0214 +0.0006 -0.0007	0.015	0.0371	3.12	125
K9L	0.0203	0.0806	0.0207 +0.0006 -0.0006	0.0141	0.0355	3.02	150
K9T	0.019	0.0616	0.0192 +0.0004 -0.0005	0.0136	0.0331	2.51	126
K9T/T	0.0205	0.0761	0.0209 +0.0006 -0.0007	0.0122	0.0384	3.11	150
K0L	0.0186	0.0728	0.0189 +0.0006 -0.0005	0.0125	0.0343	2.99	125
K0T	0.0185	0.0616	0.0187 +0.0005 -0.0005	0.0141	0.0306	2.67	115
K0T/T	0.0195	0.0745	0.0198 +0.0007 -0.0006	0.0132	0.0322	3.22	125
K1L	0.0186	0.0671	0.0189 +0.0005 -0.0005	0.0139	0.031	2.82	120

TABLE: D21. CONT.

Steel Code	Transformed Mean	S.D.	95% C.L. about Normal Mean	Min. Value	Max. Value	% R.A.	No. of Fields
K1T	0.0197	0.0843	+0.0007 0.0201 -0.0007	0.0136	0.0477	3.44	126
K1T/T	0.0207	0.0841	+0.0007 0.0212 -0.0007	0.0137	0.0403	3.44	120
M75L	0.0273	0.0889	+0.0008 0.0289 -0.0007	0.0175	0.0503	2.62	240
M75T	0.0261	0.09	+0.0008 0.0267 -0.0007	0.0165	0.0648	2.78	220
M75T/T	0.0281	0.1042	+0.001 0.029 -0.0009	0.172	0.0848	3.22	240
M9L			NOT DETERMINED				
M9T			NOT DETERMINED				
M9T/T			NOT DETERMINED				
M0L	0.0279	0.1086	+0.001 0.0288 -0.0009	0.0154	0.0919	3.27	233
M0T	0.0249	0.0825	+0.0007 0.0254 -0.0007	0.0165	0.0749	2.67	200
M0T/T	0.0268	0.1037	+0.001 0.0277 -0.0009	0.0134	0.1106	3.37	233
M1L	0.0253	0.0806	+0.0006 0.0258 -0.0007	0.0165	0.0525	2.54	210
M1T	0.0247	0.0781	+0.0006 0.0252 -0.0007	0.0147	0.0441	2.52	202
M1T/T	0.0255	0.0797	+0.0007 0.0259 -0.0006	0.0149	0.047	2.56	210

TABLE: D22. DISTRIBUTION OF AREA DETERMINED BY MOMENTS.
TRANSFORMATION LOG-NORMAL

Steel Code	NORMAL DATA			TRANSFORMED DATA		
	Extreme Value	Skewness	Kurtosis	Extreme Value	Skewness	Kurtosis
L75L	1.17	0.67	3.61	1.01	-0.26	3.4
L75T	1.12	0.53	3.7	1.01	-0.2	3.39
L9L	1.33	5.4	12.78	1.01	0.00	3.45
L9T	1.27	4.16	11.07	1.01	0.00	3.33
L0L	1.21	1.61	5.37	1.01	-0.27	3.96
L0T	1.44	13.54	19.7	1.01	1.84	6.29
L1L	1.21	1.09	3.95	1.01	-0.11	3.26
L1T	1.11	0.52	3.87	1.01	-0.12	2.96
F75L	1.27	1.73	4.75	1.02	-0.02	2.81
F75T	1.35	3.78	6.9	1.02	0.16	3.13
F9L	1.21	1.32	5.15	1.01	-0.28	3.56
F9T	1.16	1.45	4.91	1.01	0.01	2.73
F0L	1.19	1.66	5.79	1.01	-0.4	3.4
F0T	1.91	1.48	4.99	1.01	-0.01	2.82
F1L	1.15	0.33	3.11	1.01	-0.31	3.15
F1T	1.33	8.61	17.43	1.01	0.34	4.07
K75L	1.49	11.76	23.24	1.02	0.01	4.07
K75T	1.12	0.23	3.15	1.01	-0.38	3.26
K9L	1.53	12.34	25.38	1.02	0.08	3.27
K9T	1.2	2.45	6.95	1.01	0.00	3.46
K0L	1.18	0.7	3.53	1.01	-0.34	3.73
K0T	1.18	1.17	4.96	1.01	-0.28	3.86
K1L	1.62	16.2	29.14	1.02	0.197	3.69
K1T	1.15	0.51	2.97	1.01	-0.27	3.7
M75L	1.4	5.36	12.73	1.03	-0.07	3.79
M75T	1.49	6.39	13.94	1.05	-0.41	4.74
M9L			NOT DETERMINED			
M9T			NOT DETERMINED			
M0L	1.3	1.39	4.55	1.05	-0.69	4.33
M0T	1.31	2.73	7.61	1.03	-2.6	11.52
M1L	1.3	3.0	7.69	1.03	-0.19	4.36
M1T	1.19	1.41	5.13	1.02	-0.03	3.06

TABLE: D23. DISTRIBUTION OF INCLUSION COUNTS DETERMINED BY MOMENTS. SQUARE ROOT TRANSFORMATION

Steel Code	NORMAL DATA			TRANSFORMED DATA		
	Extreme Value	Skewness	Kurtosis	Extreme Value	Skewness	Kurtosis
L75L	1.09	0.21	2.82	1.03	0.00	2.68
L75T	1.07	0.08	2.31	1.02	0.00	2.37
L9L	1.11	0.13	2.19	1.03	0.0	2.12
L9T	1.12	0.57	3.64	1.03	0.05	3.1
L0L	1.12	0.44	3.55	1.03	0.03	2.77
L0T	1.2	6.51	12.49	1.04	2.72	7.49
L1L	1.12	0.38	3.22	1.03	0.03	2.63
L1T	1.06	0.03	2.74	1.01	-0.41	3.76
F75L	1.11	0.71	5.16	1.03	0.02	3.75
F75T	1.3	4.99	9.34	1.06	1.67	5.73
F9L	1.11	0.27	3.68	1.03	-0.01	3.18
F9T	1.06	0.15	2.79	1.02	0.01	2.61
F0L	1.1	0.22	2.67	1.03	0.01	2.47
F0T	1.07	0.08	2.43	1.02	-0.01	2.54
F1L	1.1	0.36	3.66	1.03	0.01	3.06
F1T	1.06	0.15	3.17	1.02	0.00	2.88
K75L	1.11	0.42	3.19	1.03	0.05	2.71
K75T	1.06	0.00	2.55	1.02	-0.09	2.69
K9L	1.08	0.01	2.32	1.02	-0.08	2.46
K9T	1.07	0.21	3.41	1.02	0.00	3.21
K0L	1.08	0.17	2.94	1.02	0.00	2.97
K0T	1.06	0.00	2.75	1.02	-0.09	2.86
K1L	1.07	0.03	2.98	1.02	-0.06	3.03
K1T	1.1	0.12	2.8	1.03	-0.02	2.82
M75L	1.13	0.45	3.03	1.04	0.03	2.8
M75T	1.1	0.09	3.07	1.03	-0.07	3.0
M9L	NOT DETERMINED					
M9T	NOY DETERMINED					
M0L	1.18	0.98	4.31	1.05	0.08	3.14
M0T	1.1	0.23	3.64	1.03	-0.04	3.65
M1L	1.09	0.09	3.01	1.03	-0.04	3.1
M1T	1.12	0.87	5.03	1.03	0.08	3.51

TABLE: D24. DISTRIBUTION OF TOTAL INCLUSION LENGTHS DETERMINED BY MOMENTS. TRANSFORMATION LOG-NORMAL.

Steel Code	NORMAL DATA			TRANSFORMED DATA		
	Extreme Value	Skewness	Kurtosis	Extreme Value	Skewness	Kurtosis
L75L	1.12	0.34	3.42	1.01	-0.26	3.41
L75T	1.09	0.2	2.94	1.01	-0.23	3.2
L9L	1.22	2.69	7.25	1.01	0.01	3.17
L9T	1.1	0.23	2.79	1.01	-0.14	2.78
L0L	1.17	1.34	5.14	1.01	-0.26	4.26
L0T	1.24	9.75	16.79	1.01	1.14	5.76
L1L	1.24	2.07	6.28	1.01	-0.01	2.95
L1T	1.09	0.52	3.65	1.01	-0.04	2.95
F75L	1.18	1.14	4.14	1.01	-0.01	2.69
F75T	1.29	3.63	6.95	1.02	0.2	3.34
F9L	1.12	0.15	3.0	1.01	-0.56	3.43
F9T	1.08	0.44	4.43	1.01	-0.02	2.57
F0L	1.11	0.39	3.42	1.01	-0.41	4.66
F0T	1.08	0.1	2.41	1.01	-0.12	2.61
F1L	1.12	0.23	3.08	1.01	-0.62	4.14
F1T	1.12	2.35	7.62	1.01	0.06	3.44
K75L	1.11	0.42	3.26	1.01	0.06	2.93
K75T	1.08	0.04	2.63	1.01	-0.32	2.86
K9L	1.11	0.14	2.8	1.01	-0.33	2.98
K9T	1.09	0.75	3.98	1.01	-0.08	4.2
K0L	1.14	0.69	4.03	1.01	-0.21	3.38
K0T	1.09	0.24	3.3	1.01	-0.43	4.14
K1L	1.14	0.87	3.82	1.01	0.00	2.58
K1T	1.11	0.2	2.84	1.01	-0.71	4.75
M75L	1.18	1.19	4.83	1.03	-0.17	3.46
M75T	1.15	0.32	3.16	1.03	-0.84	4.47
M9L			NOT DETERMINED			
M9T			NOT DETERMINED			
M0L	1.23	1.08	3.99	1.04	-0.72	5.26
M0T	1.14	0.45	3.98	1.02	-3.24	12.19
M1L	1.15	0.69	4.05	1.02	-0.33	3.83
M1T	1.13	0.83	4.42	1.02	-0.05	2.94

ABLE: D25. DISTRIBUTION OF PROJECTED LENGTHS AS DETERMINED BY MOMENTS. TRANSFORMATION LOG-NORMAL.

teel ode	NORMAL DATA			TRANSFORMED DATA		
	Extreme Value	Skewness	Kurtosis	Extreme Value	Skewness	Kurtosis
75L	1.13	0.45	3.23	1.29	-0.11	2.78
75T	1.08	0.16	2.65	1.34	-0.13	2.96
75T/T	1.11	0.34	3.34	1.3	-0.26	3.41
9L	1.14	0.32	2.59	1.25	-0.04	2.29
9T	1.21	2.39	7.2	1.35	-0.02	3.26
9T/T	1.22	2.69	7.25	1.34	0.01	3.17
0L	1.15	0.94	4.24	1.2	-0.04	2.99
0T	1.27	7.42	12.55	1.25	1.04	4.88
0T/T	1.17	1.34	5.14	1.4	-0.26	4.26
1L	1.13	0.2	2.34	1.17	-0.06	2.18
1T	1.06	0.03	2.82	1.33	-0.39	3.36
1T/T	1.24	2.07	6.28	1.31	-0.01	2.95
75L	1.13	0.63	3.9	1.14	-0.35	4.01
75T	1.35	5.49	9.71	1.15	0.12	4.02
75T/T	1.18	1.14	4.14	1.29	-0.01	2.69
9L	1.16	0.88	4.17	1.16	-0.27	3.62
9T	1.12	1.5	5.68	1.15	0.00	3.08
9T/T	1.12	0.15	3.0	1.43	-0.56	3.43
0L	1.11	0.28	3.24	1.12	-0.21	2.93
0T	1.11	0.41	3.2	1.18	-0.07	2.8
0T/T	1.11	0.39	3.42	1.49	-0.41	4.66
1L	2.54	89.01	98.49	1.18	1.12	11.02
1T	1.11	1.49	4.87	1.15	0.05	3.18
1T/T	1.12	0.23	3.08	1.48	-0.62	4.14
K75L	1.13	0.62	3.27	1.14	-0.03	2.85
K75T	1.08	0.00	2.42	1.19	-0.63	3.37
K75T/T	1.11	0.42	3.2	1.19	-0.06	2.93
K9L	1.15	1.14	5.53	1.16	-0.1	3.08
K9T	1.14	2.09	7.24	1.16	0.01	3.29
K9T/T.	1.11	0.14	2.8	1.21	-0.33	2.98
K0L	1.1	0.11	2.8	1.2	-0.58	3.92
K0T	1.11	0.4	3.67	1.22	-0.24	3.45
K0T/T	1.14	0.68	4.03	1.28	-0.21	3.38
K1L	1.31	9.76	21.24	1.15	0.06	4.25
K1T	1.11	0.22	2.98	1.2	-0.43	3.88
K1T/T	1.14	0.87	3.82	1.18	0.00	2.58
M75L	1.2	2.03	6.97	1.08	-0.23	4.19
M75T	1.17	0.6	3.91	1.12	-0.92	5.13
M75T/T	1.18	1.19	4.83	1.09	-0.17	3.46
M9L			NOT DETERMINED			
M9T			NOT DETERMINED			
M9T/T			NOT DETERMINED			
M0L	1.21	0.79	3.82	1.13	-0.54	3.9
M0T	1.23	2.48	9.23	1.17	-2.66	11.31
M0T/T	1.23	1.08	3.99	1.15	-0.72	5.26
M1L	1.13	0.6	3.78	1.09	-0.41	4.32
M1T	1.13	1.06	5.14	1.07	-0.04	3.26
M1T/T	1.15	0.69	4.05	1.1	-0.33	3.83

TABLE: D26. DISTRIBUTION OF MEAN FREE DISTANCE AS DETERMINED BY MOMENTS. TRANSFORMATION LOG-NORMAL.

Steel Code	NORMAL DATA			TRANSFORMED DATA		
	Extreme Value	Skewness	Kurtosis	Extreme Value	Skewness	Kurtosis
L75L	1.19	1.82	4.73	1.34	0.11	2.78
L75T	1.14	2.27	7.18	1.25	0.13	2.95
L75T/T	1.21	3.52	7.78	1.22	0.26	3.4
L9L	1.19	1.27	4.08	1.29	0.04	2.29
L9T	1.21	2.06	4.95	1.32	0.02	3.26
L9T/T	1.2	2.11	6.92	1.28	-0.01	3.17
L0L	1.19	2.11	5.78	1.27	0.04	2.99
L0T	1.08	0.08	3.31	1.46	-1.06	4.9
L0T/T	1.43	10.91	19.9	1.29	0.26	4.25
L1L	1.17	1.01	3.36	1.22	0.06	2.19
L1T	1.12	2.57	6.49	1.41	0.38	3.36
L1T/T	1.26	2.51	6.27	1.29	0.01	2.95
F75L	1.31	6.97	12.93	1.2	0.35	4.01
F75T	1.27	3.82	9.9	1.2	-0.13	4.03
F75T/T	1.2	1.5	4.48	1.29	0.01	2.69
F9L	1.32	5.14	9.97	1.21	0.26	3.61
F9T	1.11	0.79	3.75	1.22	0.00	3.08
F9T/T	1.29	4.12	7.45	1.32	0.55	3.42
F0L	1.18	2.04	4.93	1.17	0.21	2.92
F0T	1.15	1.56	4.71	1.25	0.07	2.8
F0T/T	1.41	16.16	30.36	1.44	0.41	4.65
F1L	1.25	3.51	7.58	1.27	-1.11	10.99
F1T	1.09	0.65	4.19	1.22	-0.05	3.19
F1T/T	1.06	5.76	14.18	1.00	0.89	5.88
K75L	1.18	1.99	6.0	1.19	0.03	2.86
K75T	1.2	3.58	7.48	1.28	0.63	3.36
K75T/T	1.16	2.21	6.81	1.27	0.06	2.93
K9L	1.18	1.82	4.44	1.22	0.1	3.08
K9T	1.12	1.21	5.1	1.23	-0.01	3.3
K9T/T	1.21	2.64	5.89	1.29	0.33	2.98
K0L	1.25	5.19	9.54	1.29	0.58	3.92
K0T	1.2	3.7	8.68	1.31	0.23	3.44
K0T/T	1.25	3.8	7.89	1.37	0.21	3.38
K1L	1.16	1.55	5.15	1.21	-0.06	4.27
K1T	1.29	6.93	13.62	1.29	0.43	3.88
K1T/T	1.13	0.76	3.44	1.24	0.00	2.58
M75L	1.45	10.79	21.07	1.11	0.23	4.19
M75T	2.02	35.14	53.18	1.15	0.92	5.13
M75T/T	1.33	5.31	10.73	1.11	0.17	3.46
M9L			NOT DETERMINED			
M9T			NOT DETERMINED			
M9T/T			NOT DETERMINED			
M0L	1.91	22.56	38.66	1.17	0.54	3.89
M0T	3.17	144.88	160.03	1.22	2.65	11.29
M0T/T	2.83	101.63	130.49	1.19	0.72	5.26
M1L	1.43	12.59	23.89	1.11	0.41	4.32
M1T	1.18	2.76	8.06	1.09	0.04	3.25
M1T/T	1.39	8.87	17.37	1.13	0.33	3.83

TABLE: D27. DISTRIBUTION OF NEAREST-NEIGHBOUR DISTANCE DETERMINED BY MOMENTS. TRANSFORMATION LOG-NORMAL.

Steel Code	NORMAL DATA			TRANSFORMED DATA		
	Extreme Value	Skewness	Kurtosis	Extreme Value	Skewness	Kurtosis
L75L	1.03	0.97	4.78	1.0	0.17	3.3
L75T	1.03	0.76	3.91	1.0	0.19	2.94
L75T/T	1.03	0.41	3.54	1.0	0.05	2.61
L9L	1.03	0.41	2.67	1.0	0.01	2.46
L9T	1.03	0.64	3.61	1.0	0.11	2.98
L9T/T	1.06	0.98	4.28	1.0	0.05	3.29
L0L	1.05	0.84	4.1	1.0	0.08	2.99
L0T	1.02	-0.03	3.77	1.0	-0.73	4.94
L0T/T	1.03	-0.01	3.05	1.0	-0.49	3.88
L1L	1.05	1.17	5.54	1.0	0.06	3.49
L1T	1.02	0.73	4.38	1.0	0.14	3.37
L1T/T	1.03	1.38	5.05	1.0	0.42	3.55
F75L	1.04	0.9	4.36	1.0	0.11	3.27
F75T	1.05	0.22	3.62	1.00	-0.1	3.53
F75T/T	1.07	1.67	8.13	1.0	-0.02	4.52
F9L	1.05	1.76	4.7	1.0	0.61	3.45
F9T	1.02	0.21	2.75	1.0	0.02	2.55
F9T/T	1.03	0.23	3.25	1.0	0.00	3.12
F0L	1.04	1.48	6.54	1.0	0.18	3.51
F0T	1.02	1.02	4.6	1.0	0.31	3.21
F0T/T	1.03	0.52	3.37	1.0	0.07	2.78
F1L	1.06	5.76	14.18	1.0	0.89	5.88
F1T	1.02	0.35	3.19	1.0	0.07	2.67
F1T/T	1.02	0.33	3.58	1.0	0.01	3.04
K75L	1.02	0.08	2.97	1.0	-0.02	2.7
K75T	1.02	0.8	3.6	1.0	0.28	2.87
K75T/T	1.04	1.72	4.92	1.0	0.66	3.41
K9L	1.05	1.71	4.93	1.0	0.55	3.5
K9T	1.02	1.11	6.69	1.0	0.1	4.07
K9T/T	1.04	0.9	4.56	1.0	0.09	3.53
K0L	1.03	1.28	5.64	1.0	0.2	3.59
K0T	1.03	1.48	5.2	1.0	0.51	3.68
K0T/T	1.03	0.91	3.9	1.0	0.23	3.02
K1L	1.03	1.51	4.89	1.0	0.53	3.57
K1T	1.07	5.23	13.58	1.0	0.94	5.16
K1T/T	1.05	1.6	5.85	1.0	0.29	3.46
M75L	1.05	1.04	4.12	.10	0.19	3.02
M75T	1.07	3.88	9.57	1.0	0.95	4.54
M75T/T	1.11	6.08	13.84	1.0	1.05	4.98
M9L			NOT DETERMINED			
M9T			NOT DETERMINED			
M9T/T			NOT DETERMINED			
M0L	1.12	6.19	16.97	1.0	0.44	4.58
M0T	1.09	13.09	29.1	1.0	1.56	7.95
M0T/T	1.21	23.7	43.0	1.0	1.92	9.04
M1L	1.05	2.36	6.95	1.0	0.58	3.99
M1T	1.04	0.88	4.86	1.0	0.06	3.45
M1T/T	1.04	1.0	5.09	1.0	0.09	3.43

TABLE: D28. MECHANICAL PROPERTIES
HOUNSFIELD No 14 TENSILES

Steel Code	Average Yield Stress (MPa)	Range Yield Stress (MPa)	Average UTS (MPa)	Range UTS (MPa)	Average Fracture Strain	Range Fracture Strain
L75L	356.5	355.6	456.6	458.6	1.31	1.35
		357.3		454.6		1.26
L75T	379.9	379.3	481.7	481.7	1.02	1.0
		380.5		481.7		1.03
L9L	299.7	297.3	432.7	430.4	1.52	1.49
		302.0		434.9		1.55
L9T	314.1	314.1	446.9	446.9	1.3	1.3
		314.1		446.9		1.29
L0L	306.0	305.8	431.7	431.1	1.39	1.57
		306.1		432.2		1.21
L0T	306.7	312.4	434.8	442.0	1.21	1.15
		301.0		427.5		1.27
L1L	298.5	295.9	428.2	427.3	1.63	1.63
		301.0		429.0		1.63
L1T	300.8	301.0	431.6	424.5	1.37	1.42
		300.6		438.6		1.32
F75L	317.3	318.0	423.7	423.5	1.6	1.6
		316.6		423.9		1.59
F75T	340.1	340.3	448.9	446.7	1.26	1.24
		339.9		451.1		1.28
F9L	287.6	287.7	395.7	396.9	1.85	1.85
		287.4		394.5		1.85
F9T	303.5	305.0	412.5	411.3	1.61	1.61
		302.0		412.5		1.61
F0L	283.2	282.8	391.6	392.9	1.91	1.95
		283.5		390.2		1.86
F0T	290.2	288.7	395.0	395.0	1.68	1.66
		291.7		395.0		1.69
F1L	242.4	243.9	391.7	390.2	1.83	1.79
		240.8		393.2		1.86
F1T	244.3	244.6	395.4	394.5	1.64	1.59
		243.9		396.3		1.68
K75L	393.5	395.6	555.9	558.7	1.12	1.14
		391.4		553.0		1.1
K75T	424.6	421.1	586.2	591.3	0.99	0.9
		428.1		581.0		1.07
K9L	317.6	323.1	461.1	461.8	1.69	1.71
		312.0		460.4		1.66
K9T	340.8	336.2	477.1	478.6	1.69	1.69
		345.3		475.6		1.69
K0L	316.8	316.0	469.5	468.0	1.63	1.67
		317.5		471.0		1.59
K0T	320.6	322.1	473.6	472.4	1.7	1.89
		319.0		474.8		1.61
K1L	324.2	328.2	477.9	477.1	1.62	1.66
		320.1		478.6		1.57
K1T	317.0	317.0	477.8	478.6	1.54	1.52
		317.0		477.0		1.56
M75L	402.3	403.9	546.5	545.6	1.34	1.35
		400.6		547.3		1.33
M75T	416.8	404.2	574.8	577.4	1.25	1.41
		429.4		572.1		1.08
M9L	349.0	347.7	502.7	503.0	1.62	1.58
		350.2		502.4		1.65
M9T	359.0	357.5	513.2	514.4	1.47	1.36
		360.5		511.9		1.58
M0L	330.8	332.3	494.6	493.8	1.73	1.7
		329.2		495.3		1.76
M0T	329.7	329.2	491.6	490.8	1.64	1.63
		330.2		492.3		1.65
M1L	333.4	338.5	497.0	501.6	1.71	1.69
		328.2		492.3		1.73
M1T	327.7	322.1	496.1	495.3	1.73	1.69
		333.2		496.8		1.76

TABLE: D29. MECHANICAL PROPERTIES
NOTCHED TENSILES - UNCHARGED

Steel Code	Average Yield Stress (MPa)	Range Yield Stress (MPa)	Average UTS (MPa)	Range UTS (MPa)	Average Fracture Strain	Range Fracture Strain
L75L	564.9	577.6 552.1	744.2	730.3 758.1	0.32	0.26 0.37
L75T	604.7	622.1 587.2	746.5	761.9 731.2	0.18	0.18 0.17
L9L	459.6	453.6 465.6	679.3	668.8 689.7	0.46	0.43 0.48
L9T	525.8	508.1 543.5	693.2	669.7 716.6	0.19	0.18 0.19
L0L	464.2	455.9 472.4	690.2	669.0 711.4	0.6	0.56 0.63
L0T	471.0	460.0 482.0	681.0	676.3 685.7	0.25	0.24 0.25
L1L	441.0	425.9 456.0	676.2	667.0 685.4	0.57	0.55 0.58
L1T	461.3	463.6 459.0	672.0	666.3 677.6	0.27	0.23 0.3
F75L	532.8	537.8 527.8	690.7	706.1 675.2	0.4	0.4 0.4
F75T	566.6	566.0 567.2	710.2	717.8 702.6	0.3	0.28 0.32
F9L	456.7	450.7 462.7	658.3	635.0 681.6	0.72	0.57 0.86
F9T	471.7	495.0 448.4	645.8	659.8 631.8	0.41	0.47 0.35
F0L	419.7	418.8 420.6	661.1	652.4 669.8	0.72	0.71 0.72
F0T	444.4	445.3 443.5	668.8	678.6 659.0	0.61	0.62 0.59
F1L	396.8	413.9 379.6	667.4	662.3 672.4	0.74	0.69 0.78
F1T	334.0	334.0 334.1	687.0	693.9 680.0	0.56	0.51 0.6
K75L	736.8	701.0 772.5	912.9	919.8 906.0	0.28	0.32 0.23
K75T	650.4	624.4 676.3	930.6	938.4 922.8	0.23	0.28 0.17
K9L	485.4	505.8 465.0	788.1	775.7 800.4	0.69	0.67 0.7
K9T	525.2	514.6 535.7	751.3	717.3 785.2	0.57	0.6 0.53
K0L	487.3	513.7 461.0	778.4	786.9 769.9	0.72	0.7 0.73
K0T	550.7	545.8 555.5	774.4	778.9 769.8	0.6	0.57 0.62
K1L	492.5	498.5 486.4	796.4	780.6 812.2	0.68	0.67 0.69
K1T	514.9	515.6 514.1	767.6	769.1 766.0	0.59	0.62 0.57
M75L	675.0	669.7 680.2	919.9	931.2 908.6	0.41	0.43 0.38
M75T	661.1	671.1 651.1	896.5	900.5 892.4	0.41	0.38 0.43
M9L	550.7	584.9 552.5	840.0	867.0 812.9	0.53	0.57 0.49
M9T	546.9	532.9 540.9	838.9	856.6 821.1	0.65	0.76 0.54
M0L	514.5	503.9 525.1	822.4	821.0 823.8	0.59	0.58 0.59
M0T	534.4	528.5 540.2	854.1	837.6 870.6	0.58	0.59 0.57
M1L	517.1	517.1 ND	828.3	828.3 ND	0.7	0.7 ND
M1T	437.3	437.6 437.0	809.4	799.3 819.4	0.72	0.7 0.73

TABLE: D30. MECHANICAL PROPERTIES
NOTCHED TENSILES - HYDROGEN CHARGED

Steel Code	Average Weld Stress (MPa)	Range Yield Stress (MPa)	Average UTS (MPa)	Range UTS (MPa)	Average Fracture Strain	Range Fracture Strain
L75L	504.5	508.4	505.7	508.4	0.04	0.04
		500.6		502.9		0.04
L75T	519.5	500.7	562.8	580.8	0.07	0.05
		538.3		544.8		0.09
L9L	399.4	399.4	403.9	403.9	0.05	0.05
		ND		ND		ND
L9T	539.6	555.9	578.1	544.3	0.1	0.1
		523.3		611.8		0.9
L0L	421.7	385.1	527.7	487.0	0.13	0.13
		458.3		568.4		0.13
L0T	452.2	452.2	577.2	577.2	0.12	0.12
		ND		ND		ND
L1L	470.2	451.6	628.4	620.0	0.15	0.16
		488.7		636.7		0.14
L1T	463.4	470.7	570.2	573.1	0.11	0.9
		456.1		567.3		0.13
F75L	488.0	473.7	593.7	575.5	0.12	0.1
		502.5		611.9		0.13
F75T	529.2	500.1	653.5	657.4	0.13	0.13
		558.2		649.5		0.13
F9L	517.9	530.1	655.6	665.5	0.38	0.44
		505.7		645.7		0.32
F9T	540.0	545.3	647.1	642.8	0.25	0.21
		534.6		651.3		0.29
F0L	430.0	409.8	618.2	630.2	0.2	0.23
		450.2		606.2		0.16
F0T	398.5	383.8	605.1	605.1	0.16	0.17
		413.2		605.1		0.15
F1L	404.6	399.9	582.4	564.0	0.13	0.13
		409.3		600.8		0.13
F1T	421.1	392.3	587.4	575.0	0.11	0.12
		450.0		599.8		0.09
K75L	569.4	574.8	718.2	712.6	0.04	0.04
		563.9		723.8		0.03
K75T	506.2	450.6	674.4	654.9	0.03	0.02
		561.8		693.9		0.04
K9L	540.7	509.7	692.8	697.2	0.16	0.14
		499.7		688.3		0.18
K9T	528.0	518.5	672.6	673.6	0.13	0.14
		537.5		671.6		0.12
K0L	514.4	512.7	677.2	695.3	0.11	0.12
		516.0		659.0		0.1
K0T	494.2	493.2	623.2	607.7	0.1	0.1
		495.3		638.6		0.1
K1L	529.3	545.3	648.8	665.4	0.1	0.1
		513.3		632.1		0.09
K1T	520.6	527.9	659.7	664.0	0.12	0.13
		513.2		655.4		0.11
M75L	722.6	695.8	858.3	809.1	0.13	0.14
		749.3		907.4		0.12
M75T	712.8	706.6	818.2	784.5	0.11	0.08
		719.0		851.8		0.14
M9L	536.3	539.6	662.7	676.3	0.09	0.09
		533.0		649.1		0.09
M9T	562.5	566.2	736.5	751.8	0.19	0.23
		558.7		721.2		0.14
M0L	541.2	559.2	704.2	707.4	0.12	0.11
		523.2		700.9		0.13
M0T	555.2	547.9	724.0	717.5	0.17	0.17
		562.5		730.5		0.16
M1L	528.4	535.7	653.5	671.7	0.08	0.08
		521.1		635.3		0.07
M1T	515.0	522.7	707.4	722.9	0.16	0.14
		507.2		691.8		0.18

TABLE D31 : % AREA FRACTION OF VOIDS MEASURED FROM THE MINIMUM NOTCH CROSS SECTION IN THE Z DIRECTION

Distance from Zmm	Steel L Long . UC	Steel L Trans . UC	Steel L Long . UC	Steel L Trans . UC	Steel F Long . UC	Steel F Trans . UC	Steel F Long . UC	Steel F Trans . UC	Steel F Long . UC	Steel K Trans . UC	Steel K Long . UC	Steel K Trans . UC	Steel K Long . UC	Steel M Trans . UC	Steel M Long . UC	Steel M Trans . UC
0.085	1.341	1.0	0.749	0.566	1.49	1.297	0.893	0.993	1.51	0.863	0.386	0.99	1.796	0.446	2.567	0.339
0.254	0.91	0.794	0.555	0.091	1.034	0.822	1.086	1.094	1.016	1.034	1.068	0.445	1.235	0.464	0.901	0.529
0.423	0.75	0.529	0.39	0.222	0.655	1.088	0.703	1.082	0.796	0.652	0.75	0.645	0.466	0.42	0.58	0.384
0.592	0.843	0.473	0.368	0.962	0.924	0.891	0.749	1.29	0.489	0.556	0.505	0.446	0.464	1.633	0.876	0.221
0.761	0.88	0.447	0.418	1.791	1.043	0.83	0.776	0.984	0.306	0.537	0.257	0.355	0.328	0.4	0.492	0.498
0.93	0.382	0.552	0.577	0.509	1.086	0.853	0.557	1.58	0.381	0.442	0.428	0.329	0.369	0.477	1.062	0.439
1.099	0.458	0.472	0.18	0.492	0.723	0.941	0.622	1.33	0.172	0.217	0.324	0.442	0.231	0.81	0.591	0.556
1.268	0.518	0.356	0.317	0.678	0.686	0.61	0.453	0.753	0.312	0.38	0.186	0.445	0.342	0.539	0.185	0.365
1.437	0.703	0.634	0.323	0.714	0.754	0.667	0.567	0.441	0.466	0.318	0.244	0.441	0.171	0.562	0.28	0.471
1.606	0.453	0.322	0.651	0.367	0.472	0.511	0.446	0.607	0.227	0.3	0.124	0.298	0.177	0.298	0.186	0.218
1.944	0.473	0.403	0.331	0.391	0.625	1.003	0.385	0.718	0.224	0.168	0.314	0.332	0.227	0.597	0.33	0.341
2.282	0.822	0.433	0.947	0.515	0.488	0.498	0.355	0.848	0.27	0.31	0.237	0.279	0.227	0.903	0.26	0.39
2.958	0.807	0.4	0.273	0.358	0.406	0.952	0.305	0.905	0.213	0.181	0.126	0.201	0.211	0.427	0.297	0.401
3.634	0.513	0.34	0.229	0.442	0.579	0.608	0.418	0.766	0.153	0.208	0.18	0.268	0.169	0.55	0.248	0.3

TABLE: D32 TOTAL LENGTH OF VOIDS IN THE DIRECTION OF PRINCIPLE STRESS MEASURED FROM THE MINIMUM NOTCH CROSS SECTION IN THE Z DIRECTION

Distance from Zmm	Steel L Long . UC	Steel L Trans . UC	Steel L Long . UC	Steel L Trans . UC	Steel F Long . UC	Steel F Trans . UC	Steel F Long . UC	Steel F Trans . UC	Steel K Long . UC	Steel K Trans . UC	Steel K Long . UC	Steel K Trans . UC	Steel M Long . UC	Steel M Trans . UC	Steel M Long . UC	Steel M Trans . UC
0.085	4.57	3.06	3.14	1.08	4.48	4.33	3.37	3.81	4.17	2.79	1.39	2.26	3.6	1.43	3.28	1.63
0.254	3.81	3.18	2.9	0.29	3.37	3.03	3.68	4.05	3.05	3.11	2.11	1.99	3.1	1.73	1.63	1.92
0.423	3.2	2.34	2.1	0.75	2.54	3.75	2.58	4.15	2.89	2.35	2.12	2.16	1.64	1.5	1.24	1.45
0.592	3.0	1.91	1.55	1.55	3.15	3.52	2.97	4.33	1.84	2.05	1.51	1.51	1.47	1.62	1.4	1.05
0.761	2.46	1.9	1.5	1.16	2.92	3.35	3.26	3.52	1.27	1.87	1.06	1.5	1.27	1.59	1.33	1.9
0.93	1.9	2.11	2.32	1.02	3.35	3.47	2.17	5.57	1.48	1.77	1.45	1.5	0.9	1.53	1.82	1.84
1.099	1.91	2.11	0.79	0.79	2.45	3.51	2.47	4.43	0.77	0.92	1.15	1.97	0.82	1.44	1.88	2.01
1.268	2.21	1.71	1.69	1.62	2.71	2.21	1.89	2.98	1.17	1.7	0.79	2.17	1.22	1.43	0.79	1.36
1.437	2.61	2.68	1.22	1.31	2.96	2.62	2.25	1.97	1.85	1.37	1.08	1.91	0.76	1.67	1.18	1.55
1.606	2.19	1.39	2.01	0.69	1.99	1.97	1.84	2.64	1.15	1.19	0.53	1.55	0.75	1.23	0.85	0.93
1.944	1.8	1.89	1.21	0.82	2.35	3.57	1.72	2.89	0.95	0.81	1.37	1.37	0.65	1.2	1.13	1.18
2.282	2.69	1.8	3.93	1.24	2.32	1.97	1.63	3.48	1.15	1.37	0.53	1.1	0.9	1.88	0.71	1.62
2.958	2.22	1.72	0.95	0.89	1.78	3.34	1.55	3.32	0.96	0.86	0.58	1.08	0.67	1.24	1.04	1.54
3.634	2.72	1.76	1.47	0.89	2.2	2.01	1.99	2.79	0.92	1.02	0.94	1.2	0.7	1.47	0.9	1.21

TABLE: D33 A REAL FRACTION OF VOIDS MEASURED FROM THE MINIMUM NOTCH CROSS SECTION IN THE Z DIRECTION

Distance from Zmm	Steel L Long UC	Steel L Trans UC	Steel L Long UC	Steel L Trans UC	Steel F Long UC	Steel F Trans UC	Steel F Long UC	Steel F Trans UC	Steel K Long UC	Steel K Trans UC	Steel K Long UC	Steel K Trans UC	Steel M Long UC	Steel M Trans UC	Steel M Long UC	Steel M Trans UC
0.085	929	690	637	319	1142	1275	1062	1328	1009	770	505	850	876	451	744	637
0.254	903	797	611	159	1036	1062	1089	1461	744	797	451	850	690	690	558	770
0.423	1195	717	451	212	956	1089	903	1407	717	797	558	876	584	637	425	451
0.592	770	584	319	186	921	1222	1195	1381	505	664	425	637	531	478	398	319
0.761	770	584	319	186	956	876	1381	1036	372	584	345	770	345	637	478	637
0.93	531	637	531	239	956	876	1381	1036	398	505	451	690	239	505	531	876
1.099	451	531	239	186	664	1115	823	1248	292	372	425	956	266	478	690	690
1.268	876	584	425	505	850	823	664	744	345	823	292	983	398	505	345	478
1.437	584	584	292	319	1062	903	929	717	611	505	425	983	239	478	531	425
1.606	717	451	372	186	744	584	690	903	451	425	266	823	266	584	425	372
1.944	398	611	372	292	850	1195	664	956	319	398	478	611	186	292	398	425
2.282	664	531	637	292	921	637	664	1089	398	505	239	478	319	584	292	584
2.958	717	584	319	212	823	1248	690	1036	345	398	212	690	239	425	425	611
3.634	929	690	637	266	903	505	903	929	372	505	292	611	292	425	345	451

REFERENCES

1. Paxton,H.W. - The Changing Scene in Steel.
Met.Trans., Vol.10A, Dec.79, p.1815.

2. Rothwell, A.B. and Cooke,R.J. - Linepipe Requirements in The Eighties.
Alloys For The Eighties, Climax Molybdenum Co., 1980, p.171.

3. Nara,Y.et al. - The Production of Linepipe in Japan.
Conf.on: Steels for Linepipe and Pipeline Fittings Grosvenor House, London - 21/23 Oct.1981 - Paper 22.

4. Pickering,F.B. - HSLA Steels - A decade of Progress.
Microalloying 75, Union Carbide Corp., New York, 1977, p.9.

5. Gray,R.J., Irving,W.R. and Baker,R. - Steelmaking, Casting and Rolling of Pipeline Steels in BSC.
Ironmaking and Steelmaking, 1983, Vol.10, No.4, p.185

6. Pircher,H. and Klapdar,W. - Controlling inclusions in steel by injecting calcium into the ladle.
Microalloying 75, Union Carbide Corp., New York, 1977, p.232.

7. Moore,E.M. and Warga,J.J. - Factors Influencing The Hydrogen Cracking Sensitivity of Pipeline Steels.
Corrosion 76, Houston, Texas, March 1976, Paper 144.

8. Miyoshi, E. et al - Hydrogen-Induced Cracking of Steels Under Wet Hydrogen Sulphide Environment.
J.of Eng. for Industry, Nov.1976, p.1221

9. Obinata,T.- An Introductory Overview of the Effect of Steelmaking Practice on The development of high-Strength steels for pipeline.
Conf. on: Steels For Linepipe and Pipeline Fittings. Grosvenor House, London, Oct.1981, Paper 19.

10. Mitchell,P.S. and Barr, R.R. - Manufacture of High Quality S.A.W. Linepipe at B.S.C.
Iron and Steel International, Feb.84, p.9

11. Nakai,Y., Kurahasi,H. and Totsuka,N. - Hydrostatic Burst Tests of Pipe with Hydrogen Induced Cracking.
Materials Performance, Feb.1983, p.37.

12. Zapffe,C.A. and Sims,C.E. - Hydrogen Embrittlement, Internal Stress and Defects in Steel.
Trans. AIME, Vol.145, 1941.

13. Moser,M. and Schmidt,V.- Fractography and Mechanisms of Hydrogen Cracking - The Fisheye Concept.
6th Int.Conf. Advances in Fracture Research, New Delhi, India, 1984, Vol.4, p.2459.

14. Ciaraldi,S.W. - Microstructural Observations On the Sulphide Stress Cracking of Low Alloy Steel Tubulars.
Corrosion - NACE, Vol.40, No.2, Feb, 1984, p.77.

15. Craig,B.D.- A Fracture Topographical Feature Characteristic of Hydrogen Embrittlement.
Corrosion-NACE, Vol.37, No.9, Sept.1981, p.530.

16. Riboud,P.V.and Gatellier,C. - New Products: What should be done in Secondary Steelmaking.
Ironmaking and Steelmaking, 1985, Vol.12, No.2, p.79.

17. Turkdogan,E.T.- Physical Chemistry of High Temperature Technology.
Chap.9, Physical Chemistry of Ironmaking and Steelmaking. Academic Press, 1980.

18. Fruehan,R.J. - Thermodynamics and Kinetics of Reactions involving Elements in Ladle Metallurgy.
Iron and Steelmaker, March 1983, p.33.

19. Kiessling, R. and Lange, N. - Non-Metallic Inclusions in Steel. Part IIK and Part III O, The Metals Society, London, 1978.

20. Plockinger,E. - Influence of Deoxidation Practice On Cleanness of Steel.
'Clean Steel', 1963, 64, London, I.S.I., p.51.

21. Bodsworth,C. and Bell,H.B. - Physical Chemistry of Iron and Steel Manufacture.
Second Ed., Longmans, London, 1972

22. Pickering,F.B. - Effect of Processing Parameters on the Origin of non-metallic Inclusions.
Int.Conf. Production and Application of Clean Steels.
Balatonfured, Hungary, June, 1970, p.75.

23. Samarin,A.M. - Physical Chemistry of the Deoxidation of Metal Alloys.
Ibid - p.17.

24. Holappa,L. - Injection Metallurgy and Inclusion Control
Swedish Symp., - Non-Metallic Inclusions In steel.
Swedish Inst. for Metals Research, April 1981, p.19.

25. Turkdogan,E.T. - Review Paper; Deoxidation of Steel.
Chemical Metallurgy of Iron and Steel, I.S.I. London, 1973, p.153.

26. Pomey,G. and Trentini,B Introductory Address: Some Aspects of Cleanness in Steels.
See Ref. 22, p.1.

27. Lindon, P.H. and Billington, J.C. - Deoxidation of Steel with Ca-Si-Al and Mg-Si-Al Alloys.
Journal of Iron and Steel Inst., March, 1969, p.340.

28. Pickering,F.B. - The Constitution of Non-Metallic Inclusions in Steel.
Inclusions - The Inst. of Metallurgists, Monograph No.3, 1979, Chap.4, p.47.

29. McLean,A. and Kay,D.A.R. - Control of Inclusions in HSLA Steels
See Ref.4, p.215.

30. Lindenberg,H.U. and Vorwerk,H. - Influence of Atmospheric Oxidation on the Cleanness of Steel.
Clean Steel, Balatonfured 1981, The Metals Society 1983, p.241.

31. Turkdogan,E.T.- Ladle Deoxidation, Desulphurisation, and Inclusions in Steel - Fundamentals and Observations in practice.
Ibid - p.75.

32. Palmaers,A. et al - Parameters influencing the steel cleanliness of continuously cast billets.
Ibid - p.318.

33. Kay,D.A.R., Lu,W.K. and McLean,A. - Rare earth Oxygen-sulphur reactions in molten steel.
Sulphide inclusions in Steel - Proc. of Int. Conf., New York 1974 American Society For metals, p.23.

34. Usui,T.et al. - Production of Linepipe Steel for Sour Gas Services By Gas and Powder Injection.
Scanject II, Lulea, Sweden, June 1980, Paper 12.

35. Janke,D - Electrochemical Measurement Techniques for Determining dissolved oxygen in liquid steel.
See Ref.30. p.202.

36. Saxena,S.K. - Use of Lime Based Powders for improving inclusion morphology cleanness and mechanical properties of aluminium Killed Steels.
See Ref.24. p.69.

37. Saxena,S.K., Engh,T.A. and Tveit,H. - Effect of Injection of Solid CaO - Containing Powders on Deoxidation, Delsulphurisation and inclusion morphology in Al Killed Steels.
Steelmaking Proc., 1978 Chicago, Vol.16, p.561.

38. Gaspard,C., Messein, P. and Greday,T. - MnS Inclusions in Hot-Rolled Mild Steel Sheets.
Metal Science, Vol.16, Feb. 1982, p.105.

39. Ikeda,T., Fujino,N and Ichihashi,H. - Shape control mechanisms of non-metallic inclusions by Calcium Treatment.
Solidification Tech. in Foundry and Cast House, England, 1980, The Met. Soc., 1983 p.268-274.

40. Lehner,T. - Homogenisation, Desulphurisation and Deoxidation of Liquid Steel by Powder Injection.
Proc.McMasters Symposium on Iron and Steelmaking 1979 Paper 7.

41. Carlsson,G and Bramming,M. - Reactions between Slag and Metal Phases during Ladle Metallurgical Treatments.
See Ref:30 p.122.

42. Fujisawa,T. and Sakao.H. - Equilibrium Relations between liquid Iron Alloys and Deoxidation products Resulting from Mn-Si-Al Complex Deoxidation AND: Equillibrium between $MnO-SiO_2-Al_2O_3$ - FeO Slags and Liquid Steel.
Tetsu-To-Hagané (1977), No.9, p.1494 and p.1504.

43. Walsh,R.A. and Ramachandran.S. - Equilibrium in The Fe-Mn-Si-O System.
Trans.Met.Soc. of AIME. Vol.227 June 1963 p.560.

44. Kubaschewski,O., Evans,E.C. and Alcock,C.B. - Metallurgical Thermochemistry.
Pergamon, Oxford, 1967.

45. Elliott,J.F. Gleiser,M. and Ramakrishna,V. Thermochemistry for Steelmaking.
Addison-Wesley, Reading, Massachusetts, 1963.

46. Turkdogan,E.T.
See Ref.17 - chap.1.

47. Parker,R.H. - An Introduction to Chemical Metallurgy
Pergamon Press, 1967, Chap.7.

48. Sigworth,G.K. and Elliott,J.F. - The Thermodynamics of Liquid dilute Iron Alloys.
Met.Sci.J. 1974 Vol.8. p.298.

49. Turkdogan,E.T.
See Ref: 17, Chap.3.

50. Olette,M. and Gatellier,C. - Effect of Additions of Calcium, Magnesium or Rare Earth Elements on the Cleanness of Steels.
See Ref:30 p.165.

51. Gustafsson,S. and Mellberg,P.O. - On the Free Energy Interaction between some Strong Deoxidisers, especially Calcium and Oxygen in Liquid Iron.
Scand. J of Met.9 (1980), p.111.

52. Ozturk,B. and Turkdogan,E.T.- Equilibrium S Distribution Between Molten Calcium Aluminate and Steel Parts 1 and 2, Metal Science Vol.18 June 1984, p.299 and p.306.

53. El.Gammal,T. - Control of Inclusion Morphology by Selection of suitable desulphurising and deoxidizing reagents.
Radex-Rundschau, 1981, Heft 1/2, p.380.

54. Riboud,P.V. and Motte,J.P.- Steel Desulphrising in the ladle and calcium treatment.
See Ref:37 - Paper 10.

55. Tahtinen,K., Vainola,R, and Sandholm,R. - Ladle injection - A way to continuously cast aluminium-killed steels for billets at Ovako.
See Ref:34, - Paper 24.

56. Forster,E. et al - Deoxidation and Desulphurisation by blowing of calcium compounds into molten steel and its effects on the mechanical properties of heavy plate.
Stahl u. Eisen 94(1974) Nr.11, May. p.474.

57. Tivelius,B. et al - Sulphide shape control at the steel processing of heavy gauge Z-plate.
See Ref:24, p.116.

58. Haastert,H.P et al - The use of various desulphurising Agents and their effects on steel cleanness and service properties.
See Ref:30, p.281.

59. Shalimov,A.G, and Kosoi,L.F. - Non-Metallic Inclusions in steel treated with synthetic slag and pulverized silicocalcium.
See Ref:30, p.232.

60. Holappa.L.E.K.- Review of Ladle Metallurgy
Scaniject II, Lulea Sweden,June 1980, Paper 1.

61. Forster,E. and Richter,H. - Kinetics of the deoxidation of Steel.
See Ref:22, p.24.

62. Grethen,E. and Philippe,L. - Kinetics of Deoxidation Reactions.
Ibid - p.29.

63. Plöckinger,E.- Influence of deoxidation practice on cleanness of steel.
Special Report 77, JISI, July, 1963, p.576.

64. Parker,R.H. - The kinetics of deoxidation and the removal of inclusions from liquid steel.
See Ref: 28, p.1.

65. Turkdogan,E.T. - Deoxidation of steel - What happens from tap to solidification.
J.of Metals, Jan.1967, p.38.

66. Luyckx,L. - Mechanisms of inclusion separation in carbon steel ladles.
See Ref:37, paper 12.

67. Tardy,P. - Data for research and production by using a complex system for the investigation of non-metallic inclusions.
See Ref:30, p.22.

68. Gatellier,C. and Olette,M. - Kinetic study of deoxidation of liquid steel.
See Ref: 25, p.191.

69. Olette,M. et al
Berg - Hutten, Montash, 1968. 113, 11 p.484.

70. Abratis,H. and Langhammer,H.J. - Application of the injection technique in steel alloying.
See Ref: 34, Paper 27.

71. Gutherie,R.I.L., Gourtsoyannis,L. and Henein,H. - Some kinetic and hydrodynamic aspects of making aluminium and ferro-alloy additions to steel baths.
Can.metall.Q.15 (1976), p.145.

72. Kusakawa,T. and Shiohara,Y.- Deoxidation effects of molten iron by different deoxidisers using various adding methods.
Steelmaking Proc. 1978, Chicago, Vol.61, p.537.

73. Fujii,T.et al - Development of pulsating mixing process for ladle refining of molten steel.
See Ref. 30, p.261.

74. Von Bogandandy,L.
Arch Eisen., 1961,32 (7), p.451.

75. Turkdogan,M.L. and Elliott, J.F. - Nucleation of oxide inclusions in Iron melts.
J. of Iron and Steel Ins., March 1966, p.217.

76. Waudby,P.E. - Some aspects of the formation of inclusions during deoxidation.
See Ref: 28, p.13.

77. Lindborg, U. and Torssell, K. - A Collis ion model for the growth and spraration of deoxidation products.
Trans. of Met. Soc. of AIME Vo.242, Jan.1968, p.94.

78. Robinson,S.W., Martin,I.W. and Pickering,F.B. - Formation of Alumina in steel and its dissemination during mechanical working.
Metals Technology, May, 1979, p.157.

79. Faulring, G.M., Farrell, J.W. and Hilty, D.C. - Steel flow through nozzles; influence of calcium
Iron and Steelmaker,. Feb. 1980, p.14.

80. Kozakevitch,P. and Olette, M. - Role of surface phenomena in the mechanisms of removal of solid inclusions.
See Ref.22, p.42.

81. Waudby,P.E. - Oxides and deoxidation Practice.
Conf. on Inclusions and their effects on steel properties. BSC Conf. Leeds, Sept.74.

82. Brunner,M. and Carlsson, G. - Refining of steel in the ladle.
See Ref. 30. p.256.

83. Torssell,K. and Olette,M. - Influence of Agitiation of the Bath on the rate of equillibrium of inclusions formed during deoxidation of liquid iron.
Comptes. Rend., 268,5,1969, p.399.

84. Luyckx,L.et al. - Sulphide shape control in high strength low alloy steels.
Met.Trans.A.Vol.1, Dec.1970, p.3341.

85. Pehlke,R.D. and Fuwa,T. - Control of Sulphur in liquid iron and steel. Int.Mets.Review, 1985, Vol.30, No.3, p.125.

86. Salmon Cox, P.H. and Charles,J.A. - Observations on the analysis and distribution of non-metallic inclusions in killed 0.2% C Steel Ingots.
JISI. Oct.1963, p.863.

87. Bergh,S
Jernkont Ann., 1962,146, p.748.

88. Narita,k. et al
Tetsu-to-Hagane, 64,1978, p.118.

89. Gustafsson,S. and Mellberg,P.O. - Inclusion picture and inclusion origin in a calcium treated steel.
See Ref.24, p.35.

90. El Gammal,T. and Kroker,M. - Metallurgical aspects of the treated steel with magnesium and calcium
See Ref.72, p.546.

91. Kitamura,M. et al - Desulphurisation process and shape control of inclusion by the addition of calcium or rare earth metals.
Kobe Steel. Technical Report 1979.

92. Emi,T. et al; - mechanisms of sulphide precipitation during solidication of calcium and rare earth treated ingots.
See Ref. 72, p.574.

93. Sanbongi,K. - Controlling sulphide shape with rare earth or calcium during the processing of molten steel.
Trans. ISIJ.Vol.19, 1979, p.1.

94. Luyckx,L. - Techniques for controlling sulphide inclusions in steel - Primary processing aspects
See Ref.33, p.44.

95. De Barbadillo, J.J. - Reactivity of magnesium and calcium in liquid steel.
See Ref.33, p.70.

96. Kozasu,I. and Tanaka,J. - The effects of sulphide inclusions on notch toughness and ductility of structural steels.
See Ref.33, p.286.

97. De Ardo,A.J and Hamburg,E.G. - Influence of elongated inclusions on the mechanical properties of high strength steel plate.
See Ref. 33, p.309.

98. Grip,C.E. - Metallurgical Control of inclusions.
See Ref.24, p.91.

99. Pickering F.B. - Inclusion Shape Control.
See Ref.28 Chap.7, p.108.

100. Scott,W.W. and Swift,R.A. - Advantages of ladle injection of calcium and magnesium reagents for steel desulphursiation.
See Ref.37, p.143.

101. Herman,J.C., Messien,P., and Greday.T. - Inclusion Globularisation by precipitation of titanium compounds.
C.R.M. no.59, June 1982, p.11.

102. Udea,T.et al.- On the production method of clean steel with ladle treatment.
Symp.-Ladle Treatment of carbon steel McMasters Univ.Canada, 1979, paper 5.

103. Selleck,L.J.et al.- High Quality steels treated with REMS in the steelmaking ladle.
See Ref.37, p.143.

104. David,M. et al. - "The Ladle Treatment of Steel by the Injection of Silico-Calcium-Industrial Practice".
See Ref.34, paper 25.

105. Davies,I.G., Randle, M. and Widdowson,R. - Distribution of inclusions in rare earth treated steel ingots.
Metals Technology, May 1974, p.241.

106. Bennett,H.W. and Sandell,L.P. - Rare Earth Additions to electric furnace steels for sulphide shape control.
J.of Metals, Feb. 1974, p.21.

107. Banks,T.M. and Gladman,T. - Sulphide Shape Control.
Metals Tech., Mar. 1979, p.81.

108. Luyckx,L., Ferry,B.N. and McLean.A, - Spinel inclusions in steel.
J.of Metals, June, 1974, p.35.

109. Wilson,W.G. and McLean,A. - Desulphurisation of iron and steel and sulphide shape control.
Iron and Steel Soc, AIME. Warrendale, PA, 1980.

110. Nakai. et al. - Development of steels resistant to Hydrogen induced cracking in wet hydrogen sulphide environments.
Kawasaki steel Tech.report. No.1 Sept.1980.

111. Plöckinger,E., Holzgruber,W. and Kuhnelt,G. Deoxidation with Ca-Si Alloys containing Barium and Strontium.
Radex Runschau, 2, p.508.

112. Turkdogan,E.T. - Theroetical aspects of sulphide formation in steel.
See Ref.33, p.1.

113. Gschneidner,K.A.- Thermodynamic stability and physical properties of metallic sulphides and oxides.
See Ref.33, p.159.

114. Taira,T.et al - Resistance of pipeline steels to wet sour gas.
Conf. on Hydrogen effects in steels, ASM, 1982, p.173.

115. Iino,M.et al - Engineering solutions to the H_2S problem in linepipe.
Ibid. p.159.

116. Johnson,W.H. - On some remarkable changes produced in iron and steel by the action of hydrogen and acids.
Proc. of Royal Society, London, Vol.23, 1875.

117. Interrante,C.G. - Basic aspects of the problems of hydrogen in steels.
See Ref.114, p.3.

118. Beachem,C.D. - Hydrogen Damage - Introduction.
Hyrogen Damage - A metal science source book. Ed.C.D. Beachem AMS.1977, p.1X.

119. Hirth,J.P. - Effects of Hydrogen on the properties of iron and steel.
Met.Trans. A. Vol.11, June 1980, p.861.

120. Parades,F. and Mize,W.W. - The Oil and Gas Journal, Vol.53, No.12, 1954.p.99.

121. API Spec.5LX (23rd Edition) for High-Test Linepipe - 1980 (and supplement 1) 1981
American Petroleum Institute, Prod.Dept., Dallas.

122. Moore,E.M. - Hydrocarbon induced damage in sour, wet crude Pipelines.
Mid.East Oil Tech. Conf., Soc. of Petro.Engs., Bahrain, March 1983, p.587.

123. Biefner,G.J. - The Stepwise Cracking of Linepipe Steels in Sour Environments.
Materials Performance, June, 1982, P.19.

124. Bruno,T.V. and Hill, R.T. - Stepwise Cracking of Pipeline Steels - A Review of the work of task Group T-1F-20.
Corr.80, NACE, Chicago, U.S.A. March, 1980, Paper.G.

125. NACE Standard TM-02-84 - Test Method for the evaluation of Pipeline Steels for Resistance to Stepwise Cracking.
Materials Performance, May 1984, p.10.

126. Herbsleb,G., Poepperling, R.K. and Schwenk,W. - Occurrence and Prevention of Hydrogen Induced Stepwise Cracking and Stress Corrosion Cracking of Low Alloy Pipeline Steels.
Corrosion NACE, Vol.36, No.5, May 1981, p.247.

127. Taira,T. et al - Sulphide Corrosion Cracking of Linepipe for Sour Gas Service.
Corr.79,Atlanta,USA, March 1979, Paper 171.

128. Iino, M. - The Extension of Hydrogen Blister-Crack Arrays in linepipe steels.
Met.Trans., Vol.9A, Nov. 1978, p.1581.

129. Burns,D.S. - Laboratory Test for Evaluating Alloys for H_2-S Service.
Corr.75. Toronto, Can, April, 1975.

130. Turn,J.C., Wilde,B.E., and Troianos,C.A. - On Sulphide stress Cracking of Corr.
NACE. Vol.39, No.9 Sept. 1983, p.364.

131. Brown,A and Jones,C.L. - Hydrogen induced Cracking in Linepipe Steels.
Corr.83.California,U.S.A. April, 1983.

132. Hill, R.T. and IIno,M. - Correlation between Hydrogen Induced Blister Cracking of Stressed and unstressed specimens.
See Ref. 114, p.196.

133. Jones,C.L., Rodgerson, P. and Brown,A., - Mechanisms of Hydrogen induced cracking in pipeline steels.
Int.Conf. on Tech. and Appl. of HSLA Steels, Philadelphia, USA, Oct.1983.

134. Troianos,A.R. and Henemann,R.F. - Hydrogen Embrittlement and Stress Corrosion in Cracking in Sour Environment.
See Ref.114, p.299.

135. Parrini,C. and De Vito,A - High Strength Microalloyed Pipe Steel Resistant to Hydrogen-Induced Failures.
Micon.78; ASTM STP672, 1979, p.53.

136. Greer,J.B. - Factors Affecting the Sulphide Stress cracking performance of high Strength Steels.
Mats.Perf.Vol.14, No.3, 1975. p.11.

137. Iino,M. - Influence of sulphur content on the hydrogen - Induced Fracture in Linepipe steels.
Met.Trans.Vol.10A, Nov.79, p.1691.

138. Taira,T. and Kobayash,Y. - Development of linepipe for Sour Gas Service.
See Ref. 3, Paper 18.

139. Iino,M. et al. - Linepipe steels resistant to hydrogen blistering and cracking..
AIME/SPM, Int.Conf. HSLA Steels - Experience in Application, France, Jan.1979.

140. Taira,T. et al - Sulphide Corrosion Cracking of Linepipe for Sour Gas.
Corr. NACE, Vol.37,No.1, Jan.1981,p.5.

141. Troiano,A.R. - General Keynote Lecture.
Hydrogen in Metals ASM. 1974, p.3.

142. NACE Standard TM-01-77. - Testing of Metals for Resistance to sulphide stress cracking at ambient temperatures.
July, 1977.

143. Groeneveld,T.P. and Fessler,R.R. - Hydrogen Induced Damage in Sour Gas Gathering Lines.
Proc.NACE. Conf.Calgary, Feb.1979, (Western Region).

144. Ikeda,A., Kaneko,T. and Terasaki,F. - Influence of Environmental Conditions and Metallurgical Factors on Hydrogen Induced Cracking of Linepipe Steels.
NACE. Corr.80, Chicago, USA, March 1980, paper 8.

145. Ikeda,A. et al - Hydrogen Induced Cracking (HIC) Susceptibility of Various Steel Linepipes in Wet H_2S Environment.
NACE. 78, Houston, USA, March 1978, paper 43.

146. NACE: Material Requirement - Sulphide Stress Cracking Resistant material for oilfield equipment.
Standard MR.-01-75 (1980 Rev.), 1980.

147. McCright,R.D. - Effects of environmental Species and Metallurgical Structure on the Hydrogen Entry into Steel.
Conf: SSC and HE or Iron Base Alloys. France - June 1973, p.306.

148. Chan,S.L.I., Martinez - Madrid,M. and Charles,J.A. - Evaluation of Three Different Test methods for Charging Hydrogen into Iron.
Mets.Tech.Dec.1983, Vol.10, p.464.

149. Oriani,R.A. - Hydrogen Embrittlement of Steels.
Ann.Rev. Mater.Sci., 1978,8, p.327.

150. Wilde,B.E., Kim,C.D. and Phelps,E.H. - Some observations on the role of inclusions in the Hydrogen induced blister cracking of linepipe steels in sulphide environments.
Corr. NACE. Vol.36, No.11, Nov.1980, p.625.

151. Thomas,D.B.J. and Doble,K.R. - Steel requirements for Submarine Pipe.
See Ref.9, paper 3.

152. Jones,B.L. and Johnson, D.L. - Metallurgical Design of Major pipelines.
See Ref.9, Paper 2.

153. Shelton,E., Rothwell,A.B. and Coote,R.I. - Steel Requirements for Current and Future Canadian Gas Pipeline Systems.
See Ref.9, p.1.

154. Golovanenko,S.A. - Steels for the Gas and Oil Industry.
See Ref.2, p.251.

155. Pressourye,G.M. - Current Solution to Hydrogen Problems in Steel.
See Ref.114, p.18.

156. Olette,M., Gatellier,C. and Vasse,R. - Progress in Ladle Steel Refining.
Int.Symp. on the Physical Chemistry of Iron and Steelmaking, Toronto, Canada, Aug./Sept. 1982, VII-1.

157. Saxena,S.K. - Refining Reactions of Magensium in Steel at Steelmaking Temperatures.
Ibid, VII-17.

158. Subramanian,S.V. and Kay,D.A.R. - Inclusion Engineering.
Ibid, VII-41.

159. Pressourye,G.M. and Zmudzinski,C. - Influence of Inclusion on Hydrogen Embrittlement.
Proc.22nd Mech. Working and Steel Processing Conf. AIME.ISS, Toronto, Canada, 1980.

160. Pressourye,G.M. et al - Very Low Inclusion of Impurity Content Steels as a solution to resist sour environments.
See Ref.114, p.212.

161. Coldren,A.P. and Tither,G. - Metallographic Study of Hydrogen Induced cracking in Linepipe Steels.
J.O.M, May, 1976, p.5.

162. Fujii, H., Watanabe,T. and Yamamoto,K. - Hydrogen Induced Cracking on Seamless Linepipe Steel Produced by Continuous Casting Process.
101st, ISIJ meeting, April, 1981, Lecture No.5450.

163. Murayama,H. et al - Decreasing Crack Propagation by Improving Microstructure.
Ibid: Lecture No. 5481.

164. Murayama,H. et al - Effect of some Metallurgical Factors on Hydrogen Induced Fracture.
Ibid: Lecture No. 5480.

165. Thompson,A.W. and Bernstein,I.M. - Microstructure and Hydrogen Embrittlement.
Hydrogen Effects in Metals TMS.AIME, Warrendale, P.A., 1981.

166. Iino,M. - Analysis of Irreversible Hydrogen Trapping.
Acta Met. Vol.30, 1982, p.377.

167. Iino,M. - A more Generalised Analysis of Hydrogen Trapping.
Acta Met. Vol.30, 1982, p.367.

168. Pressourye,G.M. - Trap Theory of Hydrogen Embrittlement.
Acta Met. Vo.28, 1980, p.895.

169. Bernstein, I.M. et al - Microstructural Control of Hydrogen Embrittlement in Steels.
See Ref.114, p.259.

170. Lothan, M.R. and McNitt.R.P. - The Role of Test Technique in Evaluating Hydrogen Embrittlement Mechanisms.
Effect of Hydrogen on the behaviour of Materials (ed.Thompson & Bernstein), AIME, New York, 1976, p.496.

171. Thompson,A.W. and Bernstein, I.M. - The influence of Hydrogen on plastic fracture processes.
Second Int. Conf. on Hydrogen in Metals. Paris, France, June 1977, paper 3A6, p.1172.

172. Tuyen,D.L. and Wilde, B.E. - An Autoradiographic Technique for Studying the Segregation of Hydrogen Absorbed into Carbon and low-Alloy Steels.
See Ref.114, p.413.

173. Baker,T.J. - Use of SEM in Studying Sulphide Morphology on Fracture Surfaces.
See Ref. 33, p.135.

174. Zapffe,C.A. and Sims,C.E. - Hydrogen Embrittlement, Internal Stress and defects in Steel.
Trans. AIME Vol.145, 1941.

175. Tyson,W.R. - Hydrogen in Steel
Mech. Working and Steel Processing XVIII, Conf., Canada, Oct. 1980, Iron and Steel Soc.AIME 1981.

176. Troiano,R.A. - The Role of Hydrogen and Other Interstitials in Mechanical Behaviour of Metals.
Trans.ASM. Vol.52,1960.

177. Oriani,R.A. - A Mechanical Theory of Hydrogen Embrittlement of Steels.
Berichte Der Bunsen-Gesellscaft Fur Physikalische Chemie, Vol.76, 1972.

178. Petch,N.J. and Stables,P. - Delayed Fracture of Metals under static load.
Nature, Vol.169, May. 1954

179. Beachem,C.D. - A New Model for Hydrogen Assisted Cracking (Hydrogen "Embrittlement").
Met.Trans., Vol.3, Feb.1972.

180. Bastien,P. and Azou, P. - Effect of Hydrogen on the Deformation and Fracture of Iron and Steel in Simple Tension.
Proc.First World Met. Cong., ASM, 1951.

181. Tien, J.K. et al.- Hydrogen Transport by Dislocations.
Met.Trans.A., Vol.7A, June 1976, p.821.

182. Nair,S.V., Jensen,R.R. and Tien,J.K. - Kinetic Enrichment of Hydrogen at Interfaces and Voids by Dislocation Sweep in of Hydrogen.
Met. Trans A., Vol.14A, March.1983, p.385.

183. Louthan,M.R., McNitt,R.P. and Sission,R.D.- Importance of Stress State on Hydrogen Embrittlement.
See Ref.165, p.25.

184. Ikeda,A. et al.- On the Hydrogen Induced Cracking of Linepipe Steels under Wet Hydrogen Sulphide Environment.
See Ref.171,Paper 4A7.

185. Knott,J.F. - Micro-Mechanisms of Fracture and the Fracture Toughness of Engineering Materials.
Proc.4th Intl. Cong. on Fracture, Waterloo; Ed. D.M.R. Taplin, 63, 1977 Pergamon, p.61.

186. Thomson,R. - Fracture.
Physical Metallurgy Chap. D. Ed. R.W. Cann and P. Hassen.

187. Rice,J.R. and Thomson,R. - Ductile versus Brittle Behaviour of Crystals.
Phil. Mag., 29, 1974, p.73.

188. Kelly,A., Tyson,W.R. and Cottrell, A.H. - Ductile and Brittle Crystals.
Phil.Mag., 15, 1967, p.567.

189. Vehoff,H. and Neuman,P. - Crack Propagation and Cleavage Initiation in Fe-2.6% Si Single Crystals under Controlled Plastic Crack Tip Opening Rate in Various Gaseous Environments.
ACTA.Met., Vol.28, p.265.

190. Pressourye,G.M. - Hydrogen Traps, Repellers, and Obstacles in Steel; Consequences of Hydrogen Diffusion, Solubility, and Embrittlement.
Met.Trans. A, Vol.14A, Oct. 1983, p.2189.

191. Pressourye,G.M. - A Classification of Hydrogen Traps in Steel.
Met.Trans.A, Vol.10A, Oct. 1979, p.1571.

192. Thompson,A.W. - The Mechanisms of Hydrogen Participation in ductile Fracture.
See Ref. 170, p.467-477.

193. Pressourye,G.M. and Bernstein,I.M. - A Quantitative Analysis of Hydrogen Trapping.
Met.Trans.A, Vol.9A, Nov. 1978, p.1571.

194. Nakasugi,H. et al - Development of New Linepipe Steels for Sour Gas Service.
Nippon Steel Technical Report. Vol.14, No.12, 1979, p.66.

195. Vander Voort G.F. - Inclusion Measurement
Metallography As a Quality Control Tool, Ed.McCall and French Plenum Press, New York, 1979, p.1.

196. Pressourye,G.M. -
Third Int. Cong. on Hydrogen and Materials, Paris (1982), Pergamon Press.

197. Baker, T.J. and Charles,J.A. - Influence of Deformed Inclusions on the Short Transverse Ductility of Hot-Rolled Steel.
The Effect of 2nd Phase Particles on the Mechanical Poperties of Steels, I.S.I. Publication, 1971, p.79.

198. Baker,T.J., Gove, K.B. and Charles,J.A. - Inclusion Deformation and Toughness Anisotropy in Hot-Rolled Steels.
Metals Tech., April, 1976, p.183.

199. Yu,H.S. and Li,J.C.M. - Hydrogen Embrittlement Due to Hydrogen-Inclusion Interaction.
Proc.Conf. Computer Simulation for Materials Applications, Gaithersburg, 1976, Vol.2, p.872.

200. Shibata,A.M. and Ono,K. - Stress Concentration due to an Oblate Spheroidal Inclusion.
Mats.Sci. and Eng.N., 34 (1978), p.131-137.

201. Li,J.C.M. - Physical Chemistry of Some Microstructural Phenomena.
Met.Trans. A. Vol.9A, 1978, p.1353.

202. Cialone,H. and Asaro,R.J. - Hydrogen Assisted Fracture of Spheroidized Plain Carbon Steels.
Met.Trans.A, Vol.12A, Aug. 1981, p.1373 - 1387.

203. Cialone,H. and Asaro,R.J. - The role of Hydrogen in the Ductile Fracture of plain carbon steel.
Met.Trans.A. Vol.10A, March 1979, p.357-375.

204 Bernstein, I.M., Garber,R. and Pressourye.G.M. - The effect of dissolved Hydrogen on Mechanical behaviour of Metals.
Effect of hydrogen on behaviour of Mats., Conf., 1976, p.37-58.

205. Lin,J.K. and Oriani,R.A. - The Effect of Hydrogen on the initiation of shear localisation in plain carbon steels.
Acta. Met., Vol.31, No.7, 1983,p.1071-1077.

206. Costa,J.E. and Thompson,A.W. - Effect of Hydrogen on Fracture behaviour of a quenched and tempered medium - carbon Steel.
Met.Trans.A., Vol.12A, May 1981, p.761-771.

207. Garber,R., Bernstein,I.M. and Thompson,A.W. - Hydrogen Assisted Ductile Fracture of Spheroidized Carbon Steels.
Met.Trans.A, Vol.12A, Feb. 1981, p.225 - 234.

208. French,I.E., Weinrich, P.F. and Weaver,C.W. - Hydrogen Embrittlement of Spheroidised Steel.
Scripta.Met., Vol.13,1979, p.285 - 288.

209. Thompson,A.W., and Bernstein.I.M. - Quantitative Metallography and fractography in Hydrogen Embrittlement.
Private Communication.

210. Thompson,A.W. - The Relation Between Changes in Ductility and in Ductile fracture topography:Control by microvoid nucleation,
Acta.Met.Vol.31, No.10, 1983, p.1517-1523.

211. Van Stone,R.H., Cox,T.B., Low,J.R. and Psioda,J.A. - Microstructural Aspects of Fracture by Dimpled Rupture.
Int.Met.Review, 1985, Vol.30, No.4, p.157-179.

212. Speich,G.R. and Dabkowski,D.S. - Influence of Sulphur Content Rolling Practice, and Specimen Orientation on the Tensile Ductility of Mn-Nb Plate Steels.
Toughness Characterisation and Spec. in HSLA and structural steels, P.L. Mangonon, JR. Ed., AIME, 1980, p.257-285.

213. Spitzig,W.A. and Sober,R.J. - Influence of sulphide inclusions and pearlite content on the mechanical properties of Hot-Rolled Carbon Steel.
Met.Trans.A, Vol.12A, Feb.1981, p.281-291.

214. Melander,A. and Steninger,J. - The Role of Sulphide, Oxides and Pearlite in Ductile Fracture of a Niobium Micro-Alloyed Steel.
Report lM-1511, Swed.Inst. For Metals Research, (1980).

215. Takada,H. et al - Effect of the Amount and Shape of inclusions on the directionality of ductility in carbon manganese steels.
Fractography in failure analysis, ASTM, Special Tech. Pub. 645, p.335-350.

216. Tyson,W.R. - Hydrogen Embrittlement and Hydrogen Dislocation Interactions - Discussion.
Corr., NACE, Vol.36, No.8 August, 1980.

217. Rosenfield,A.R. - Criteria For Ductile Fracture of Two-Phase Alloys.
Met. Reviews,, No.121, 1968. p.29-40.

218. Wilsdorf,H.G.F. - The Ductile Fracture of Metals: A Microstructural Viepoint
Mat.Science and Eng. Review paper, 59 (1983), p.1-39.

219. Howard,I.C. and Willougby,A.A. - Mechanics and Mechanisms of Ductile Fracture.
Developments in Fracture,Vol.2, Ed.C.G.Chell, Chap.2, App. Science Publishers.

220. Leslie,W.C. - Inclusions and Mechanical Properties.
Trans. Iron Steel Soc.,
1983, 2,6 p.1.

221. Embury,J.D. - Dutcile Fracture.
Strength of Metals and Alloys, Proc. 6th Int. Conf., Melbourne, Australia, Aug. 1982, Vol.3, p.1089-1104.

222. Hancock,J.W. and Mackenzie,A.C. - On the Mechanisms of Ductile failure in high strength-steels subjected to multi-axial stress states.
Mech. Phys.Solids, 1976, Vol.24, p.147 - 169.

223. Bridgeman,P.W. - Studies in Large Plastic Flow and Fracture.
McGraw Hill Book Company, New York, 1952.

224. Argon,A.S., Im,J. and Needleman,A. - Distribution of Plastic Strain and negative Pressure in Necked Steel and Copper Bars.
Met.Trans.A, Vol.6A, April 1975, p.815-824.

225. Beremen,F.M. - Cavity Formation from inclusions in Ductile Fracture of A 508 Steel.
Met.Trans.A, Vol.12A, May 1981, p.723-731.

226. Argon,A.S., Im, J. and Safoglu,R. - Cavity Formation from Inclusions in Ductile Fracture.
Met.Trans. A. Vol.12A, April, 1975 p.825-837.

227. Goods,S.H. and Brown,L.M. - The Nucleation of Cavities by Plastic Deformation.
Overview No.1 Acta. Met. Vol.27, (1979) p.1-15.

228. Thomson,R.D. and Hancock,J.W. - Ductile Failure by Void Nucleation, Growth and Coalescence.
Inst.J. of Fracture, 26,(1984) p.99-112.

229. Gladman,T., Holmes,B. and McIvor,I.D. - Effects of Second Phase Particles on Strength, Toughness, and Ductility.
See Ref, 197, p.68.

230. Evensen,J.D., Lereim,J. and Embury,J.D. - Microstructural Apsects of the Fracture Parameters of Controlled Rolled HSLA Steels.
See Ref.211, p.187.

231. Spitzig,W.A. - Effect of Sulphides and Sulphide Morphology on Anisotropy of Tensile Ductility and Toughness of Hot Rolled C-Mn Steels.
Met.Trans.A, Vol.14A March, 1983, p.471-484.

232. Fisher,J.R. and Gurland,J. - Void Nucleation in Spheriodized Carbon Steels Part 2: Model.
Metal Science, May 1981, p.193-202.

233. Shehata,M.T. and Boyd,J.D. - Quantitative Correlations between Toughness and Microstructure for Commercial Linepipe Steel.
Advanced in Phy.Met. and Appl. of Steel, Mets. Soc., England, Sept. 81.p.11.

234. Spitzig,W.A. - Effect of Sulphide Inclusion Morphology and Pearlite Banding on Anisotropy of Mechanical Properties in normalized C-Mn Steels.
Met.Trans. A, Vol.14A, Feb. 1983, p.271-283.

235. Spitzig,W.A. - Effect of Shape of Sulphide Inclusions on Anisotropy of Inclusion Spacings and on Directionality of ductility in Hot-Rolled C-Mn Steels.
Met.Trans. A, Vol.15A, June 1984, p.1259-1264.

236. Thompson,A.W. and Bernstein,I.M. - The Role of Plastic Fracture Processes in Hydrogen Embrittlement.
See. Ref: 185, p.249-254.

237. Beachem,C.D. - Microscopic Analysis of Cleavage Mechanisms (Cohesion vs Cleavage).
2nd Int.Conf. on Mechanical Behaviour of Materials, 1976. p.322-347.

238. Nelson,J.A. and Blann,G.A. - Improving metallographic sample Preparation for inclusion Analysis by Automatic Methods.
Metal Progress, May 1984, p.39-44.

239. Murdoch,J. and Barnes,J.A. - Statistical Tables.
2nd Ed. MacMillan 1982.

240. De Hoff, R.T. and Rhines,F.N. - Quantitative Micoroscopy.
McGraw-Hill Book Comapny, 1968.

241. Underwood,E.E. - Quantitative Stereology.
Addison-Wesley Publishing Company , Inc., Reading, Mass., 1970.

242. Vander Voort,G.F. - Metallography: Principles and Practice.
Chap.6 Quantitative Microscopy. McGaw-Hill. 1984.

243. Pickering,F.B. - The Basis of Quantitative Metallography.
Inst. of Met. Techs, Monograph No.1, 1976.

244. Nicholson,W.L. - Invited Review - Application of Statistical methods in Quantitative Microscopy.
J. of Microscopy, Vol.113, Pt3, August 1978, p.223-239.

245. Stanz,A., Dressel,P.G., Kuhlmeyer,M. - Characteristics of Microstructure in Alloy Steels - Considered Statistically.
Praktische Metallography, 15 (1978), p.159-170.

246. Johansson,S. - How to Quantify Steel Cleanliness.
See Ref: 24,p.221.

247. Elliot,J.M. - Statistical Analysis of Benthic Invertebrates.
Freshwater Biological Assn., Scientific Publication No.25, 1977 Titus Wilson & Son Ltd., Kendal.

248. Simpson,I.D. et al - The Effect of Non-Metallic Inclusions on Mechanical Properties.
Metals Forum,Vol.2,No.2,1979,p.108-117.

249. Spitzig,W.A. - SEM Based Automatic Image Analysis of Sulphide Inclusions in Hot Rolled Carbon Steels.
Metallography 16: p. 171-198,(1983).

250. Corti,C.W., Coterill,P. and Fitzpatrick,G.A. - Review 182 - The Evaluation of the interparticle Spacing in Dispersion Alloys.
Int.Mets.Reviews, 1974,Vol.19, p.77-88.

251. Quenoille,M.H. - Introductory Statistics.
Pergamon Press, Second Addition, 1966.

252. Aitchison,J and Brown,J.A.C. - The Lognormal Distribution,
University of Cambridge, Deptn. of Applied Economics, Monograph:5, Cambridge University Press, 1957.

253. Baker,T.J. and Charles,J.A. - Deformation of MnS inclusions in Steel.
J. of Iron and Steel Institute, Sept. 1972, p.680-690.

254. LeRoy,G. et al - A model of ductile fracture based on the nucleation and growth of voids.
Acta Met., Vol.29, p.1509-1522, 1981.

255. Samuels,H.E. - Optical Microscopy of Carbon Steels.
ASTM. Metals Park, Ohio 44073, Chap. 4 and 5. p 59-167.

256. Asante,J.C.B. - Hot Deformation Characteristics of Oxide/Sulphide Inclusions in Low Carbon Steels.
Ph.D Thesis, Aston University 1980.

257. Honeycombe,R.W.K. - Steels, Microstructure and Properties.
Edward Arnold, 1981.

258. Leslie,W.C. - The Physical Metallurgy of Steels.
McGraw-Hill, 1981.

259. Kiessling,R. - Clean Steel - A Debatable Concept.
Clean Steel - 2nd.Int.Conf.Balatonfured, Hungary.
Metals Society, London, 1983, pp.1-9.

260. Pumphrey,K.N. and Akhurst,P.H. - Hydrogen Cracking in Mild Steel.
See Ref.196, p.547.

261. Brookbanks,O. and Andrews,K.W. - Inclusions.
See Ref.22.